
**STRUCTURAL SYSTEMS**

**RESEARCH PROJECT**

Report No.
SSRP–06/16
**FINAL**

# AXIAL FORCE TRANSFER MECHANISMS WITHIN CAST-IN-STEEL-SHELL PILES

**by**

**MICHAEL J. GEBMAN**

**SCOTT A. ASHFORD**

**JOSÉ I. RESTREPO**

Final Report Submitted to the California Department of Transportation Under Contract No. 59A0337.

June 2006

Department of Structural Engineering
University of California, San Diego
La Jolla, California 92093-0085

University of California, San Diego
Department of Structural Engineering
Structural Systems Research Project

Report No. SSRP–06/16
**FINAL**

# Axial Force Transfer Mechanisms within Cast-In-Steel-Shell Piles

by

**Michael Gebman**
*Graduate Student Researcher*

**Scott A. Ashford**
*Professor of Geotechnical Engineering*

**José I. Restrepo**
*Associate Professor of Structural Engineering*

Final Report Submitted to the California Department of Transportation
Under Contract No. 59A0337.

Department of Structural Engineering
University of California, San Diego
La Jolla, California 92093-0085

June 2006

Technical Report Documentation Page

| 1. Report No. | 2. Government Accession No. | 3. Recipient's Catalog No. |
|---|---|---|
| | | |

| 4. Title and Subtitle | 5. Report Date |
|---|---|
| Axial Force Transfer Mechanisms within Cast-In-Steel-Shell Piles | July, 2006 |
| | 6. Performing Organization Code |

| 7. Author(s) | 8. Performing Organization Report No. |
|---|---|
| Michael Gebman, Scott Ashford, José Restrepo | UCSD / SSRP-06/16 |

| 9. Performing Organization Name and Address | 10. Work Unit No. (TRAIS) |
|---|---|
| Department of Structural Engineering<br>School of Engineering<br>University of California, San Diego<br>La Jolla, California 92093-0085 | 11. Contract or Grant No.<br>59A0337 |

| 12. Sponsoring Agency Name and Address | 13. Type of Report and Period Covered |
|---|---|
| California Department of Transportation<br>Division of Engineering Services<br>1801 30th St., West Building MS-9<br>Sacramento, California 95807 | Final Report – 07/01/02 to 06/30/06 |
| | 14. Sponsoring Agency Code |

15. Supplementary Notes

Prepared in cooperation with the State of California Department of Transportation.

16. Abstract

In this research, the axial force transfer within Cast-In-Steel-Shell (CISS) piles through the surface bond and through mechanisms fixed to the steel shell internal surface was studied. Mechanisms studied included a shear ring, welded bar, weld bead, shear studs, cross bar, and tread plate. Other parameters studied in this experiment included the effect of shear ring spacing, the effect of the D/t ratio on the shear ring, and the effects of expansive concrete, D/t ratio, and surface condition. Test units were subjected to a quasi-static reversed cyclic axial loading. All mechanisms exhibited a noticeable increase in the axial force capacity, in both compression and tension. Test units with a circumferential mechanism (e.g. shear ring) had a ductile performance, whereas distributed mechanisms had a non-ductile performance. Circumferential mechanisms were effective to the extent that either the steel shell capacity was obtained, through circumferential yielding at the mechanism, or the reinforced concrete core capacity was obtained. This report will present the experimental results, a prediction method using a plastic hinge formulation and results from finite element modeling.

| 17. Key Words | 18. Distribution Statement |
|---|---|
| Cast-In-Steel-Shell Pile, Shear Ring, Pile Foundations | No restrictions |

| 19. Security Classification (of this report) | 20. Security Classification (of this page) | 21. No. of Pages | 22. Price |
|---|---|---|---|
| Unclassified | Unclassified | | |

## DISCLAIMER

The contents of this report reflect the views of the authors who are responsible for the facts and the accuracy of the data presented herein. The contents do not necessarily reflect the official views or policies of the State of California. This report does not constitute a standard, specification or regulation.

# ACKNOWLEDGEMENTS

This study was made possible by funding from the California Department of Transportation under contract No. 59A0337. The financial support of the California Department of Transportation and the technical input from Ron Bromenshenkel and Dr. Charles Sikorsky is hereby acknowledged. The hard work of the UCSD Charles Lee Powell Structural Engineering Laboratory Staff is greatly appreciated.

# ABSTRACT

In this research, the axial force transfer within Cast-In-Steel-Shell (CISS) piles through the surface bond and through mechanisms fixed to the steel shell internal surface was studied. Mechanisms studied included a shear ring, welded bar, weld bead, shear studs, cross bar, and tread plate. Other parameters studied in this experiment included the effect of shear ring spacing, the effect of the D/t ratio on the shear ring, and the effects of expansive concrete, D/t ratio, and surface condition. Test units were subjected to a quasi-static reversed cyclic axial loading. All mechanisms exhibited a noticeable increase in the axial force capacity, in both compression and tension. Test units with a circumferential mechanism (e.g. shear ring) had a ductile performance, whereas distributed mechanisms had a non-ductile performance. Circumferential mechanisms were effective to the extent that either the steel shell capacity was obtained, through circumferential yielding at the mechanism, or the reinforced concrete core capacity was obtained. This report will present the experimental results, a prediction method and results from finite element modeling.

# TABLE OF CONTENTS

# LIST OF FIGURES

# LIST OF TABLES

# LIST OF SYMBOLS

| | |
|---|---|
| a | Weld throat size |
| $A_{core}$ | Cross sectional area of the concrete core |
| $A_{mech}$ | Area of the mechanism protruding into the concrete core |
| $A_{shell}$ | Cross sectional area of the steel shell |
| $A_{surface}$ | Surface area of the steel shell-reinforced concrete interface |
| $A_{sy}$ | Area of steel shell in yielding |
| $A_{weld}$ | Weld effective area |
| $C$ | Initial kinematic hardening |
| $C_L$ | Coefficient for grouted length to pile diameter ratio |
| $C_S$ | Surface condition factor |
| $d_c$ | Compression damage variable |
| $d_c$ | Exponential decay constant |
| $d_t$ | Tension damage variable |
| $D$ | Steel shell internal diameter |
| $D_g$ | Grout external diameter (API code) |
| $D_p$ | Pile external diameter (API code) |
| $D_s$ | Steel sleeve external diameter (API code) |
| $D_{stud}$ | Shear stud diameter |
| $E$ | Elastic modulus |
| $E_c$ | Concrete modulus of elasticity |
| $E_o$ | Unloading stiffness |
| $E_s$ | Steel modulus of elasticity |
| $F_{exx}$ | Electrode yield stress |
| $f_{2\sigma}$ | Bond stress two standard deviations above the mean (Virdi and Dowling) |
| $f_{ba}$ | Allowable axial load transfer stress (API code) |
| $f_{b\max}$ | Maximum axial load transfer stress |
| $f_{buc}$ | Characteristic bond strength of a grouted steel shell-sleeve connection (UK DOE code) |
| $f_c^{'}$ | Concrete compressive strength |
| $f_{ct}$ | Tensile yield stress |
| $f_{cu}$ | Unconfined grout compressive strength |
| $f_u$ | Ultimate stress for steel |
| $f_y$ | Yield stress for steel |
| $f_{ymech}$ | Mechanism yield stress |
| $E_c$ | Modulus of Elasticity for concrete |

| | |
|---|---|
| $E_{shell}$ | Modulus of Elasticity for the steel shell |
| $F$ | Von Mises yield surface function |
| $FS$ | Factor of safety |
| $h$ | Shear ring radial thickness (API code) |
| $h_{sr}$ | Shear ring height |
| $I$ | Moment of inertia |
| $I_t$ | Identity tensor |
| $k$ | Constant for confinement contribution to axial stress |
| $k_{load}$ | Loading stiffness for axial force-axial displacement response |
| $k_{unload}$ | Unloading stiffness for axial force-axial displacement response |
| $K$ | Dimensionless stiffness factor |
| $\ell$ | Length of concrete core |
| $l_e$ | Effective length |
| $\ell_f$ | Distance between plastic hinges, or points of inflection |
| $\ell_o$ | Steel shell height through which bond occurs (no strain continuity) |
| $\ell_r$ | Distance between plastic hinge zones |
| $L$ | Grouted connection length (UK DOE code) |
| $L_{stud}$ | Shear stud length |
| $m$ | modular ratio of steel to grout |
| $M$ | Moment |
| $M_p$ | Plastic moment |
| $N$ | Normal force on the concrete core |
| $N_{mech}$ | Number of mechanisms |
| $N_{rings}$ | Number of shear rings |
| $N_{studs}$ | Number of shear studs |
| $p$ | Equivalent pressure stress |
| $P$ | Applied axial force |
| $P_{applied}$ | Applied axial force |
| $P_{cm}$ | Axial force at which concrete crushing initiates at a mechanism |
| $P_{fric}$ | Axial force transferred through friction bond |
| $P_{hinge}$ | Force to develop a plastic hinge |
| $P_\ell$ | Lateral force on mechanism |
| $P_{mech}$ | Governing axial force transfer at a mechanism |
| $P_{mech-lower}$ | Axial force transfer through a mechanism other than the first mechanism resisting axial force |
| $P_{sc}$ | Axial force at strain compatibility |
| $P_{shell}$ | Steel shell axial force capacity |
| $P_{sm}$ | Lateral force capacity of the steel shell at the mechanism |

| | |
|---|---|
| $P_{sm-axial}$ | Axial force capacity of the steel shell and mechanism |
| $P_{T,Peak}$ | Peak cyclic axial tension force |
| $P_{unload}$ | Axial force at zero displacement, after obtaining the peak cyclic axial tension force |
| $P_{weld}$ | Axial force capacity of the weld |
| $R^2$ | Linear regression correlation coefficient |
| $s$ | Shear ring center to center spacing |
| $s_r$ | Radial spacing of shear studs |
| $s_v$ | Vertical spacing of shear studs |
| $S$ | Deviatoric stress tensor |
| $t$ | Steel shell thickness |
| $t_{cover}$ | Concrete cover (distance) between mechanism face and longitudinal reinforcement bar |
| $t_g$ | Grout thickness (API code) |
| $t_p$ | Pile steel shell thickness (API code) |
| $t_{ring}$ | Radial thickness of shear ring |
| $t_s$ | Steel sleeve thickness (API code) |
| $t_{sr}$ | Shear ring radial thickness |
| $t_{weld}$ | Fillet weld effective throat thickness |
| $v$ | Deformation |
| $V_{stud}$ | Shear force capacity of a single shear stud |
| $V$ | Shear force |
| $w$ | Total mechanism height, including welds |
| $W_{hinge}$ | Internal work at a plastic hinge |
| $x$ | Distance from fixed end support |
| $Z$ | Plastic section modulus |
| $\alpha$ | Angle at which resultant force is applied to a mechanism |
| $\alpha_{vm}$ | Von Mises backstress |
| $\alpha^{dev}$ | Deviatoric part of the backstress tensor |
| $\beta$ | Angle of tension tie or compression strut |
| $\Delta$ | Out-of-plane displacement |
| $\Delta\ell$ | Strain induced displacement |
| $\Delta_y$ | Axial displacement at yield |
| $\Delta_{yt}$ | Yield displacement in axial tension |
| $\Delta_{yc}$ | Yield displacement in axial compression |
| $\varepsilon_c$ | Strain in concrete |
| $\varepsilon_s$ | Strain in steel shell |
| $\varepsilon_{sc}$ | Strain at compatibility condition |

| | |
|---|---|
| $\varepsilon_y$ | Yield strain |
| $\dot{\bar{\varepsilon}}^{pl}$ | Equivalent plastic strain rate |
| $\dot{\varepsilon}^{pl}$ | Rate of plastic flow |
| $\gamma$ | Rate at which the kinematic hardening modulus decreases as plastic deformation increases |
| $\gamma_{eq}$ | Slip rate |
| $\phi$ | Curvature |
| $\phi_{ba}$ | Bond stress reduction factor for API-LRFD code |
| $\phi_y$ | Yield Curvature |
| $\mu$ | Friction coefficient |
| $\mu_s$ | Static friction coefficient |
| $\mu_k$ | Kinetic friction coefficient |
| $\upsilon$ | Poissons ratio |
| $\rho_\ell$ | Longitudinal reinforcement ratio |
| $\theta$ | Angle of rotation |
| $\theta_y$ | Angle of rotation at yield |
| $\sigma^0$ | Yield stress |
| $\sigma_1$ | Axial stress |
| $\sigma_3$ | Lateral confinement pressure |
| $\sigma$ | Stress tensor |
| $\sigma_{bond}$ | Bond stress between steel shell and concrete core |
| $\sigma_{Bond}$ | Bond stress at zero axial displacement after obtaining the peak axial tension force |
| $\sigma_{Bond,T}$ | Bond stress calculated from the peak axial tension force |
| $\sigma_c$ | Concrete stress |
| $\sigma_{ci}$ | Initial yield stress |
| $\sigma_{mech}$ | Normal stress on the mechanism |
| $\sigma_s$ | Steel shell stress |
| $\sigma_{shell}$ | Normal stress in the steel shell |
| $\sigma_{ti}$ | Tensile failure stress |
| $\sigma_{Transfer}$ | Axial transfer stress |

# 1 INTRODUCTION

## 1.1 Cast-In-Steel-Shell Pile Foundation Background and Bond Design Issues

Cast-In-Steel-Shell (CISS) pile foundations, also known as drilled piers with permanent steel casing, consist of a circular steel shell section filled with reinforced concrete. The California Department of Transportation (Caltrans) uses this construction technique in bridge foundations, with diameters typically ranging from 0.61 to 3.0 m (24 to 120 in.), and pile lengths in some cases exceeding 100 m (328 ft). The construction technique typically consists of driving a steel shell to the desired depth, followed by removal of the soil within the steel shell. The interior surface is cleaned to remove any soil or mud. This cleaning is followed by placement of a reinforcement bar cage, as shown in Figure 1.1. Concrete is placed with the aide of a tremie in either a dry steel shell or a steel shell filled with a bentonite slurry. To ensure a reliable bond between the reinforced concrete core and the steel shell, mechanisms can be welded to the steel shell interior surface in either a continuous circumferential design or in a spatial distribution.

Mechanisms are used in large diameter CISS piles because designers have been concerned about the shrinkage potential of the reinforced concrete core (Roeder, 1999). This shrinkage potential could have an adverse effect on the reinforced concrete core bond to the steel shell. The use of mechanisms, such as shear rings, or shear studs (see Figure 1.2) can resolve this issue and have been used by Caltrans in many CISS pile foundations, including the new east span of the San Francisco-Oakland Bay Bridge.

**Figure 1.1 Placement of a Reinforcement Bar Cage into a Steel Shell at the new East Span of the San Francisco-Oakland Bay Bridge (SFOBB) – Photo: Caltrans**

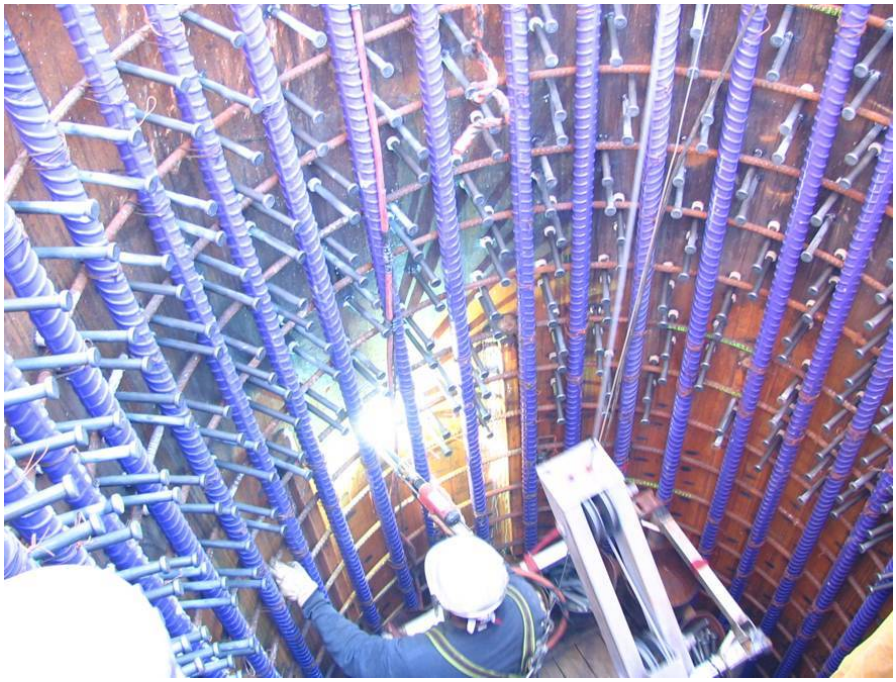

**Figure 1.2 Shear Stud Installation within a CISS Pile at the new East Span of the SFOBB – Photo: Caltrans**

CISS piles must resist not only the dead load of the superstructure, but also seismic forces in both horizontal and vertical directions. When bridge structures are subjected to seismic forces, the superstructure will undergo cyclic displacements in the transverse and longitudinal directions. As an abutment, or bent (column), is displaced cyclically in the lateral direction, its pile foundation may be subject to moment reversals. This moment reversal can cause the axial force within the pile to alternate between tension and compression, as shown in Figure 1.3. Such a reversal in the forces could result in high bond stress demands between the reinforced concrete core and the steel shell, and potential slip, provided the steel shell has adequate skin friction resistance with the soil.

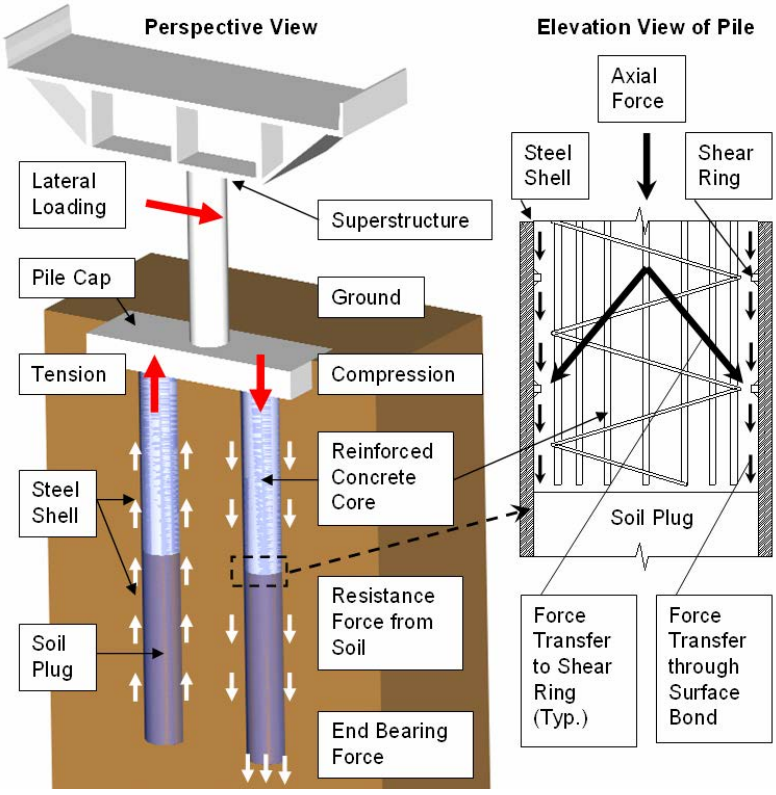


**Figure 1.3 Force Transfer for a CISS Pile Supported Bridge Superstructure Subjected to a Lateral Loading**

In some CISS pile designs, the reinforced concrete core extends only into a portion of the upper steel shell. In such a case, the axial force transfer from the concrete core to the steel shell occurs in the upper portion of the pile. The additional hollow steel

shell length transfers axial force from the steel shell to the soil through the steel shell-soil surface contact as shown in Figure 1.3. The transfer of axial force into the soil through end bearing is not commonly relied on due to concerns with the cleanliness of the bottom of the hole.

## 1.2 Research Significance

A reinforced concrete core confined by a circular steel shell can transfer axial force in tension and compression to the steel shell through surface bond and through mechanisms welded to the steel shell interior surface. These mechanisms have been used within CISS pile foundations, as well as other structural elements, to transfer axial forces between the reinforced concrete core and the steel shell. However, large-scale experimental verification of these mechanisms is very limited in the published research literature, as presented in Chapter 2.0.

## 1.3 CISS Pile Foundation System at the New San Francisco-Oakland Bay Bridge

The east span of the new San Francisco-Oakland Bay Bridge makes extensive use of mechanisms within its CISS pile foundation. This new bridge is supported by 160 CISS piles, with a typical diameter of 2.5 m (8.2 ft) and lengths up to 107 m (350 ft). Six to eight CISS piles support a typical bridge column, as shown in the view of a foundation under construction within a cofferdam, in Figure 1.1, and the plan view in Figure 1.4. In this pile design, the upper half of the steel shell is filled with reinforced concrete, as shown in Figure 1.5. A composite bond between the steel shell and reinforced concrete core was provided with shear rings in the lower core section and shear studs in the upper core section. Approximately 1,462 shear studs were placed in the upper core section of the pile. Studs had a diameter of 22 mm (0.87 in.), a length of 203 mm (8 in.), and an arrangement of 34 studs per circumferential row. Studs were placed in 43 circumferential rows, with a vertical spacing of 135 mm (5.3 in.) as shown in Figure 1.6. Shear studs were attached after the soil (bay mud) was removed from the interior of the driven steel shell and after the reinforcement bar cage was placed within a clean steel shell.

Placement of the shear studs, with a stud gun, is shown in Figure 1.2, in which a worker has been lowered on a platform into the steel shell.

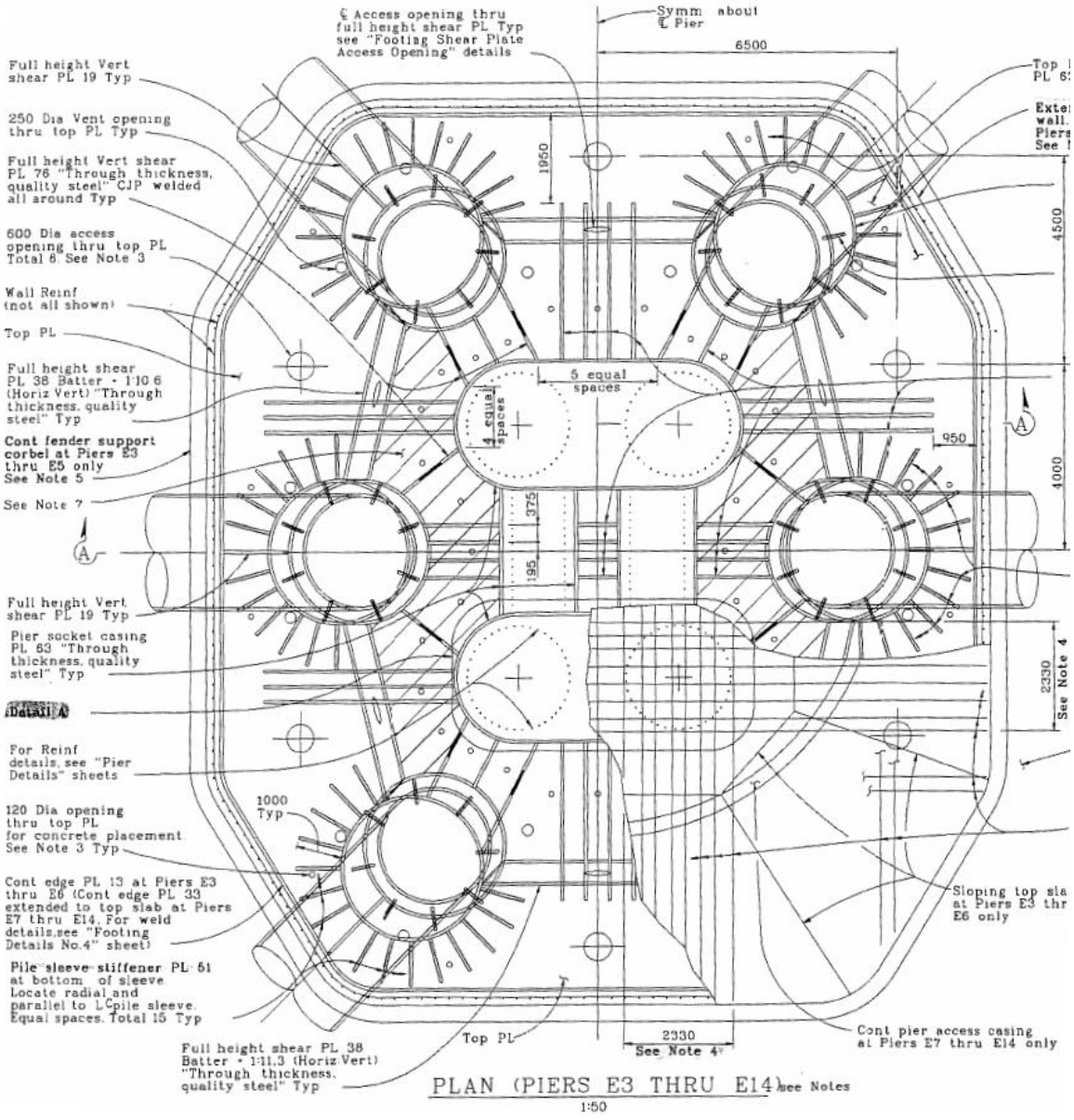


**Figure 1.4 Plan View of a Typical SFOBB Foundation – Plans: Caltrans**

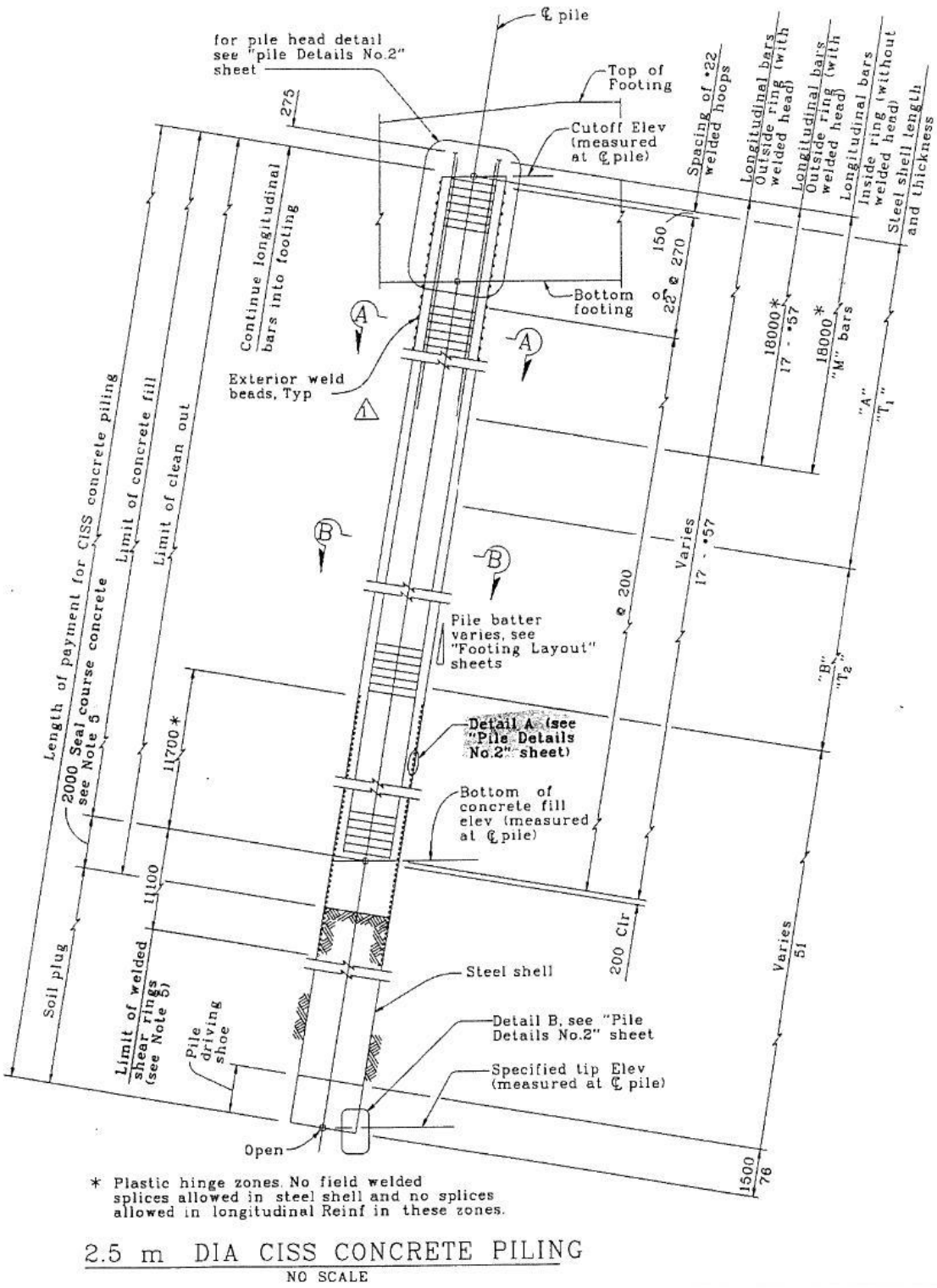


**Figure 1.5 Elevation View of a Typical SFOBB CISS Pile, showing Shear Studs and Shear Rings – Plans: Caltrans**

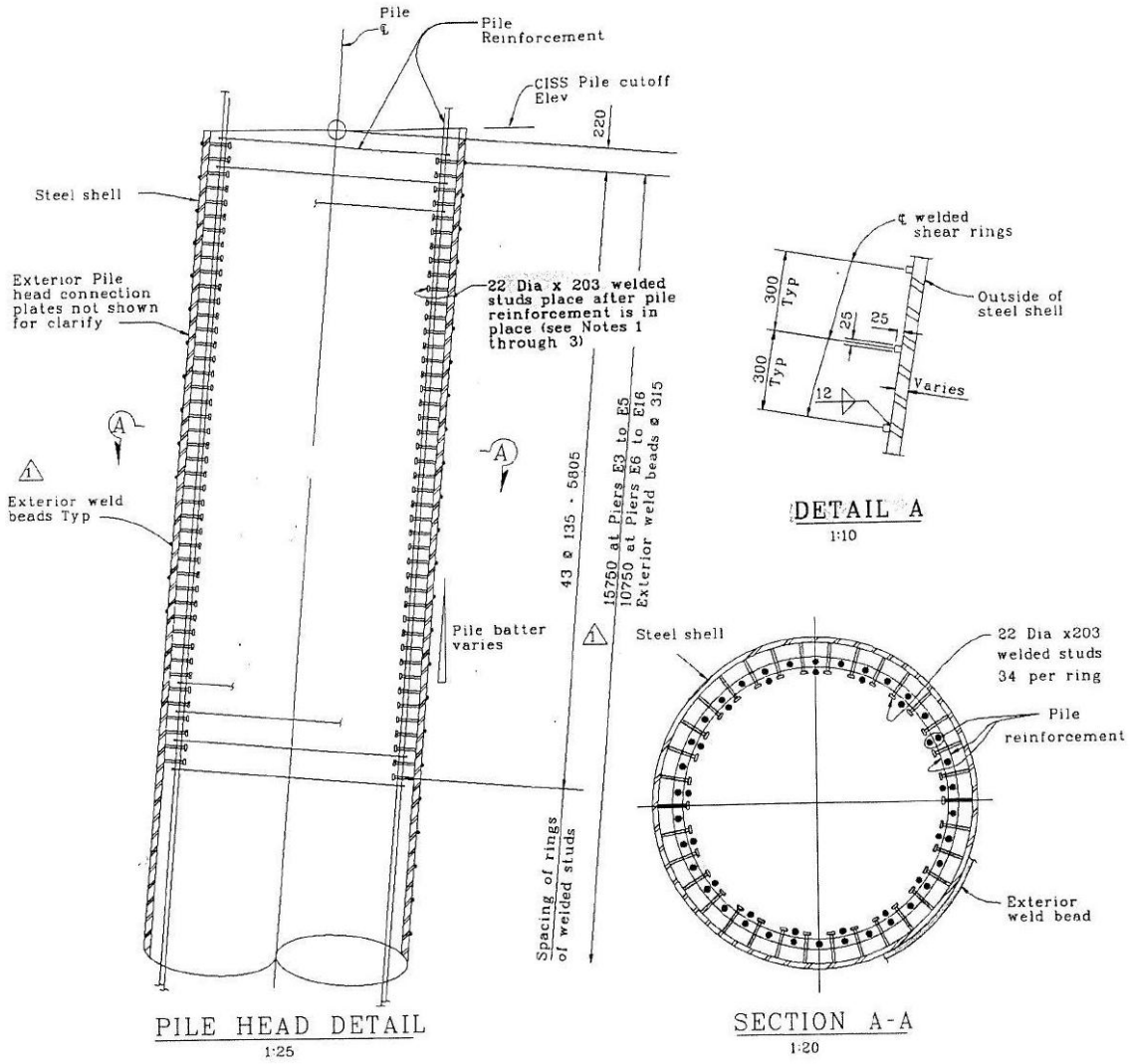


**Figure 1.6 Details for Shear Studs and Shear Rings for SFOBB – Plans: Caltrans**

In the lower portion of the reinforced concrete core, 74 shear rings were welded to the steel shell. The shear rings had a square cross section, of 25 mm (1 in.). Continuous fillet welds were placed along the top and bottom of each shear ring to the steel shell interior surface. Welding of the shear rings occurred prior to driving the steel shell into the bay mud. After the steel shell, with rings, was driven into the bay mud, this mud was removed, and the steel shell interior surface was cleaned with a scrub brush system and water at a high pressure. A video camera system inspected the steel shell to ensure the cleaning of the steel shell was successful and that no soil would prevent a bond between the steel shell and the reinforced concrete core.

## 1.4 Experimental Program Overview

The focus of this study is the axial force transfer within CISS piles, through mechanisms fixed to the steel shell and/or through the surface bond between the steel shell and reinforced concrete core. This was investigated through full-scale laboratory testing at the Charles Lee Powell Structural Engineering Laboratory of the University of California, San Diego. Surface bond issues investigated included the effects of the steel shell diameter to thickness (D/t) ratio, the steel shell interior surface condition, and the effect of expansive concrete on the D/t ratio. Issues for the mechanisms that were investigated included the effect of the mechanism design, the effect of the D/t ratio on the shear ring mechanism, and the effect of shear ring spacing.

Nineteen CISS pile test units were studied, with a typical diameter of 0.61 m (24 in.), and two CISS pile test units were studied with a diameter of 0.39 m (15.25 in.). A summary of the test unit details is shown in Table 4.1. A reversed cyclic axial compression and tension loading was applied to the test units. Mechanisms studied included three designs fixed circumferentially to the steel shell and three designs distributed within the steel shell, as shown in Figure 1.7. Mechanisms fixed circumferentially to the steel shell included a shear ring, a circumferentially welded reinforcement bar, and a weld bead. Mechanisms distributed within the steel shell included shear studs, a cross bar, and a tread plate. A majority of these mechanism designs have been used by design engineers at Caltrans. Concreting conditions included normal and expansive concrete. The steel shell interior surface was clean for all test units except one which had a water-bentonite mud coating to simulate a tremie pour condition. The effect of the D/t ratio was studied with five test units for normal concrete, and with three test units for expansive concrete.

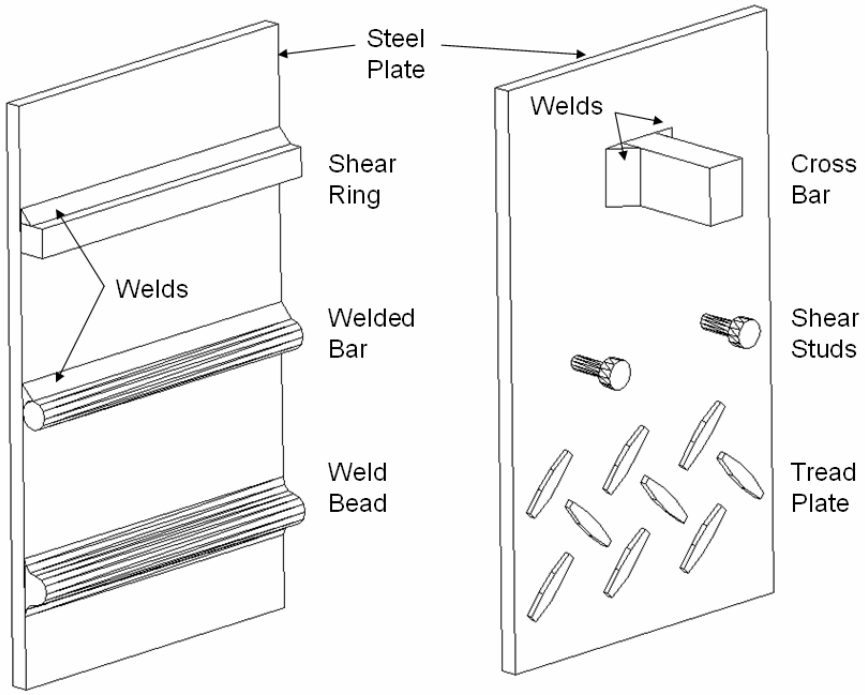


**Figure 1.7 Mechanisms Studied in this Research**

Three test units examined the effect of the D/t ratio on the axial force transfer through a single shear ring. One test unit had a lining on the steel shell to isolate the axial force transfer through the shear ring. The role of shear ring spacing was studied with three test units, each with two shear ring.

## 1.5 Analytical Research Overview

Nonlinear finite element modeling was conducted using ABAQUS/EXPLICIT (ABAQUS, 2005) to model the axial force transfer through the shear ring mechanism, and through the surface bond. Details for the selection of model characteristics, such as geometry, material properties, and interaction are presented in Appendix Chapter 9. Results from the modeling are compared to experimental results and are presented in Appendix Chapter 9.

## 1.6 Report Outline and Chapter Summary

This report is organized into chapters focusing on the various research initiatives undertaken. A review of previous literature and design codes are presented in Chapter Two. The experimental program, test unit design, and experimental setup are presented in Chapter Three. Experimental results are presented in Chapter Four. A finite element analysis of the axial force transfer through the shear ring mechanism is presented in Chapter Five. Analysis of the experimental results, a comparison to previous research, and design recommendations are presented in Chapter Six. A summary and conclusions are presented in Chapter Seven. A brief overview of each chapter is presented below.

### 1.6.1 Chapter 1 Summary

This chapter introduces the axial force transfer design issues for the CISS pile and the solutions that designers have implemented, such as in the design of the new San Francisco-Oakland Bay Bridge. An overview of the research program to verify these axial force transfer issues through experimental study and finite element modeling, and an outline for other chapters in this report was presented.

### 1.6.2 Chapter 2 Summary

Previous experimental studies conducted on test units with similar loading conditions to this research, and the shrinkage concern is presented. Design recommendations from the American Petroleum Institute and the United Kingdom Department of Energy show the importance of this research to improving the design procedure.

### 1.6.3 Chapter 3 Summary

This chapter presents the theory behind the axial force transfer through surface bond and through mechanisms. A method to predict the axial transfer through surface bond and through mechanisms is presented.

### 1.6.4 Chapter 4 Summary

Details of the experimental program, parameters, test unit design, construction, and instrumentation are presented in this chapter. The test protocol and test setup is presented as well.

### 1.6.5 Chapter 5 Summary

This chapter presents experimental results for all test units. Axial force-axial displacement hysteretic responses for each test unit are presented along with pertinent strain profiles from the steel shell and longitudinal reinforcing bars. Photographic evidence of key findings is presented.

### 1.6.6 Chapter 6 Summary

This chapter presents an analysis of experimental results, comparison to other research, comparison to design codes, and design recommendations. A capacity prediction for the shear ring mechanism using a plastic hinge formulation and an estimation of the concrete capacity at the mechanism is compared to experimental results.

### 1.6.7 Chapter 7 Summary

This chapter presents the design procedure to predict the axial force transfer through surface bond, circumferential mechanisms and distributed mechanisms. The design procedure is demonstrated in three examples.

### 1.6.8 Chapter 8 Summary

This chapter presents a summary of the key findings from this research and the original contributions to the design of CISS piles. Concluding remarks and recommendations for future research through experimental investigation and analytical studies are presented.

### 1.6.9 Appendix Chapter 8 Strain Profiles

Strain profiles for the steel shell and longitudinal reinforcement are presented in this appendix chapter. Strain profiles are presented for test units of the second phase of the experimental program, which focused on the shear ring mechanism.

### 1.6.10 Appendix Chapter 9 Finite Element Analysis

Finite element modeling of the shear ring mechanism using ABAQUS/EXPLICIT is presented in this appendix chapter. Details for the selection of model characteristics, such as geometry, material properties, and interaction are presented. Results from the modeling of the axial force transfer through the shear ring mechanism and surface bond are presented and compared to test results of the axial force-axial displacement hysteretic response.

# 2 LITERATURE REVIEW

## 2.1 Introduction

This chapter reviews relevant research and design codes from the American Petroleum Institute and the United Kingdom Department of Energy.

## 2.2 Previous Studies on the Effect of the D/t Ratio and Mechanisms

Published research on the effect of the D/t ratio or mechanisms fixed to the steel shell surface is presented in this section. Numerous researchers have conducted bond testing of steel shells filled with concrete. Published results for a true bond test in which the axial force was applied to the concrete core and support at the base was provided only through the steel shell, as shown in Table 2.1, is limited. Published results for the testing of mechanisms was obtained from Tomii *et al*. (1980) and Sato *et al*. (1981) only for the tread plate mechanism. Published results for a shear ring mechanism were found only for testing of a grouted connection between two steel shells.

**Table 2.1 Summary of Bond Stress Data Obtained from Literature Review**

| Researcher | Mechanism | Diameter, D mm (in.) | Thickness, t mm (in.) | D/t Ratio | Bond Stress MPa (psi) | Void at Base? |
|---|---|---|---|---|---|---|
| Roeder | Moderate Shrinkage | 248, (9.75) | 13.5, (0.53) | 18.4 | 0.01, (1.5) | Yes |
| Roeder | Moderate Shrinkage | 248, (9.75) | 13.5, (0.53) | 18.4 | 0.026, (3.8) | Yes |
| Roeder | Moderate Shrinkage | 341, (13.4) | 7.1, (0.28) | 48 | 0.031, (4.5) | Yes |
| Roeder | Moderate Shrinkage | 341, (13.4) | 7.1, (0.28) | 48 | 0.037, (5.4) | Yes |
| Roeder | Moderate Shrinkage | 341, (13.4) | 7.1, (0.28) | 48 | 0.094, (14) | Yes |
| Roeder | Moderate Shrinkage | 341, (13.4) | 7.1, (0.28) | 48 | 0.043, (6.2) | Yes |
| Roeder | Moderate Shrinkage | 598, (23.6) | 5.6, (0.22) | 107 | 0.052, (7.5) | Yes |
| Roeder | Moderate Shrinkage | 598, (23.6) | 5.6, (0.22) | 107 | 0.068, (9.9) | Yes |
| Roeder | Minimal Shrinkage | 248, (9.75) | 13.5, (0.53) | 18.4 | 0.77, (112) | Yes |
| Roeder | Minimal Shrinkage | 248, (9.75) | 13.5, (0.53) | 18.4 | 0.79, (114) | Yes |
| Roeder | Minimal Shrinkage | 248, (9.75) | 13.5, (0.53) | 18.4 | 0.78, (112) | Yes |
| Roeder | Minimal Shrinkage | 248, (9.75) | 13.5, (0.53) | 18.4 | 0.32, (46) | Yes |
| Roeder | Minimal Shrinkage | 341, (13.4) | 7.1, (0.28) | 48 | 0.28, (41) | Yes |
| Roeder | Minimal Shrinkage | 341, (13.4) | 7.1, (0.28) | 48 | 0.36, (52) | Yes |
| Roeder | Minimal Shrinkage | 341, (13.4) | 7.1, (0.28) | 48 | 0.18, (25) | Yes |
| Roeder | Minimal Shrinkage | 341, (13.4) | 7.1, (0.28) | 48 | 0.19, (27) | Yes |
| Roeder | Minimal Shrinkage | 598, (23.6) | 5.6, (0.22) | 107 | 0.15, (21) | Yes |
| Roeder | Minimal Shrinkage | 598, (23.6) | 5.6, (0.22) | 107 | 0.18, (26) | Yes |
| Roeder | Minimal Shrinkage | 598, (23.6) | 5.6, (0.22) | 107 | 0.093, (14) | Yes |
| Roeder | Minimal Shrinkage | 598, (23.6) | 5.6, (0.22) | 107 | 0.093, (14) | Yes |
| Sato | None | 600, (23.6) | 9.0, (0.35) | 66.7 | 0.39, (57) | Yes |
| Sato | Tread Plate (3 checker) | 600, (23.6) | 9.0, (0.35) | 66.7 | 4.9, (711) | Yes |
| Sato | Tread Plate (2 checker) | 600, (23.6) | 9.0, (0.35) | 66.7 | 5.5, (798) | Yes |
| Tomii | Expansive Conc. | 150, (5.91) | 3.2, (0.13) | 46.9 | 0.69, (100) | No |
| Tomii | Expansive Conc. | 150, (5.91) | 3.2, (0.13) | 46.9 | 0.49, (71) | No |
| Tomii | None | 150, (5.91) | 3.2, (0.13) | 46.9 | 0.39, (57) | No |
| Tomii | Tread Plate | 150, (5.91) | 3.2, (0.13) | 46.9 | 0.59, (86) | No |
| Tomii | Tread | 150, (5.91) | 3.2, (0.13) | 46.9 | 0.59, (86) | No |

### 2.2.1 Tomii *et al* (1980)

Tomii *et al*. (1980) conducted monotonic axial compression testing of steel shells filled with plain concrete or expansive concrete. Test units had a steel shell length of 735 mm (28.9 in.), a diameter of 150 mm (5.9 in.), and a steel shell diameter to thickness ratio (D/t) of 47. Several test units had a steel shell with a tread plate mechanism. Axial compression was applied to the top of the steel shell, and support at the base was provided by both the concrete core and the steel shell, as shown in Figure 2.1 (loading case 4). Longitudinal steel shell strains were measured along the height of a typical test unit. This allowed for determination of the regions where bond stress existed, since a

constant strain distribution (continuity between steel shell and concrete core) indicated no change in the axial force transfer. A region of the steel shell in which the strain changes with height indicates a bond stress. The bond stress, $\sigma_{bond}$, was calculated for these two cases by subtracting the stress in the steel shell, $\sigma_{shell}$, from the applied stress, as stated in Equation 2.1:

$$\sigma_{bond} = \left( \left( \frac{N}{A_{shell}} \right) - \sigma_{shell} \right) \cdot \left( \frac{t}{\ell_o} \right) \tag{2.1}$$

In Equation 2.1, $N$ is the axial compression force applied to the concrete core and steel shell, and $t$ is the steel shell thickness. For the case in which a continuity in the strain existed, the steel shell height over which there was no strain continuity was used for $\ell_o$. The steel shell stress in the section where strain continuity existed, as calculated from measured strains, was used for $\sigma_{shell}$. For the case in which no continuity in the strain existed (a completely bonded interface), the steel shell height was used for $\ell_o$. The steel shell stress, $\sigma_{shell}$, was calculated from the measured strains at the base.

Bond stress values ranging from 0.20 MPa (28 psi) to 0.39 MPa (57 psi) were obtained for a test unit with a smooth steel shell interior surface, and ordinary concrete. When expansive concrete was used, a maximum bond stress increase of 75% was obtained. The use of tread plate resulted in a maximum bond stress increase of 49% over the test unit with a smooth steel shell. The use of tread plate and expansive concrete, together, resulted in a maximum bond stress increase of 161%. Bond stress values are listed in Table 2.1.

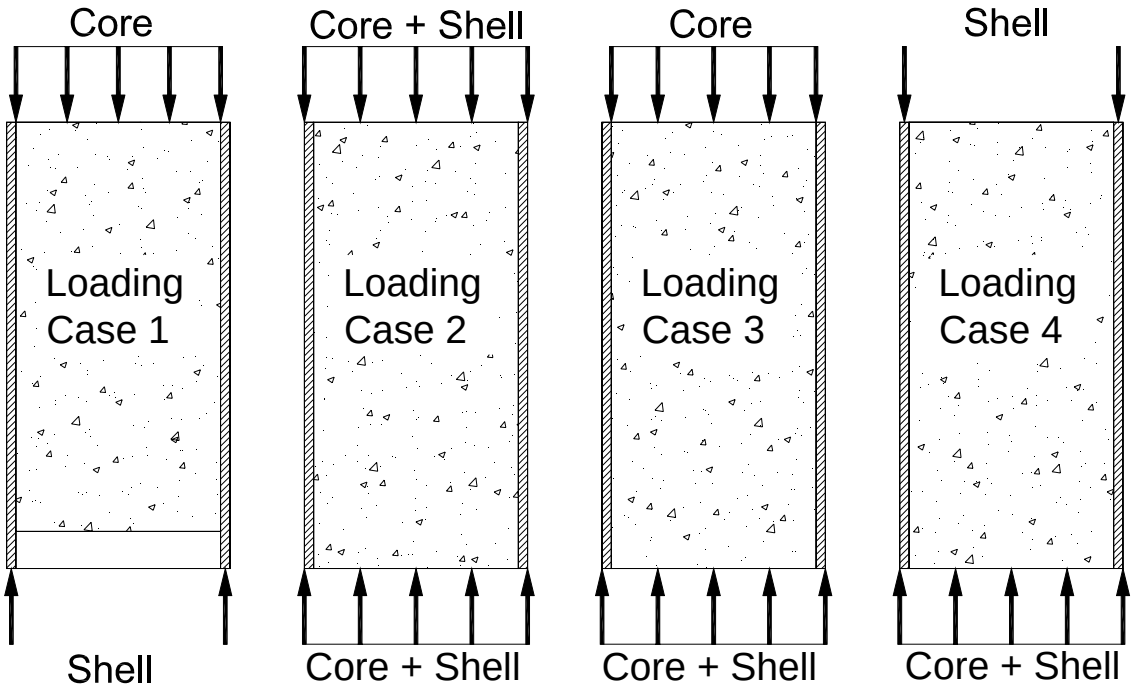


**Figure 2.1 Loading Conditions Used in Testing of Steel Shells Filled with Concrete**

### 2.2.2 Sato *et al*. (1981)

Sato *et al*. (1981) conducted monotonic axial compression testing of steel shells filled with unreinforced concrete. A typical test unit had a steel shell with a length of 300 mm (11.8 in.), a diameter of 600 mm (23.6 in.), a thickness of 9 mm (0.35 in.) and a D/t ratio of 66.7. Issues investigated included the use of tread plate, the presence of oil or mud on the steel shell surface and the variation of the steel shell length. Axial force was applied to the concrete core, at the top, and supported at the base only by the steel shell, as shown in Figure 2.1 (loading case 1). A bond stress of 4.9 MPa (0.71 ksi) was obtained for a test unit with a tread plate mechanism which was approximately 13 times that of a steel shell with a smooth interior surface. The maximum bond stress was found to decrease by 20% when a mud coating was present on the steel shell interior surface. Sato *et al*. concluded that the steel shell with the tread plate could be used in place of a steel shell with a smooth interior surface and expansive concrete.

A comparison of bond stress versus D/t ratio for results obtained by Sato *et al*. and Tomii *et al*. is shown in Figure 2.2. In this plot, the bond stress data for normal

concrete test units had approximately the same value for both researchers, with D/t ratios of 66.7 for Sato *et al.* and 47 for Tomii *et al*. However, the bond stress data for the tread plate mechanism did not match up between these two researchers, as shown in Figure 2.3. This difference in results could be attributed to the bond stress calculation procedure. Tomii *et al*. calculated the bond stress as a force per steel shell surface area whereas Sato *et al*. might have calculated the bond stress as a force per tread area protruding into the core. The procedure for calculating the bond stress for the tread plate mechanism was not reported by Sato *et al*.

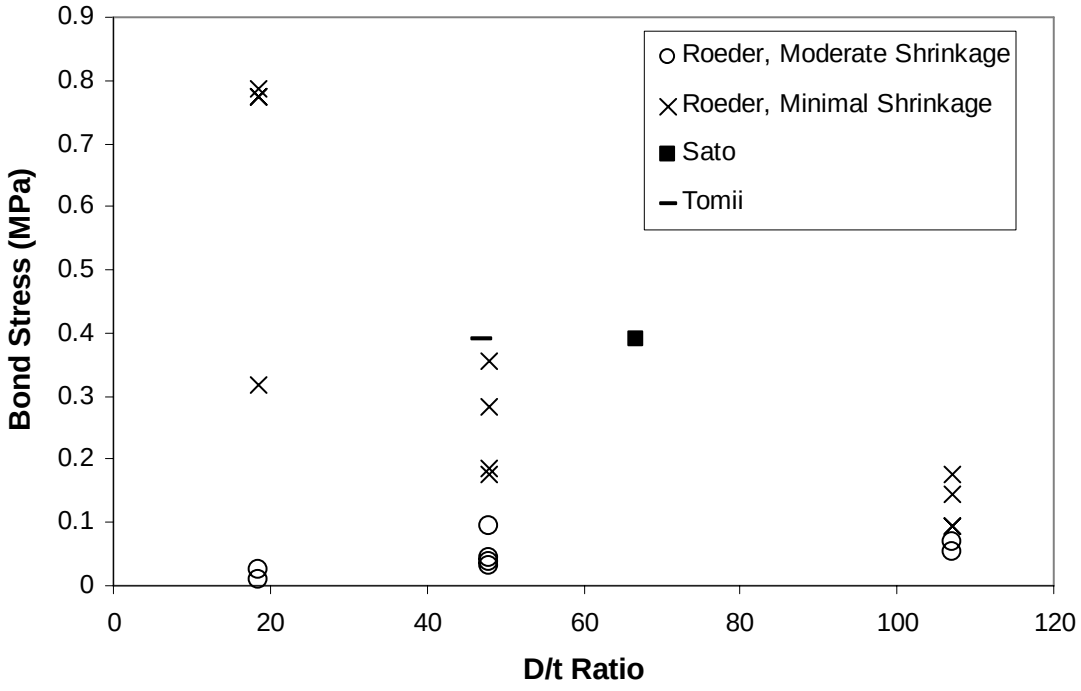


**Figure 2.2 Bond Stress for Normal Concrete**

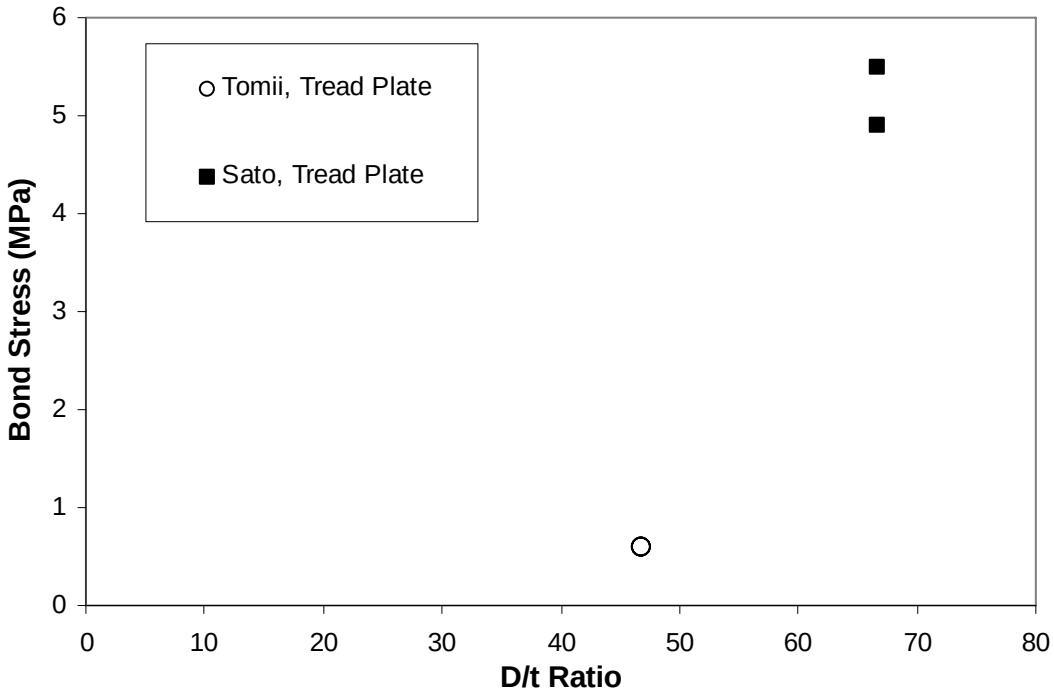


**Figure 2.3 Bond Stress for Expansive Concrete**

## 2.3 Shrinkage Potential

The effect of shrinkage on steel shells filled with concrete was investigated by Ichinose, *et al.* (2001). The shrinkage of concrete within a steel shell was compared to test units which lacked a steel shell. Test units with a steel shell, had a height of 1.0 m (39.4 in.), an external diameter of 165.2 mm (6.5 in.) and thicknesses of 4.5 mm (0.18 in.) or 5.0 mm (0.20 in.). This resulted in test units with D/t ratios of 34.7 and 31.0. Concrete shrinkage strains were measured for 280 days, with no external loading applied, through an embedded gauge in the test unit. The test units with a steel shell were found to obtain approximately 9% of the strain values measured in the test units which lacked a steel shell. Ichinose *et al*. concluded that shrinkage strain could be considered negligible in the design of steel shells filled with concrete.

The shrinkage potential for steel shells filled with concrete subjected to a monotonic axial compression loading was investigated by Roeder *et al*. (1999). Test units had a steel shell with external diameters between 275 mm (10.8 in.) and 610 mm

(24.0 in.) and D/t ratios between 18 and 107, respectively. Steel shell lengths ranged from 758 mm (29.8 in.), for a D/t ratio of 18, to a length of 1,927 mm (75.9 in.) for a D/t ratio of 107. Monotonic axial compression was applied to the concrete core, with support at the base provided through only the steel shell. Roeder *et al.* conducted a linear regression analysis on bond stress data versus D/t ratio for his data and for data obtained from Virdi *et al.* (1981) and Virdi and Dowling (1983) as stated in Equation 2.2.

$$f_{2\sigma} = 2.109 - 0.026 \cdot (D/t) \tag{2.2}$$

In this equation, $f_{2\sigma}$ is the bond stress two standard deviations above the mean. This equation results in a decreasing bond stress as the D/t ratio increases which suggests no bond stress for D/t ratios greater than 80. Roeder *et al*. concluded this potential lack of bond stress at high D/t ratios, to highlight the importance of shrinkage of the concrete core.

Roeder *et al*. found the bond stress to occur over a length of D/2, with an exponential distribution, if slip between the steel shell-concrete interface was prevented. After slip, the bond stress was found to have a uniform distribution over the length of slip. The bond length, prior to slip, was found to be shorter than D/2 for high D/t ratios and longer than D/2 for a lower D/t ratio.

A comparison of results from Roeder *et al*., Tomii *et al*., and Sato *et al*. is shown in Figure 2.2. One of the test units from Roeder *et al*. at a D/t ratio of 48, with minimal shrinkage, had a close match to a test unit of Tomii *et al*. at a D/t ratio of 47. Test units from Roeder *et al*. with minimal shrinkage appear to show a trend of decreasing bond stress with D/t ratio. A linear regression of this data with data from Sato *et al*. and Tomii *et al*. would produce such a trend. Bond stress data from Roeder *et al*. for moderate shrinkage showed a low bond stress, at a wide range of D/t ratios, in comparison to Sato *et al*. and Tomii *et al*.

## 2.4 Design Code Recommendations

Provisions for the design of composite columns (or piles) currently do not exist in any of the major design codes used by structural engineers, such as the American Concrete Institute (ACI), the American Institute for Steel Construction (AISC), or the Uniform Building Code (UBC). Currently design equations and recommendations are made only in the American Petroleum Institute (API) code, and in the United Kingdom Department of Energy (UK DOE) code, both of which are used for offshore structural design. These codes have recommendations for the strength of a grouted connection between a steel shell pile and an internal steel shell (sleeve) using shear rings, as shown in Figure 2.4. Several tests included mechanisms attached to both the steel shell pile and steel sleeve, as studied by Billington (1978 and 1980), Lewis (1980) and Loset (1981). The effects of the steel shell surface condition and scale effects were examined by Yamasaki (1980). Results from the aforementioned experiments were used to develop the equations presented in this section. Experimental results will not be discussed because of the difference between this connection type and the CISS pile (focus of this research). However, the API and UK DOE codes will be presented as they have been applied by bridge designers to design mechanisms within CISS piles.

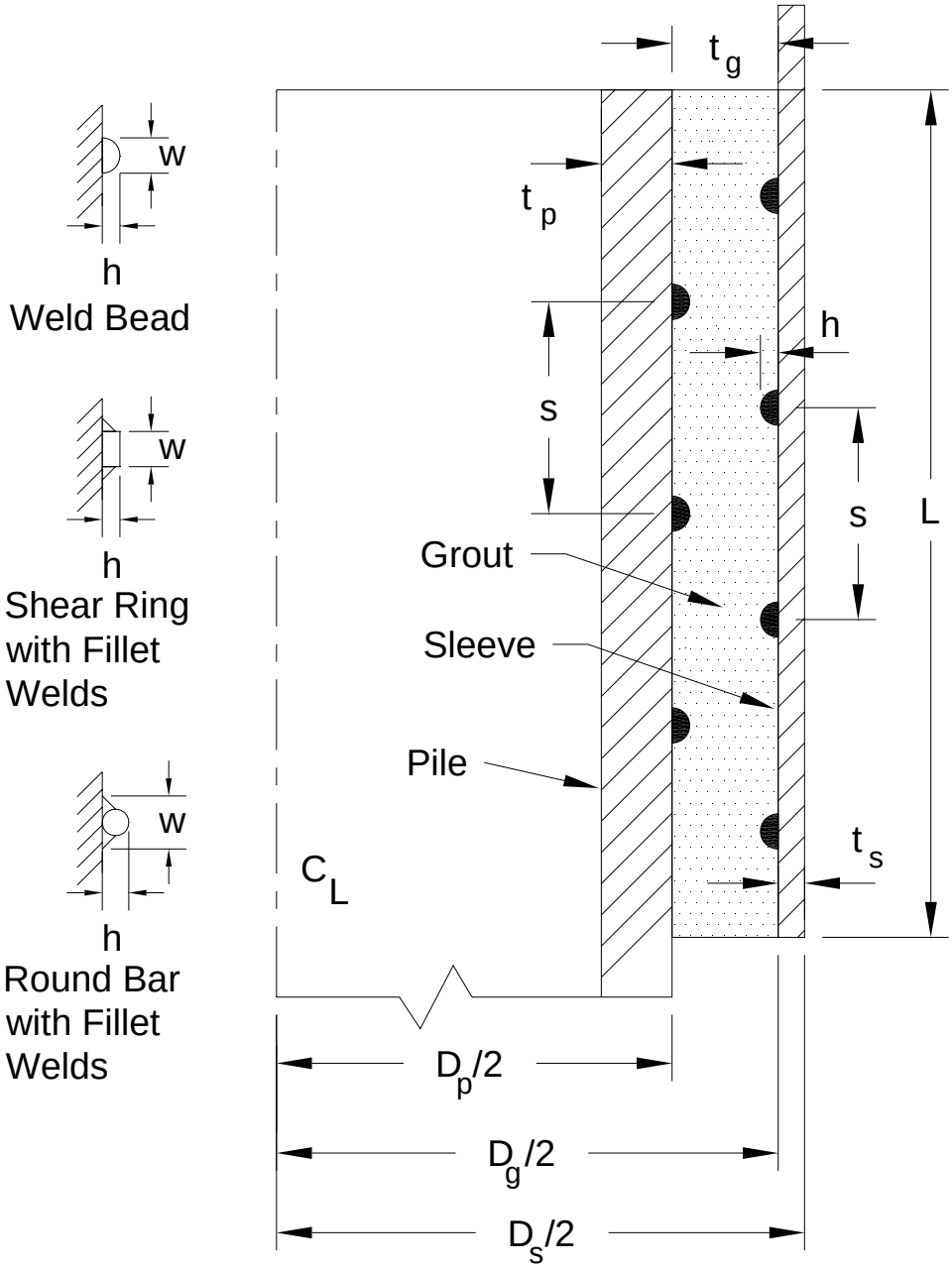


**Figure 2.4 Steel Shell Pile to Steel Sleeve Connection Detail using Mechanisms**

### 2.4.1 American Petroleum Institute Code - Working Stress Design

The API code has recommendations for both working stress design and load and resistance factor design (LRFD) as presented in the following sections. In the working stress design method of the American Petroleum Institute Code (API, 2002), axial load transfer stresses can be calculated for two loading cases. In the first loading case, the

dead load and live load are of concern. In the second loading case, dead load and live load are of concern under extreme environmental loading conditions. Using either loading case, the axial force transfer is the product of the allowable axial load transfer stress, $f_{ba}$, and the contact area between the steel shell or sleeve and the grout. The minimum contact area, between the steel shell and grout or sleeve and grout should be used. Equations for the nominal allowable axial load transfer stress, $f_{ba}$, were presented for two loading cases. The nominal allowable axial load transfer stress, $f_{ba}$, for the first case was stated as:

$$f_{ba} = 0.138 + 0.5 \cdot f_{cu} \cdot \left(\frac{h}{s}\right) \quad \text{(SI Units: MPa)} \tag{2.3}$$

$$f_{ba} = 20 + 0.5 \cdot f_{cu} \cdot \left(\frac{h}{s}\right) \quad \text{(USCS Units: psi)} \tag{2.4}$$

The nominal allowable axial load transfer stress, $f_{ba}$, for the second case was stated as:

$$f_{ba} = 0.184 + 0.67 \cdot f_{cu} \cdot \left(\frac{h}{s}\right) \quad \text{(SI Units: MPa)} \tag{2.5}$$

$$f_{ba} = 26.7 + 0.67 \cdot f_{cu} \cdot \left(\frac{h}{s}\right) \quad \text{(USCS Units: psi)} \tag{2.6}$$

In the nominal allowable load transfer stress equations presented above (Equations 2.3, 2.4, 2.5, and 2.6), the stress is calculated for a shear ring with radial thickness, $h$, and a shear ring center to center spacing of $s$. The total mechanism height, including welds, as shown in Figure 2.4, is defined as $w$. The stress is calculated for a grout with an unconfined compressive strength, $f_{cu}$, obtained from a cube strength test. The cube strength test is used in the United Kingdom, Europe, and Russia as a measure of the concrete strength, instead of concrete cylinder testing conducted in the U.S.A. The unconfined compressive strength, $f_{cu}$, is obtained from the concrete compressive strength based on cylinder testing, $f_c^{'}$, using the equation below (Day, 1999):

$$f_{cu} = f_c^{'} + \left(\frac{19}{\sqrt{f_c^{'}}}\right) \quad \text{(SI Units: MPa)} \tag{2.7}$$

$$f_{cu} = f_c^{'} + \left( \frac{33193}{\sqrt{f_c^{'}}} \right) \qquad \text{(USCS Units: psi)} \qquad (2.8)$$

Equations 2.3, 2.4, 2.5 and 2.6 can also be used for design cases in which no mechanisms are used, as the second term simply drops out. This results in the axial load transfer stresses as stated below.

For Loading Condition 1 and 2: $f_{ba}$ = 0.138 MPa (20 psi) (2.9)

For Loading Condition 3 and 4: $f_{ba}$ = 0.184 MPa (26.7 psi) (2.10)

The mechanisms recommended for use by the API code include a weld bead, a shear ring (rectangular cross section) with fillet welds or a welded bar (circular cross section) with fillet welds. The API code recommended the mechanisms should be connected to the steel shell in a series of circular hoops with a vertical spacing of $s$, or be connected to the steel shell as a spiral with a pitch of $s$. Mechanisms should be designed for allowable steel and weld stresses to transfer a part of the connection capacity (stress multiplied by surface area) as stated in the equation below.

$$P = A_{mech} \cdot 1.7 \cdot f_{cu} \qquad (2.11)$$

In Equation 2.11, $A_{mech}$ is the area of the shear key protruding into the concrete core. Equation 2.11 is recommended for the steel shell-sleeve connection region between two pile diameters from the top and bottom. Equation 2.12, as stated below, should be used for the connection region within two pile diameters from the top and bottom.

$$P = A_{mech} \cdot 2.5 \cdot f_{cu} \qquad (2.12)$$

Application of the API code equations for the axial load transfer stress has the limitations as listed below.

1. Unconfined compressive strength:

17.25 MPa (2,500 psi) $\leq f_{cu} \leq$ 110 MPa (16,000 psi)

2. Sleeve geometry: $\frac{D_s}{t_s} \leq 80$

3. Pile geometry: $\frac{D_p}{t_p} \leq 40$

4. Grout annulus geometry: $7 \le \frac{D_g}{t_g} \le 45$

5. Mechanism spacing ratio: $2.5 \le \frac{D_p}{s} \le 8$

6. Mechanism ratio: $\frac{h}{s} \le 0.10$

7. Mechanism shape factor: $1.5 \le \left(\frac{w}{h}\right) \le 3$

8. Product of $f_{cu}$ and $\frac{h}{s}$: $f_{cu} \cdot \left(\frac{h}{s}\right) \le 5.5$ MPa (800 psi)

### 2.4.2 American Petroleum Institute Code - Load and Resistance Factor Design

In the load and resistance factor design (LRFD) method (API, 1993), the axial load transfer stress is calculated for only one loading case, consisting of dead and live load. The LRFD equation has the same limitations for use as the working stress equation, as stated in the previous section. The equations for the nominal allowable axial load transfer stress, $f_{ba}$, are similar to the working stress equations, and are stated below:

$$f_{ba} = 0.248 + 0.9 \cdot f_{cu} \cdot \left(\frac{h}{s}\right) \quad \text{(SI Units: MPa)} \tag{2.13}$$

$$f_{ba} = 36 + 0.9 \cdot f_{cu} \cdot \left(\frac{h}{s}\right) \quad \text{(USCS Units: psi)} \tag{2.14}$$

Equations 2.13 and 2.14 can also be used for design cases in which no mechanisms are used, as the second term simply drops out. This results in an axial load transfer stress, $f_{ba}$, of 0.248 MPa (36 ksi) as stated below, in Equation 2.15. A reduction factor, $\phi_{ba}$, of 0.9 is used to obtain the maximum axial load transfer stress, as stated below, in Equation 2.16.

$$f_{ba} = 0.248 \text{ MPa (36 psi)} \tag{2.15}$$

$$f_{b\max} \le \phi_{ba} \cdot f_{ba} \tag{2.16}$$

Axial load transfer stresses obtained using the LRFD equation predict a greater stress than working stress design equations for both API loading cases. This is shown in Figure 2.5 in which the axial load transfer stress is plotted versus the ratio of shear ring radial width to spacing, $h/s$, for the ratio over which the equations are valid: $0 < h/s < 0.1$.

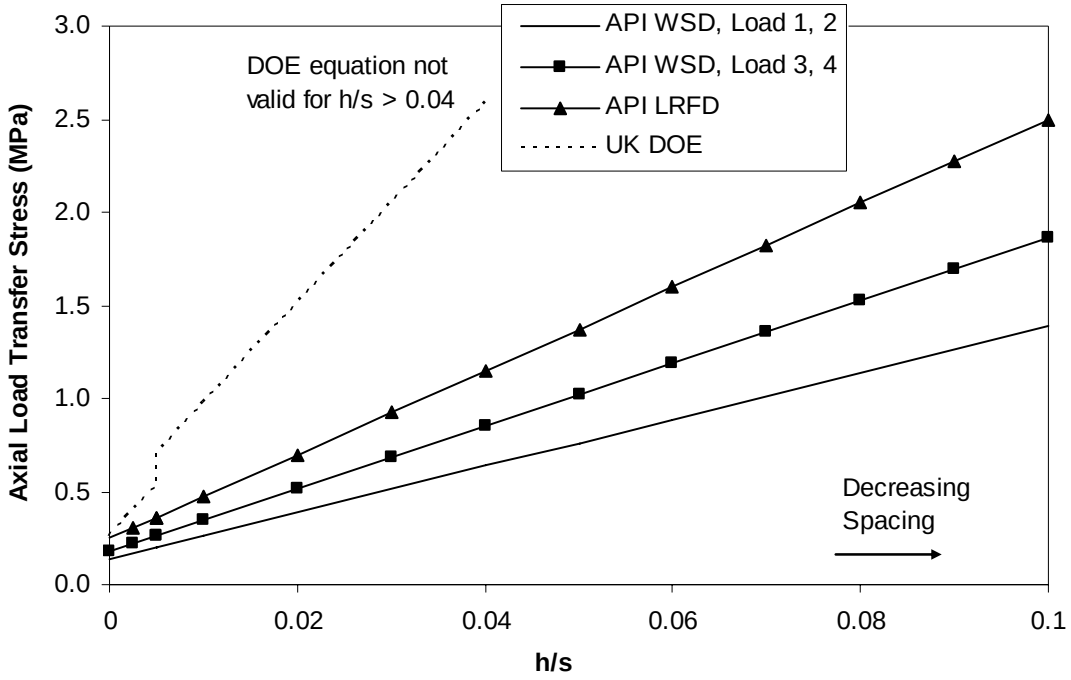


**Figure 2.5 Comparison of Axial Load Transfer Stress for Design Code**

### 2.4.3 United Kingdom Department of Energy Code

Recommendations for the design of a grouted connection between a steel shell pile and a steel sleeve through mechanisms, as shown in Figure 2.4, can also be found in the United Kingdom Department of Energy (UK DOE) code (1982). This code has an equation for what is termed the characteristic bond strength, $f_{buc}$, of a grouted steel shell-sleeve connection. This stress is applicable to the contact area between the steel shell (pile) and the grout. This equation was developed from the results of approximately 450 tests of steel shell piles grouted to a steel sleeve (Billington and Tebbett, 1980). Some tests included mechanisms attached to both the steel shell pile and the steel sleeve, as

studied by Billington and Lewis (1978), Lewis *et al.* (1980) and Loset (1981). The aforementioned characteristic bond strength, $f_{buc}$, is stated as:

$$f_{buc} = K \cdot C_L \cdot \left(9 \cdot C_s + 1100 \cdot \frac{h}{s}\right) \cdot \left(f_{cu}\right)^{1/2} \qquad \text{(MPa)} \tag{2.17}$$

The characteristic bond strength, of Equation 2.17, is valid for grouted connections with and without mechanisms. In Equation 2.17, $K$ is a dimensionless stiffness factor, and is stated as:

$$K = \frac{1}{m} \cdot \left(\frac{D}{t}\right)_g^{-1} + \left[\left(\frac{D}{t}\right)_p + \left(\frac{D}{t}\right)_s\right]^{-1} \tag{2.18}$$

The subscripts g, p and s refer to the grout, pile and sleeve, respectively. The other variables in Equation 2.18 are listed below.

$C_L$: coefficient for grouted length to pile diameter ratio

$C_S$: surface condition factor

$D$: external diameter (mm)

$f_{cu}$: characteristic grout compressive strength based on testing of 75 mm (2.9 in.) cubes at 28 days (MPa)

$h$: minimum mechanism radial width (mm)

$m$: modular ratio of steel to grout

$s$: nominal shear connector spacing (mm)

$t$: wall thickness (mm)

The UK DOE code recommends a conservative value of 18 for the modular ratio, $m$, if no data is otherwise available. The length coefficient, $C_L$, has values of 1.0, 0.9, 0.8 and 0.7 for ratios of grouted connection length to pile diameter, $L/D_P$, of 2, 4, 8 and 12 or greater, respectively. The surface condition factor, $C_S$, has a value of 1.0 if mechanisms are used and if the ratio of mechanism width to spacing, $h/s \geq 0.005$. If $h/s < 0.005$, or if no mechanisms are used, than a value of 0.6 should be used for $C_S$.

The allowable load transfer stress, $f_{ba}$, is calculated by dividing the characteristic bond strength, $f_{buc}$, by a factor of safety, $FS$, as stated below.

$$f_{ba} = \left(\frac{1}{FS}\right) \cdot f_{buc} \tag{2.19}$$

The factor of safety, $FS$, depends on the conditions under which grout is placed and on the loading condition. If grout is placed in a manner such that it displaces water (in the case of a submerged pile-sleeve connection) then $FS$ values of 4.5 and 6.0 should be used for extreme loading and operating loading conditions, respectively. If grout is placed in a manner such that it displaces drilling mud or a similar material then $FS$ values of 6.0 and 8.0 should be used for extreme loading and operating loading conditions, respectively.

The characteristic bond strength, $f_{buc}$, equation must satisfy the requirements as stated below.

1. Sleeve geometry: $50 \le \left(\frac{D_s}{t_s}\right) \le 140$
2. Pile geometry: $24 \le \left(\frac{D_p}{t_p}\right) \le 40$
3. Grout annulus geometry: $10 \le \left(\frac{D_g}{t_g}\right) \le 45$
4. Grouted connection length to pile diameter ratio: $\left(\frac{L}{D_p}\right) \ge 2$
5. Mechanism height ratio: $0 \le \left(\frac{h}{D_P}\right) \le 0.006$
6. Mechanism spacing ratio: $0 \le \left(\frac{D_P}{s}\right) \le 8$
7. Mechanism ratio: $0 \le \left(\frac{h}{s}\right) \le 0.04$
8. Mechanism shape factor: $1.5 \le \left(\frac{h}{s}\right) \le 3$

Mechanisms recommended for use, by the UK DOE code, include welded bars or a weld bead with either a circumferential layout or a spiral configuration. The mechanism spacing is recommended to be uniform throughout the steel shell-sleeve connection region.

### 2.4.4 Comparison of Codes

A numerical comparison of the API code and the UK DOE code was done by Karsan *et al*. (1984) for grouted connections between a steel shell and a steel sleeve. Karsan *et al*. noted the UK DOE code required greater knowledge of the connection, as this code is a function of ten independent variables, whereas the API code is a function of three independent variables. A database of 117 tests with sufficient information to meet the requirements of both code equations was used by Karsan *et al*. to evaluate the two design codes. The UK DOE equation was found to have a higher factor of safety for grouted connections relying on surface bond than the API equation. The API equation was found to have a higher factor of safety for connections with a mechanism in comparison to the UK DOE equation.

Application of the API equation to CISS piles is clearly more straightforward than using the UK DOE equation, due to the fewer number of variables involved in the calculation. The API equation can be applied to predict the bond stress within a CISS pile without axial force enhancing mechanisms, and with axial force enhancing mechanisms as well. The UK DOE equation can also be applied to both, however, in the calculation of the stiffness factor, $K$, the D/t term for the steel sleeve section is nonexistent. Both equations have numerous limitations as listed in the previous sections, such as the steel shell diameter to thickness ratio $D/t \leq 40$ for both equations. As a result of this, these equations cannot be applied to all of the test units in this research study as the D/t ratio varied from 24 to 128. A comparison of the code equations to test results will be presented in Section 6.8.

A comparison of the axial load transfer stresses, predicted using the code equations in Figure 2.5 shows the stress to increase linearly with the $h/s$ ratio, for both cases. The UK DOE equation could only be applied over a range of $0<h/s<0.04$ and clearly predicted a greater stress at all $h/s$ ratios. A discontinuity in the stress prediction of the UK DOE equation occurred at a $h/s$ ratio of 0.005 due to the change in the value of $C_s$ from 0.6 to 1.0 as shown in Figure 2.5. The axial load transfer stresses predicted by the codes were close at low $h/s$ ratios; however the predicted stresses diverged as the $h/s$ ratio increased. At an $h/s$ ratio of 0.04 the stress predicted by the UK DOE code was approximately 2.5 times the maximum stress predicted by the API code, as shown in Figure 2.5. The difference in the predicted stresses for these two codes shows the need for additional studies into the axial force transfer through a shear ring. In addition, the difference shows the need for investigation into the axial force transfer from a reinforced concrete core to a shear ring and a steel shell.

# 3 AXIAL FORCE TRANSFER PREDICTION

## 3.1 Introduction

This chapter presents the theory for the prediction of the axial force transfer through mechanisms and through surface bond. A prediction for the axial force transfer through surface bond is presented using strain compatibility between the steel shell and concrete core. The prediction of axial force transfer through a mechanism is presented for two failure modes: obtaining the capacity of the steel shell and mechanism, and obtaining the capacity of the concrete core. A plastic hinge formulation is used to predict the steel shell and mechanism capacity. A confined concrete model is used to predict the stresses in the concrete (and capacity) at the mechanism.

## 3.2 Surface Bond

The application of an axial force to a reinforced concrete core within a steel shell will initially result in a minimal axial displacement. A minimal displacement will occur due to strain compatibility between the concrete core and the steel shell. After the strain compatibility is exceeded, the concrete core will slip relative to the steel shell. Prior to attainment of the strain at compatibility, $\varepsilon_{sc}$, the axial force transfer occurs as if the concrete core and steel shell were both supported at the base. This is due to the minimal initial axial displacement, which can be assumed to occur within the concrete core. The axial force at strain compatibility, $P_{sc}$, can be expressed as a function of the concrete stress, $\sigma_c$, the steel shell stress, $\sigma_s$, and the cross sectional area of the concrete core, $A_{core}$, and the steel shell, $A_{shell}$, as stated below.

$$P_{sc} = \sigma_c \cdot A_{core} + \sigma_{shell} \cdot A_{shell} \tag{3.1}$$

The stresses and strains at the strain compatibility state are within the elastic range. Hooke's Law relations for the concrete and steel stresses and strains are stated below in Equations 3.2 and 3.3.

$$\sigma_c = E_c \cdot \varepsilon_c \tag{3.2}$$

$$\sigma_{shell} = E_{shell} \cdot \varepsilon_{shell} \tag{3.3}$$

In Equations 3.2 and 3.3, the modulus of elasticity for concrete and steel are $E_c$ and $E_{shell}$, respectively. The strains are expressed as $\varepsilon_c$, for concrete, and $\varepsilon_{shell}$ for steel. Substitution of the above Hooke's Law relations into Equation 3.1 results in the following axial force at the strain compatibility condition, $P_{sc}$:

$$P_{sc} = E_c \cdot \varepsilon_c \cdot A_{core} + E_{shell} \cdot \varepsilon_{shell} \cdot A_{shell} \tag{3.4}$$

At strain compatibility the concrete and steel are both at the same strain, $\varepsilon_{sc}$, such that Equation 3.4 can be re-stated in Equation 3.5. This strain will result in a compression displacement, $\Delta\ell$, of the concrete core (with a length of $\ell$) as stated in Equation 3.6, based on the definition of strain.

$$P_{sc} = \varepsilon_{sc} \cdot \left(E_c \cdot A_{core} + E_{shell} \cdot A_{shell}\right) \tag{3.5}$$

$$\Delta\ell = \varepsilon_c \cdot \ell \tag{3.6}$$

After the axial force at strain compatibility is obtained, the concrete core will slip relative to the steel shell and will result in a variation of the strains in the concrete core and the steel shell. As the concrete core slips, a friction bond will dominate the response, $P_{fric}$, which is equated to the axial force in the concrete core as stated in Equations 3.7, with a strain, $\varepsilon_c$, assumed equal to $\varepsilon_{sc}$.

$$P_{fric} = \varepsilon_{sc} \cdot E_c \cdot A_{core} \tag{3.7}$$

After the peak axial force transfer is obtained at the strain compatibility condition, as shown in Figure 3.1, the axial force is assumed to decrease with the same initial stiffness. The axial force decreases until the axial force transfer as predicted in Equation 3.7 is obtained, after which the axial force remains constant as axial displacement increases.

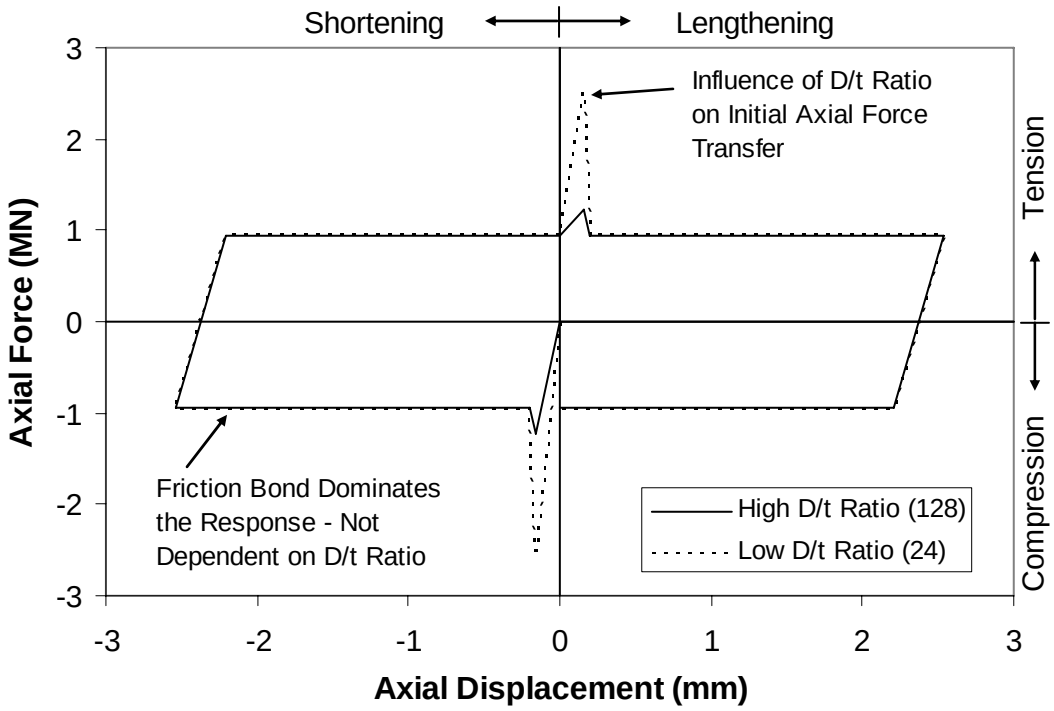


**Figure 3.1 Effect of the D/t Ratio on the Initial Hysteretic Response for Surface Bond**

After the desired axial displacement is obtained, the concrete core is unloaded with a stiffness assumed as the original stiffness for loading, as shown in Figure 3.1. Unloading of the concrete core will have a friction force, $P_{fric}$, as predicted from Equation 3.7. After the axial displacement is returned to zero, axial tension loading results in a slight axial force transfer increase due to an initial elongation of the concrete core, similar to the initial peak in axial compression force. After this peak in the axial tension occurs, the axial force is assumed to decrease with the original axial stiffness until an axial force, as predicted by Equation 3.7 is obtained. The axial force remains constant, until the desired displacement, as shown in Figure 3.1, followed by an unloading process similar to the aforementioned unloading from axial compression.

The axial force transfer at the strain compatibility condition is affected by the D/t ratio. As the D/t ratio decreases, the axial force transfer increases due to the increasing steel shell cross sectional area. However, after strain compatibility, the D/t ratio is

expected to not have an effect on the axial force transfer, as shown in Figure 3.1. This is due to a friction bond dominating the response as the axial displacement increases.

## 3.3 Axial Force Transfer through a Circumferential Mechanism

In this section the prediction of the axial force transfer through circumferential mechanisms will be presented. The axial force transfer through a mechanism fixed to the steel shell internal surface will be controlled by either attainment of the mechanism connection capacity, the steel shell and mechanism capacity, or the concrete capacity. One of these controlling factors combined with the previously presented frictional response will allow for prediction of the axial force transfer. The prediction of the axial force transfer through the three controlling parameters will be presented in the following sections.

### 3.3.1 Mechanism Connection Capacity

The axial force transfer can be limited by the capacity of the mechanism if the weld capacity does not exceed the capacity of the steel shell or concrete core. Failure of the welded connection of a circumferential mechanism, such as a shear ring, to the steel shell is not desired. If such a failure occurred, than the axial force transfer would depend primarily on the surface bond between the steel shell and the concrete core. The roughness of the failed welded surface remaining on the steel shell could provide some axial force transfer; however, this is a highly undesired design situation. The capacity of the weld, $P_{weld}$, with an electrode yield stress, $F_{exx}$, and an effective area, $A_{weld}$, is stated below in Equation 3.8 (LRFD) for a weld subject to shear on the effective area.

$$P_{weld} = 0.75 \cdot (0.6 \cdot F_{exx}) \cdot A_{weld} \tag{3.8}$$

In the weld capacity equation the stress is multiplied by a nominal resistance factor of 0.75. The effective area of the weld, $A_{weld}$, is the product of the steel shell circumference and the effective throat thickness of the fillet weld, $t_{weld}$, as stated in Equation 3.9. For fillet welds made by submerged arc welding of 10 mm (3/8 in.) or

smaller, the weld leg size (weld dimension along mechanism face) can be used as the throat thickness (LRFD). For fillet welds greater than 10 mm (3/8 in.) the theoretical throat size plus 3 mm (0.11 in.) should be used (LRFD). The theoretical throat size is the minimum distance from the weld joint (intersection of mechanism and steel shell) to the weld face.

$$A_{weld} = \pi \cdot D \cdot t_{weld} \tag{3.9}$$

The capacity of the weld should be equal to or exceed the yield stress of the mechanism, $f_{ymech}$, as stated below.

$$P_{weld} = 0.6 \cdot F_{exx} \cdot A_{weld} \geq A_{mech} \cdot f_{ymech} \tag{3.10}$$

### 3.3.2 Plastic Hinge Prediction

The transfer of axial force through a mechanism fixed circumferentially to the steel shell results in a high lateral pressure on the steel shell. This lateral pressure is limited by the capacity of the steel shell and mechanism through the formation of three circumferential plastic hinges as shown in Figure 3.2. In Figure 3.2 one plastic hinge is assumed to form at the mechanism location and two additional hinges are assumed to form at the points of inflection in the steel shell (at a distance $l_f$ from the mechanism). The steel shell will deform circumferentially out-of-plane through a steel shell height of $l_e$ as shown in Figure 3.2. The plastic moment, $M_p$, which develops at each of the three plastic hinge locations is stated in Equation 3.11.

$$M_p = f_y \cdot Z \tag{3.11}$$

The plastic moment, $M_p$, is the product of the steel shell yield stress, $f_y$, and the plastic section modulus, $Z$, as stated below in Equation 3.12. The plastic section modulus, $Z$, is obtained with the assumed stress distribution, as shown in Figure 3.3.

$$Z = \left( \frac{t^2}{4} \right) \tag{3.12}$$

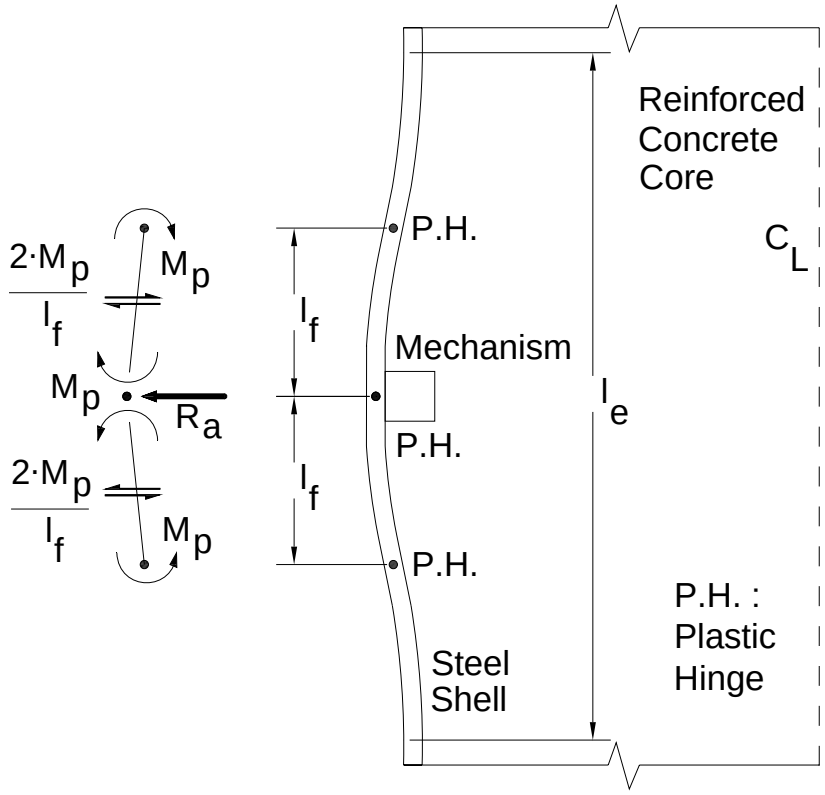


**Figure 3.2 Formation of Plastic Hinges in a Steel Shell**

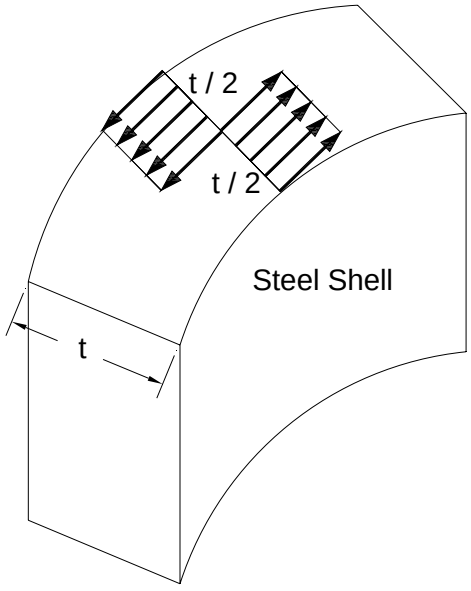


**Figure 3.3 Assumed Stress Distribution in the Steel Shell**

Substitution of Equation 3.12 into Equation 3.11 results in the following expression for the plastic moment, $M_p$, per unit length [F*L/L]:

$$M_p = \frac{t^2 \cdot f_y}{4} \tag{3.13}$$

The plastic moments will result in a shear force in the steel shell sections between the hinges as shown in Figure 3.2 and as stated:

$$V = \frac{2 \cdot M_p}{l_f} \tag{3.14}$$

The shear forces in Figure 3.2 will resist a lateral force, $R_a$, with units of force per length [F/L] as stated:

$$R_a = \frac{4 \cdot M_p}{l_f} \tag{3.15}$$

This lateral force per length, $R_a$, is applied circumferentially to the steel shell interior surface as shown in Figure 3.4. The product of this force per length and the steel shell diameter, $D$, results in the plastic hinge force as shown in the free-body diagram of Figure 3.5. This figure shows the contribution of the mechanism, the steel shell and the plastic hinge formation to the lateral force capacity of the steel shell and mechanism, $P_{sm}$. The lateral force capacity of the steel shell and the mechanism is stated as:

$$P_{sm} = t \cdot f_y \cdot \left( \frac{t \cdot D}{l_f} + 2 \cdot l_e \right) + 2 \cdot A_{mech} \cdot f_{ymech} \tag{3.16}$$

In the lateral force capacity equation, $P_{sm}$, the cross sectional area of the circumferential mechanism is $A_{mech}$ and the yield stress of the mechanism is $f_{ymech}$. The plastic hinge length, $l_f$, and the height through which the steel shell deforms, $l_e$, are determined with experimental results as presented in Section 6.10.

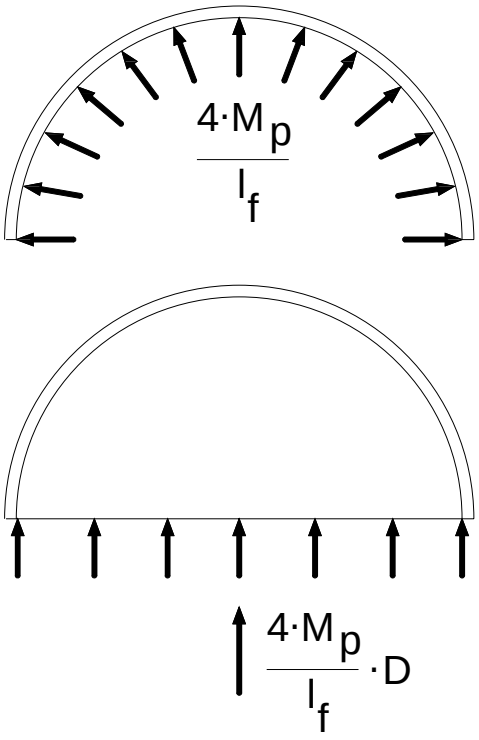


**Figure 3.4 Lateral Pressure and Resultant Force Exerted by Plastic Hinges**

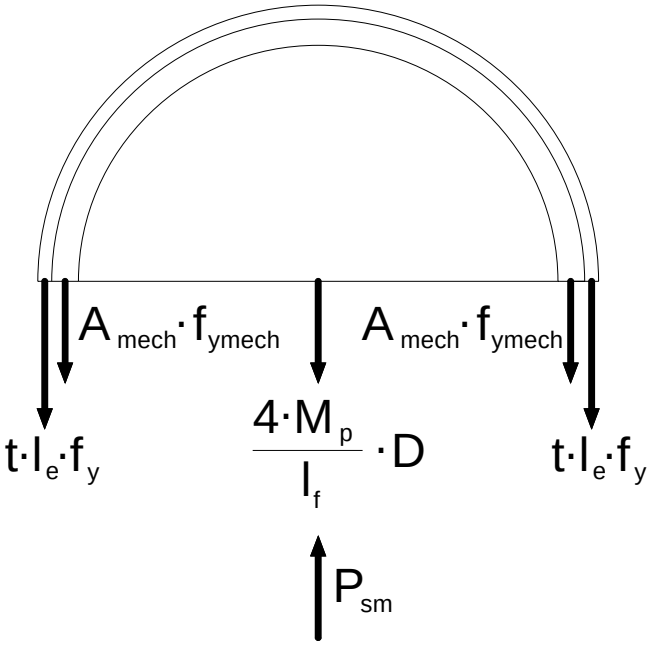


**Figure 3.5 Free Body Diagram for the Steel Shell and Mechanism Capacity**

The axial force capacity, $P_{sm-axial}$, of the steel shell and the mechanism is obtained with the trigonometric relationship shown in Figure 3.6 and is stated as:

$$P_{sm-axial} = \left( \frac{P_{sm}}{\tan(\alpha)} \right) \tag{3.17}$$

The angle $\alpha$ is the angle at which the resultant axial force transfer strut occurs as shown in Figure 3.6. This angle is determined with experimental results as presented in Section 6.10.

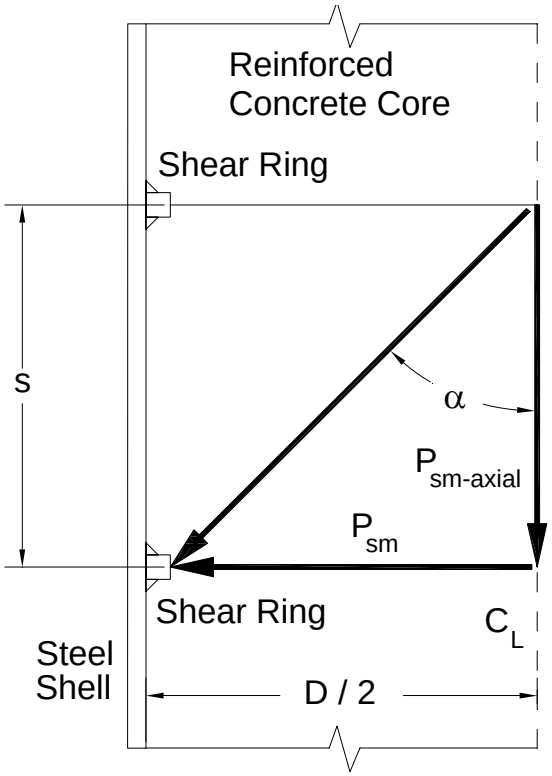


**Figure 3.6 Shear Ring Spacing**

### 3.3.3 Mechanism Quantity and Spacing for the Steel Shell and Mechanism Capacity Prediction

If the steel shell and mechanism capacity, $P_{sm-axial}$, governs the failure mode and is less than the applied axial force then multiple circumferential mechanisms are needed. The quantity of mechanisms, $N_{mech}$, required is determined by division of the product of the applied axial force, $P$, (to be transferred through mechanisms) and a factor of safety, $FS$, by the mechanism axial force capacity, $P_{sm-axial}$, as stated:

$$N_{mech} = \left( \frac{P \cdot FS}{P_{sm-axial}} \right) \tag{3.18}$$

In Equation 3.18 it is up to the designers discretion to determine a reasonable factor of safety, $FS$, to use. This factor of safety should account for the mechanism fabrication quality. In addition, if it is desired to have the pile remain within the elastic range then the factor of safety should increase the applied axial force, $P$, to ensure an elastic response (and no plastic hinge formation). In Equation 3.18 the applied axial force, $P$, cannot exceed the concrete core capacity or the steel shell capacity as stated in the condition below. The applied axial compression or axial tension forces are typically in the range of 2 – 20% of the concrete core capacity.

$$P < \left\{ \begin{array}{c} \left( \frac{\pi \cdot D^2 \cdot f_c^{'}}{4} \right) \\ \left( \frac{\pi}{4} \right) \cdot \left( (D + 2 \cdot t)^2 - D^2 \right) \cdot f_y \end{array} \right\} \tag{3.19}$$

If the mechanism spacing is too close than the steel shell section between the plastic hinge zones, with a length $l_r$, (as shown in Figure 3.7) will provide an insufficient restraining force to prevent this section from deforming out-of-plane with the shear rings. In this case the two plastic hinges between the shear rings will not develop. The resulting steel shell deformation could diminish the effectiveness of the shear rings. However, if the spacing between the plastic hinge zones, $l_r$, is adequate than the expected plastic hinge formations will develop as shown in Figure 3.7. The spacing between the plastic hinge zones, $l_r$, is estimated with an equilibrium of the forces in the free-body diagram of Figure 3.7.

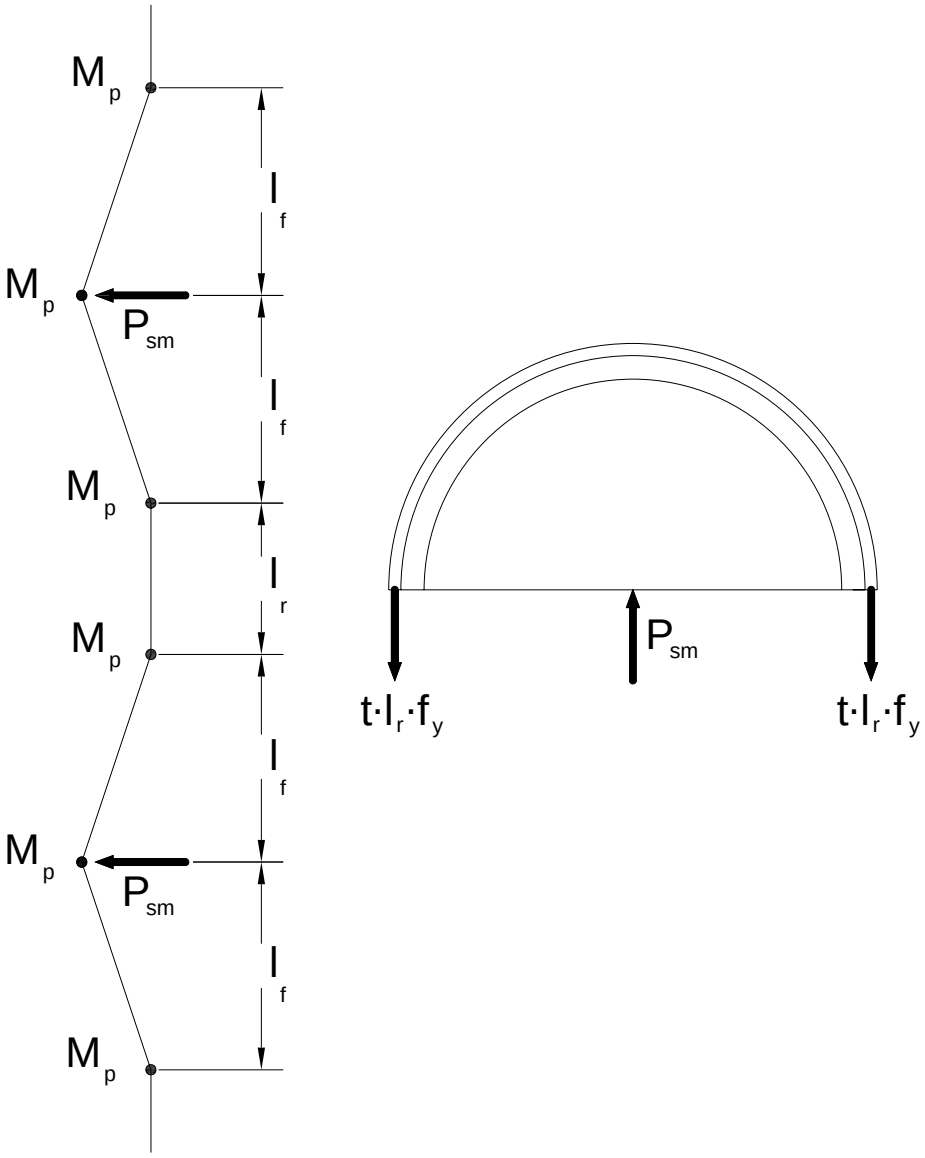


**Figure 3.7 Spacing between Plastic Hinges Zones**

Solving the force equilibrium for $l_r$ results in:

$$l_r = \left( \frac{P_{sm}}{2 \cdot t \cdot f_y} \right) \tag{3.20}$$

Substitution of Equation 3.16 into 3.20 results in:

$$l_r = 2 \cdot l_e + \left( \frac{t \cdot D}{l_f} \right) + \left( \frac{A_{mech}}{t} \right) \tag{3.21}$$

Experimental results are used to determine $l_e$ and $l_f$, and is presented in Section 6.10. The center to center spacing between circumferential mechanisms, $s$, is the sum of the spacing between the plastic hinge zones, $l_r$, and the distance between the plastic hinges, $2 \cdot l_f$, as shown in Figure 3.7 and as stated:

$$s = l_r + 2 \cdot l_f \tag{3.26}$$

This equation represents the minimum required spacing to allow for the plastic hinge formation to develop.

### 3.3.4 Concrete Capacity Prediction

The elastic capacity of the concrete core is determined by assuming the concrete core to be locked in place due to the presence of a mechanism. In this condition, no concrete has crushed. This locked condition will result in the steel shell providing a lateral confinement pressure on the concrete core, $\sigma_3$, as shown in Figure 3.8. This confinement pressure will increase the axial stress in the concrete core, $\sigma_1$, as stated:

$$\sigma_1 = f_c^{'} + k \cdot \sigma_3 \tag{3.27}$$

In Equation 3.27 the constant, $k$, is assumed to have a value of 4 as determined by Richart, *et al*. (1928). The lateral confinement from the steel shell can be obtained by examining the free body diagram of Figure 3.8. For a unit height of 1, the confinement of the steel shell is the product of twice the thickness and the yield stress of the steel shell. This confinement can be equated to the product of the diameter and the internal pressure, $\sigma_3$. Equilibrium of these forces, and solving for $\sigma_3$ results in:

$$\sigma_3 = \left( \frac{2 \cdot t \cdot f_y}{D} \right) \tag{3.28}$$

Substitution of Equation 3.28 into Equation 3.27, results in the concrete axial stress, at the circumferential mechanism, as stated:

$$\sigma_1 = f_c^{'} + k \cdot \left( \frac{2 \cdot t \cdot f_y}{D} \right) \tag{3.29}$$

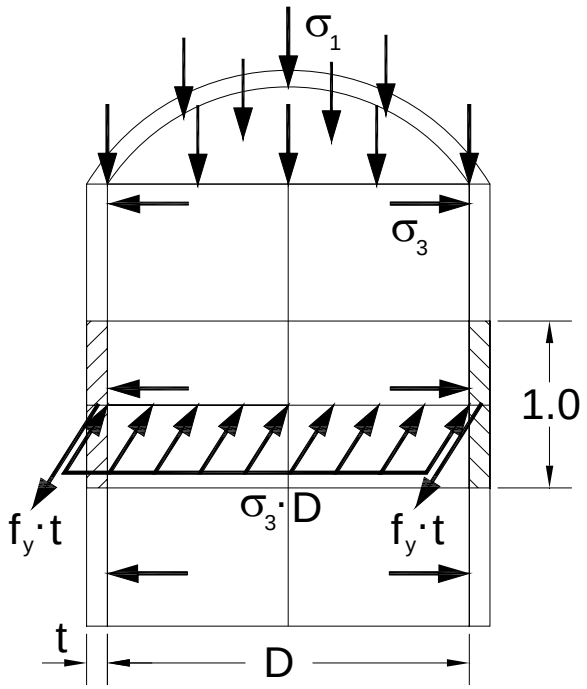


**Figure 3.8 Lateral Pressure Exerted by the Steel Shell on the Concrete Core**

This predicted axial stress, $\sigma_1$, is the stress in the concrete at the mechanism location after which crushing and displacement of the core will initiate. The product of this axial stress and the mechanism surface area perpendicular to the concrete core predicts the mechanism axial force capacity, $P_{cm}$. In the case of a shear ring mechanism, the mechanism axial force capacity is determined with Equation 3.30, in which $t_{ring}$ is the radial thickness of the shear ring.

$$P_{cm} = \left(\frac{\pi}{4}\right) \cdot \left(D^2 - \left(D - 2 \cdot t_{ring}\right)^2\right) \cdot \left(f_c^{'} + k \cdot \left(\frac{2 \cdot t \cdot f_y}{D}\right)\right) \tag{3.30}$$

In the case where multiple circumferential mechanisms are required, the mechanism spacing will have an effect on the efficiency of the mechanisms. As the circumferential mechanism spacing decreases, the angle, $\alpha$, at which the resultant force acts increases, and the vertical (axial) force transferred into the lower mechanism, $P_{cm-lower}$, will decrease. This force is related to the mechanism axial force capacity, $P_{cm}$, through division by the tangent of the angle $\alpha$ as stated in Equation 3.31.

$$P_{cm-lower} = \left( \frac{P_{cm}}{\tan(\alpha)} \right) \tag{3.31}$$

If the spacing provides an angle of $\alpha$ equal to $45^{o}$ (one half of the steel shell diameter) the axial force transferred into the lower mechanism, $P_{cm-lower}$, will equal $P_{cm}$. However, for larger diameter piles this spacing of D/2 results in a high spacing which might not be needed. An alternative relationship for the spacing is to relate the spacing with the distance between the mechanism face and the longitudinal reinforcement, $t_{cover}$, as shown in Figure 3.9. A strut and tie mechanism will form between the circumferential mechanisms and the longitudinal reinforcement as shown in Figure 3.9. As axial tension is applied to the longitudinal reinforcement a tension tie will form between the mechanism and the upper section of the reinforcement. A compression strut will form between the mechanism and lower section of the reinforcement. The tension tie and compression strut are assumed to develop at the same angle, $\beta$, as shown in Figure 3.9. This angle will be determined through testing to allow for determination of recommendations for spacing at which mechanisms behave independently.

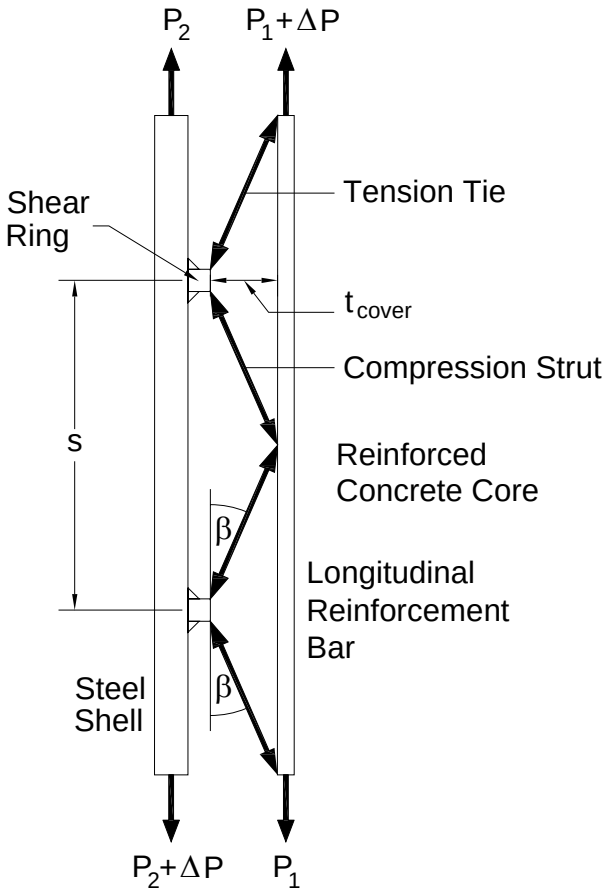


**Figure 3.9 Shear Ring Spacing at a Low D/t Ratio**

The mechanism which has the first contact with the applied axial force will be assumed to be fully effective, such that the axial force transfer predicted with Equation 3.30 is obtained. The axial force transfer obtained in the lower mechanism, $P_{cm-lower}$, at a spacing, $s$, is estimated by substitution of Equation 3.30 into Equation 3.31 as stated:

$$P_{cm-lower} = \left(\frac{\pi}{4}\right)\cdot\left(D^2 - \left(D - 2\cdot t_{ring}\right)^2\right)\cdot\left(f_c^{'} + k\cdot\left(\frac{2\cdot t\cdot f_y}{D}\right)\right)\cdot\left(\frac{1}{\tan(\alpha)}\right) \tag{3.32}$$

Equation 3.32 can also be expressed in terms of the axial stress on the lower circumferential mechanism, as stated:

$$\sigma_{cm-lower} = \left(f_c^{'} + k\cdot\left(\frac{2\cdot t\cdot f_y}{D}\right)\right)\cdot\left(\frac{1}{\tan(\alpha)}\right) \tag{3.33}$$

The prediction of the axial force transfer through multiple shear rings will be compared to experimental results in Section 6.11.

### 3.3.5 Mechanism Quantity for Concrete Capacity Prediction

The quantity of mechanisms can be determined using a similar procedure as presented in Section 3.3.3 and in Equation 3.18. In this case the concrete capacity at the mechanism, $P_{cm}$, governs. If the applied loading is greater than the concrete capacity at the mechanism, $P_{cm}$, then multiple mechanisms are needed. However, in this case the axial force transfer through mechanisms below the first mechanism resisting the applied loading is $P_{cm-lower}$. This axial force transfer, $P_{cm-lower}$, can be less than $P_{cm}$ depending on the spacing. The axial forces transferred through mechanisms are equated to the applied axial force, $P$, and a factor of safety, $FS$, as stated:

$$P_{cm} + \left(N_{mech-lower} \cdot P_{cm-lower}\right) = P \cdot FS \tag{3.34}$$

In the above equation the quantity of mechanisms below the first mechanism resisting the applied loading is $N_{mech-lower}$. Solving Equation 3.34 for $N_{mech-lower}$ result in:

$$N_{mech-lower} = \left(\frac{P \cdot FS - P_{cm}}{P_{cm-lower}}\right) \tag{3.35}$$

The total quantity of mechanisms is the summation of lower mechanisms, $N_{mech-lower}$, and the one upper mechanism a stated:

$$N_{mech} = 1 + N_{mech-lower} \tag{3.36}$$

Substitution of Equation 3.35 into 3.36 results in the following equation for the total number of mechanisms:

$$N_{mech} = 1 + \left(\frac{P \cdot FS - P_{cm}}{P_{cm-lower}}\right) \tag{3.37}$$

If the axial force transfer through the lower mechanisms, $P_{cm-lower}$, is equal to $P_{cm}$ than Equation 3.37 simplifies to:

$$N_{mech} = \left(\frac{P \cdot FS}{P_{cm}}\right) \tag{3.38}$$

## 3.4 Mechanisms Distributed within the Steel Shell

Mechanisms which are distributed within the steel shell, such as a series of shear studs, are prone to fail at the connection. This type of mechanism has a small contact area with the steel shell, which results in a minor weld. The shear capacity of the shear stud weld, $V_{stud}$, is calculated based on the weld electrode strength, $F_{exx}$, the throat size, $a$, and the diameter as stated below:

$$V_{stud} = \pi \cdot D_{stud} \cdot a \cdot 0.75 \cdot (0.6 \cdot F_{exx}) \tag{3.39}$$

The quantity of shear studs, $N_{studs}$, is determined by dividing the product of the applied axial force, $P$, and a factor of safety, $FS$, by the shear stud capacity, $V_{stud}$:

$$N_{studs} = \left( \frac{P \cdot FS}{V_{stud}} \right) \tag{3.40}$$

A description of the selection of the factor of safety, $FS$, is presented in Section 3.3.3.

## 3.5 Steel Shell Deformation at Mechanism Location

If the steel shell capacity is obtained at the location of a circumferential mechanism, as presented in Section 3.3.2, than an out-of-plane deformation occurs. This deformation is predicted by analyzing one half of the deformed profile as a cantilevered beam, as shown in Figure 3.10, with a fixed support condition at one end and a rigid guide block at the other support. The rigid guide block allows for a displacement, but no rotation. The expected deformation of this cantilevered beam is also shown in Figure 3.10. This represents one half of the theoretical out-of-plane deformation of the steel shell, at the mechanism location. The mechanism is assumed at the guide support location. The solution to this problem can be obtained from most mechanics of materials textbooks, such as Craig (1996), and is explained in greater detail here within.

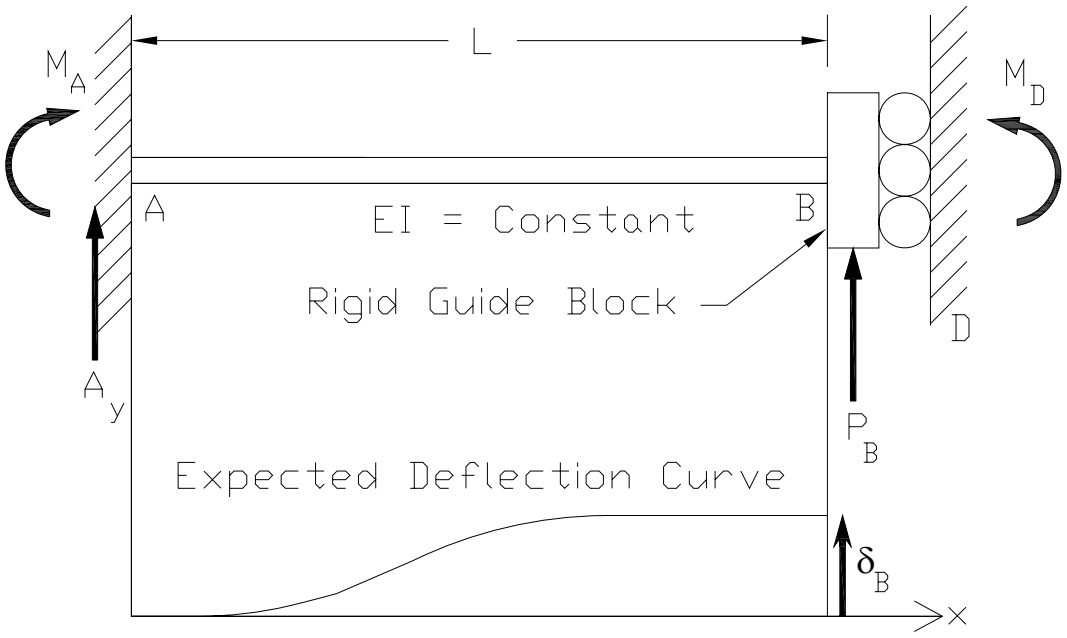


**Figure 3.10 Cantilevered Beam with Rigid Guide Block Support (right) and Expected Deformation (bottom)**

The deformed shape is predicted by integration of the fourth order load-deflection equation, as stated:

$$P = E \cdot I \cdot \frac{d^4 v}{dx^4} \tag{3.41}$$

In Equation 3.41, $E$ is the elastic modulus of the beam material, $I$ is the moment of inertia of the beam material, $v$ is the deformation, and $x$ is the distance from the fixed end support. This relationship can be derived from the moment-curvature relationship, $M - \phi$, the load-shear relationship, $P - V$, and the moment-shear relationship, $M - V$, as stated in the equations:

$$M = E \cdot I \cdot \frac{d^2 v}{dx^2} = E \cdot I \cdot \phi \tag{3.42}$$

$$P = \frac{dV}{dx} \tag{3.43}$$

$$V = \frac{dM}{dx} \tag{3.44}$$

The boundary conditions for integration of the load-deflection equation are:

Deflection: $v(x = 0) = 0$ (3.45)

Reaction: $$V(x = L) = -P_B \tag{3.46}$$

Slope: $$\frac{dv}{dx}(x = 0) = 0 \tag{3.47}$$

Slope: $$\frac{dv}{dx}(x = L) = 0 \tag{3.48}$$

Load: $$P(x) = 0 \tag{3.49}$$

It should be noted that in the boundary condition for the load (Equation 3.49) there is no distributed load on the beam. However, there is a reaction at the guide support, as shown in the boundary condition of Equation 3.46. In the boundary conditions presented in Equations 3.46 and 3.48, $L$, is one half of the length of the steel shell deformation, or the deformation of the cantilevered beam as shown in Figure 3.9. Substitution of Equation 3.49 into the load-deflection relationship, of Equation 3.41, results in:

$$P = E \cdot I \cdot \frac{d^4 v}{dx^4} = 0 \tag{3.50}$$

The first integration of the above equation results in the shear equation:

$$V = \int P dx = E \cdot I \cdot \frac{d^3 v}{dx^3} = C_1 \tag{3.51}$$

The second integration results in the moment equation:

$$M = \int V dx = E \cdot I \cdot \frac{d^2 v}{dx^2} = C_1 \cdot x + C_2 \tag{3.52}$$

The third integration results in:

$$E \cdot I \cdot \frac{dv}{dx} = \left( \frac{C_1 \cdot x^2}{2} \right) + C_2 \cdot x + C_3 \tag{3.53}$$

The fourth and final integration results in:

$$E \cdot I \cdot v = \left( \frac{C_1 \cdot x^3}{6} \right) + \left( \frac{C_2 \cdot x^2}{2} \right) + C_3 \cdot x + C_4 \tag{3.54}$$

Application of the boundary conditions presented in Equations 3.45 – 3.48 to the differential equations above, results in constants $C_1$, $C_2$, $C_3$, and $C_4$ as stated:

$$C_1 = -P_B \tag{3.55}$$

$$C_2 = \left( \frac{P_B \cdot L}{2} \right) \tag{3.56}$$

$$C_3 = 0 \tag{3.57}$$

$$C_4 = 0 \tag{3.58}$$

Substitution of the above constants into Equation 3.54 and solving for the deflection, $v$, results in the prediction presented in Equation 3.59. Substitution of the constants into Equation 3.53, and solving for the slope, $\theta$, results in the prediction presented in Equation 3.60.

$$v = \left( \frac{P_B \cdot L^3}{12 \cdot E \cdot I} \right) \cdot \left( -2 \cdot \left( \frac{x}{L} \right)^3 + 3 \cdot \left( \frac{x}{L} \right)^2 \right) \tag{3.59}$$

$$\theta = \left( \frac{P_B \cdot L^2}{2 \cdot E \cdot I} \right) \cdot \left( -\left( \frac{x}{L} \right)^2 + \left( \frac{x}{L} \right) \right) \tag{3.60}$$

## 3.6 Summary

This chapter presents the theory for the prediction of the axial force transfer through surface bond and through a circumferential mechanism. The initial surface bond, which includes an adhesive bond, can be predicted using strain compatibility as restated below from Equation 3.5. After the initial bond is overcome, the adhesive bond diminishes, resulting in a frictional bond, as restated below from Equation 3.7.

$$P_{sc} = \varepsilon_c \cdot \left( E_c \cdot A_{core} + E_{shell} \cdot A_{shell} \right) \tag{3.5}$$

$$P_{fric} = \varepsilon_c \cdot E_c \cdot A_{core} \tag{3.7}$$

The use of circumferential mechanisms will result in either obtaining the steel shell and mechanism capacity or the concrete capacity at the mechanism. The steel shell and mechanism capacity is predicted using a plastic hinge formulation as restated below from Equation 3.16. The plastic hinge zones should have a vertical spacing, $l_r$, as restated below from Equation 3.21. The mechanisms should have a center-to-center spacing, $s$, as restated from Equation 3.26. Experimental results will be used to determine $l_e$ and $l_f$, as presented in Section 6.10.

$$P_{sm} = t \cdot f_y \cdot \left( \frac{t \cdot D}{l_f} + 2 \cdot l_e \right) + 2 \cdot A_{mech} \cdot f_{ymech} \tag{3.16}$$

$$l_r = 2 \cdot l_e + \left( \frac{t \cdot D}{l_f} \right) + \left( \frac{A_{mech}}{t} \right) \tag{3.21}$$

$$s = l_r + 2 \cdot l_f \tag{3.26}$$

$$N_{mech} = \left( \frac{P \cdot FS}{P_{sm-axial}} \right) \tag{3.18}$$

In the case in which the steel shell capacity exceeds the concrete core capacity the axial force transfer through a circumferential mechanism is estimated with Equation 3.30. The quantity of circumferential mechanisms is estimated with Equation 3.18. The axial force transfer through mechanisms, below the uppermost mechanism resisting axial force, is predicted with Equation 3.32 as restated below.

$$P_{cm} = \left( \frac{\pi}{4} \right) \cdot \left( D^2 - \left( D - 2 \cdot t_{ring} \right)^2 \right) \cdot \left( f_c^{'} + k \cdot \left( \frac{2 \cdot t \cdot f_y}{D} \right) \right) \tag{3.30}$$

$$P_{cm-lower} = \left( \frac{\pi}{4} \right) \cdot \left( D^2 - \left( D - 2 \cdot t_{ring} \right)^2 \right) \cdot \left( f_c^{'} + k \cdot \left( \frac{2 \cdot t \cdot f_y}{D} \right) \right) \cdot \left( \frac{1}{\tan(\alpha)} \right) \tag{3.32}$$

$$N_{mech} = 1 + \left( \frac{P \cdot FS - P_{cm}}{P_{cm-lower}} \right) \tag{3.37}$$

If the capacity of the steel shell and mechanism through the plastic hinge formulation (Equation 3.16) is obtained than circumferential yielding occurs. This circumferential yielding of the steel shell and mechanism is predicted with the deflection and slope equations (Equations 3.59 and 3.60) as restated below.

$$v = \left( \frac{P_B \cdot L^3}{12 \cdot E \cdot I} \right) \cdot \left( -2 \cdot \left( \frac{x}{L} \right)^3 + 3 \cdot \left( \frac{x}{L} \right)^2 \right) \tag{3.59}$$

$$\theta = \left( \frac{P_B \cdot L^2}{2 \cdot E \cdot I} \right) \cdot \left( -\left( \frac{x}{L} \right)^2 + \left( \frac{x}{L} \right) \right) \tag{3.60}$$

The theory restated above for predicting the axial force transfer through surface bond, through a circumferential mechanism, and through multiple circumferential mechanisms will be compared to experimental results in Chapter 7.0.

# 4 EXPERIMENTAL PROGRAM

## 4.1 Introduction

This chapter will present the parameters of study for the experimental program, the test unit design, the test setup, and the test protocol. The construction procedure for the test units is presented as well.

## 4.2 Test Specimens

The experimental program consisted of fifteen full-scale test units in a first phase of testing, followed by six test units in a second phase of testing, as listed in Table 4.1. In the first phase of testing five test units studied the effect of the D/t ratio, one test unit studied the surface condition, and three test units examined the effect of the D/t ratio on expansive concrete (Gebman *et al.*, 2004). Also in the first phase of testing six test units studied the mechanism design. The second phase of testing focused on the shear ring mechanism design (Gebman *et al.*, 2005). In this second phase, two test units studied the effect of the D/t ratio on the shear ring axial force transfer, three test units studied the effect of shear ring spacing, and one test unit studied the shear ring axial force transfer with a disbond between the steel shell and the concrete core.

Test units were designed to study the transfer of axial force from the reinforced concrete core to the steel shell through surface bond and through mechanisms. This is shown in the graphic of Figure 4.1 which depicts Test Unit # 17 with a single shear ring at a D/t ratio of 24. All test units had a void space inside the steel shell base with a height of 127 mm (5.0 in.), as shown in the graphic of Figure 4.1 and in the elevation view for Test Unit # 5 of Figure 4.2. This allowed free movement of the reinforced concrete core within the steel shell once the initial surface bond was broken. This void was provided to ensure that axial force was transferred only through the steel shell at the base of the test unit. Access openings were placed in the steel shell base, as shown in Figure 4.2, to allow for monitoring of the base void during testing, and to allow for any loose concrete at the base to fall out.

**Table 4.1 Test Unit Specifications**

| Test Unit # | Internal Diameter, D mm (in.) | Thickness, t mm (in.) | D/t | Steel Shell Length m (in.) | Bond Length m (in.) | Connection Type |
|---|---|---|---|---|---|---|
| 1 | 610 (24.0) | 4.8 (3/16) | 128 | 1.22 (48.0) | 1.09 (43.0) | None |
| 2 | 597 (23.5) | 6.4 (1/4) | 94 | 1.22 (48.0) | 1.09 (43.0) | None |
| 3 | 584 (23.0) | 12.7 (1/2) | 46 | 1.22 (48.0) | 1.09 (43.0) | None |
| 4 | 610 (24.0) | 4.8 (3/16) | 128 | 1.22 (48.0) | 1.09 (43.0) | Weld Bead |
| 5 | 610 (24.0) | 4.8 (3/16) | 128 | 1.22 (48.0) | 1.09 (43.0) | Shear Ring |
| 6 | 610 (24.0) | 4.8 (3/16) | 128 | 1.22 (48.0) | 1.09 (43.0) | Cross Bar |
| 7 | 610 (24.0) | 4.8 (3/16) | 128 | 1.22 (48.0) | 1.09 (43.0) | Welded Bar |
| 8 | 610 (24.0) | 4.8 (3/16) | 128 | 1.22 (48.0) | 1.09 (43.0) | Shear Studs |
| 9 | 610 (24.0) | 4.8 (3/16) | 128 | 1.22 (48.0) | 1.09 (43.0) | Tread Plate |
| 10 | 610 (24.0) | 4.8 (3/16) | 128 | 1.22 (48.0) | 1.09 (43.0) | Water-Bentonite |
| 11 | 387 (15.25) | 9.5 (3/8) | 40.7 | 1.22 (48.0) | 1.09 (43.0) | None |
| 12 | 387 (15.25) | 9.5 (3/8) | 40.7 | 1.22 (48.0) | 1.09 (43.0) | None |
| 13 | 610 (24.0) | 4.8 (3/16) | 128 | 1.22 (48.0) | 1.09 (43.0) | Expansive Concrete |
| 14 | 597 (23.5) | 6.4 (1/4) | 96 | 1.22 (48.0) | 1.09 (43.0) | Expansive Concrete |
| 15 | 584 (23.0) | 12.7 (1/2) | 46 | 1.22 (48.0) | 1.09 (43.0) | Expansive Concrete |
| 16 | 597 (23.5) | 6.35 (1/4) | 94 | 1.22 (48.0) | 1.09 (43.0) | Shear Ring |
| 17 | 610 (24.0) | 25.4 (1.0) | 24 | 1.22 (48.0) | 1.09 (43.0) | Shear Ring |
| 18 | 610 (24.0) | 25.4 (1.0) | 24 | 1.22 (48.0) | 1.09 (43.0) | Shear Ring |
| 19 | 610 (24.0) | 25.4 (1.0) | 24 | 1.52 (60.0) | 1.40 (55.0) | Shear Rings |
| 20 | 610 (24.0) | 25.4 (1.0) | 24 | 1.52 (60.0) | 1.40 (55.0) | Shear Rings |
| 21 | 610 (24.0) | 25.4 (1.0) | 24 | 1.52 (60.0) | 1.40 (55.0) | Shear Rings |

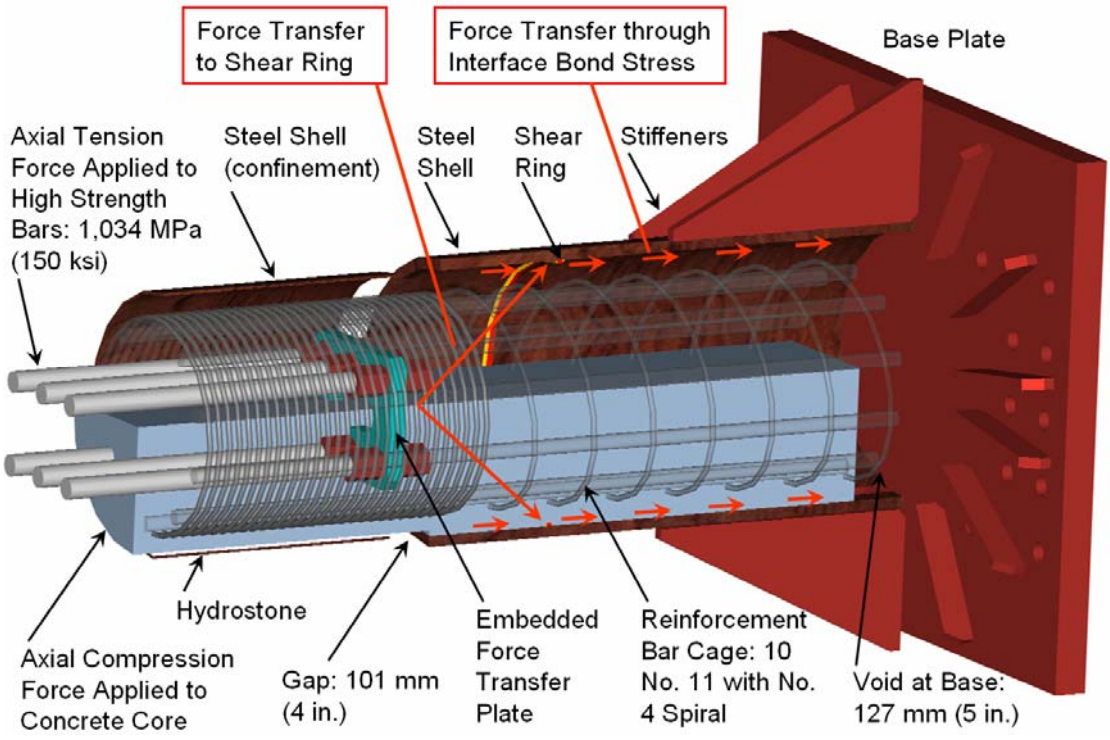


**Figure 4.1 Test Unit 3-D Perspective**

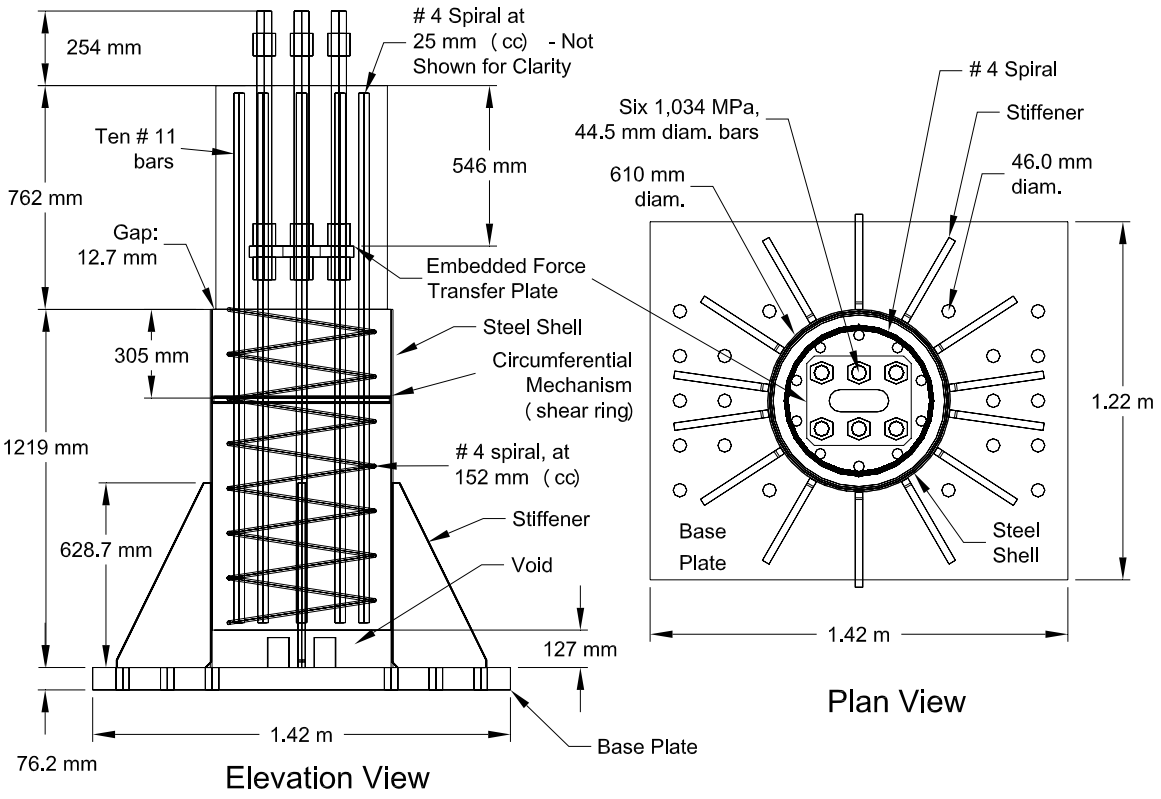


**Figure 4.2 Elevation and Plan Views for a Typical Test Unit with a Circumferential Mechanism (Test Units # 4, # 5, # 7 and # 16)**

At the top of each test unit, the reinforced concrete core extended 0.76 m (30.0 in.) beyond the steel shell to allow axial compression and tension force from the test setup to fully develop in the reinforced concrete core prior to its transfer to the steel shell. Special care was made in the design and construction of the test units to ensure the applied axial force would be carried by the reinforced concrete core, and transferred only through the mechanisms and bond with the steel shell interior surface. This was achieved by constructing the upper reinforced concrete force transfer section at a diameter slightly less than the internal diameter of the steel shell, as shown by the radial gap of 12.7 mm (0.5 in.) in Figure 4.2. This radial gap ensured that no axial force was transferred into the top of the steel shell as also shown in the photograph of a test unit with a D/t ratio of 24 in Figure 4.3.


**Figure 4.3 Radial Gap between the Concrete Core and Steel Shell (Top Surface)**

## 4.3 Phase I Experimental Program

The specifications for each test unit in the first phase of the experimental program are listed in Table 4.1. Test Unit #1 was used as a baseline case with a D/t ratio of 128. Test Units #1- #15, which comprised the first phase of the experimental program, all had a steel shell length of 1.22 m (48.0 in.). The steel shells for test units which had a mechanism along with steel shells for Test Units # 1, # 10 and # 13 were fabricated from rolled steel plate, A572 Grade 50. These steel shells had an internal diameter of 0.61 m (24 in.) and a thickness of 4.8 mm (0.19 in.) resulting in a D/t ratio of 128. These test units had a vertical seam weld as the steel shell was fabricated from a rolled plate.

### 4.3.1 Variation of the Steel Shell Diameter to Thickness Ratio

The effect of the D/t ratio on the surface bond axial force transfer was investigated with five test units with D/t ratios ranging from 128 to 40.7. A D/t ratio of 128 was used in Test Unit # 1 as previously mentioned. Test Unit # 2 had a D/t ratio of 94 which was obtained with a steel shell of internal diameter 0.60 m (23.5 in.) and a thickness of 6.4 mm (0.25 in.). Test Unit # 3 had a D/t ratio of 46 which was obtained with a steel shell of internal diameter 0.58 m (23.0 in.) and a thickness of 12.7 mm (0.5 in.). Test Unit # 3 and # 2 were similar to Test Unit # 1 with the only difference being the steel shell diameter and thickness. A plan view and elevation view for Test Units #1, # 2, and #3 is shown in Figure 4.4.

A D/t ratio of 40.7 was simulated in Test Units # 11 and # 12 with a steel shell internal diameter of 0.39 m (15.25 in.) and a thickness of 9.5 mm (0.38 in.). A plan view and elevation view for Test Units # 11 and # 12 are shown in Figure 4.5. Test units with D/t ratios of 40.7, 46 and 94 were fabricated from pipe sections of A53 Grade B.

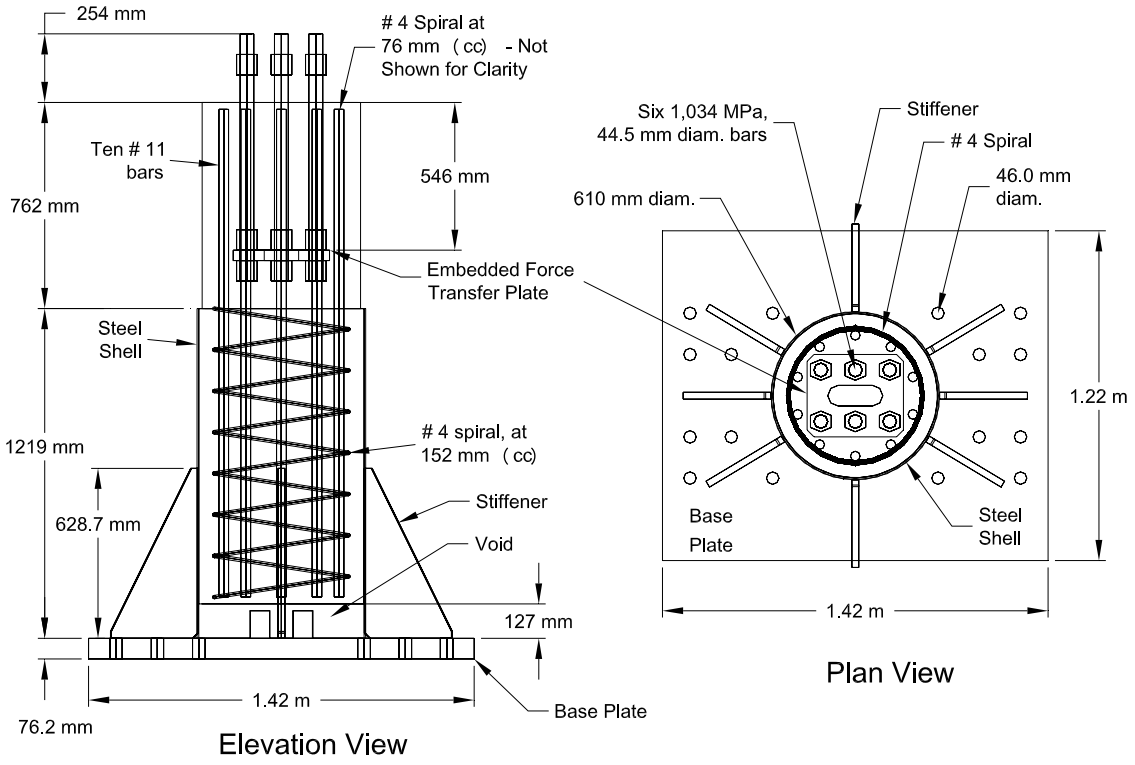


**Figure 4.4 Elevation and Plan Views of a Typical Test Unit without a Mechanism (Test Units #1, #2, #3, #10)**

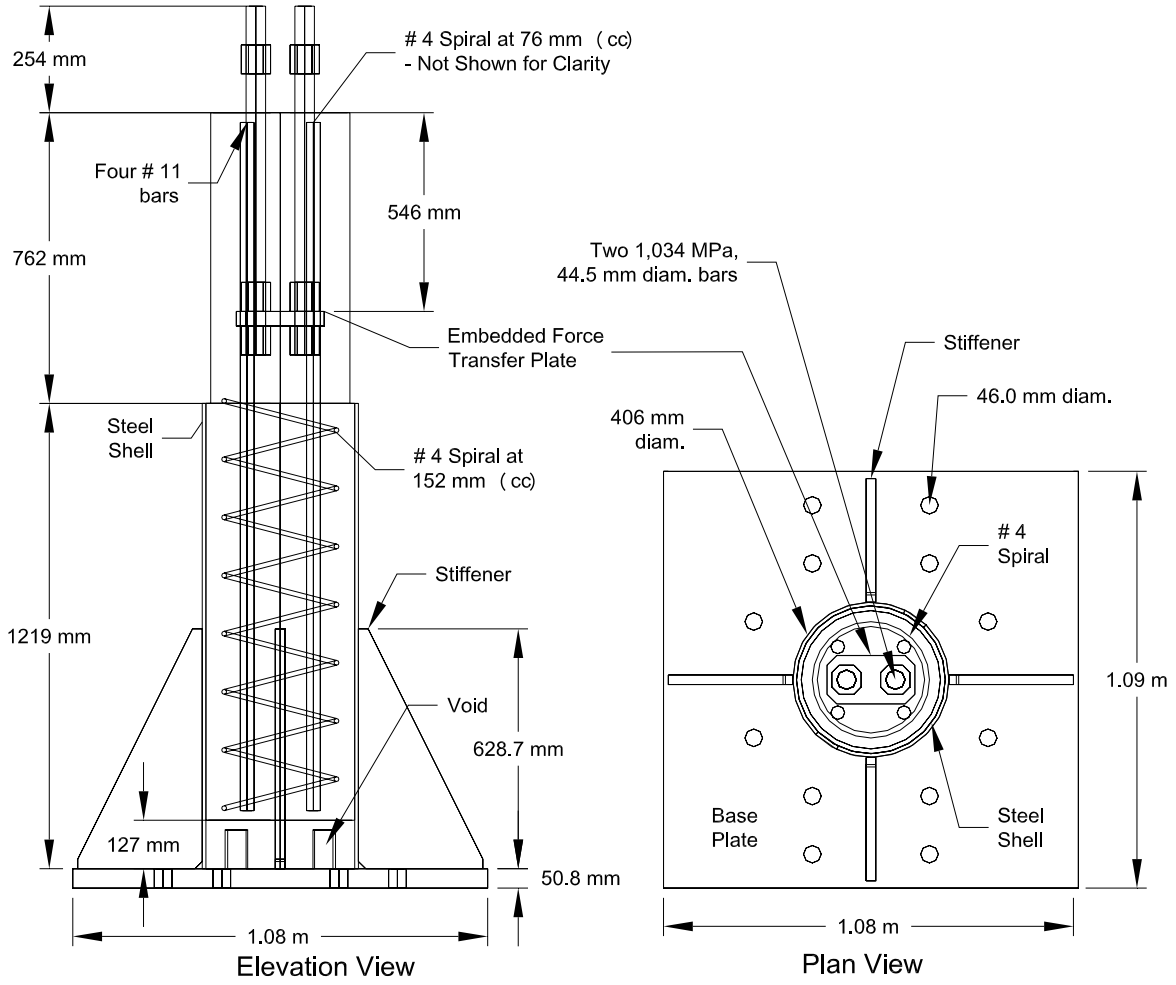


**Figure 4.5 Elevation and Plan Views of Test Units at a D/t Ratio of 40.7 (Test Units # 11 and # 12)**

### 4.3.2 Surface Condition

In the construction of some CISS piles, a drilling fluid or slurry polymer is temporarily placed within the steel shell for lateral support after the soil is removed. A reinforcement bar cage is placed within the steel shell containing the drilling fluid followed by concrete placement. This procedure can result in a slurry residue on the steel shell interior surface which can result in a reduction of bond between the reinforced concrete core and the steel shell. This effect was simulated in Test Unit #10 by coating the steel shell interior surface (D/t ratio of 128) and the reinforcement bar cage with a water-bentonite mixture prior to placement of the concrete. This coating is shown in

Figure 4.6 for the steel shell interior surface, and in Figure 4.7 for the reinforcement bar cage. A plan view and elevation view is shown in Figure 4.4 for this test unit.

**Figure 4.6 Water-Bentonite Coating on Steel Shell Internal Surface of Test Unit # 10**

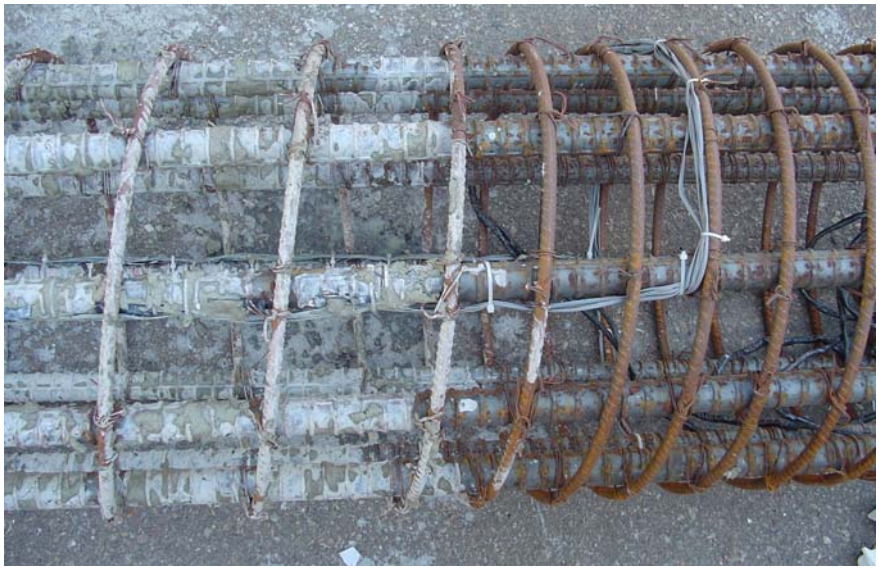

**Figure 4.7 Water-Bentonite Coating on Reinforcement Bar Cage Section Confined by Steel Shell (left) of Test Unit # 10**

### 4.3.3 Expansive Concrete

Test Units # 13, # 14, and # 15 were constructed with expansive concrete, and had D/t ratios of 128, 94 and 46, respectively to allow for comparison to Test Units # 1, # 2 and # 3. A plan view and elevation view for test units with expansive concrete is shown

in Figure 4.8. An expansive Type K cement was added at a quantity of 40.8 kg (90 lb) per 0.764 $m^3$ (1 cubic yard) of concrete. A concrete mix with an $f'_c$ of 14 MPa (2.0 ksi) was specified.

The addition of an expansive admixture to Portland Type II cement results in an ASTM C 845 Type K Cement. Upon mixing of this cement with water, ettringite will form, and will continue to form as the concrete sets and gains strength. Ettringite formation will stop when either the sulfite ($SO_3$) or aluminum oxide ($Al_2O_3$) is completely consumed. The formation of ettringite does not cause the concrete to expand in its volume instead the shrinkage is reduced as the concrete sets after immediate placement. During the drying phase shrinkage can occur, however, the shrinkage will be accompanied by a reduction in tensile stresses in the reinforcement (ACI, 2005).

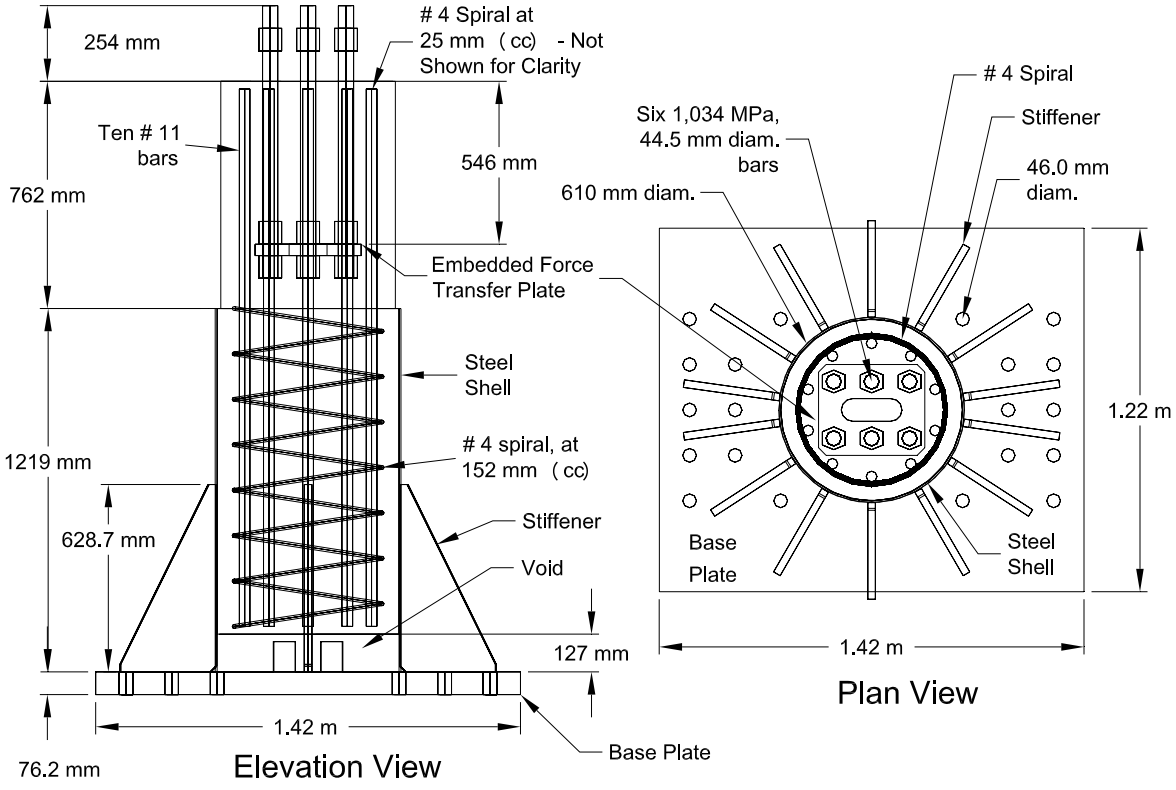


**Figure 4.8 Elevation and Plan Views for Test Units with Expansive Concrete (Test Units # 13, # 14 and # 15)**

### 4.3.4 Mechanism Designs Studied

Six types of mechanism designs were studied at a D/t ratio of 128 as shown in plan details in Figure 4.9 and in the photographs in Figure 4.10. Three mechanisms were welded circumferentially to the steel shell which consisted of a shear ring, a welded reinforcement bar, and a weld bead. Two mechanism designs were distributed throughout the steel shell, which consisted of shear studs, and tread plate. The sixth mechanism design studied was the cross bar which spanned the internal diameter of a steel shell, and passed through the reinforcement bar cage. Details of these mechanism designs will be presented in the following sections.

#### 4.3.4.1 Shear Ring

Test Unit #5 had a single shear ring with a cross section of 12.7 mm (0.50 in.) square as shown in Figures 4.9(a) and 4.10(a). The shear ring was fabricated from A 572 Grade 50 hot rolled flat bar bent to fit the internal diameter of the steel shell. The shear ring was placed at 0.3 m (12.0 in.) from the top of the steel shell which corresponds to D/2 as shown in the plans of Figure 4.2. This shear ring location allows for a compression strut to develop with a maximum expected angle of $45^{o}$ between the shear ring and the concrete core at the top of the steel shell. A continuous 4.8 mm (0.19 in.) fillet weld connected the top surface of the shear ring to the steel shell.

#### 4.3.4.2 Welded Reinforcement Bar

A single No. 3 reinforcement bar (Grade 60) with a diameter of 9.5 mm (0.38 in.) was placed within the steel shell of Test Unit # 7. This reinforcing bar was bent to fit the internal diameter of the steel shell. The reinforcing bar was welded circumferentially at 305 mm (12.0 in.) from the top of the steel shell with a continuous 4.8 mm (0.19 in.) fillet weld along the top face to the steel shell as shown in Figure 4.9(b) and 4.10(b). A plan view and elevation view for this test is shown in Figure 4.2.

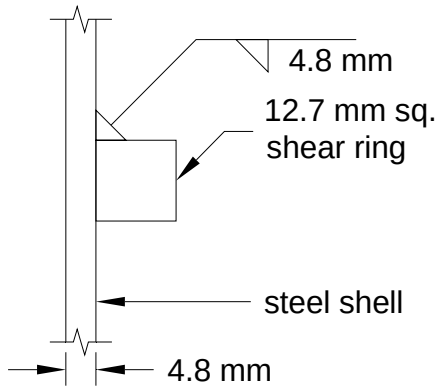


(a) Shear Ring - Elevation View

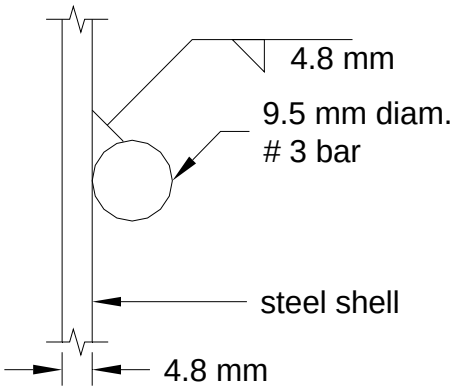


(b) Welded Bar - Elevation View

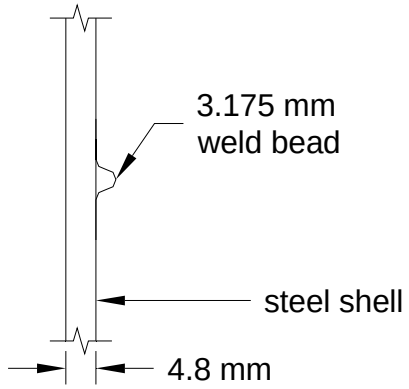


(c) Weld Bead - Elevation View

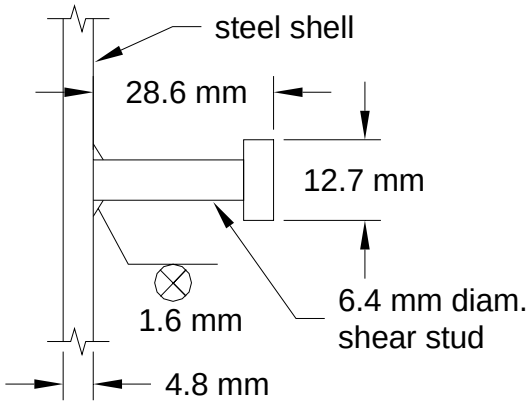


(d) Shear Stud - Elevation View

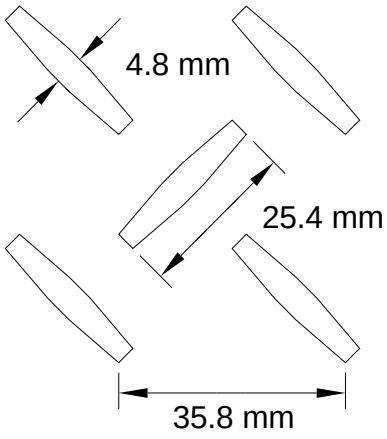


(e) Tread Plate - Elevation View

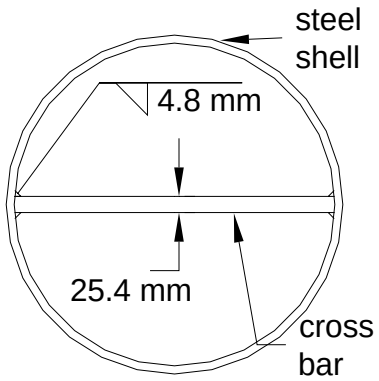


(f) Cross Bar - Plan View

**Figure 4.9 Mechanism Design Details**

(a) Shear Ring (After Test)

(b) Welded Bar (After Test)

(c) Weld Bead (After Test)

(d) Shear Studs (Fabrication)

(e) Tread Plate (After Test)

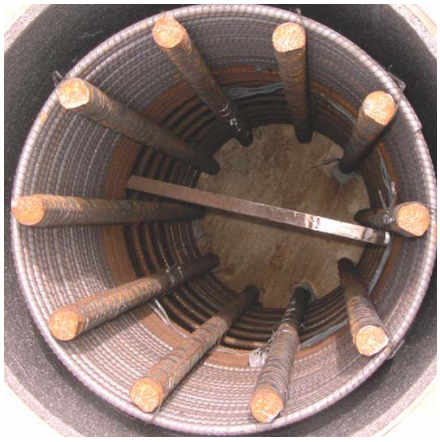

(f) Cross Bar (Fabrication)

**Figure 4.10 Mechanism Photographs**

#### 4.3.4.3 Weld Bead

A single weld bead with a size of 3.2 mm (0.13 in.), as shown in Figures 4.9(c) and 4.10(c) was placed circumferentially within the steel shell of Test Unit #4. The weld bead was placed at 305 mm (12.0 in.) from the top of the steel shell as shown in the plan view and elevation view in Figure 4.2.

#### 4.3.4.4 Shear Studs Mechanism

Twenty-one shear studs were placed within the steel shell of Test Unit #8 in an arrangement of three circumferential rows with seven studs evenly distributed per row. Studs were placed with a 76.2 mm (3.0 in.) vertical spacing and a 274.3 mm (10.8 in.) radial spacing. The uppermost row was at 0.3 m (12.0 in.) from the top of the steel shell which corresponds to D/2. This allows for a compression strut to develop with a maximum expected angle of $45^{o}$ between the shear studs and the concrete core at the top of the steel shell. The aforementioned distribution of shear studs was used to ensure independent behavior of the shear studs. Studs had a total length of 30.1 mm (1.19 in.), a diameter of 6.4 mm (0.25 in.), a head diameter of 12.7 mm (0.5 in.), and a head length of 4.8 mm (0.19 in.) as shown in Figures 4.9(d) and 4.10(d). Studs were fabricated from A108 steel with a minimum yield stress of 344.7 MPa (50 ksi). A plan view and elevation view for this test unit is shown in Figure 4.11.

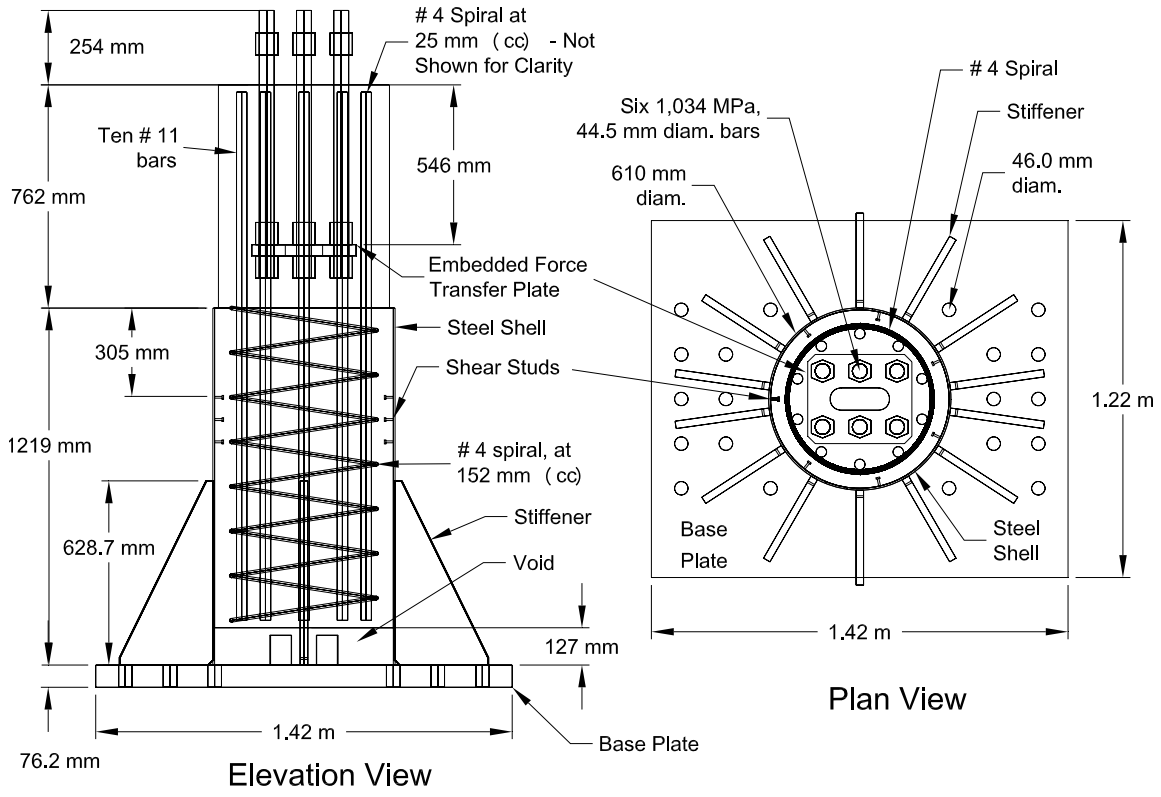


**Figure 4.11 Elevation and Plan Views for Test Unit # 8 with Shear Studs (tot. 21)**

### 4.3.4.5 Tread Plate Mechanism

Test Unit # 9 had a tread plate surface as shown in Figures 4.9(e) and 4.10(e). This test unit was fabricated using two steel shell sections. The lower non-test region was fabricated from a steel shell section using a rolled plate of A 572 Grade 50 with an internal diameter of 0.61 m (24.0 in.), a thickness of 4.8 mm (0.19 in.), and a height of 0.76 m (30 in.). A tread plate with a height of 0.46 m (18.0 in.) and a thickness of 6.4 mm (0.25 in.) was rolled and welded to form the upper steel shell section (test region). These two sections were welded together to form a steel shell with a height of 1.22 m (48.0 in.), similar to the other test units. The tread plate had approximately 1,695 treads each with a length of 25.4 mm (1.0 in.), and a depth of 2.54 mm (0.10 in.). A plan view and elevation view for this test is shown in Figure 4.12.

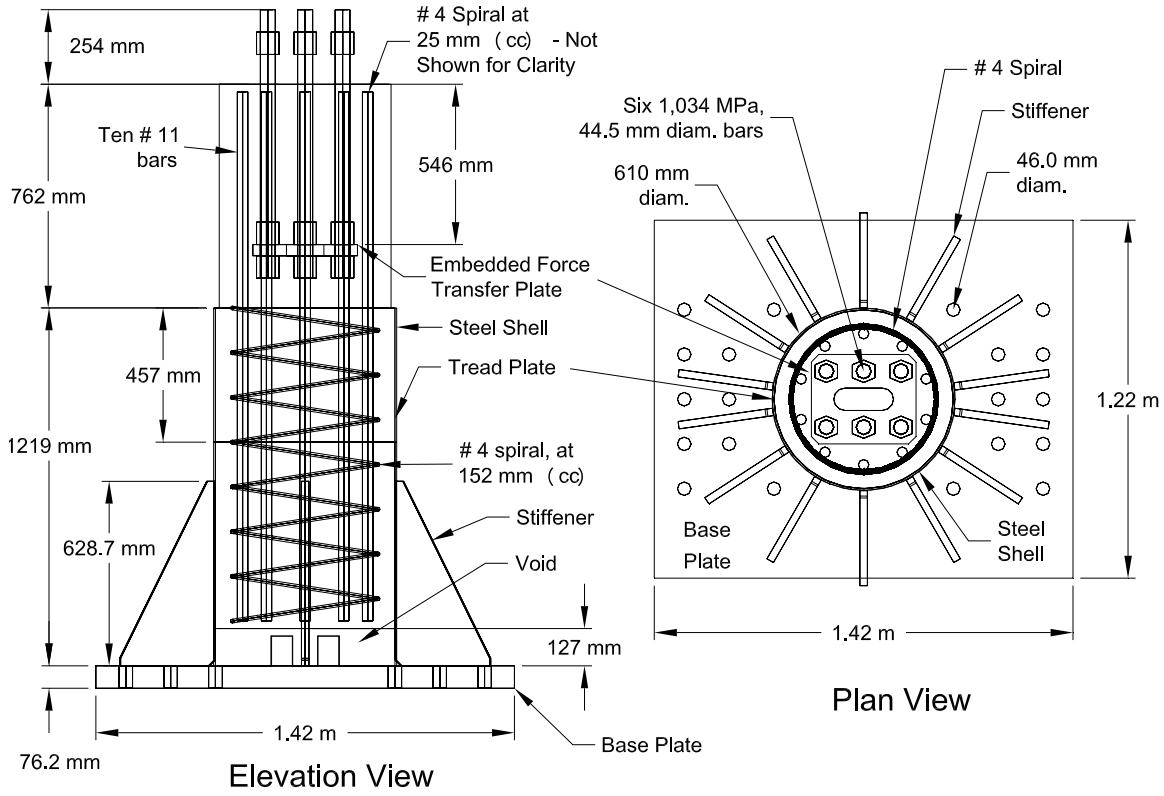


**Figure 4.12 Elevation and Plan Views for Test Unit # 9 with Tread Plate**

### 4.3.4.6 Cross Bar Mechanism

A single cross bar (A 572 Grade 50) was placed inside the reinforcement bar cage to span the internal diameter of a steel shell, of Test Unit #6, as shown in Figures 4.9(f) and 4.10(f). The cross bar had a cross section with a height of 50.8 mm (2.0 in.), and a width of 25.4 mm (1.0 in.). A vertical 4.8 mm (0.19 in.) fillet weld, connected the cross bar ends to the uppermost steel shell section, as shown in Figures 4.9(f). A plan view and elevation view for this test is shown in Figure 4.13.

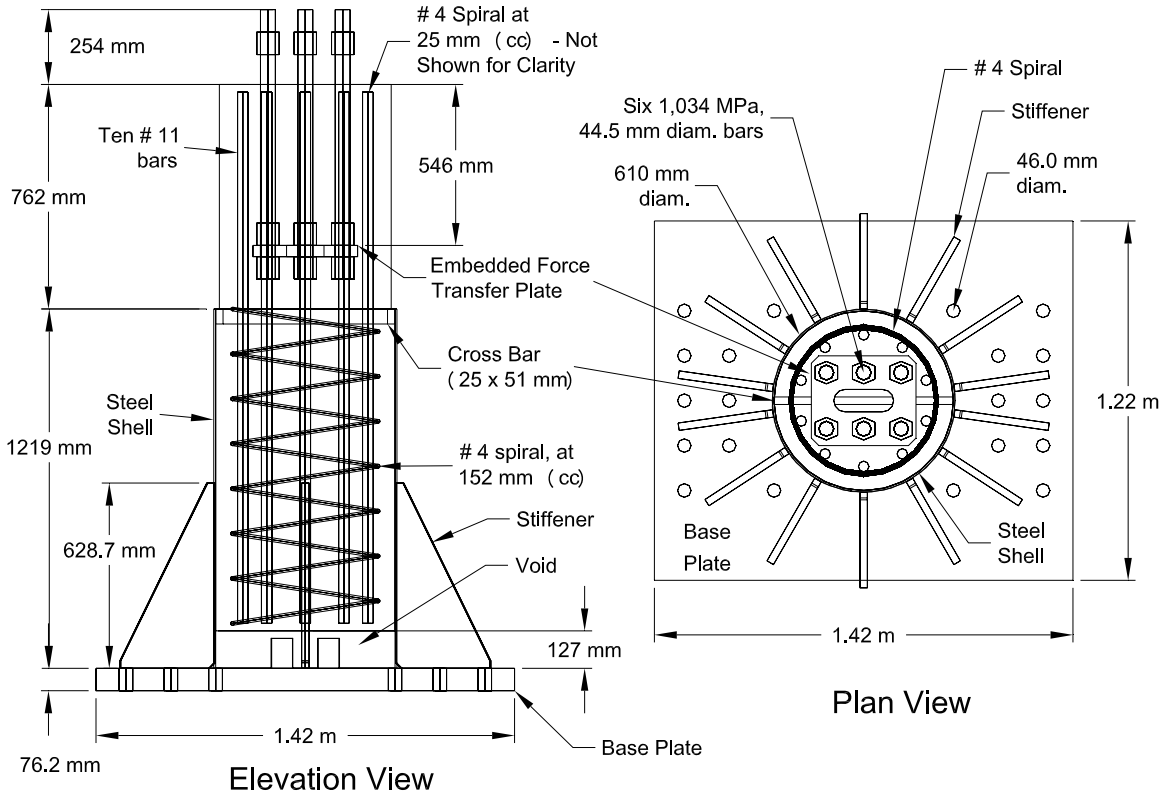


**Figure 4.13 Elevation and Plan Views for Test Unit # 6 with a Cross Bar**

## 4.4 Phase II Experimental Program

Results from the first phase of testing as presented in Chapter 5 indicated the shear ring mechanism to have the best overall axial force-axial displacement hysteretic behavior. To further evaluate the effectiveness of the shear ring at transferring axial force to the steel shell six 610 mm (24.0 in.) diameter test units were designed and tested under reversed cyclic axial loading as listed in Table 4.1. Three parameters were investigated in this phase of testing which included: the role of the D/t ratio on the axial force transfer through a shear ring, the effect of a disbond between the concrete core and the steel shell, and the effect of shear ring spacing. Table 4.2 lists the specifications for the shear rings in this second phase: Test Units # 16 - #21, along with the shear ring of Test Unit # 5 (from the first phase). A plan view and elevation view for Test Units # 17 - # 21 is shown in Figure 4.14. Photographs of the shear ring configurations for Test Units

# 16 - # 21 are shown in Figure 4.15. Details for the test units studied in this second phase of testing will be presented in the following sections.

**Table 4.2 Shear Ring Details**

| Test Unit # | Radial Width mm (in.) | Height mm (in.) | Quantity | Spacing mm (in.) | Fillet Weld mm (in.) | Weld Location |
|---|---|---|---|---|---|---|
| 5 | 12.7 (0.50) | 12.7 (0.50) | 1 | | 4.8 (0.19) | Top |
| 16 | 6.35 (0.25) | 12.7 (0.50) | 1 | | 6.4 (0.25) | Top and Bottom |
| 17 | 6.35 (0.25) | 12.7 (0.50) | 1 | | 6.4 (0.25) | Top and Bottom |
| 18 | 6.35 (0.25) | 12.7 (0.50) | 1 | | 6.4 (0.25) | Top and Bottom |
| 19 | 6.35 (0.25) | 12.7 (0.50) | 2 | 106 (3.0) | 6.4 (0.25) | Top and Bottom |
| 20 | 6.35 (0.25) | 12.7 (0.50) | 2 | 152 (6.0) | 6.4 (0.25) | Top and Bottom |
| 21 | 6.35 (0.25) | 12.7 (0.50) | 2 | 305 (12.0) | 6.4 (0.25) | Top and Bottom |

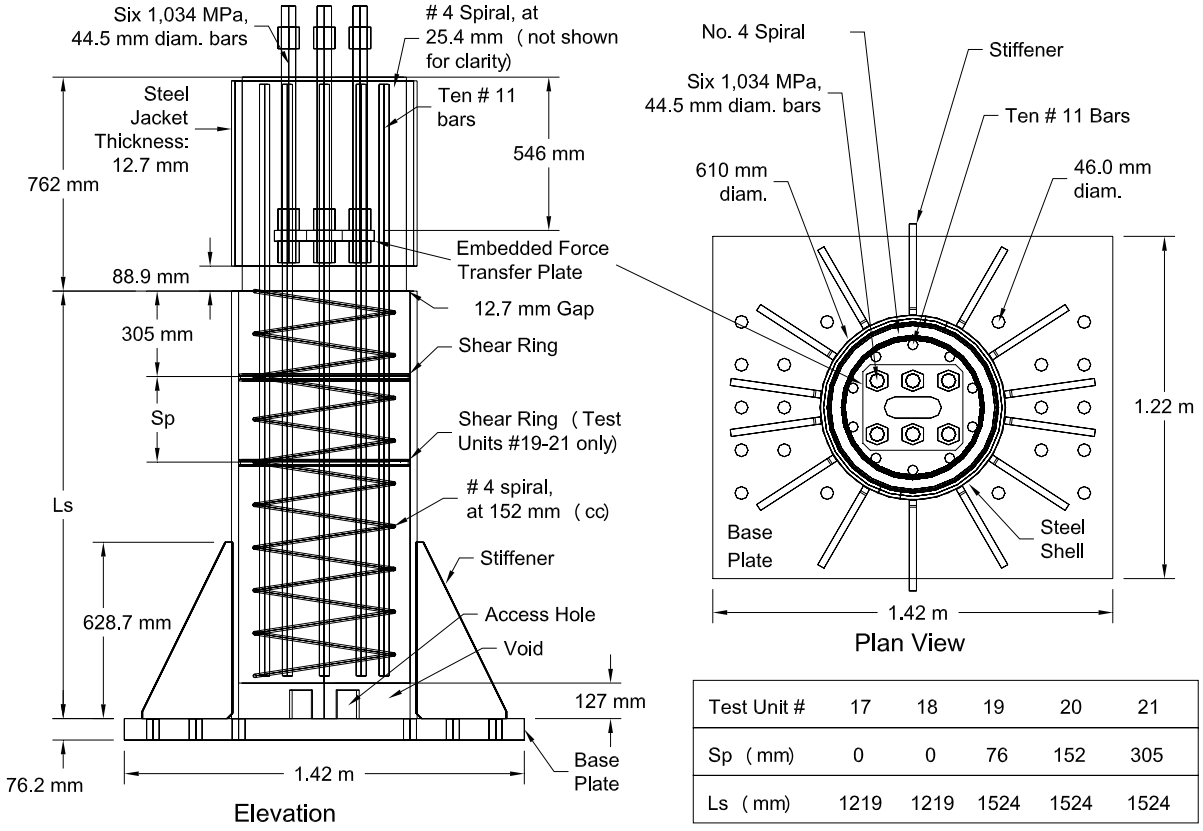


| Test Unit # | 17 | 18 | 19 | 20 | 21 |
|---|---|---|---|---|---|
| Sp (mm) | 0 | 0 | 76 | 152 | 305 |
| Ls (mm) | 1219 | 1219 | 1524 | 1524 | 1524 |

**Figure 4.14 Elevation and Plan Views for a Typical Test Unit of the Phase II Experimental Program (with Retrofit Steel Shell)**


(a) Test Unit # 16


(b) Test Unit # 17


(c) Test Unit # 18

(d) Test Unit # 19

(e) Test Unit # 20

(f) Test Unit # 21

**Figure 4.15 Shear Ring Placement**

### 4.4.1 Shear Rings for Test Units # 16-21

The shear rings for Test Units # 16-21 had a radial thickness, $t_{sr}$, of 6.4 mm (0.25 in.), a height, $h_{sr}$, of 13 mm (0.50 in.) and were fabricated from A 572 Grade 50 hot rolled flat bar bent to fit the internal diameter of the steel shell. Shear rings for Test Units # 16-21 were welded along the top and bottom of the shear ring with a continuous 6.4 mm (0.25 in.) fillet weld. Figure 4.16 shows a comparison of the shear ring details used in Test Unit # 5 and Test Units #16-21.

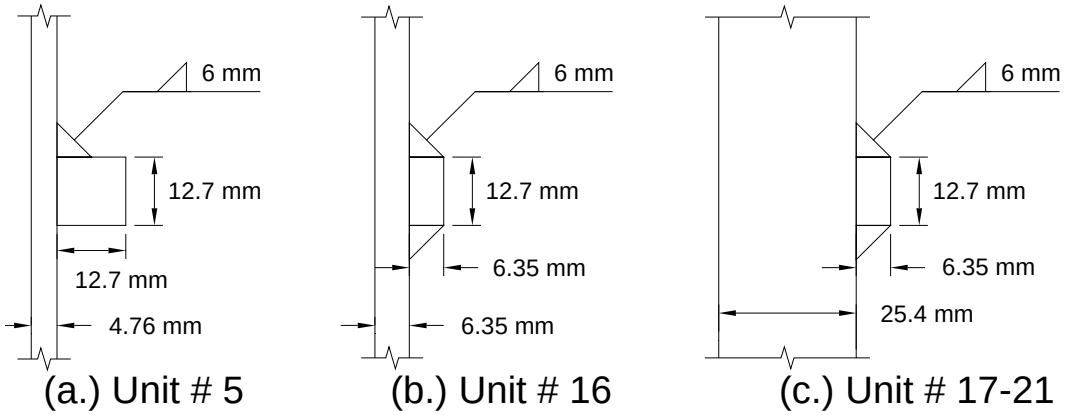


**Figure 4.16 Comparison of Shear Ring Design Details**

### 4.4.2 Test Unit # 16 at a D/t Ratio of 94

Test Unit # 16 investigated the shear ring axial force transfer capacity at a D/t ratio of 94 to complement previous shear ring testing (Test Unit # 5) at a D/t ratio of 128. A steel pipe section of A 53 Grade B with a length of 1.22 m (48.0 in.), an internal diameter of 0.60 m (23.5 in.), and a thickness of 6.4 mm (0.25 in.) was used. This test unit had a single shear ring at 305 mm (12.0 in.) from the top of the steel shell as shown in the plan view and elevation view in Figure 4.2.

### 4.4.3 Test Unit # 17 at a D/t Ratio of 24

Test Unit # 17 also investigated the shear ring axial force transfer capacity at a D/t ratio of 24 to complement results from Test Units # 5 and # 16. This test unit was

fabricated from a rolled steel plate, A 572 Grade 50, with a length of 1.22 m (48.0 in.), an internal diameter of 0.61 m (24.0 in.), and a thickness of 25.4 mm (1.0 in.). A single shear ring was located at 305 mm (12.0 in.) from the top of the steel shell as shown in Figure 4.14. It should be noted that Test Unit # 17 lacked a second steel shell (for additional confinement of the force transfer region) as shown in Figure 4.14.

### 4.4.4 Test Unit # 18 at a D/t Ratio of 24

Test Unit # 18 had the same steel shell specification and shear ring placement as Test Unit # 17. However, a polyethylene lining was placed within the steel shell of Test Unit # 18 to minimize the bond between the reinforced concrete core and the steel shell so that axial force would be transferred primarily through the shear ring. The lining covered only the steel shell internal surface, and did not cover the shear ring or shear ring welds. Test Unit # 18 had additional confinement provided for the axial force transfer region through the use of a second steel shell as shown in Figure 4.14. Details for this additional confinement are presented in Section 4.4.6.

### 4.4.5 Test Units # 19, # 20, and # 21 with Two Shear Rings

Test Units # 19-21 each had two shear rings and were studied to investigate the influence of spacing between shear rings on the axial force-axial displacement capacity and hysteretic response. Test Units # 19-21 had a steel shell with a length of 1.5 m (60.0 in.) to accommodate two shear rings. Test Units # 19, # 20 and # 21 were fabricated from a rolled steel plate, A 572 Grade 50, with an internal diameter of 0.61 m (24.0 in.), and a thickness of 25.4 mm (1.0 in.) which resulted in a D/t ratio of 24. The center-to-center spacing between shear rings in these test units was 76, 152 and 305 mm (3.0, 6.0, and 12.0 in.) for Test Units # 19, # 20, and # 21 respectively. The uppermost shear ring for each of these test units was located at 305 mm (12.0 in.) from the top of the steel shell, as shown in Figure 4.14. The placement of the shear rings for Test Units # 19, # 20 and # 21 is shown in Figure 4.15.

### 4.4.6 Additional Confinement of the Axial Force Transfer Section for Test Units # 18-21

Testing of Test Unit # 17 resulted in crushing of the cover concrete in the reinforced concrete force transfer section as presented in Chapter 5. Additional confinement of this section for the remaining Phase II test units (Test Units # 18-21) was provided by adding an oversized steel shell whose gap was filled with hydrostone to provide additional confinement (a retrofit measure). Placement of a retrofit steel shell is shown in Figure 4.17. Test Unit # 18 was retrofitted with a steel shell section cut from Test Unit # 14. This retrofit steel shell, of grade A53, had a length of 584 mm (23.0 in.), an internal diameter of 597 mm (23.5 in.) and a thickness of 12.5 mm (0.5 in.). This retrofit steel shell was placed over the reinforced concrete force transfer section such that a gap of 127 mm (5.0 in.) was provided between this steel shell and the test unit steel shell as shown in Figure 4.18. Retrofit steel shells for Test Units # 19-21 were fabricated from A53 grade B (pipe section) with a length of 660 mm (26.0 in.), an internal diameter of 635 mm (25.0 in.), and a thickness of 12.7 mm (0.5 in.). Retrofit steel shells for Test Units # 19-21 were placed over the reinforced concrete force transfer section such that a vertical gap of 88.9 mm (3.5 in.) was provided between this steel shell and the test unit steel shell as shown in Figure 4.14. This gap ensured that an axial compression displacement of 76 mm (3.0 in.) could be applied without contact between the test unit steel shell and the retrofit steel shell.


**Figure 4.17 Placement of a Retrofit Steel Shell**

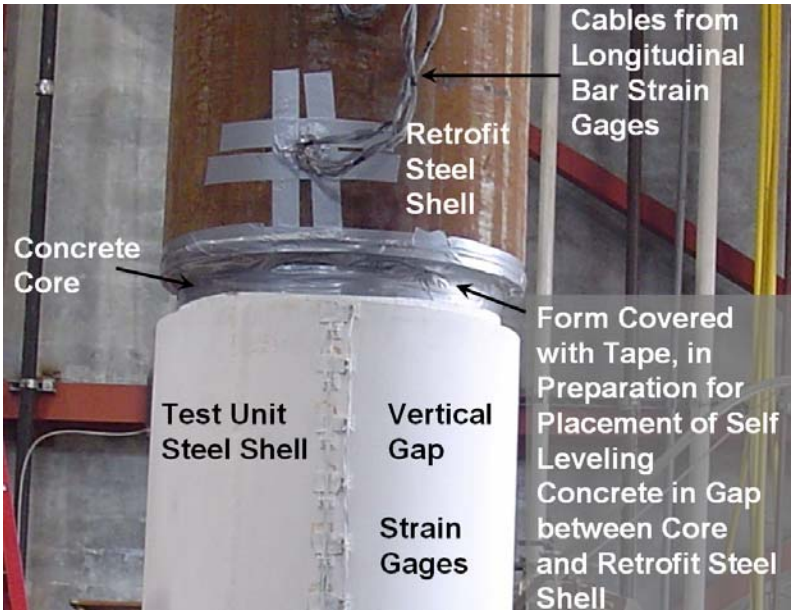


**Figure 4.18 Vertical Gap between Retrofit Steel Shell and Test Unit Steel Shell (Test Unit # 19-21)**

## 4.5 Reinforced Concrete

Details of the longitudinal and transverse steel reinforcement for the test units are presented in this section. The concrete specifications for test units in both experimental phases are also presented.

### 4.5.1 Reinforcement

Test Units # 1-10 and # 13-21 had a 508 mm (20.0 in.) diameter (external) reinforcement bar cage with longitudinal reinforcement provided by ten # 11 bars (Grade 60). This resulted in a longitudinal reinforcement ratio, $\rho_\ell$, of 3.4%. This high reinforcement ratio was used to ensure that the predicted mechanism strength would be attained prior to yielding of the longitudinal reinforcement when subjecting the test unit to axial tension. Confinement was provided by a # 4 reinforcement bar spiral (Grade 60) with a pitch of 152 mm (6.0 in.) for the reinforcement bar cage section confined by the steel shell. Confinement outside of the steel shell, in the 762 mm (30.0 in.) force transfer region, was provided by a # 4 reinforcement bar spiral (Grade 60). This reinforcement bar spiral had a pitch of 25 mm (1.0 in.) for Test Units # 4-9 and # 13-21, and a pitch of 75 mm (3.0 in.) for Test Units # 1-3 and # 10-12. Reinforcement bar cages were constructed with two instrumented bars per cage as presented in Section 4.7.

Test Units # 11 and # 12 were reinforced with a 305 mm (12.0 in.) external diameter bar cage with longitudinal reinforcement provided by four # 11 bars (Grade 60). This resulted in a longitudinal reinforcement ratio, $\rho_\ell$, of 3.1%. Confinement of the reinforcement bar cage, within the steel shell, was provided by a # 4 reinforcement bar spiral (Grade 60) with a pitch of 152.4 mm (6.0 in.). Confinement of the reinforcement bar cage outside of the steel shell was provided by a # 4 reinforcement bar spiral (Grade 60) with a pitch of 76.2 mm (3.0 in.).

### 4.5.2 Concrete Mix Design Specification

A concrete mix design with a specified compressive strength, $f_c^{'}$, of 14 MPa (2.0 ksi) at 28 days was procured to ensure strength on the day of test would not exceed 21 MPa (3.0 ksi). Specifications for the concrete mix design obtained from the supplier (Vulcan Materials Company) are listed in Table 4.3. If the concrete strength exceeded this value then the ultimate strength of the longitudinal reinforcement would be obtained prior to the axial force capacity of the test unit; a highly undesirable outcome. The

maximum aggregate size used in the mix was 9.53 mm (3/8 in.). A sieve analysis of the aggregate and sand used in the mix is listed in Table 4.4.

**Table 4.3 Concrete Mix Design Specifications**

| Material | Batch Quantity | Percentage of Aggregate | Specific Gravity | Absolute Volume |
|---|---|---|---|---|
| Cement | 212.74 kg (469.00 lb) | | 3.15 | 0.0677 $m^3$ (2.39 $ft^3$) |
| Flyash | 39.01 kg (86.00 lb) | | 2.05 | 0.019 $m^3$ (0.67 $ft^3$) |
| WCS (Sand) | 850.032 kg (1874.00 lb) | 64.95 | 2.67 | 0.3186 $m^3$ (11.25 $ft^3$) |
| 3/8 inch Coarse Gravel | 446.79 kg (985.00 lb) | 35.05 | 2.6 | 0.172 $m^3$ (6.07 $ft^3$) |
| Water | 20.66 kg (45.55 lb) | | | 0.172 $m^3$ (6.08 $ft^3$) |
| Admixtures (WRDA-64) | 8.618 kg (19.00 lb) | | | 0 |
| Air Percentage | 2 | | | 0.0153 $m^3$ (0.54 $ft^3$) |
| W / (C + F) Ratio | 0.68 | | | |
| Total | 1577.8 kg (3478.6 lb) | | | 0.765 $m^3$ (27.0 $ft^3$) |

**Table 4.4 Concrete Mix Aggregate Sieve Analysis**

| Sieve Size: No. or mm (in.) | WCS (Sand) | 9.5 mm (3/8 in.) Coarse Gravel |
|---|---|---|
| 51 (2) | 100 | 100 |
| 38 (1.5) | 100 | 100 |
| 25 (1) | 100 | 100 |
| 19 (0.75) | 100 | 100 |
| 13 (0.5) | 100 | 100 |
| 9.5 (3/8) | 100 | 90 |
| No. 4 | 97 | 20 |
| No. 8 | 89 | 3 |
| No. 16 | 68 | 0 |
| No. 30 | 49 | 0 |
| No. 50 | 26 | 0 |
| No. 100 | 5 | 0 |
| No. 200 | 2 | 0 |

## 4.6 Test Unit End Reactions

Details for the end reactions of the test units will be discussed in this section.

### 4.6.1 Top Reaction of Test Units (Concrete Core)

The transfer of axial tension force at the top of the test units was obtained by using 44.5 mm (1.75 in.) diameter high strength threaded bars with a yield stress, $f_y$, of 1,034 MPa (150 ksi). The high strength threaded bars extended out from the top of the test unit a length of 254 mm (10.0 in.) to allow for the connection of the test unit to the test setup as presented in Section 4.9. The high strength threaded bars were embedded within the reinforced concrete (force transfer region) a length of 660 mm (26.0 in.), and were fastened to a steel fabricated plate also embedded within the concrete core. This plate allowed for the transfer of axial tension to the reinforcement bar cage.

The transfer of axial tension force at the top of Test Units #1-10 and #13-21 was obtained with six 44.5 mm (1.75 in.) diameter high strength threaded bars. The threaded bars were fastened to a 38.1 mm (1.5 in.) thick steel force transfer plate, A572 Grade 50, with hex nuts. This assembly was placed within the reinforcement bar cage such that the steel plate was 546 mm (21.5 in.) from the top of the test unit, and 216 mm (8.5 in.) above the steel shell-reinforced concrete interface. Placement of the high strength threaded bars and force transfer plate is shown in the test unit plan views and elevation views in Figures 4.2, 4.4, 4.5, 4.8, 4.11, 4.12, 4.13 and 4.14.

The transfer of axial tension force at the top of Test Units # 11 and # 12 was obtained with two 44.5 mm (1.75 in.) diameter high strength threaded bars. The threaded bars were fastened to a 38.1 mm (1.5 in.) thick steel force transfer plate, A572 Grade 50, with hex nuts as shown in the test unit plan views and elevation views.

### 4.6.2 Base Reaction of Test Units (Steel Shell)

Axial force transfer at the base of each test unit to the test setup was achieved with a base reaction consisting of a steel base plate and welded stiffener plates (A572 grade 50). The base plate had a hole pattern corresponding to the test setup which allowed for the base of the test unit to be post-tensioned to the test setup. Test units with a mechanism or expansive concrete had fourteen stiffener plates for the transfer of axial tension as shown in Figures 4.2, 4.8, 4.11, 4.12, 4.13, and 4.14. Test Units # 1, # 2, # 3, and # 10 had eight stiffener plates as shown in Figure 4.4. Test Units # 11, and # 12 had four stiffener plates as shown in Figure 4.5. All stiffener plates had a length of 629 mm (24.75 in.) along the steel shell, a width of 324 mm (12.75 in.) at the base, and a thickness of 25.4 mm (1.0 in.).

Stiffener plates for Test Units # 1-16 were welded to the steel shell with a 4.8 mm (3/16 in) fillet weld to minimize thermal effects on the concrete within the steel shell as shown in Figure 4.19. Stiffener plates for Test Units # 17-21 were welded to the steel shell with a 7.9 mm (5/16 in.) fillet weld also as shown in Figure 4.19. All stiffener plates were welded to the base plate with a 9.5 mm (3/8 in.) fillet weld as shown in Figures 4.19. Test Units # 4-9 and # 13-21 had a steel fabricated base plate, A572 grade 50, with dimensions of 1,420 mm (56.0 in.) x 1,220 mm (48.0 in.) and a thickness of 76 mm (3.0 in.). Test Units # 1, # 2, # 3, and # 10 had a steel fabricated base plate, A572 grade 50, with dimensions of 1,420 mm (56.0 in.) x 1,220 mm (48.0 in.) and a thickness of 51 mm (2.0 in.). Test Units # 11, # 12 had a steel fabricated base plate, A572 grade 50, with dimensions of 1,090 mm (43.0 in.) x 1,080 mm (42.5 in.) and a thickness of 51 mm (2.0 in.).

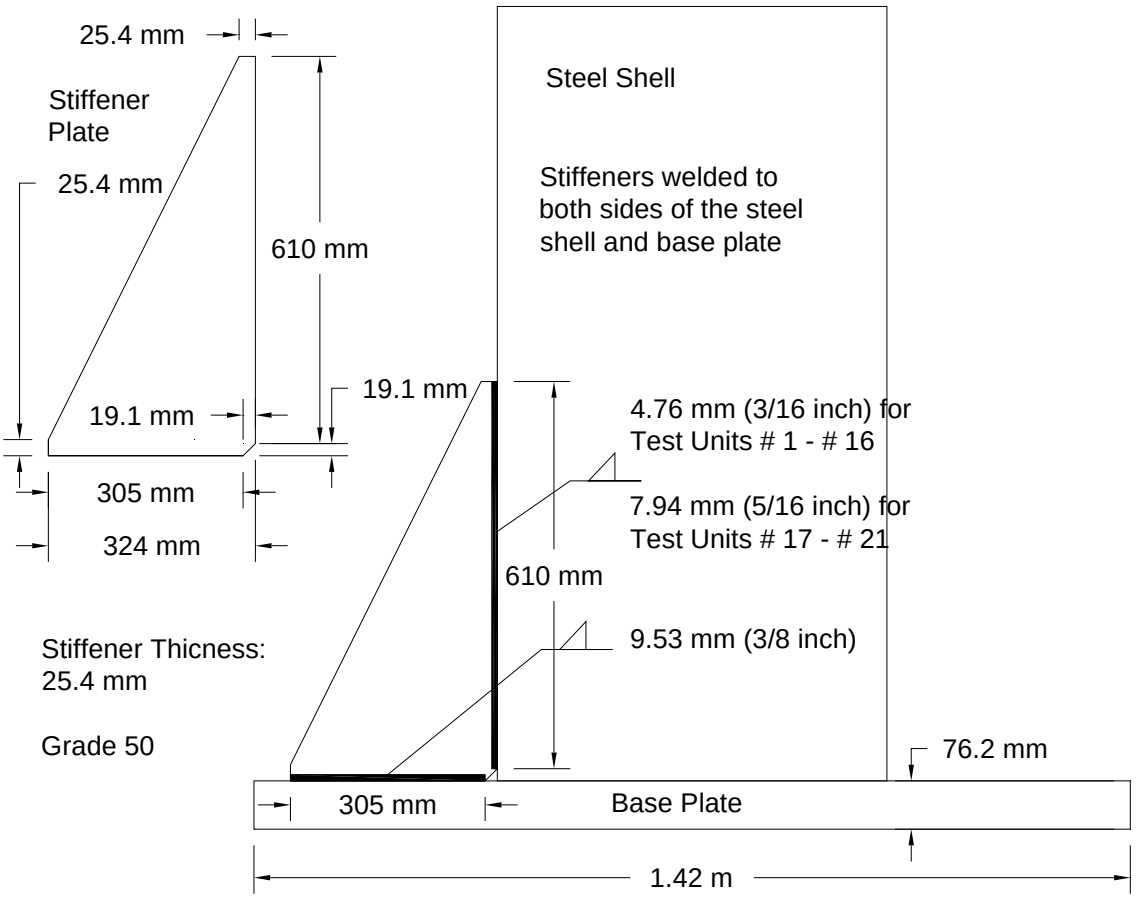


**Figure 4.19 Stiffener Plate Welds**

## 4.7 Instrumentation

Electrical resistance strain gauges were applied to # 11 bars, with a majority placed in the primary test region: the steel shell section not confined by stiffeners. Strain gauges were applied to two No. 11 bars for each test unit with a typical layout as shown in the instrumentation plans for Test Unit # 21 in Figure 4.20. Strain gauges were also applied to the steel shell in the longitudinal and transverse directions in the section not confined by stiffeners. A strain gauge layout for the steel shell of Test Unit # 21 is shown in Figure 4.21. Strain gauges were covered with a waterproof coating and with a pad to provide protection. Strain gauges on the reinforcement bars had the cables routed and secured to the bar length to minimize any interaction of the cables with a concrete vibrator during concrete placement.

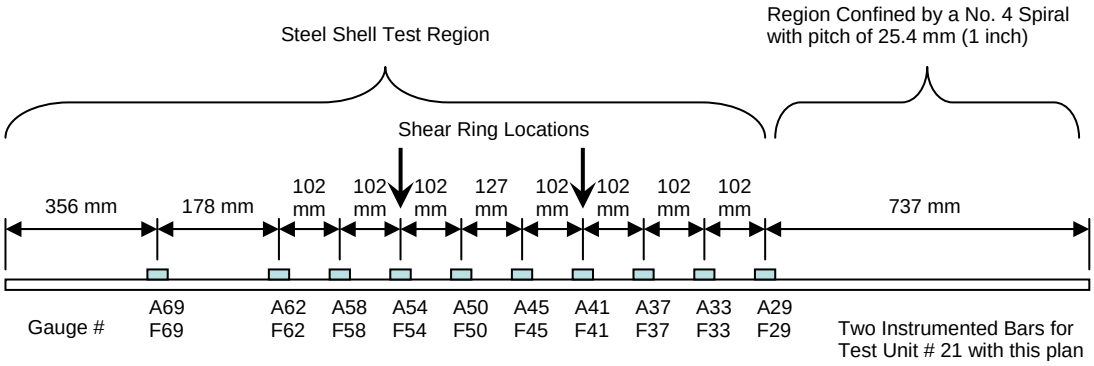


**Figure 4.20 Typical Longitudinal Reinforcement Bar Instrumentation Plan (Test Unit # 21)**

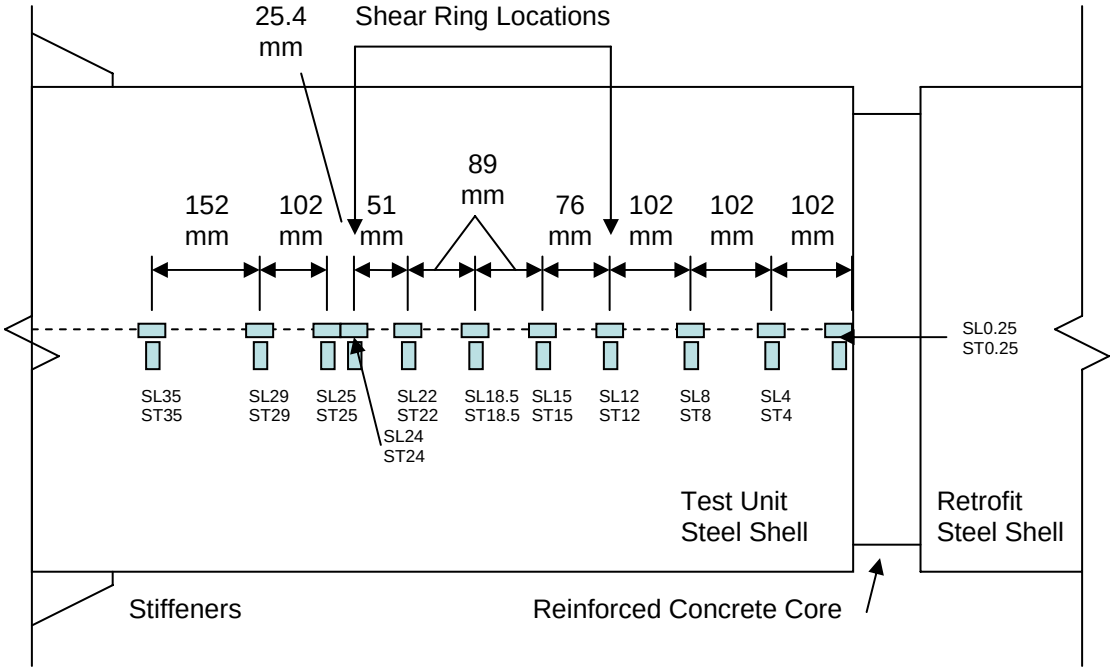


**Figure 4.21 Typical Steel Shell Instrumentation Plan (Test Unit # 21)**

## 4.8 Test Unit Construction

Test Units were constructed by the Staff of the Charles Lee Powell Structural Engineering Laboratories at UCSD. Details pertaining to the fabrication and construction of the test units will be discussed in the following sections.

### 4.8.1 Reinforcement Bar Cage Construction and Instrumentation

Construction commenced with application of electrical resistance strain gauges to the No. 11 longitudinal reinforcement bars. After instrumentation of the longitudinal reinforcement was completed, the reinforcement bar cages were constructed, as shown in Figure 4.22 for a typical 610 mm (24.0 in.) diameter test unit, and in Figure 4.23 for a typical 387 mm (15.25 in.) diameter test unit. Strain gauge cables were routed and secured to each reinforcement bar cage to minimize any interaction of the cables with a concrete vibrator during concrete placement. Cables were routed out of the test units at approximately 200 mm (8.0 in.) above the steel shell top surface.

**Figure 4.22 Reinforcement Bar Cage for a Typical 610 mm (24.0 in.) Diameter Test Unit**

**Figure 4.23 Reinforcement Bar Cage for a Typical 387 mm (15.25 in.) Diameter Test Unit**

### 4.8.2 Steel Shell Fabrication

Fabrication of the steel shell which for some test units included rolling and welding of steel plates was performed by an outside fabricator. The longitudinal weld within the steel shell of Test Units # 17-21 (fabricated from a rolled plate) was grinded to a smooth finish to prevent any weld surface irregularities from increasing the axial force transfer. Figure 4.24 shows a typical steel shell internal surface with a weld ground smooth, whereas a rough vertical seam weld from a test unit with a D/t ratio of 128 is shown in Figure 4.25. After the steel shell fabrication was completed mechanisms were welded to the steel shells per the experimental plan. Welding of the shear ring for Test Unit # 17 is shown in Figure 4.26. Placement of the shear studs for Test Unit # 8 required splitting the steel shell into two equal sections to allow for shear stud attachment using a shear stud gun as shown in Figure 4.27. Studs were attached using electric arc stud welding after which the steel shell was rewelded.

**Figure 4.24 Test Unit with a Steel Shell Vertical Seam Weld Grinded Smooth**

**Figure 4.25 Test Unit with a Steel Shell Vertical Seam Weld – not Grinded**

**Figure 4.26 Shear Ring Welding for Test Unit # 17**

**Figure 4.27 Shear Stud Attachment with Stud Gun**

### 4.8.3 Setup on Casting Bed

Upon completion of the welding of the mechanisms to the steel shells, and completion of the reinforcement bar cages, the test units were setup on a casting bed in preparation for concrete placement. Each steel shell had a 127 mm (5.0 in.) thick polystyrene form, as shown in Figure 4.28, cut to fit the internal diameter of the steel shell. This provided a void at the steel shell base. Placement of this form, within a steel shell, is shown in Figure 4.29. A 3.2 mm (1/8 in.) thick sheet of plywood was placed on top of this polystyrene form to distribute the weight of the reinforcement bar cage. Concrete spacer cubes with a dimension of 25.4 mm (1.0 in.) were attached to the base of each reinforcement bar to provide a 25.4 mm (1.0 in.) concrete cover at the base. A polyethylene lining was placed within the steel shell of Test Unit # 18 such that the shear ring and welds were not covered by this lining, as shown in Figure 4.30.

**Figure 4.28 Polystyrene Base Form for a Typical Test Unit Steel Shell**

**Figure 4.29 Placement of a Polystyrene Base Form**

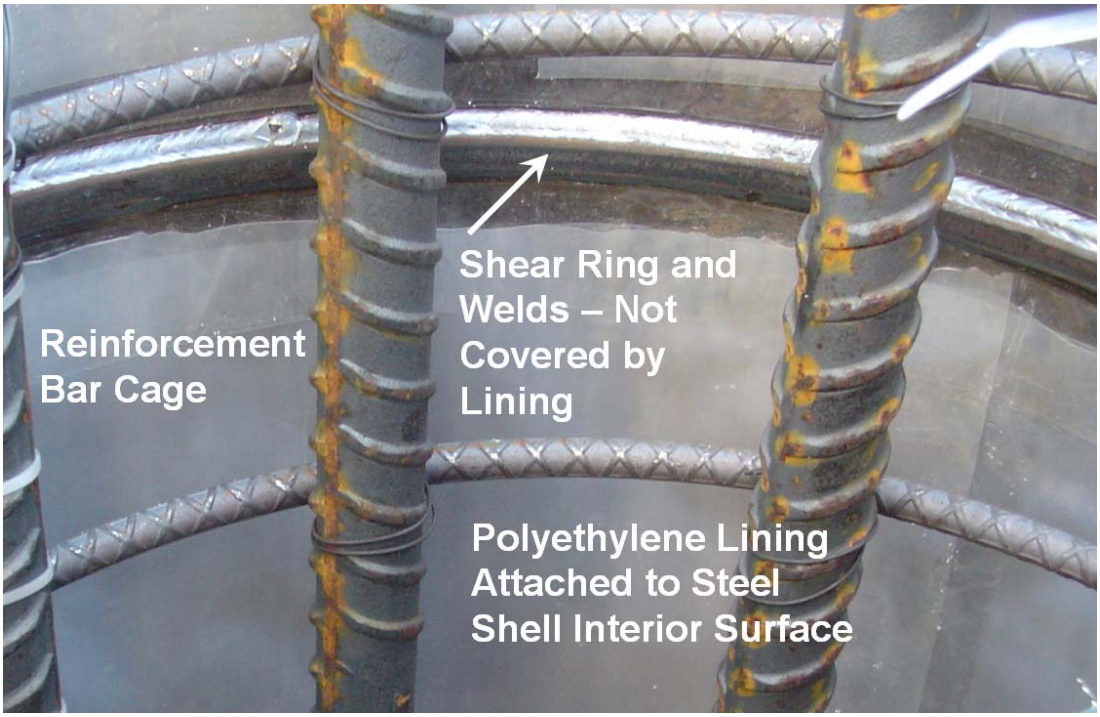


**Figure 4.30 Polyethylene Lining Placed within the Steel Shell of Test Unit # 18**

Reinforcement bar cages were carefully placed within the steel shells as shown in Figure 4.31 and centered. After the reinforcement bar cages were placed a tube form with a diameter of 610 mm (24.0 in.) and a length of 762 mm (30.0 in.), was used to form the upper reinforced concrete axial force transfer section. Each tube form was lined with a layer of polystyrene foam insulation, as shown in Figure 4.32, with a thickness of 12.5 mm (0.5 in.). This lining was used to ensure the diameter of the reinforced concrete axial force transfer section was less than the diameter of the reinforced concrete core within the steel shell. This would ensure no contact between the upper reinforced concrete section and the top of the steel shell. Tube forms with the interior lining were then glued to the top of the steel shells followed by formwork. After the formwork was completed the high strength threaded bar assembly with steel plate anchorage, as discussed in Section 4.6.1 and as shown in Figure 4.33, was placed within the reinforcement bar cage. This assembly was secured to the formwork as shown in Figure 4.34. A view of the test units formed and ready for concrete placement is shown in Figure 4.35.

**Figure 4.31 Placement of Reinforcement Bar Cages**

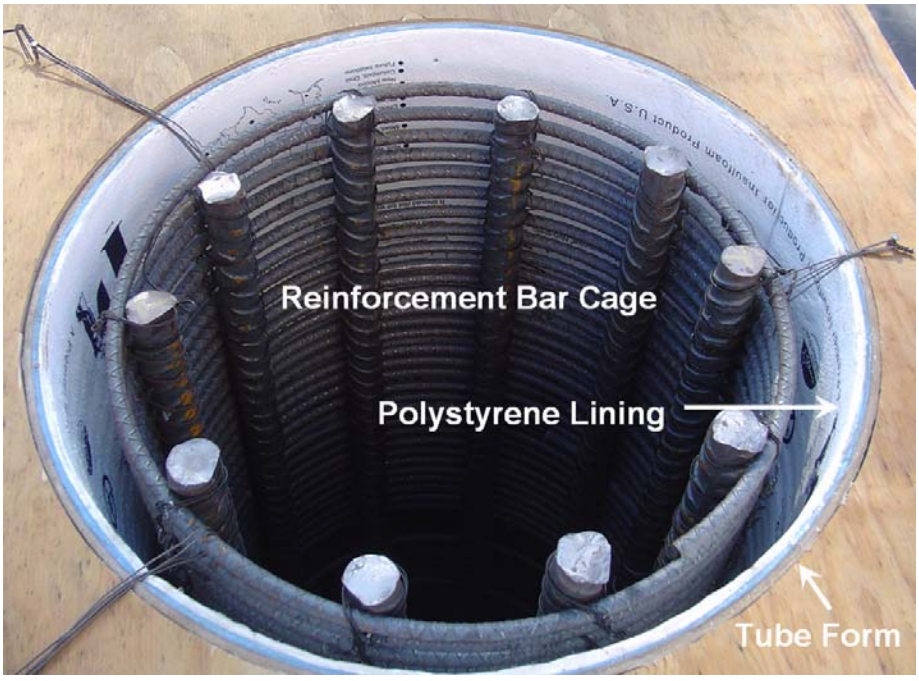


**Figure 4.32 Tube Form Lined with Polystyrene Foam Insulation**

**Figure 4.33 High Strength Threaded Bar Assembly with Steel Plate Anchorage**

**Figure 4.34 High Strength Threaded Bar Assembly Secured to Formwork**


**Figure 4.35 Test Units Formed and Ready for Concrete Placement**

### 4.8.4 Concrete Placement

Concrete was placed with the aide of a pump truck and a vibrator in four lifts with a typical lift height of 1/4 of the overall test unit height as shown in Figure 4.36. Concrete was placed to within approximately 12.5 mm (0.5 in.) of the top of the tube form, as shown in Figure 4.37, to allow for future placement of a self leveling concrete (hydrostone). In Figure 4.37 it should be noted that this photograph was taken after the top form assembly for the high strength threaded bars was removed approximately five hours after concrete placement. After the test units had cured for one day the formwork was removed except for the tube forms and polystyrene base form. The polystyrene base form and the 3.2 mm (1/8 in.) thick plywood base form were removed after the test units had cured for at least three weeks (Figure 4.38) at which time welding of the base reactions began. Tube forms were removed after the test unit concrete had cured for 28 days.


**Figure 4.36 Concrete Placement**

**Figure 4.37 Rough Top Surface to Allow Bond with a Layer of Self Leveling Concrete**


**Figure 4.38 Removal of Base form**

### 4.8.5 Base Reaction

Each test unit had its own base reaction consisting of a steel base plate and stiffeners as discussed in Section 4.6.2. Base plates with the required test setup hole pattern were fabricated prior to welding of the base reaction of each test unit. Alignment of the base plate hole pattern with the high strength threaded bars extending from the top of each test unit was critical. A proper alignment was needed because rotation of the SRMD shake table (platen) about the longitudinal axis for connection of the test unit and for operation of the test was not desired. A proper alignment was obtained by using plumb bobs and levels to insure that an axis through the high strength threaded bars was parallel to an axis through the base plate hole pattern. After a proper alignment of the test unit and base plate was achieved, stiffeners were then placed and welded to the steel shell as shown in Figure 4.39. A lifting point was welded to each base plate so that an overhead laboratory bridge crane could lift each test unit (in a horizontal orientation) from two points: the base plate and the high strength threaded bars extending from the reinforced concrete axial force transfer section. Access holes for the base void, as presented in Section 4.2, were marked and cut.

**Figure 4.39 Welding of Stiffeners to Steel Shell**

### 4.8.6 Final Test Unit Preparation

After welding of the base reaction was completed final preparation for testing was conducted. A 12.5 mm (0.5 in.) layer of self leveling concrete (hydrostone), as shown in Figure 4.40, was placed on the top of each test unit (reinforced concrete core) to provide a smooth surface for the test setup to apply axial compression. Strain gauges were applied to the surface of the steel shell in the longitudinal and transverse directions per the instrumentation plan. The steel shell and reinforced concrete axial force transfer section were painted white to allow for greater visibility of cracks and yielding of the steel shell. Three linear potentiometers were placed across the steel shell-reinforced concrete interface at a circumferential spacing of $120^{o}$ to measure axial displacement of the reinforced concrete core relative to the steel shell. These devices were placed with the anticipation of a crack opening at the location of the embedded axial force transfer plate (fastened to the high strength threaded bars) at 191 mm (7.5 in.) from the steel shell-reinforced concrete interface. These devices were attached on the steel shell side of the anticipated crack. A completed test unit ready for placement in the test setup is shown in Figure 4.41, and a test unit with a steel shell retrofit is shown in Figure 4.42.

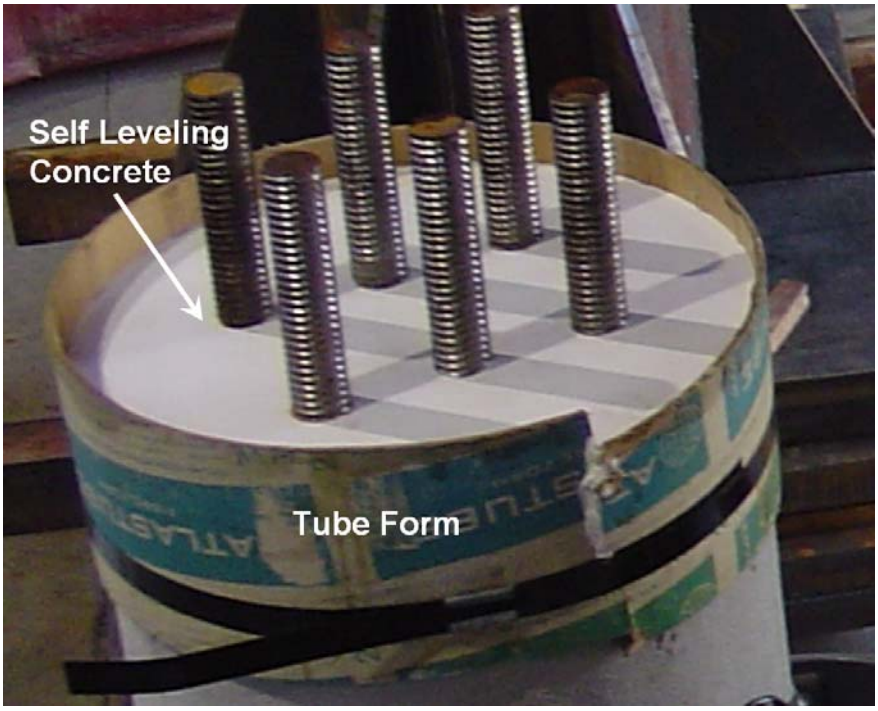


**Figure 4.40 Placement of Self Leveling Concrete**

**Figure 4.41 Test Unit Ready for Placement in the Test Setup**

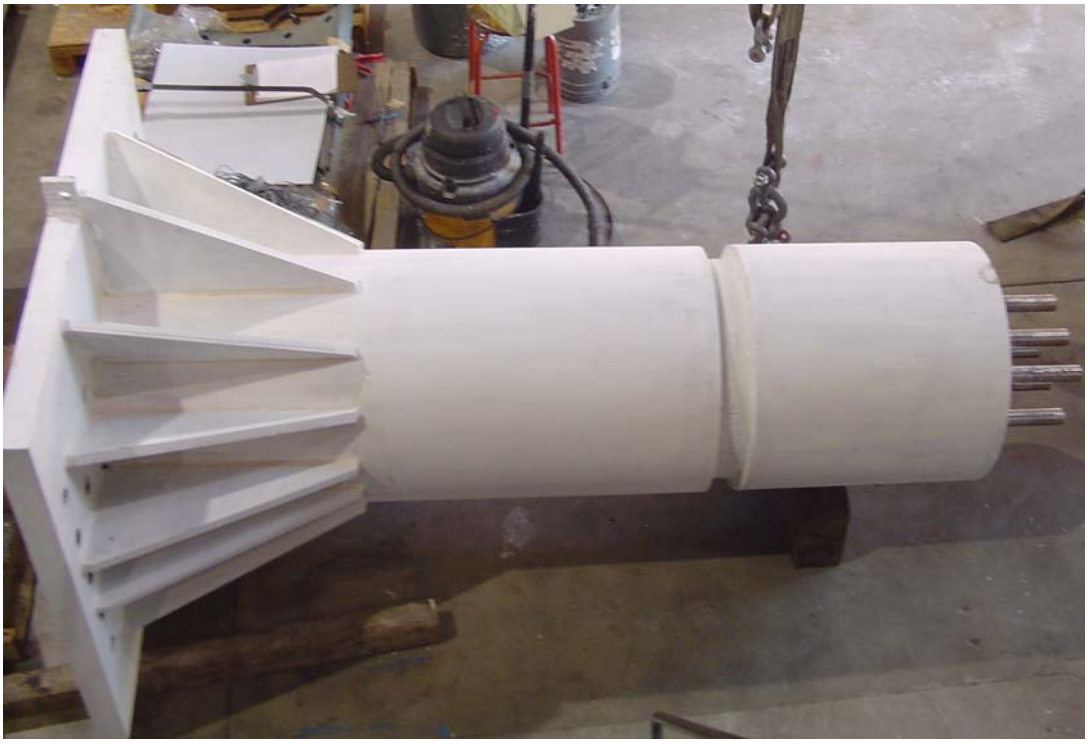

**Figure 4.42 Test Unit with Steel Shell Retrofit Ready for Placement in Test Setup**

## 4.9 Test Setup

Details of the test setup and data acquisition will be presented in the following section.

### 4.9.1 Test Setup at the SRMD

A test setup at the UCSD-Caltrans Seismic Response Modification Device (SRMD) Test Facility was utilized as this provided an economical solution to generate potential axial force demands up to 8.9 MN (2,000 kips). A three dimensional perspective of the test setup is shown in Figure 4.43 in which the horizontal testing configuration of a test unit can be noted.

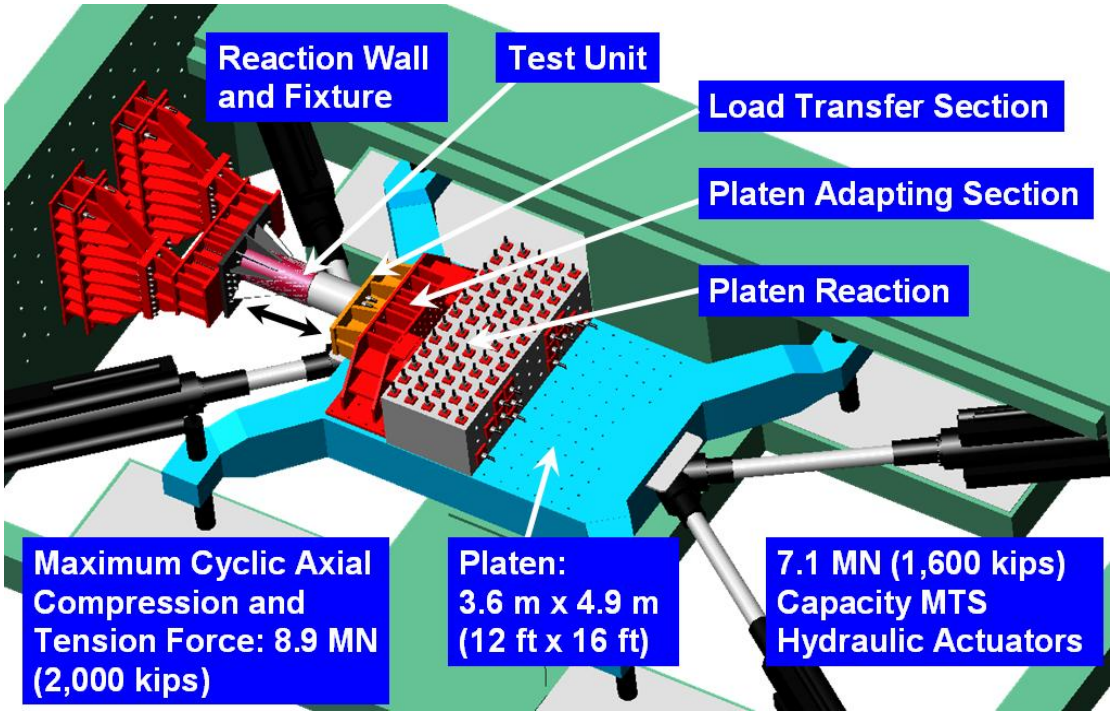


**Figure 4.43 SRMD Test Setup Perspective**

In the test setup four 7.1 MN (1,600 kip) capacity servo controlled MTS hydraulic actuators applied load to the steel fabricated platen (shake table). Load was transferred from the platen to a reinforced concrete reaction mass with a height of 1.07 m (42.0 in.), a longitudinal length of 1.52 m (60.0 in)., and a transverse width of 3.66 m (144 in.). This reaction mass was post-tensioned to the platen using fifty-eight A449 rods with a diameter of 38.1 mm (1.5 in.). A steel fabricated platen adapting section was post-tensioned horizontally to the reaction block with fourteen 1,030 MPa (150 ksi) high strength threaded bars, with a 44.5 mm (1.75 in.) diameter. The platen adapting fixture was also post-tensioned to the platen using eight A449 rods. A steel fabricated load transfer section was post-tensioned to the platen adapting fixture with twenty-eight A449 rods, with a diameter of 38 mm (1.5 in.). This fixture was designed to allow for the connection of the high strength threaded bars extending from the reinforced concrete axial force transfer section of a typical test unit.

At the strong wall reaction of the test setup, a pair of steel fabricated reaction wall brackets was post-tensioned to the reaction wall. Each bracket was post-tensioned with

twelve 44.5 mm (1.75 in.) diameter high strength threaded bars with a yield stress, $f_y$, of 1,030 MPa (150 ksi). A steel fabricated beam section, referred to as the wall adapting fixture, was post-tensioned to the pair of reaction wall brackets using twenty-two A325 bolts with a diameter of 38 mm (1.5 in.). This reaction wall bracket had a hole pattern, at 152.4 mm (6.0 in.) on center, which allowed for post-tensioning of the steel base of a typical test unit. This strong wall reaction had sufficient capacity to allow a typical test unit to remain cantilevered from this strong wall reaction.

Test units were placed in the setup initially with only the base post-tensioned to the wall adapting fixture. On the day of test the platen was raised to the elevation of the test unit and moved towards the test unit. The high strength threaded bars extending from the test unit were carefully aligned with the holes in the steel fabricated load transfer section, and passed through by moving the platen. The platen was moved to pass the high strength threaded bars through the load transfer section so that the top of the test unit was firm against the load transfer section. After contact was made hex nuts were placed and hand tightened as shown in Figure 4.44. Aluminum shims were placed between the test unit and load transfer section as needed as shown in Figure 4.44. The hex nuts were also tightened at the maximum axial compression displacement obtained in the first applied cycle. An overall view of the test setup with a test unit in place and ready for testing is shown in Figure 4.45.

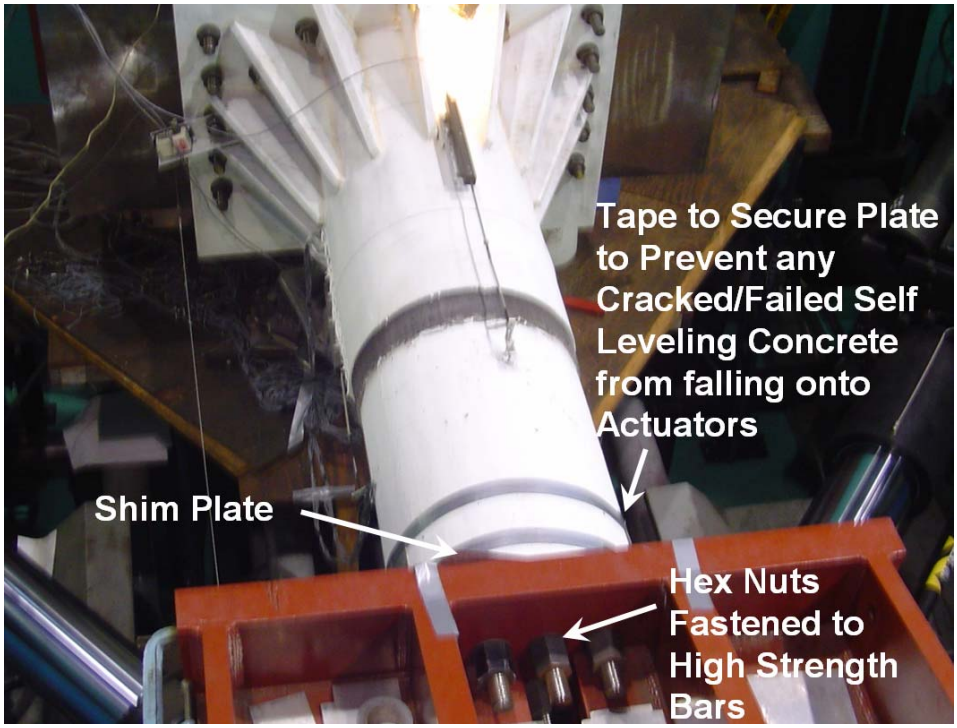


**Figure 4.44 Hex nuts fastening a Test Unit to Steel Fabricated Load Transfer Section**

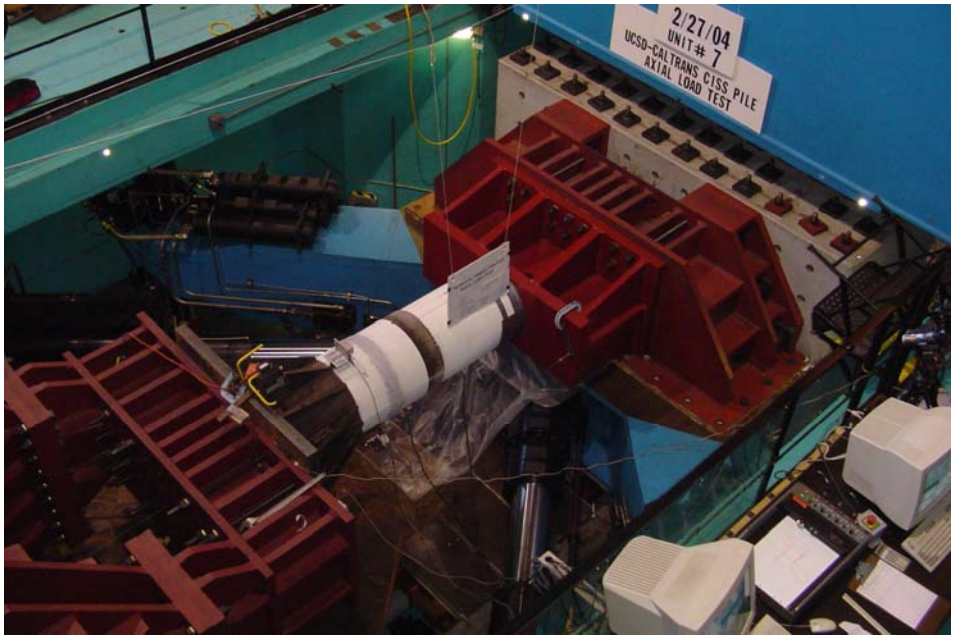


**Figure 4.45 Overall view of Test Setup, Test Underway (Axial Tension Applied to Test Unit # 7)**

### 4.9.2 Data Acquisition

A data acquisition system was used to record displacements, strains, and forces. Axial displacement of the reaction block, reaction wall, strong wall bracket, wall adapting fixture, load transfer section, and platen adapting section were measured with linear potentiometers. The displacement of the reinforced concrete core relative to the steel shell was measured with three linear potentiometers placed across the steel shell-reinforced concrete interface at a radial spacing of $120^{o}$.

Axial force and displacement of the platen was calculated by the SRMD control system based on data obtained from load cells on each of the four hydraulic actuators. Forces and displacements in the longitudinal, transverse, and vertical directions were obtained and recorded by the data acquisition system. Each test was recorded by two video cameras along with extensive digital photography.

## 4.10 Test Protocol

A reversed quasi-static cyclic axial compression and tension displacement was applied to each test unit using the SRMD. A displacement based test protocol was used because the SRMD is a displacement controlled system. The protocol consisted of eight displacement levels each with three cycles in axial compression and axial tension. Displacement levels consisted of target displacements of $\pm 2.54$, $\pm 5.08$, $\pm 7.6$, $\pm 12.7$, $\pm 25.4$, $\pm 50.8$, $\pm 76.2$, and $\pm 101.6$ mm ($\pm 0.1$, $\pm 0.2$, $\pm 0.3$, $\pm 0.5$, $\pm 1$, $\pm 2$, $\pm 3$, and $\pm 4$ in.), as shown in Figure 4.46.

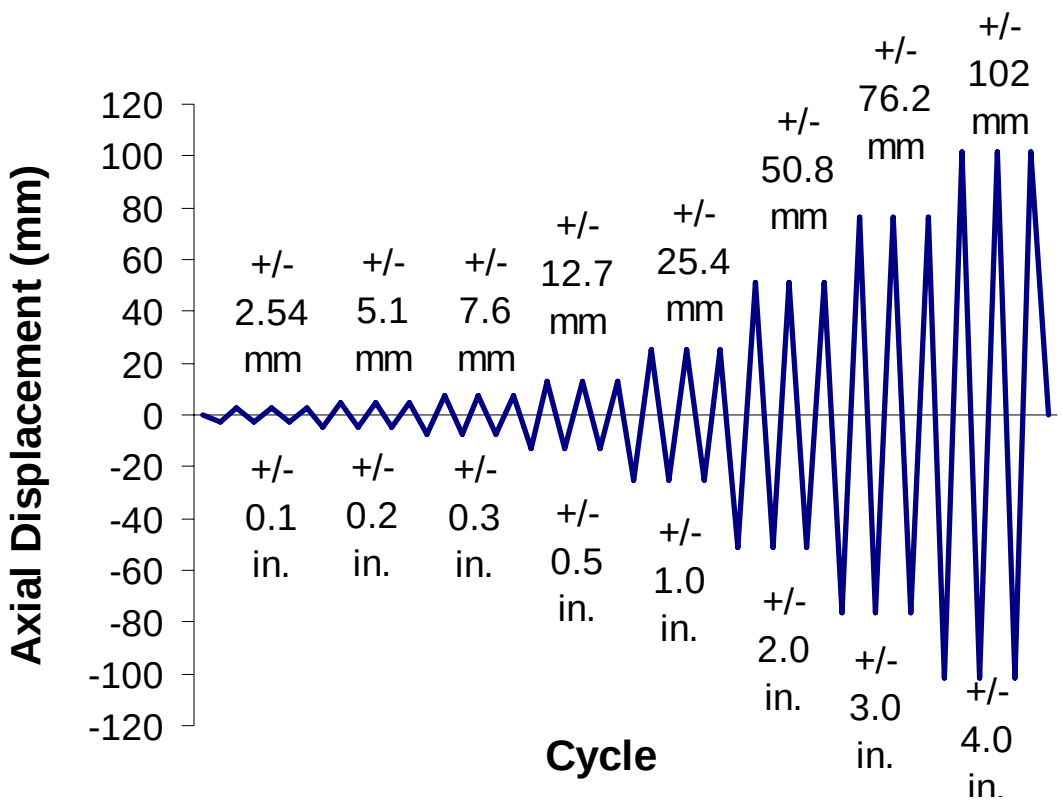


**Figure 4.46 Test Protocol**

# 5 EXPERIMENTAL RESULTS

## 5.1 Introduction

This chapter presents the experimental results of this research. Results include axial force-axial displacement hysteretic response of all test units, relevant strain data histories, and photographic evidence of key findings. Results for material testing are presented as well.

## 5.2 Typical Axial Force-Axial Displacement Hysteretic Response

In a typical plot of the applied axial force-axial displacement hysteretic response (of the reinforced concrete core) the application of axial compression force is shown in the two lower quadrants in Figure 5.1. The application of axial tension force is shown in the two upper quadrants in Figure 5.1. The upper left and lower right quadrants show the return of the reinforced concrete core to zero axial displacement.

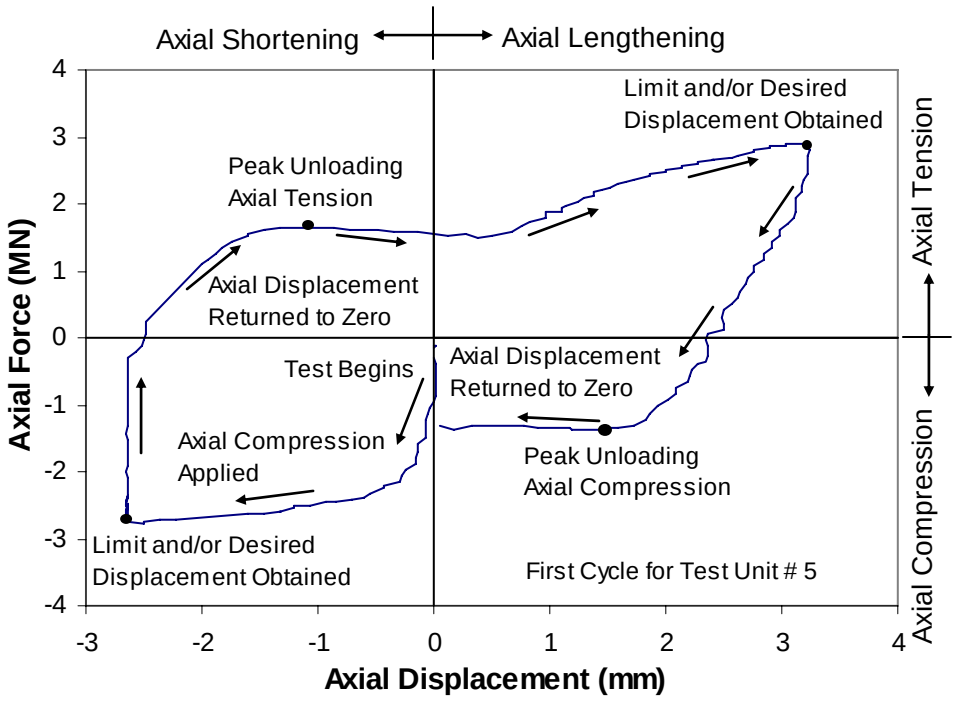


**(a) First Cycle at 2.54 mm for Test Unit # 5**

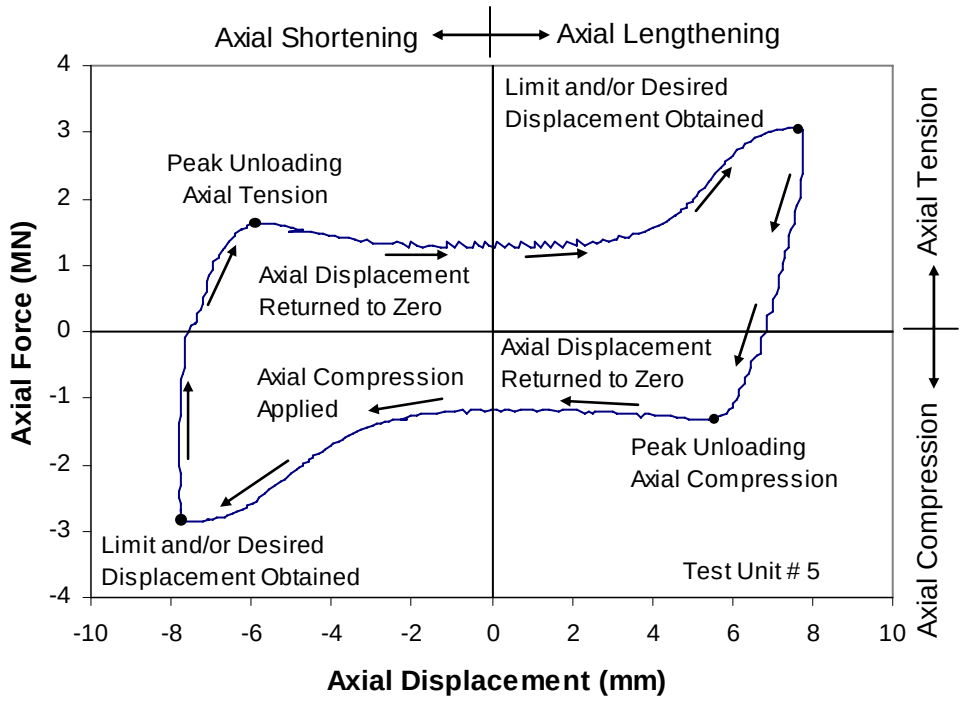


**(b) First Cycle at 7.6 mm for Test Unit # 5**

**Figure 5.1 Explanation of a Typical Axial Force-Axial Displacement Hysteretic Response**

Axial compression was applied until the desired axial compression displacement in the test protocol was obtained. This is shown in Figure 5.1(a) in which axial compression was applied for the first cycle of Test Unit # 5. After obtaining the desired axial compression displacement the axial compression force was returned to zero with a partial elastic recovery. This was followed by the application of axial tension force which typically had no major change in axial displacement until after a peak unloading axial tension force was obtained as shown in Figures 5.1(a) and 5.1(b). This peak as shown in the upper left quadrant of a typical hysteretic response was due to a jamming of the reinforced concrete core relative to the steel shell. Peaks were more pronounced for cycles at greater axial displacements as shown in Figure 5.1(b). This jamming of the concrete core was relieved through an unlocking process in which axial displacement returned to zero with a softening of the hysteretic response (decrease in the axial force). As axial tension displacement was applied in the upper right quadrant of a typical hysteretic response the axial tension force increased until either the desired displacement

was obtained or until a limiting axial force transfer (as discussed in the following sections) was obtained. After the desired axial tension displacement and force were obtained the axial force was returned to zero and axial compression was applied, similar to the previous process in which axial tension was applied with peaks obtained in the response.

Examination of a typical hysteretic response for test units without a mechanism shows a slightly unsymmetric response. In the unsymmetric response axial tension forces obtained were usually less than the axial compression forces at the same axial displacement (magnitude). This unsymmetric response was due to the formation of microcracks during the application of axial tension force.

Test units which lacked a mechanism obtained peak axial forces at the initial cyclic axial displacements as shown in a typical hysteretic response for Test Unit # 1, in Figure 5.2. These peaks are the result of an adhesive bond at the steel shell-reinforced concrete core interface.

## 5.3 Response for Test Units with a Variation of D/t Ratio

Results for test units in which the D/t ratio was the parameter of variation will be presented.

### 5.3.1 Test Unit # 1 at a D/t Ratio of 128

Test Unit # 1 obtained a maximum axial compression force of -1.03 MN (-233 kips) at -0.025 mm (-0.001 in.) and a maximum axial tension force of 0.950 MN (214 kips) at 2.4 mm (0.09 in.) as shown in Figure 5.2. Softening of the response was observed when the axial tension displacements increased. In axial compression the axial force transfer diminished after obtaining the aforementioned peak force during the first cycle. However, the axial force transfer increased at greater axial compression displacements, and had a typical maximum cyclic force of approximately -0.950 MN (-

214 kips). In axial tension the axial force transfer decreased after the aforementioned peak force was obtained as shown in Figure 5.2.

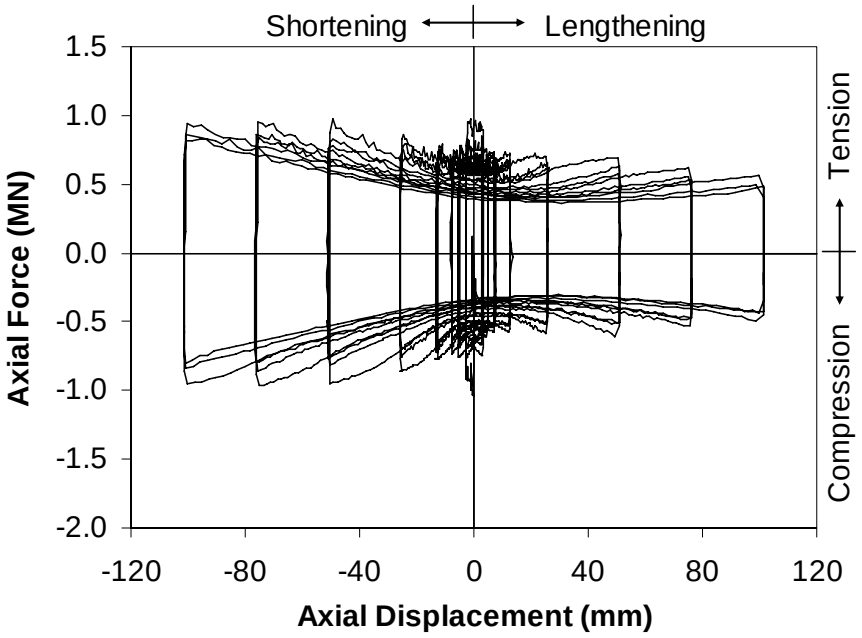


**Figure 5.2 Hysteretic Response for Test Unit # 1 at a D/t Ratio of 128**

### 5.3.2 Test Unit # 2 at a D/t Ratio of 94

Test Unit # 2 obtained a maximum axial compression force of -1.27 MN (-286 kips) at -0.35 mm (-0.014 in.) after which a sharp decrease in the axial force transfer occurred as shown in Figure 5.3. At axial compression displacements beyond this maximum a typical maximum cyclic force transfer of approximately -0.56 MN (-126 kips). During the last axial compression cycle a slight contact occurred between the upper reinforced concrete force transfer section and the top of the steel shell. This contact resulted in an increase in the stiffness of the hysteretic response as shown by the peak at a displacement of -98 mm (3.86 in.) in Figure 5.3. In axial tension a maximum axial force of 1.08 MN (242 kips) at 2.1 mm (0.08 in.) was obtained after which a sharp decrease in the axial force transfer occurred. At axial tension displacements beyond this maximum a typical maximum cyclic force of 0.67 MN (150 kips) was obtained.

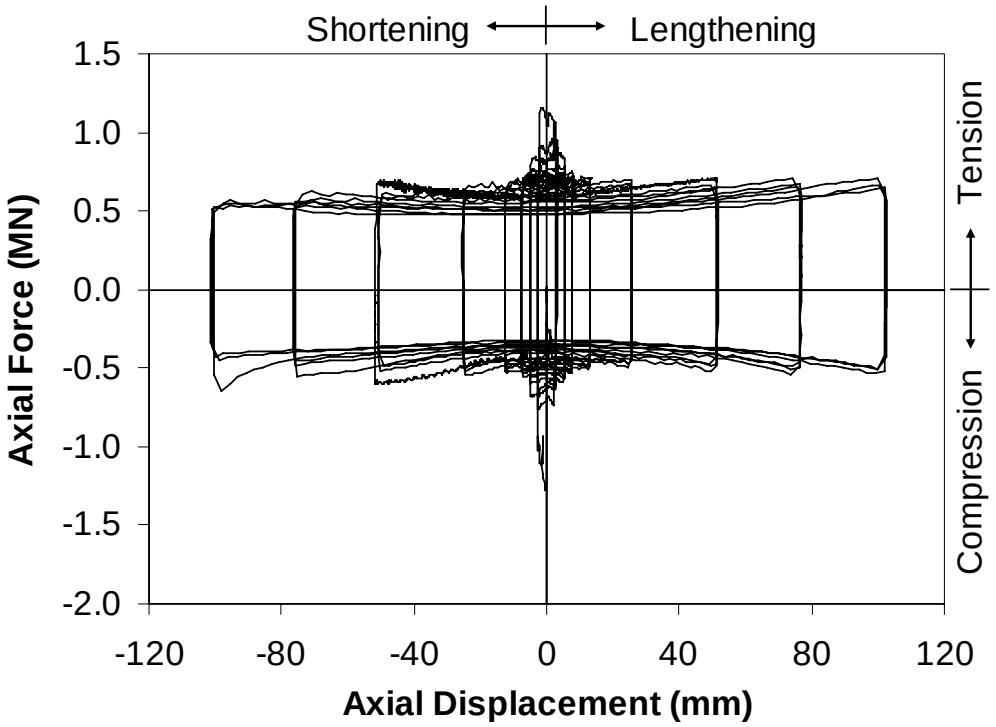


**Figure 5.3 Hysteretic Response for Test Unit # 2 at a D/t Ratio of 94**

### 5.3.3 Test Unit # 3 at a D/t Ratio of 46

Test Unit # 3 obtained a maximum axial compression force of -1.74 MN (-391 kips) at -0.41 mm (-0.02 in.) after which a sharp decrease in the axial force transfer occurred as shown in Figure 5.4. At axial compression displacements beyond this peak a typical maximum cyclic force of -0.81 MN (-182 kips) was obtained. During the last axial compression cycle some loose concrete collected inside the base void which resulted in contact between the reinforced concrete core and the base plate. This contact resulted in an increase in the stiffness of the hysteretic response as shown by the peak at a displacement of -100 mm (3.9 in.) in Figure 5.4. In axial tension a maximum axial force of 1.23 MN (276 kips) at 1.9 mm (0.074 in.) was obtained after which a sharp decrease in the axial force transfer occurred. At axial tension displacements beyond this maximum a typical maximum cyclic force of 0.6 MN (135 kips) was obtained.

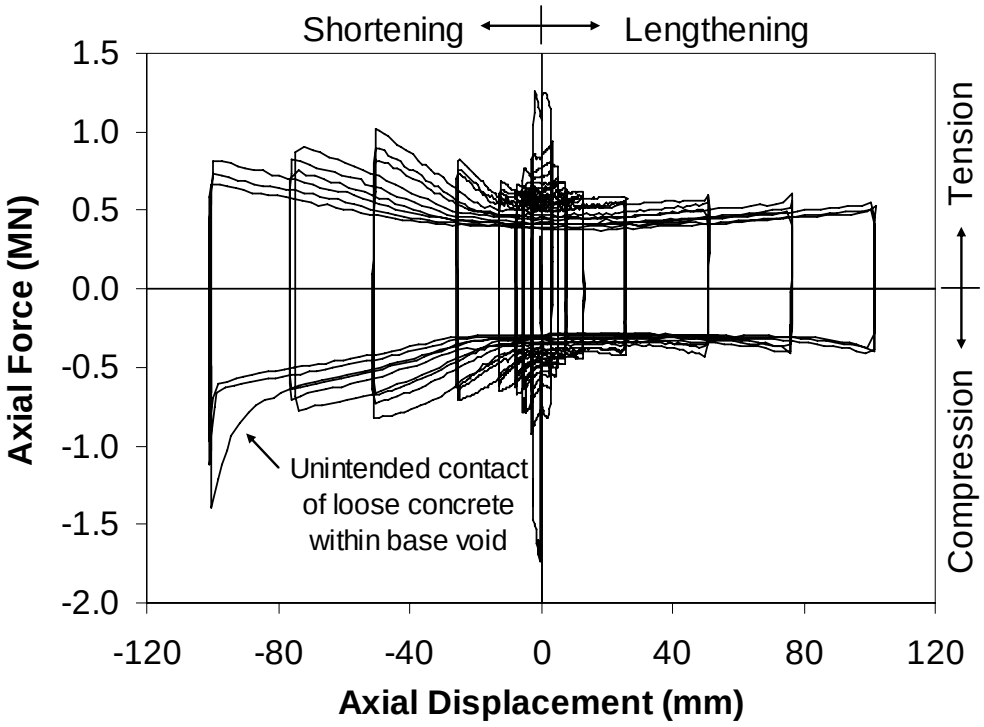


**Figure 5.4 Hysteretic Response for Test Unit # 3 at a D/t Ratio of 46**

### 5.3.4 Test Unit # 11 at a D/t Ratio of 40.7

Test Unit # 11 obtained a maximum axial compression force of -1.11 MN (-249 kips) at -1.26 mm (-0.05 in.) after which a sharp decrease in the axial force transfer occurred as shown in Figure 5.5. At axial compression displacements beyond this maximum a slight softening in the hysteretic response occurred. In axial tension a maximum axial force of 0.75 MN (169 kips) at 2.46 mm (0.10 in.) was obtained after which a sharp decrease in the axial force transfer occurred. At axial tension displacements beyond this maximum, a slight softening in the hysteretic response occurred as well.

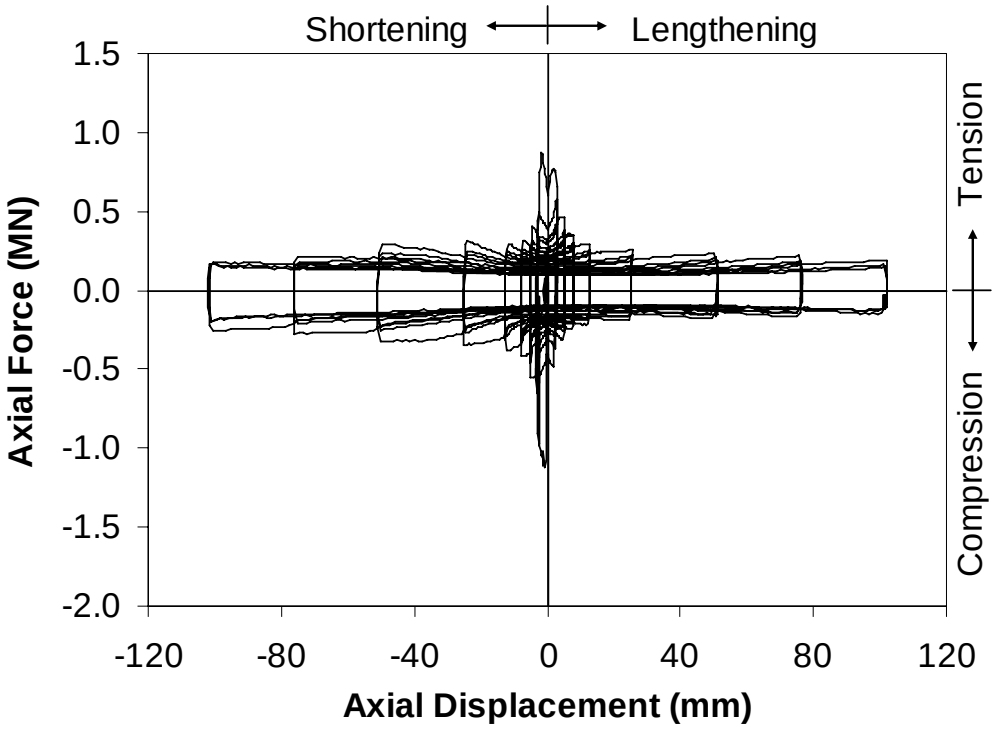


**Figure 5.5 Hysteretic Response for Test Unit # 11 at a D/t Ratio of 40.7**

### 5.3.5 Test Unit # 12 at a D/t Ratio of 40.7

Test Unit # 12 obtained a maximum axial compression force of -1.07 MN (-241 kips) at -0.28 mm (-0.01 in.) after which a sharp decrease in the axial force transfer occurred as shown in Figure 5.6. At axial compression displacements beyond this maximum a slight softening in the hysteretic response occurred. In axial tension a maximum axial force of 0.78 MN (176 kips) at 2.83 mm (0.11 in.) was obtained after which a sharp decrease in the axial force transfer occurred. At axial tension displacements beyond this maximum a slight softening in the hysteretic response occurred.

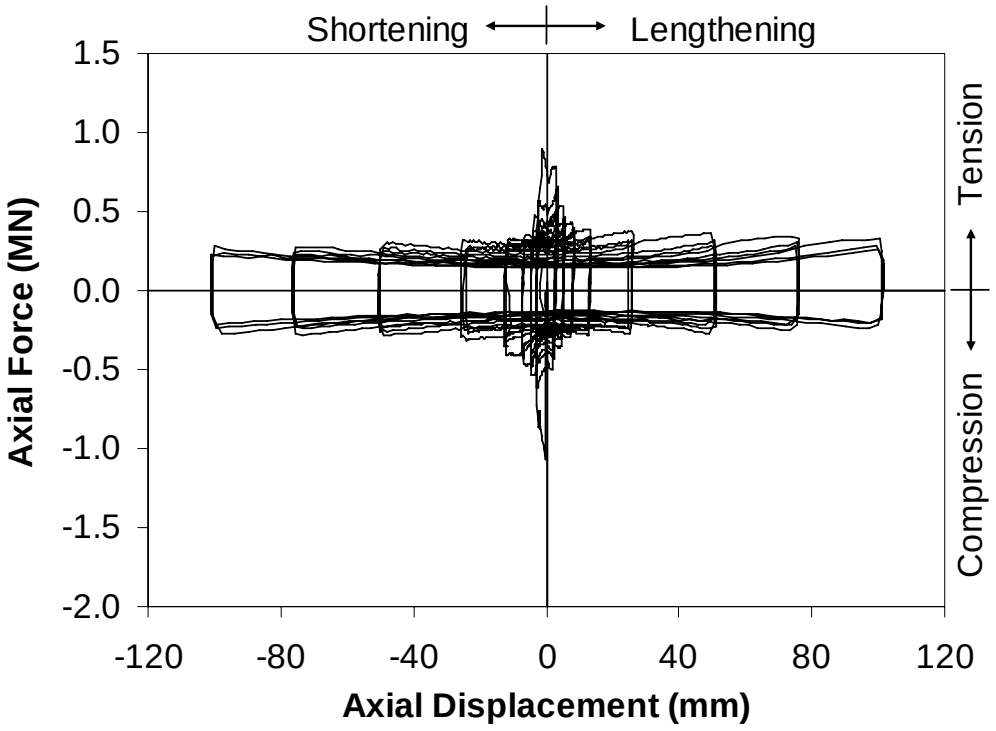


**Figure 5.6 Hysteretic Response for Test Unit # 12 at a D/t Ratio of 40.7**

### 5.3.6 Test Unit # 10 at a D/t Ratio of 128 (Surface Condition Study)

The test unit with a water-bentonite surface coating on the steel shell lacked the initial peaks in the axial compression and axial tension forces which were present in Test Unit # 1, also at a D/t ratio of 128. As shown in Figure 5.7, Test Unit # 10 obtained relatively constant axial forces at all axial compression and axial tension displacements. In axial compression a typical maximum cyclic force of -0.74 MN (-166 kips) was obtained. In axial tension a typical maximum cyclic force of 0.62 MN (139 kips) was obtained. The lack of initial peaks in the response is a result of the surface condition which prevented formation of an adhesive bond.

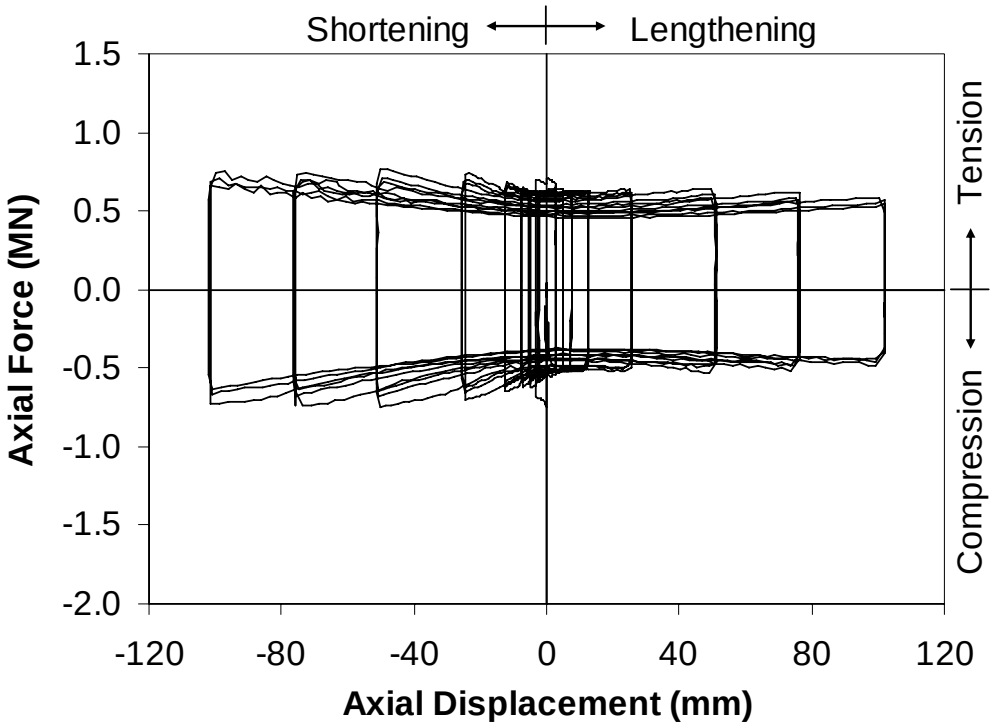


**Figure 5.7 Hysteretic Response for Test Unit # 10 at a D/t Ratio of 128 and a Water-Bentonite Coating on the Steel Shell**

## 5.4 Response for Test Units with Expansive Concrete

Results for test units with expansive concrete in which the D/t ratio was the parameter of variation will be presented.

### 5.4.1 Test Unit # 13 at a D/t Ratio of 128

Test Unit # 13 obtained a maximum axial compression force of -1.46 MN (-328 kips) at -0.13 mm (-0.01 in.) after which a sharp decrease in the axial force transfer occurred as shown in Figure 5.8. At axial compression displacements beyond this maximum a typical maximum cyclic force of -1.08 MN (-243 kips) was obtained. In axial tension a maximum axial force of 1.03 MN (231 kips) at 2.91 mm (0.11 in.) was obtained after which a sharp decrease in the axial force transfer occurred. A softening in the response occurred during the last two displacement levels as shown in Figure 5.8 with an axial tension force of 0.66 MN (148 kips) obtained at the maximum applied displacement of 98.6 mm (3.88 in.).

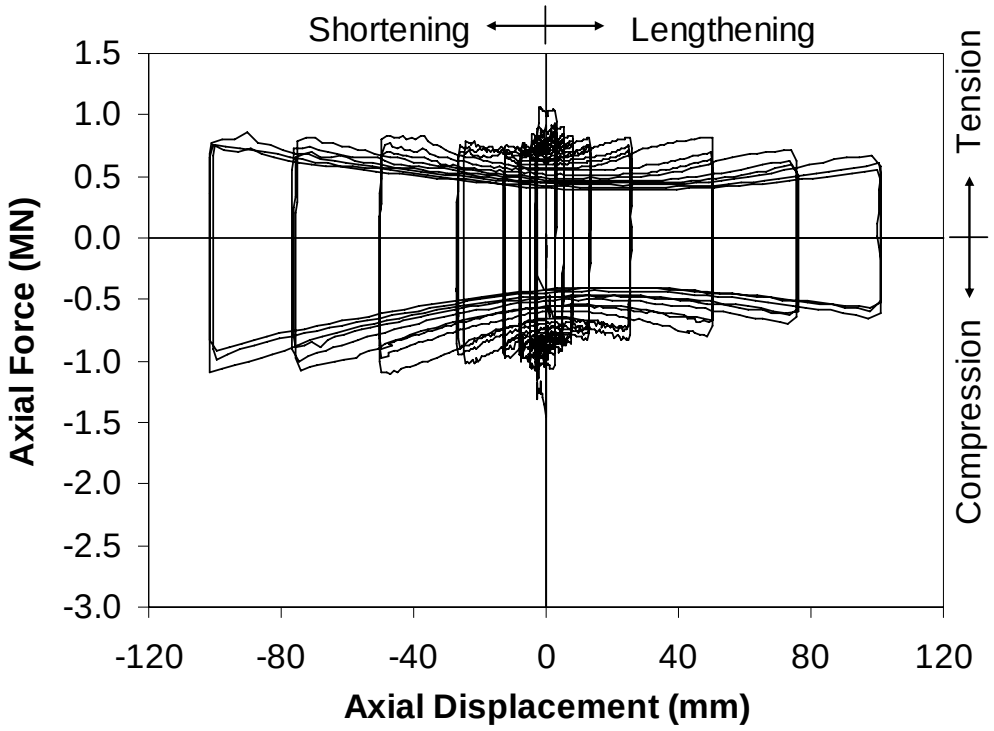


**Figure 5.8 Hysteretic Response for Test Unit # 13, with Expansive Concrete, at a D/t Ratio of 128**

### 5.4.2 Test Unit # 14 at a D/t Ratio of 94

Test Unit # 14 obtained a maximum axial compression force of -2.39 MN (-537 kips) at -0.44 mm (-0.02 in.) after which a sharp decrease in the axial force transfer occurred as shown in Figure 5.9. At axial compression displacements beyond this maximum a typical maximum cyclic force of -0.83 MN (-186 kips) was obtained. In axial tension a maximum axial force of 1.23 MN (276 kips) at 2.1 mm (0.08 in.) was obtained after which a sharp decrease in the axial force transfer occurred. At axial tension displacements beyond this peak a typical maximum cyclic force of 0.65 MN (146 kips) was obtained.

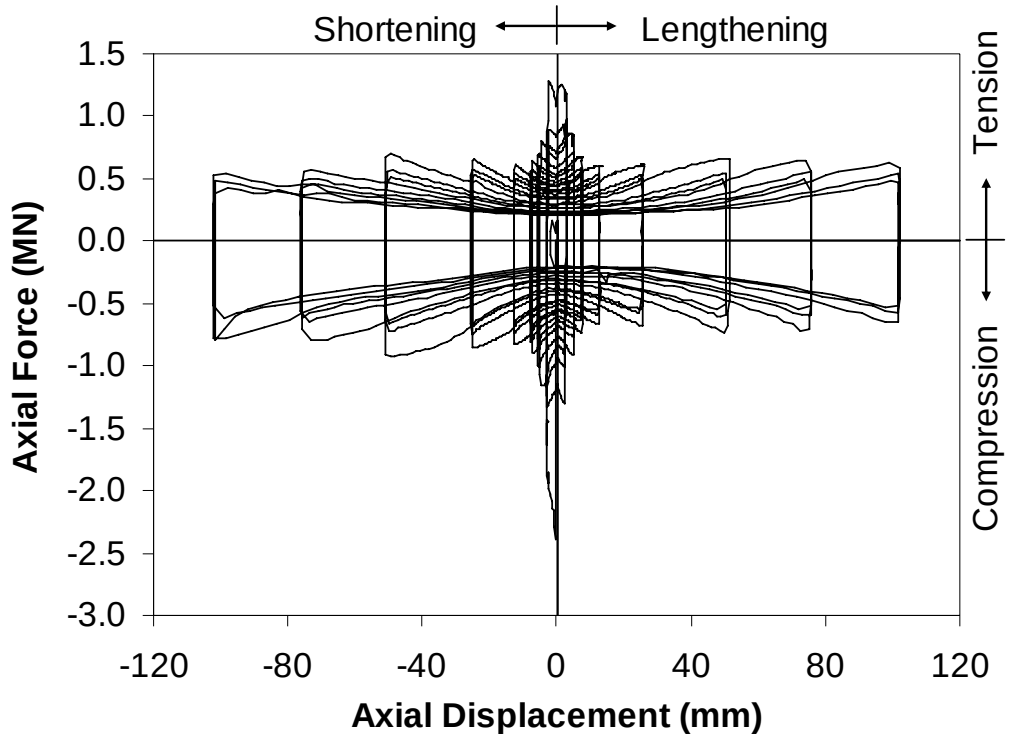


**Figure 5.9 Hysteretic Response for Test Unit # 14, with Expansive Concrete, at a D/t Ratio of 94**

### 5.4.3 Test Unit # 15 at a D/t Ratio of 46

Test Unit # 15 obtained a maximum axial compression force of -2.87 MN (-645 kips) at -0.72 mm (-0.03 in.) after which a sharp decrease in the axial force transfer occurred as shown in Figure 5.10. A noticeable softening of the response occurred during the last two axial compression displacement levels as shown in Figure 5.10. In axial tension a maximum axial force of 1.16 MN (261 kips) at 2.0 mm (0.08 in.) was obtained after which a sharp decrease in the axial force transfer occurred. At axial tension displacements beyond this peak a slight softening of the response occurred.

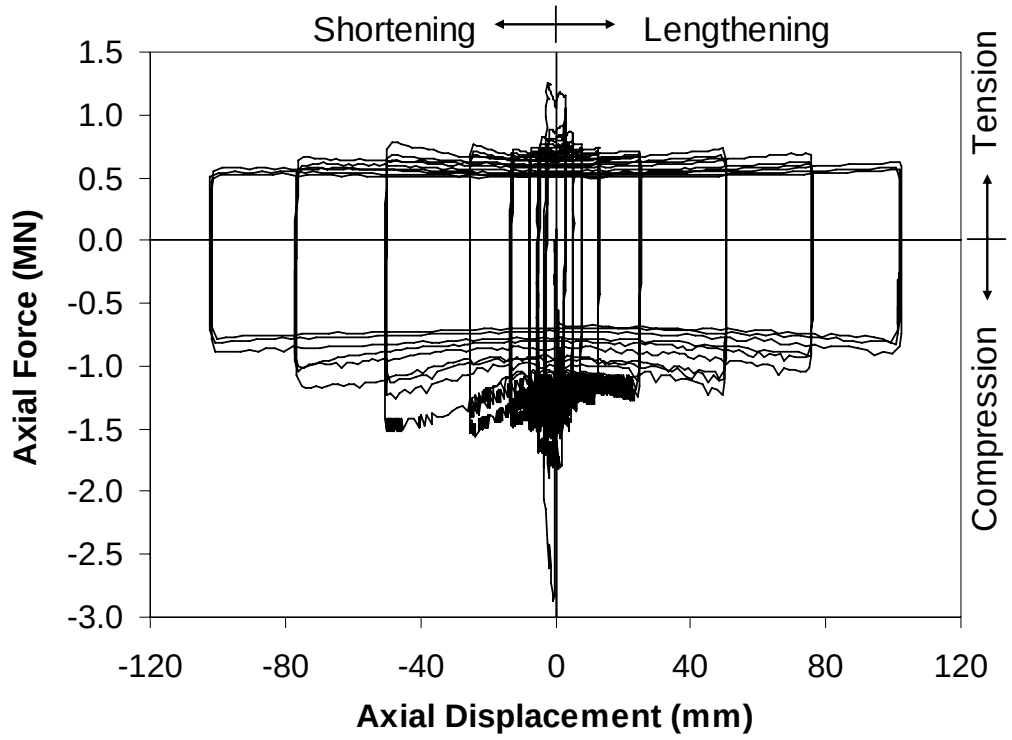


**Figure 5.10 Hysteretic Response for Test Unit # 15, with Expansive Concrete, at a D/t Ratio of 46**

## 5.5 Response for Test Units with a Mechanism

The hysteretic response of each mechanism design tested, at a D/t ratio of 128, will be presented. Relevant photographic evidence will be presented from testing as well as photographs from failure inspections conducted after testing. Failure inspections involved using a torch to extract the steel shell to reveal the mechanism condition, and the extent of concrete crushing.

### 5.5.1 Test Unit # 4 with a Weld Bead

The weld bead mechanism (Test Unit # 4) obtained relatively constant maximum cyclic forces throughout all axial compression and axial tension displacements as shown in Figure 5.11. This test unit obtained a maximum axial compression force of -2.29 MN (-514 kips) at -48.1 mm (-1.89 in.) and a maximum axial tension force of 2.10 MN (473 kips) at 49.8 mm (1.96 in.). The axial force transfer was limited by circumferential

yielding of the steel shell and the weld bead at the mechanism location as shown in Figure 5.12. A residual radial deformation of approximately 9.5 mm (0.38 in.) was observed at the end of the test. This circumferential steel shell deformation occurred over a length of approximately 127 mm (5.0 in.), and had no noticeable change in shape when subjected to axial tension. After the test a portion of the steel shell was removed to allow examination of the internal failure. This revealed the weld bead deformed with the steel shell and did not fracture as shown in Figure 5.13. Concrete above and below the weld bead crushed to lengths corresponding to the applied axial displacements.

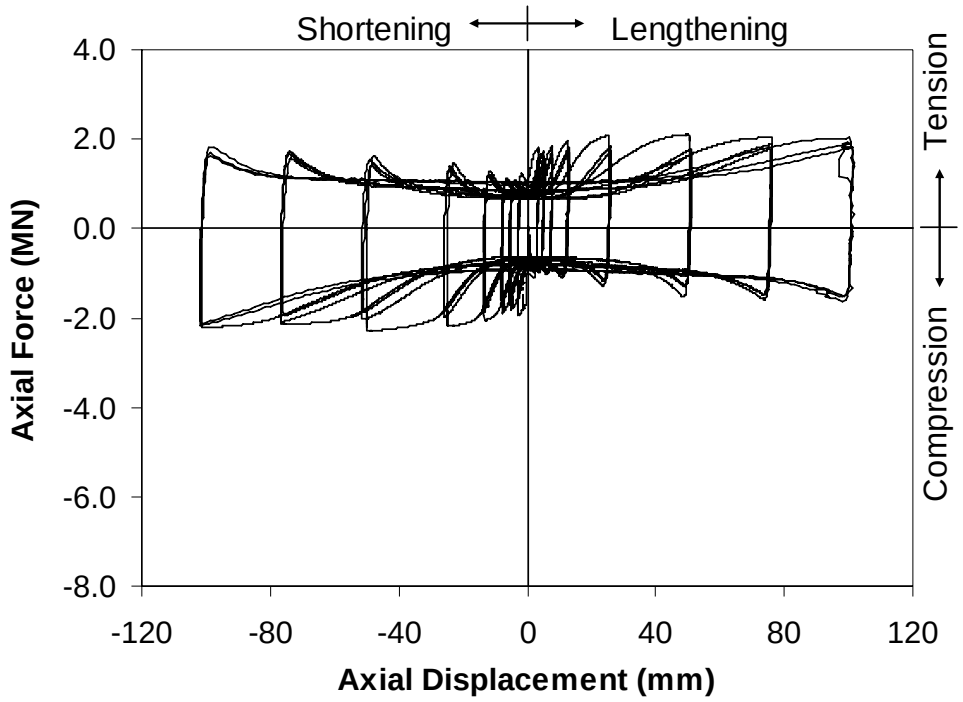


**Figure 5.11 Hysteretic Response for Test Unit # 4, with a Weld Bead, at a D/t Ratio of 128**


**Figure 5.12 Circumferential Yielding of the Steel Shell and Weld Bead at the Mechanism Location (Test Unit # 4)**

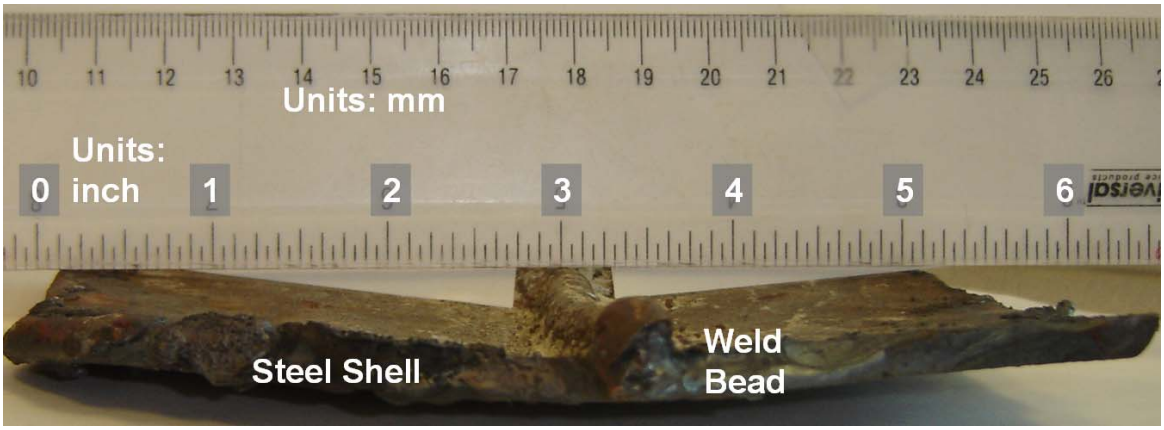


**Figure 5.13 Failure Inspection of the Steel Shell and Weld Bead – After Test (Test Unit # 4)**

### 5.5.2 Test Unit # 5 with a Shear Ring

Test Unit #5 with a shear ring at a D/t ratio of 128 obtained relatively constant maximum cyclic forces in axial compression. A maximum axial compression force of -3.09 MN (-695 kips) was obtained at -50.7 mm (2.0 in.). When axial compression was applied to displacement of -76 mm (-3.0 in.) the axial force transfer increased due to contact between the steel base plate and reinforced concrete core as shown in Figure 5.14. This contact was caused by concrete debris at the base of the reinforced concrete core which accumulated to the extent that the base void became partially filled due to

insufficient openings in the base to allow removal of loose concrete. In axial tension this test unit obtained a maximum axial force of 3.48 MN (783 kips) at a displacement of 24.1 mm (0.95 in.). Beyond this displacement there was a slight softening of the response.

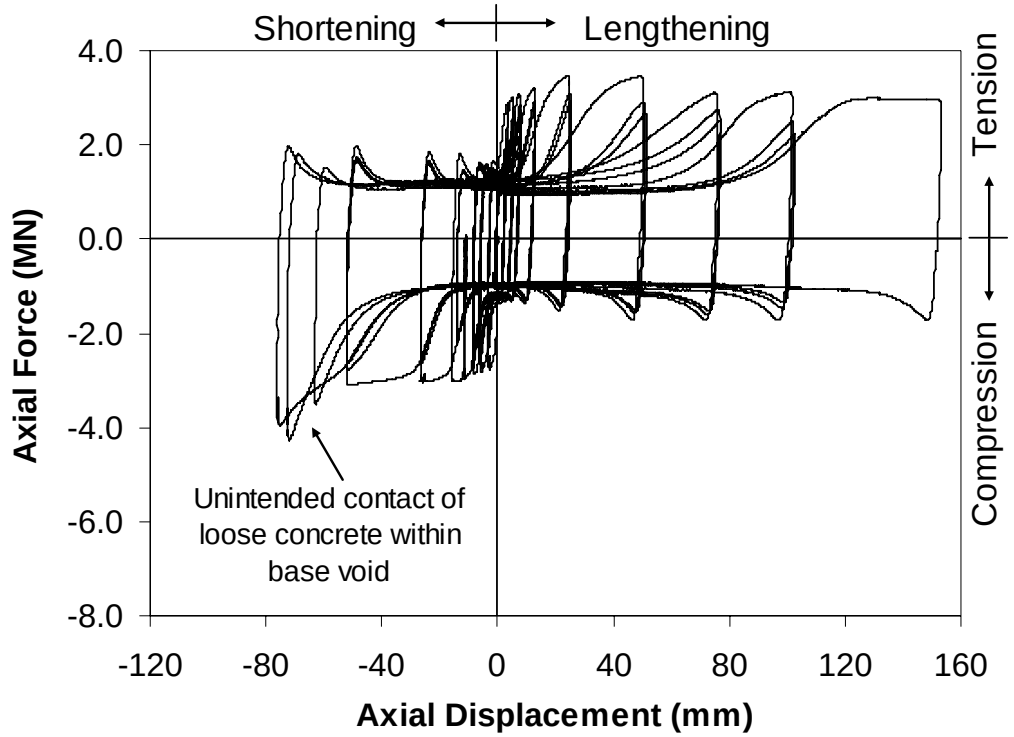


**Figure 5.14 Hysteretic Response for Test Unit # 5, with a Shear Ring, at a D/t Ratio of 128**

The capacity of this test unit was obtained through circumferential yielding of the steel shell and the shear ring at the mechanism location as shown in Figure 5.15. This yielding resulted in a residual radial deformation of approximately 9.5 mm (0.4 in.) observed at the end of the test. The steel shell deformation had a length of approximately 152 mm (6.0 in.) and had no noticeable change in shape when subjected to axial tension. The shear ring deformed with the steel shell and did not fracture or have any weld failure as shown in Figure 5.16 after the test. Concrete above and below the shear ring crushed to lengths corresponding to the applied axial displacements.

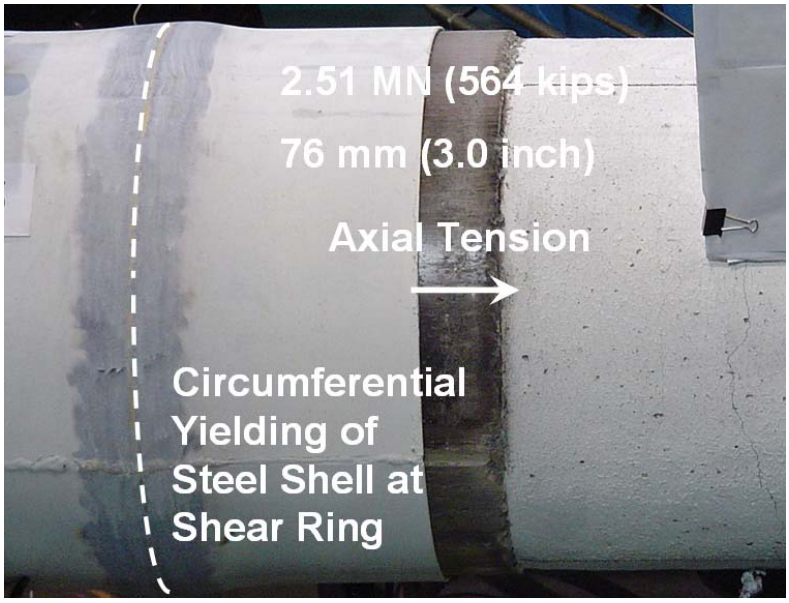


**Figure 5.15 Circumferential Yielding of the Steel Shell and Shear Ring at the Mechanism Location (Test Unit # 5)**

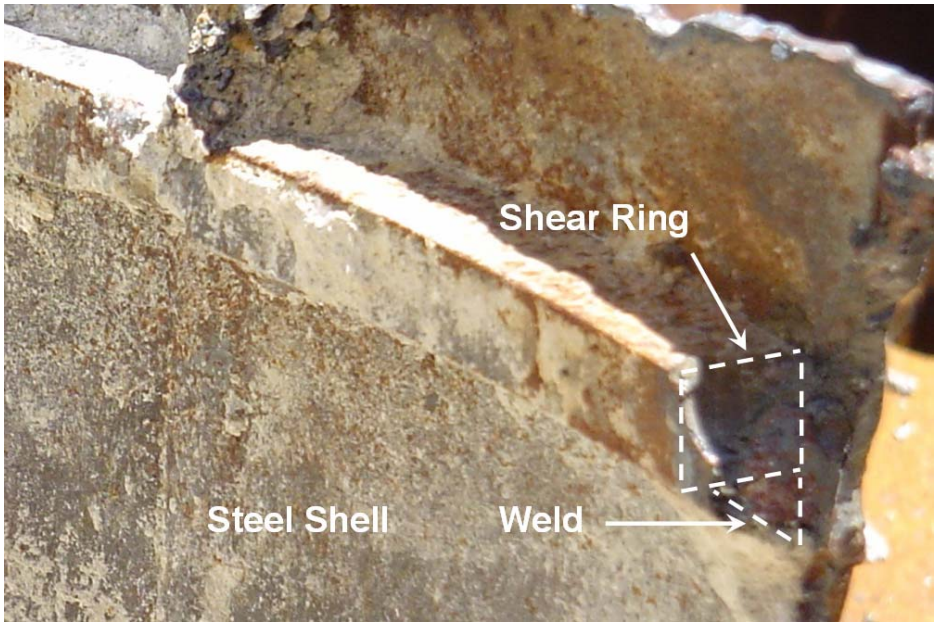


**Figure 5.16 Failure Inspection of the Steel Shell and Shear Ring – After Test (Test Unit # 5)**

### 5.5.3 Test Unit # 6 with a Cross Bar

The cross bar mechanism (Test Unit # 6) was initially effective at transferring axial force, however, this diminished after the initial cyclic axial displacements, as shown

in Figure 5.17. This test unit obtained a maximum axial compression force of -2.43 MN (-546 kips) at -2.46 mm (-0.10 in.) and a maximum axial tension force of 1.60 MN (359 kips) at 2.74 mm (0.11 in.). The axial force transferred decreased after these peak axial forces and obtained a relatively constant axial force transfer at greater cyclic axial displacements. This was a result of failure of the cross bar weld, leaving the friction bond as essentially the only mechanism of force transfer. The separation of the cross bar from the steel shell is shown in Figure 5.18, in which the cross bar can be seen to be embedded within the concrete core.

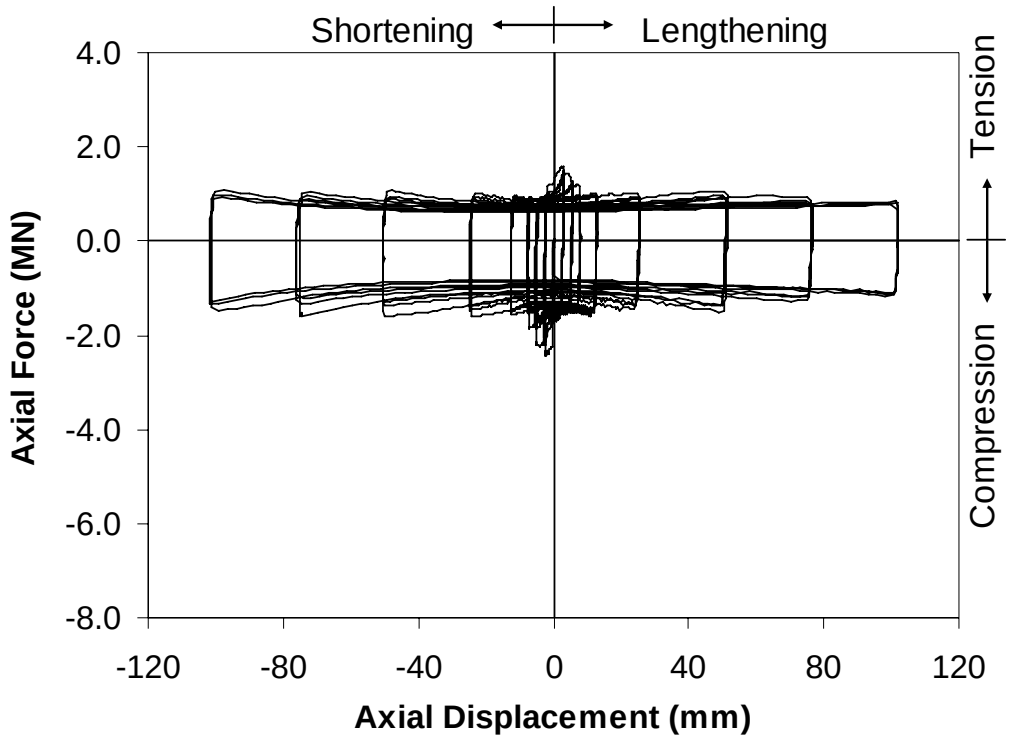


**Figure 5.17 Hysteretic Response for Test Unit # 6, with a Cross Bar, at a D/t Ratio of 128**


**Figure 5.18 Separation of the Cross Bar from the Steel Shell (Test Unit # 6)**

### 5.5.4 Test Unit # 7 with a Welded Reinforcement Bar

The circumferentially welded reinforcement bar mechanism (Test Unit # 7) obtained relatively constant maximum cyclic forces throughout all axial compression displacements, as shown in Figure 5.19. A maximum axial compression force of -3.0 MN (-674 kips) was obtained at -74.8 mm (-2.94 in.) after which the axial force increased due to contact between the steel base plate and concrete debris dislodged from the reinforced concrete core as shown in Figure 5.19. This was the first test unit tested and lacked openings in the base of the steel shell to allow for loose concrete to fall out. Loose concrete accumulated due to failure of concrete at the steel shell-concrete interface at the base. In axial tension this test unit obtained a maximum axial force of 3.33 MN (748 kips) at a displacement of 36.4 mm (1.43 in.). After this displacement a softening in the response occurred. Softening of the response was caused by circumferential yielding of the steel shell and the reinforcing bar at the mechanism location as shown in Figure 5.21. This yielding resulted in a residual radial deformation of approximately 9.5 mm (0.38 in.) observed at the end of the test. This steel shell deformation had a length of approximately 127 mm (5.0 in.) and had no noticeable change in shape when subjected to axial tension. Removal of a steel shell section after testing revealed the # 3 bar did not fracture or sustain any fracture damage to the weld, as shown in Figure 5.21. Concrete

above and below the # 3 bar crushed to lengths corresponding to the applied axial displacements, as shown in Figure 5.22.

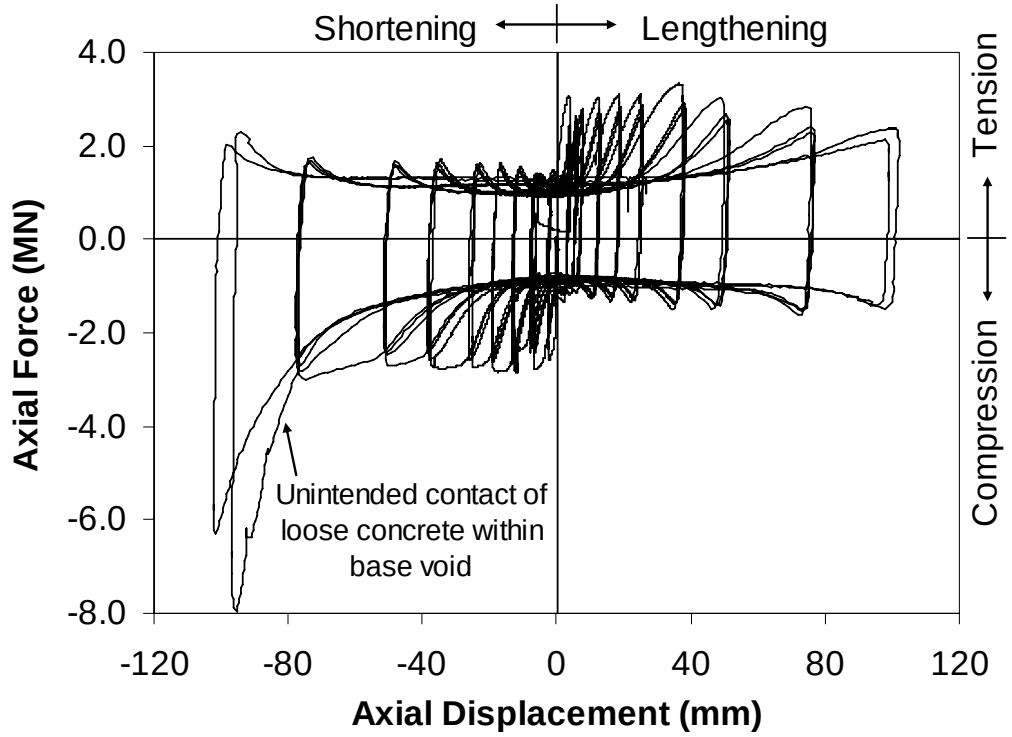


**Figure 5.19 Hysteretic Response for Test Unit # 7, with a Welded Reinforcement Bar, at a D/t Ratio of 128**

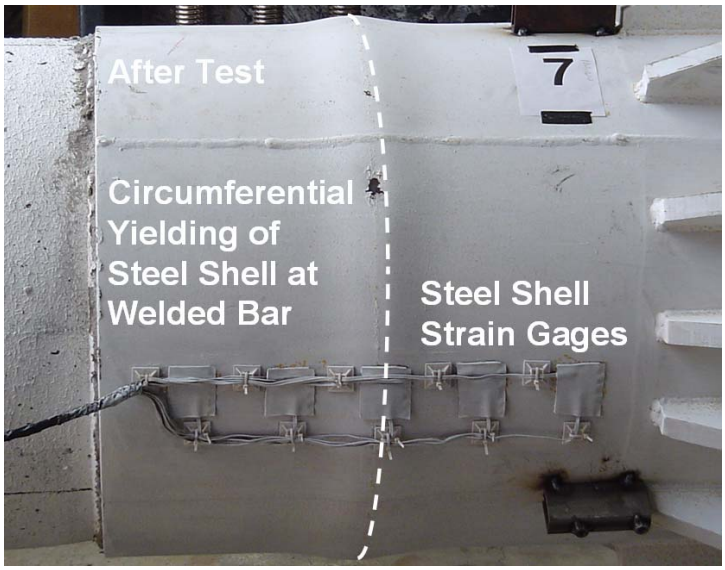


**Figure 5.20 Circumferential Yielding of the Steel Shell and Welded Bar at the Mechanism Location (Test Unit # 7)**

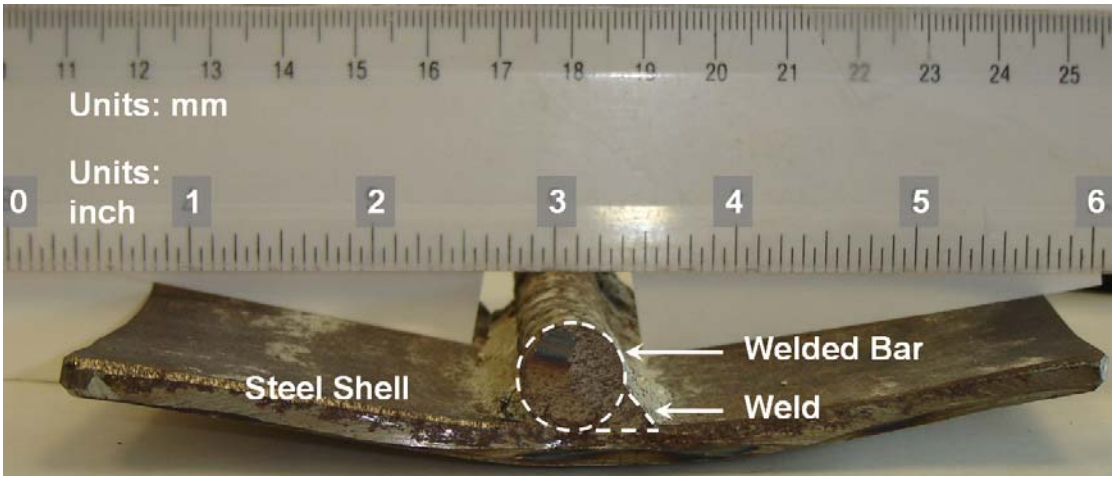


**Figure 5.21 Failure Inspection of the Steel Shell and Welded Bar – After Test (Test Unit # 7)**

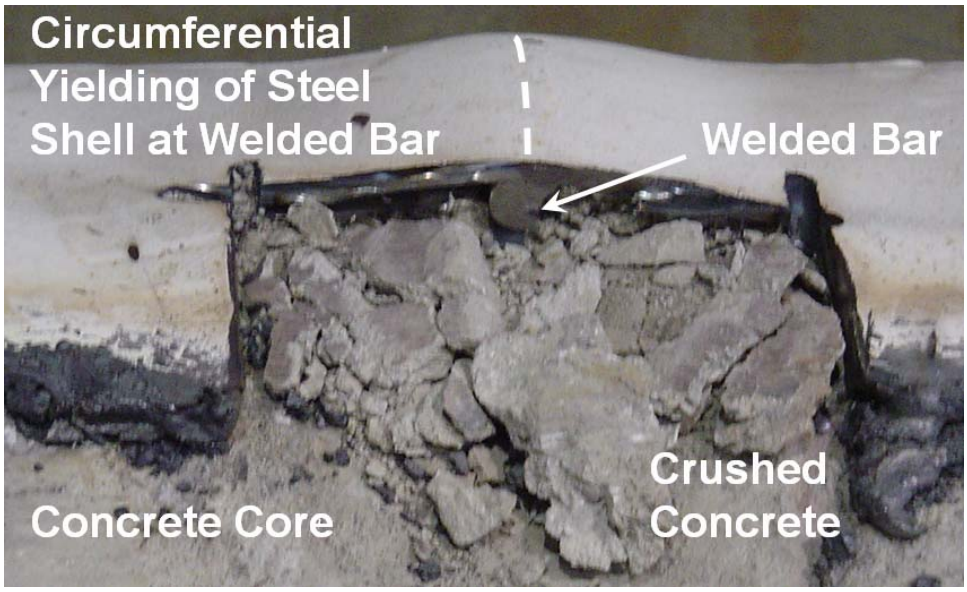


**Figure 5.22 Failure Inspection of the Steel Shell, Welded Bar, and Core – After Test (Test Unit # 7)**

### 5.5.5 Test Unit # 8 with Shear Studs

The shear stud mechanism (Test Unit # 8) was initially effective at transferring axial force; however, this mechanism was quickly rendered ineffective due to failure of the shear stud welds. This test unit obtained a maximum axial compression force of -1.70 MN (-382 kips) at -52.0 mm (-2.05 in.) and a maximum axial tension force of 1.68 MN (377 kips) at 41.7 mm (1.64 in.). Therefore, at large cyclic axial displacements the axial force transferred was essentially a result of the friction bond mechanism, as shown in

Figure 5.23. A constant axial compression and tension force transfer was obtained at the axial displacements after the initial peaks. Shear studs embedded in the concrete core are shown in the photograph of the concrete core after the test in Figure 5.24. The weld remaining on the steel shell from the shear stud connection can also be seen in Figure 5.24.

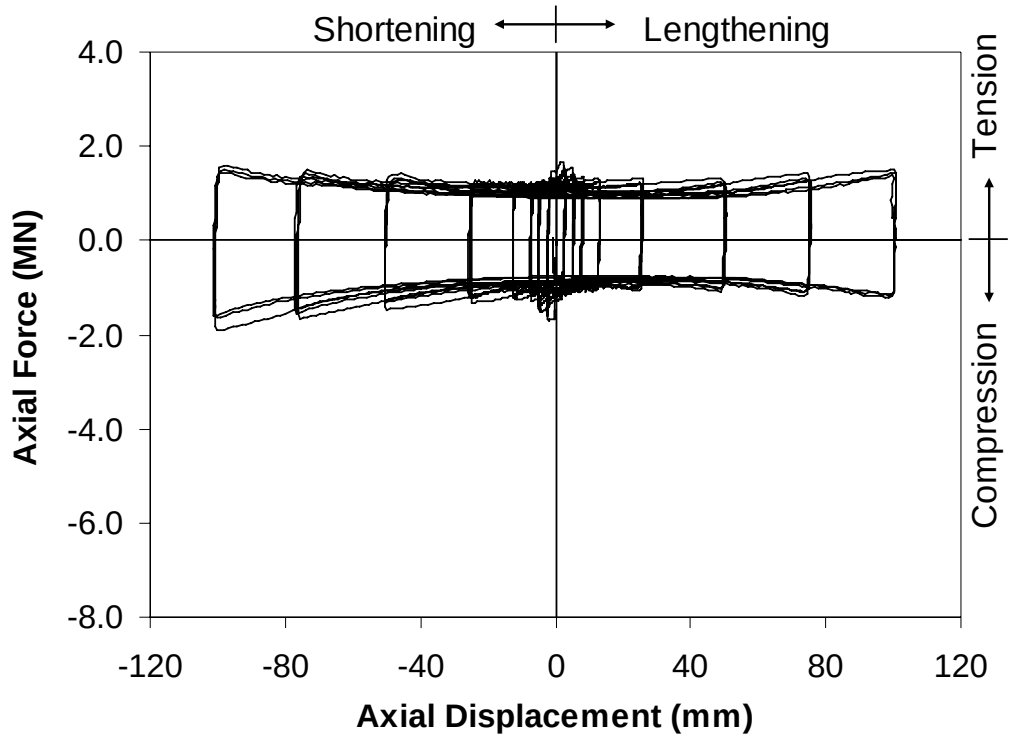


**Figure 5.23 Hysteretic Response for Test Unit # 8, with a Shear Studs, at a D/t Ratio of 128**

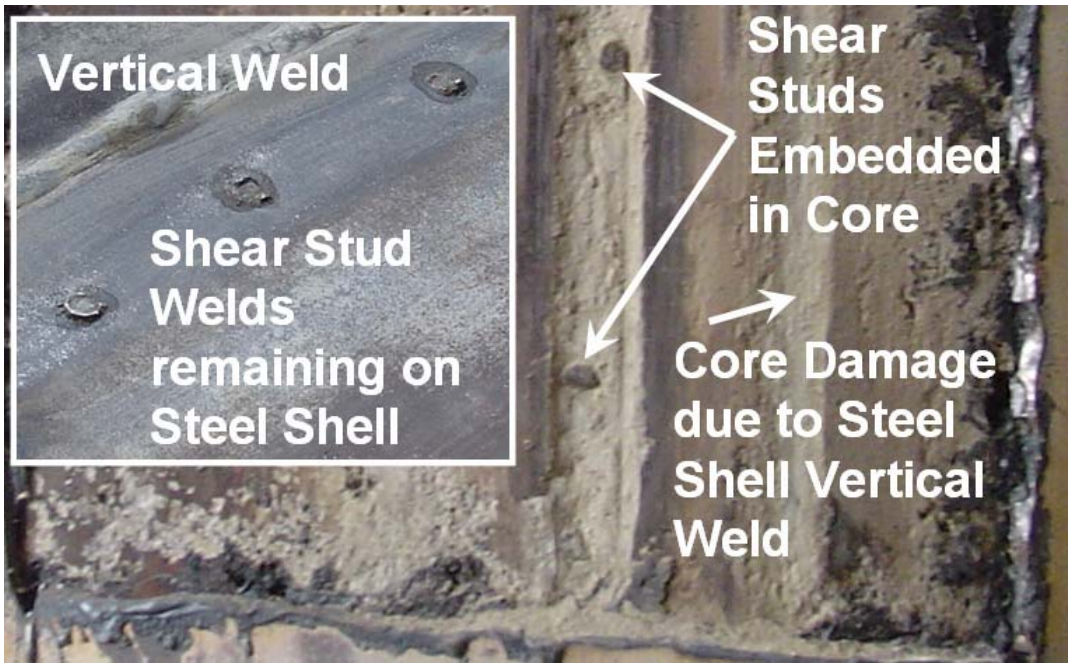


**Figure 5.24 Test Unit # 8 Shear Stud Failure (After Test): Stud Welds on Shell (left) and Studs Embedded in Concrete Core (right)**

### 5.5.6 Test Unit # 9 with Tread Plate

The tread plate mechanism (Test Unit # 9) was initially very effective at transferring axial force, however, the mechanism deteriorated very quickly as the axial displacement increased, as shown in Figure 5.25. A maximum axial compression force of -3.86 MN (-868 kips) was obtained at -5.1 mm (-0.2 in.), and a maximum axial tension force of 3.31 MN (745 kips) was obtained at 5.1 mm (0.2 in.). After these peak forces, the axial force had a sharp decrease as shown in Figure 5.25. This decrease in the axial force was due to the crushing of concrete between the treads, which resulted in a diminished contact between the reinforced concrete core and the treads. At axial compression displacements after the sharp decrease in axial force transfer, a softening of the response occurred as the contact between the concrete core and the treads continued to diminish. This softening effect was not observed in axial tension, as shown in Figure 5.25.

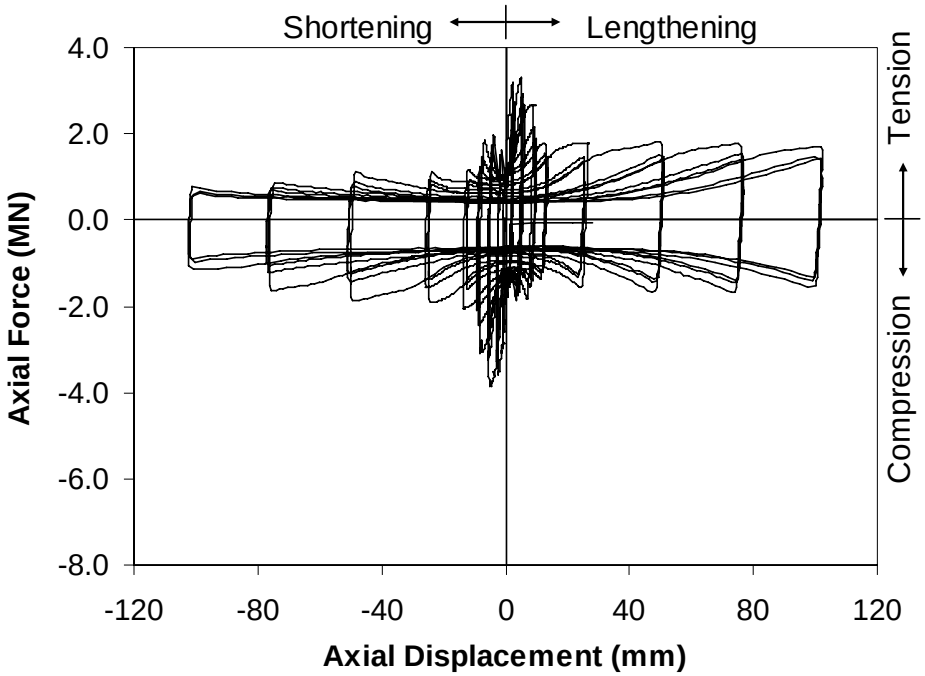


**Figure 5.25 Hysteretic Response for Test Unit # 9, with a Tread Plate, at a D/t Ratio of 128**

The extent of concrete crushing, below the lowermost circumferential row of treads, did not extend beyond approximately the maximum applied axial compression displacement. In axial compression, after the concrete between treads crushed, there was no concrete remaining with sufficient strength to provide a bond with the concrete core. This concrete crushing is shown in Figure 5.26 in which alternating lines of crushed and non-crushed concrete can be seen extending from the concrete core. A view of the concrete crushing is also shown in Figure 5.27 which shows the tread plate section (after the test) with crushed concrete between the treads. As a result of this concrete crushing, a softening of the response occurred as the contact diminished. However, in axial tension a softening of the response was not obtained. This is due to the confinement of the crushed concrete, around the lowermost circumferential row of treads, such that in axial tension this crushed concrete was in a state of compression. This compression state, as shown in Figure 5.28, allowed the lowermost row of treads to remain active in axial tension which resulted in no softening of the hysteretic response.

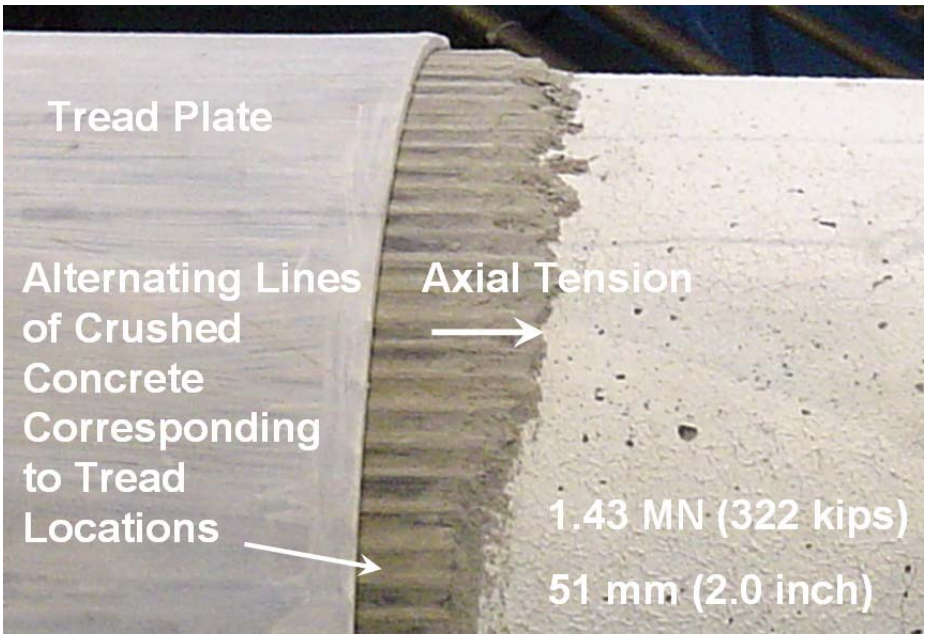


**Figure 5.26 Test Unit # 9 Concrete Crushing between Treads – During Test**

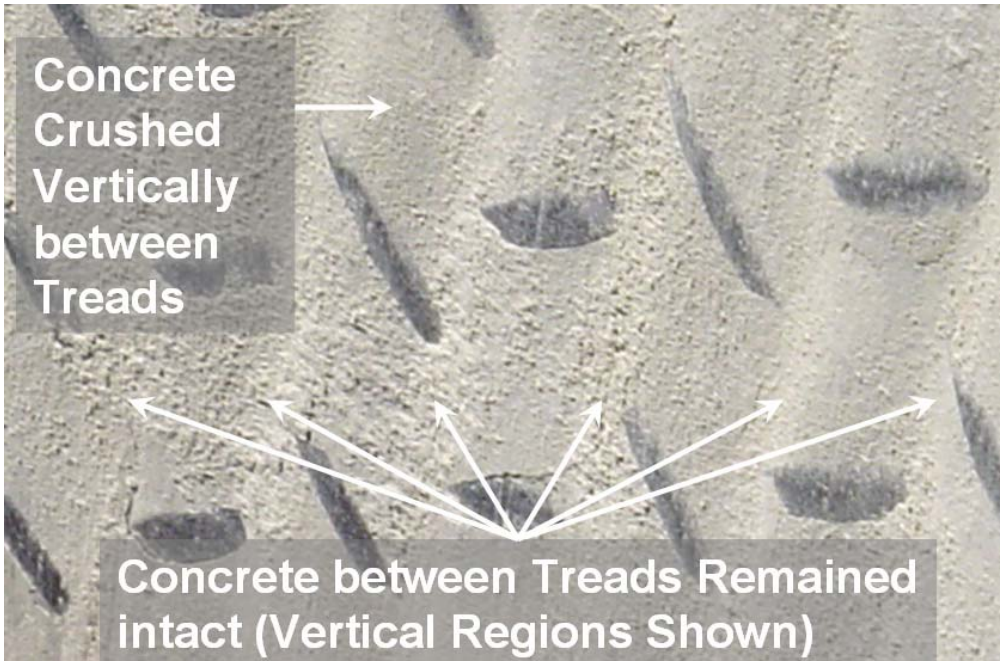


**Figure 5.27 Test Unit # 9 Concrete Crushing between Treads – View of Steel Shell After Test**

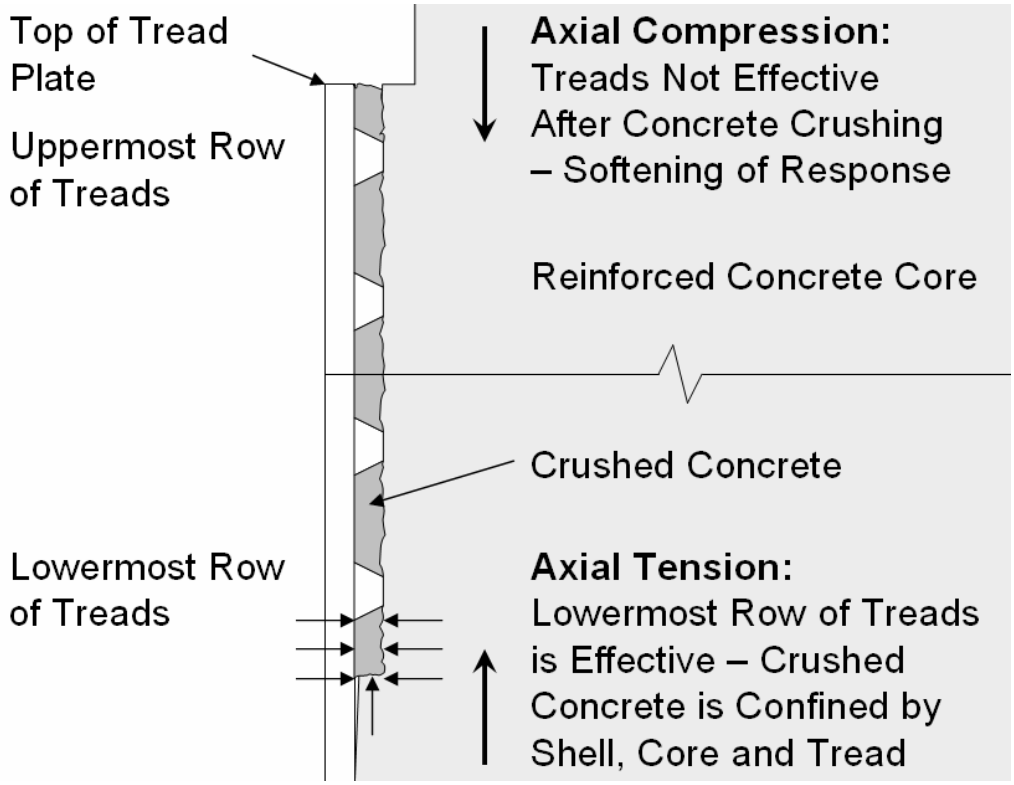


**Figure 5.28 Confinement of Concrete with respect to Steel Shell and Treads**

## 5.6 Response for Test Units Studying the Shear Ring Mechanism (Phase 2)

The axial force-axial displacement hysteretic response for test units in the Phase 2 experimental program (shear ring study), in which the D/t ratio or surface condition was varied, is presented.

### 5.6.1 Test Unit # 16 with a D/t Ratio of 94

The test unit with a single shear ring and a D/t ratio of 94 (Test Unit # 16) had a similar performance to the shear ring test unit at a D/t ratio of 128, in that the capacity was limited by circumferential yielding of the steel shell and shear ring. A maximum axial compression force of -2.62 MN (-589 kips) was obtained at a displacement of -47.9 mm (-1.9 in.). A maximum axial tension force of 2.78 MN (624 kips) was obtained at a displacement of 48.4 mm (1.9 in.) as shown in Figure 5.29. Softening of the response was caused by circumferential yielding of the steel shell and the shear ring at the mechanism location, as shown in Figure 5.30, with a residual radial deformation of

approximately 4.8 mm (0.19 in.) observed at the end of the test. This steel shell deformation had a length of approximately 178 mm (7.0 in.), and had no noticeable change in shape when subjected to reversals in the applied axial displacement and force. The shear ring deformed with the steel shell and did not fracture or have any weld failure, as shown in the failure inspection conducted after the test, as shown in Figure 5.31. Concrete crushed above and below the shear ring to lengths corresponding to the applied axial displacement.

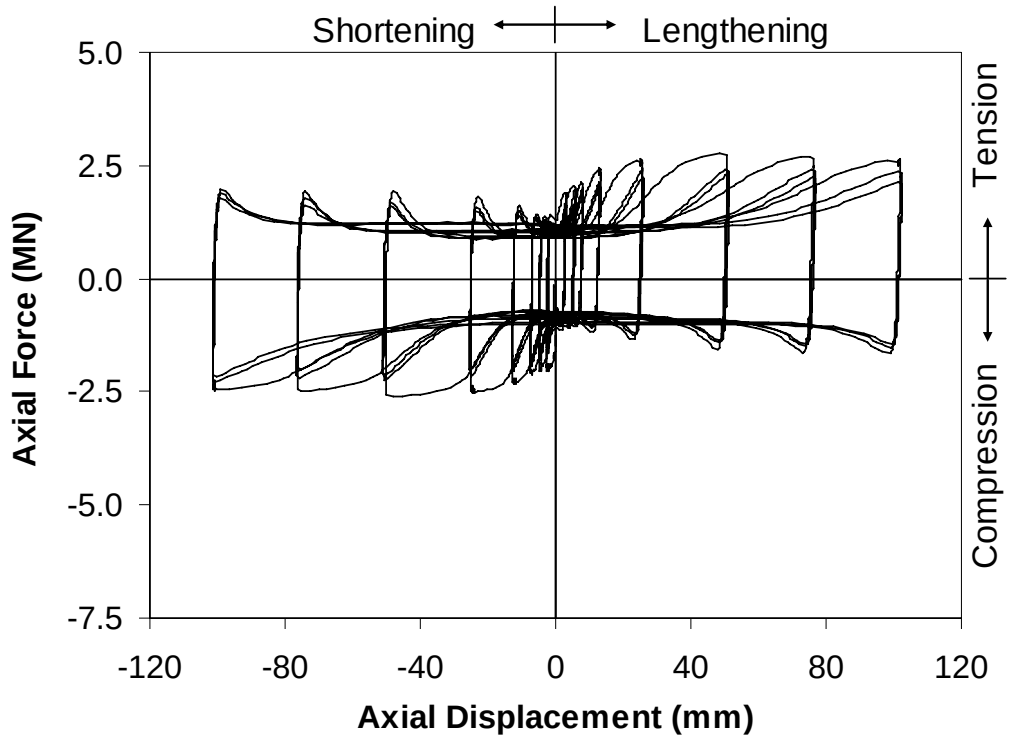


**Figure 5.29 Hysteretic Response for Test Unit # 16, with a Shear Ring (D/t of 94)**

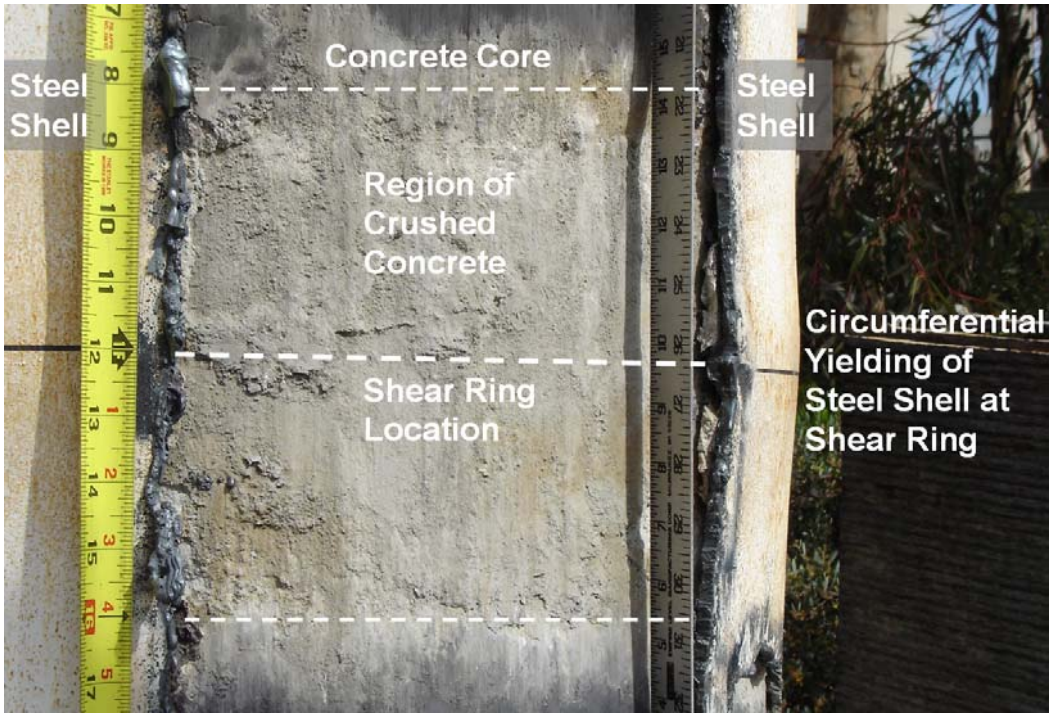


**Figure 5.30 Circumferential Yielding of the Steel Shell and Shear Ring at the Mechanism Location (Test Unit # 16)**

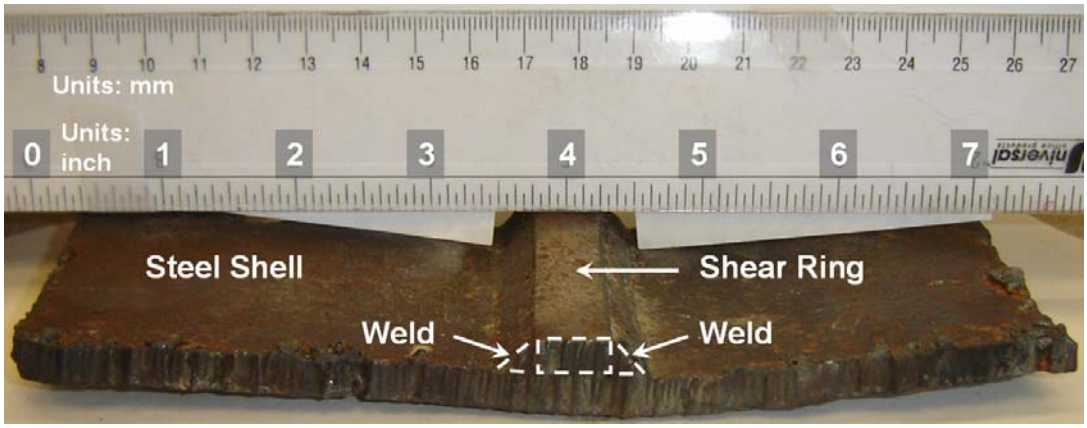


**Figure 5.31 Steel Shell and Shear Ring – After Test (Test Unit # 16)**

### 5.6.2 Test Unit # 17 with a D/t Ratio of 24

The test unit with a D/t ratio of 24 and a single shear ring (Test Unit # 17) had a hysteretic response in which the axial force transfer increased as axial displacements increased, as shown in Figure 5.32. A maximum axial tension force of 4.37 MN (983 kips) was obtained at a displacement of 16.5 mm (0.65 in.), as shown in Figure 5.33.

Axial tension was not applied beyond this displacement due to cracking and spalling of the concrete cover (surrounding the reinforcement bar cage) in the force transfer section of the test unit. This was a result of the longitudinal bar reinforcement exceeding its yield stress, as observed in the strain profile in Appendix Figures 8.10 and 8.12. After this cycle monotonic axial compression was applied to -6.04 MN (-1,360 kips) with a corresponding displacement of -43.9 mm (-1.73 in.), as shown in Figure 5.34. At this point the test had to be stopped for safety reasons as reinforced concrete in the force transfer section of the test unit attained its compressive strength and began to crush. The return of the concrete core to zero axial force and zero axial displacement was problematic due to the damage incurred in the reinforced concrete force transfer section. The axial force was returned to approximately zero with a permanent axial compression displacement of -47.8 mm (-1.88 in.), as shown in Figure 5.32.

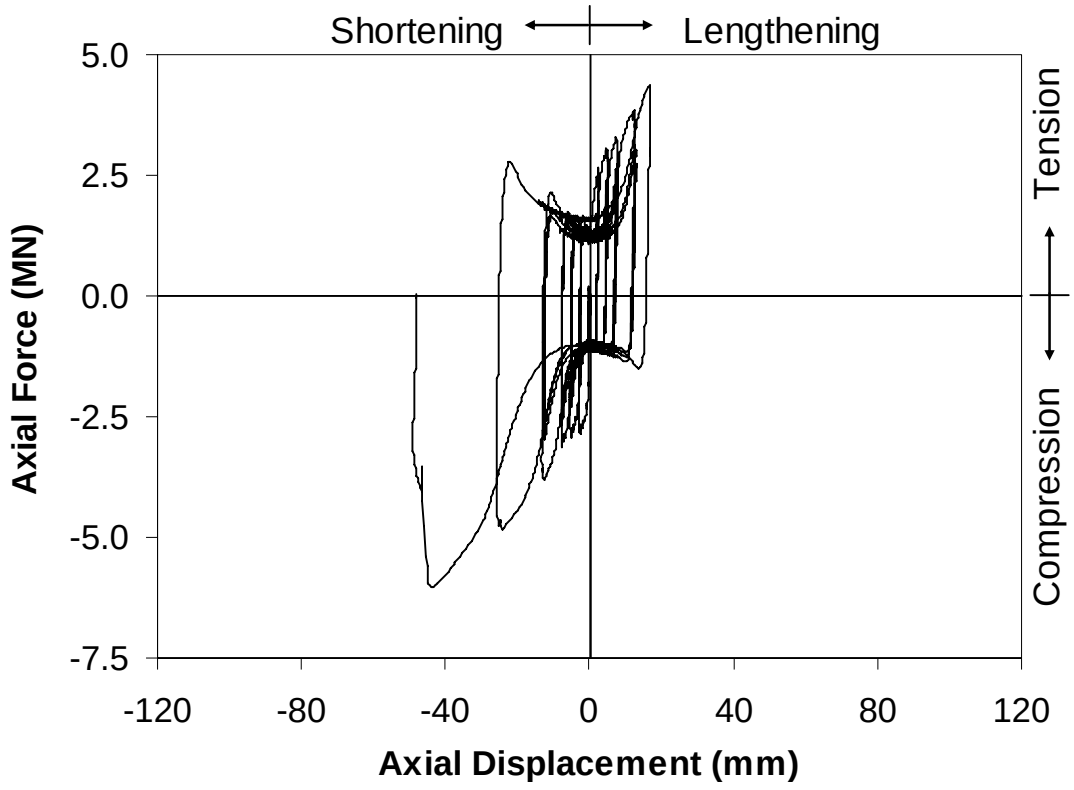


**Figure 5.32 Hysteretic Response for Test Unit # 17, with a Shear Ring (D/t of 24)**

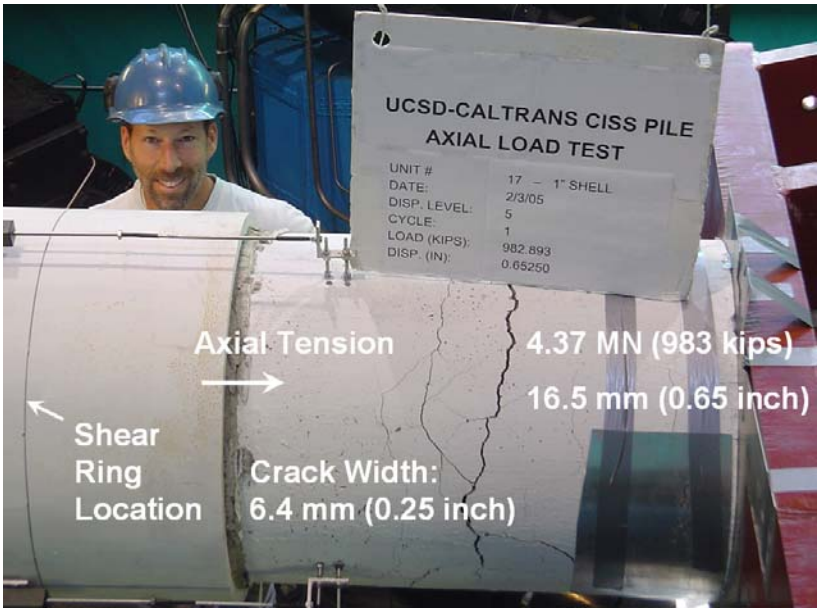


**Figure 5.33 Test Unit # 17 at the Maximum Applied Axial Tension Displacement**

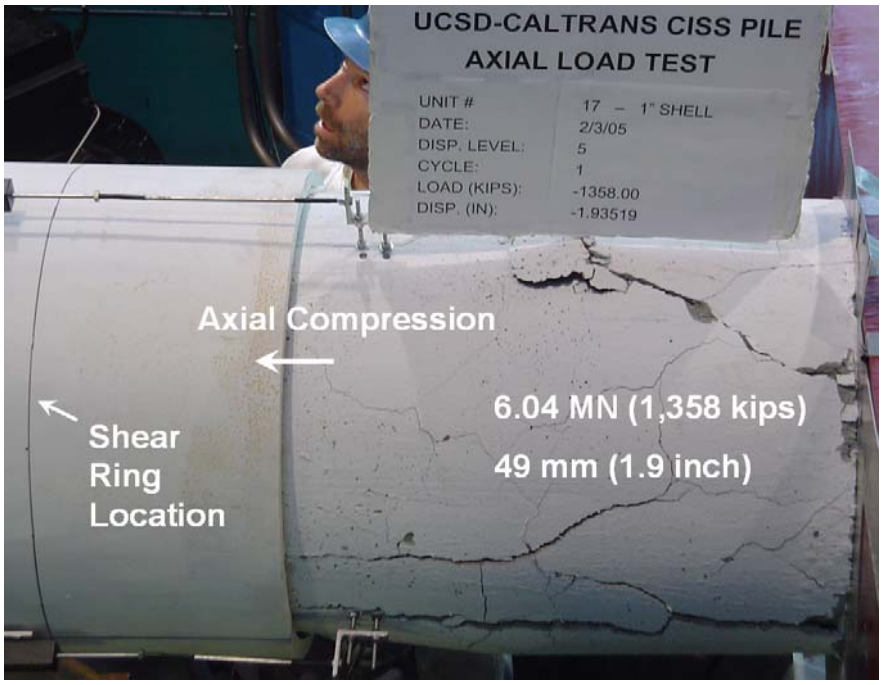


**Figure 5.34 Test Unit # 17 at the Maximum Applied Axial Compression Displacement**

The steel shell and shear ring remained elastic throughout the test, as shown in the longitudinal and transverse steel shell strain profiles in Appendix Figures 8.13-8.16. Removal of the cracked concrete cover, after the test, from the upper reinforced concrete

force transfer section revealed the longitudinal and hoop reinforcement to be intact, as shown in Figure 5.35. Removal of the steel shell revealed concrete adjacent to the shear ring crushed to a distance of 50.8 to 76.2 mm (2.0 to 3.0 in.) below the shear ring. Note that the maximum axial tension displacement was 16.5 mm (0.65 in.). Concrete above the shear ring failed in a circumferential plane with a length of approximately 50.8 mm (2.0 in.). This failure plane was intersected by a second failure plane with a slope of approximately 2:5 (transverse to longitudinal), as shown in Figure 5.35. A third failure plane corresponding to the spalled concrete from the upper reinforced concrete force transfer section intersected the failure plane with a slope of 2:5, as shown in Figure 5.35.

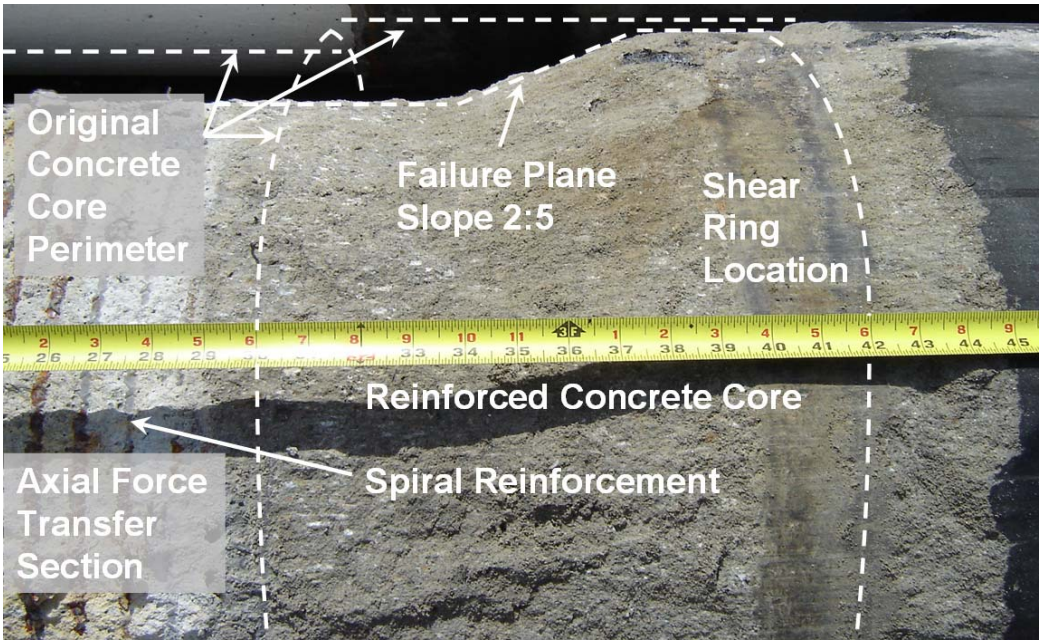


**Figure 5.35 Concrete Core with Spalled/Cracked Concrete Removed – After Test (Test Unit # 17)**

### 5.6.3 Test Unit # 18 with a D/t Ratio of 24 and a Debonded Core

Test Unit # 18 with a debonded steel shell-concrete interior surface had a hysteretic response in which the axial force increased as axial displacement increased, for most displacement levels, as shown in Figure 5.36. Some difficulty was encountered with the first cycle to an axial compression displacement of -2.5 mm (-0.1 in.) due to control issues with the SRMD, which resulted in exceeding this targeted displacement, as shown in Figure 5.36. Some difficulties were also had when applying axial compression

to a displacement of -50.8 mm (-2.0 in.), during the first cycle. As axial compression was applied, an axial compression force of -3.64 MN (-819 kips) was obtained at a displacement of -31.8 mm (-1.25 in.), after which the force decreased as displacement increased to the targeted displacement, as shown in Figure 5.36. A similar effect was obtained when applying axial displacement to 50.8 mm (2.0 in.), ± 76.2 mm (3.0 in.), and ± 101.6 mm (4.0 in.), as shown in Figure 5.36. A maximum axial tension force of 4.54 MN (1,020 kips) was obtained at a displacement of 125 mm (4.93 in.), which was beyond the test protocol.

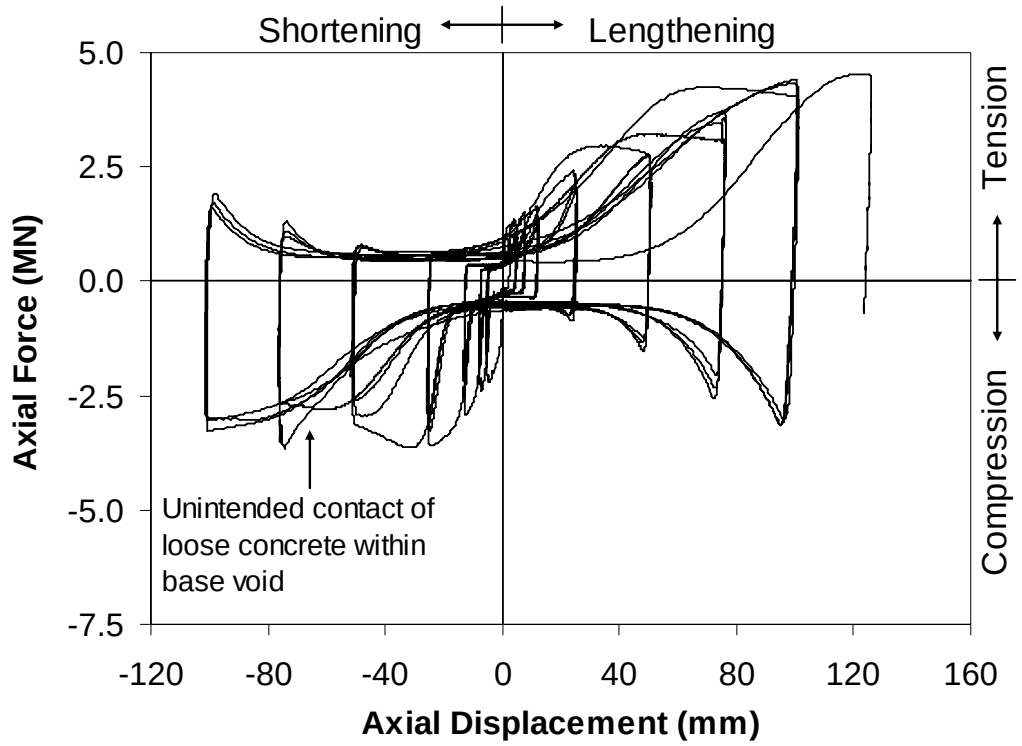


**Figure 5.36 Hysteretic Response for Test Unit # 18, with a Shear Ring and a Debonded Core (D/t of 24)**

The reinforced concrete core made contact with the base plate due to concrete debris accumulating inside the base void during the last axial compression cycle to a displacement of -76.2 mm (-3.0 in.), as shown by the increased stiffness in Figure 5.36. This loose concrete was removed from the base void prior to application of greater axial compression displacements.

Strains on the longitudinal reinforcement bars were below yield. The steel shell and shear ring remained elastic throughout the test, as shown in the steel shell longitudinal strain and transverse strain profiles in Appendix Figures 8.17-8.20. After testing, the steel shell was removed to allow for examination of the concrete core. Removal of the test unit steel shell revealed a region of moist and loose concrete, from approximately 127 mm (5.0 in.) below the shear ring to 152.4 mm (6.0 in.) above the shear ring. The region extended in the radial direction to a typical distance of 25.4 mm (1.0 in.) and a maximum distance of 50.8 mm (2.0 in.). Figure 5.37 shows the reinforced concrete core with this moist concrete removed. As this material was removed a high water content was observed. This high water to cement ratio was the result of the shear ring preventing the escape of water from the test unit during concrete placement and during the curing process. Despite the presence of this moist and loose material at the shear ring location (Figure 5.38), the shear ring was still effective at transferring axial force due to the confinement.

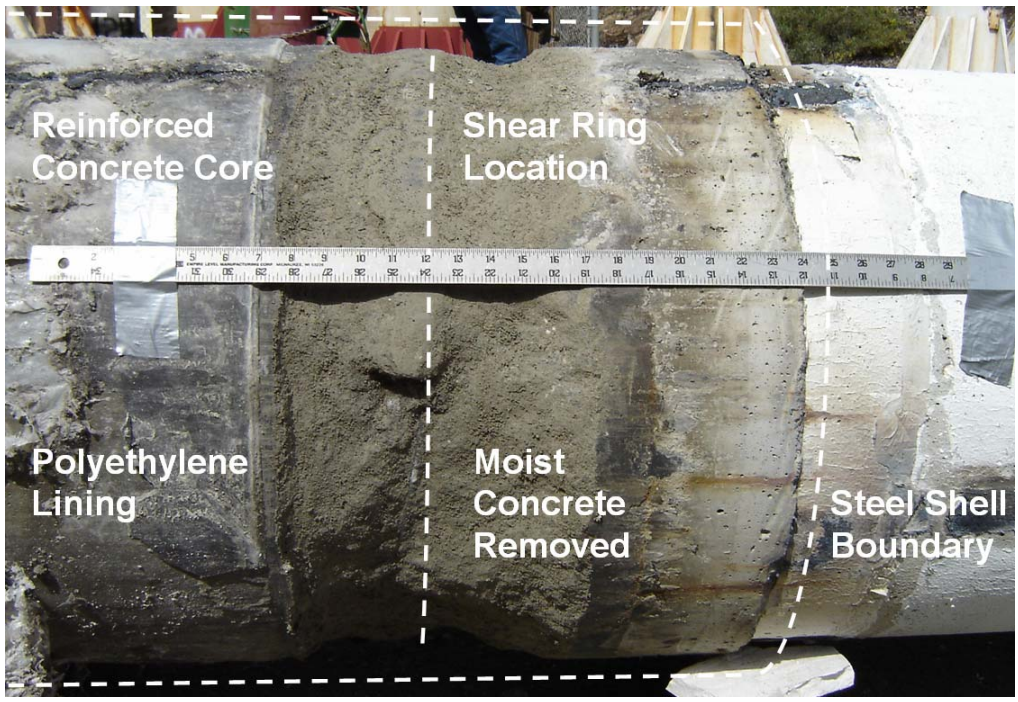


**Figure 5.37 Concrete Core after Test with Moist Concrete removed (Test Unit # 18)**

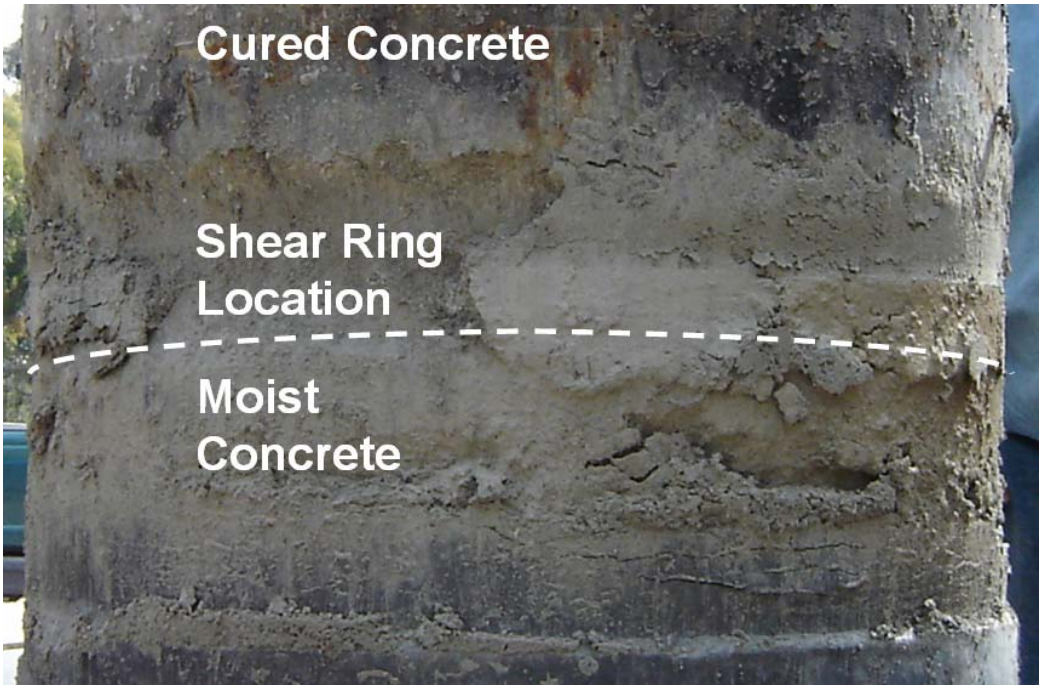


**Figure 5.38 Moist Concrete at Shear Ring Region of Concrete Core**

## 5.7 Response for Test Units Studying the Shear Ring Spacing

Results for test units which studied the effect of shear ring spacing will be presented in this section.

### 5.7.1 Test Unit # 19 with a Spacing of 76 mm (3.0 in.)

The test unit with two shear rings at a spacing of 76 mm (3.0 in.) and a D/t ratio of 24 (Test Unit # 19) typically increased in axial force as axial displacement increased, as shown in Figure 5.39. However, this behavior was not followed initially in axial compression as a slight decrease in axial compression force occurred after the initial peak in the axial compression force at -2.54 mm (-0.1 in.). A maximum axial compression force of -6.28 MN (-1,410 kips) was obtained at an axial displacement of -72.9 mm (-2.87 in.). A maximum axial tension force of 5.60 MN (1,260 kips) was obtained at a displacement of 24.9 mm (0.98 in.). Axial tension displacement was not applied beyond this displacement, because the test unit was still increasing in axial force and would have resulted in increased reinforcement bar strains, which were beyond yield. The reinforcement bar strain profile is shown in Appendix Figures 8.22 and 8.24, in which the strain clearly reached yield, at 0.02% (2000 micro strain). Failure of the longitudinal bar

reinforcement (fracture) or damage to the reinforced concrete force transfer section was not desired.

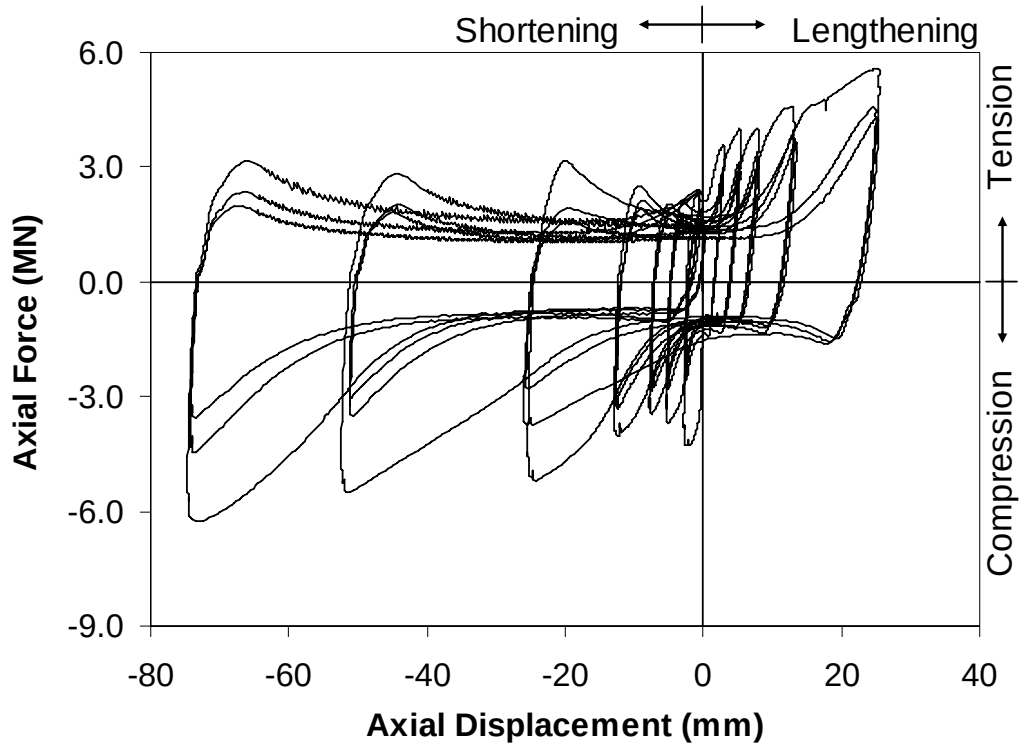


**Figure 5.39 Hysteretic Response for Test Unit # 19: Two Shear Rings with a Spacing of 76 mm (3.0 in.) at a D/t Ratio of 24**

In this test unit the steel shell and shear rings remained elastic, as shown in the steel shell longitudinal strain and transverse strain profiles of Appendix Figures 8.25-8.28. Minimal damage occurred to the reinforced concrete force transfer section, and consisted primarily of a crack opening in the region between the test unit steel shell and the steel shell confining the force transfer section. Removal of the steel shell after testing revealed concrete crushed above the uppermost shear ring to a height typically of 152 mm (6.0 in.). Concrete crushing below the lowermost shear ring extended to at most 76 mm (3.0 in.). Concrete between the shear rings also crushed (failed in shear). The concrete core of this test unit with the crushed concrete removed is shown in Figure 5.40 whereas the steel shell with crushed concrete between the shear rings is shown in Figure 5.41.


**Figure 5.40 Concrete Core after Test, with Crushed Concrete at Shear Ring Locations Removed (Test Unit # 19)**

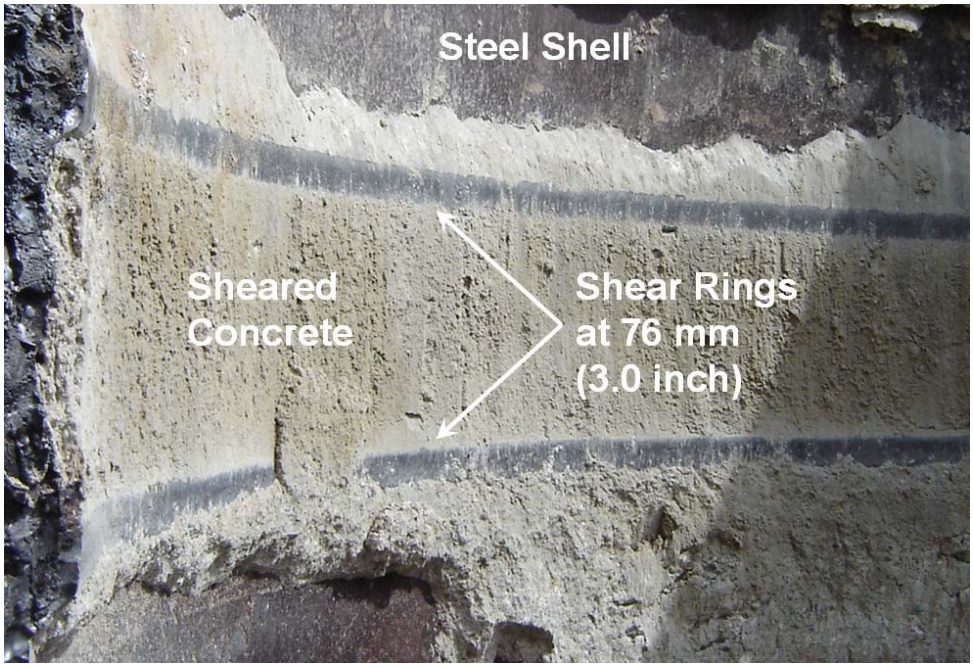


**Figure 5.41 Steel Shell after Test, with Crushed Concrete between Shear Rings (Test Unit # 19)**

### 5.7.2 Test Unit # 20 with a Spacing of 152 mm (6.0 in.)

Test Unit # 20 with two shear rings at a spacing of 152 mm (6.0 in.) showed an improved hysteretic response over that observed for Test Unit # 19. As axial displacements increased this test unit typically increased in axial force as shown in Figure 5.42. A maximum axial compression force of -6.22 MN (-1,400 kips) was obtained at a displacement of -51.6 mm (-2.03 in.). However, as the test unit was returned to zero displacement the axial tension force increased as shown in the upper left quadrant of Figure 5.42, with a peak axial tension force near zero displacement. This behavior occurred after subsequent axial compression displacements as well. A maximum axial tension force of 5.80 MN (1,300 kips) was obtained at 24.9 mm (0.98 in.). Axial tension displacements were not applied beyond this displacement because reinforcement bar strains were beyond yield, as shown in Appendix Figures 8.30 and 8.32.

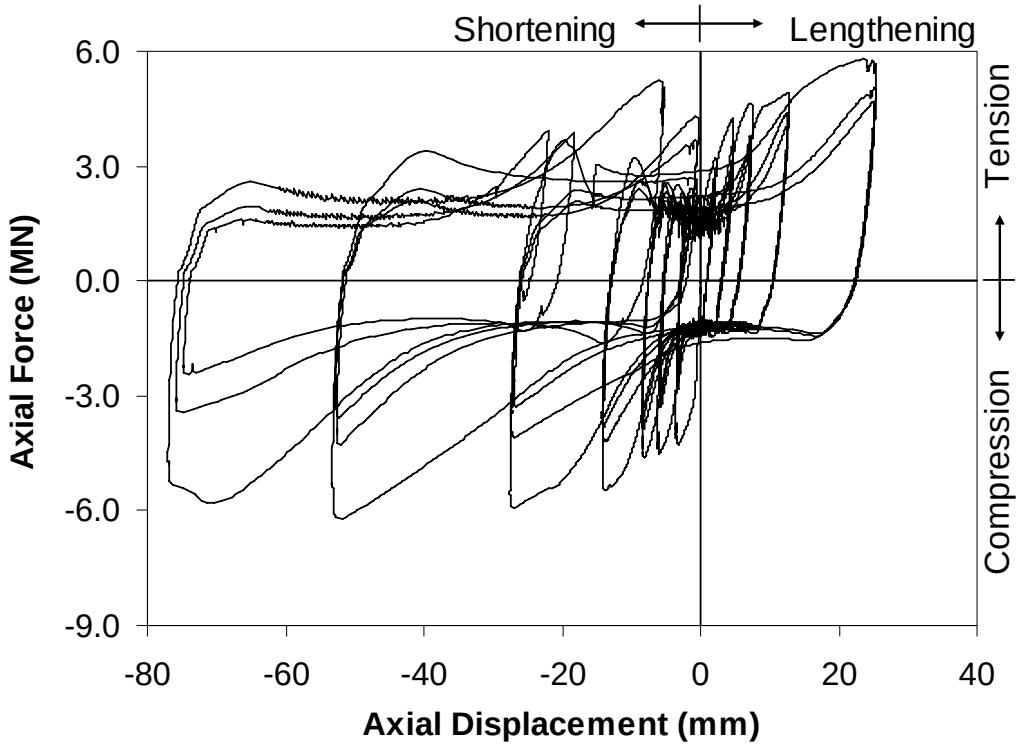


**Figure 5.42 Hysteretic Response for Test Unit # 20: Two Shear Rings with a Spacing of 152 mm (6.0 in.) at a D/t Ratio of 24**

In this test unit, the steel shell and the shear rings remained elastic, as shown in the steel shell longitudinal and transverse strain profiles in Appendix Figures 8.33-8.36.

Removal of the steel shell revealed that concrete around the shear rings was in a moist and loose state, similar to Test Unit # 18. This moist and loose concrete was within a region from near the top of the steel shell, to approximately 25.4 mm (1.0 in.) below the lower shear ring. The concrete core with moist concrete removed is shown in Figure 5.43. A moist band of concrete (dark gray color) between the shear rings and cured concrete (light gray) attached to the steel shell is shown in Figure 5.44. The presence of this loose and moist concrete was due to a high water to cement ratio, as explained previously for Test Unit #18.

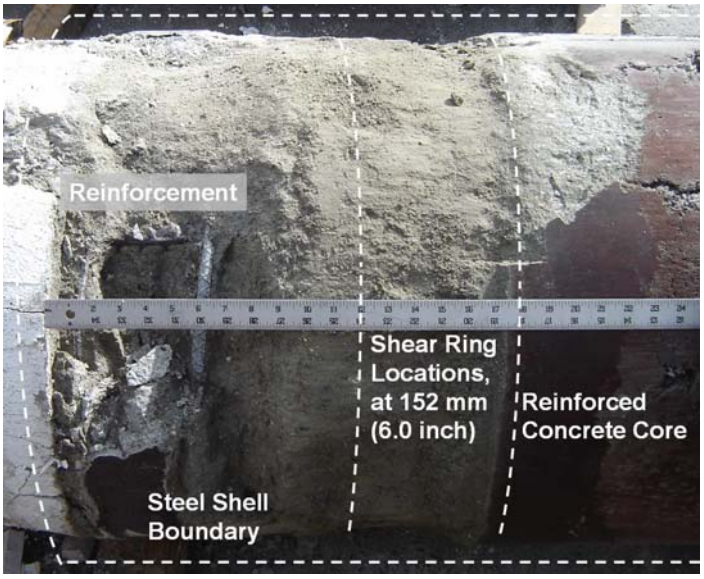


**Figure 5.43 Moist Concrete Removed from the Concrete Core, after Test (Test Unit # 20)**

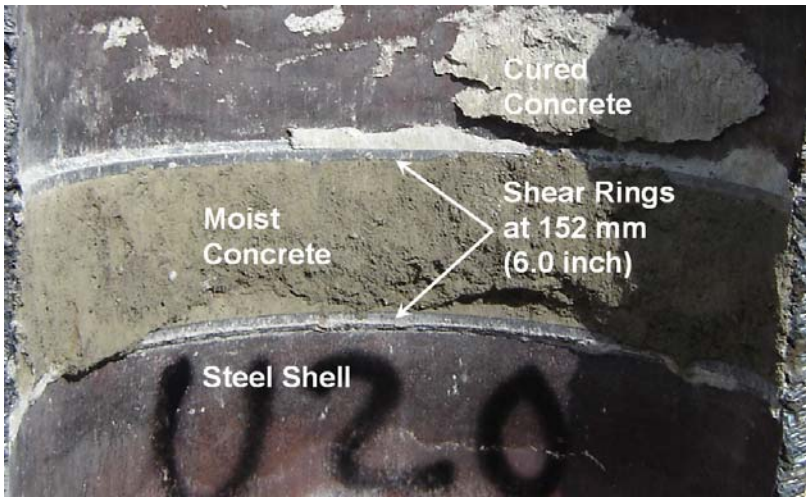


**Figure 5.44 Steel Shell after Test, with Moist Concrete between Shear Rings (Test Unit # 20)**

### 5.7.3 Test Unit # 21 with a Spacing of 305 mm (12.0 in.)

The test unit with two shear rings at a spacing of 305 mm (12.0 in.) and a D/t ratio of 24 (Test Unit # 21) exhibited the best overall performance, as shown in Figure 5.45 and obtained the greatest axial forces. As axial displacements increased, the axial force increased as well. A maximum axial compression force of -8.48 MN (-1,960 kips) was obtained at -25.1 mm (-0.99 in.) after which the test was stopped. This axial force was near the capacity of the test setup: 8.90 MN (2,000 kips). A maximum axial tension force of 5.44 MN (1,220 kips) was obtained at an axial displacement of 12.4 mm (0.49 in.). After this displacement no greater axial tension displacements were applied because longitudinal reinforcement bar strains were beyond yield, as shown in Appendix Figures 8.38 and 8.40.

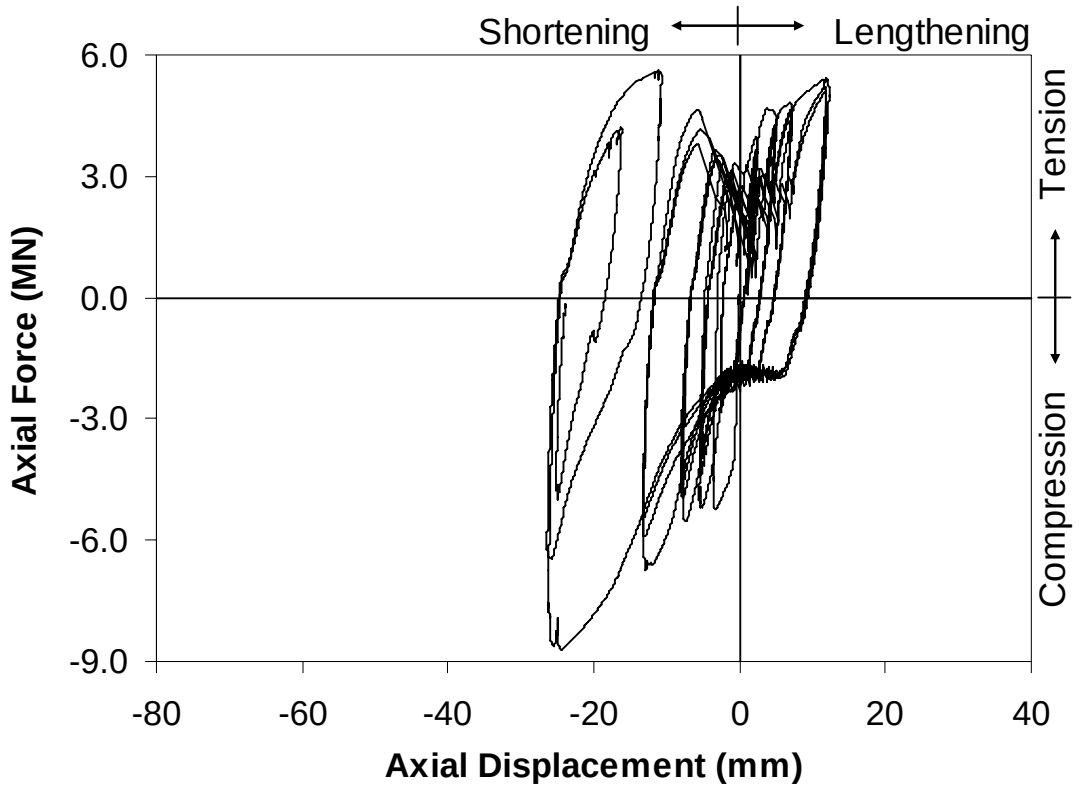


**Figure 5.45 Hysteretic Response for Test Unit # 21: Two Shear Rings with a Spacing of 305 mm (12.0 in.) at a D/t Ratio of 24**

The steel shell and shear rings remained elastic throughout the testing as shown in the steel shell longitudinal and transverse strain profiles, in Appendix Figures 8.41-8.44. Removal of the steel shell after testing revealed concrete crushed above and below the shear rings to lengths corresponding to the applied axial displacements, as shown in Figure 5.46. Concrete between the shear rings remained intact and free of any cracking, with only a minor amount of crushed concrete at the shear ring locations as shown in the view of the steel shell, in Figure 5.47.

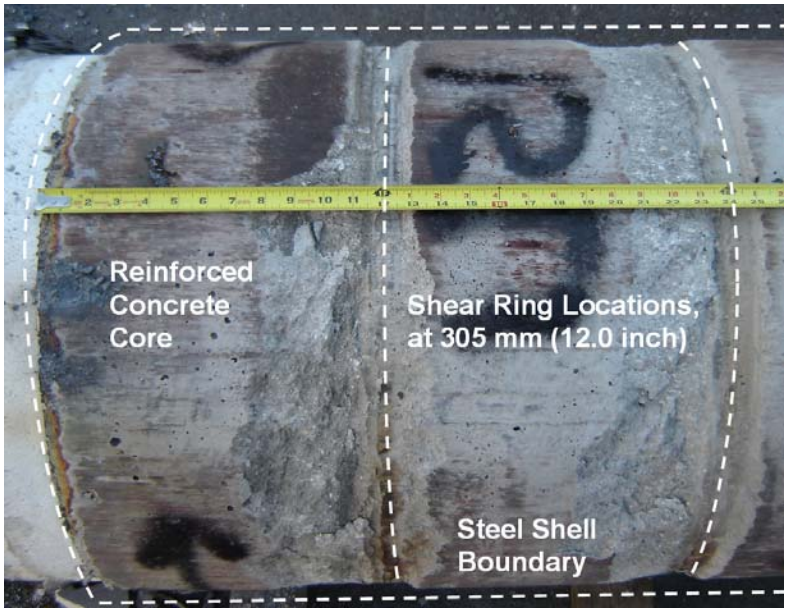


**Figure 5.46 Concrete Core after Test, with Concrete intact between Shear Ring Locations (Test Unit # 21)**

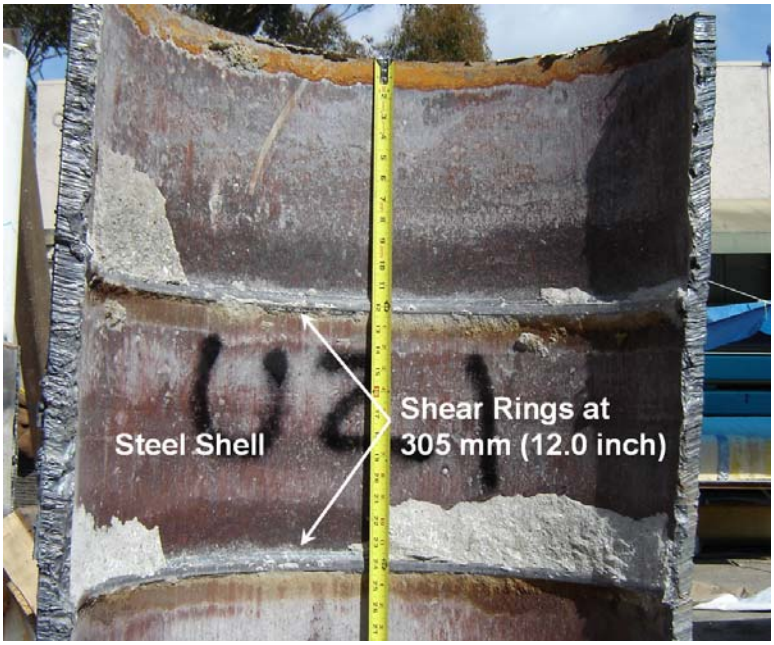


**Figure 5.47 Steel Shell after Test, (Test Unit # 21)**

## 5.8 Material Testing

Testing of materials for verification of individual material properties, used in the construction and fabrication of the test units is presented.

### 5.8.1 Concrete

Concrete compression strengths were obtained per ASTM Standard (ASTM 2004a) by testing cylinders with a height of 305 mm (12.0 in.) and a diameter of 152 mm (6.0 in.). Three cylinders were tested to obtain concrete strengths at 28 days and on the day of a full-scale test. Test Units # 1-9, # 11 and # 12 had an $f_c^{'}$ of 16.9 MPa (2.45 ksi) at 28 days. Test Unit # 10 had an $f_c^{'}$ of 19.6 MPa (2.84 ksi) at 28 days. Test units with expansive concrete (Test Units # 13, # 14, and # 15) had an $f_c^{'}$ of 16.5 MPa (2.39 ksi) at 28 days. Test Units # 16-21 had an $f_c^{'}$ of 16.1 MPa (2.34 ksi) at 28 days. Compressive strengths, on the day of test for each test unit, are listed in Table 5.1.

**Table 5.1 Concrete Compressive Strength**

| Test Unit # | Cylinder Compressive Strength, $f'_c$ MPa (ksi) | Cure Time (days) |
|---|---|---|
| 1 | 19.7 (2.86) | 74 |
| 2 | 22.1 (3.21) | 100 |
| 3 | 20.7 (3.00) | 78 |
| 4 | 20.0 (2.90) | 89 |
| 5 | 20.1 (2.92) | 53 |
| 6 | 22.1 (3.21) | 72 |
| 7 | 20.0 (2.90) | 50 |
| 8 | 21.0 (3.05) | 67 |
| 9 | 20.6 (2.99) | 63 |
| 10 | 21.0 (3.05) | 33 |
| 11 | 20.5 (2.97) | 80 |
| 12 | 21.6 (3.13) | 85 |
| 13 | 15.2 (2.20) | 22 |
| 14 | 14.8 (2.15) | 26 |
| 15 | 16.5 (2.39) | 29 |
| 16 | 18.4 (2.67) | 49 |
| 17 | 18.4 (2.67) | 51 |
| 18 | 20.5 (2.97) | 55 |
| 19 | 20.2 (2.93) | 57 |
| 20 | 20.3 (2.94) | 59 |
| 21 | 20.9 (3.03) | 62 |

### 5.8.2 Reinforcement

Tensile tests were conducted per ASTM Standard (ASTM 2004b) to obtain the yield, $f_y$, and ultimate stresses, $f_u$, of the longitudinal # 11 reinforcement bars, and of the # 4 reinforcement bar spiral. Yield and ultimate stresses are listed in Table 5.2.

### 5.8.3 Steel Shell

Tensile tests were also conducted on steel shell coupons extracted from test units, per ASTM Standard (ASTM 2004a) to obtain the yield, $f_y$, and ultimate stresses, $f_u$. Yield and ultimate stresses are listed in Table 5.2. A typical setup for tensile testing of a steel shell coupon is shown in Figure 5.48 with the necking behavior (elongation at the narrowed section) clearly visible prior to ultimate failure.

**Table 5.2 Steel Material Properties**

| Material | Yield Stress, $f_y$ MPa (ksi) | Ultimate Stress, $f_u$ MPa (ksi) |
|---|---|---|
| # 11 Bars (Test Units # 1-12) | 464 (67.3) | 734 (106.5) |
| # 11 Bars (Test Units # 13-15) | 473 (68.6) | 762 (110.5) |
| # 11 Bars (Test Units # 16-21) | 475 (68.9) | 653 (94.7) |
| # 4 Spiral Bar (Test Units # 1-12) | 437 (63.4) | 683 (99.1) |
| # 4 Spiral Bar (Test Units # 13-15) | 421 (61.0) | 687 (99.7) |
| # 4 Spiral Bar (Test Units # 16-21) | 413 (59.9) | 709 (102.9) |
| Steel Shell: D/t = 128 | 473 (68.7) | 623 (90.4) |
| Steel Shell: D/t = 96 | 447 (64.8) | 594 (86.2) |
| Steel Shell: D/t = 24 | 436 (63.2) | 569 (82.5) |

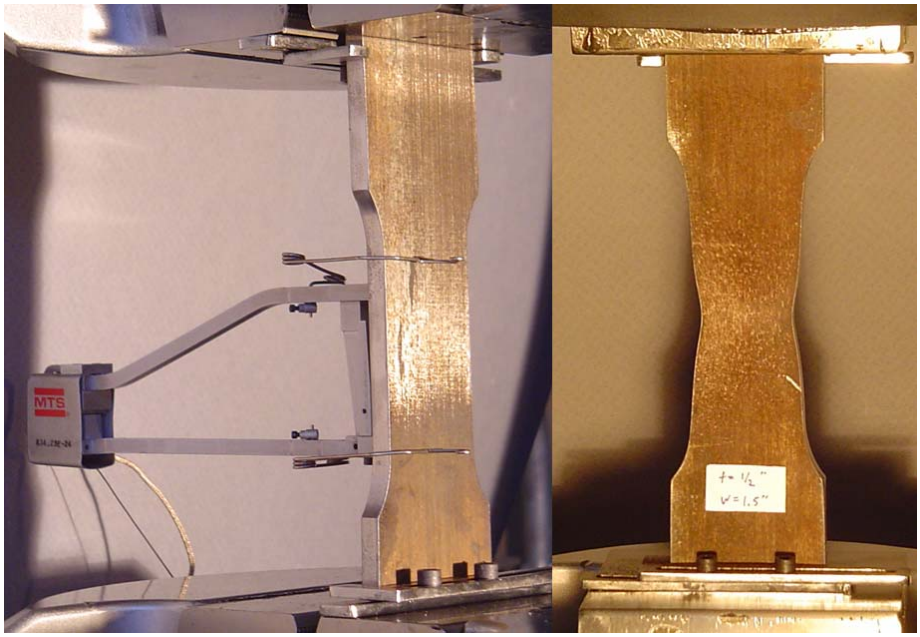


**Figure 5.48 Tensile Test of a Steel Shell Coupon: Test Setup (left) and Necking Behavior prior to Ultimate Failure (right)**

# 6 ANALYSIS OF RESULTS

## 6.1 Introduction

In this chapter, the results obtained from the experimental program, the prediction, and the finite element analysis will be compared in order to develop design recommendations. Data from other researchers along with the design codes of the American Petroleum Institute and the United Kingdom Department of Energy will be compared to the experimental results. Comparisons of the measured hysteretic response envelopes will be used to compare overall performance of the parameters investigated in this study. The calculation of friction bond and elastic stiffness will be presented for test units without a mechanism.

## 6.2 Explanation of a Typical Hysteretic Response and Transverse Steel Shell Strain Profile for a Test Unit at a D/t Ratio of 128

A plot of the transverse steel shell strain measured at the shear ring location versus applied axial force for Test Unit # 5 is shown in Figure 6.1. This figure shows the transverse strain for each cycle of the first five displacement levels, with axial displacements of: 2.5, 5.1, 7.6, 12.7 and 25.4 mm (0.1, 0.2, 0.3, 0.5, 1.0 in.). Yielding of the steel shell in the transverse direction occurred during the second displacement level, to an axial displacement of 5.1 mm (0.2 in.), as noted by the transverse strain plot exceeding 0.2%. The transverse steel shell strain exceeded 2% when an axial displacement of 50.8 mm (2.0 in.) was applied, beyond which strains were not recorded.

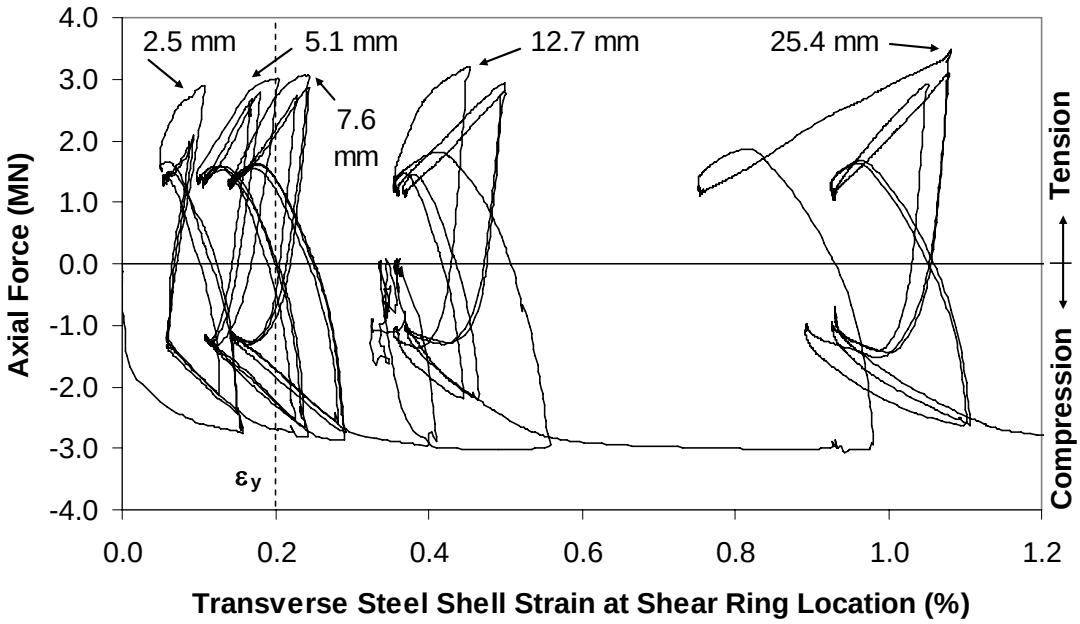


**Figure 6.1 Transverse Steel Shell Strain Profile, measured at the Shear Ring Mechanism Location for Test Unit # 5 (D/t Ratio of 128)**

The transverse steel shell strain data, presented in Figure 6.1 is best explained through a side-by-side comparison of the axial force-axial displacement hysteretic response and the transverse steel shell strain of Test Unit # 5. A comparison for the first cycle of displacement level 3 to an axial displacement of 7.6 mm (0.3 in.) is shown in Figure 6.2. This cycle began at point *a*, with axial compression force applied to the test unit. A maximum axial compression force and a maximum axial compression transverse strain were obtained at point *b*. The increase in transverse strain indicated that a jamming process of the concrete core relative to the steel shell occurred, because the concrete immediately adjacent to the shear ring was crushed and expanded against the steel shell. After this point, the axial force was returned to zero with a partial elastic recovery at point *c*. As axial tension force was applied, a peak was obtained at point *d*, with a similar peak in the transverse strain. This portion of the response appears to be largely influenced by residual hoop stresses in the steel shell and shear ring. Axial displacement was then returned to zero at point *e* and some softening was observed in the response. This portion of the response seems to be due to an unlocking process and the steel shell-concrete core friction. As the concrete core was displaced under axial tension, a peak axial tension force, and a peak transverse strain were obtained at the desired displacement

at point *f*. Again, the jamming process was observed and the subsequent response was similar to that from points *b* to *e*.

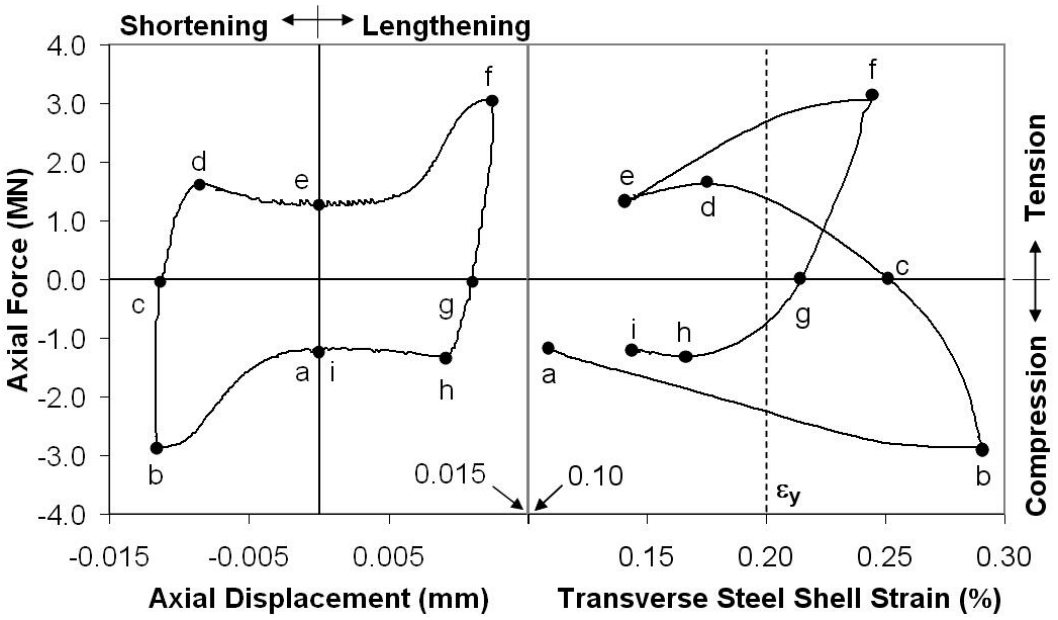


**Figure 6.2 Explanation of a Transverse Steel Shell Strain Response: Transverse Strain Response (left) and Corresponding Hysteretic Loop (right) for Test Unit # 5 (D/t Ratio of 128)**

This comparison of the axial force-axial displacement hysteretic behavior to the transverse strain profile at a mechanism shows the effectiveness of a mechanism and the highly nonlinear behavior. The complexity in the behavior of the response of a test unit demonstrates the need to carefully understand the test data in terms of the frictional response and mechanism effectiveness, as will be presented in the following sections.

## 6.3 Performance Comparison

In this section, a comparison is made between the test units of this study by generating envelopes of the axial force-axial displacement hysteretic response. The envelopes are a plot of the peak cyclic axial forces obtained at each axial displacement level, as shown in Figures 6.4 through 6.10.

### 6.3.1 Effect of D/t Ratio and Surface Condition

A comparison of the hysteretic envelopes for test units with a variation of the D/t ratio is shown in Figure 6.3. Test Units # 11 and # 12 had a D/t ratio of 40.7 and exhibited a similar performance. However, results from Test Unit #11 will be used for comparison in Figure 6.3 because this test unit obtained slightly lower axial compression forces. A comparison of test units with D/t ratios of 128, 94 and 46 and with approximately the same steel shell diameter of 610 mm (24 in.) can be made at the initial axial displacements of +/- 2.54 mm (0.1 in.), as shown in Figure 6.3(a). In Figure 6.3(a) the test unit with a D/t ratio of 40.7, which had a diameter of 387 mm (15.25 in.), is also plotted for a comparison of the influence of the D/t ratio. This test unit had an axial force transfer that was less than the axial force transfer of test units with D/t ratios of 46 and 94. As a result of this, the D/t ratio cannot be concluded to influence the axial force transfer. However, the axial force transfer increased as the steel shell thickness increased for a constant steel shell diameter (for D/t ratios of 128, 94 and 46), as shown in Figure 6.3(a). This shows the importance of the steel shell thickness in the axial force transfer at the initial axial displacements which agrees with the strain compatibility prediction as presented in Section 3.2. A comparison of the prediction to the experimental results is presented in Section 6.9.

At greater axial displacements, as shown in Figure 6.3(b), a trend for the relationship between the axial force transfer and the D/t ratio or steel shell thickness cannot be deduced. At the greater axial displacements, the axial force transfer occurs primarily through a friction bond which is independent of the steel shell thickness.

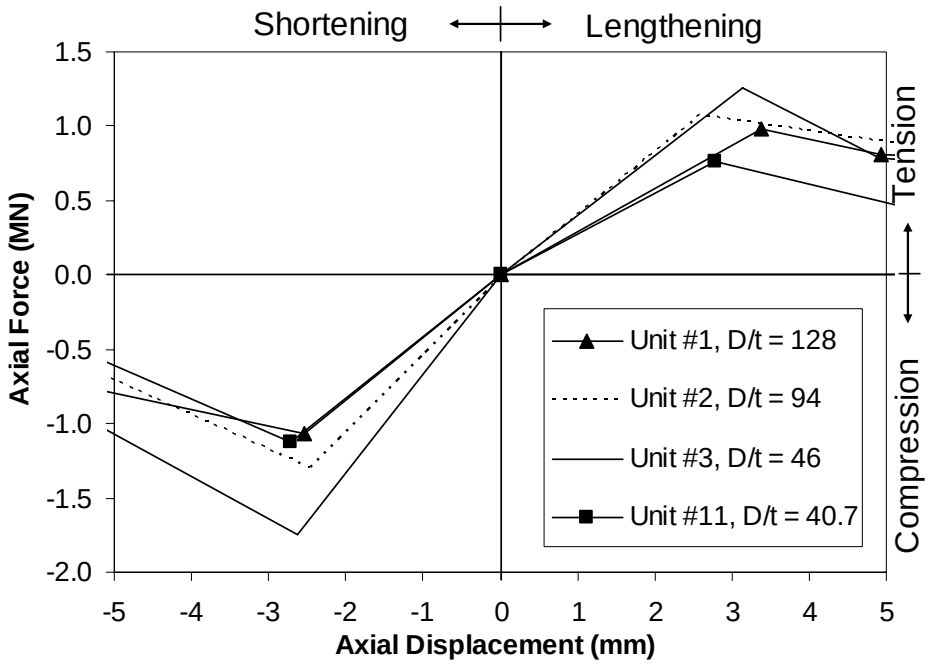


**(a.) Effect of Steel Shell Thickness at Initial Displacement**

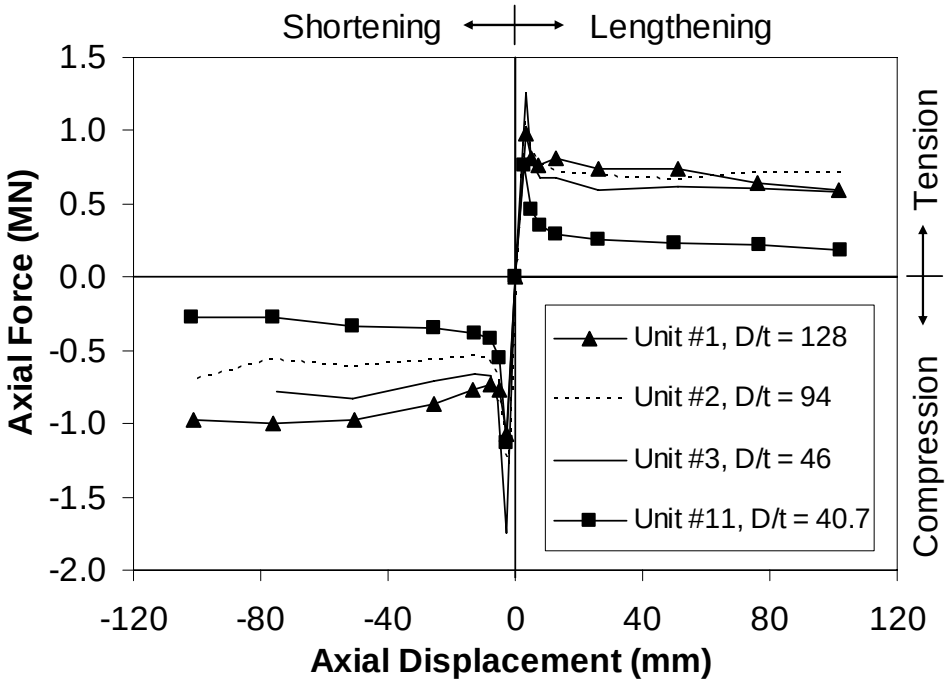


**(b.) Overall Performance**

**Figure 6.3 Hysteretic Envelope Comparison for Test Units with a Variation of the D/t Ratio and no Mechanism**

The influence of the surface bond on the axial force is shown in the comparison of Figure 6.4 for Test Units # 1 and # 10, at a D/t ratio of 128. The presence of a water-bentonite coating on the steel shell interior surface of Test Unit # 10 decreased the axial force transfer and prevented peaks in the axial force transfer at the initial axial displacements. The axial compression force transfer decreased by 29% and by 24% at the initial and maximum axial displacements of -2.54 mm (-0.1 inch) and -101.6 mm (-4 inch), respectively. In axial tension, the water-bentonite surface coating decreased the axial force transfer by 28% at a displacement of 2.54 mm (0.1 inch). A slight increase in the axial force transfer of 6% occurred at an axial displacement of 101.6 mm (4 inch). On average, a 27% reduction in the axial compression force transfer and an 11% reduction in the axial tension force transfer occurred when a water-bentonite coating was present on the steel shell interior surface.

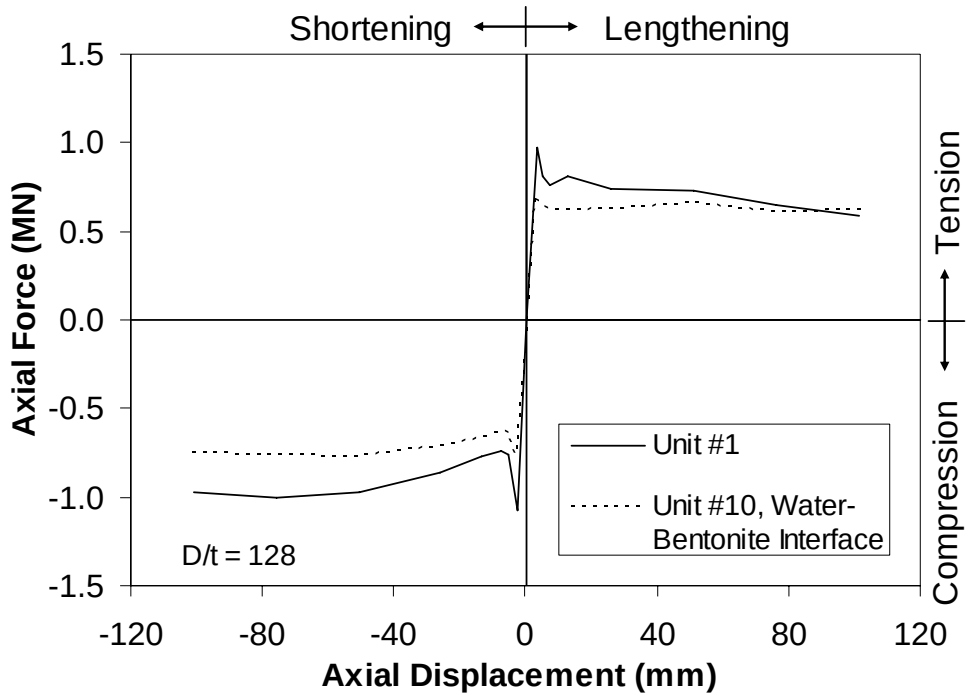


**Figure 6.4 Hysteretic Envelope Comparison for the Effect of the Steel Shell Internal Surface Condition**

### 6.3.2 Effect of Expansive Concrete

A comparison of the hysteretic envelopes for all expansive concrete test units and the test unit at a D/t ratio of 128 with normal concrete is shown in Figure 6.5. The axial force transfer increased at the initial displacements; however, this increase was not prevalent at greater axial displacements. Figure 6.5 shows a slight improvement in the axial load transfer at greater displacements for a D/t ratio of 128. The expansive concrete test unit with a D/t ratio of 46 obtained the greatest axial compression force, and on average maintained the highest axial compression forces at greater axial displacements. In axial tension all three expansive concrete test units and the test unit at a D/t ratio of 128 with normal concrete had a similar performance.

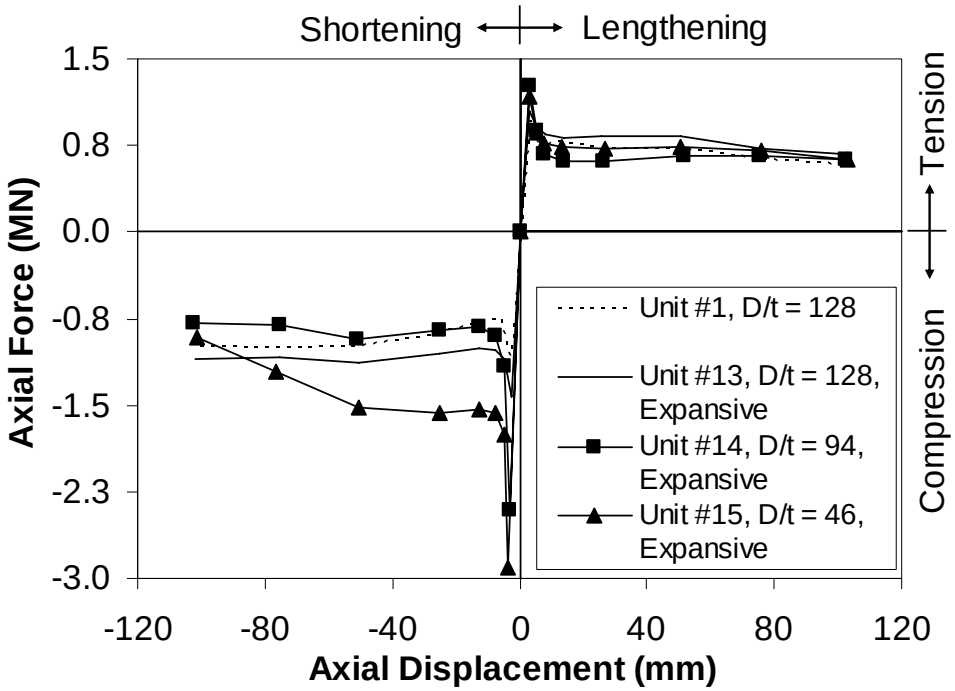


**Figure 6.5 Hysteretic Envelope Comparison for Test Units with Expansive Concrete**

A comparison of the hysteretic envelopes of Test Unit # 14, with expansive concrete at a D/t ratio of 94, and Test Unit # 2, also at a D/t ratio of 94, is shown in Figure 6.6. In this figure it can be seen that expansive concrete clearly increased the initial adhesive bond. However, at greater axial tension displacements expansive concrete had no improvement in the axial force transfer. At greater axial compression displacements, expansive concrete increased the axial force transfer, however, at the

maximum applied axial displacement, expansive concrete had a similar performance as the test unit with normal concrete.

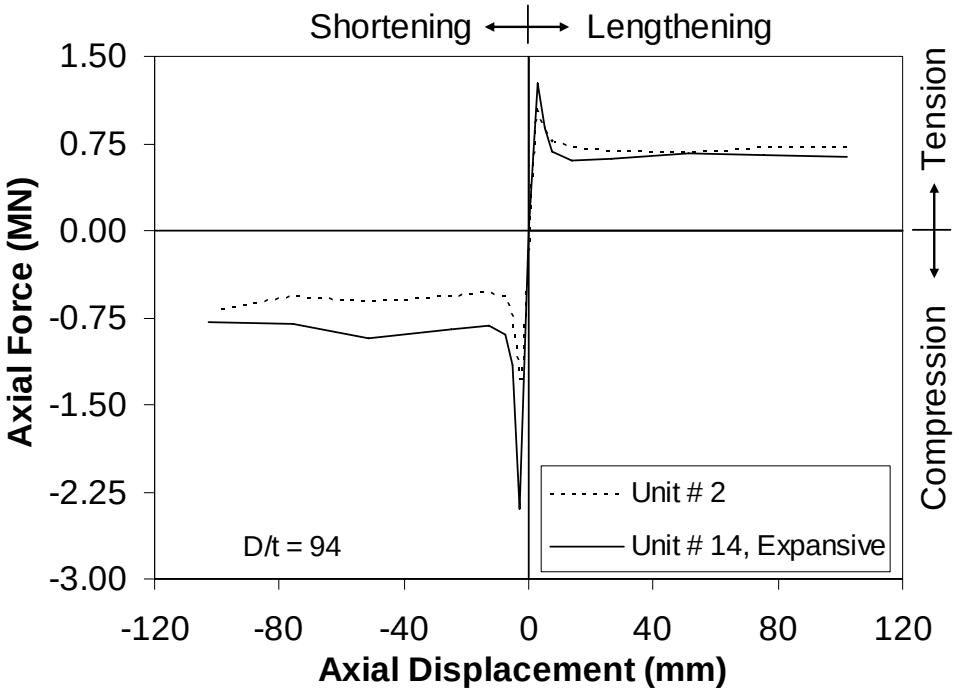


**Figure 6.6 Hysteretic Envelope Comparison for the Effect of Expansive Concrete at a D/t Ratio of 94**

A comparison of the hysteretic envelopes of Test Unit # 15 with expansive concrete at a D/t ratio of 46, and Test Unit # 3 also at a D/t ratio of 46, is shown in Figure 6.7. In this figure, expansive concrete clearly increased the initial adhesive bond. However, at greater axial tension displacements expansive concrete had no improvement in the axial force transfer. At greater axial compression displacements, expansive concrete increased the axial force transfer. As the axial compression displacement increased to -101.6 mm (-4.0 in.), the axial force transferred by expansive concrete had a noticeable decrease.

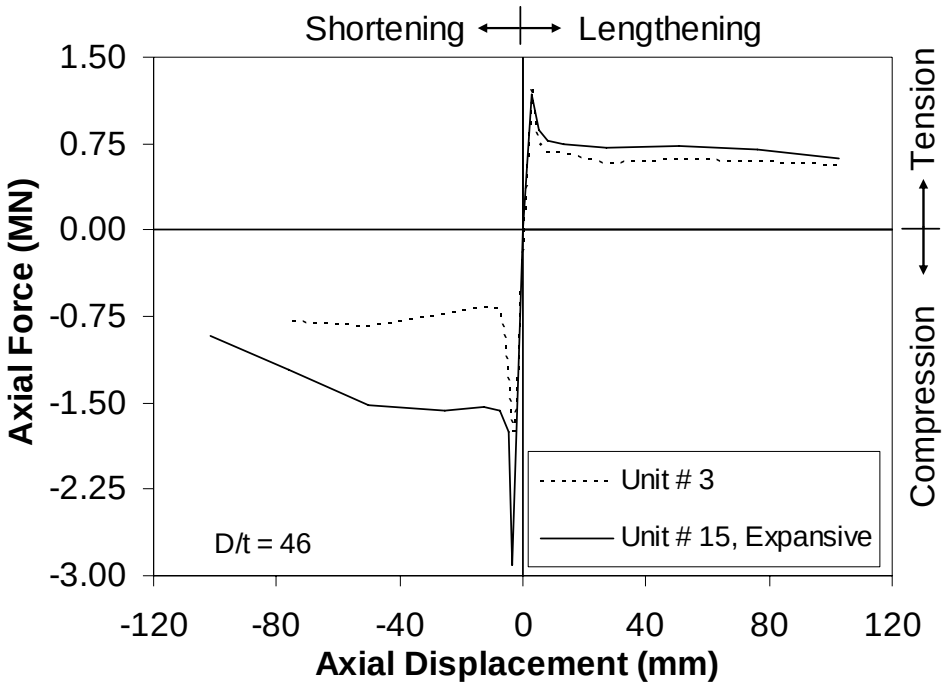


**Figure 6.7 Hysteretic Envelope Comparison for the Effect of Expansive Concrete at a D/t Ratio of 46**

Expansive concrete was found to increase the initial axial force transfer or adhesion for test units with a D/t ratio of 128, 94 and 46. However, after the adhesion was overcome, and as the axial displacements increased, expansive concrete did not significantly increase the axial force transfer through friction bond.

### 6.3.3 Effect of Mechanism Design

A comparison was made for test units with mechanisms by generating monotonic envelopes, as shown in Figure 6.8. Mechanisms with a substantial weld contact area with the steel shell (e.g. the shear ring, circumferentially welded reinforcement bar, and weld bead) were able to maintain high levels of axial compression and axial tension force transfer at all axial displacements. The shear stud mechanism and cross bar both had small weld contact areas with the steel shell, which resulted in a shear failure of the connection at low axial displacements. This failure resulted in a highly non-ductile behavior, as the axial force transfer had a sharp decrease until a friction bond dominated

the response, as shown in Figure 6.8. The tread plate mechanism also initially obtained high axial forces. However, this mechanism also had a non-ductile behavior, as the axial force transfer decreased at greater axial displacements as the concrete between treads failed. This failure reduced the number of treads actively in contact with the reinforced concrete core, as explained in Section 5.5.6, leaving a friction bond.

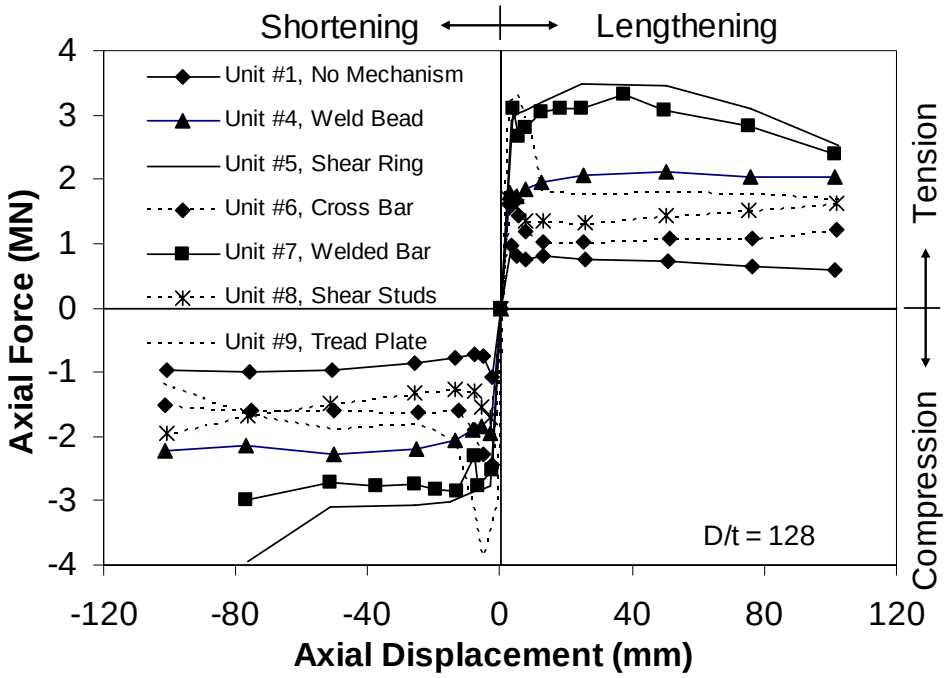


**Figure 6.8 Hysteretic Envelope Comparison for Test Units with a Mechanism**

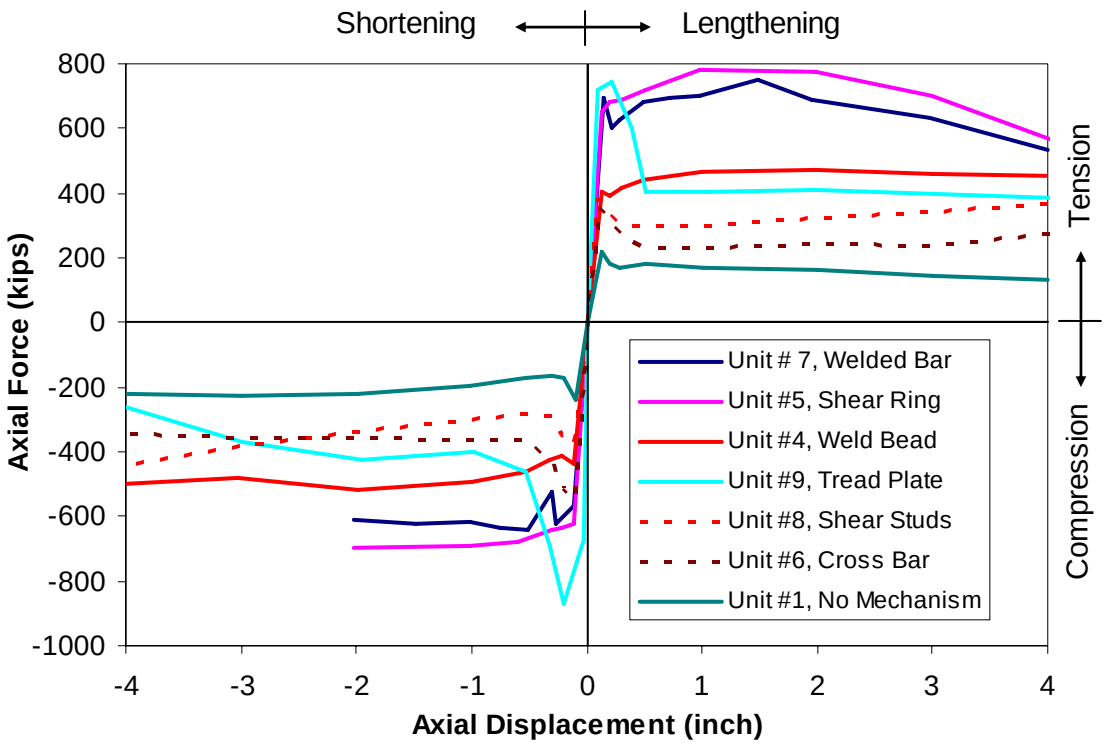


**Figure 6.9 Hysteretic Envelope Comparison for Test Units with a Mechanism – USCS Units and in Color**

### 6.3.4 Effects of D/t Ratio and Spacing on Shear Ring

A hysteretic envelope comparison is presented in Figures 6.9 and 6.10 for test units which had a single shear ring and a variation of the D/t ratio. The axial force transfer through the shear ring mechanism was expected to increase as the steel shell thickness increased, or as the D/t ratio decreased. However, this expected trend did not hold for the Test Unit # 16, at a D/t ratio of 94. This test unit obtained an axial compression and axial tension force transfer that was less than Test Unit # 5, at a D/t ratio of 128. Both of these units had a similar failure mode, which consisted of circumferential yielding of the steel shell, at the shear ring location. As the steel shell deformed out-of-plane with the shear ring, the contact between the shear ring and concrete core diminished. This was more pronounced for Test Unit # 16, which had a shear ring radial width of 6.35 mm (0.25 in.) which was half of the radial width of Test Unit # 5.

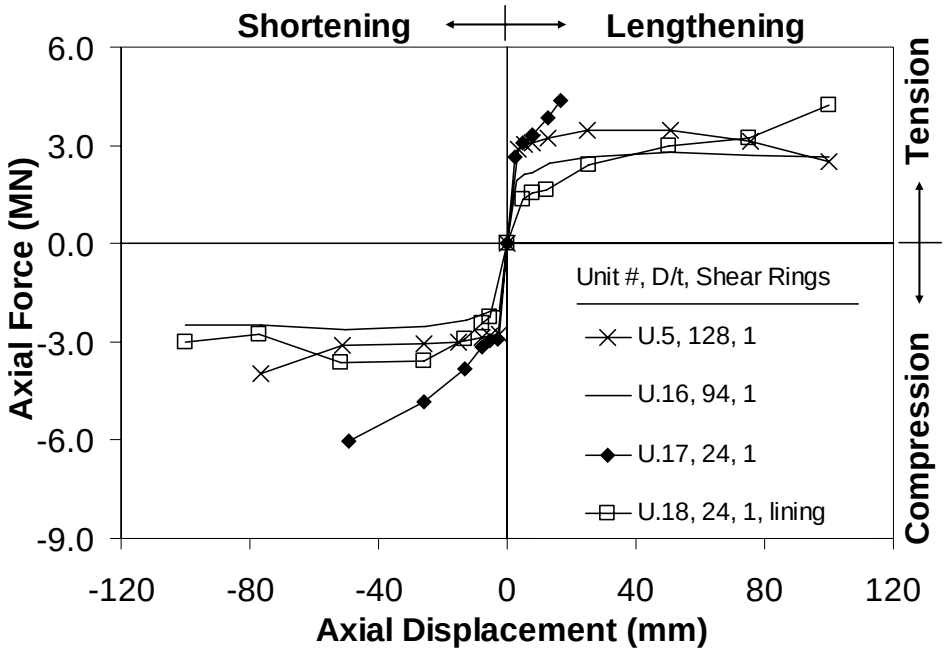


**Figure 6.10 Hysteretic Envelope Comparison for Test Units with a Single Shear Ring**

Test Units # 16, # 17, and # 18 all had the same shear ring radial width. These test units met the expectation of increased axial force transfer as the steel shell thickness increased, as shown in Figure 6.10. A comparison of Test Unit # 18, with a debonded core, and the similar test unit without a lining (Test Unit # 17) shows a noticeable difference in the axial tension and compression forces transferred at greater displacements. However, it should be noted that the test unit with the debonded core also had moist concrete at the shear ring location, hence it cannot be concluded that the lack of a friction bond between the steel shell and the reinforced concrete core was the primary reason for the difference in axial forces between these two test units.

A hysteretic envelope comparison is presented in Figure 6.11 for test units which had two shear rings and a D/t ratio of 24. In this figure, the axial compression and axial tension force increased if two shear rings were used, and increased further if the shear ring spacing was increased from 76 mm (3.0 in.) to 305 mm (12.0 in.). The shear ring spacing of 305 mm (12.0 in.) corresponds to one half of the steel shell diameter. At this shear ring spacing, the concrete between the shear rings remained intact and bonded to

the reinforced concrete core, as presented in Section 5.7.3. Test units with a lesser shear ring spacing had concrete crush between the shear rings as shown in Figure 5.41. The crushing of concrete between the shear rings resulted in Test Units # 19 and # 20 obtaining similar axial forces to the test unit with a single shear ring (Test Unit # 17) at greater axial displacements, as shown in Figure 6.11.

Shear rings used in a steel shell with a high D/t ratio (128 or 94) were effective at transferring axial force despite a softening in the hysteretic response because of circumferential yielding of the steel shell at the mechanism location. In test units with multiple shear rings, the axial force transfer was found to increase as the shear ring spacing increased to one half of the steel shell diameter. At a lesser shear ring spacing, concrete between the shear rings crushed and sheared completely between rings at the greater axial displacements similar to a test unit with a single shear ring.

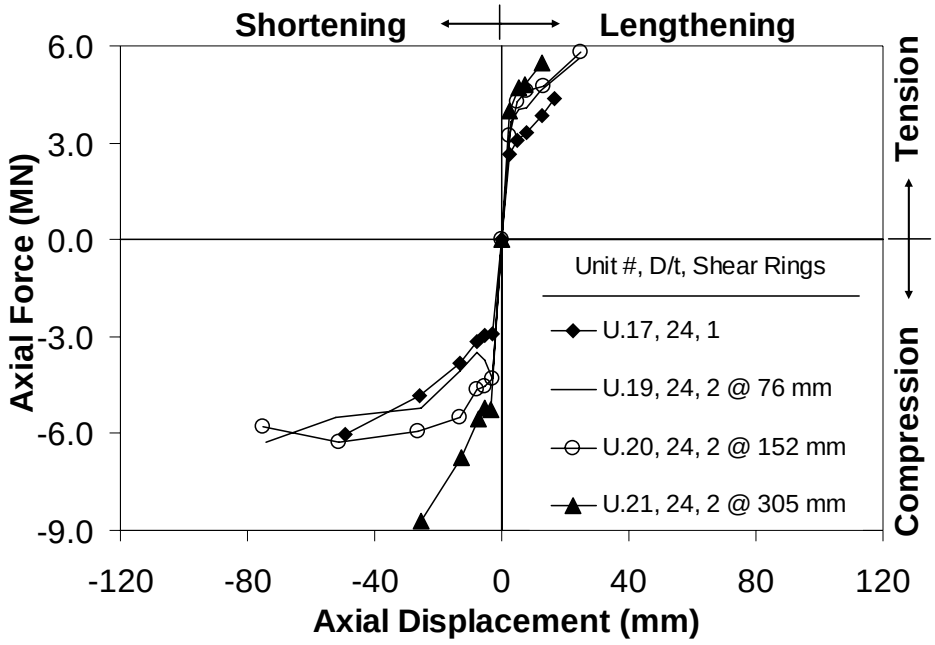


**Figure 6.11 Hysteretic Envelope Comparison for Test Units with Two Shear Rings**

## 6.4 Initial Steel Shell-Concrete Core Surface Bond

The initial bond through surface contact between the steel shell and the reinforced concrete core was through an adhesive bond. This adhesive bond resulted in peaks in the

axial force transfer at displacements of ± 2.54 mm (0.1 in.) for test units without a mechanism. The adhesive bond will be evaluated as an elastic axial stiffness, and is presented.

### 6.4.1 Computation of Elastic Stiffness

Elastic axial stiffness for axial compression and axial tension were calculated based on experimentally determined peak axial compression and tension forces as listed in Table 6.1. Prior to obtaining the peak response, the axial force-axial displacement response changes from a linear relationship to a nonlinear relationship, as shown by the hardening in a typical hysteretic response (Figures 5.2, 5.3 and 5.4). As a result of this behavior, the axial stiffness was calculated at 75% of the peak axial compression and tension forces obtained during the first axial displacement cycle. Stiffness was calculated at 75% of the peak force (as an estimate of the yield) to account for the hardening in the response typically occurred prior to attainment of the peak forces. Axial forces were divided by the corresponding axial displacement, at approximately 2.54 mm (0.1 in.) to obtain the elastic axial stiffness.

**Table 6.1 Elastic Axial Stiffness at the Maximum Axial Compression and Tension Displacements Obtained in the First Cycle**

| Test Unit # | Test Unit Description | Compression Stiffness MN/mm (kip/in) | Tension Stiffness MN/mm (kip/in) |
|---|---|---|---|
| 1 | D/t = 128 | 0.316 (1790) | 0.216 (1230) |
| 2 | D/t = 94 | 0.388 (2200) | 0.315 (1790) |
| 3 | D/t = 46 | 0.497 (2820) | 0.299 (1700) |
| 10 | D/t = 128, Surface Condition | 0.178 (1010) | 0.202 (1140) |
| 11 | D/t = 40.7 | 0.312 (1770) | 0.207 (1170) |
| 12 | D/t = 40.7 | 0.274 (1550) | 0.233 (1320) |
| 13 | D/t = 128, Expansive | 0.391 (2210) | 0.253 (1430) |
| 14 | D/t = 94, Expansive | 0.609 (3450) | 0.31 (1760) |
| 15 | D/t = 46, Expansive | 0.626 (3550) | 0.294 (1660) |

### 6.4.2 Elastic Stiffness for Surface Bond

The elastic axial compression stiffness was plotted versus the steel shell thickness, in Figure 6.12, and versus the D/t ratio, in Figure 6.13, for plain concrete test units

without a mechanism. Compression and tension stiffness was plotted for Test Units # 1, #, 2, # 3, and # 11, at D/t ratios of 128, 94, 46, and 40.7, respectively. A linear regression was then conducted to determine if the stiffness had a greater correlation to the steel shell thickness or to the D/t ratio. Greater correlation coefficients, $R^2$, were obtained for the axial compression stiffness relationship to the steel shell thickness ($R^2$ of 0.4945) than to the D/t ratio ($R^2$ of 0.1582). A similar result was obtained for the axial tension stiffness, though the coefficients were not as large. This result, of a stronger relationship between the axial stiffness and the steel shell thickness was clearly expected, per the comparison of test units presented in Section 6.3.1. However, the stiffness had a greater correlation to the D/t ratio for test units with expansive concrete (Test Units # 13, # 14, and # 15) as shown in Figures 6.14 and 6.15.

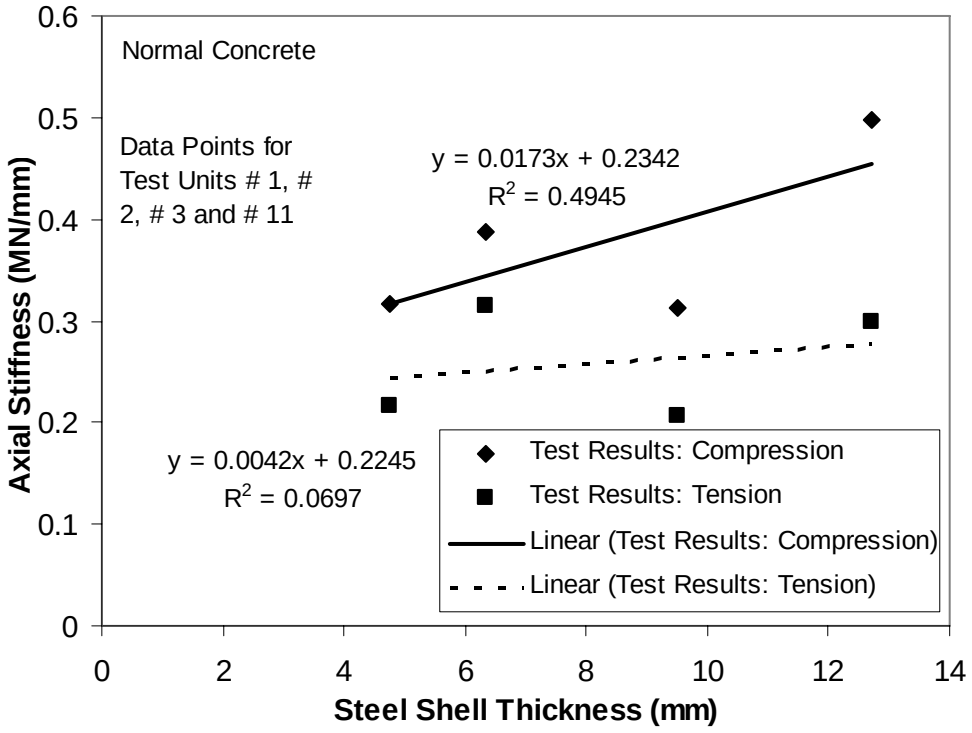


**Figure 6.12 Elastic Axial Stiffness versus Steel Shell Thickness**

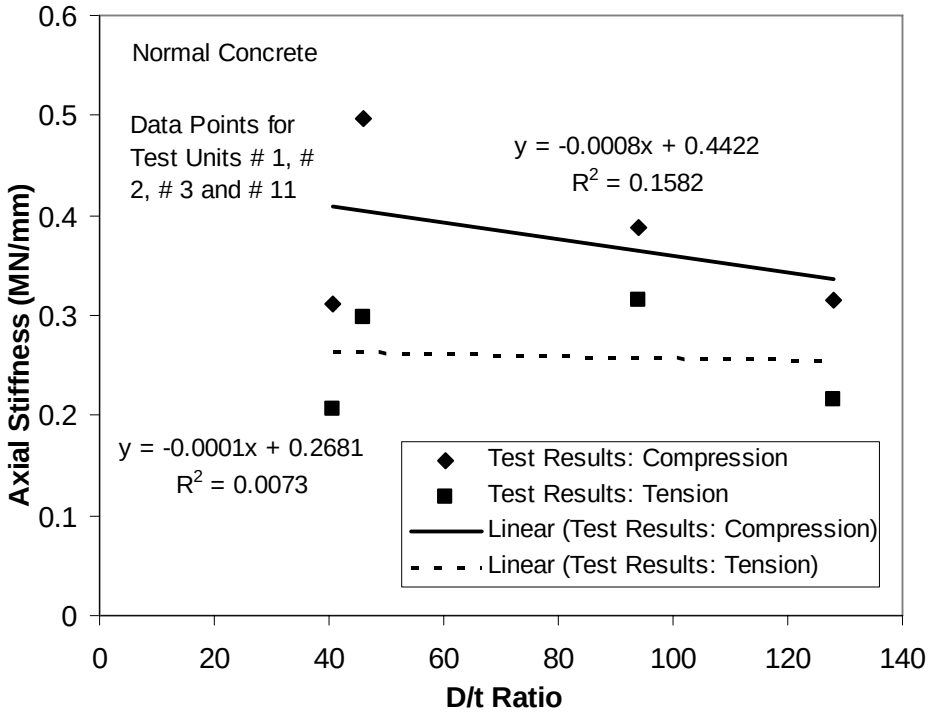


**Figure 6.13 Elastic Axial Stiffness versus D/t Ratio**

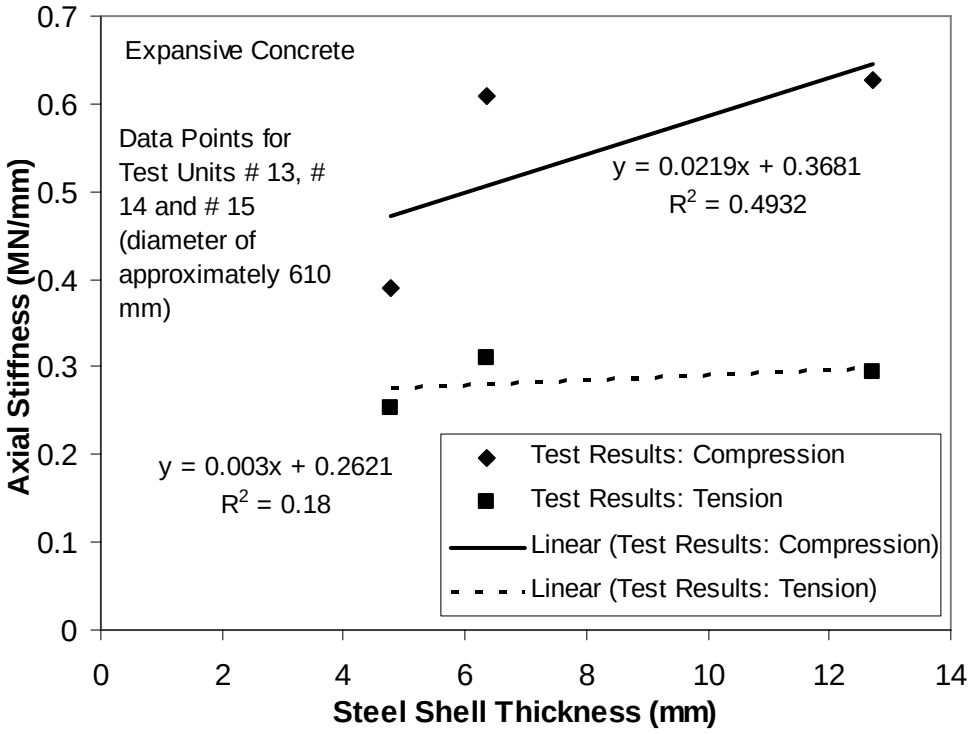


**Figure 6.14 Elastic Axial Stiffness versus Steel Shell Thickness for Expansive Concrete**

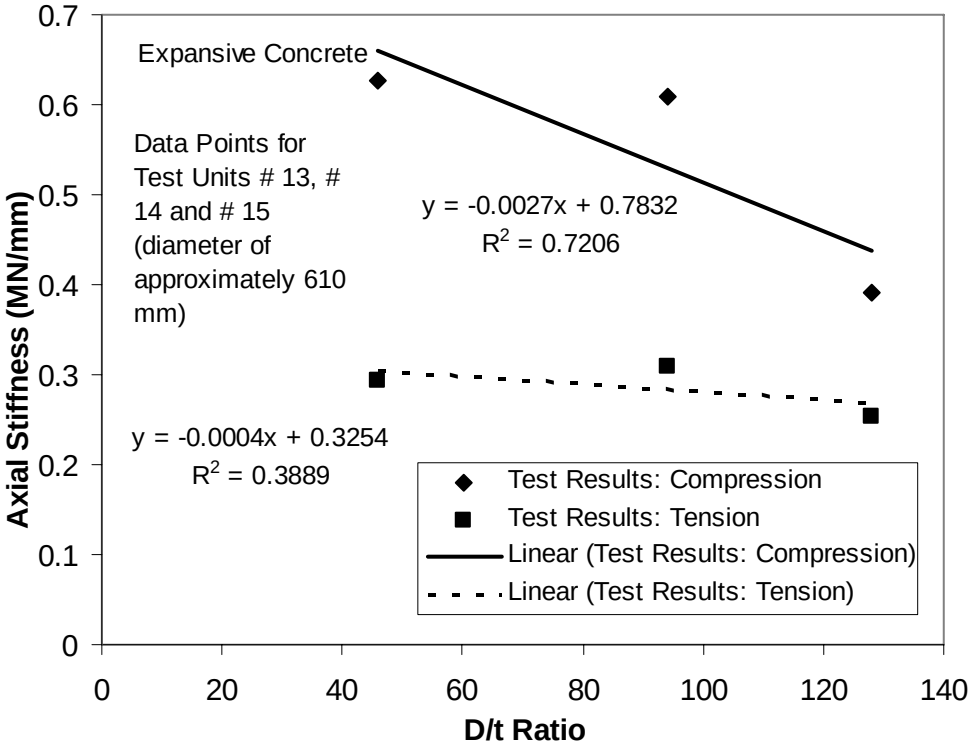


**Figure 6.15 Elastic Axial Stiffness versus D/t Ratio for Expansive Concrete**

## 6.5 Friction Bond

The adhesive bond, as presented in the previous section, diminished after the initial axial displacements after which a friction bond dominated the hysteretic response, as presented in this section. Friction bond stress was calculated for test units which lacked a mechanism.

### 6.5.1 Calculation of Friction Bond

Frictional bond stress values for axial compression and axial tension are reported in Table 6.2. These values were obtained by averaging the peak cyclic axial forces from axial displacements of 12.7 to 101.6 mm (0.5 to 4.0 in.) and dividing by the steel shell interior surface area. This axial displacement range was used because displacements less than a magnitude of 12.7 mm (0.5 in.) had some influence from the initial adhesive bond. Bond stresses were calculated at the peak cyclic axial tension forces, and at the subsequent axial force at zero displacement. The bond stress calculated from the peak

axial tension force, $\sigma_{Bond,T}$, and the bond stress at zero axial displacement after obtaining the peak axial tension force, $\sigma_{Bond,O}$ can be expressed as:

$$\sigma_{Bond,T} = \left( \frac{P_{T,Peak}}{A_{surface}} \right) \tag{6.1}$$

$$\sigma_{Bond,O} = \left( \frac{P_{unload}}{A_{surface}} \right) \tag{6.2}$$

$A_{surface}$: Surface area of the steel shell-reinforced concrete interface

$P_{T,Peak}$: Peak cyclic axial tension force

$P_{unload}$: Axial force at zero displacement, after obtaining the peak cyclic axial tension force

The bond stress equations presented above will be used in the following sections to allow for an evaluation of the effect of the D/t ratio on the bond stress for plain concrete and expansive concrete test units.

**Table 6.2 Friction Bond Stress**

| Test Unit # | Axial Compression Bond Stress MPa (ksi) | Axial Tension Bond Stress MPa (ksi) |
|---|---|---|
| 1 | 0.44 (0.063) | 0.34 (0.049) |
| 2 | 0.28 (0.041) | 0.35 (0.051) |
| 3 | 0.37 (0.054) | 0.31 (0.045) |
| 10 | 0.35 (0.051) | 0.31 (0.045) |
| 11 | 0.16 (0.023) | 0.12 (0.017) |
| 12 | 0.16 (0.023) | 0.18 (0.026) |
| 13 | 0.53 (0.076) | 0.38 (0.055) |
| 14 | 0.41 (0.06) | 0.31 (0.045) |
| 15 | 0.66 (0.096) | 0.34 (0.05) |

### 6.5.2 Friction Bond for Variation of D/t Ratio

A performance comparison to examine the friction bond for test units without a mechanism was made by plotting bond stress versus axial displacement. Bond stresses calculated at the peak axial tension force, $\sigma_{Bond,T}$, versus cyclic axial displacement are

plotted in Figure 6.16. Bond stresses at zero displacement, $\sigma_{Bond,O}$, versus axial tension displacement is plotted in Figure 6.17. The curves presented in Figures 6.16 and 6.17 differ as a result of the increase in the longitudinal reinforcement bar strain, under applied axial tension. When the reinforcing bars were subject to axial tension, radial strains formed in the surrounding concrete, and small splitting (microcracks) occurred. This resulted in a lateral pressure on the steel shell, which increased the axial force transfer thus providing a force transfer mechanism in addition to the force transfer through surface bond. The bond stress, $\sigma_{Bond,O}$, shown in Figure 6.17 represents the true bond stress due to friction at the steel shell-reinforced concrete interface, because reinforcement bar strains were at a minimum at zero displacement. These bond stress values, $\sigma_{Bond,O}$, will be used for comparison to test data from other researcher in Section 6.7.

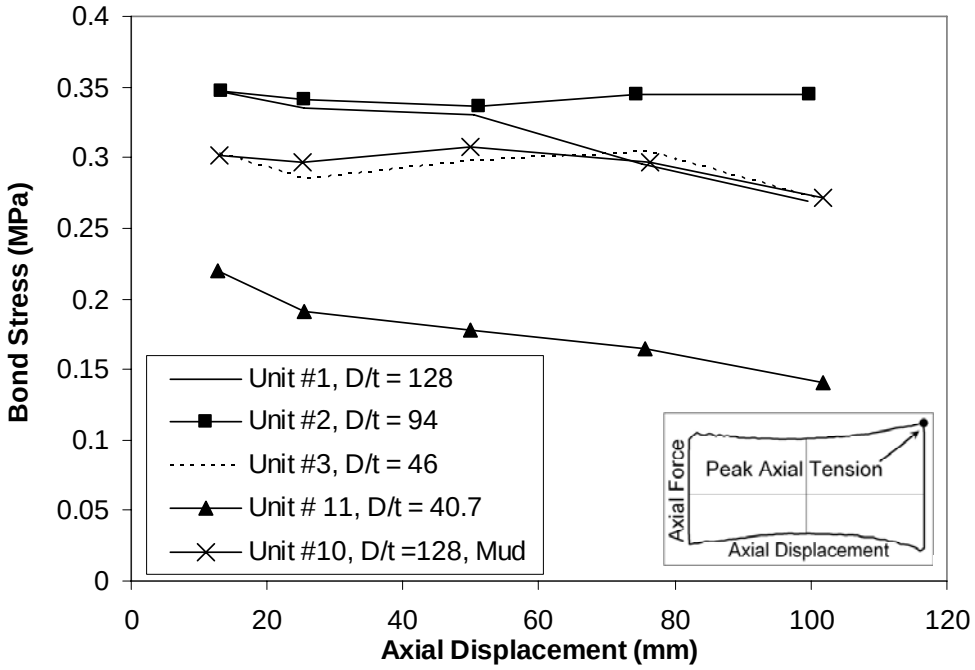


**Figure 6.16 Axial Tension Bond Stress at Maximum Cyclic Axial Displacement for Test Unit with a variation of the D/t Ratio**

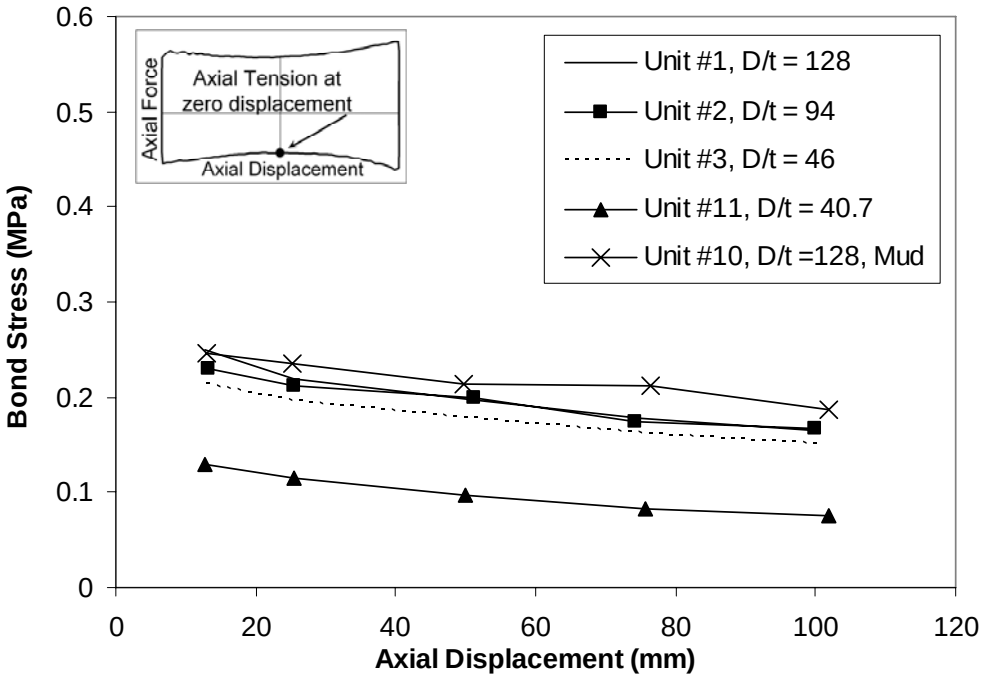


**Figure 6.17 Axial Tension Bond Stress at Zero Cyclic Axial Displacement for Test Unit with a variation of the D/t Ratio**

Bond stresses calculated for Test Unit #11 were used for comparison in Figures 6.16 and 6.17 because this test unit obtained slightly lower axial tension forces than Test Unit # 12 which had the same D/t ratio. A comparison of Test Units # 11 and # 2 with approximately the same steel shell cross sectional area, (D/t ratios of 40.7 and 94), shows the higher D/t ratio reached greater bond stresses at the peak axial tension forces and at zero axial displacement. This implies the importance of the steel shell diameter, D, (greater surface area) in the axial force transfer through friction bond. A trend for test units with the same steel shell diameter, D, (D/t ratios of 128, 94 and 46) cannot be obtained from Figures 6.16 and 6.17.

The water-bentonite surface coating within Test Unit # 10 typically decreased the bond stress under axial tension, in comparison to the test unit with a clean surface at the same D/t ratio (Test Unit # 1), as shown in Figure 6.16. However, this was not the case for the bond stress at zero axial displacement, as shown in Figure 6.17, as the test unit with the water-bentonite surface coating obtained the greatest bond stress, in comparison to Test Units # 1, # 2, # 3, and # 11 at D/t ratios of 128, 94, 46 and 40.7, respectively.

### 6.5.3 Friction Bond for Expansive Concrete

Bond stress plots for test units with expansive concrete are shown in Figures 6.18 and 6.19. These plots are similar to the previously presented bond stress plots. At the initial axial displacements, when an adhesive bond dominated, the bond stress was found to increase as the D/t ratio decreased. After the adhesive bond was overcome, the bond stress had a sharp decrease until a friction bond dominated the response. As shown in Figure 6.18 the friction bond under axial tension typically remained constant until an axial displacement of 50.8 mm (2.0 in.) after which a gradual decrease occurred for all expansive concrete test units. A trend of increasing bond stress with D/t ratio or steel shell thickness cannot be obtained from either Figure 6.18 or 6.19. In Figure 6.19 the friction bond at zero axial displacement had a clear trend of decreasing bond stress with increasing axial displacement.

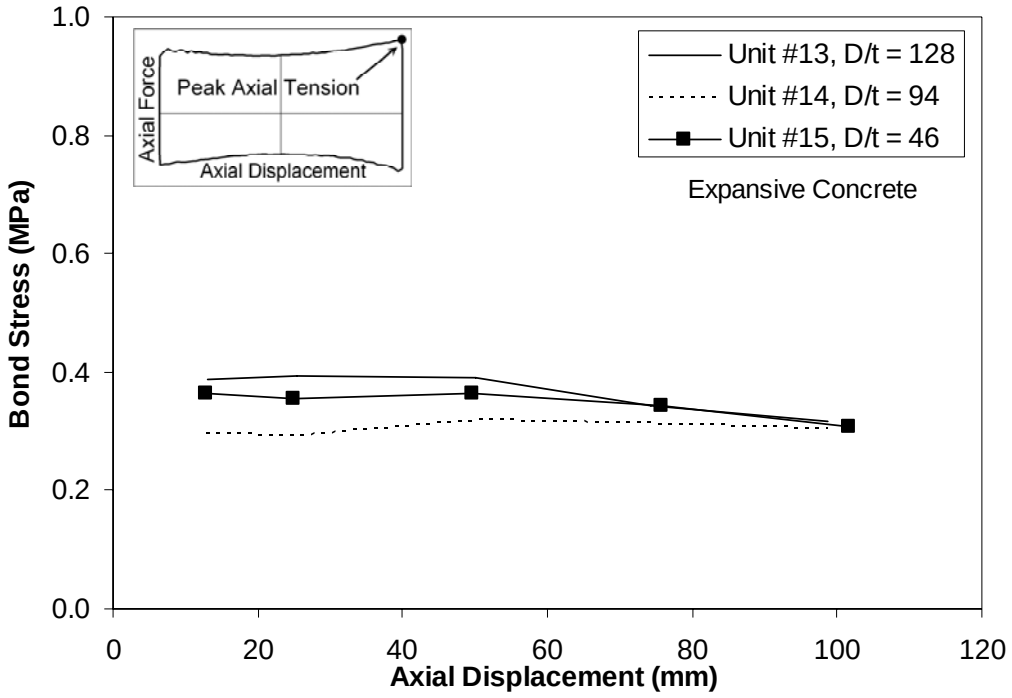


**Figure 6.18 Axial Tension Bond Stress at Maximum Cyclic Axial Displacement for Expansive Concrete Test Units**

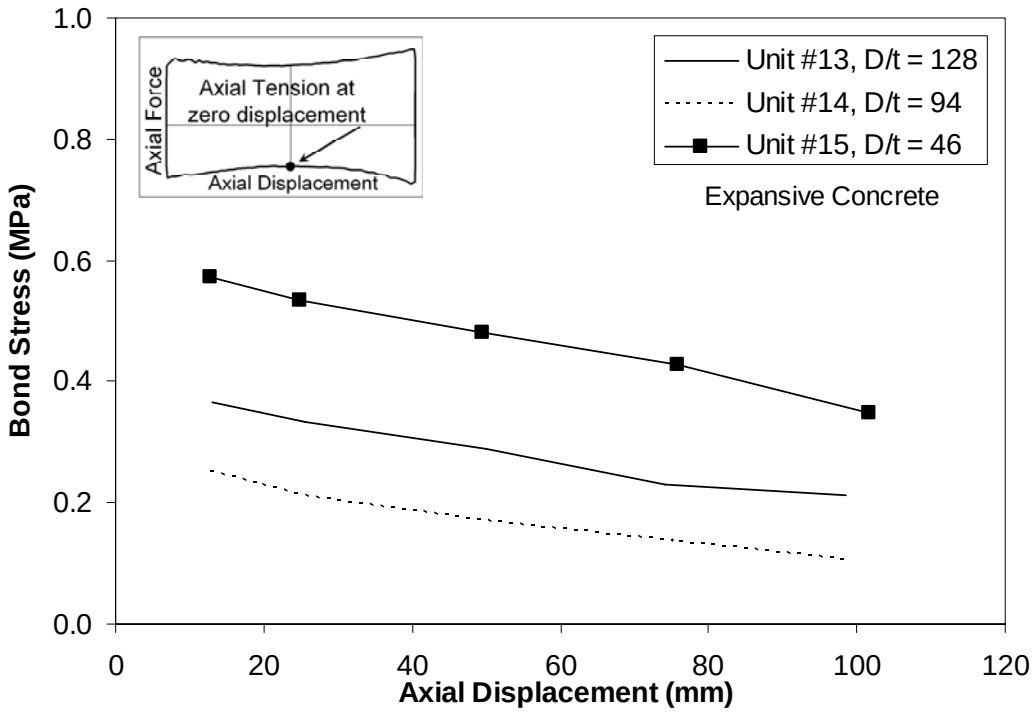


**Figure 6.19 Axial Tension Bond Stress at Zero Cyclic Axial Displacement for Expansive Concrete Test Units**

A comparison between the bond stresses obtained by expansive concrete and plain concrete test units is shown in Figure 6.20 for the friction bond under axial tension and in Figure 6.21 for the friction bond at zero axial displacement. In both figures the test units at D/t ratios of 128 and 46 with expansive concrete obtained greater bond stresses than their respective plain concrete counterparts. This trend was not true at a D/t ratio of 94. In most cases, the increase in bond stress gained by using expansive concrete was not substantial. As a result the use of expansive concrete is concluded to not have a substantial increase in the friction bond.

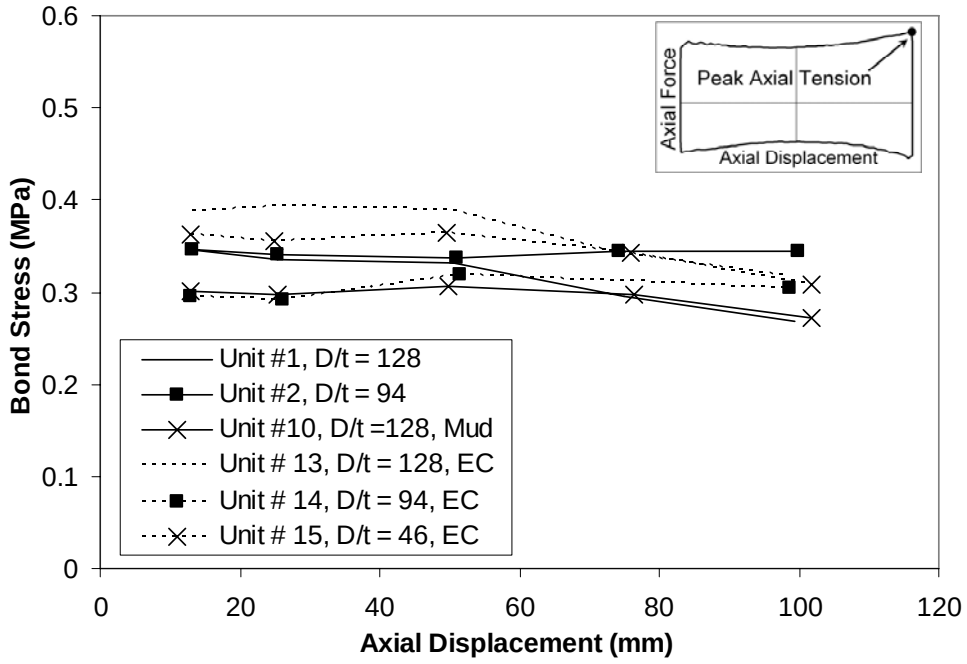


**Figure 6.20 Axial Tension Bond Stress at Maximum Cyclic Axial Displacement for Plain Concrete and Expansive Concrete Test Units**

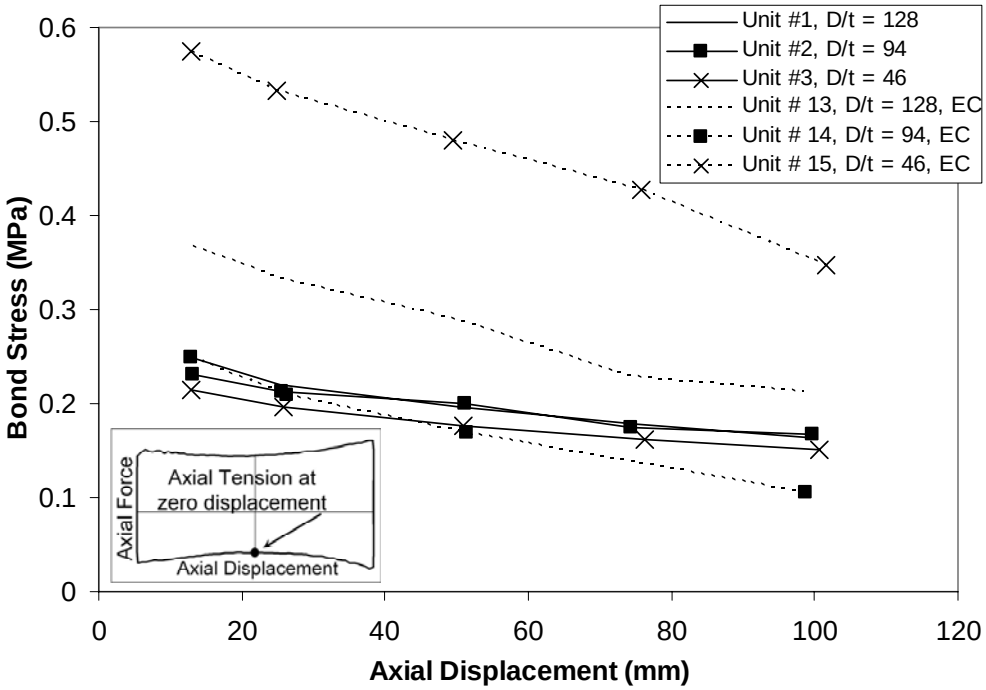


**Figure 6.21 Axial Tension Bond Stress at Zero Cyclic Axial Displacement for Plain Concrete and Expansive Concrete Test Units**

## 6.6 Axial Transfer Stress on Mechanisms

The effectiveness of an axial force transfer mechanism, welded circumferentially to the steel shell, can be determined by calculating the axial transfer stress. This stress is the axial force per mechanism area, protruding into the concrete core, which will be presented in the following section.

### 6.6.1 Calculation of Axial Transfer Stress on Mechanisms

The axial transfer stress, $\sigma_{Transfer}$, was calculated using the estimated axial compression and axial tension yield forces, $P_{applied}$, as obtained from the hysteretic response. The yield point, in the hysteretic response, was estimated as the maximum axial force at the target displacement of the first cycle: +/- 2.54 mm (0.1 in.). A friction, $P_{fric}$, of 0.89 MN (200 kips) was assumed based on results of test units without a mechanism and subtracted from the yield force to obtain the force transferred through the mechanism. This force was divided by the area of the mechanism protruding into the reinforced concrete core, $A_{mech}$, and also divided by the number of mechanisms (if two shear rings), $N_{mech}$, to obtain the axial transfer stress. This is shown in Equation 6.3 below. Axial transfer stresses are listed in Table 6.3 for test units which had a circumferential mechanism at a high D/t ratio. Axial transfer stresses are listed in Table 6.4 for test units which had a circumferential mechanism at a low D/t ratio.

$$\sigma_{Transfer} = \left( \frac{P_{applied} - P_{fric}}{A_{mech} \cdot N_{mech}} \right) \tag{6.3}$$

Equation 6.3 will be used in the following sections to calculate the axial transfer stress to a circumferential mechanism.

**Table 6.3 Calculation of Transfer Stresses for Test Units with a Circumferential Mechanism and a High D/t Ratio**

| Property or Calculation | Units | Test Unit # 4 | # 5 | # 7 | # 16 |
|---|---|---|---|---|---|
| Internal Diameter, D | mm, (inch) | 610, (24.0) | 610, (24.0) | 610, (24.0) | 597, (23.5) |
| Steel Shell Thickness, t | mm, (inch) | 4.8, (0.19) | 4.8, (0.19) | 4.8, (0.19) | 6.4, (0.25) |
| Mechanism Radial Width, h | mm, (inch) | 3.3, (0.13) | 12.7, (0.5) | 9.5, (0.38) | 6.4, (0.25) |
| Mechanism Area, $A_{mech}$ | $m^2$, ($inch^2$) | 0.0063, (9.75) | 0.024, (36.9) | 0.018, (27.8) | 0.012, (18.3) |
| Compression Force at Yield | MN, (kips) | 1.94, (436) | 2.77, (623) | 2.52, (567) | 1.94, (435) |
| Tension Force at Yield | MN, (kips) | 1.80, (405) | 2.90, (652) | 3.09, (695) | 1.94, (436) |
| Assumed Core-Shell Friction | MN, (kips) | 0.89, (200) | 0.89, (200) | 0.89, (200) | 0.89, (200) |
| Compression Force, per Ring | MN, (kips) | 1.05, (236) | 1.88, (423) | 1.63, (367) | 1.05, (235) |
| Tension Force, per Ring | MN, (kips) | 0.91, (205) | 2.01, (452) | 2.20, (495) | 1.05, (236) |
| Compression Transfer Stress | MPa, (ksi) | 167, (24.2) | 79.0, (11.5) | 90.8, (13.2) | 88.9, (12.9) |
| Tension Transfer Stress | MPa, (ksi) | 145, (21) | 84.4, (12.2) | 123, (17.8) | 89.3, (13) |

**Table 6.4 Calculation of Transfer Stresses per Shear Ring for Test Units at a Low D/t Ratio**

| Property or Calculation | Units | Test Unit # 17 | # 18 | # 19 | # 20 | # 21 |
|---|---|---|---|---|---|---|
| Internal Diameter, D | mm, (inch) | 610, (24.0) | 610, (24.0) | 610, (24.0) | 610, (24.0) | 610, (24.0) |
| Steel Shell Thickness, t | mm, (inch) | 25.4, (1) | 25.4, (1) | 25.4, (1) | 25.4, (1) | 25.4, (1) |
| Mechanism Radial Width, h | mm, (inch) | 6.4, (0.25) | 6.4, (0.25) | 6.4, (0.25) | 6.4, (0.25) | 6.4, (0.25) |
| Shear Ring Spacing, s | mm, (inch) | | | 76.2, (3.0) | 152.4, (6.0) | 304.8, (12.0) |
| Mechanism Area, $A_{mech}$ | $m^2$, ($inch^2$) | 0.012, (18.7) | 0.012, (18.7) | 0.012, (18.7) | 0.012, (18.7) | 0.012, (18.7) |
| Axial Compression Force at Yield | MN, (kips) | 2.87, (646) | 2.08, (469) | 4.09, (920) | 4.12, (927) | 5.20, (1170) |
| Axial Tension Force at Yield | MN, (kips) | 2.81, (633) | 1.36, (305) | 3.44, (774) | 3.28, (738) | 3.94, (885) |
| Assumed Core-Shell Friction | MN, (kips) | 0.89, (200) | 0.89, (200) | 0.89, (200) | 0.89, (200) | 0.89, (200) |
| Number of Shear Rings | | 1 | 1 | 2 | 2 | 2 |
| Axial Compression Force at Yield, per Ring | MN, (kips) | 1.98, (446) | 1.2, (269) | 1.6, (360) | 1.62, (364) | 2.15, (484) |
| Axial Tension Force at Yield, per Ring | MN, (kips) | 1.92, (433) | 0.47, (105) | 1.28, (287) | 1.2, (269) | 1.52, (343) |
| Axial Compression Transfer Stress | MPa, (ksi) | 165, (23.9) | 99.4, (14.4) | 133, (19.3) | 134, (19.5) | 179, (26.0) |
| Axial Tension Transfer Stress | MPa, (ksi) | 160, (23.2) | 38.8, (5.6) | 106, (15.4) | 99.4, (14.4) | 127, (18.4) |

### 6.6.2 Axial Transfer Stress on Circumferential Mechanisms

A comparison of the transfer stresses for the three circumferential mechanism designs, tested at a D/t ratio of 128, is shown in the column chart of Figure 6.22. The weld bead mechanism obtained the greatest transfer stresses of the three designs, however, it should be noted this mechanism had a radial width that was approximately 1/3 of the shear ring radial width. This would indicate that mechanisms (tested) with a greater radial width did not need to have a greater thickness: an ineffective use of material. However, a mechanism with a greater radial width resulted in an axial force

transfer at a lower stress, and maintained contact with the concrete core as the steel shell deformed out-of-plane, which is critical for a high D/t ratio.

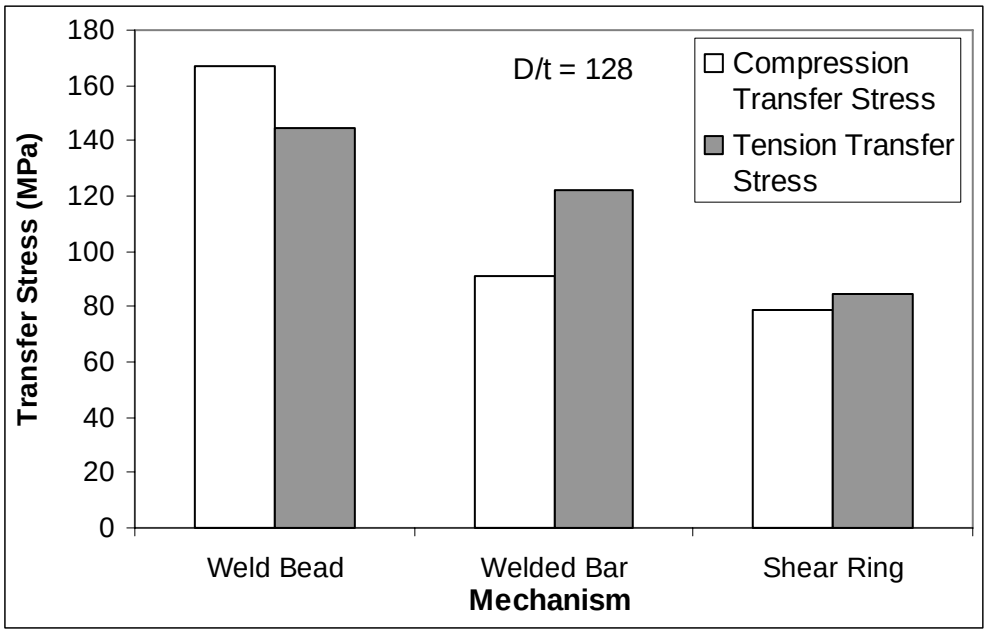


**Figure 6.22 Effect of Mechanism Design on Transfer Stress at a D/t Ratio of 128**

The welded bar, which had a radial width that was 3/4 of the shear ring, also obtained transfer stresses greater than the shear ring, as shown in Figure 6.22. This behavior, of greater axial transfer stress with decreasing mechanism radial width is due to the attainment of the steel shell capacity. After the steel shell capacity was obtained, and circumferential yielding of the steel shell and mechanism occurred, no further increase in the axial force transfer could occur. This axial force transfer limit governed by the steel shell, clearly demonstrates the inefficiency of a mechanism with a large radial width.

A comparison of the effect of the D/t ratio on the shear ring transfer stresses is shown in the column chart of Figure 6.23. The test unit with a D/t ratio of 96 obtained a slightly greater axial transfer stresses than the test unit at a D/t ratio of 128. Both test units obtained the steel shell capacity; however, the shear ring at a D/t ratio of 96 had one half the radial width of the shear ring at a D/t ratio of 128, hence a greater difference in the axial transfer stresses would have been expected. At the lowest D/t ratio tested, of 24, the axial transfer stresses nearly doubled due to the steel shell remaining in the elastic range. In this test unit an axial compression transfer stress of 164.8 MPa (23.9 ksi) was

obtained which represents an axial transfer stress that is eight times the concrete compressive strength, $f_c^{'}$. However, in this test unit the concrete core governed the capacity with axial force increasing as axial displacement increased as shown in Figure 5.32. A stress of 428 MPa (62.1 ksi) was obtained at the maximum axial compression force of 6.04 MN (1360 kips). This stress was twenty-one times the concrete compressive strength, $f_c^{'}$.

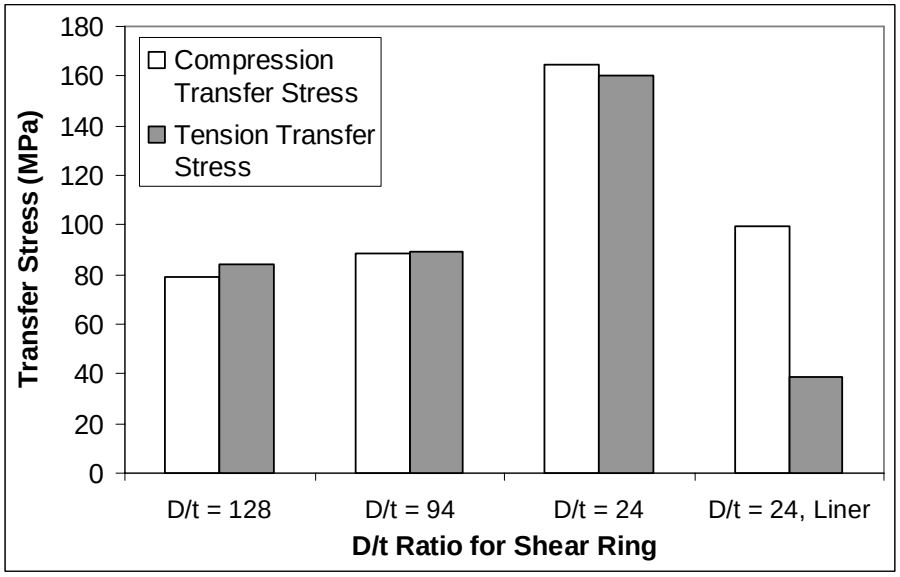


**Figure 6.23 Effect of D/t Ratio on Transfer Stress for Shear Ring Mechanism**

The test unit at a D/t ratio of 24 with a polyethylene lining obtained a lower axial transfer stress due to the minimization (or attempted prevention) of the surface bond between the steel shell and core, with the lining, and also due to the presence of moist concrete, as presented in Section 5.6.3. However, it should be noted that in the calculation of the axial transfer stress, using Equation 6.3, a friction, $P_{frict}$, of 0.89 MN (200 kips) was assumed and used for all of the aforementioned test units. Test Unit # 18 had a level of friction (Figure 5.36) that was typically less than the aforementioned assumed value, however, this value was used for consistency.

### 6.6.3 Axial Transfer Stress on Multiple Shear Rings

Axial transfer stresses were calculated for test units with two shear rings, as shown in Table 6.4 and as shown in the column chart of Figure 6.24. Stresses were calculated using Equation 6.3. Figure 6.24 shows lower transfer stresses for test units with a shear ring spacing of 76 mm (3.0 in.) and 152 mm (6.0 in.) when compared to the test unit with a single shear ring (at the same D/t ratio of 24). As the shear ring spacing increased to 305 mm (12.0 in.), the transfer stress increased (for Test Unit # 21), such that the axial compression transfer stress exceeded that of Test Unit # 17 with a single shear ring. Test Unit # 17 obtained an axial compression transfer stress of 165 MPa (23.9 ksi), whereas Test Unit # 21 obtained an axial compression transfer stress of 179 MPa (26.0 ksi): an increase of 8.5%. Test Unit # 21 was not expected to have an axial transfer stress greater than the single shear ring of Test Unit # 17. This high level of axial transfer stress is due to a proper spacing of the shear rings, at a spacing of D/2. Comparisons between the prediction and the experimental hysteretic response for test units with a shear ring(s) will be presented in Section 6.11.

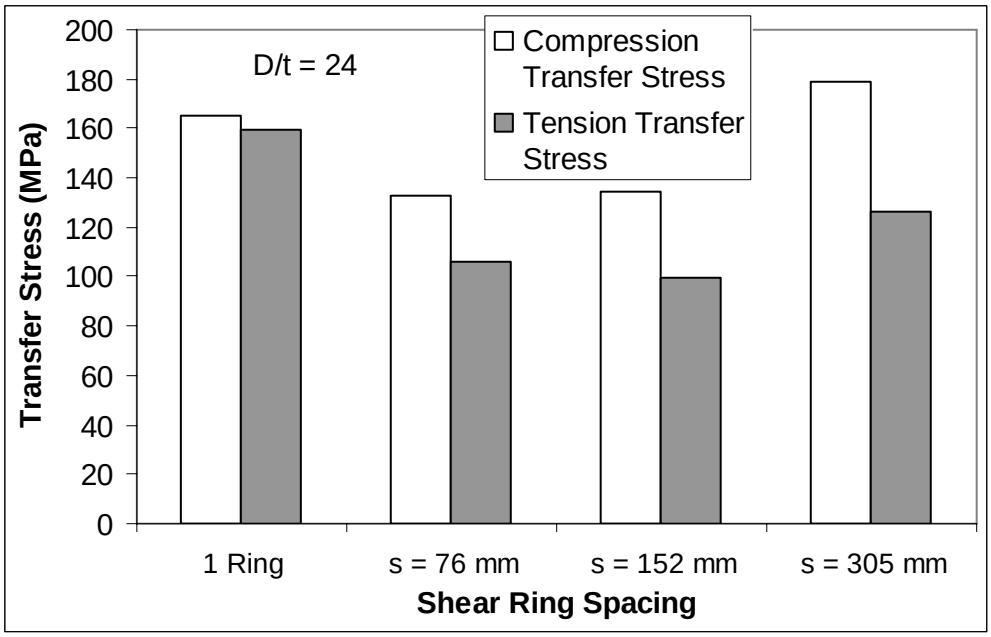


**Figure 6.24 Effect of Shear Ring Spacing on Transfer Stress**

### 6.6.4 Axial Transfer Stress on Distributed Mechanisms

The axial transfer stress was calculated for test units with mechanisms distributed throughout the steel shell, such as the cross bar, shear studs, and tread plate are listed in Table 6.5. The axial transfer stress for these mechanisms was calculated using Equation 6.3. A uniform axial transfer stress distribution was assumed on the mechanisms surface area. The shear stud mechanism obtained axial compression and axial tension transfer stresses of 158 MPa (22.8 ksi) and 152 MPa (22.1 ksi), respectively. These stresses were close to the stresses obtained by a single shear ring at a D/t ratio of 24 (Test Unit # 17). However, these stresses did not last beyond the initial axial displacements due to failure of the shear studs: a non-ductile performance. The tread plate mechanism obtained axial transfer stresses that were approximately 1/5 of the shear stud axial transfer stress, as shown in Table 6.5. This is a result of the large quantity of treads used. However, as the axial displacements increased, the bond deteriorated as the concrete between the treads crushed, rendering this mechanism ineffective: a non-ductile performance.

The cross bar mechanism obtained the lowest stresses of the distributed mechanisms due to its greater surface area, and as a result of the minimal weld contact area with the steel shell. This stress transfer also lasted only until the yield strength of the welded connection was obtained, after which the mechanism and weld separated from the steel shell thus rendering the mechanism ineffective; also a non-ductile performance.

The aforementioned distributed mechanisms had a significant drop in the axial force transfer after obtaining a high axial force transfer (yield). Such mechanisms, if used, should be used in a sufficient quantity such that a factor of safety will exist between the capacity of the mechanism and the maximum applied force. This will ensure the mechanisms will remain within the elastic range.

**Table 6.5 Calculation of Transfer Stresses for Test Units with Distributed Mechanisms**

| | | Test Unit | | |
|---|---|---|---|---|
| **Property/Calculation** | **Units** | **# 6 (Cross Bar)** | **# 8 (Shear Studs)** | **# 9 (Tread Plate)** |
| Internal Diameter, D | mm, (inch) | 609.6, (24) | 610, (24) | 610, (24) |
| Steel Shell Thickness, t | mm, (inch) | 4.8, (0.19) | 4.8, (0.19) | 4.8, (0.19) |
| Mechanism Length | mm, (inch) | 25.4, (1) | 33.5, (1.32) | 25.4, (1) |
| Mechanism Radial Width | mm, (inch) | 610, (24) | 6.35, (0.25) | 2.54, (0.1) |
| Mechanism Area | $m^2$, ($inch^2$) | 0.015, (24) | 0.00024, (0.38) | 4.6E-05, (0.071) |
| Number of Mechanisms | | 1 | 21 | 1695 |
| Total Mechanism Area | $m^2$, ($inch^2$) | 0.015, (24) | 0.0051, (7.90) | 0.077, (120) |
| Axial Compression Force at Yield | MN, (kips) | 2.42, (545) | 1.69, (380) | 3.62, (813) |
| Axial Tension Force at Yield | MN, (kips) | 1.60, (359) | 1.67, (375) | 3.18, (715) |
| Assumed Core-Shell Friction | MN, (kips) | 0.89, (200) | 0.89, (200) | 0.89, (200) |
| Axial Compression Force at Yield | MN, (kips) | 1.53, (345) | 0.80, (180) | 2.73, (613) |
| Axial Tension Force at Yield | MN, (kips) | 0.71, (159) | 0.78, (175) | 2.29, (515) |
| Axial Compression Transfer Stress | MPa, (ksi) | 99.1, (14.4) | 158, (22.8) | 35.3, (5.11) |
| Axial Tension Transfer Stress | MPa, (ksi) | 45.7, (6.63) | 152, (22.1) | 29.7, (4.30) |

## 6.7 Bond Stress Comparison to Other Researchers

A comparison of bond stress data, as obtained from testing conducted by other researchers (Sections 2.2 and 2.3) with bond stress data from this research is presented in this section. The bond stress used from this research, for comparison in this section, is an average of the stresses at zero axial displacement obtained after the peak axial cyclic tension forces, $\sigma_{Bond}$. This stress is presented in Section 6.5 and is stated in Equation 6.2.

### 6.7.1 Bond Stress for Normal Concrete

Bond stress data is listed in Table 6.6 for testing conducted by Roeder (1999), Tomii (1980), and Sato (1981), and for test units from this research. Test results listed in Table 6.6 included test units which had normal concrete, expansive concrete, reinforced

concrete, and either a smooth steel shell interior surface, or a steel shell interior surface lined with treads (a tread plate). It should be noted that test data obtained for Tomii had a support condition in which the base of the concrete core and steel shell were both supported. However, this data will be presented as it includes data for a tread plate mechanism. Testing conducted by Tomii would have been expected to obtain the greatest bond stress, as the base was supported by both the steel shell and the concrete core. However, in the calculation of bond stress, Tomii accounted for this support condition, as presented in Section 2.2.1.

In Figure 6.25, the bond stresses obtained by Roeder, Sato, Tomii and for this research, for normal concrete are plotted versus the D/t ratio. A general trend of decreasing bond stress with increasing D/t ratio cannot be inferred upon comparison of all data points. Such a trend was inferred by Roeder, as presented in Section 2.3. A comparison of only the bond stress data points obtained from this research shows no significant change in the bond stress as the D/t ratio increases.

**Table 6.6 Bond Stresses Obtained in Research Literature and Test Program**

| Researcher | Mechanism | Diameter, D mm (in.) | Thickness, t mm (in.) | D/t Ratio | Bond Stress MPa (psi) |
|---|---|---|---|---|---|
| Tomii | Expansive Conc. | 150, (5.91) | 3.2, (0.13) | 46.9 | 0.69, (100) |
| Tomii | Expansive Conc. | 150, (5.91) | 3.2, (0.13) | 46.9 | 0.49, (71) |
| Tomii | None | 150, (5.91) | 3.2, (0.13) | 46.9 | 0.39, (57) |
| Tomii | Tread Plate | 150, (5.91) | 3.2, (0.13) | 46.9 | 0.59, (86) |
| Tomii | Tread | 150, (5.91) | 3.2, (0.13) | 46.9 | 0.59, (86) |
| Roeder | Moderate Shrinkage | 248, (9.75) | 13.5, (0.53) | 18.4 | 0.01, (1.5) |
| Roeder | Moderate Shrinkage | 248, (9.75) | 13.5, (0.53) | 18.4 | 0.026, (3.8) |
| Roeder | Moderate Shrinkage | 341, (13.4) | 7.1, (0.28) | 48 | 0.031, (4.5) |
| Roeder | Moderate Shrinkage | 341, (13.4) | 7.1, (0.28) | 48 | 0.037, (5.4) |
| Roeder | Moderate Shrinkage | 341, (13.4) | 7.1, (0.28) | 48 | 0.094, (14) |
| Roeder | Moderate Shrinkage | 341, (13.4) | 7.1, (0.28) | 48 | 0.043, (6.2) |
| Roeder | Moderate Shrinkage | 598, (23.6) | 5.6, (0.22) | 107 | 0.052, (7.5) |
| Roeder | Moderate Shrinkage | 598, (23.6) | 5.6, (0.22) | 107 | 0.068, (9.9) |
| Roeder | Minimal Shrinkage | 248, (9.75) | 13.5, (0.53) | 18.4 | 0.77, (112) |
| Roeder | Minimal Shrinkage | 248, (9.75) | 13.5, (0.53) | 18.4 | 0.79, (114) |
| Roeder | Minimal Shrinkage | 248, (9.75) | 13.5, (0.53) | 18.4 | 0.78, (112) |
| Roeder | Minimal Shrinkage | 248, (9.75) | 13.5, (0.53) | 18.4 | 0.32, (46) |
| Roeder | Minimal Shrinkage | 341, (13.4) | 7.1, (0.28) | 48 | 0.28, (41) |
| Roeder | Minimal Shrinkage | 341, (13.4) | 7.1, (0.28) | 48 | 0.36, (52) |
| Roeder | Minimal Shrinkage | 341, (13.4) | 7.1, (0.28) | 48 | 0.18, (25) |
| Roeder | Minimal Shrinkage | 341, (13.4) | 7.1, (0.28) | 48 | 0.19, (27) |
| Roeder | Minimal Shrinkage | 598, (23.6) | 5.6, (0.22) | 107 | 0.15, (21) |
| Roeder | Minimal Shrinkage | 598, (23.6) | 5.6, (0.22) | 107 | 0.18, (26) |
| Roeder | Minimal Shrinkage | 598, (23.6) | 5.6, (0.22) | 107 | 0.093, (14) |
| Roeder | Minimal Shrinkage | 598, (23.6) | 5.6, (0.22) | 107 | 0.093, (14) |
| Sato | None | 600, (23.6) | 9.0, (0.35) | 66.7 | 0.39, (57) |
| Sato | Tread Plate (3 checker) | 600, (23.6) | 9.0, (0.35) | 66.7 | 4.9, (711) |
| Sato | Tread Plate (2 checker) | 600, (23.6) | 9.0, (0.35) | 66.7 | 5.5, (798) |
| UCSD, U.1 | None | 610, (24) | 4.8, (0.19) | 128 | 0.21, (31) |
| UCSD, U.2 | None | 597, (23.5) | 6.4, (0.25) | 94 | 0.2, (30) |
| UCSD, U.3 | None | 584, (23) | 12.7, (0.5) | 46 | 0.19, (27) |
| UCSD, U.11 | None | 610, (24) | 4.8, (0.19) | 42.7 | 0.11, (16) |
| UCSD, U.12 | None | 387, (15.2) | 9.5, (0.37) | 42.7 | 0.15, (22) |
| UCSD, U.13 | Expansive Conc. | 610, (24.0) | 4.8, (0.19) | 128 | 0.3, (44) |
| UCSD, U.14 | Expansive Conc. | 597, (23.5) | 6.4, (0.25) | 94 | 0.21, (30) |
| UCSD, U.15 | Expansive Conc. | 584, (23.0) | 12.7, (0.50) | 46 | 0.49, (72) |
| UCSD, U.9 | Tread Plate | 610, (24.0) | 4.8, (0.19) | 128 | 0.32, (46) |

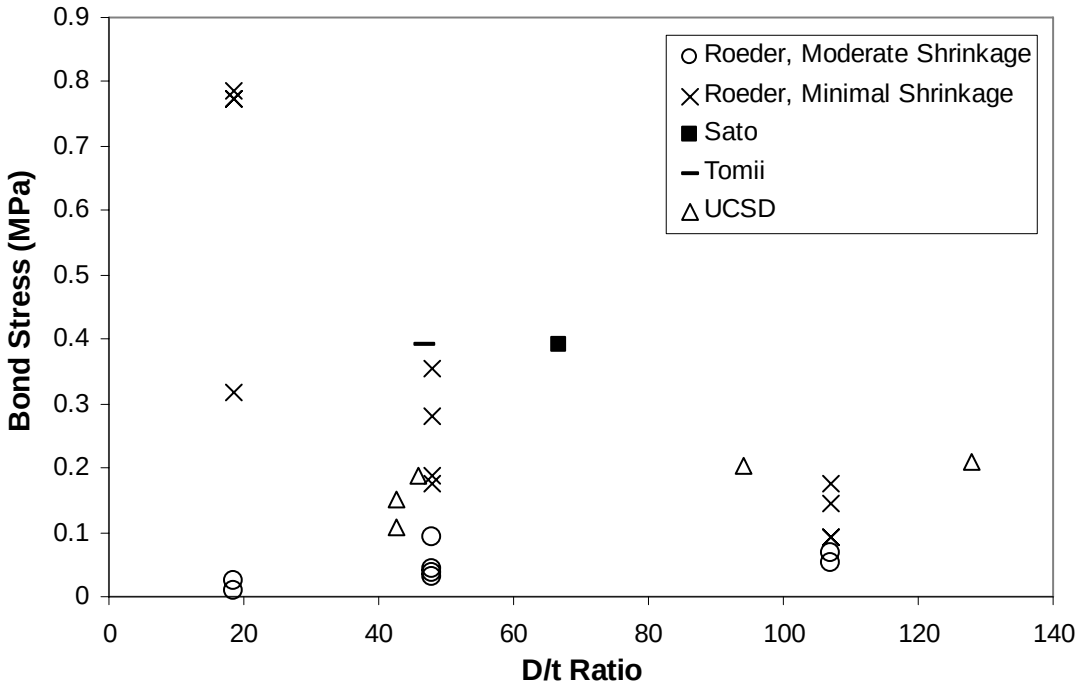


**Figure 6.25 Bond Stress Comparison as a Function of D/t Ratio**

### 6.7.2 Bond Stress for Expansive Concrete

A comparison of the effect of expansive concrete is shown in Figure 6.26. A general trend of decreasing bond stress with increasing D/t ratio can be observed from the plot. Despite the difference in base support conditions between Tomii and the test units in this research, the scatter between the data points was small at a low D/t ratio. A linear regression line for the three data points from this research, is shown in Figure 6.26, and stated below in Equation 6.4. The linear regression equation for the expansive concrete bond stress is stated below, and had a correlation coefficient, $R^2$, of 0.523.

$$\sigma_{Bond} = -0.0026 \cdot \left( \frac{D}{t} \right) + 0.5629 \qquad (6.4)$$

Equation 6.4 presents an estimate for the bond stress obtained at zero axial displacement, after obtaining the peak axial tension force. This equation is based on data from test units with D/t rations ranging from 46 to 128.

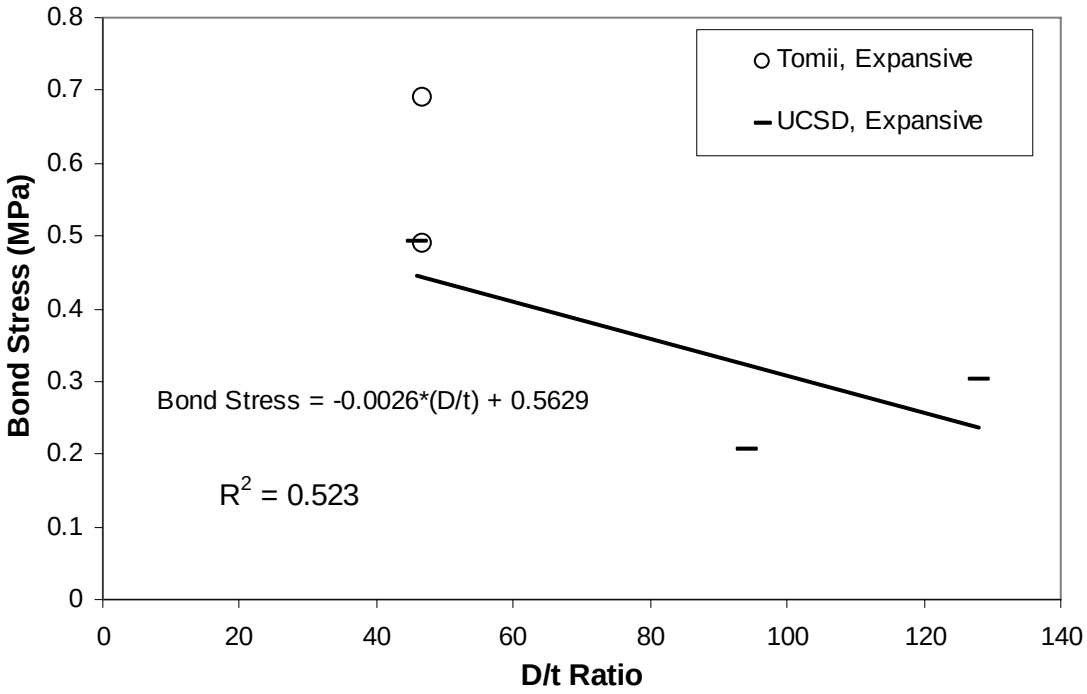


**Figure 6.26 Bond Stress Comparison as a Function of D/t Ratio for Expansive Concrete**

### 6.7.3 Bond Stress for Tread Plate Mechanism

A comparison of the bond stress data for test units with a tread plate is shown in Figure 6.27. Testing conducted by Sato (1981) resulted in bond stresses greater than the stresses obtained by Tomii (1980), and greater than the result obtained in this study for Test Unit # 9. In Figure 6.27, the bond stress for the tread plate mechanism was calculated by Tomii, and for Test Unit # 9, as the force per steel shell surface area lined with treads. From the research literature available, for Sato, it is not clear if the bond stress data reported followed this aforementioned calculation procedure, or if the bond stress was calculated as force per tread area perpendicular to loading. A bond stress calculated per unit area of tread perpendicular to loading, for Test Unit # 9, resulted in compression and tension transfer stresses of 35.3 MPa (5.11 ksi) and 29.7 MPa (4.30 ksi), respectively, as shown in Table 6.5. However, when compared to the maximum bond stress obtained by Sato, which was 5.5 MPa (0.80 ksi), a scatter in the data is still present. As a result of this scatter, the calculation procedure does not seem to be the explanation for this difference.

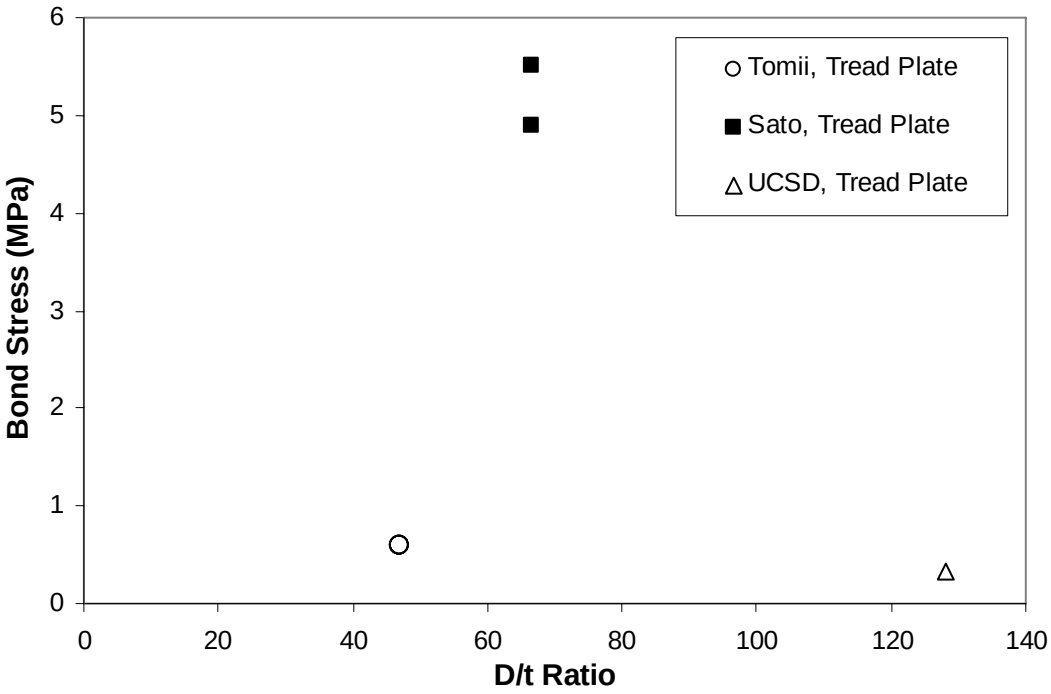


**Figure 6.27 Bond Stress Comparison as a Function of D/t Ratio for Tread Plate Mechanism**

## 6.8 Design Codes

This section will present a comparison of the experimental results with the design codes of the American Petroleum Institute and the United Kingdom Department of Energy.

### 6.8.1 API Code

The API code equations for the calculation of the axial load transfer stress using working stress or LRFD (Section 2.4.2) was valid for test units with multiple shear rings or test units that relied on the surface bond between the steel shell and reinforced concrete core. The calculation and required checks for the axial load transfer stress of test units with two shear rings, Test Units # 19, # 20, and # 21, is shown in Table 6.7. This equation was also applied to Test Units # 3 and # 11, which had D/t ratios of 46 and 40.7, respectively. These D/t ratios exceed the requirement of $D/t \leq 40$, however, the test units were judged to be within reason for comparison purposes. The test units with shear rings did not fully satisfy the requirement for the ratio of shear ring height

(including welds) to shear ring radial width: $1.5 \leq w/h \leq 3$. Test Units # 19, # 20 and # 21 all had a ratio, of $w/h$, of 4. In addition, Test Unit # 21, did not fully satisfy the requirement for the pile diameter to shear ring spacing ratio, of $2.5 \leq D/s \leq 8$, with a ratio of 2. Despite these shortcomings, a comparison was made to the two API equations using working stress design for two load cases: dead load and live load under normal conditions and under extreme loading conditions. A comparison was also made to the API LRFD equation.

Application of the API equation to Test Units # 19, # 20, and # 21 resulted in axial load transfer stresses as shown in Table 6.7. Multiplication of these stresses by the steel shell-concrete core contact surface area results in the axial transfer forces as shown in Table 6.7. These forces were plotted versus the ratio of shear ring radial width to spacing, $h/s$, as shown in Figure 6.28. A comparison of the forces obtained using the API equations, was made to the experimental axial compression forces at the first cycle, at a displacement of -2.54 mm (-0.1 in.), as shown in Figure 6.28. This axial displacement was selected as it provided an approximation to the yield point. The API working stress equation (for extreme loading conditions) made a close prediction of the experimental result at a $h/s$ ratio of 0.083, with a corresponding shear ring spacing of 76 mm (3.0 in.). However, as the shear ring spacing increased (decreasing $h/s$ ratio) the force predicted by the API equations and by the experimental result diverged, as shown in Figure 6.28. At a shear ring spacing of 305 mm (12.0 in.) the API predictions were approximately 1/3 of the experimental axial force.

**Table 6.7 Calculation of API Code Bond Stress for Shear Ring Mechanism**

| | | Test Unit | | |
|---|---|---|---|---|
| **Property/Calculation** | **Units** | **# 19** | **# 20** | **# 21** |
| Internal Diameter, D | mm, (inch) | 609.6, (24) | 609.6, (24) | 609.6, (24) |
| Steel Shell Thickness, t | mm, (inch) | 25.4, (1) | 25.4, (1) | 25.4, (1) |
| Shear Ring Height with Welds, w | mm, (inch) | 25.4, (1) | 25.4, (1) | 25.4, (1) |
| Shear Ring Radial Width, h | mm, (inch) | 6.35, (0.25) | 6.35, (0.25) | 6.35, (0.25) |
| Shear Ring Spacing, s | mm, (inch) | 76.2, (3) | 152.4, (6) | 304.8, (12) |
| Shear Ring Area, Aring | $mm^2$, ($inch^2$) | 12034, (18.7) | 12034.3, (18.7) | 12034.3, (18.7) |
| Connection Length | mm, (inch) | 1397, (55) | 1397, (55) | 1397, (55) |
| Concrete Compressive Strength, f'c | MPa, (psi) | 20.7, (3000) | 20.7, (3000) | 20.7, (3000) |
| Unconfined Grout Strength, fcu | MPa, (psi) | 24.9, (3606) | 24.9, (3606) | 24.9, (3606) |
| **Checks for API:** | | | | |
| Sleeve: $D_s/t_s < 80$ | | N/A | N/A | N/A |
| Pile: $D_p/t_p < 40$ | | 24 | 24 | 24 |
| Grout: $7 < D_g/t_g < 45$ | | N/A | N/A | N/A |
| $2.5 < (D_p/s) < 8$ | | 8 | 4 | 2 |
| $h/s < 0.1$ | | 0.083 | 0.042 | 0.021 |
| $1.5 < w/h < 3$ | | 4 | 4 | 4 |
| (17 MPa, 2.5 ksi) < fcu < (110 MPa, 16 ksi) | MPa, (ksi) | 24.9, (3.6) | 24.9, (3.6) | 24.9, (3.6) |
| fcu * (h/s) < (5.5 MPa, 800 psi) | MPa, (psi) | 2.07, (301) | 1.04, (150) | 0.52, (75) |
| **API (Working Stress Design, Load Conditions 1 and 2 - Dead and Live Load):** | | | | |
| Nominal Allowable Axial Load Transfer Stress, $f_{ba}$ | MPa, (psi) | 1.17, (170) | 0.66, (95) | 0.4, (58) |
| Axial Force Transfer | MN, (kips) | 3.14, (706) | 1.75, (394) | 1.06, (239) |
| Axial Force Transfer to One Mechanism | MN, (kips) | 0.75, (168) | 0.75, (168) | 0.75, (168) |
| **API (Working Stress Design, Load Conditions 3 and 4 - Dead, and Live Load Under Extreme Conditions):** | | | | |
| Nominal Allowable Axial Load Transfer Stress, $f_{ba}$ | MPa, (psi) | 1.57, (228) | 0.88, (127) | 0.53, (77) |
| Axial Force Transfer | MN, (kips) | 4.21, (946) | 2.35, (528) | 1.42, (319) |
| Axial Force Transfer to One Mechanism | MN, (kips) | 0.75, (168) | 0.75, (168) | 0.75, (168) |
| **API (LRFD):** | | | | |
| Nominal Axial Load Transfer Stress, $f_{ba}$ | MPa, (psi) | 2.11, (306) | 1.18, (171) | 0.71, (104) |
| Resistance Factor for Axial Load Transfer, $\phi_{ba}$ | | 0.9 | 0.9 | 0.9 |
| Maximum Axial Load Transfer Stress, $f_{ba} * \phi_{ba}$ | MPa, (psi) | 1.9, (276) | 1.06, (154) | 0.64, (93) |
| Axial Force Transfer | MN, (kips) | 5.09, (1144) | 2.84, (639) | 1.72, (387) |
| Axial Force Transfer to One Mechanism | MN, (kips) | 0.75, (168) | 0.75, (168) | 0.75, (168) |

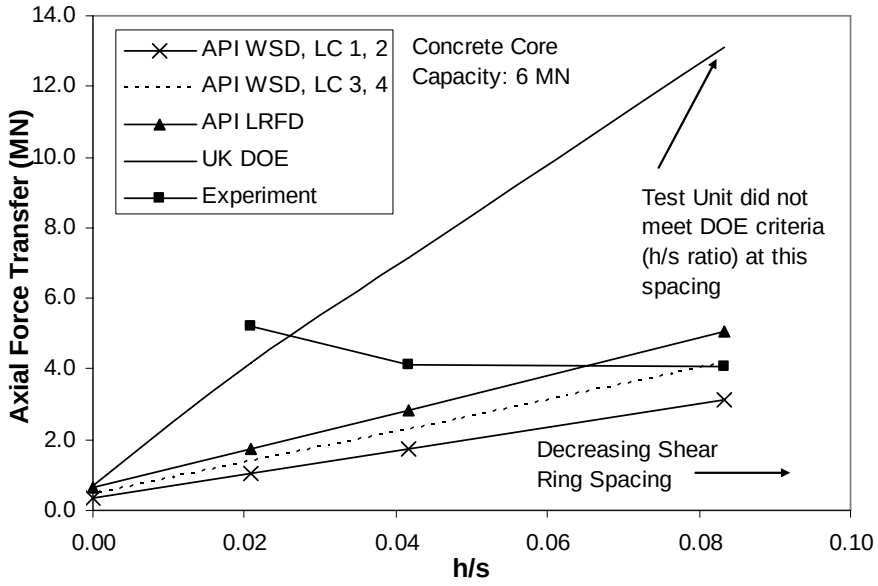


**Figure 6.28 Prediction of the Effect of Shear Ring Spacing on the Axial Force Transfer by API and UK DOE Codes**

A comparison of the API equations and the experimental axial transfer forces for Test Units # 3 and # 11, with D/t ratios of 46 and 40.7, is shown in Figure 6.29. This comparison was made despite the API equation requirement of D/t < 40. The axial force transfer predicted by the API equations and the experimental results increased with D/t ratio, however, the difference between the two increases as the D/t ratio increases. The API equations did not match the experimental results, as the predicted values were only a fraction of the experimental results, at all D/t ratios. The calculation and required checks for the application of the API equations to Test Units # 3 and # 11 are shown in Table 6.8.

**Table 6.8 Calculation of API Code Bond Stress for No Mechanism**

| Property/Calculation | Units | Test Unit # 3 | # 11 |
|---|---|---|---|
| Internal Diameter, D | mm, (inch) | 584.2, (23) | 387.4, (15.25) |
| Steel Shell Thickness, t | mm, (inch) | 12.7, (0.5) | 9.5, (0.375) |
| Shear Ring Height with Welds, w | mm, (inch) | N/A | N/A |
| Shear Ring Radial Width, h | mm, (inch) | N/A | N/A |
| Shear Ring Spacing, s | mm, (inch) | N/A | N/A |
| Shear Ring Area, Aring | $mm^2$, ($inch^2$) | N/A | N/A |
| Connection Length | mm, (inch) | 1092, (43) | 1092, (43) |
| Concrete Compressive Strength, f'c | MPa, (psi) | 20.7, (3000) | 20.7, (3000) |
| Unconfined Grout Strength, fcu | MPa, (psi) | 24.9, (3606) | 24.9, (3606) |
| **Checks for API:** | | | |
| Sleeve: $D_s/t_s < 80$ | | N/A | N/A |
| Pile: $D_p/t_p < 40$ | | 46 | 40.7 |
| Grout: $7 < D_g/t_g < 45$ | | N/A | N/A |
| $2.5 < (D_p/s) < 8$ | | N/A | N/A |
| $h/s < 0.1$ | | N/A | N/A |
| $1.5 < w/h < 3$ | | N/A | N/A |
| (17 MPa, 2.5 ksi) < fcu < (110 MPa, 16 ksi) | MPa, (ksi) | 24.9, (3.6) | 24.9, (3.6) |
| fcu * (h/s) < (5.5 MPa, 800 psi) | MPa, (psi) | N/A | N/A |
| **API (Working Stress Design, Load Conditions 1 and 2 - Dead and Live Load):** | | | |
| Nominal Allowable Axial Load Transfer Stress, $f_{ba}$ | MPa, (psi) | 0.14, (20) | 0.14, (20) |
| Axial Force Transfer | MN, (kips) | 0.28, (62.1) | 0.18, (41.2) |
| Axial Force Transfer to One Mechanism | MN, (kips) | N/A | N/A |
| **API (Working Stress Design, Load Conditions 3 and 4 - Dead, and Live Load Under Extreme Conditions):** | | | |
| Nominal Allowable Axial Load Transfer Stress, $f_{ba}$ | MPa, (psi) | 0.18, (26.7) | 0.18, (26.7) |
| Axial Force Transfer | MN, (kips) | 0.37, (83) | 0.24, (55) |
| Axial Force Transfer to One Mechanism | MN, (kips) | N/A | N/A |
| **API (LRFD):** | | | |
| Nominal Axial Load Transfer Stress, $f_{ba}$ | MPa, (psi) | 0.25, (36) | 0.25, (36) |
| Resistance Factor for Axial Load Transfer, $\phi_{ba}$ | | 0.9 | 0.9 |
| Maximum Axial Load Transfer Stress, $f_{ba} * \phi_{ba}$ | MPa, (psi) | 0.22, (32.4) | 0.22, (32.4) |
| Axial Force Transfer | MN, (kips) | 0.45, (100.7) | 0.3, (66.7) |
| Axial Force Transfer to One Mechanism | MN, (kips) | N/A | N/A |

### 6.8.2 UK DOE Code

Application of the UK DOE equation was valid for test units in which two shear rings were used (Test Units # 19, # 20 and # 21), or for the test units which had no mechanism. The equation was also applied to Test Units # 3 and # 11, with D/t ratios of 46 and 40.7, respectively, despite the D/t requirement of: $24 < D/t < 40$. These two test units were judged to be within reason for comparison to the UK DOE equation. The test units with shear rings did not fully satisfy four of the six requirements, as shown in the required checks and load transfer stress calculation in Table 6.9. Test Units # 20 and # 21 were within reason of meeting the requirements such that the equation could be applied for comparison purposes. Test Unit # 19, with the smallest shear ring spacing of 76 mm (3.0 in.) had a ratio of shear ring width to spacing, h/s, of 0.8, which was twice the maximum value allowed. This close shear ring spacing resulted in a high axial force transfer as shown in Table 6.9, which is greater than the concrete core capacity. For these reasons, the UK DOE equation could not be reasonably applied to Test Unit # 19, however, this data point will be included in Figure 6.28 to demonstrate the over-prediction of the axial force transfer at a small shear ring spacing.

In the calculation of the load transfer stress, using the UK DOE equation, a conservative value of 18 was used for the modular ratio of steel to grout, m, as recommended by this code for cases lacking test data. A safety factor of 4.5 was used to obtain the allowable load transfer stress, $f_{ba}$, from the characteristic bond stress, $f_{buc}$. The axial load transfer was obtained by taking the product of the allowable load transfer stress, $f_{ba}$, and the steel shell-concrete core contact area.

**Table 6.9 Calculation of UK DOE Bond Stress for Shear Ring Mechanism**

| Property/Calculation | Units | Test Unit # 19 | # 20 | # 21 |
|---|---|---|---|---|
| **Checks for UK DOE:** | | | | |
| Sleeve: $50 < D_s/t_s < 140$ | | | | |
| Pile: $24 < D_p/t_p < 40$ | | 24 | 24 | 24 |
| Grout: $10 < D_g/t_g < 45$ | | | | |
| $L_{grout}/D_p > 2$ | | 2.3 | 2.3 | 2.3 |
| $0 < (h/D_p) < 0.006$ | | 0.01 | 0.01 | 0.01 |
| $0 < (D_p/s) < 8$ | | 8.0 | 4.0 | 2.0 |
| $0 < (h/s) < 0.04$ | | 0.083 | 0.042 | 0.021 |
| $1.5 < (w/h) < 3$ | | 4.0 | 4.0 | 4.0 |
| **Calculations for UK DOE:** | | | | |
| Grouted Length to Pile Diameter Ratio, $C_L$ | | 1 | 1 | 1 |
| Surface Condition Factor, $C_s$ | | 1 | 1 | 1 |
| Modular Ratio of Steel to Grout, m | | 18 | 18 | 18 |
| Stiffness Factor (dimensionless), K | | 0.04 | 0.04 | 0.04 |
| DOE Characteristic Bond Stress, $f_{buc}$ | MPa, (psi) | 22.1, (3202) | 12, (1744) | 7, (1015) |
| Factor of Safety, FS | | 4.5 | 4.5 | 4.5 |
| DOE Allowable Load Transfer Stress, $f_{ba}$ | MPa, (psi) | 4.9, (712) | 2.7, (388) | 1.6, (226) |

### 6.8.3 Code Comparisons

A comparison of the axial load transfer, for test units with two shear rings, calculated using the UK DOE equation, and the API equation with the experimental results is shown in Figure 6.28. In this figure, the axial force transfer predicted by the UK DOE equation exceeded the experimental result, and exceeded the concrete core capacity of 6.0 MN (1,360 kips) at two of the three tested shear ring spacings. At the greatest shear ring spacing of 305 mm (12.0 in.) ($h/s$ ratio of 0.021), the UK DOE equation slightly under-predicted the axial force transfer, however, the prediction held better than the API equation at this spacing. The API equation had a better prediction at the smallest shear ring spacing, of 76 mm (3.0 in.), with a corresponding $h/s$ ratio of 0.083. It should be noted that the test units with two shear rings did not fully satisfy the criteria for using the UK DOE equation, as several parameters were out of range, such as the ratio of grout length to diameter, and the ratio of shear ring width to diameter, as

shown in Table 6.9. These discrepancies could explain the over-prediction of the axial force transfer at two of the shear ring spacings.

A comparison of the axial load transfer, for test units without shear rings, calculated using the UK DOE equation, and the API equation with the experimental results is shown in Figure 6.29. In Figure 6.29, the axial load transfer is plotted versus the D/t ratio despite the fact that both the API and UK DOE equations require a D/t ratio less than 40. The data plotted for Test Units # 3 and # 11, in Figure 6.29, only needed to satisfy the criteria that the D/t ratio be within a range of 24<D/t<40 and the ratio of grouted connection length to diameter, L/D, to exceed 2. Test Unit # 11 had a D/t ratio of 40.7, which slightly exceeded the maximum, and a L/D ratio of 2.8. This test unit was judged to be within reason for comparison to the UK DOE equation. Test Unit # 3 had a D/t ratio of 46 and an L/D ratio of 1.87. Although this test unit did not satisfy either criteria, the UK DOE equation was applied to provide an additional point of comparison. The axial force transfer predicted by the UK DOE equation was a fraction of the experimental results, as shown in Figure 6.29, and was slightly less than the axial force transfer predicted by the API equation. The calculation and required checks for the UK DOE equation are shown in Table 6.10.

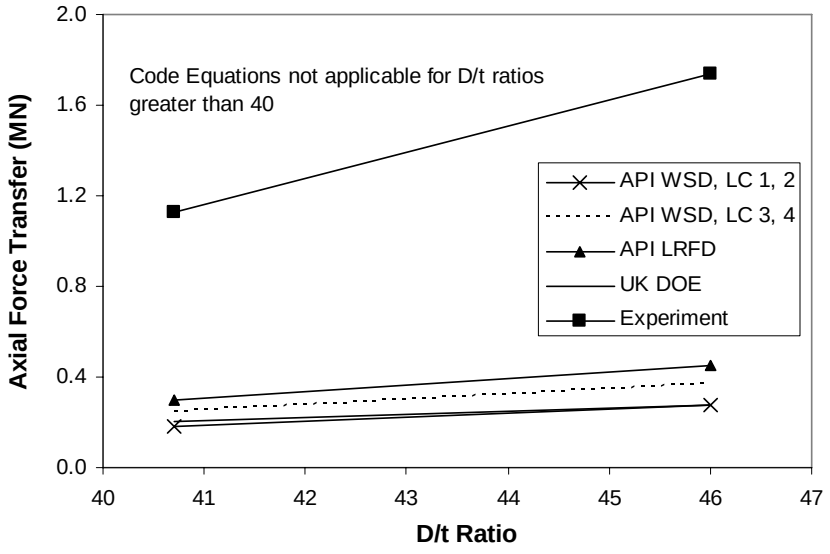


**Figure 6.29 Prediction of the Effect of D/t Ratio on the Axial Force Transfer by API and UK DOE Codes**

**Table 6.10 Calculation of UK DOE Bond Stress for No Mechanism**

| Property/Calculation | Units | Test Unit # 3 | # 11 |
|---|---|---|---|
| **Checks for UK DOE:** | | 0 | 0 |
| Sleeve: $50 < D_s/t_s < 140$ | | N/A | N/A |
| Pile: $24 < D_p/t_p < 40$ | | 46 | 40.7 |
| Grout: $10 < D_g/t_g < 45$ | | N/A | N/A |
| $L_{grout}/D_p > 2$ | | 1.9 | 2.8 |
| $0 < (h/D_p) < 0.006$ | | N/A | N/A |
| $0 < (D_p/s) < 8$ | | N/A | N/A |
| $0 < (h/s) < 0.04$ | | N/A | N/A |
| $1.5 < (w/h) < 3$ | | N/A | N/A |
| **Calculations for UK DOE:** | | | |
| Grouted Length to Pile Diameter Ratio, $C_L$ | | 1 | 1 |
| Surface Condition Factor, $C_s$ | | 0.6 | 0.6 |
| Modular Ratio of Steel to Grout, m | | 18 | 18 |
| Stiffness Factor (dimensionless), K | | 0.02 | 0.03 |
| DOE Characteristic Bond Stress, $f_{buc}$ | MPa, (psi) | 0.62, (89.6) | 0.7, (101.4) |
| Factor of Safety, FS | | 4.5 | 4.5 |
| DOE Allowable Load Transfer Stress, $f_{ba}$ | MPa, (psi) | 0.14, (19.9) | 0.16, (22.5) |
| Axial Force Transfer | MN, (kips) | 0.28, (61.9) | 0.21, (46.4) |

### 6.8.4 Code Conclusions

The API code and UK DOE code equations under-predicted the surface bond at a D/t ratio of 40.7, which slightly exceeded the code limitations of 40 for the D/t ratio. The codes predicted an increase in the axial force transfer through a shear ring as the ratio of the shear ring radial width to spacing, $h/s$, increased (or as spacing decreased for a constant shear ring width). Experimental results showed the opposite to occur. At a low h/s ratio, the UK DOE code provided a close prediction to the experimental results. At a high h/s ratio, the API code provided a close prediction to the experimental results. These aforementioned discrepancies between the codes and the experimental results are due to the differences in the test units and the limitations of the code application, which were not all satisfied for the test units of this research. The API and UK DOE codes are based on testing of a grouted connection of a steel shell to a steel sleeve. This reinforces

the need for a code design procedure based on research and testing of the bond between a steel shell and a reinforced concrete core.

## 6.9 Prediction of Surface Bond

The prediction of the axial force transfer for test units relying on only the surface bond between the steel shell and reinforced concrete core was presented in Section 3.2, using strain compatibility. Application of this method of prediction to the test units without a mechanism, Test Unit # 1, # 2, # 3, and # 11 will be presented in this section. The calculation for this prediction is shown in Table 6.11 for SI units and Table 6.12 for USCS units.

**Table 6.11 Calculation of Strain Compatibility Prediction (SI Units)**

| | | Test Unit | | | |
|---|---|---|---|---|---|
| **Parameter** | | **# 1** | **# 2** | **# 3** | **# 11** |
| f'c | MPa | 20.7 | 20.7 | 20.7 | 20.7 |
| E concrete | MPa | 21523 | 21523 | 21523 | 21523 |
| E steel | MPa | 206820 | 206820 | 206820 | 206820 |
| $\varepsilon$ compatibility | | 0.00015 | 0.00015 | 0.00015 | 0.00015 |
| Internal Diameter | mm | 609.6 | 596.9 | 584.2 | 387.4 |
| Shell Thickness | mm | 4.8 | 6.4 | 12.7 | 9.5 |
| Core Length | mm | 1092 | 1092 | 1092 | 1092 |
| Core Area | $mm^2$ | 291864 | 279829 | 268048 | 117841 |
| Shell Area | $mm^2$ | 9192 | 12034 | 23815 | 11876 |
| Strain Compatibility Force | MN | 1.23 | 1.28 | 1.60 | 0.75 |
| Friction Force | MN | 0.94 | 0.90 | 0.87 | 0.38 |
| Compatibility Displacement | mm | 0.164 | 0.164 | 0.164 | 0.164 |
| Initial Friction Displacement | mm | 0.202 | 0.212 | 0.239 | 0.244 |

**Table 6.12 Calculation of Strain Compatibility Prediction (USCS Units)**

| | | Test Unit | | | |
|---|---|---|---|---|---|
| **Parameter** | | **# 1** | **# 2** | **# 3** | **# 11** |
| f'c | psi | 3000 | 3000 | 3000 | 3000 |
| E concrete | psi | 3122019 | 3122019 | 3122019 | 3122019 |
| E steel | psi | 30000000 | 30000000 | 30000000 | 30000000 |
| $\varepsilon$ compatibility | | 0.00015 | 0.00015 | 0.00015 | 0.00015 |
| Internal Diameter | inch | 24 | 23.5 | 23 | 15.25 |
| Shell Thickness | inch | 0.1875 | 0.25 | 0.5 | 0.375 |
| Core Length | inch | 43 | 43 | 43 | 43 |
| Core Area | $inch^2$ | 452.4 | 433.7 | 415.5 | 182.7 |
| Shell Area | $inch^2$ | 14.2 | 18.7 | 36.9 | 18.4 |
| Strain Compatibility Force | lb | 275969 | 287059 | 360680 | 168372 |
| Friction Force | lb | 211855 | 203120 | 194568 | 85537 |
| Compatibility Displacement | inch | 0.0065 | 0.0065 | 0.0065 | 0.0065 |
| Initial Friction Displacement | inch | 0.0079 | 0.0083 | 0.0094 | 0.0096 |

### 6.9.1 Prediction at a D/t Ratio of 128

The strain compatibility prediction method provides a reasonably accurate estimate of the axial force-axial displacement hysteretic response for the first axial displacement level to +/- 2.54 mm (0.1 in.). A comparison between the prediction and the hysteretic response for the first displacement level of Test Unit # 1 (D/t ratio of 128) is shown in Figure 6.30. The prediction results in an initial peak in axial compression which decreases more sharply than the experimental result. In axial tension, a peak occurs in the prediction, whereas the experimental result lacks a peak. However, the overall prediction provides a reasonably accurate approximation throughout the first axial displacement level.

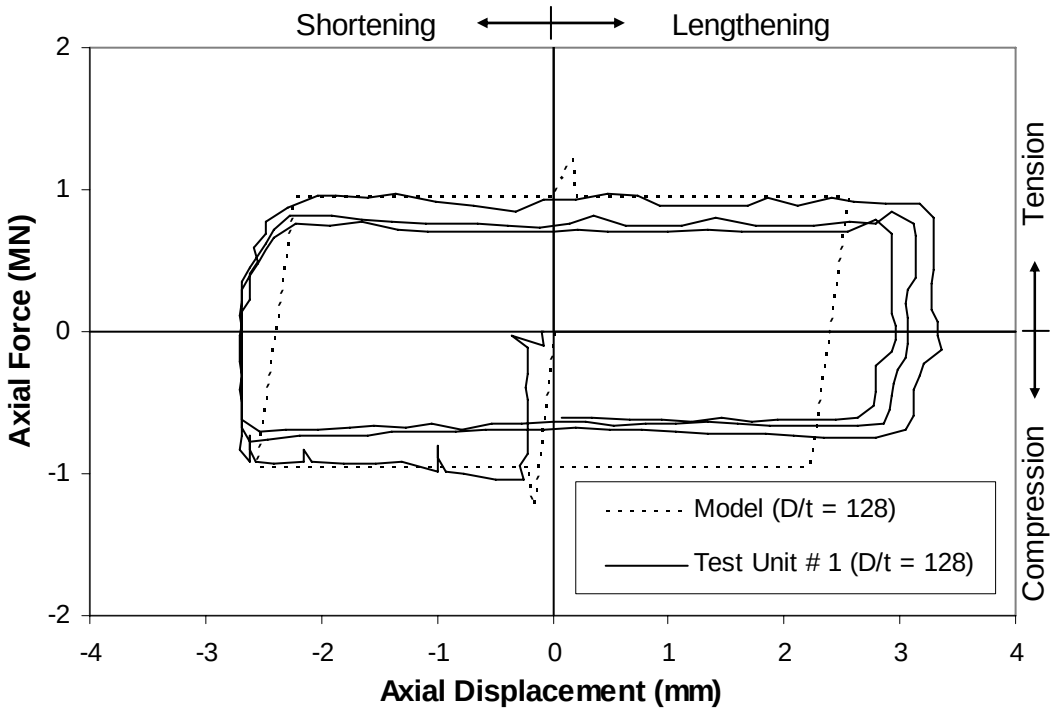


**Figure 6.30 Strain Compatibility Prediction for the First Cycle of Test Unit # 1 (D/t = 128)**

The strain compatibility method of prediction was plotted versus the overall hysteretic response as shown in Figure 6.31. The prediction provides a reasonable envelope to the hysteretic response, for axial compression loading and unloading, as shown in the two left quadrants of Figure 6.31. However, the method results in an envelope which over-predicts the axial tension loading and unloading. This method should over-predict the response at greater axial displacements, as it was derived for the state in which no slip between the entire concrete core and steel shell has occurred. The method might have provided a reasonably accurate envelope in axial compression because of the presence of a vertical seam weld in the steel shell internal surface.

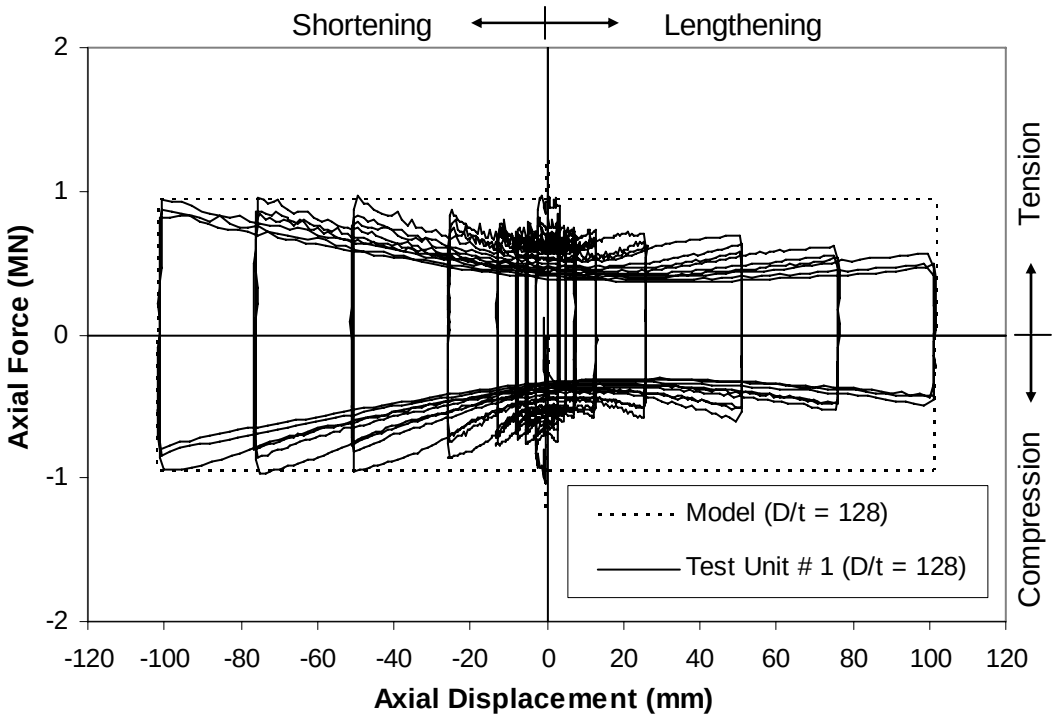


**Figure 6.31 Strain Compatibility Prediction Compared to all Cycles of Test Unit # 1 (D/t = 128)**

### 6.9.2 Prediction at a D/t Ratio of 94

The strain compatibility prediction method provides a reasonably accurate estimate of the axial force-axial displacement hysteretic response for the first axial displacement level, to +/- 2.54 mm (0.1 in.). A comparison between the prediction and the hysteretic response for the first displacement level of Test Unit # 2 (D/t ratio of 94) is shown in Figure 6.32. The prediction results in an initial peak in axial compression which decreases more sharply than the experimental result. The decrease in the axial force obtained at the initial peak to the axial force at the peak displacement is, however, approximately the same for the prediction and experiment. In axial tension, a peak occurs in the prediction, whereas the experimental result lacks a major peak. The overall prediction provides a reasonably accurate approximation throughout the first axial displacement level.

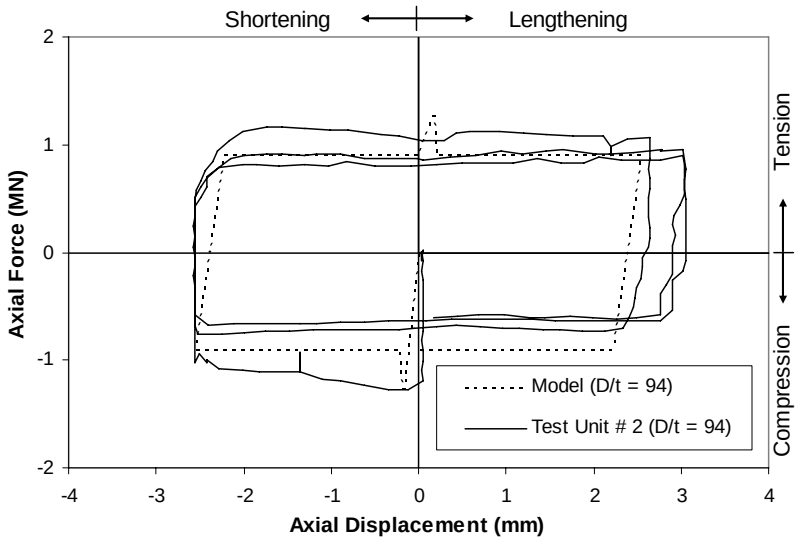


**Figure 6.32 Strain Compatibility Prediction for the First Cycle of Test Unit # 2 (D/t = 94)**

The strain compatibility method of prediction was plotted versus the overall hysteretic response as shown in Figure 6.33. This method clearly over-predicts the response, throughout the axial displacement levels beyond the initial level to +/- 2.54 mm (0.1 in.), as expected.

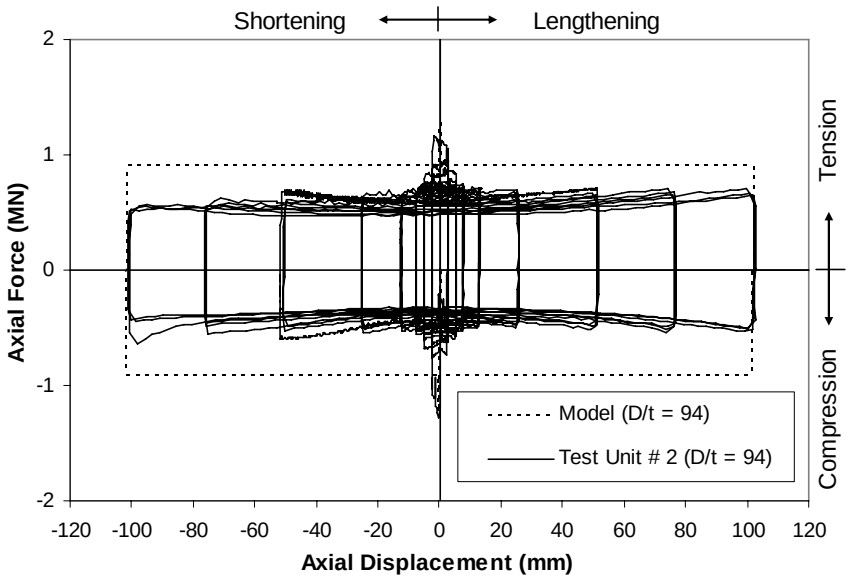


**Figure 6.33 Strain Compatibility Prediction Compared to all Cycles of Test Unit # 2 (D/t = 94)**

### 6.9.3 Prediction at a D/t Ratio of 46

The strain compatibility prediction method provides a reasonably accurate estimate of the axial force-axial displacement hysteretic response for the first axial displacement level to +/- 2.54 mm (0.1 in.). A comparison between the prediction and the hysteretic response for the first displacement level of Test Unit # 3 (D/t ratio of 46) is shown in Figure 6.34. The prediction results in an initial peak in axial compression which decreases more sharply than the experimental result. The decrease in the axial force obtained at the initial peak to the axial force at the peak displacement of the second cycle, is approximately the same for the prediction and experiment. In axial tension, a peak occurs in the prediction, whereas the experimental result lacks a major peak. The overall prediction provides a reasonably accurate approximation throughout the first axial displacement level.

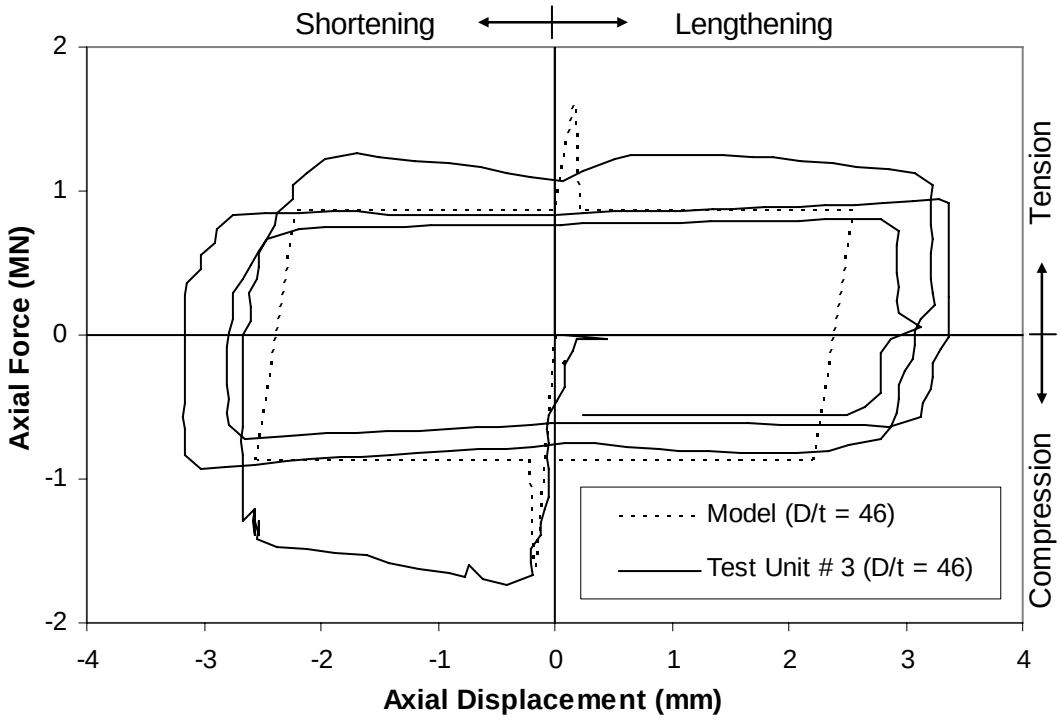


**Figure 6.34 Strain Compatibility Prediction for the First Cycle of Test Unit # 3 (D/t = 46)**

The strain compatibility method of prediction was plotted versus the overall hysteretic response as shown in Figure 6.35. This method clearly over-predicts the

response for axial tension loading and unloading beyond the initial level to +/- 2.54 mm (0.1 in.), as expected. However, the prediction results in a reasonably accurate approximation for axial compression loading and unloading, which was not expected.

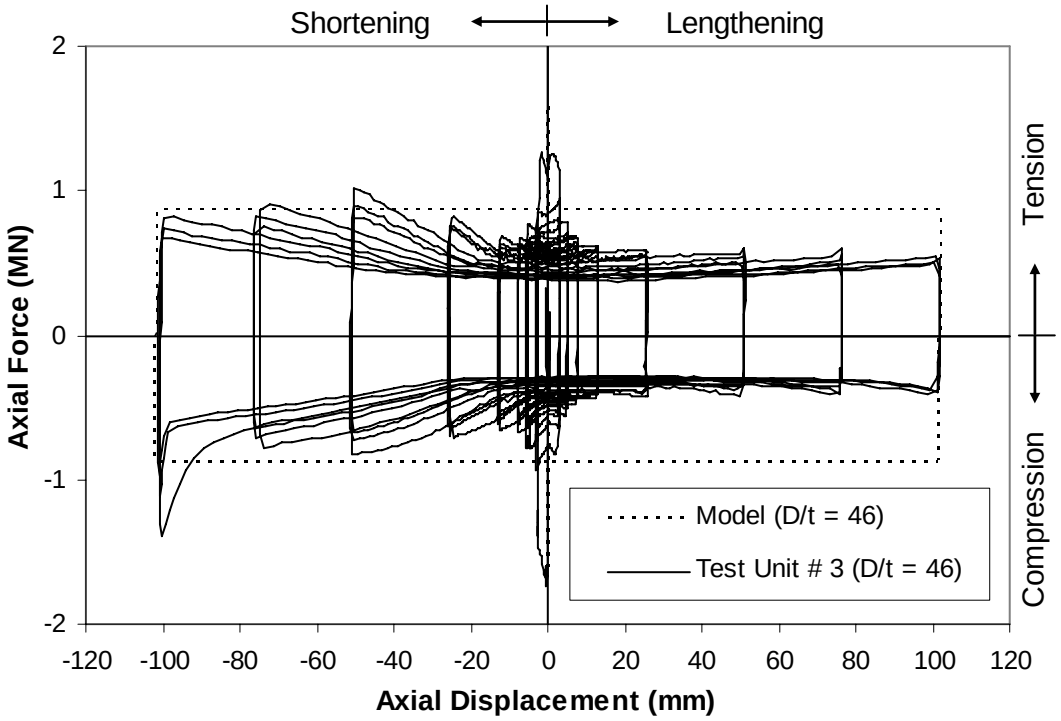


**Figure 6.35 Strain Compatibility Prediction Compared to all Cycles of Test Unit # 3 (D/t = 46)**

### 6.9.4 Prediction at a D/t Ratio of 40.7

The strain compatibility prediction method provides a reasonably accurate estimate of the axial force-axial displacement hysteretic response for the first axial displacement level to +/- 2.54 mm (0.1 in.). A comparison between the prediction and the hysteretic response for the first displacement level, of Test Unit # 11 (D/t ratio of 40.7) is shown in Figure 6.36. The first cycle of the experimental hysteretic response is under-predicted by this method; however, a reasonably accurate approximation is obtained when compared to the second and third loops of the hysteretic response.

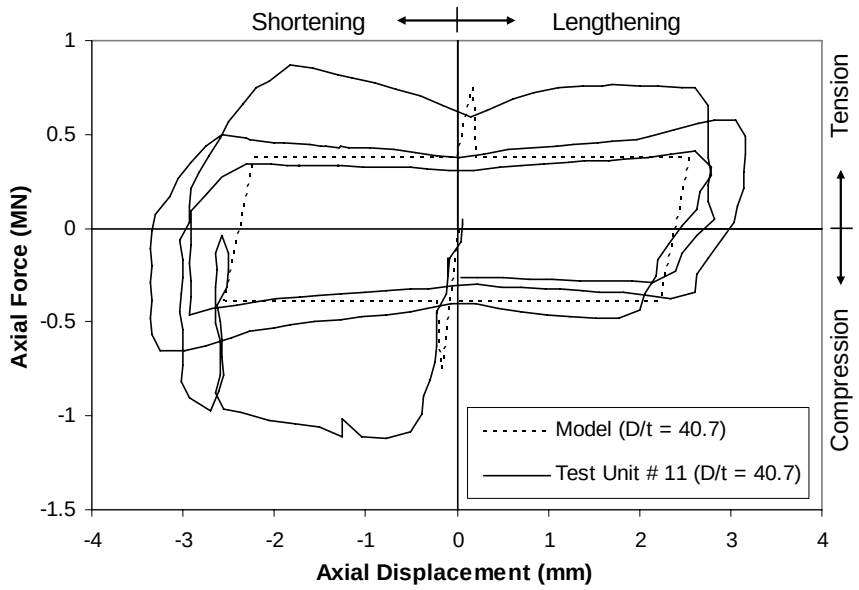


**Figure 6.36 Strain Compatibility Prediction for the First Cycle of Test Unit # 11 (D/t = 40.7)**

The strain compatibility method of prediction was plotted versus the overall hysteretic response as shown in Figure 6.37. This method clearly over-predicts the hysteretic response for all displacement levels beyond the initial level to +/- 2.54 mm (0.1 in.), as expected.

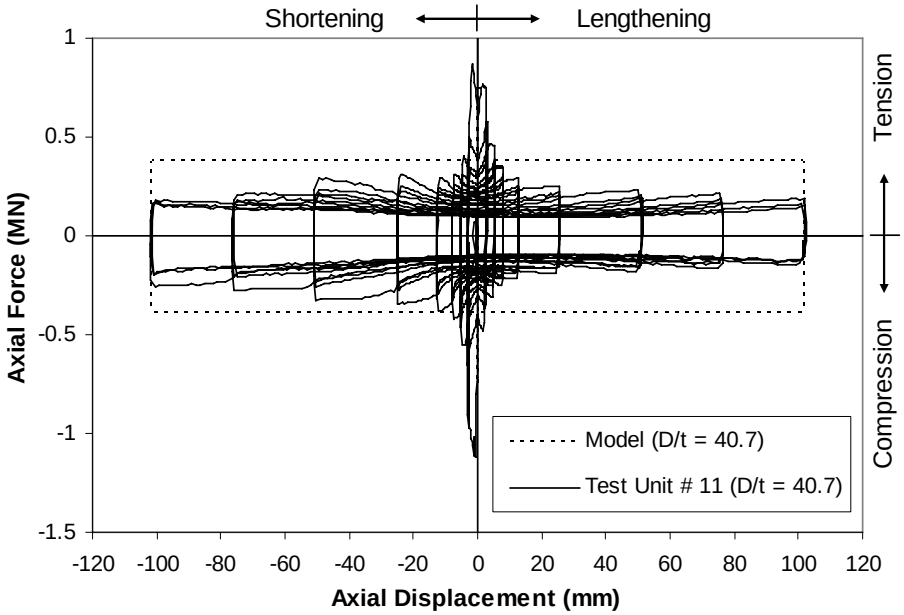


**Figure 6.37 Strain Compatibility Prediction Compared to all Cycles of Test Unit # 11 (D/t = 40.7)**

### 6.9.5 Summary of Surface Bond Prediction

A reasonably accurate prediction of the axial force transfer through the initial adhesion bond and surface bond was provided by a strain compatibility approach. This approach provided a simplified technique to estimate the envelope of an axial force-axial displacement hysteretic response. The approach provided the best match to the first hysteretic cycle of all D/t ratios tested. For cycles at greater axial displacements, the approach provided a reasonable estimate for the axial compression envelope for almost all D/t ratios, however the approach over-predicted the axial tension envelope for all D/t ratios tested.

## 6.10 Capacity Prediction for Circumferential Mechanisms

The prediction of the axial force transfer for test units with a circumferential mechanism fixed to the steel shell was presented in Chapter 3. The prediction involves either the formation of three plastic hinges in the steel shell (Equations 3.16 and 3.17), or attainment of the concrete core capacity (Equation 3.30). Experimental results are used to determine relationships for the variables in steel shell and mechanism capacity equation (Equation 3.16) as presented. Predictions of the hysteretic envelopes for test units with a single circumferential mechanism are presented.

### 6.10.1 Determination of the Steel Shell and Mechanism Capacity Equation Terms

The height of the steel shell deformation, $l_e$, and the plastic hinge length, $l_f$, were determined by measurement of steel shell sections extracted from the test units. Steel shell samples containing the out-of-plane deformation at the mechanism location were obtained for Test Units # 4, # 7, and # 16, which had a weld bead, welded bar and shear ring, respectively. The height of the steel shell deformation, $l_e$, was measured as 127 mm (5.0 in.) for Test Units # 4 and # 7. Test Unit # 16 had a steel shell deformation height, $l_e$, of 152 mm (6.0 in.). The plastic hinge length, $l_f$, was measured as 38 mm (1.5 in.) for Test Units # 4 and # 7. Test Unit # 16 had a plastic hinge length, $l_f$, of 44.5 mm (1.75 in.).

An equation for the height of the steel shell deformation, $l_e$, as a function of the D/t ratio is determined through linear regression of the measured values, as shown in Figure 6.38 (SI units) and in Figure 6.39 (USCS units). The expressions are:

$$l_e = -0.7471 \cdot \left(\frac{D}{t}\right) + 222.62 \qquad \text{(SI Units: mm)} \tag{6.5}$$

$$l_e = -0.0294 \cdot \left(\frac{D}{t}\right) + 8.7647 \qquad \text{(USCS Units: inch)} \tag{6.6}$$

The steel shell deformation height equations are valid for D/t ratios from 94 to 128 and had a correlation coefficient, $R^2$, of 1.

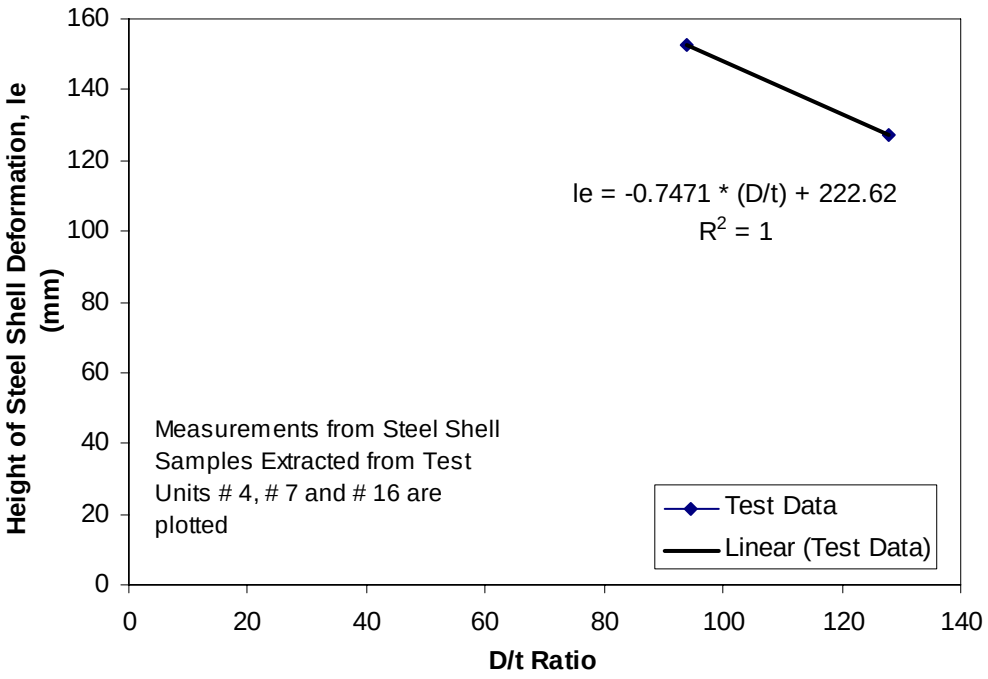


**Figure 6.38 Correlation of the Steel Shell Deformation Height to the D/t Ratio (SI Units)**

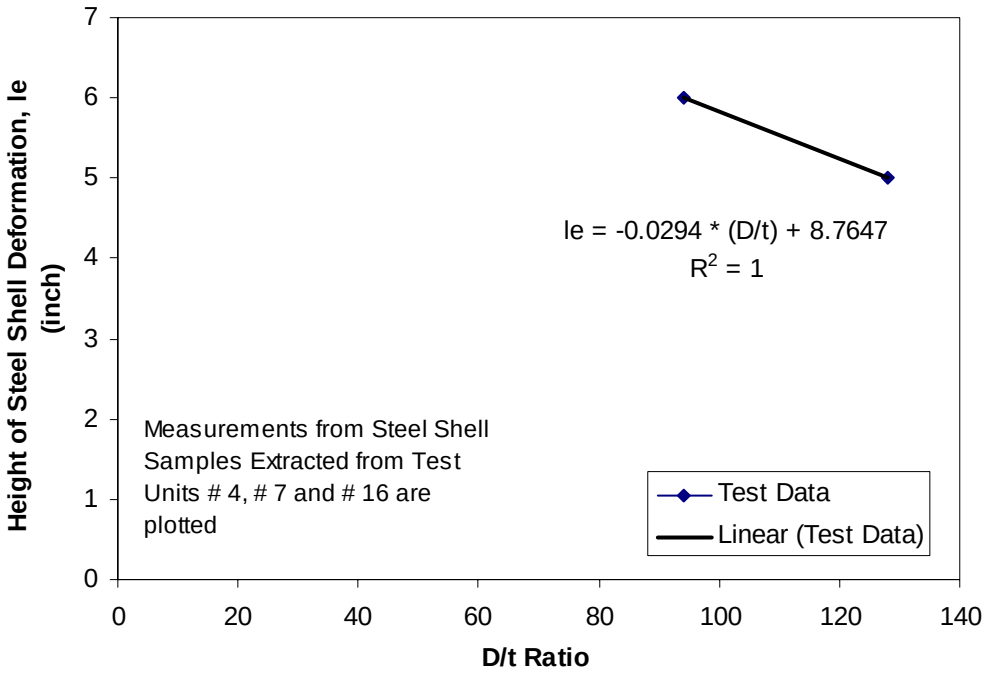


**Figure 6.39 Correlation of the Steel Shell Deformation Height to the D/t Ratio (USCS Units)**

An equation for the plastic hinge length, $l_f$, as a function of the D/t ratio is determined through linear regression of the measured values, as shown in Figure 6.40 (SI units) and in Figure 6.41 (USCS units). The expressions are:

$$l_f = -0.1868 \cdot \left(\frac{D}{t}\right) + 62.006 \quad \text{(SI Units: mm)} \tag{6.7}$$

$$l_f = -0.0074 \cdot \left(\frac{D}{t}\right) + 2.4412 \quad \text{(USCS Units: inch)} \tag{6.8}$$

The plastic hinge length equations are valid for D/t ratios from 94 to 128 and had a correlation coefficient, $R^2$, of 1.

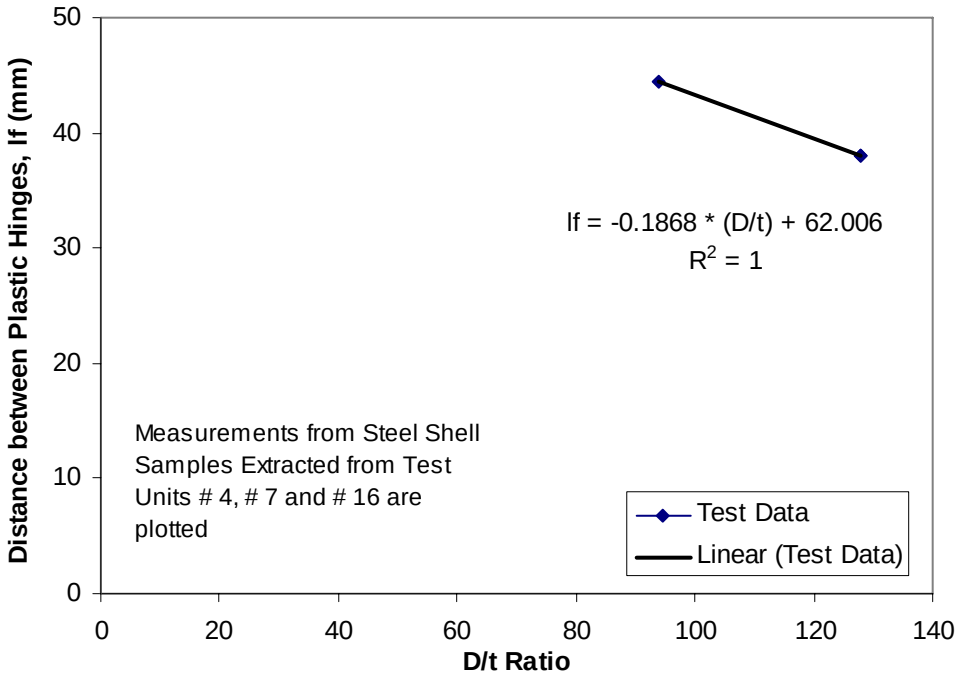


**Figure 6.40 Correlation of the Distance between Plastic Hinges to the D/t Ratio (SI Units)**

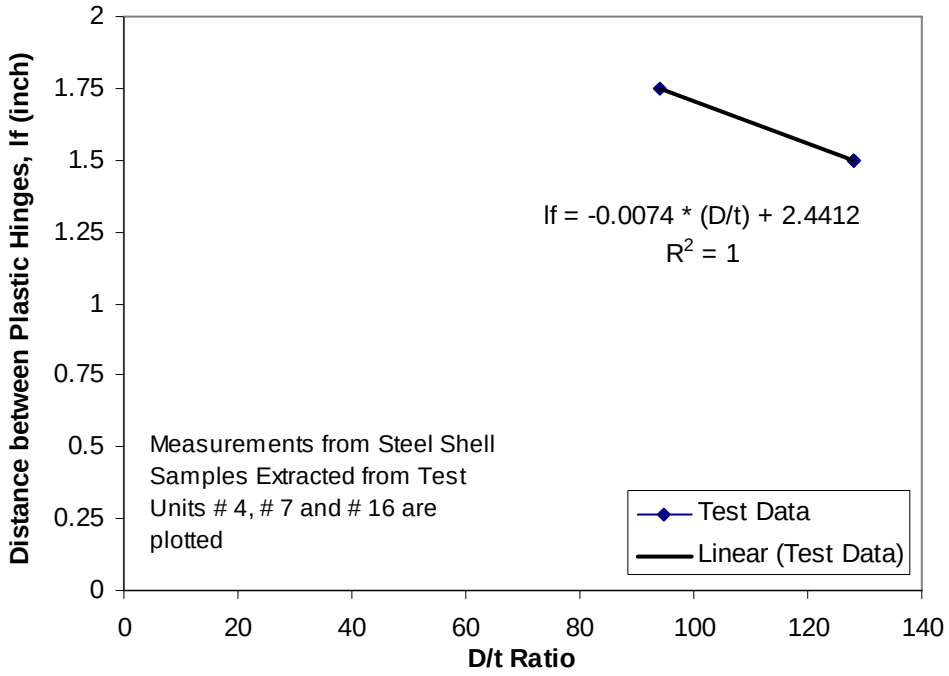


**Figure 6.41 Correlation of the Distance between Plastic Hinges to the D/t Ratio (USCS Units)**

The angle at which the resultant axial force transfer acts on the mechanism, $\alpha$, as shown in Figure 3.6 is determined using experimental results and the predicted steel shell and mechanism capacity (Equation 3.16). The peak applied axial compression force transfer, $P_{applied}$, obtained in the first cycle at -2.54 mm (-0.1 in.) is used. A friction of 0.89 MN (200 kips) is assumed and subtracted from this force. This net axial force (axial force transferred through a circumferential mechanism) is divided by the lateral force: as predicted from the steel shell and mechanism capacity, $P_{sm}$, (Equation 3.16). The inverse tangent of this ratio results in the angle, $\alpha$, as stated:

$$\alpha = TAN^{-1}\left(\frac{P_{applied} - 0.89MN}{P_{sm}}\right) \tag{6.9}$$

An relationship for the angle at which the resultant axial force transfer acts on the mechanism, $\alpha$, with known test unit geometric properties is examined with linear regression analysis. The correlation of the angle, $\alpha$, with the ratio of the mechanism radial thickness to the steel shell thickness, $t_r / t$, is shown in Figure 6.42. Data points for Test Units # 4, # 5, # 7 and # 16 are plotted which cover a $t_r / t$ range from 0.7 to 2.7. A correlation coefficient, $R^2$, of 0.593 is obtained for the $\alpha$ - $t_r / t$ expression as stated:

$$\alpha = -8.41 \cdot \left(\frac{t_r}{t}\right) + 46.91 \tag{6.10}$$

The correlation of the angle, $\alpha$, with the D/t ratio is shown in Figure 6.43. A correlation coefficient, $R^2$, of 0.7947 is obtained for the $\alpha$ - D/t expression as stated:

$$\alpha = -0.53 \cdot \left(\frac{D}{t}\right) + 96.41 \tag{6.11}$$

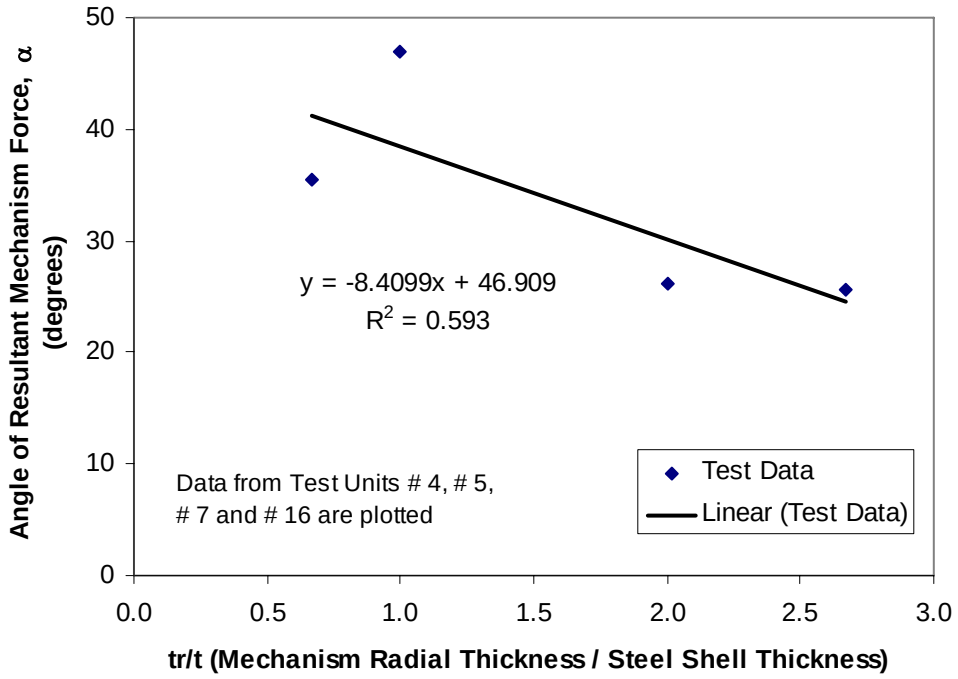


**Figure 6.42 Correlation of the Resultant Mechanism Force Angle to the Ratio of the Mechanism Thickness to the Steel Shell Thickness**

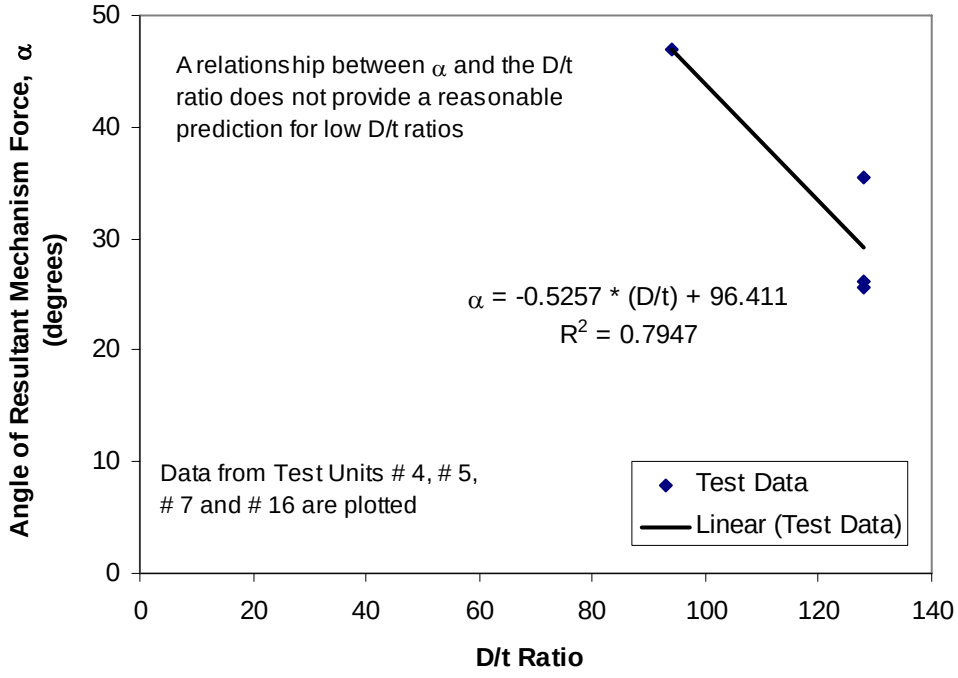


**Figure 6.43 Correlation of the Resultant Mechanism Force Angle to the D/t Ratio**

The $\alpha$ - D/t relationship is valid for D/t ratios from 94 to 128. However, this relationship cannot readily be extrapolated to lower D/t ratios, as that results in a high value for $\alpha$. The $\alpha$ - $t_r / t$ expression does not have this problem at lower $t_r / t$ ratios. Therefore a relationship between the angle at which the resultant axial force transfer acts on the mechanism, $\alpha$, and the ratio of the mechanism radial thickness to the steel shell thickness, $t_r / t$, (Equation 6.10) is recommended despite a lower correlation coefficient, $R^2$.

The measured values obtained for the height of the steel shell deformation, $l_e$, and the plastic hinge length, $l_f$, is presented in Table 6.13 for Test Units # 4, # 5, # 7, # 16 and # 17. The prediction or measurement of the angle at which the resultant axial force transfer acts on the mechanism, $\alpha$, is presented in Table 6.14. Equation 6.9 is used to determine the measured angle, $\alpha$, despite the use of the predicted lateral force in the equation. Equation 6.10 is used to determine the predicted angle, $\alpha$.

**Table 6.13 Steel Shell Deformation Height and Distance between Plastic Hinges**

| Test Unit # | Mechanism | Measured $l_e$ mm (inch) | $l_f$ mm (inch) |
|---|---|---|---|
| 4 | Weld Bead | 127 (5.0) | 38 (1.5) |
| 7 | Welded Bar | 127 (5.0) | 38 (1.5) |
| 16 | Shear Ring | 152 (6.0) | 44.5 (1.75) |

**Table 6.14 Angle of the Resultant Axial Force Transfer on a Circumferential Mechanism**

| Test Unit # | Mechanism | Measured | | Predicted | |
|---|---|---|---|---|---|
| | | $\alpha$ (rad) | $\alpha$ (deg) | $\alpha$ (rad) | $\alpha$ (deg) |
| 4 | Weld Bead | 0.7 | 41.3 | 0.62 | 35.5 |
| 7 | Welded Bar | 0.5 | 30.1 | 0.46 | 26.1 |
| 5 | Shear Ring | 0.4 | 24.5 | 0.45 | 25.7 |
| 16 | Shear Ring | 0.7 | 38.5 | 0.82 | 47 |
| 17 | Shear Ring | 0.8 | 44.8 | 0.79 | 45 |

The prediction of the steel shell and mechanism capacity, $P_{sm-axial}$, using Equations 3.16 and 3.17 is shown in Table 6.15. Yield stresses obtained from tensile tests of coupons, as presented in Section 5.8, are used in the prediction of the lateral force, $P_{sm}$. This lateral force is then divided by the tangent of the measured angle, $\alpha$, (determined from Equation 6.9) to obtain the predicted axial force transfer, $P_{sm-axial}$, through the circumferential mechanism. The spacing between plastic hinge zones, $l_f$, and the center to center mechanism spacing, $s$, is shown in Table 6.16. These spacings are predicted for test units with a single circumferential mechanism to determine the ideal spacing for multiple mechanisms. Test units with a circumferential mechanism at a D/t ratio of 128 had a spacing that was on average 72% of the steel shell diameter, $D$. Test Unit # 17 had a spacing that was 131% of the steel shell diameter, $D$. However, attainment of the steel shell and mechanism capacity for Test Unit # 17 (or the test units with multiple shear rings) was not obtained in the experiment due to test setup load restrictions and potentially could not be obtained as the concrete core governed the response.

**Table 6.15 Predicted Axial Force Transfer through a Circumferential Mechanism**

| Test Unit # | Mechanism | $P_{sm-axial}$ MN (kips) | $P_{sm-axial}/\tan(\alpha)$ MN (kips) |
|---|---|---|---|
| 4 | Weld Bead | 0.753 (169.3) | 0.857 (192.7) |
| 7 | Welded Bar | 0.820 (184.3) | 1.415 (318.1) |
| 5 | Shear Ring | 0.879 (197.5) | 1.929 (433.6) |
| 16 | Shear Ring | 1.173 (263.8) | 1.475 (331.6) |
| 17 | Shear Ring | 7.580 (1704) | 7.631 (1715) |

**Table 6.16 Spacing for Circumferential Mechanisms**

| Test Unit # | Mechanism | $l_r$ mm (inch) | s mm (inch) | s/D |
|---|---|---|---|---|
| 4 | Weld Bead | 334 (13.1) | 410 (16.1) | 0.67 |
| 7 | Welded Bar | 363 (14.3) | 440 (17.3) | 0.72 |
| 5 | Shear Ring | 389 (15.3) | 466 (18.3) | 0.76 |
| 16 | Shear Ring | 414 (16.3) | 503 (20.0) | 0.85 |
| 17 | Shear Ring | 685 (27.0) | 800 (31.5) | 1.31 |

### 6.10.2 Hysteretic Envelope Prediction

Hysteretic envelopes are predicted by combining the predicted axial force transfer through the circumferential mechanism and the predicted axial force transfer through friction bond. The strain compatibility force and friction force are calculated to account for the axial force transfer through the surface bond, although only the friction force was added to the predicted mechanism axial force transfer to obtain the predicted axial force transfer. The predicted axial force was assumed to occur at the strain compatibility displacement, as shown in the figures comparing the prediction and hysteretic response. In the predictions of Figures 6.44 through 6.53, unloading was assumed to occur with a stiffness equal to the initial loading stiffness.

A procedure to estimate the concrete capacity at a circumferential mechanism was presented in Section 3.3.4. The concrete capacity at the mechanism is estimated with Equation 3.30, in which the axial force transfer is the product of the mechanism area, perpendicular to the core, and the stress obtained by the concrete. The stress obtained by the concrete is the summation of the concrete compressive strength, $f_c^{'}$, and the confinement pressure provided by the steel shell. The contribution of the confinement pressure was multiplied by a factor, $k$, which for this prediction was assumed to have a value of 4 as presented in Section 3.3.4.

### 6.10.3 Capacity Prediction for the Shear Ring at a D/t Ratio of 128

The concrete capacity prediction under-predicted the response, as shown in Figures 6.44 and 6.45, for Test Unit # 5 at a D/t ratio of 128. After the concrete at the mechanism location reached the yield point, the axial force transfer was able to increase due to the confinement provided by the steel shell and the mechanism. This allowed the response to exceed the concrete capacity prediction, and to obtain the plastic hinge prediction. The radial thickness of the shear ring, at 12.7 mm (0.5 in.), allowed for the mechanism to remain in contact with the concrete core as the steel shell and mechanism deformed out of plane.

A comparison between the capacity predictions and the hysteretic response is shown in Figure 6.44 for the first axial displacement level of +/- 2.54 mm (0.1 in.). The plastic hinge method initially over-predicts the axial tension stiffness; however, the capacity is close to the actual maximum axial tension force transferred. A comparison between the capacity predictions and the overall hysteretic response is shown in Figure 6.45. With the exception of two cycles in axial tension, the method provides a reasonably accurate estimate. It should be noted that the last axial compression cycles increased in stiffness due to contact within the base void, as presented in Section 5.5.2.

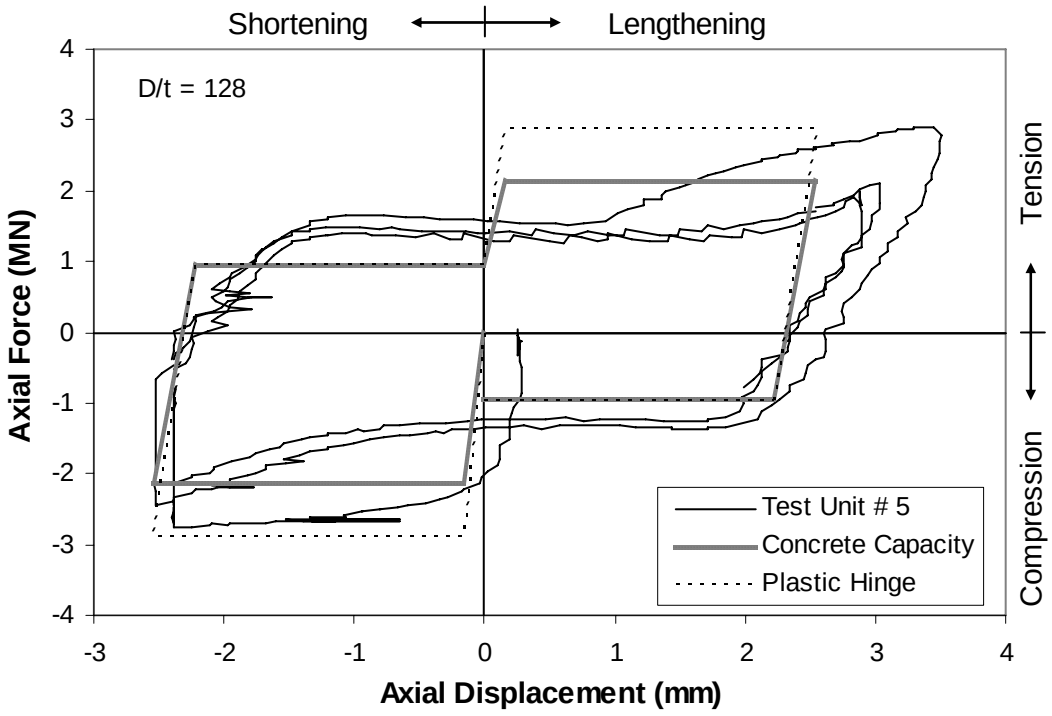


**Figure 6.44 Prediction for the First Cycle of Test Unit # 5 (D/t = 128) with a Shear Ring**

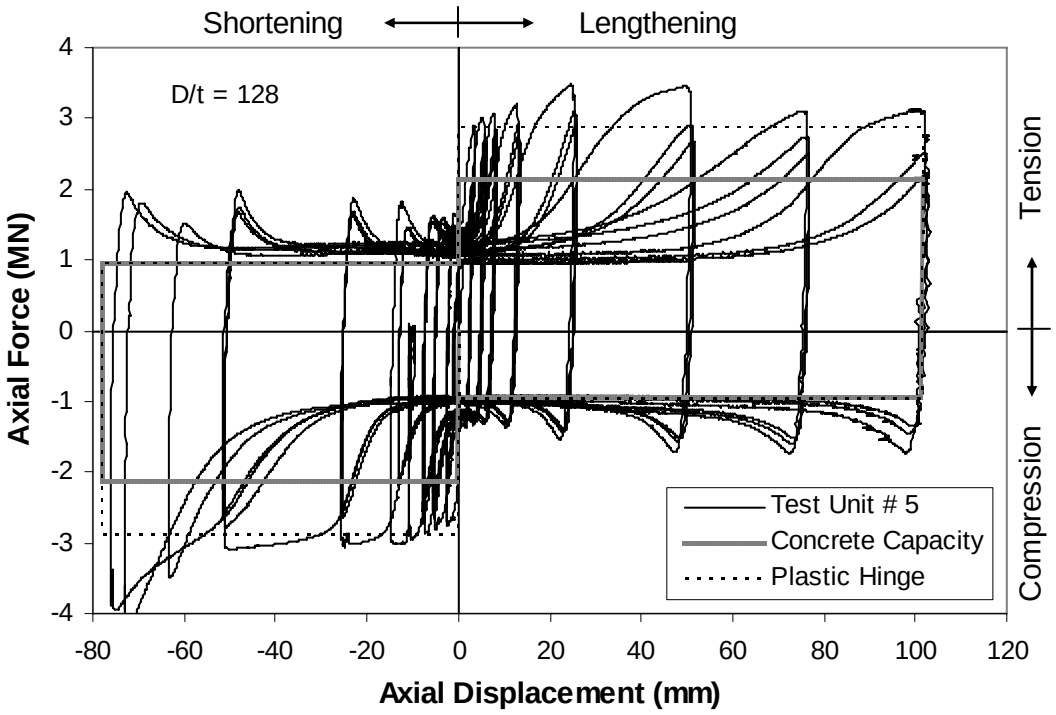


**Figure 6.45 Prediction for Test Unit # 5 (D/t = 128) with a Shear Ring**

### 6.10.4 Capacity Prediction for the Welded Bar at a D/t Ratio of 128

The concrete capacity prediction under-predicted the response, as shown in Figures 6.46 and 6.47, for Test Unit # 7 at a D/t ratio of 128. After the concrete at the mechanism location reached the yield point, the axial force transfer was able to increase due to the confinement provided by the steel shell and the sufficient radial thickness of the mechanism. This allowed the response to exceed the concrete capacity prediction, and to obtain the plastic hinge prediction. The radial thickness of the welded bar, at 9.5 mm (0.375 in.), allowed for the mechanism to remain in contact with the concrete core as the steel shell and mechanism deformed out of plane.

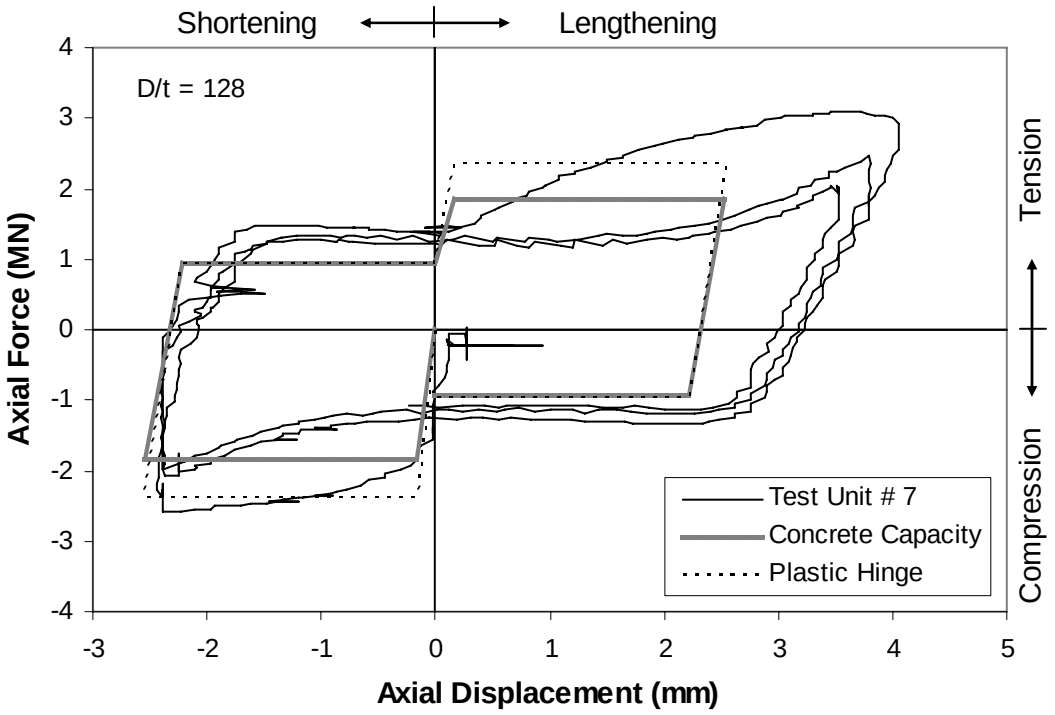


**Figure 6.46 Prediction for the First Cycle of Test Unit # 7 (D/t = 128) with a Welded Bar**

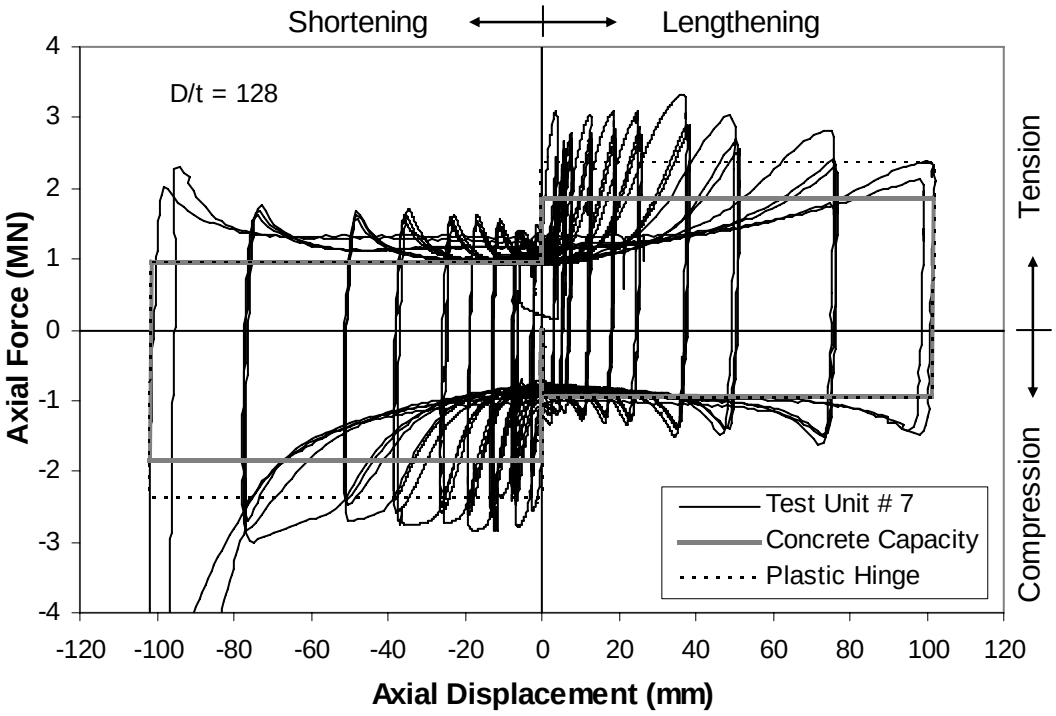


**Figure 6.47 Prediction for Test Unit # 7 (D/t = 128) with a Welded Bar**

A comparison between the capacity predictions and the hysteretic response is shown in Figure 6.47 for the first axial displacement level of +/- 2.54 mm (0.1 in.). The plastic hinge method initially over-predicts the axial tension stiffness; however, the capacity is close to the actual maximum axial tension force transferred. A comparison between the capacity predictions and the overall hysteretic response is shown in Figure 6.47. With the exception of two cycles in axial tension, the method provides a reasonably accurate estimation. It should be noted that the last axial compression cycles increased in stiffness due to contact within the base void, as presented in Section 5.5.4.

### 6.10.5 Capacity Prediction for the Weld Bead at a D/t Ratio of 128

The concrete capacity prediction under-predicted the response, as shown in Figures 6.48 and 6.49 for Test Unit # 4 with a weld bead at a D/t ratio of 128. After the concrete at the mechanism location reached the yield point, the axial force transfer was able to increase due to the confinement provided by the steel shell, such that the response exceeded the concrete capacity prediction, yet did not obtain the plastic hinge prediction. The plastic hinge prediction was not obtained due to radial deformation of the steel shell and the mechanism, such that the contact area between the weld bead and the concrete core diminished. The weld bead had a radial thickness of 3.175 mm (0.125 in.) which was one-quarter of the radial thickness of the shear ring used in Test Unit # 5. As a result, this mechanism lost a substantial contact area with the concrete core as the steel shell deformed out-of-plane, thus the plastic hinge capacity was not obtained due to an insufficient mechanism radial thickness.

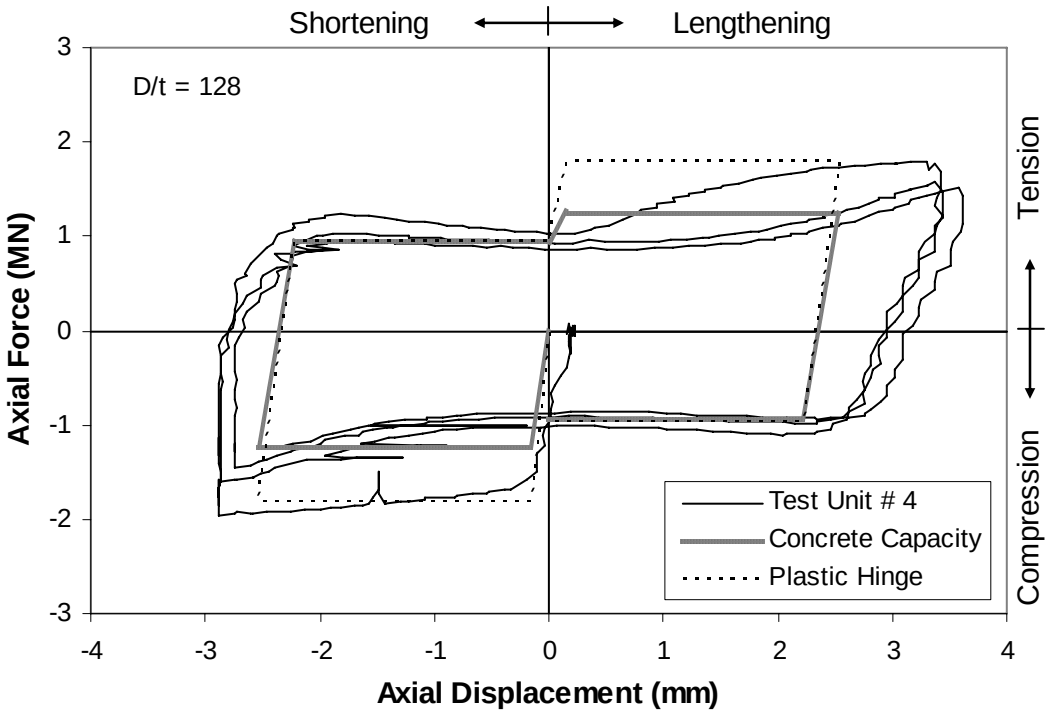


**Figure 6.48 Prediction for the First Cycle of Test Unit # 4 (D/t = 128) with a Weld Bead**

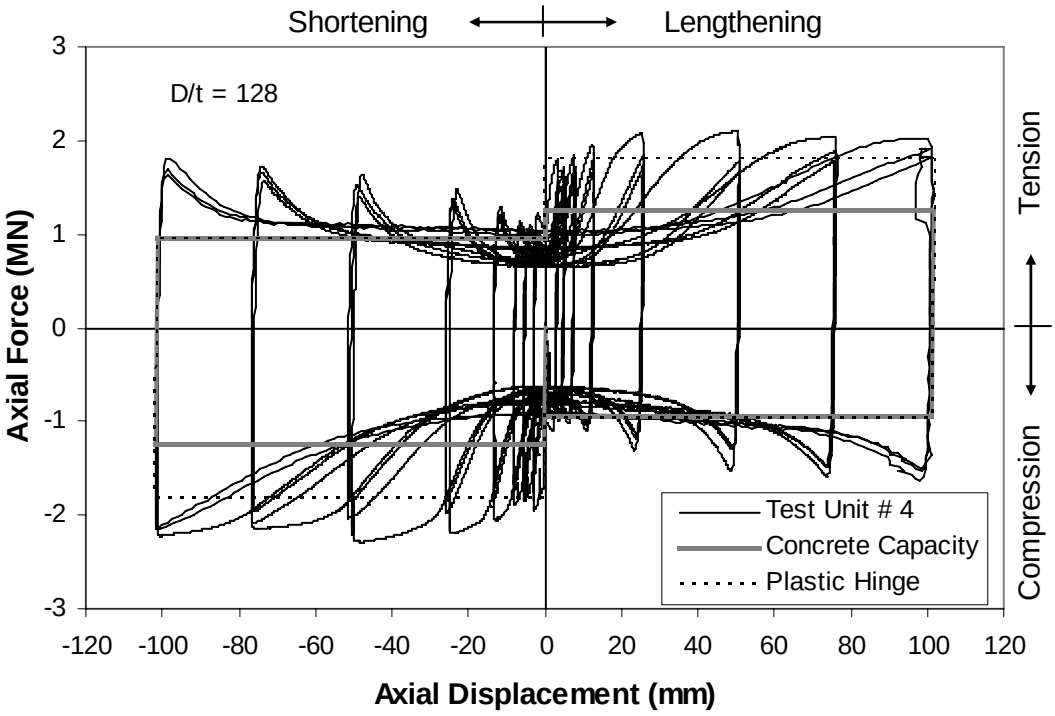


**Figure 6.49 Prediction for Test Unit # 4 (D/t = 128) with a Weld Bead**

### 6.10.6 Capacity Prediction for the Shear Ring at a D/t Ratio of 94

The concrete capacity prediction under-predicted the response, as shown in Figures 6.50 and 6.51. After the concrete at the mechanism location reached the yield point, the axial force transfer was able to increase due to the confinement provided by the steel shell, such that the response exceeded the concrete capacity prediction, yet did not obtain the plastic hinge prediction. The plastic hinge prediction was not obtained due to radial deformation of the steel shell and the mechanism, such that the contact area between the shear ring and the concrete core diminished. The shear ring had a radial thickness of 6.4 mm (0.25 in.) which was one-half of the radial thickness of the shear ring used in Test Unit # 5. As a result, this mechanism lost contact area with the concrete core as the steel shell deformed out-of-plane, thus the plastic hinge capacity was not obtained due to an insufficient mechanism radial thickness.

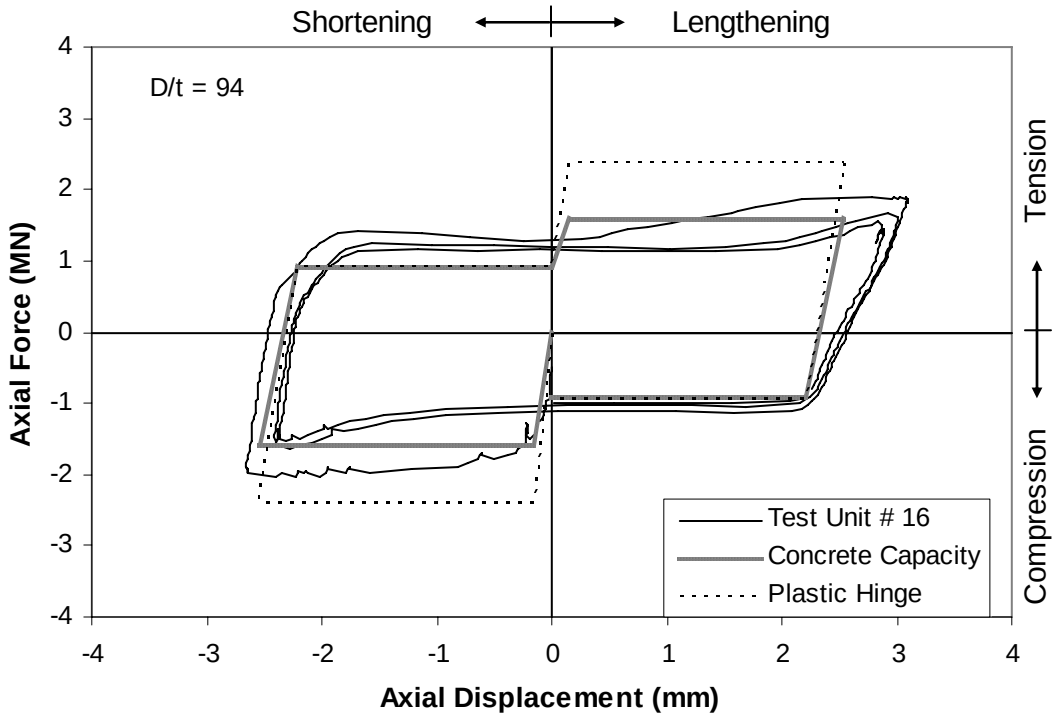


**Figure 6.50 Prediction for the First Cycle of Test Unit # 16 (D/t = 94) with a Shear Ring**

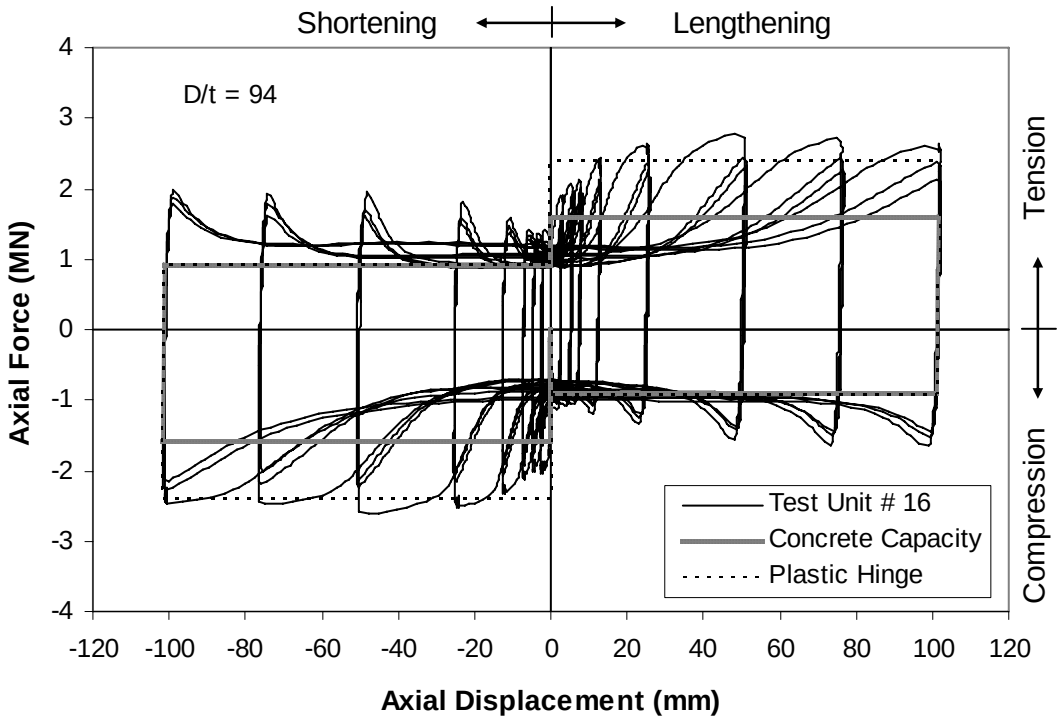


**Figure 6.51 Prediction for Test Unit # 16 (D/t = 94) with a Shear Ring**

### 6.10.7 Capacity Prediction for the Shear Ring at a D/t Ratio of 24

The concrete capacity prediction for Test Unit # 17, with a shear ring at a D/t ratio of 24, provided a reasonably accurate estimation of the axial force transfer. This is shown in a comparison between the concrete capacity prediction and the hysteretic response, in Figure 6.52, for the first axial displacement level of +/- 2.54 mm (0.1 in.). As the axial displacement increased, the prediction did not hold up as well as the initial response, as shown in Figure 6.53. The plastic hinge prediction is not shown in Figures 6.52 and 6.53 because the steel shell capacity exceeds the reinforced concrete core capacity. As a result the steel shell would be expected to remain within the elastic range with the concrete core capacity governing. This expectation was found in the experiment.

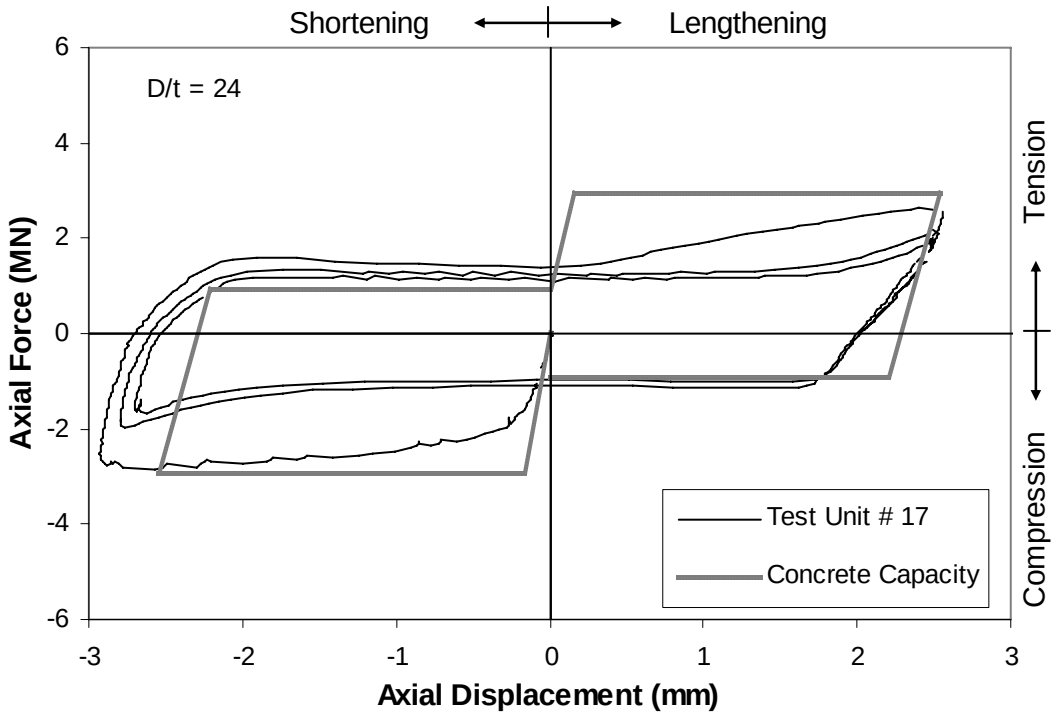


**Figure 6.52 Prediction for the First Cycle of Test Unit # 17 (D/t = 24) with a Shear Ring**

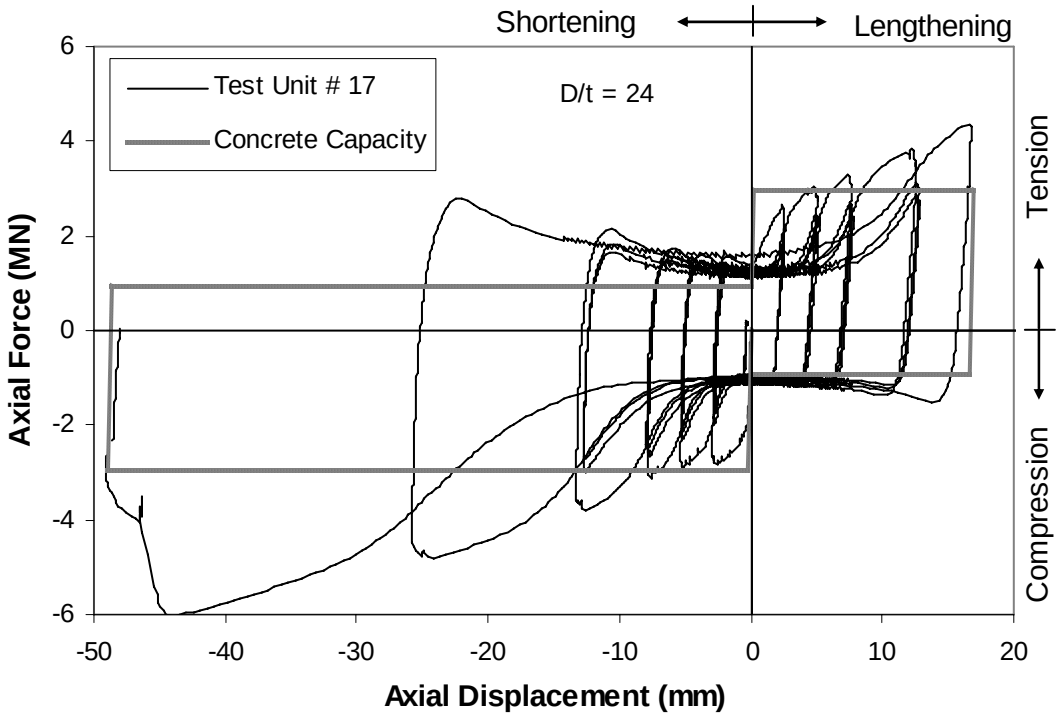


**Figure 6.53 Prediction for Test Unit # 17 (D/t = 24) with a Shear Ring**

### 6.10.8 Capacity Prediction for the Shear Ring at a D/t Ratio of 24 and a Debonded Interface

In the concrete capacity prediction for Test Unit # 18, with a D/t ratio of 24 and a disbond between the concrete core and the steel shell, friction was neglected in the calculation. A relatively low level of friction was present in the test unit, as shown in the hysteretic response; however, this term was neglected in the calculation of the concrete capacity. The prediction provided a reasonably accurate estimation of the axial force transfer as shown in Figure 6.54, for the first axial displacement level of +/- 2.54 mm (0.1 in.). The prediction held up well in axial compression, however, a slight over-prediction resulted in axial tension. As the axial displacement increased, the prediction did not hold up as well, as shown in Figure 6.55. This is partly due to the neglected friction. The plastic hinge prediction is not shown for the same reason as presented in the previous section.

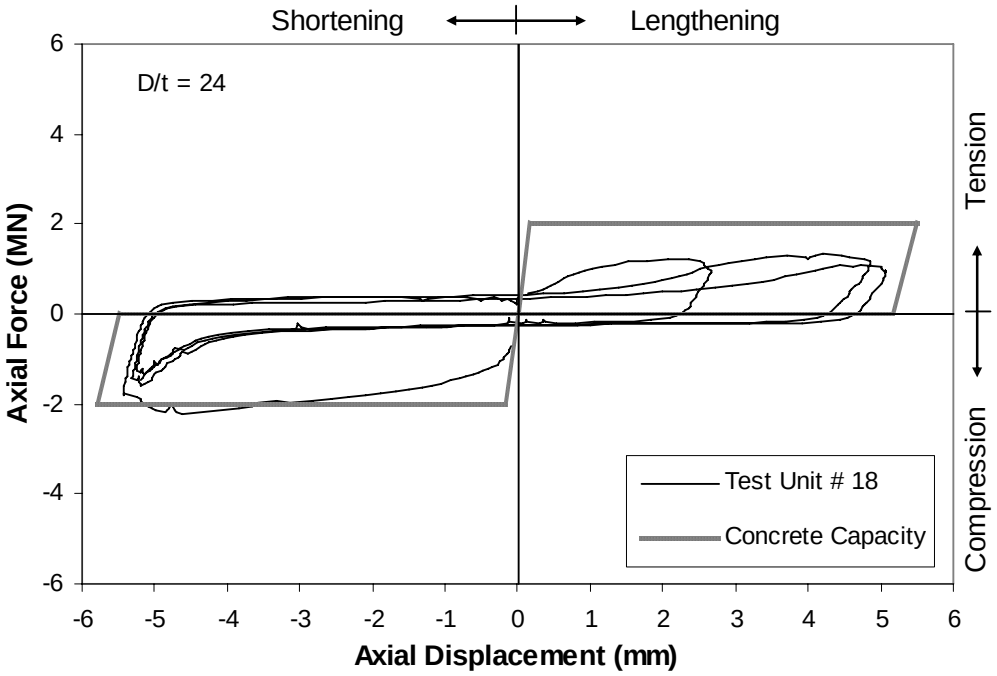


**Figure 6.54 Prediction for the First Cycle of Test Unit # 18 (D/t = 24) with a Shear Ring and a Debonded Interface**

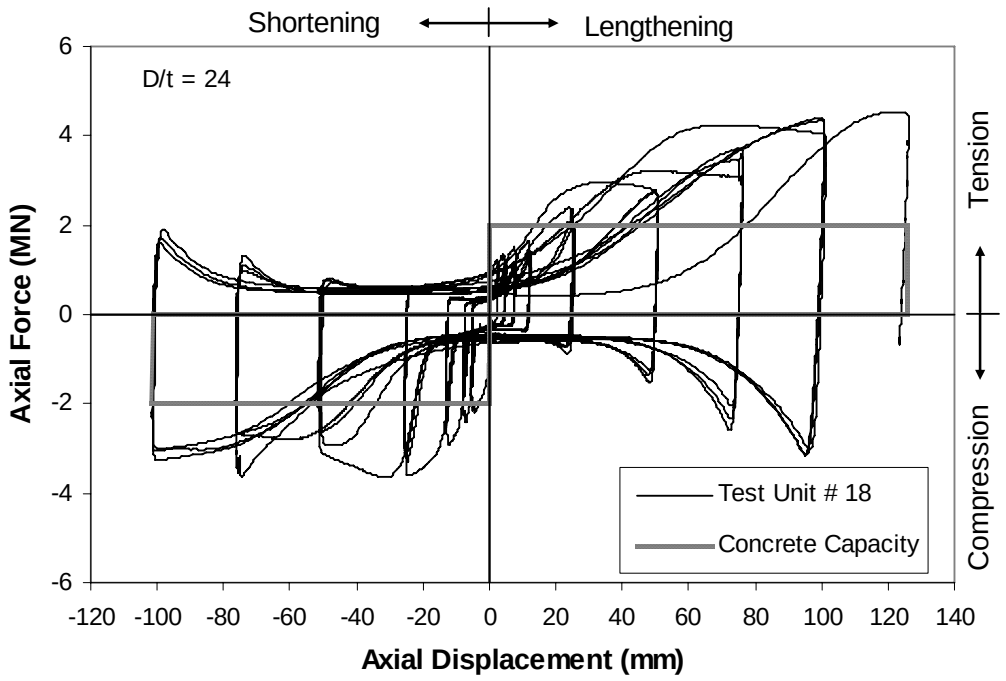


**Figure 6.55 Prediction for Test Unit # 18 (D/t = 24) with a Shear Ring and a Debonded Interface**

### 6.10.9 Summary of Capacity Prediction for Circumferential Mechanisms

The prediction of the axial force transfer through a circumferential mechanism involves the calculation of the steel shell and mechanism capacity through an assumed plastic hinge formation and the concrete capacity at the mechanism. This prediction provides a reasonably accurate estimation of the axial force-axial displacement hysteretic response. Mechanisms with an adequate radial thickness and a high D/t ratio were able to obtain the axial force predicted by the steel shell and mechanism capacity (Equation 3.16). However, mechanisms without an adequate radial thickness, and/or a high D/t ratio, did not able to obtain the axial force predicted by the steel shell and mechanism capacity. Instead, the response was bounded by the steel shell and mechanism capacity, and by the concrete capacity prediction. Mechanisms with a steel shell of a low D/t ratio, had a steel shell which remained elastic, therefore the axial force predicted by the steel shell and mechanism capacity equation could not be obtained as the concrete capacity at the mechanism controlled.

## 6.11 Capacity Prediction for Multiple Shear Rings at a D/t Ratio of 24

The three test units with two shear rings each had a steel shell with a capacity greater than the reinforced concrete capacity. In this case, the failure mode consisted of internal crushing of the concrete at the shear rings. The steel shell remained elastic therefore the steel shell and mechanism capacity (Equation 3.16) is not shown in Figures 6.56-6.61 as it would be great enough that it would be off of the scale. The concrete capacity at the mechanisms is predicted by applying Equation 3.30 to the uppermost shear ring and by applying Equation 3.32 to the lower shear ring at a spacing, $s$. Both equations make use of a factor, $k$, which increases the contribution of the steel shell. In this prediction, $k$, was assumed a have a value of 4. The capacity is assumed to occur at the strain compatibility displacement, as shown in the figures comparing the prediction and the hysteretic response. Unloading is assumed to occur with a stiffness equal to the initial loading stiffness.

### 6.11.1 Capacity Prediction for Test Unit # 19 with Two Shear Rings at 76 mm

The concrete capacity prediction for Test Unit # 19 with two shear rings at a spacing of 76 mm (3.0 in.) has a reasonable match to the hysteretic response. The initial axial compression stiffness and force transfer matched well to the hysteretic response. The prediction is shown to have a reasonable match to the hysteretic response at all axial displacements in Figure 6.56. The axial force transfer for the first cycle at greater displacements exceeds the prediction. However, the second and third cycles usually obtained an axial force transfer that was equal to or less than the predicted value, as shown in Figure 6.57.

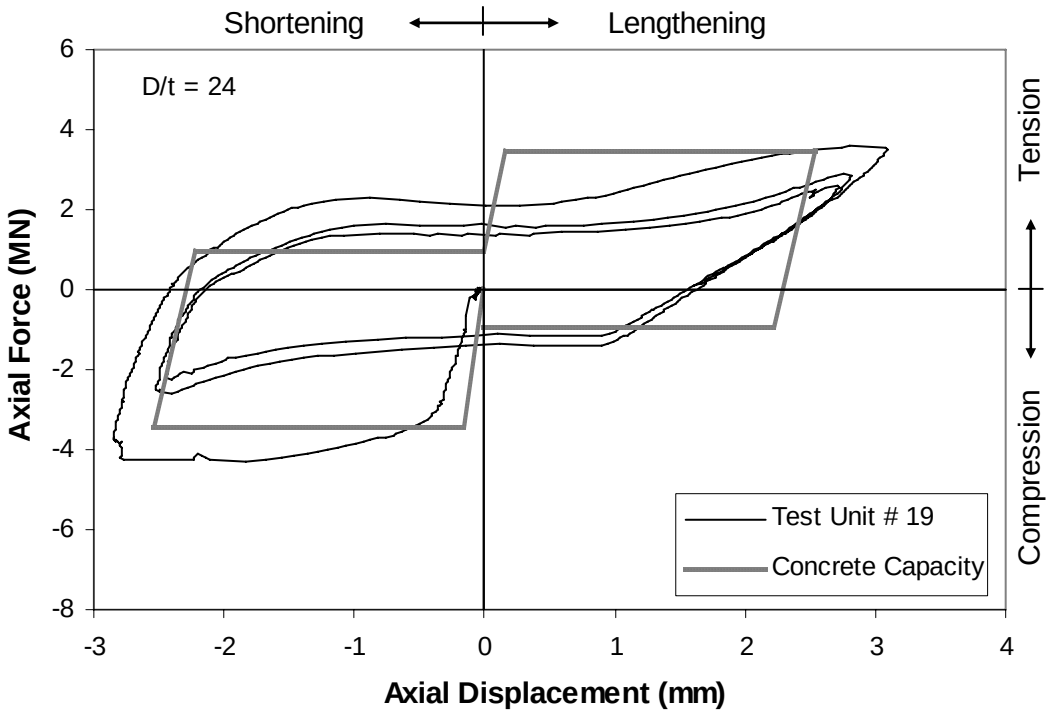


**Figure 6.56 Prediction for the First Cycle of Test Unit # 19 (D/t = 24) with Two Shear Rings at 76 mm (3.0 in.)**

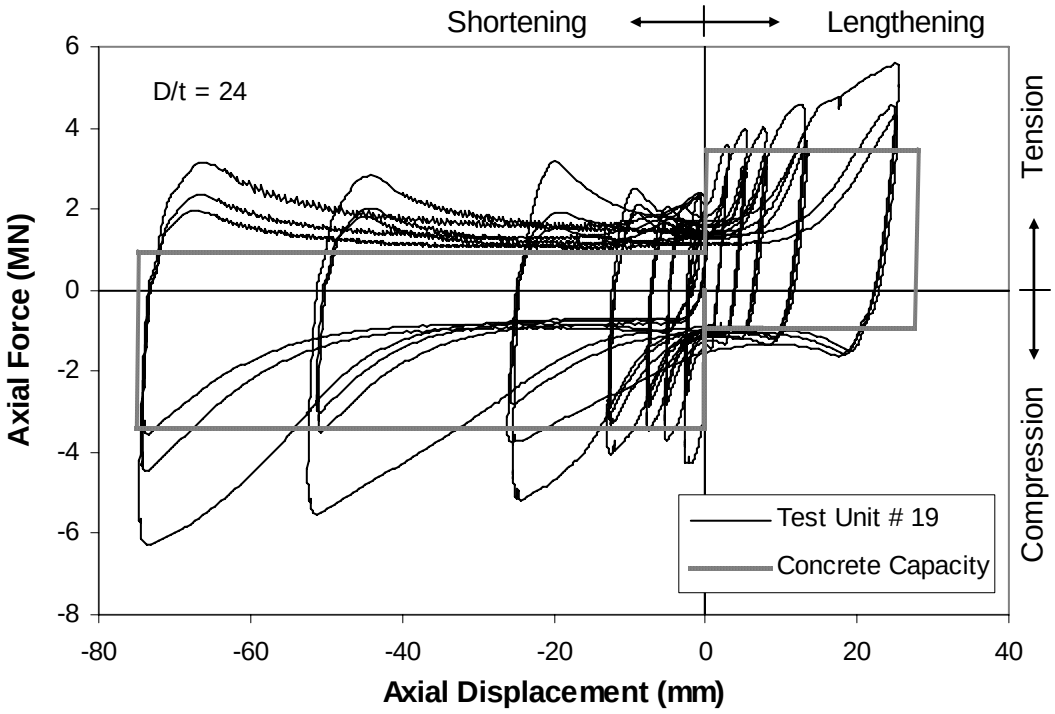


**Figure 6.57 Prediction for Test Unit # 19 (D/t = 24) with Two Shear Rings at 76 mm (3.0 in.)**

### 6.11.2 Capacity Prediction for Test Unit # 20 with Two Shear Rings at 152 mm

The concrete capacity prediction for Test Unit # 20 with two shear rings at a spacing of 152 mm (6.0 in.) has a reasonable match to the hysteretic response. The initial axial compression stiffness and axial compression force transfer matched well to the hysteretic response. However, the axial tension prediction did not hold up as well during the initial prediction, as shown in Figure 6.58. The prediction is shown to have a reasonable match to the hysteretic response at all axial displacements, in Figure 6.59. The axial force transfer, for the first cycle at greater displacements, exceeds the prediction. However, the second and third cycles usually obtained an axial force transfer that was equal to or less than the predicted value, as shown in Figure 6.59.

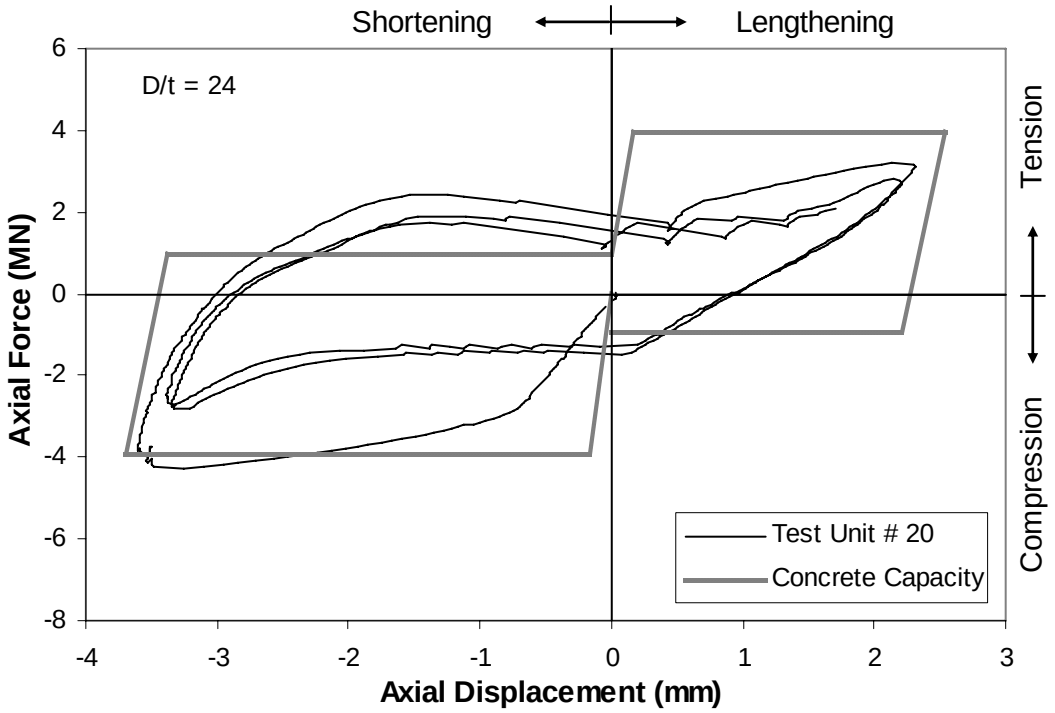


**Figure 6.58 Prediction for the First Cycle of Test Unit # 20 (D/t = 24) with Two Shear Rings at 152 mm (6.0 in.)**

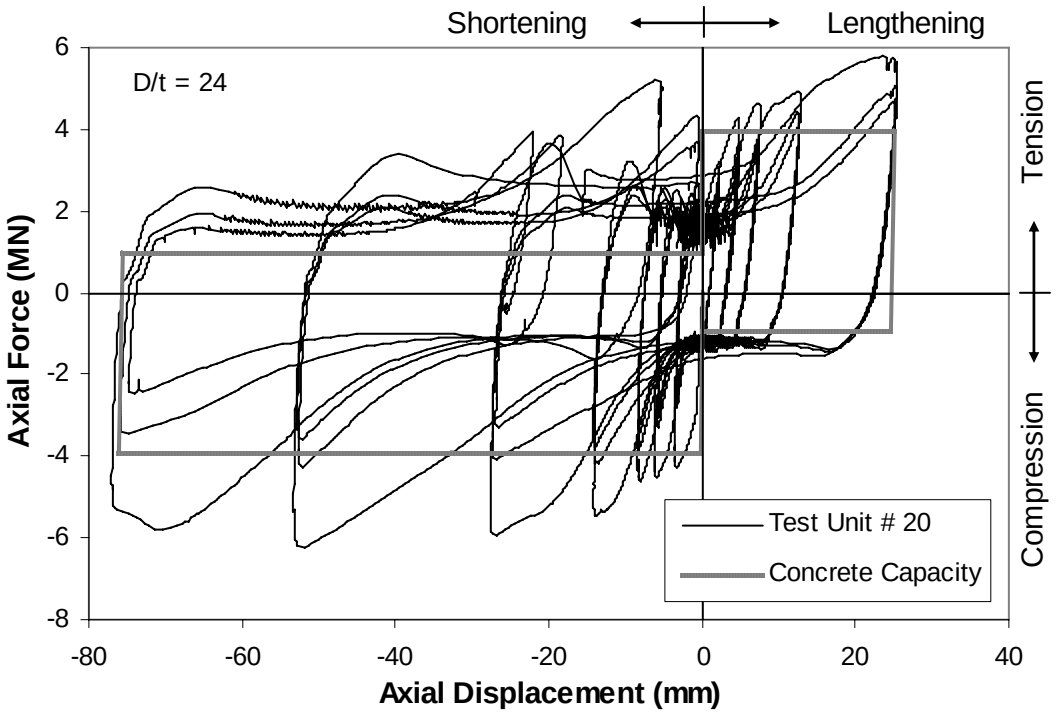


**Figure 6.59 Prediction for Test Unit # 20 (D/t = 24) with Two Shear Rings at 152 mm (6.0 in.)**

### 6.11.3 Capacity Prediction for Test Unit # 21 with Two Shear Rings at 305 mm

The concrete capacity prediction for Test Unit # 21 with two shear rings at a spacing of 305 mm (12.0 in.) has a reasonable match to the hysteretic response. The initial axial compression stiffness and axial force transfer matched well to the hysteretic response, as shown in Figure 6.60. The axial force transfer exceeded the prediction at greater axial compression displacements, as shown in Figure 6.61. However, the prediction is shown to have a reasonable match to the hysteretic response, at all axial displacements.

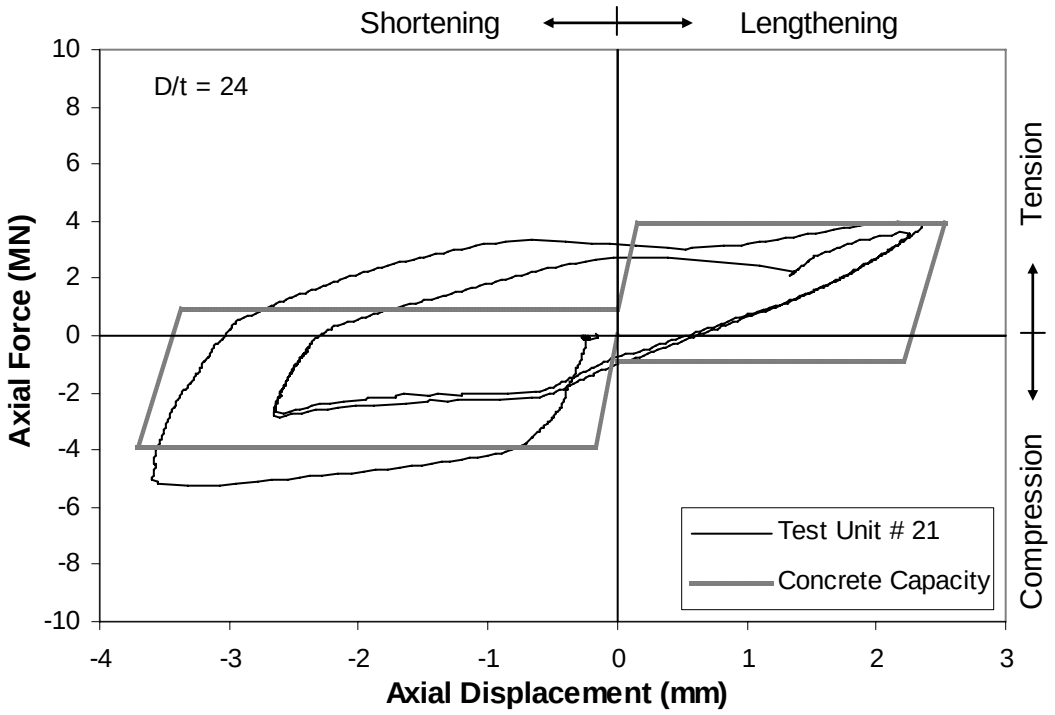


**Figure 6.60 Prediction for the First Cycle of Test Unit # 21 (D/t = 24) with Two Shear Rings at 301 mm (12.0 in.)**

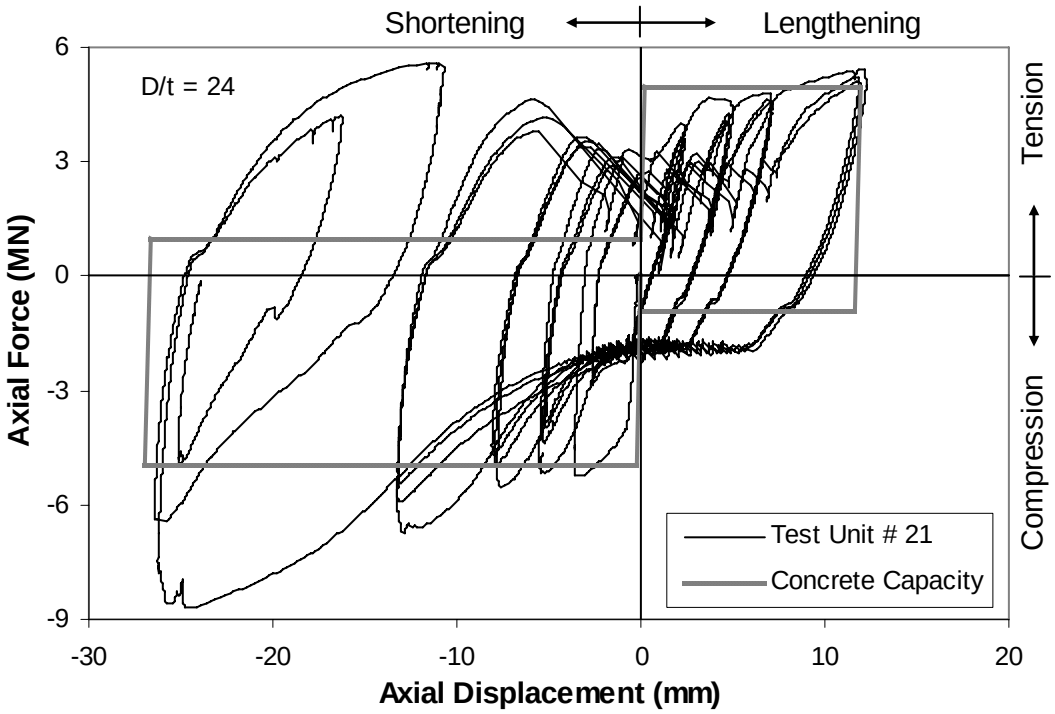


**Figure 6.61 Prediction for Test Unit # 21 (D/t = 24) with Two Shear Rings at 305 mm (12.0 in.)**

### 6.11.4 Summary of Capacity Prediction for Multiple Shear Rings

The prediction of the axial force transfer through multiple circumferential mechanisms involves the calculation of the concrete capacity at the upper mechanism resisting the applied force, and the lower mechanism which is influenced by the spacing. Mechanisms were all tested on a steel shell with a low D/t ratio (24), which remained elastic throughout testing, therefore the axial force predicted by the steel shell and mechanism capacity could not be obtained as the concrete capacity controlled. This prediction technique provides a reasonably accurate estimation of the axial force-axial displacement hysteretic response for all shear ring spacing tested.

## 6.12 Chapter Summary

This chapter presents an analysis of experimental data through comparison of hysteretic envelope curves, calculation of elastic stiffness, friction bond, and axial transfer stresses through a mechanism. A comparison of hysteretic envelope curves showed the circumferential mechanisms to have a ductile behavior, whereas mechanisms distributed throughout the steel shell interior surface had a non-ductile performance. Expansive concrete was shown in the comparisons to increase the initial axial force transfer, however, the friction bond did not substantially increase compared to plain concrete test units. The initial axial force transfer was shown to have a stronger relationship to the steel shell thickness, whereas the steel shell diameter had a greater role in the friction bond. The condition of the steel shell surface was shown to have an importance as well. When a water-bentonite coating is present on the steel shell, the initial adhesion bond is prevented, and the friction bond is decreased.

The axial transfer stress through a shear ring was approximately eight times the concrete compressive strength, $f_c^{'}$, at yield, for a steel shell within the elastic range (D/t ratio of 24). The axial transfer stress through multiple shear rings was found to increase as the spacing, $s$, increased to $D/2$ such that the shear rings behaved independently.

The API and UK DOE code predictions did not accurately predict the axial force transfer through surface bond or through a shear ring. This is due to the differences in the design of the test units which the codes are based on (a grouted connection between two steel shells) and due to code limitations. The prediction presented in this chapter, which is based on strain compatibility, the steel shell and mechanism capacity through formation of plastic hinges and the concrete capacity at the mechanism, provides a reasonable estimation of the axial force-axial displacement hysteretic response.

# 7 DESIGN

## 7.1 Introduction

This chapter presents a design procedure and recommendations for the transfer of axial force through surface bond, circumferential mechanisms and distributed mechanisms. The design procedure is demonstrated through three pile design examples.

## 7.2 Design Procedure

Design recommendations are presented in this section for the transfer of axial force through surface bond and for mechanisms fixed circumferentially to the steel shell or distributed within the steel shell.

### 7.2.1 Overview of Procedure

The first key decision as shown in the flow chart of Figure 7.1 is to determine if the surface bond between the steel shell and concrete core will be included. If the steel shell surface is cleaned prior to the placement of reinforced concrete then this bond can be included. A comparison of the predicted axial force transfer through surface bond divided by a factor of safety and the applied axial force determines if any mechanisms are needed. If mechanisms are needed, then the type of mechanism (circumferential or distributed) must be selected and evaluated for its capacity. The capacity of distributed mechanisms, such as shear studs will be governed by the connection to the steel shell (weld for shear studs). The capacity of circumferential mechanisms is governed by obtaining either the concrete core capacity or the steel shell and mechanism capacity. These axial force capacity predictions are presented in subsequent sections and are expected to be applicable to pile designs with a $f_c^{'}$ greater than 21 MPa (3.0 ksi). A comparison of these axial force transfer capacities determines which failure mode will govern the mechanism design.

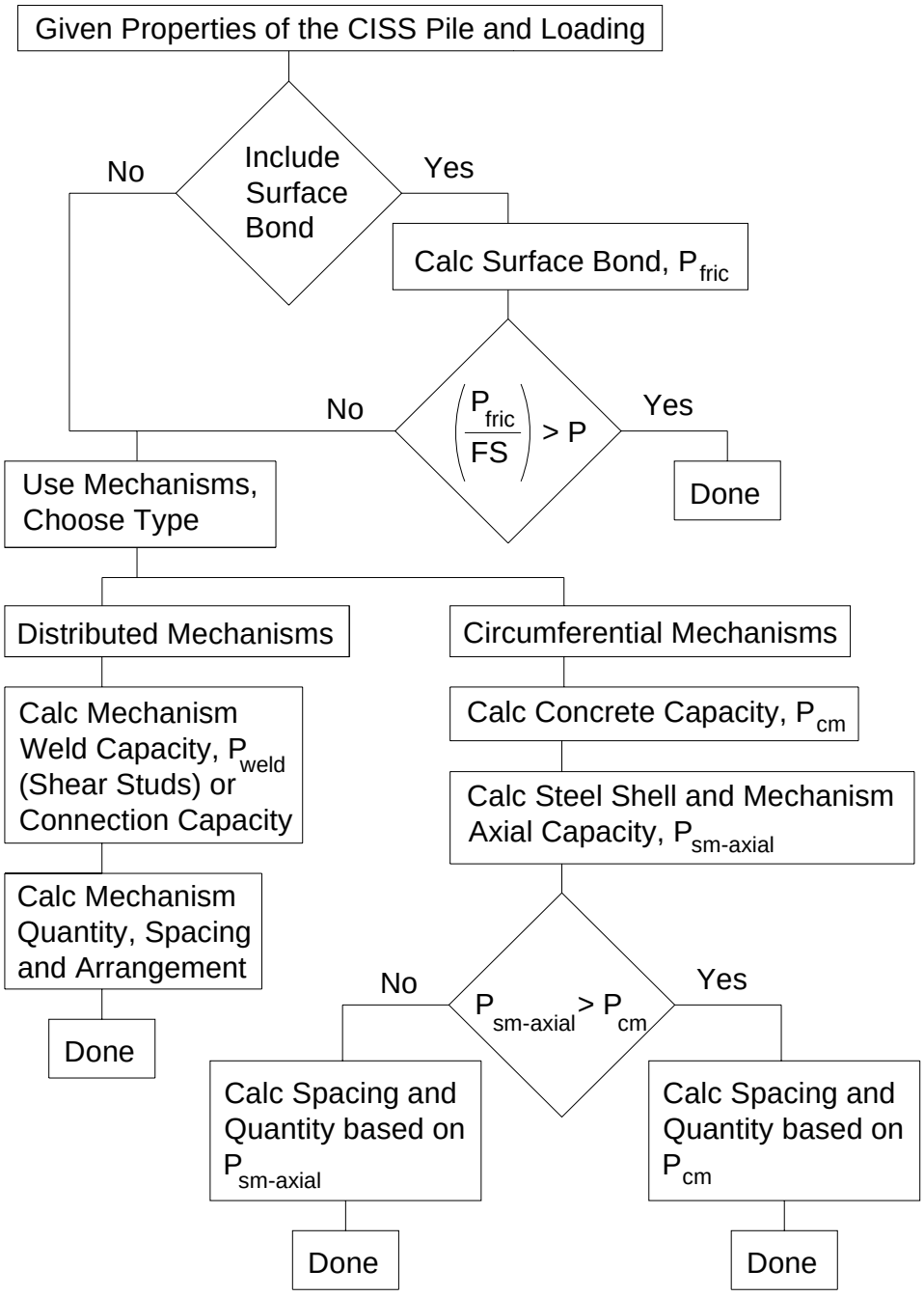


**Figure 7.1 Design Procedure Flowchart**

### 7.2.2 Prediction of the Axial Force Transfer through Surface Bond

The initial axial force transfer through surface bond obtains a peak force due to the presence of an adhesion bond. This peak force, $P_{sc}$, is predicted to be obtained at the

strain compatibility condition with a compatibility strain, $\varepsilon_{sc}$, of approximately 0.00015. This peak axial force transfer, as predicted in Equation 3.5, occurs at an axial yield displacement, $\Delta_y$, as predicted in Equation 3.6.

$$P_{sc} = \varepsilon_{sc} \cdot \left(E_c \cdot A_{core} + E_{shell} \cdot A_{shell}\right) \tag{3.5}$$

$$\Delta_y = \varepsilon_{sc} \cdot \ell \tag{3.6}$$

This peak axial force transfer is shown in the predicted axial force-axial displacement response for surface bond in Figure 7.2. After the initial peak occurs the adhesion bond is diminished which results in a decrease in the axial force as axial displacement increases. The axial force will decrease with a stiffness of $k_{unload}$ which will be assumed equal to the loading stiffness of $k_{load}$ as stated:

$$k_{load} = k_{unload} = \left(\frac{P_{sc}}{\Delta_y}\right) \tag{6.12}$$

The axial force will decrease until a frictional bond, $P_{fric}$, is obtained and dominates the response, as shown in Figure 7.2 and as stated:

$$P_{fric} = \varepsilon_{sc} \cdot E_c \cdot A_{core} \tag{3.7}$$

The axial force transfer through friction bond is assumed to remain constant as the axial displacement increases. When the concrete core is unloaded the axial displacement and axial force will increase with the unloading stiffness, $k_{unload}$, until an axial force transfer (tension) corresponding to the friction bond, $P_{fric}$, is obtained, as shown in Figure 7.2. As the axial displacement returns to zero, the axial force is assumed to remain constant.

As axial tension displacement is applied beyond zero displacement the initial adhesion bond as predicted using the strain compatibility condition is obtained. This axial force, $P_{sc}$, is obtained with a stiffness of $k_{load}$ as shown in Figure 7.2. After this axial force is obtained, the adhesion bond will diminish and result in a decrease in the axial force as axial displacement increases. The axial force will decrease with a stiffness of $k_{unload}$ until the axial force transfer corresponding to friction bond, $P_{fric}$, is obtained.

Unloading to zero axial displacement will be similar to the procedure for unloading from axial compression.

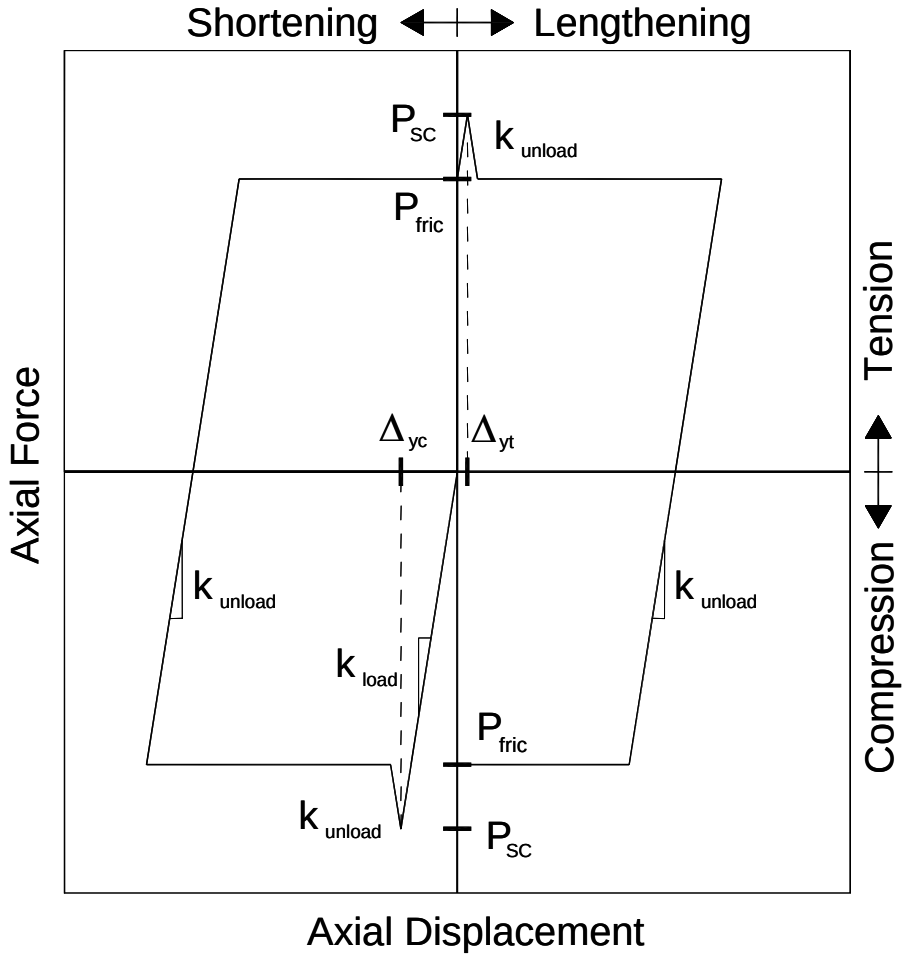


$$P_{sc} = \varepsilon_{sc} \cdot \left(E_c \cdot A_{core} + E_{shell} \cdot A_{shell}\right) \qquad \Delta_{yc} = \varepsilon_{sc} \cdot \ell$$

$$P_{fric} = \varepsilon_{sc} \cdot E_c \cdot A_{core} \qquad \Delta_{yt} = \left|\Delta_{yc}\right| - \left(\frac{P_{fric}}{k_{load}}\right)$$

$$k_{load} = k_{unload} = \left(\frac{P_{sc}}{\Delta_{yc}}\right)$$

**Figure 7.2 Axial Force-Axial Displacement Prediction for the Force Transfer through Surface Bond**

### 7.2.3 Prediction of the Axial Force Transfer through a Circumferential Mechanism and Surface Bond

The transfer of axial force through a mechanism fixed circumferentially to the steel shell results in either attainment of the steel shell and mechanism capacity or the concrete capacity. The prediction of these two failure modes is presented in detail in Sections 3.3.3 and 3.3.4 and is summarized in this section for design purposes. Both of these failure modes have an additional axial force transfer through the surface bond if it is judged as an appropriate method of axial force transfer and as presented in the previous section.

The capacity of the steel shell and a circumferential mechanism through the formation of three plastic hinges is predicted using Equations 3.16 and 3.17. Equation 3.16 estimates the lateral capacity, whereas Equation 3.17 estimates the axial capacity. In Equation 3.16, the height of the steel shell out-of-plane deformation, $\ell_e$, is predicted with Equation 6.5. The distance between the plastic hinges, $\ell_f$, is predicted with Equation 6.7. The angle at which the resultant force acts upon the mechanism, $\alpha$, is predicted from Equation 6.10.

$$P_{sm} = t \cdot f_y \cdot \left( \frac{t \cdot D}{l_f} + 2 \cdot l_e \right) + 2 \cdot A_{mech} \cdot f_{ymech} \tag{3.16}$$

$$P_{sm-axial} = \left( \frac{P_{sm}}{\tan(\alpha)} \right) \tag{3.17}$$

$$l_e = -0.7471 \cdot \left( \frac{D}{t} \right) + 222.62 \qquad \text{(SI Units: mm)} \tag{6.5}$$

$$l_f = -0.1868 \cdot \left( \frac{D}{t} \right) + 62.006 \qquad \text{(SI Units: mm)} \tag{6.7}$$

$$\alpha = -8.41 \cdot \left( \frac{t_r}{t} \right) + 46.91 \qquad \text{(Units: degrees)} \tag{6.10}$$

If the steel shell D/t ratio is low than the steel shell will likely remain elastic such that the plastic hinge prediction will not govern. In this case the concrete capacity at the circumferential mechanism will govern as presented in Section 3.3.4. The capacity of

the concrete at a circumferential mechanism, $P_{cm}$, is predicted using Equation 3.30 as stated:

$$P_{cm} = \left(\frac{\pi}{4}\right) \cdot \left(D^2 - \left(D - 2 \cdot t_{ring}\right)^2\right) \cdot \left(f_c^{'} + k \cdot \left(\frac{2 \cdot t \cdot f_y}{D}\right)\right) \tag{3.30}$$

A value of 4.0 is recommended for $k$ (Richart, 1928). The axial force transfer predicted by either the concrete capacity or the plastic hinge formulation will occur at an estimated yield axial (compression) displacement, $\Delta_{yc}$, corresponding to strain compatibility as stated:

$$\Delta_{yc} = \varepsilon_{sc} \cdot \ell \tag{3.6}$$

In the yield axial displacement equation the length of the reinforced concrete core through which surface bond is assumed to occur is $\ell$ and a strain compatibility, $\varepsilon_{sc}$, of approximately 0.00015 is used. The yield axial displacement is used to estimate the loading and unloading stiffness, as stated:

$$k_{load} = k_{unload} = \left(\frac{P_{sm} + P_{fric}}{\Delta_y}\right) \tag{6.13}$$

$$k_{load} = k_{unload} = \left(\frac{P_{cm} + P_{fric}}{\Delta_y}\right) \tag{6.14}$$

Equation 6.13 is used for the case in which the steel shell and mechanism capacity governs. Equation 6.14 is used for the case in which the concrete capacity governs. In both equations the axial force transfer through friction bond, $P_{fric}$, should be included only if judged appropriate (clean steel shell). The axial force-axial displacement response, as shown in Figure 7.3, is obtained by using the aforementioned stiffness and the predicted capacities as presented in Equations 3.16 and 3.17 for the steel shell and mechanism and Equation 3.30 for the concrete capacity. In the response it is assumed that an axial compression cycle is applied followed by an axial tension cycle (similar to the test protocol). The yield point is obtained at an axial yield displacement, $\Delta_{yc}$, and an axial force corresponding to the controlling failure mode: either Equation 3.17 or 3.30. After the yield force is obtained, the axial force remains constant until the desired axial displacement is obtained. After the desired axial displacement is obtained, the axial

displacement and the axial force decrease with the unloading stiffness, $k_{unload}$, until an axial force transfer corresponding to the friction bond, $P_{fric}$, is obtained as shown in Figure 7.3. As the axial displacement returns to zero displacement, the axial force remains constant.

As axial tension displacement is applied beyond the initial zero displacement the axial force corresponding to the controlling failure mode is obtained: either Equation 3.17 or 3.30. The yield point is obtained at an axial yield displacement, $\Delta_{yt}$, and an axial force corresponding to the controlling failure mode: either Equation 3.17 or 3.30. After the yield force is obtained, the axial force remains constant until the desired axial displacement is obtained. After the desired axial displacement is obtained, the axial displacement and axial force will decrease with the unloading stiffness, $k_{unload}$, until an axial force transfer corresponding to the friction bond, $P_{fric}$, is obtained as shown in Figure 7.3. As the axial displacement returns to zero displacement, the axial force remains constant.

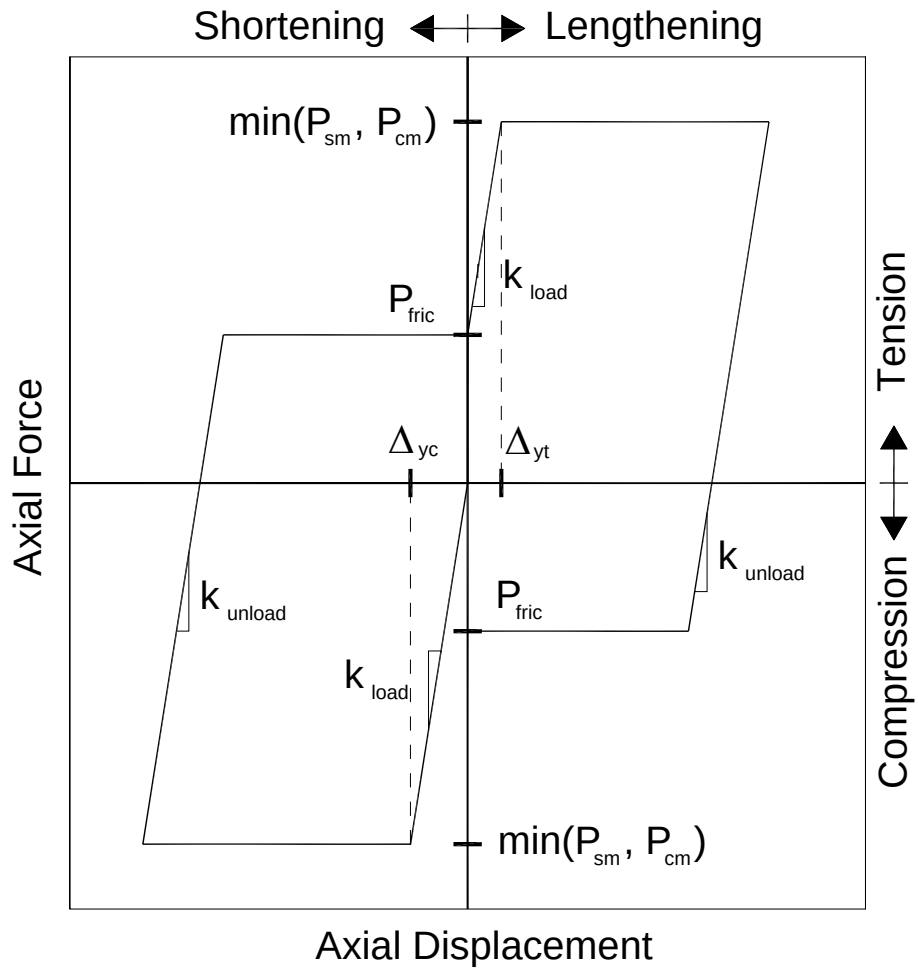


$$P_{fric} = \varepsilon_{sc} \cdot E_c \cdot A_{core}$$

$$P_{cm} = \left(\frac{\pi}{4}\right) \cdot \left(D^2 - \left(D - 2 \cdot t_{ring}\right)^2\right) \cdot \left(f_c^{'} + k \cdot \left(\frac{2 \cdot t \cdot f_y}{D}\right)\right) \qquad \Delta_{yc} = \varepsilon_{sc} \cdot \ell$$

$$P_{sm} = t \cdot f_y \cdot \left(\frac{t \cdot D}{l_f} + 2 \cdot l_e\right) + 2 \cdot A_{mech} \cdot f_{ymech} \qquad \Delta_{yt} = \left|\Delta_{yc}\right| - \left(\frac{P_{fric}}{k_{load}}\right)$$

$$P_{sm-axial} = \left(\frac{P_{sm}}{\tan(\alpha)}\right) \qquad k_{load} = k_{unload} = \left(\frac{\min(P_{sm}, P_{cm}}{\Delta_{yc}}\right)$$

**Figure 7.3 Axial Force-Axial Displacement Prediction for the Force Transfer through a Circumferential Axial Force Transfer Mechanism**

### 7.2.4 Axial Force Transfer through Multiple Mechanisms

The quantity of mechanisms, $N_{mech}$, required is determined by dividing the product of the applied axial force, $P$, and a factor of safety, $FS$, by the governing mechanism capacity, $P_{mech}$, as stated below.

$$N_{mech} = \left( \frac{P \cdot FS}{P_{mech}} \right) \tag{7.1}$$

Selection of the factor of safety is presented in Section 3.3.3. The governing mechanism capacity, $P_{mech}$, depends on the expected failure mode at the mechanism. Failure will be obtained through the formation of plastic hinges, as predicted by $P_{sm-axial}$, or through concrete crushing at the mechanism as predicted by $P_{cm}$. The lower value of these two predicted axial forces is the governing mechanism capacity, $P_{mech}$. This force determines the failure mode and the quantity of mechanisms, $N_{mech}$.

$$P_{mech} = \text{minimum}\left(P_{sm-axial}, P_{cm}\right) \tag{7.2}$$

In the mechanism quantity equation, the applied axial force, $P$, cannot exceed the concrete core capacity or the steel shell capacity as stated in the condition below. The applied axial compression or tension forces are typically in the range of 2 – 20% of the concrete core capacity.

$$P < \left\{ \begin{array}{c} \left( \frac{\pi \cdot D^2 \cdot f_c^{'}}{4} \right) \\ \left( \frac{\pi}{4} \right) \cdot \left( \left( D + 2 \cdot t \right)^2 - D^2 \right) \cdot f_y \end{array} \right\}$$

The axial force transferred through multiple circumferential mechanisms in which the plastic hinge formulation governs can be predicted for each mechanism using Equations 3.16 and 3.17. An adequate spacing (Equation 3.26) for the mechanisms is required to allow for the formation of the plastic hinges and thus individual action of the mechanisms. Mechanism spacing is addressed in the next section.

The axial force transferred through multiple circumferential mechanisms in which the concrete capacity equation governs (low D/t) is estimated from Equation 3.32. This equation should be used for the mechanisms below the uppermost mechanism providing resistance to the applied axial force. The concrete capacity for the first mechanism providing resistance to the applied axial force is estimated from Equation 3.30. For the uppermost circumferential mechanism:

$$P_{cm} = \left(\frac{\pi}{4}\right) \cdot \left(D^2 - \left(D - 2 \cdot t_{ring}\right)^2\right) \cdot \left(f_c^{'} + k \cdot \left(\frac{2 \cdot t \cdot f_y}{D}\right)\right) \tag{3.30}$$

For subsequent lower circumferential mechanisms:

$$P_{cm} = \left(\frac{\pi}{4}\right) \cdot \left(D^2 - \left(D - 2 \cdot t_{ring}\right)^2\right) \cdot \left(f_c^{'} + k \cdot \left(\frac{2 \cdot t \cdot f_y}{D}\right)\right) \cdot \left(\frac{1}{\tan(\alpha)}\right) \tag{3.32}$$

The axial forces transferred by the circumferential mechanisms are added to the axial force transferred through surface bond (if included), as predicted in Equation 3.7, which results in the total predicted axial force capacity. This predicted capacity is obtained at the yield axial displacement as shown in Figure 7.3 and remains constant until the desired axial displacement is obtained. Unloading occurs to the axial force transferred through friction bond, similar to the procedure in the previous section. In axial tension the predicted axial force capacity for the arrangement of multiple circumferential mechanisms and surface bond is obtained in axial tension at the yield axial displacement as shown in Figure 7.3. This axial force transfer remains constant until the expected axial tension displacement is obtained. Unloading from the desired axial displacement occurs to an axial force transfer corresponding to the friction bond, as shown in Figure 7.3. This axial force transfer remains constant as the axial displacement is returned to zero.

### 7.2.5 Spacing of Circumferential Mechanisms

The spacing of circumferential mechanisms will depend on the expected failure mode. For low D/t ratios the concrete capacity (Equation 3.30) will likely govern whereas for high D/t ratios the steel shell and mechanism capacity (Equations 3.16 and

3.17) will likely govern. If the concrete capacity equation governs then a shear ring spacing, $s$, as stated below is recommended:

$$s = 6.5 \cdot t_{cover} \tag{6.15}$$

In Equation 6.15 $t_{cover}$ is the concrete cover (distance) between the mechanism and the longitudinal reinforcement as shown in Figure 3.9. The spacing predicted by Equation 6.15 is recommended based on results of Test Unit # 21 which had a shear ring spacing corresponding to Equation 6.15 of 305 mm (12.0 in.). This spacing exhibited the most independent behavior of the range of shear ring spacing tested. This spacing also corresponds to an angle, $\alpha$, between the mechanism and concrete core center of $45^o$ (see Figure 3.6). However, if an angle, $\alpha$, of $45^o$ was used to determine the spacing then a spacing of one half the steel shell diameter would be concluded as the ideal spacing. At larger diameters this would clearly result in a high mechanism spacing therefore Equation 6.15 is recommended.

If the steel shell and mechanism capacity governs then the spacing, $s$, as stated below is recommended:

$$s = l_r + 6 \cdot l_f \tag{3.26}$$

In this prediction the recommended spacing, $s$, is a function of the distance between the plastic hinges, $l_f$, and the distance between plastic hinge zones, $l_r$. This spacing is a minimum recommended spacing, and is depicted in Figure 3.7.

### 7.2.6 Axial Force Transfer through Distributed Mechanisms

Mechanisms which are distributed throughout the steel shell, such as shear studs or a cross bar, will have an expected failure mode consisting of a shear failure of the welded connection between the steel shell and the mechanism. After the mechanism connections fail only the surface bond remains, if fabricated under ideal conditions such that this bond can be relied upon. The axial force-axial displacement response for distributed mechanisms can be predicted following the procedure presented in Section

7.2.3. The governing axial force transfer will be the weld shear capacity of the shear studs or cross bar.

The axial force transfer through a tread plate mechanism is estimated with the experimentally determined bond stress calculated per area of tread perpendicular to loading. Bond stresses for axial compression and axial tension of 35.3 MPa (5.11 ksi) and 29.7 MPa (4.30 ksi), respectively, were obtained. These bond stresses can be used to estimate the governing axial force transfer.

### 7.2.7 Mechanism Design Recommendations

A comparison of the mechanism design advantages and disadvantages is presented in Table 7.1. Circumferential mechanisms are recommended for all pile diameters because of their ductile performance. For piles with a diameter greater than 0.91 m (36 inch) a shear ring or welded reinforcement bar is recommended to provide the necessary mechanism radial width. For piles with a diameter less than 0.91 m (36 inch) a weld bead connection is recommended because the radial width required is potentially close to the size of a typical weld pass. In addition for a pile with a high D/t ratio a weld bead might be the ideal mechanism for the aforementioned reason.

Installation of shear studs typically requires placing a welder on a platform and lowering the welder into the pile with the reinforcement bar cage already placed. Shear studs are then attached in the spaces between the longitudinal reinforcement and transverse reinforcement as shown in Figure 1.2. This installation procedure works well for pile diameters around 2.7 m (108 inch) diameter, and clearly does not work for small pile diameter piles. This fabrication issue combined with the non-ductile performance renders the shear stud not recommended for small diameter piles. For large diameter piles the shear stud mechanism should be used with caution due to its non-ductile performance.

**Table 7.1 Connection Type Advantages and Disadvantages**

| Design Concern | Welded Bar or Shear Ring | Weld Bead | Cross Bar | Shear Studs | Tread Plate | Expansive Concrete |
|---|---|---|---|---|---|---|
| **Mechanism Fabrication Location** | Shop | Shop | Field | Field | Field/Shop | Field |
| **Ease of Mechanism Fabrication** | Bar or ring has to be bent to match the diameter | Applied directly to shell | Obtain from supplier | Obtain from supplier | Purchase from supplier<br><br>Tread plate has to be bent to match the diameter | Add an expansive admixture to the concrete |
| **Installation on Large Diameter Piles (>0.91 m Diam)** | Extensive welding | Extensive welding especially to build up a larger weld bead | Complicated by presence of reinforcement bar cage | Studs can be welded after the reinforcement bar cage is placed | Use the rolled tread plate section as a pile section | No issues |
| **Installation on Small Diameter Piles (<0.91 m Diam)** | Radial thickness might be small enough that a weld bead is more practical | Ideal for applications where a small radial thickness is needed | Complicated by presence of reinforcement bar cage | Difficulty placing as a welder has to be lowered into the pile and reinforcement cage | Use the tread plate section as a portion of the pipe pile section | No issues |
| **Axial Force-Axial Displacement Response** | Ductile | Ductile | Non-Ductile, failure at connection to steel shell | Non-Ductile, failure at connection to steel shell | Non-Ductile<br><br>Concrete crushes between treads | Initial increase in axial force<br><br>Not effective in reversed cyclic axial loading |
| **Installation on Piles in Wet Conditions** | Extensive welding effected by water acting as a heat sink | Extensive welding effected by water acting as a heat sink | If the cross bar passes through the steel shell and is bolted (no welds) then wet conditions are not a problem | Minor local welds at each shear stud<br><br>Wet conditions could be problematic | Not an issue<br><br>Tread plate section attached prior to pile driving | No issues |

Field welding of a mechanism to a steel shell in wet conditions can be problematic, however, in such a case the cross bar mechanism can be advantageous as it can be bolted to the steel shell (instead of welded as was done in this research).

The tread plate mechanism increased the initial axial force transfer, however, the effectiveness diminished under reversed cyclic axial loading as concrete crushed between treads. This mechanism is relatively simple to fabricate as the tread plate is rolled to form a pipe section for the pile itself. A tread plate with a thickness that is commonly used in CISS piles might not be readily available. However, the tread plate mechanism is not recommended because of its non-ductile performance.

Expansive concrete provided an increase in the axial force transfer, when compared to normal concrete, however, this increase was ineffective under reversed cyclic axial loading. Expansive concrete is not recommended for this reason.

### 7.2.8 Design Procedure Summary

This section presented a procedure to estimate the axial force transfer through mechanisms and surface bond and an envelope of the axial force-axial displacement response. The axial force transfer through circumferential mechanisms is predicted through the steel shell and mechanism capacity or through the capacity of the concrete at the mechanism. The axial force transfer for distributed mechanisms is predicted through failure of the welded connection of the steel shell (shear studs and cross bar) or through concrete crushing for the tread plate mechanism. The procedure presented in this section can be used to obtain an envelope of the axial force-axial displacement response with relative ease and provides a reasonably accurate prediction.

## 7.3 Pile Design Example

In this section design examples will be presented to demonstrate the procedure to predict the axial force transfer through mechanisms and surface bond. The axial force

transfer through the surface bond between the steel shell and the concrete core will either be included or not included as shown for the pile design examples in Table 7.2. The exclusion of the surface bond is conservative for the construction case in which the bond is diminished due to the presence of a bentonite slurry residue (a tremie pour) or if the steel shell is not thoroughly cleaned. All pile design examples listed in Table 7.2 are for CISS piles with normal reinforced concrete. Properties of the piles, shear rings and shear studs are listed in Table 7.3 for SI units and in Table 7.4 for USCS units.

**Table 7.2 Pile Design Example Cases**

| Design Example | D/t | Diameter mm (inch) | Axial Force MN (kips) | Shell-Concrete Interface Bond |
|---|---|---|---|---|
| Pile 1.a | 60 | 762 (30) | 2.67 (600) | Not Included |
| Pile 2.a | 80 | 1524 (60) | 13.34 (3000) | Not Included |
| Pile 3.a | 108 | 2743 (108) | 35.59 (8000) | Not Included |
| Pile 1.b | 60 | 762 (30) | 2.67 (600) | Included |
| Pile 2.b | 80 | 1524 (60) | 13.34 (3000) | Included |
| Pile 3.b | 108 | 2743 (108) | 35.59 (8000) | Included |

**Table 7.3 Properties for the Pile Design Examples (SI Units)**

| Property | Units | Pile 1 | Pile 2 | Pile 3 |
|---|---|---|---|---|
| ***Steel Shell*** | | | | |
| Internal Diameter, D | mm | 762 | 1524 | 2743 |
| D/t | | 60 | 80 | 108 |
| Steel Shell Thickness, t | mm | 13 | 19 | 25 |
| Concrete Cover (shell to reinforcement), $t_{cover}$ | mm | 51 | 51 | 51 |
| ***Shear Ring*** | | | | |
| Shear Ring Radial Thickness, $t_{ring}$ | mm | 13 | 19 | 25 |
| Height of Shear Ring, $h_{ring}$ | mm | 13 | 19 | 25 |
| Shear Ring Cross Sectional Area, $A_{mech}$ | $mm^2$ | 81 | 121 | 161 |
| ***Shear Studs*** | | | | |
| Shear Stud Diameter, $D_{stud}$ | mm | 12.7 | 19.1 | 25.4 |
| Shear Stud Length, $L_{stud}$ | mm | 50.8 | 76.2 | 101.6 |
| Weld Size (Throat) | mm | 3.18 | 4.8 | 6.35 |
| Electrode, $F_{exx}$ | MPa | 482.6 | 482.6 | 482.6 |
| ***Materials*** | | | | |
| f'c | MPa | 21 | 21 | 21 |
| Modulus of Elasticity for Concrete, $E_c$ | MPa | 21523 | 21523 | 21523 |
| fy, Steel Shell | MPa | 345 | 345 | 345 |
| fy, Shear Ring | MPa | 345 | 345 | 345 |

**Table 7.4 Properties for the Pile Design Examples (USCS Units)**

| Property | Units | Pile 1 | Pile 2 | Pile 3 |
|---|---|---|---|---|
| ***Steel Shell*** | | | | |
| Internal Diameter, D | inch | 30 | 60 | 108 |
| D/t | | 60 | 80 | 108 |
| Steel Shell Thickness, t | inch | 0.5 | 0.75 | 1 |
| Concrete Cover (shell to reinforcement), $t_{cover}$ | inch | 2 | 2 | 2 |
| ***Shear Ring*** | | | | |
| Shear Ring Radial Thickness, $t_{ring}$ | inch | 0.5 | 0.75 | 1 |
| Height of Shear Ring, $h_{ring}$ | inch | 0.5 | 0.75 | 1 |
| Shear Ring Cross Sectional Area, $A_{mech}$ | $inch^2$ | 0.25 | 0.5625 | 1 |
| ***Shear Studs*** | | | | |
| Shear Stud Diameter, $D_{stud}$ | inch | 0.5 | 0.75 | 1 |
| Shear Stud Length, $L_{stud}$ | inch | 2 | 3 | 4 |
| Weld Size (Throat) | inch | 0.125 | 0.1875 | 0.25 |
| Electrode, $F_{exx}$ | ksi | 70 | 70 | 70 |
| ***Materials*** | | | | |
| f'c | ksi | 3 | 3 | 3 |
| Modulus of Elasticity for Concrete, $E_c$ | ksi | 3122 | 3122 | 3122 |
| fy, Steel Shell | ksi | 50 | 50 | 50 |
| fy, Shear Ring | ksi | 50 | 50 | 50 |

In Tables 7.3 and 7.4 the shear ring cross sectional area is the product of the shear ring radial thickness, $t_{ring}$, and the shear ring height, $h_{ring}$. In Table 7.4 the modulus of elasticity for concrete is calculated from:

$$E_c = 57000 \cdot \sqrt{f_c'} \qquad \text{(USCS Units: psi)} \qquad (7.3)$$

Calculations for Pile 1.a and Pile 1.b will be explained in detail and shown in Tables 7.5, 7.6, 7.7 and 7.8. The axial force transfer through a circumferential mechanism, such as a shear ring or through a distributed mechanism (shear studs) will be calculated for all pile design examples.

### 7.3.1 Mechanism Design Example without Surface Bond

The design procedure for Pile 1.a which does not account for the surface bond will first estimate the capacity of the concrete at the location of a circumferential mechanism. Next the capacity of the steel shell at the circumferential mechanism is

estimated by assuming a series of plastic hinges in the steel shell. A comparison of these two capacities determines which failure mode will govern the design, the quantity and the spacing of circumferential mechanisms as shown in Figure 7.3. In addition to the design of circumferential mechanisms, the shear stud mechanism is also evaluated. The capacity of each shear stud is limited by the weld to the steel shell.

The capacity of the concrete at the location of a circumferential mechanism (shear ring) such that concrete crushing initiates is stated as:

$$P_{cm} = \left(\frac{\pi}{4}\right) \cdot \left(D^2 - \left(D - 2 \cdot t_{ring}\right)^2\right) \cdot \left(f_c^{'} + k \cdot \left(\frac{2 \cdot t \cdot f_y}{D}\right)\right) \tag{3.30}$$

Substitution of the given design values results in

$$P_{cm} = \left(\frac{\pi}{4}\right) \cdot \left(\left(0.762m\right)^2 - \left(0.762m - 2 \cdot \left(0.013m\right)\right)^2\right) \cdot \left(21MPa + 4 \cdot \left(\frac{2 \cdot \left(0.013m\right) \cdot \left(345MPa\right)}{0.762m}\right)\right)$$

$$P_{cm} = 2.0MN$$

This axial force represents the force which will cause the concrete at the location of a circumferential mechanism to crush. This failure mode will not fully develop if the capacity of the steel shell at the mechanism is less than this force.

The axial force transfer capacity of the steel shell at the mechanism location, $P_{sm-axial}$, is calculated using the assumed plastic hinge distribution as shown in Figure 7.4 and the trigonometric relationship in Figure 7.5. This force is calculated based on a trigonometric relationship with the lateral force capacity, $P_{sm}$, and the angle, $\alpha$, at which the resultant force develops as shown in Figure 7.5. The axial force, $P_{sm-axial}$, is determined with the trigonometric relationship stated as:

$$P_{sm-axial} = \left(\frac{P_{sm}}{\tan(\alpha)}\right) \tag{3.17}$$

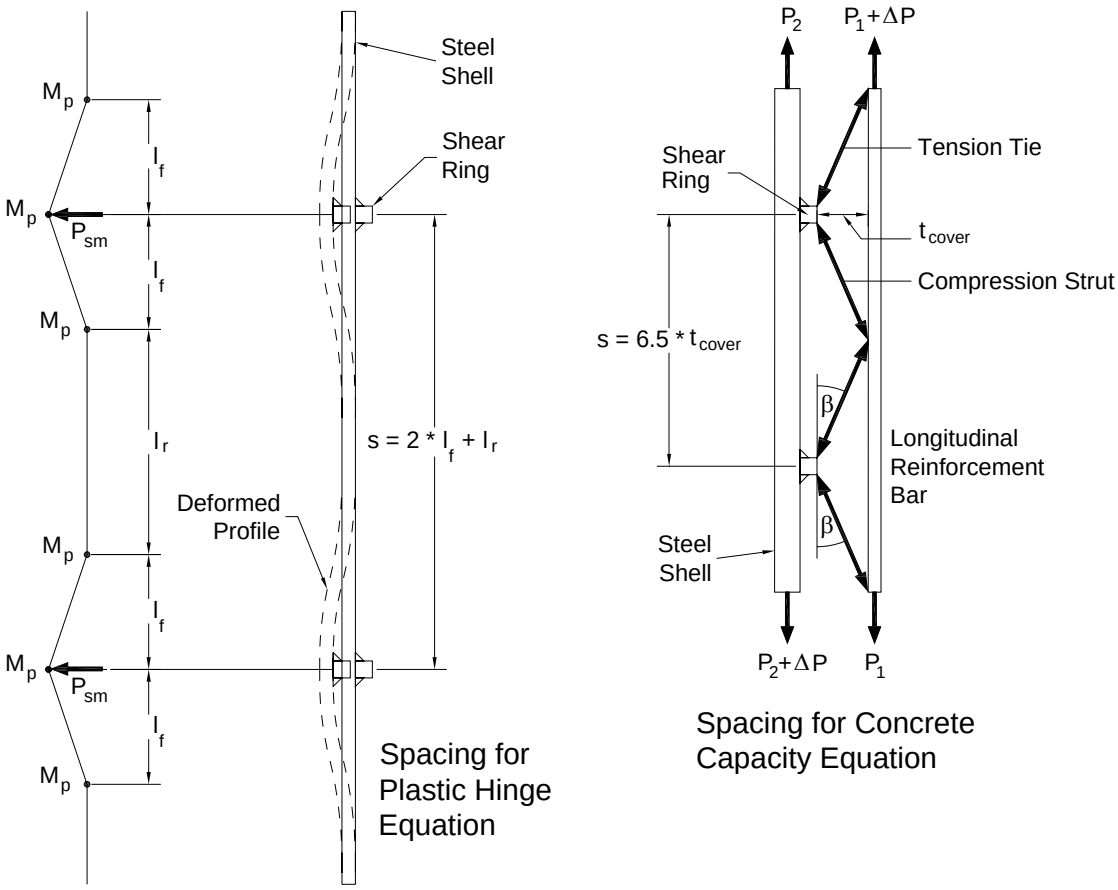


**Figure 7.4 Shear Ring Spacing**

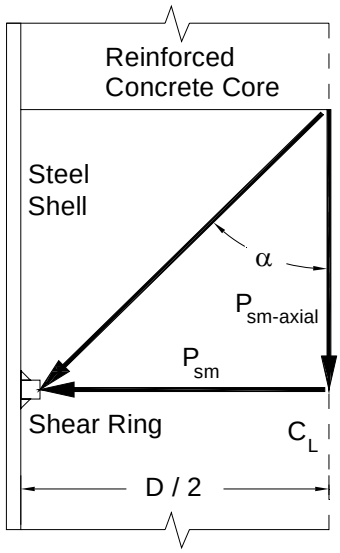


**Figure 7.5 Trigonometric Relationship for the Axial Force and Lateral Force**

In the lateral force capacity equation two plastic hinges are assumed to form at the points of inflection in the steel shell deformation (Figure 7.4) and a third hinge is assumed to form at the mechanism location with a spacing of $l_f$. The steel shell is assumed to deform out-of-plane through a height of $l_e$. Equations for $l_f$ and $l_e$ were estimated with experimental results (Equations 6.5 and 6.7) and are restated below in SI units.

$$l_f = -0.188 \cdot \left(\frac{D}{t}\right) + 62.006 \quad \text{(SI Units: mm)} \qquad (6.5)$$

$$l_e = -0.747 \cdot \left(\frac{D}{t}\right) + 222.6 \quad \text{(SI Units: mm)} \qquad (6.7)$$

Substitution of the D/t ratio into the above equations results in:

$$l_f = -0.188 \cdot (60) + 62.006 = 51mm$$

$$l_e = -0.747 \cdot (60) + 222.6 = 178mm$$

The lateral force capacity of the steel shell and mechanism through the formation of three plastic hinges (Figure 7.4) is stated as:

$$P_{sm} = t \cdot f_y \cdot \left(\frac{t \cdot D}{l_f} + 2 \cdot l_e\right) + 2 \cdot A_{mech} \cdot f_{ymech} \qquad (3.16)$$

Substitution of the given design values results in

$$P_{sm} = (0.013m) \cdot (345MPa) \cdot \left(\frac{(0.013m) \cdot (0.762m)}{0.051m} + 2 \cdot (0.178m)\right) + 2 \cdot (0.000161m^2) \cdot (345MPa)$$

$$P_{sm} = 2.58MN$$

The lateral force capacity, $P_{sm}$, is used to obtain the axial force capacity, $P_{sm-axial}$, with the trigonometric relationship of Equation 3.17. The angle $\alpha$ between the lateral capacity, $P_{sm}$, and the axial capacity, $P_{sm-axial}$, is assumed as $45^o$. Substitution of the given design values results in:

$$P_{sm-axial} = \left(\frac{2.58MN}{\tan(45^o)}\right) = 2.58MN$$

The axial force to develop the plastic hinge distribution at the shear ring, $P_{sm-axial}$, of 2.58 MN (563 kips) is greater than the axial force to initiate concrete crushing, $P_{cm}$, of

2.0 MN (448 kips). Therefore concrete crushing at the shear ring is the expected failure mode and will determine the number of shear rings and spacing.

In determining the number of shear rings, $N_{rings}$, as stated below a factor of safety should be used which is up to the designers discretion. In this example a factor of safety, $FS$, of 2 is used.

$$N_{rings} = \left( \frac{P}{P_{cm}} \right) \cdot FS \tag{7.4}$$

$$N_{rings} = \left( \frac{2.7MN}{2.0MN} \right) \cdot 2 = 2.6$$

The above calculation results in 2.6 shear rings, which will be rounded up to 3 shear rings. The shear ring spacing for the concrete crushing failure mode is a function of the concrete cover, $t_{cover}$, between the internal edge of the shear ring and the reinforcement bar cage, as stated:

$$s = 6.5 \cdot t_{cover} \tag{6.15}$$

Substitution of the known concrete cover, $t_{cover}$, results in:

$$s = 6.5 \cdot (51mm) = 332mm$$

This minimum shear ring spacing of 332 mm (13.1 in.) will ensure independent behavior of the shear rings. The upper shear ring is placed at 381 mm (15 in.) from the top of the steel shell which corresponds to D/2 as shown in Figure 7.6. This placement allows for a resultant force to develop at a $45^o$ angle relative to the center of the concrete core and ensures the mechanism effectiveness. The shear ring spacing is also calculated for the plastic hinge failure mode to demonstrate the procedure. The shear ring spacing for the plastic hinge formation is stated as:

$$s = l_r + 2 \cdot l_f \tag{3.26}$$

The shear ring spacing, $s$, is a function of the spacing between plastic hinges, $l_f$, and the distance between plastic hinge zones, $l_r$, as shown in Figure 7.4. The spacing between the plastic hinge zones, $l_r$ is stated as:

$$l_r = \left( \frac{P_{sm-axial}}{2 \cdot t \cdot f_y} \right) \tag{3.20}$$

Substitution of the given design values into the equations for the plastic hinge zone spacing, $l_r$, and the shear ring spacing, $s$, results in:

$$l_r = \left( \frac{2.58MN}{2 \cdot (0.013m) \cdot (345MPa)} \right) = 0.287m$$

$$s = 0.287m + 2 \cdot 0.051m = 0.389m = 389mm$$

The above calculation results in a shear ring spacing, $s$, of 389 mm (15.3 in.) for the plastic hinge failure mode. If a lesser spacing is used then the steel shell section between the plastic hinge zones with a spacing of $l_r$ (Figure 7.4) would provide an insufficient force to prevent this section from deforming out-of-plane. Such a deformation could result in additional loss of contact between the shear ring and the core and a decreased effectiveness.

The procedure demonstrated above can be used for circumferential mechanisms with cross sections other than a square or rectangular shear ring, such as a welded reinforcement bar or a weld bead.

A mechanism distributed throughout the steel shell internal surface can be used in place of shear rings. Distributed mechanisms include shear studs, cross bars and tread plate. The above example (for Pile 1.a) will be redone for the shear stud mechanism. A shear stud diameter, $D_{stud}$, will be assumed equal to the steel shell thickness. The length of the shear studs, $L_{stud}$, will be assumed as four times the stud diameter. The weld between the shear stud and the steel shell will have a weld throat, $a$, that is 1/4 of the shear stud diameter. The properties of the shear stud and weld are listed below:

$D_{stud}$ = 12.7 mm = 0.5 in.

$L_{stud}$ = 50.8 mm = 2.0 in.

$a$ = 3.175 mm = 0.125 in.

$F_{exx}$ = 483 MPa = 70.1 ksi

The shear capacity of the shear stud weld, $V_{stud}$, is calculated based on the weld electrode strength, $F_{exx}$, the throat size, $a$, and the diameter as stated below. It should be noted that the designer could use shear stud capacity tables provided by the manufacturer. Such tables assume the stud is fused to the steel shell which results in a greater shear capacity and fewer studs then the following procedure which relies on the weld for the capacity.

$$V_{stud} = \pi \cdot D_{stud} \cdot a \cdot 0.75 \cdot (0.6 \cdot F_{exx}) \tag{3.39}$$

Substitution of the given design values results in:

$$V_{stud} = \pi \cdot (0.0127mm) \cdot (0.003175m) \cdot 0.75 \cdot (0.6 \cdot 483MPa) = 0.028MN$$

The quantity of shear studs, $N_{studs}$, is determined by dividing the product of the applied axial force, $P$, and a factor of safety, $FS$, by the shear stud capacity, $V_{stud}$:

$$N_{studs} = \left( \frac{P \cdot FS}{V_{stud}} \right) \tag{3.40}$$

$$N_{studs} = \left( \frac{(2.7MN) \cdot 2}{0.028MN} \right) = 194$$

The shear studs need to be placed with adequate spacing to ensure independent behavior. The minimum vertical spacing, $s_v$, and minimum radial spacing, $s_r$, are recommended as:

$$s_v = 3 \cdot L_{stud} \tag{7.5}$$

$$s_r = 3 \cdot L_{stud} \quad \text{(minimum radial spacing)} \tag{7.6}$$

$$s_v = 3 \cdot (50.8mm) = 152mm$$

$$s_r = 3 \cdot (50.8mm) = 152mm$$

This spacing will ensure independent action of the shear studs. The radial spacing will be rounded up to 160 mm (6.3 in.) to provide an equal spacing for the 15 shear studs in each circumferential row. Thirteen circumferential rows of shear studs will provide 195 shear studs which meets the requirement of 194 shear studs. This design is shown in Figure 7.7.

In this design example two mechanism design options were presented to provide an axial force transfer between the steel shell and the reinforced concrete core (neglecting the surface bond). In one option three shear rings each with a cross section of 13 mm (0.51 in.) square and a spacing of 332 mm (13.1 in.) are used. An alternative to the shear rings is the use of 195 shear studs within the steel shell with 15 shear studs for each of the 13 circumferential rows. The calculations for this example are shown in Table 7.5 for SI units and in Table 7.6 for USCS units. Calculations for the two additional pile design cases (Pile 2.a and 3.a) as specified in Table 7.2 are also presented in Tables 7.5 and 7.6. The shear ring design and shear stud design are shown in Figures 7.8 and 7.9 for the CISS pile with a 1.52 m (60 in.) diameter. The shear ring design and shear stud design are shown in Figures 7.10 and 7.11 for the CISS pile with a 2.7 m (108 inch) diameter.

**Table 7.5 Shear Ring and Shear Stud Calculations – SI Units**

| Calculation | Units | Pile 1.a | Pile 2.a | Pile 3.a |
|---|---|---|---|---|
| ***Shear Ring Calculations*** | | | | |
| Applied Load, P | MN | 2.7 | 13.3 | 35.6 |
| Confinement Coefficient, k | | 4 | 4 | 4 |
| Concrete Capacity at Shear Ring, $P_{cm}$ | MN | 1.99 | 5 | 10 |
| Shear Ring Cross Sectional Area, $A_{mech}$ | $mm^2$ | 161 | 363 | 645 |
| Distance between Hinges, $l_f$ | mm | 51 | 47 | 42 |
| Height of Deformation, $l_e$ | mm | 178 | 163 | 142 |
| Lateral Force Capacity, $P_{sm}$ | MN | 2.5 | 6.4 | 17.6 |
| Strut Angle | degrees | 45 | 45 | 45 |
| Axial Force Capacity, $P_{sm\text{-}axial}$ | MN | 2.5 | 6.4 | 17.6 |
| Failure Mode | | Conc Crush | Conc Crush | Conc Crush |
| Quantity of Shear Rings | | 1.3 | 2.1 | 2 |
| Factor of Safety | | 2 | 2 | 2 |
| Final Quantity of Shear Rings | | 3 | 4 | 4 |
| Spacing between PH Zones, $l_r$ | mm | 286 | 491 | 1003 |
| Shear Ring Spacing, s for PH Formation | mm | 387 | 585 | 1086 |
| Shear Ring Spacing, s for Conc Crush | mm | 330 | 330 | 330 |
| ***Shear Stud Calculations*** | | | | |
| Shear Stud Diameter, $D_{stud}$ | mm | 12.7 | 19.1 | 25.4 |
| Shear Stud Length, $L_{stud}$ | mm | 50.8 | 76.2 | 101.6 |
| Weld Size (Throat) | mm | 3.175 | 4.763 | 6.35 |
| Electrode, $F_{exx}$ | MPa | 482.6 | 482.6 | 482.6 |
| Shear Stud Weld Capacity, $V_{stud}$ | MN | 0.028 | 0.062 | 0.11 |
| Factor of Safety | | 2 | 2 | 2 |

**Table 7.5 Continued**

| | | | | |
|---|---|---|---|---|
| Quantity of Shear Studs | | 97 | 216 | 323 |
| Quantity of Shear Studs with FS | | 194 | 431 | 647 |
| Total Capacity with FS | MN | 5.3 | 26.7 | 71.2 |
| Spacing (Vertical) | mm | 152 | 229 | 305 |
| Spacing (Radial) | mm | 160 | 239 | 287 |
| Studs per row | | 15 | 20 | 30 |
| Number of rows | | 13 | 22 | 22 |
| Final Quantity of Shear Studs | | 195 | 440 | 660 |

**Table 7.6 Shear Ring and Shear Stud Calculations – USCS Units**

| Calculation | Units | Pile 1.a | Pile 2.a | Pile 3.a |
|---|---|---|---|---|
| ***Shear Ring Calculations*** | | | | |
| Applied Load, P | kips | 600 | 3000 | 8000 |
| Confinement Coefficient, k | | 4 | 4 | 4 |
| Concrete Capacity at Shear Ring, $P_{cm}$ | kips | 448 | 1117 | 2253 |
| Shear Ring Cross Sectional Area, $A_{mech}$ | $inch^2$ | 0.25 | 0.5625 | 1 |
| Distance between Hinges, $l_f$ | inch | 2.0 | 1.8 | 1.6 |
| Height of Deformation, $l_e$ | inch | 7.0 | 6.4 | 5.6 |
| Lateral Force Capacity, $P_{sm}$ | kips | 563 | 1450 | 3948 |
| Strut Angle | degrees | 45 | 45 | 45 |
| Axial Force Capacity, $P_{sm\text{-}axial}$ | kips | 563 | 1450 | 3948 |
| Failure Mode | | Conc Crush | Conc Crush | Conc Crush |
| Quantity of Shear Rings | | 1.3 | 2.1 | 2.0 |
| Factor of Safety | | 2 | 2 | 2 |
| Final Quantity of Shear Rings | | 3 | 4 | 4 |
| Spacing between PH Zones, $l_r$ | inch | 11.3 | 19.3 | 39.5 |
| Shear Ring Spacing, s for PH Formation | | 15.3 | 23.0 | 42.8 |
| Shear Ring Spacing, s for Conc Crush | inch | 13.0 | 13.0 | 13.0 |
| ***Shear Stud Calculations*** | | | | |
| Shear Stud Diameter, $D_{stud}$ | inch | 0.5 | 0.75 | 1 |
| Shear Stud Length, $L_{stud}$ | inch | 2 | 3 | 4 |
| Weld Size (Throat) | inch | 0.125 | 0.1875 | 0.25 |
| Electrode, $F_{exx}$ | ksi | 70 | 70 | 70 |
| Shear Stud Weld Capacity, $V_{stud}$ | kips | 6.2 | 13.9 | 24.7 |
| Factor of Safety | | 2 | 2 | 2 |
| Quantity of Shear Studs | | 97 | 216 | 323 |
| Quantity of Shear Studs with FS | | 194 | 431 | 647 |
| Total Capacity with FS | kips | 1200 | 6000 | 16000 |
| Spacing (Vertical) | inch | 6 | 9 | 12 |
| Spacing (Radial) | inch | 6.28 | 9.42 | 11.31 |
| Studs per row | | 15 | 20 | 30 |
| Number of rows | | 13 | 22 | 22 |
| Final Quantity of Shear Studs | | 195 | 440 | 660 |

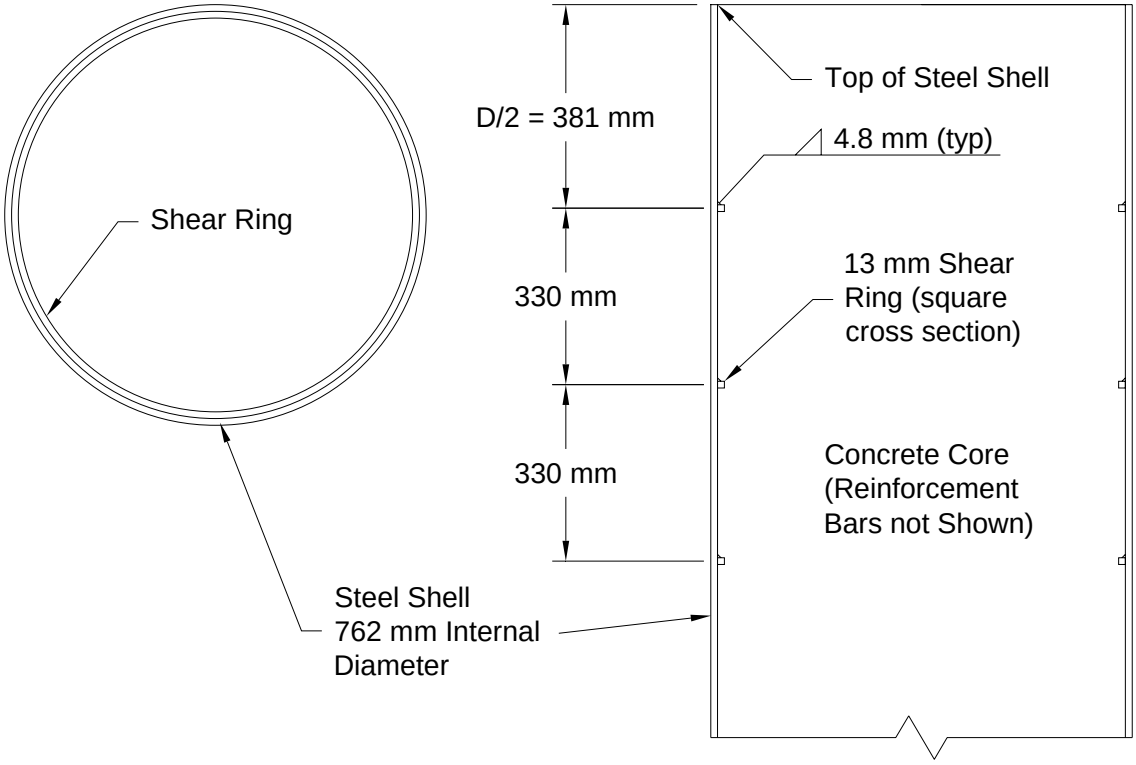


**Figure 7.6 Shear Ring Placement – 0.76 m Diameter (Pile 1.a)**

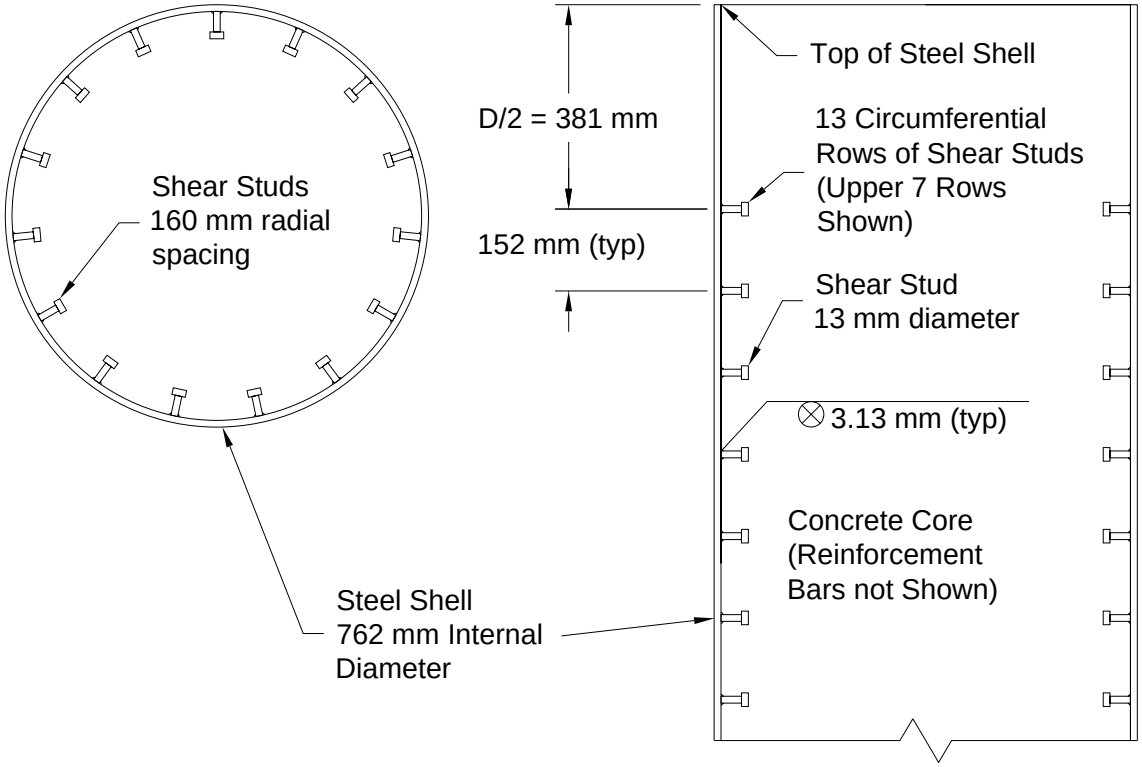


**Figure 7.7 Shear Stud Placement – 0.76 m Diameter (Pile 1.a)**

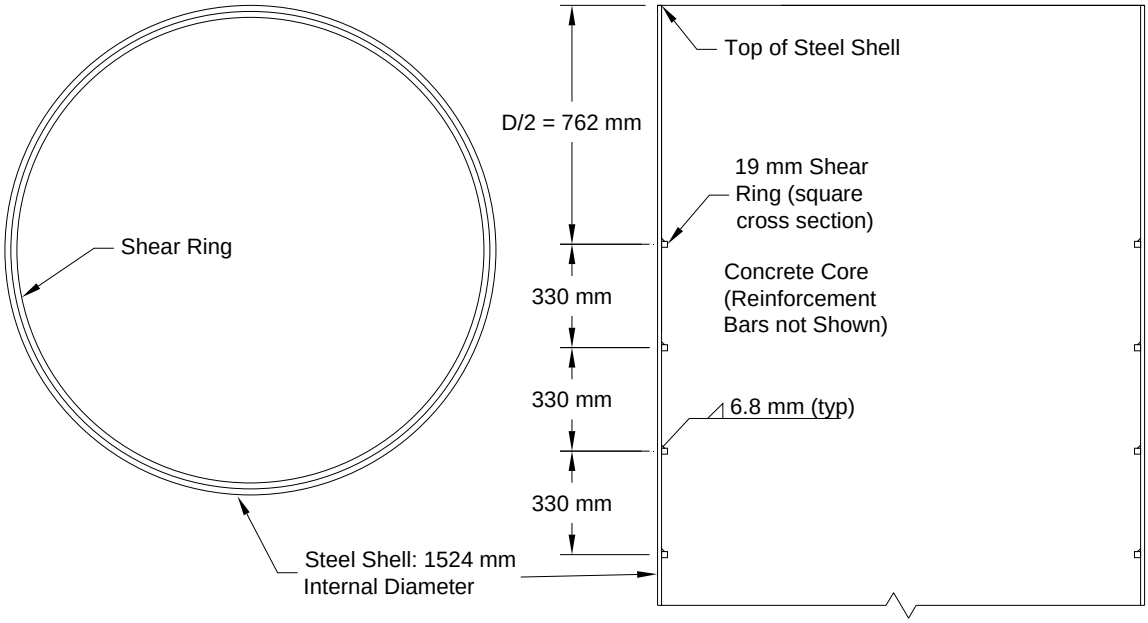


**Figure 7.8 Shear Ring Placement – 1.52 m Diameter (Pile 2.a)**

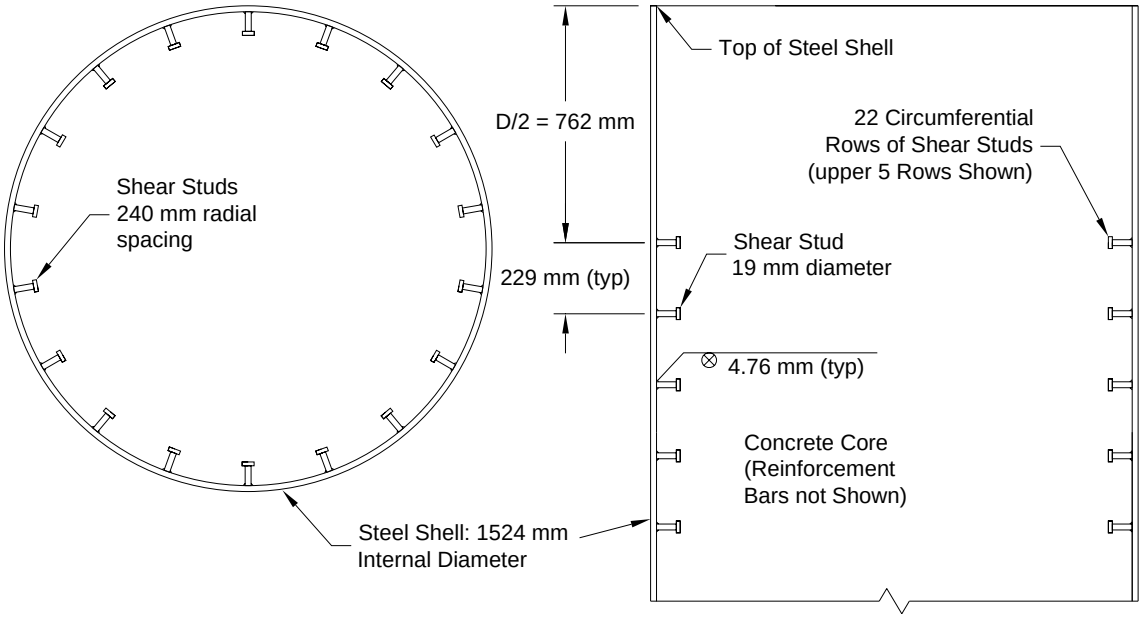


**Figure 7.9 Shear Stud Placement – 1.52 m Diameter (Pile 2.a)**

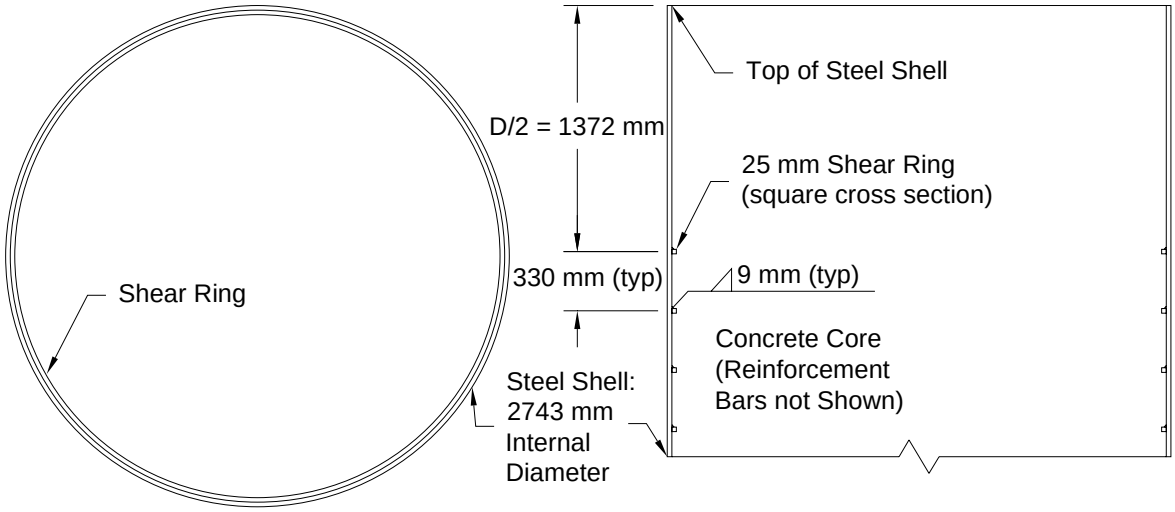


**Figure 7.10 Shear Ring Placement – 2.7 m Diameter (Pile 3.a)**

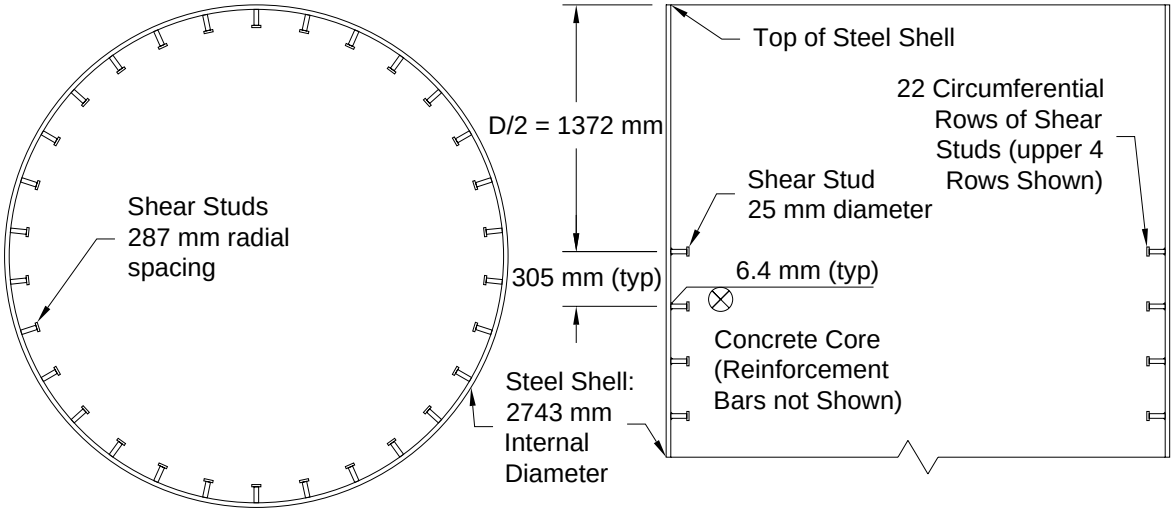


**Figure 7.11 Shear Stud Placement – 2.7 m Diameter (Pile 3.a)**

### 7.3.2 Mechanism Design Example with Surface Bond

The three pile designs analyzed in the previous section will be redone to include the axial force transfer through the surface bond between the steel shell internal surface and the reinforced concrete core. The calculation procedure for Pile 1.b will be explained in detail whereas calculated values will be shown in Tables 7.7 (SI units) and 7.8 (USCS units) for the other two pile designs. Calculations for the mechanism design will be

similar to the previous example; however, the contribution of the surface bond will result in a lower axial force transfer through the mechanisms.

The axial force transfer through the surface bond, $P_{fric}$, is estimated through a strain compatibility condition between the steel shell and concrete core as stated below. After this strain is obtained the concrete core will slip.

$$P_{fric} = E_c \cdot \varepsilon_{sc} \cdot A_{core} \tag{3.7}$$

In the surface bond equation, the cross sectional area of the concrete core is $A_{core}$, the modulus of elasticity for concrete is $E_c$ and the strain at compatibility is $\varepsilon_{sc}$. A value of 0.00015 is used for the compatibility strain. Substitution of the given design values results in the following axial force transfer through surface bond:

$$P_{fric} = (21523MPa) \cdot (0.00015) \cdot (0.456m^2) = 1.5MN$$

The axial force transferred through the surface bond, $P_{fric}$, is subtracted from the applied force, $P$, to determine the axial force transfer through mechanism, $P_{mech}$, as stated:

$$P_{mech} = P - P_{fric} \tag{7.7}$$

Substitution of the given design values results in:

$$P_{mech} = 2.7MN - 1.5MN = 1.2MN$$

In this case the surface bond transfers an axial force of 1.5 MN (331 kips) which is greater than the axial force transferred through the mechanisms of 1.2 MN (269 kips). Accounting for the surface bond clearly results in a reduced axial force transfer through the mechanisms and a reduced quantity of mechanisms. However, the effectiveness of the surface bond requires a clean steel shell internal surface. A tremie pour condition (with a bentonite slurry residue on the steel shell) will diminish the surface bond as would the presence of any other drilling fluid, soil or mud.

Shrinkage is not expected to occur such that it would diminish the surface bond as shown by the test results of Chapter 5 at a 0.6 m (24 in.) diameter. If shrinkage did occur then water would have to escape from the core in the radial and vertical directions. This

is prevented by the steel shell confinement. In two of the test units with shear rings a high water to cement ratio was found at the shear ring locations upon removal of the steel shell (after testing). This moist concrete was found as shown in Figures 5.38 and 5.44. In both cases water was trapped by the steel shell and concrete core resulting in a band of moist concrete at the shear ring locations. Additional tests of large diameter CISS piles are recommended to verify that shrinkage is not an issue.

The mechanisms are designed for an axial force of 1.2 MN (269 kips) using the same procedure as the previous example in which surface bond was not accounted for. Calculated values are shown in Table 7.7 for SI units and in Table 7.8 for USCS units. The resulting mechanism design options are either use one shear ring or use 90 shear studs (15 shear studs in 6 circumferential rows). This represents a reduction in the quantity of shear studs or shear rings by over 50% in comparison to the design which did not account for the surface bond. Mechanism designs are shown in Figure 7.12 for shear rings and Figure 7.13 for shear studs.

Calculations for the other two pile designs (Pile 2.b and Pile 3.b) with surface bond are also shown in Tables 7.7 and 7.8. In both examples the quantity of mechanisms is reduced due to the contribution of the surface bond. The quantity of shear rings was reduced by 50% for Pile 2.b and Pile 3.b. The quantity of shear studs was reduced by approximately 50% for both pile designs. The resulting mechanism design options for Pile 2.b are two shear rings with a spacing of 330 mm (13 in.) as shown in Figure 7.14 or 240 shear studs as shown in Figure 7.15. The resulting mechanism design options for Pile 3.b are two shear rings with a spacing of 330 mm (13 in.) as shown in Figure 7.16 or 308 shear studs as shown in Figure 7.17.

**Table 7.7 Shear Ring and Shear Stud Calculations with Surface Bond – SI Units**

| Calculation | Units | Pile 1.b | Pile 2.b | Pile 3.b |
|---|---|---|---|---|
| Applied Load, P | MN | 2.7 | 13.3 | 35.6 |
| ***Axial Force Transferred through Surface Bond*** | | | | |
| Concrete Core Area | $mm^2$ | 456036.7 | 1824146.9 | 5910236.0 |
| Compatibility Strain $\varepsilon_c$ | | 0.00015 | 0.00015 | 0.00015 |
| Modulus of Elasticity for Concrete, $E_c$ | MPa | 21523 | 21523 | 21523 |
| Axial Force Transferred through Bond, $P_{fric}$ | MN | 1.5 | 5.9 | 19.1 |
| Axial Force Transferred through Mechanisms, $P_{mech}$ | MN | 1.2 | 7.5 | 16.5 |
| ***Shear Ring Calculations*** | | | | |
| Confinement Coefficient, k | | 4 | 4 | 4 |
| Concrete Capacity at Shear Ring, $P_{cm}$ | MN | 2.0 | 5.0 | 10.0 |
| Shear Ring Cross Sectional Area, $A_{mech}$ | $mm^2$ | 161 | 363 | 645 |
| Distance between Hinges, $l_f$ | mm | 51 | 47 | 42 |
| Height of Deformation, $l_e$ | mm | 178 | 163 | 142 |
| Lateral Force Capacity, $P_{sm}$ | MN | 2.5 | 6.4 | 17.6 |
| Strut Angle | degrees | 45 | 45 | 45 |
| Axial Force Capacity, $P_{sm\text{-}axial}$ | MN | 2.5 | 6.4 | 17.6 |
| Failure Mode | | Conc Crush | Conc Crush | Conc Crush |
| Quantity of Shear Rings | | 0.5 | 1.2 | 0.9 |
| Factor of Safety | | 2 | 2 | 2 |
| Final Quantity of Shear Rings | | 1 | 2 | 2 |
| Spacing between PH Zones, $l_r$ | mm | 286 | 491 | 1003 |
| Shear Ring Spacing, s for PH Formation | mm | 387 | 585 | 1086 |
| Shear Ring Spacing, s for Conc Crush | mm | 330 | 330 | 330 |
| ***Shear Stud Calculations*** | | | | |
| Shear Stud Diameter, $D_{stud}$ | mm | 12.7 | 19.1 | 25.4 |
| Shear Stud Length, $L_{stud}$ | mm | 50.8 | 76.2 | 101.6 |
| Weld Size (Throat) | mm | 3.175 | 4.763 | 6.35 |
| Electrode, $F_{exx}$ | MPa | 482.6 | 482.6 | 482.6 |
| Shear Stud Weld Capacity, $V_{stud}$ | MN | 0.028 | 0.062 | 0.110 |
| Factor of Safety | | 2 | 2 | 2 |
| Quantity of Shear Studs | | 43 | 120 | 150 |
| Quantity of Shear Studs with FS | | 87 | 241 | 300 |
| Capacity | MN | 2.4 | 14.9 | 33.0 |
| Spacing (Vertical) | mm | 152 | 229 | 305 |
| Spacing (Radial) | mm | 160 | 239 | 308 |
| Studs per row | | 15 | 20 | 28 |
| Number of rows | | 6 | 12 | 11 |
| Final Quantity of Shear Studs | | 90 | 240 | 308 |

**Table 7.8 Shear Ring and Shear Stud Calculations with Surface Bond – USCS Units**

| Calculation | Units | Pile 1.b | Pile 2.b | Pile 3.b |
|---|---|---|---|---|
| Applied Load, P | kips | 600 | 3000 | 8000 |
| ***Axial Force Transferred through Surface Bond*** | | | | |
| Concrete Core Area | $inch^2$ | 706.9 | 2827.4 | 9160.9 |
| Compatibility Strain $\varepsilon_c$ | | 0.00015 | 0.00015 | 0.00015 |
| Modulus of Elasticity for Concrete, $E_c$ | ksi | 3122 | 3122 | 3122 |
| Axial Force Transferred through Bond, $P_{fric}$ | kips | 331.0 | 1324.1 | 4290.1 |
| Axial Force Transferred through Mechanisms, $P_{mech}$ | kips | 269.0 | 1675.9 | 3709.9 |
| ***Shear Ring Calculations*** | | | | |
| Confinement Coefficient, k | | 4 | 4 | 4 |
| Concrete Capacity at Shear Ring, $P_{cm}$ | kips | 448 | 1117 | 2253 |
| Shear Ring Cross Sectional Area, $A_{mech}$ | $inch^2$ | 0.25 | 0.5625 | 1 |
| Distance between Hinges, $l_f$ | inch | 2.0 | 1.8 | 1.6 |
| Height of Deformation, $l_e$ | inch | 7.0 | 6.4 | 5.6 |
| Lateral Force Capacity, $P_{sm}$ | kips | 563 | 1450 | 3948 |
| Strut Angle | degrees | 45 | 45 | 45 |
| Axial Force Capacity, $P_{sm\text{-}axial}$ | kips | 563 | 1450 | 3948 |
| Failure Mode | | Conc Crush | Conc Crush | Conc Crush |
| Quantity of Shear Rings | | 0.5 | 1.2 | 0.9 |
| Factor of Safety | | 2 | 2 | 2 |
| Final Quantity of Shear Rings | | 1 | 2 | 2 |
| Spacing between PH Zones, $l_r$ | inch | 11.3 | 19.3 | 39.5 |
| Shear Ring Spacing, s for PH Formation | inch | 15.3 | 23.0 | 42.8 |
| Shear Ring Spacing, s for Conc Crush | inch | 13 | 13 | 13 |
| ***Shear Stud Calculations*** | | | | |
| Shear Stud Diameter, $D_{stud}$ | inch | 0.5 | 0.75 | 1 |
| Shear Stud Length, $L_{stud}$ | inch | 2 | 3 | 4 |
| Weld Size (Throat) | inch | 0.125 | 0.1875 | 0.25 |
| Electrode, $F_{exx}$ | ksi | 70 | 70 | 70 |
| Shear Stud Weld Capacity, $V_{stud}$ | kips | 6.2 | 13.9 | 24.7 |
| Factor of Safety | | 2 | 2 | 2 |
| Quantity of Shear Studs | | 43 | 120 | 150 |
| Quantity of Shear Studs with FS | | 87 | 241 | 300 |
| Capacity | kips | 538 | 3352 | 7420 |
| Spacing (Vertical) | inch | 6 | 9 | 12 |
| Spacing (Radial) | inch | 6.3 | 9.4 | 12.1 |
| Studs per row | | 15 | 20 | 28 |
| Number of rows | | 6 | 12 | 11 |
| Final Quantity of Shear Studs | | 90 | 240 | 308 |

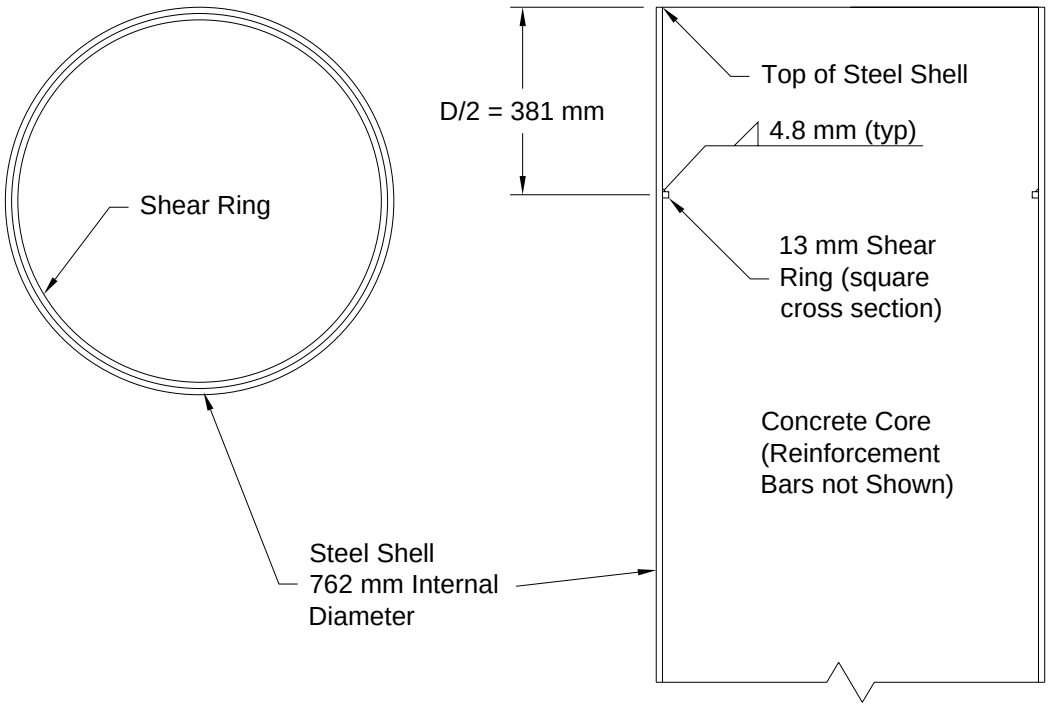


**Figure 7.12 Shear Ring Placement – 0.76 m Diameter (Pile 1.b) with Surface Bond**

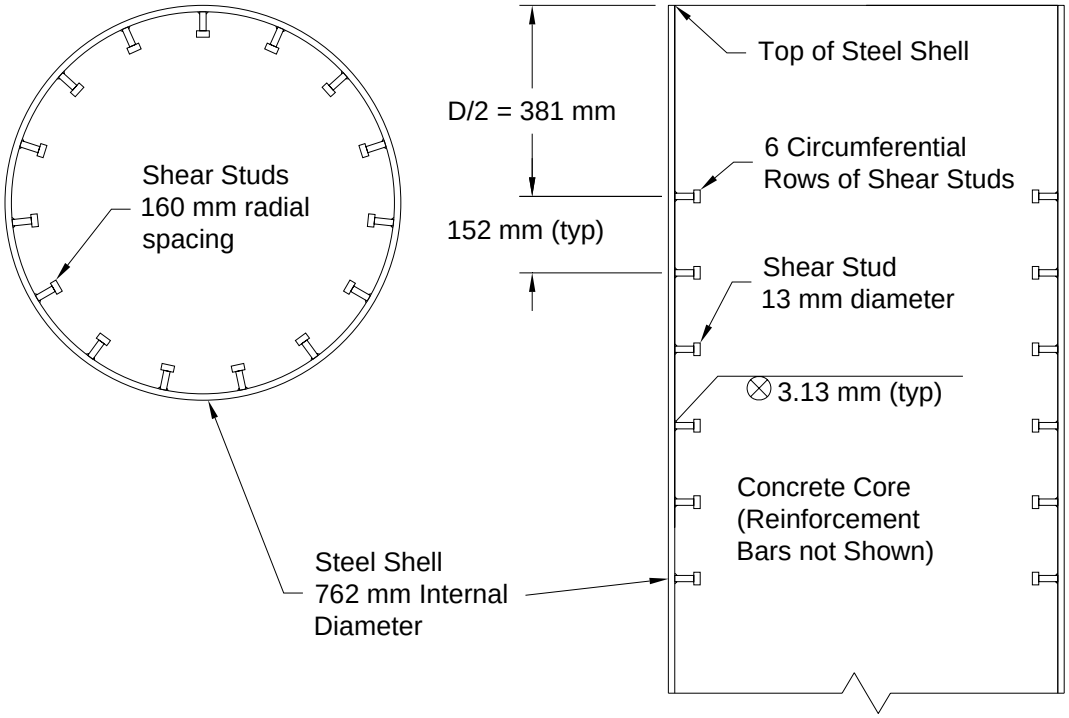


**Figure 7.13 Shear Stud Placement – 0.76 m Diameter (Pile 1.b) with Surface Bond**

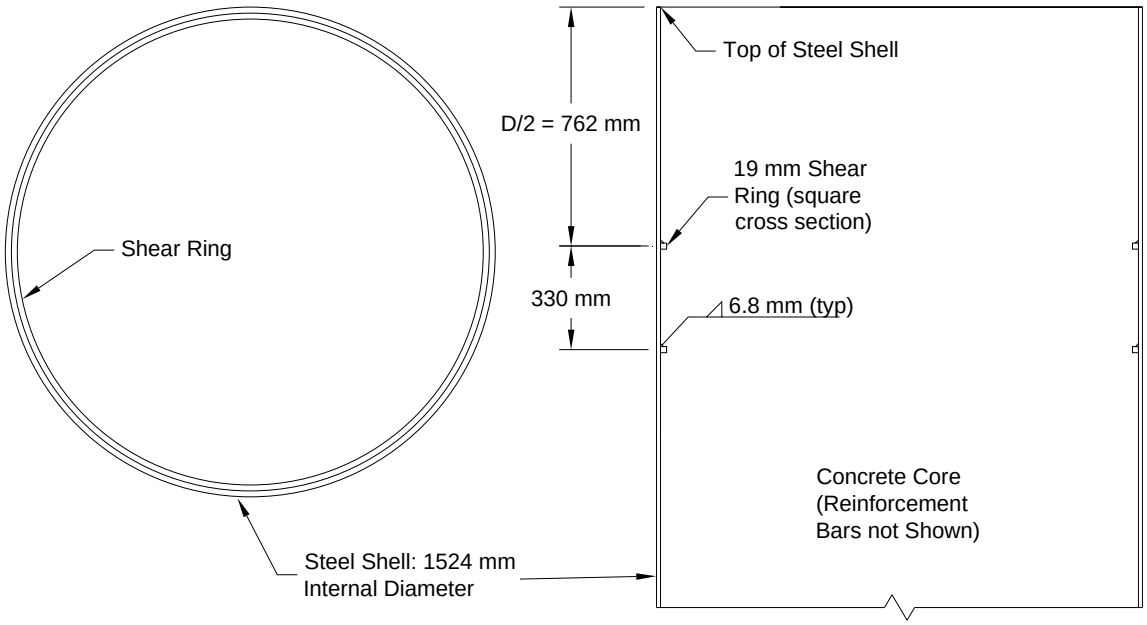


**Figure 7.14 Shear Ring Placement – 1.52 m Diameter (Pile 2.b) with Surface Bond**

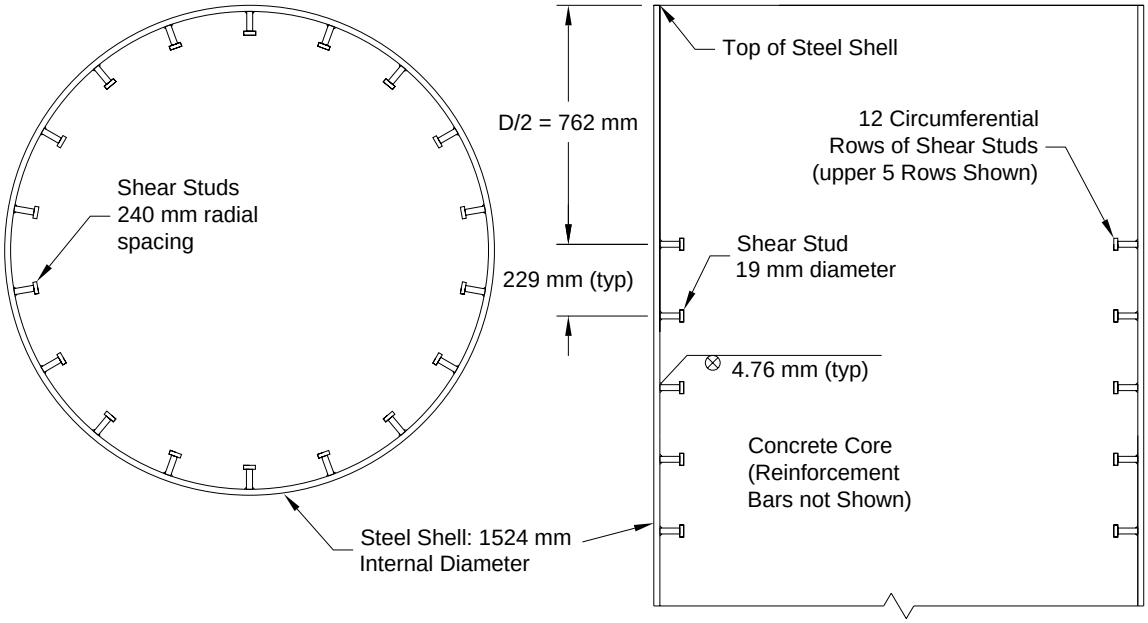


**Figure 7.15 Shear Stud Placement – 1.52 m Diameter (Pile 2.b) with Surface Bond**

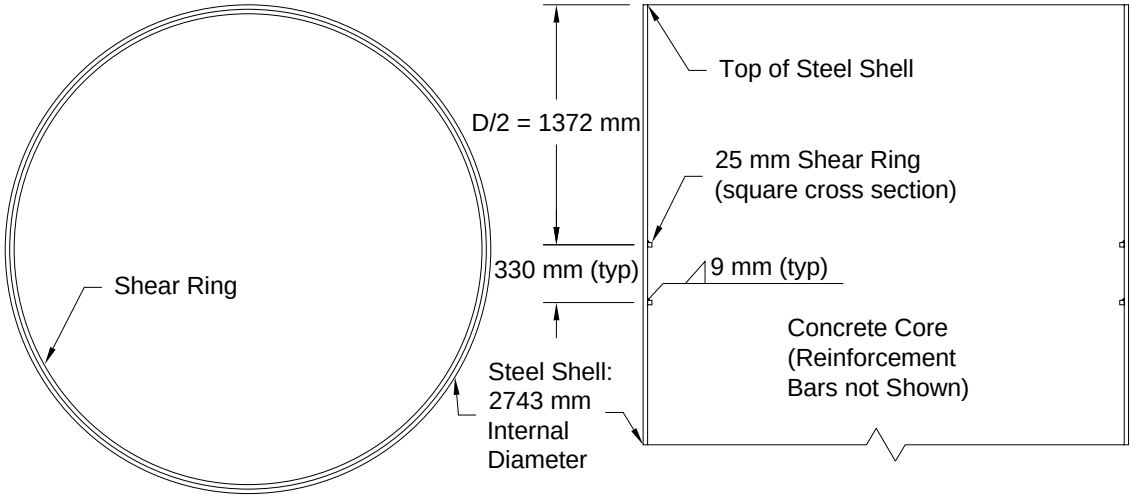


**Figure 7.16 Shear Ring Placement – 2.7 m Diameter (Pile 3.b) with Surface Bond**

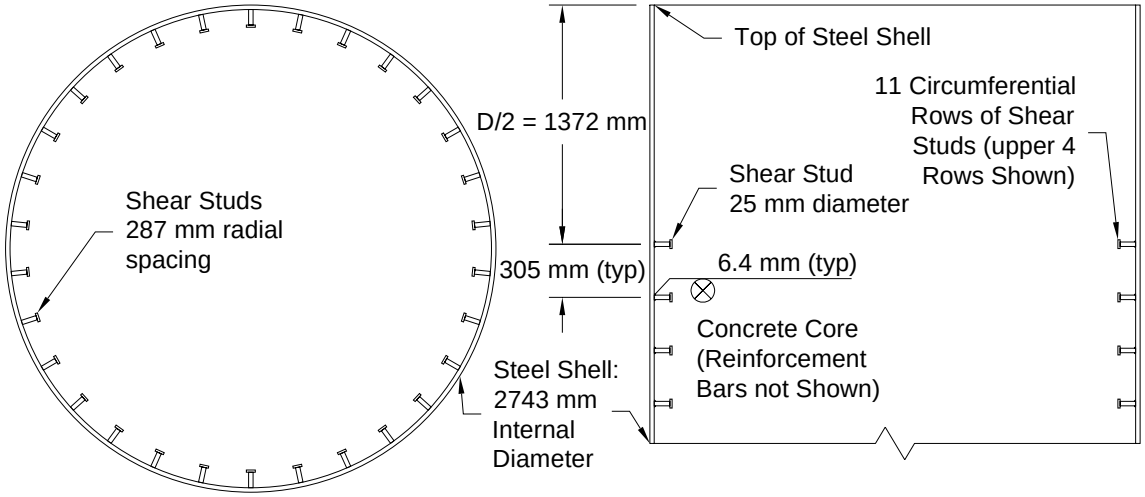


**Figure 7.17 Shear Stud Placement – 2.7 m Diameter (Pile 3.b) with Surface Bond**

### 7.3.3 Mechanism Design Summary

Accounting for the axial force transfer through the surface bond has a noticeable effect on the mechanism design with typical mechanism quantity reductions of 50% for the given loads. Table 7.9 provides a summary of the mechanism designs selected for the pile design examples presented in this section.

**Table 7.9 Mechanism Design Summary**

**Pile Design Example**

| Property | 1.a | 1.b | 2.a | 2.b | 3.a | 3.b |
|---|---|---|---|---|---|---|
| Diameter (mm) | 762 | 762 | 1524 | 1524 | 2743 | 2743 |
| Diameter (inch) | 60 | 60 | 80 | 80 | 108 | 108 |
| D/t | 60 | 60 | 80 | 80 | 108 | 108 |
| Surface Bond | No | Yes | No | Yes | No | Yes |
| Shear Ring Quantity | 3 | 1 | 4 | 2 | 4 | 2 |
| Shear Stud Quantity | 195 | 90 | 440 | 240 | 660 | 308 |
| Studs per Row | 15 | 15 | 20 | 20 | 30 | 28 |
| Number of Rows | 13 | 6 | 22 | 12 | 22 | 11 |

## 7.4 Chapter Summary

This chapter presents the design procedure, design examples and mechanism recommendations. The design examples demonstrated the procedure to determine the failure mode, design and quantity of circumferential mechanisms, design of distributed mechanisms, and the effect of surface bond. The inclusion of the axial force transfer through the surface bond reduces the quantity of mechanisms; however, the steel shell internal surface must be clean to allow for this form of axial force transfer.

# 8 SUMMARY AND CONCLUSIONS

The transfer of axial force through mechanisms fixed to the steel shell of a CISS pile provides a reliable and effective bond. Researchers have conducted experimental and analytical studies into the bond between a steel shell and concrete core. However, published results are limited for the transfer of axial force through a mechanism. Published results for reversed cyclic axial loading are also non-existant. Published results are available for only one mechanism, tread plate; however, such results are available for only monotonic loading. Through experimental investigation and analytical investigation this research has provided a much needed examination into the axial force transfer within CISS piles. Numerous discoveries into the actual physics involved in the surface bond, and mechanisms have been made that will have an impact on future bridge foundation design. The key findings are presented in the following sections for the three main study areas of this research: surface bond, mechanisms, and prediction.

## 8.1 Surface Bond

Axial force transfer through the surface bond was found to be the result of an adhesive bond at the initial cyclic axial displacements and friction bond at greater cyclic axial displacements. An additional axial force transfer was found to occur through reinforcement bars, under axial tension, which exerted a lateral pressure on the steel shell. From the observations made in the experimental program, the following conclusions can be drawn:

1. The transfer of axial force through surface bond was found to consist of two non-additive components: adhesion and frictional bond. Adhesion was present at the initial cyclic axial displacements and resulted in peak axial forces in the hysteretic response, after which it was followed by a sharp decrease and replaced by a frictional bond. Frictional bond was maintained through large amplitude reversed axial displacement cycles.

2. The presence of a water-bentonite surface coating on the steel shell interior surface prevented the formation of an adhesive bond, and lowered the friction bond. The friction bond decreased an average of 27%, in axial compression, and 11% in axial tension. For design purposes, it is recommended that adhesion not be relied upon as field construction conditions of the steel shell inner surface can vary.

3. The initial adhesion bond was found to increase as the steel shell thickness increases for a constant steel shell diameter. The frictional bond stress for plain concrete and for expansive concrete was found to have no change with the steel shell thickness.

4. Expansive concrete was found to increase the initial adhesion; however, it did not significantly increase the frictional bond.

## 8.2 Mechanisms

The axial force transfer through mechanisms fixed to the steel shell interior surface was found to be highly effective, such that either the steel shell capacity was obtained or the concrete capacity was obtained. The axial force transferred through a single shear ring was highly effective, such that at high D/t ratios (of 128 and 94), the capacity was limited by circumferential yielding of the steel shell at the mechanism location. At a low D/t ratio (of 24) the capacity of the reinforced concrete core was obtained and the steel shell and shear rings remained elastic. The axial force transferred through two shear rings improved as the shear ring spacing increased to one half of the steel shell diameter. In two of the test units, moist concrete was found adjacent to the shear rings, however; these test units were still very effective at transferring axial compression and tension force. From the observations made in the experimental program, the following conclusions can be drawn:

1. Mechanisms which had a small weld contact area to the steel shell, such as shear studs and cross bar, initially increased the axial force transfer. However, these

mechanisms had a non-ductile performance after failure of the mechanism connections to the steel shell, leaving a friction bond.

2. The tread plate mechanism was found to be effective at initial cyclic axial displacements. However, at greater cyclic axial displacements the concrete between the treads crushed, which resulted in a deterioration of the performance, also a non-ductile behavior.

3. Test units with a mechanism welded circumferentially to the steel shell, such as the shear ring, welded reinforcement bar or weld bead, maintained a high axial force transfer at all axial displacements. These mechanisms had no significant deterioration in the axial force transfer despite a circumferential yielding and radial deformation of the steel shell at the mechanism location.

4. A single shear ring, within a steel shell with a D/t ratio of 24, was found to be highly effective at developing the capacity of the reinforced concrete core. The hysteretic response had an increase in axial force throughout all reversed cyclic axial displacements. At this D/t ratio, concrete sheared above and below the shear rings to heights typically corresponding to the applied axial compression and tension displacements.

5. Shear rings used in a steel shell with a high D/t ratio (128 or 94) were effective at transferring axial force despite a softening in the hysteretic response because of circumferential yielding of the steel shell at the mechanism location.

6. In test units with multiple shear rings, the axial force transfer was found to increase as the shear ring spacing increased to one half of the steel shell diameter. At a lesser shear ring spacing, concrete between the shear rings sheared and resulted in a performance, at greater axial displacements, similar to a test unit with a single shear ring.

7. In a design situation in which multiple shear rings are required, a minimum shear ring spacing of one half of the steel shell diameter is recommended.

8. Despite the presence of moist concrete surrounding the shear rings in two of the test units, the shear rings were still very effective at transferring axial compression and tension forces.

## 8.3 Finite Element Analysis

A finite element analysis model, developed in ABAQUS/EXPLICIT (ABAQUS, 2005), provided theoretical verification of the axial force transfer through the shear ring mechanism, as presented in Appendix Chapter 9. The three dimensional finite element models developed were highly computationally intensive, as this is a complex nonlinear contact analysis problem. The computational requirements for this analysis were so great that a coarse mesh was used and only monotonic response curves could be obtained with the available computing time and resources of the San Diego Supercomputer Center, at UCSD. The coarse mesh used resulted in stress concentrations in the steel shell, mechanism and concrete core; an undesirable modeling outcome and limitation. However, the finite element models were able to simulate the surface bond axial force transfer, as well as the crushing and deformation of concrete at the circumferential mechanism and circumferential yielding of the steel shell.

Despite the use of a coarse mesh, the finite element model provided reasonably accurate results for the cases in which a mechanism, such as the welded bar of Test Unit # 7 or shear ring of Test Unit # 5 were modeled with the steel shell at a high D/t ratio of 128. These models captured both the crushing and deformation of the concrete at the mechanism location. These models also captured the yielding and the out-of-plane deformation of the steel shell at the mechanism.

Finite element modeling of the shear ring within Test Unit # 17, at a D/t ratio of 24 proved to be a challenge due to the coarse mesh used. The response obtained does not fully match the experimental results. However the model behaved similarly to the test unit in that the steel shell remained elastic and the concrete within the core crushed at the

mechanism location. The use of a more refined mesh would provide a better prediction of the experimental result, for not only this model but for all models.

The modeling of the axial force transfer through surface bond was found to have a dependence on the D/t ratio. The friction property needed adjustment if a closer match to the experimental results for D/t ratios less than 128 is desired. However, this dependence of the friction property on the D/t ratio is a result of the coarse mesh used.

## 8.4 Prediction

A procedure to predict the axial force transfer was presented in Chapter 3 and compared to experimental results in Chapter 7. This procedure, which predicts the surface bond, and the axial force transfer through a circumferential mechanism, provided a reasonably accurate prediction of the experimental hysteretic responses. For circumferential mechanisms the prediction assumes a limiting axial force transfer occurs through either the formation of three plastic hinges in the steel shell-mechanism region distribution in the steel shell, or through attainment of the concrete capacity at the mechanism location.

## 8.5 Future Work

This experimental investigation and numerical study through finite element modeling have made many important findings. At the same time, these findings have generated additional questions into aspects of the axial force transfer through additional experimental study and finite element analysis. Areas of future experimental investigation and finite element analysis which could provide further insight into CISS pile design include:

1. Hysteretic response under combined axial load and bending,
2. Larger diameter piles under reversed cyclic axial loading,
3. Prevention of uncured concrete at the shear ring,
4. Effect of soil confinement on the shear ring through a full-scale field test,
5. Further finite element analysis of the axial force transfer through a circumferential mechanism

## 8.6 Concluding Comments

This research has provided much needed insight into the transfer of axial force from a reinforced concrete core into a steel shell through experimental investigation, finite element analysis and prediction. Finite element modeling of this complex nonlinear contact analysis problem proved to be a computational challenge. However, results were obtained, and in a majority of cases provided a reasonable axial compression envelope to the hysteresis and modeled the physical failure modes obtained experimentally. A method to predict the axial force transfer through the surface bond, and through circumferential mechanisms allows for a straightforward estimate of the effectiveness and failure mode. Additional concerns have developed as a result of the findings, and will likely keep researchers throughout the world busy for some time to come.

For design purposes a mechanism fixed circumferentially to the steel shell is recommended because of its ductile performance. A weld bead should be considered for piles with a diameter less than 0.91 m (36 inch). For CISS piles with a diameter greater than 0.91 m (36 inch) a shear ring or welded reinforcement bar is recommended. The use of expansive concrete or mechanisms distributed throughout the steel shell internal surface (such as shear studs, cross bars, or tread plate) is not recommended.

# 9 APPENDIX - STRAIN PROFILES

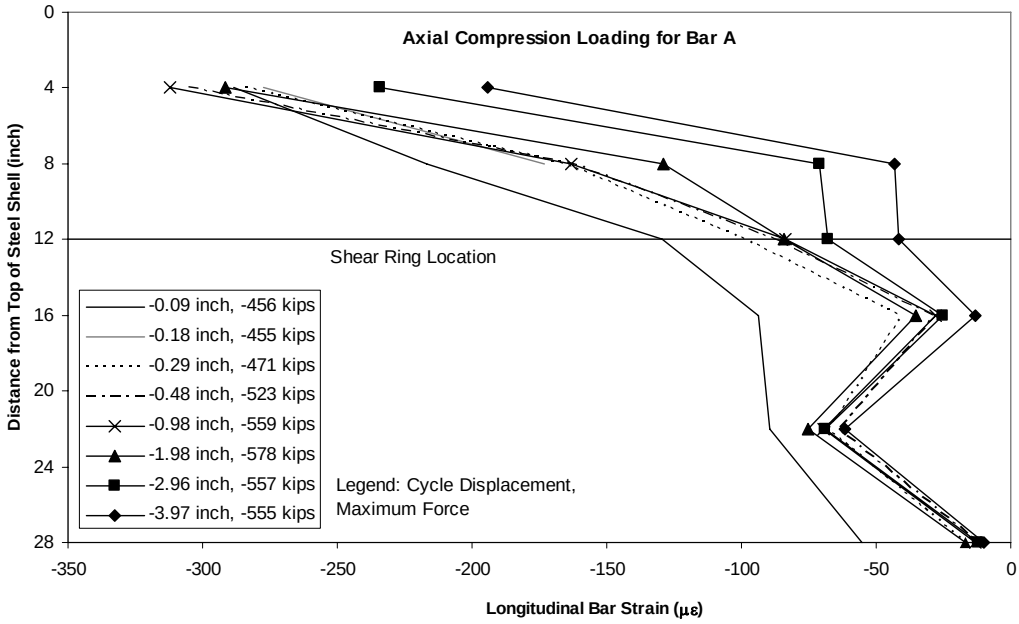


**Figure 9.1 Longitudinal Bar Strain Profiles at Peak Cyclic Axial Compression Forces for Test Unit # 16, Reinforcement Bar A**

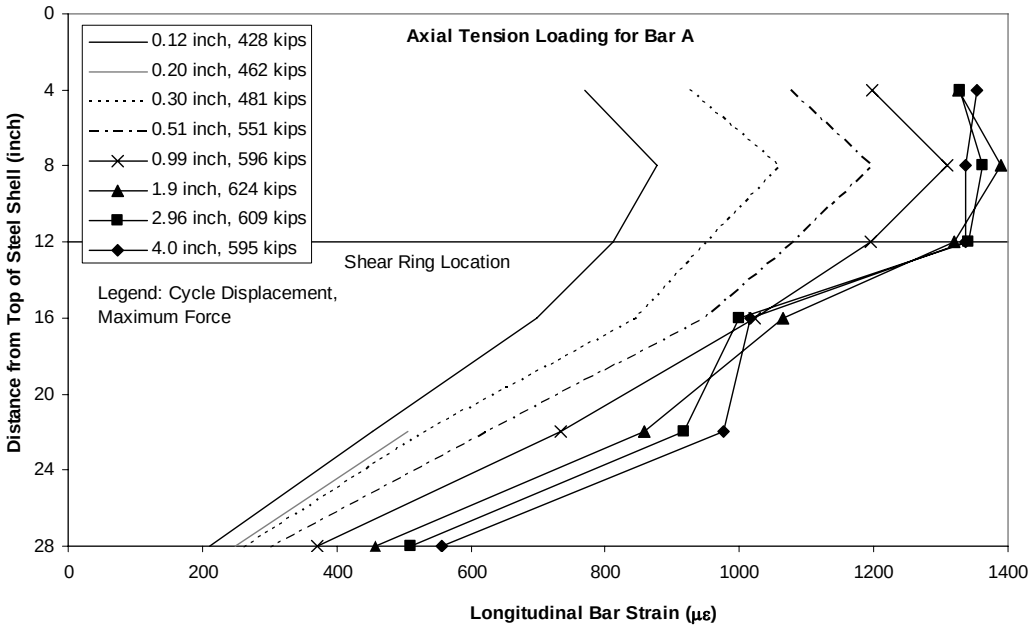


**Figure 9.2 Longitudinal Bar Strain Profiles at Peak Cyclic Axial Tension Forces for Test Unit # 16, Reinforcement Bar A**

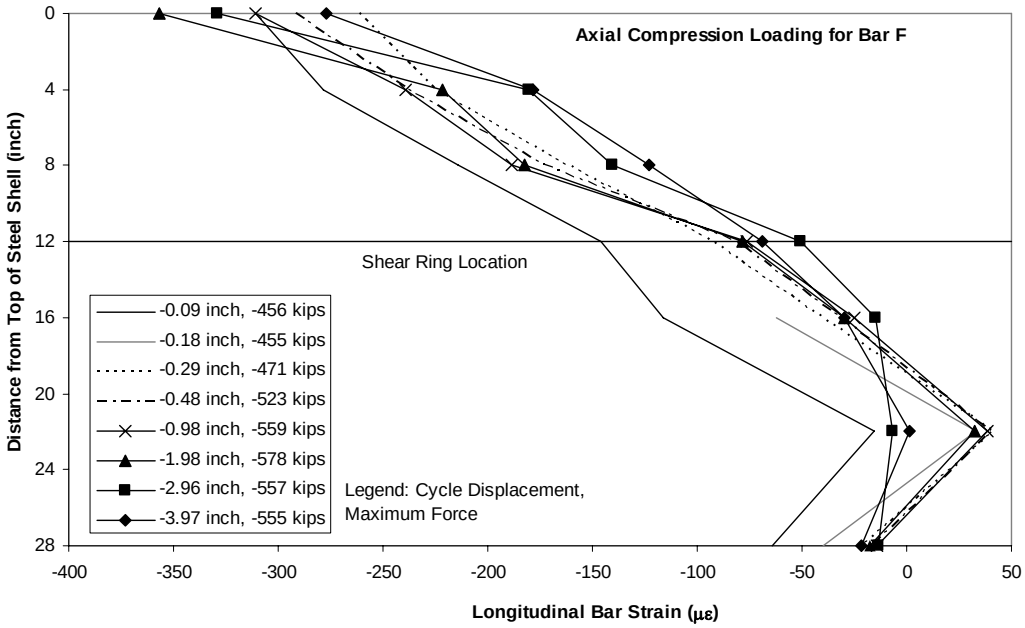


**Figure 9.3 Longitudinal Bar Strain Profiles at Peak Cyclic Axial Compression Forces for Test Unit # 16, Reinforcement Bar F**

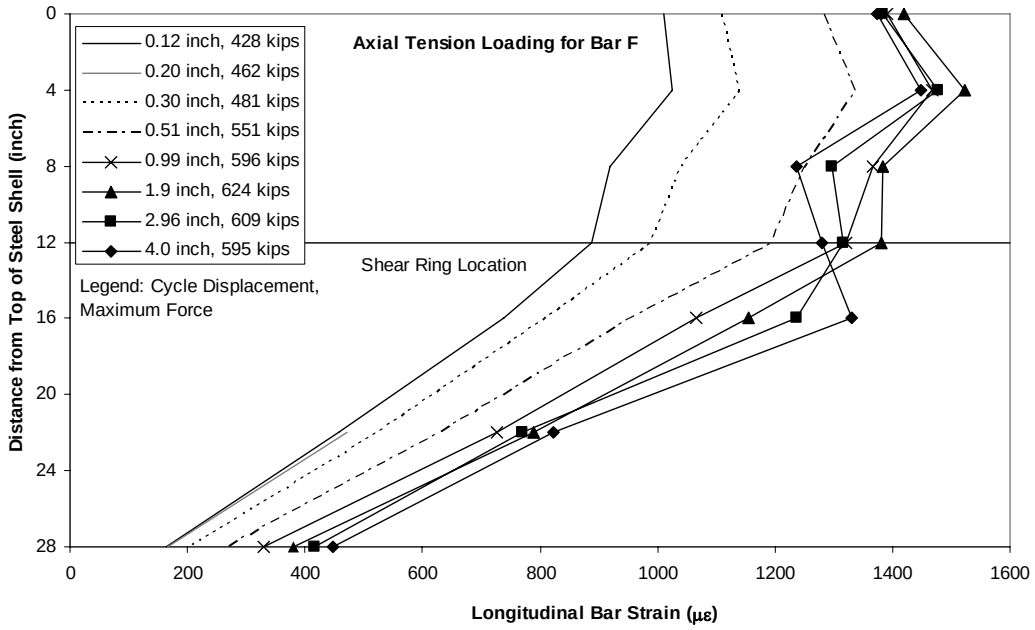


**Figure 9.4 Longitudinal Bar Strain Profiles at Peak Cyclic Axial Tension Forces for Test Unit # 16, Reinforcement Bar F**

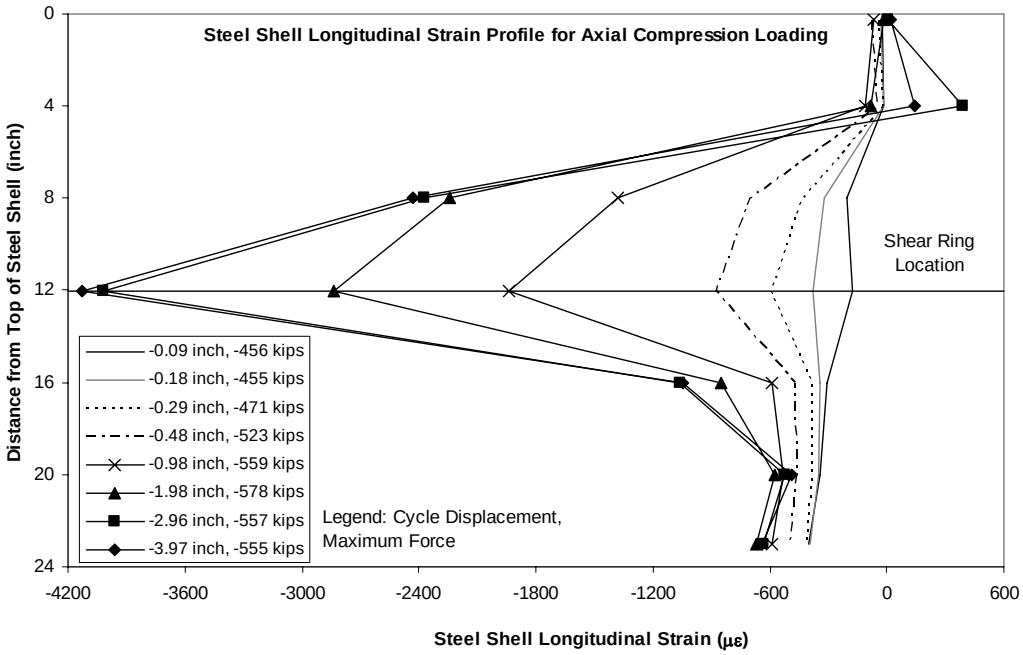


**Figure 9.5 Steel Shell Longitudinal Strain Profiles at Peak Cyclic Axial Compression Forces for Test Unit # 16**

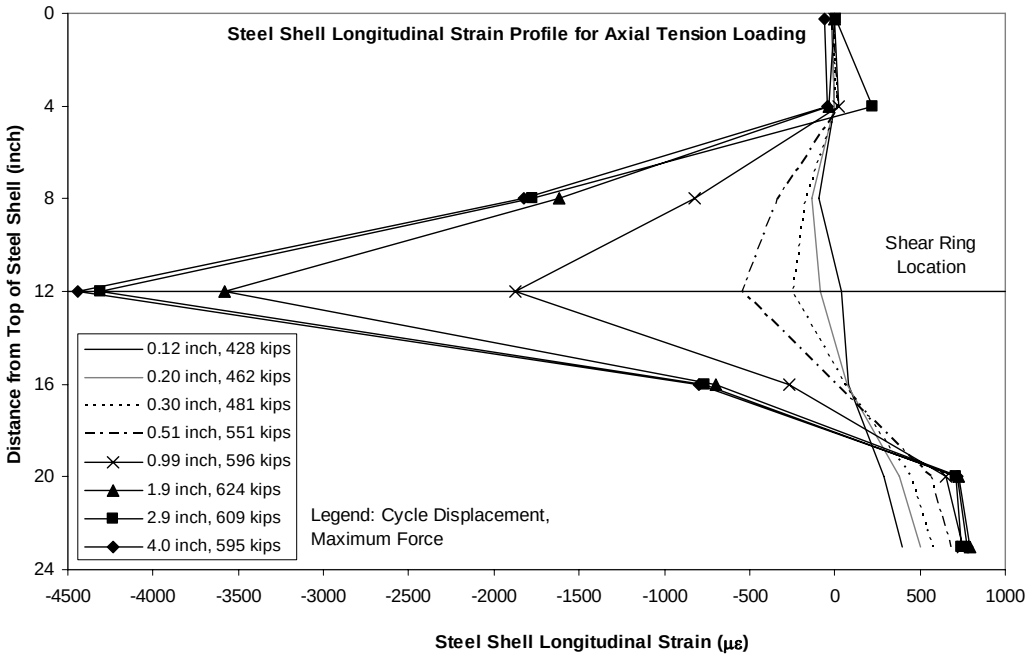


**Figure 9.6 Steel Shell Longitudinal Strain Profiles at Peak Cyclic Axial Tension Forces for Test Unit # 16**

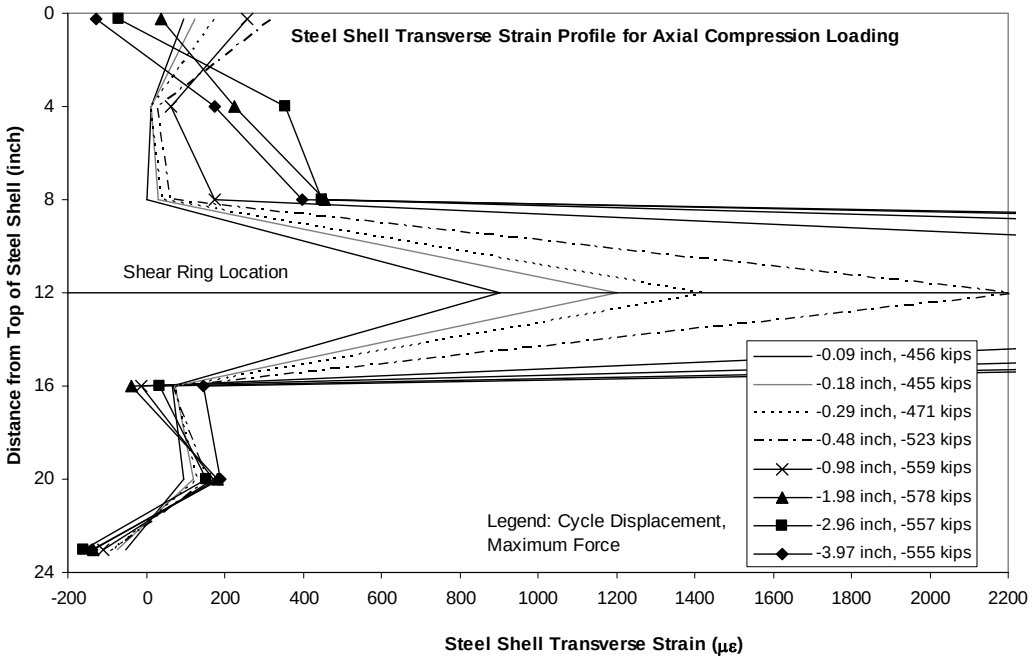


**Figure 9.7 Steel Shell Transverse Strain Profiles at Peak Cyclic Axial Compression Forces for Test Unit # 16**

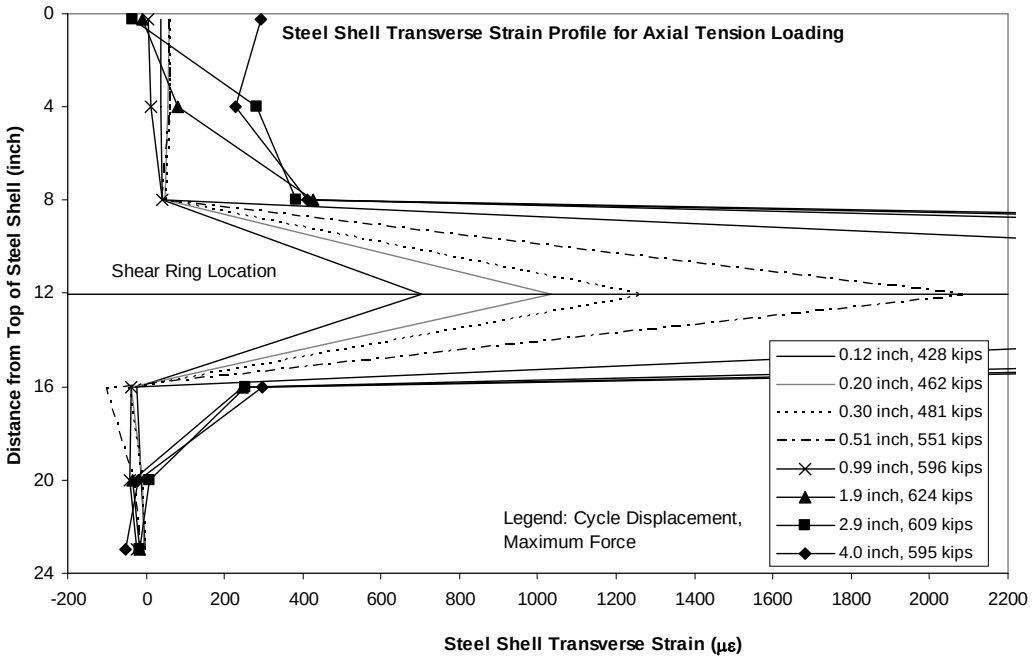


**Figure 9.8 Steel Shell Transverse Strain Profiles at Peak Cyclic Axial Tension Forces for Test Unit # 16**

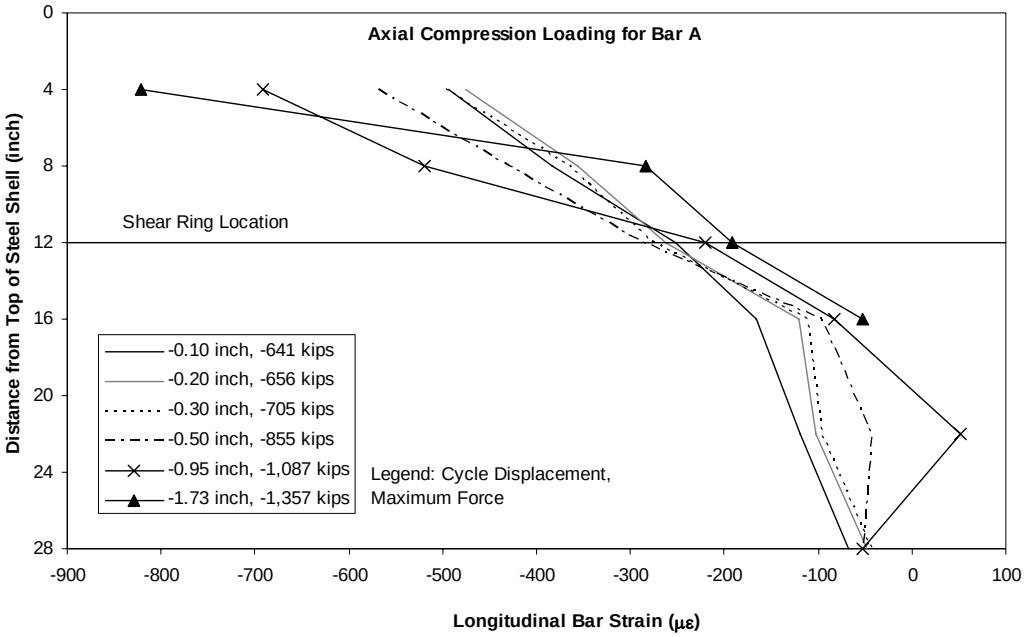


**Figure 9.9 Longitudinal Bar Strain Profiles at Peak Cyclic Axial Compression Forces for Test Unit # 17, Reinforcement Bar A**

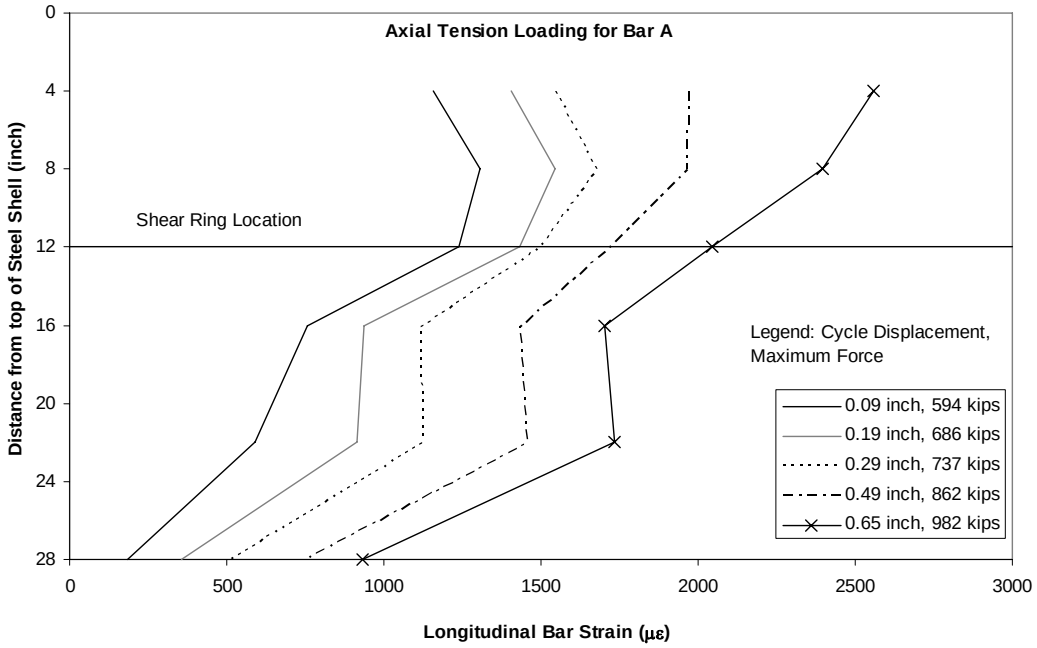


**Figure 9.10 Longitudinal Bar Strain Profiles at Peak Cyclic Axial Tension Forces for Test Unit # 17, Reinforcement Bar A**

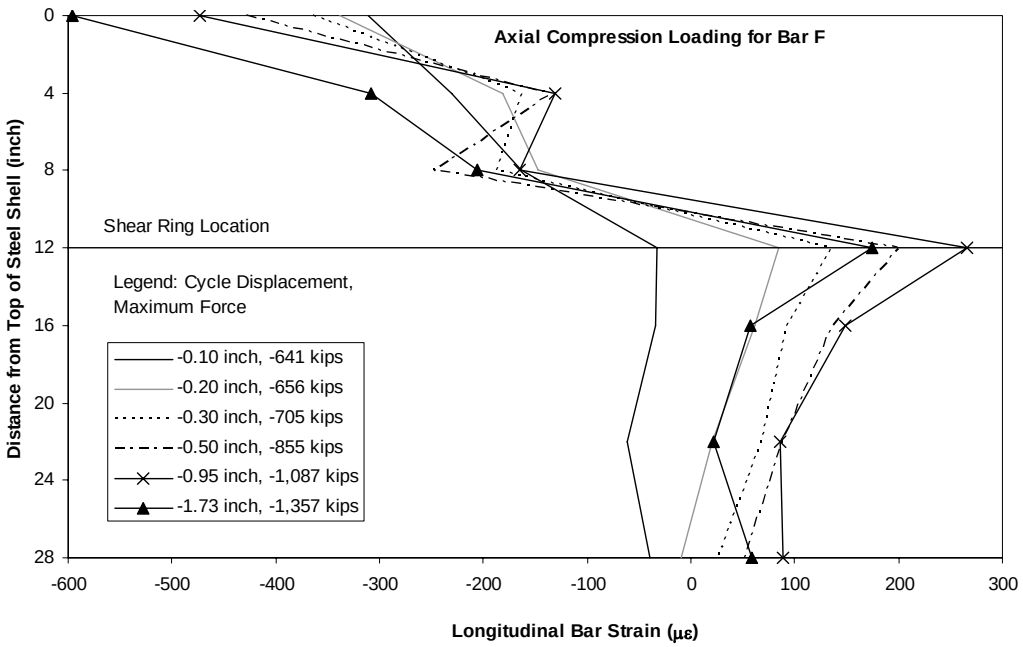


**Figure 9.11 Longitudinal Bar Strain Profiles at Peak Cyclic Axial Compression Forces for Test Unit # 17, Reinforcement Bar F**

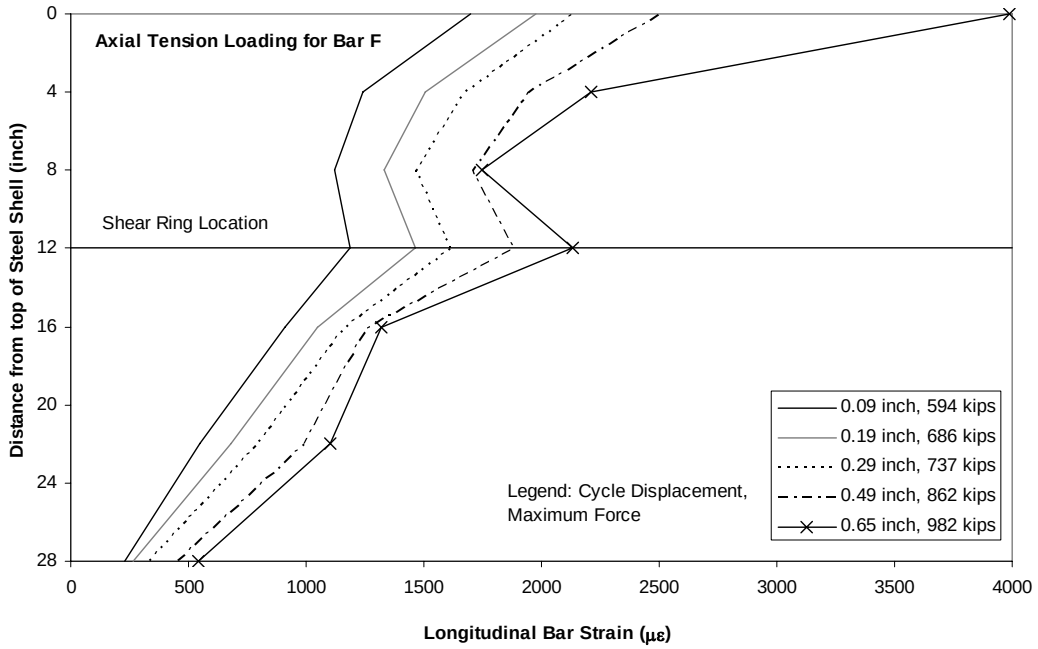


**Figure 9.12 Longitudinal Bar Strain Profiles at Peak Cyclic Axial Tension Forces for Test Unit # 17, Reinforcement Bar F**

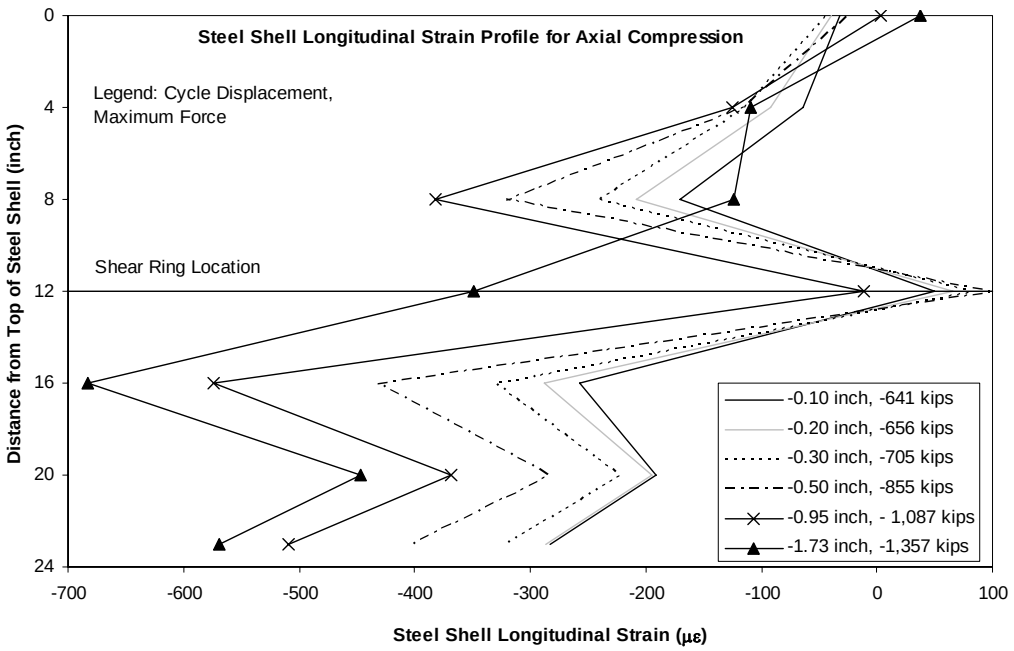


**Figure 9.13 Steel Shell Longitudinal Strain Profiles at Peak Cyclic Axial Compression Forces for Test Unit # 17**

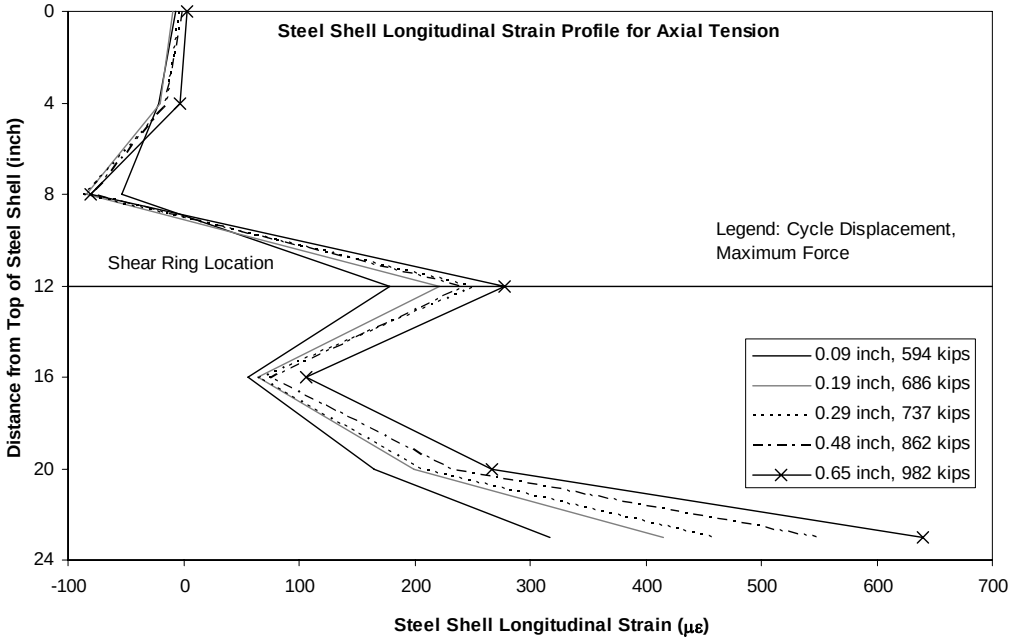


**Figure 9.14 Steel Shell Longitudinal Strain Profiles at Peak Cyclic Axial Tension Forces for Test Unit # 17**

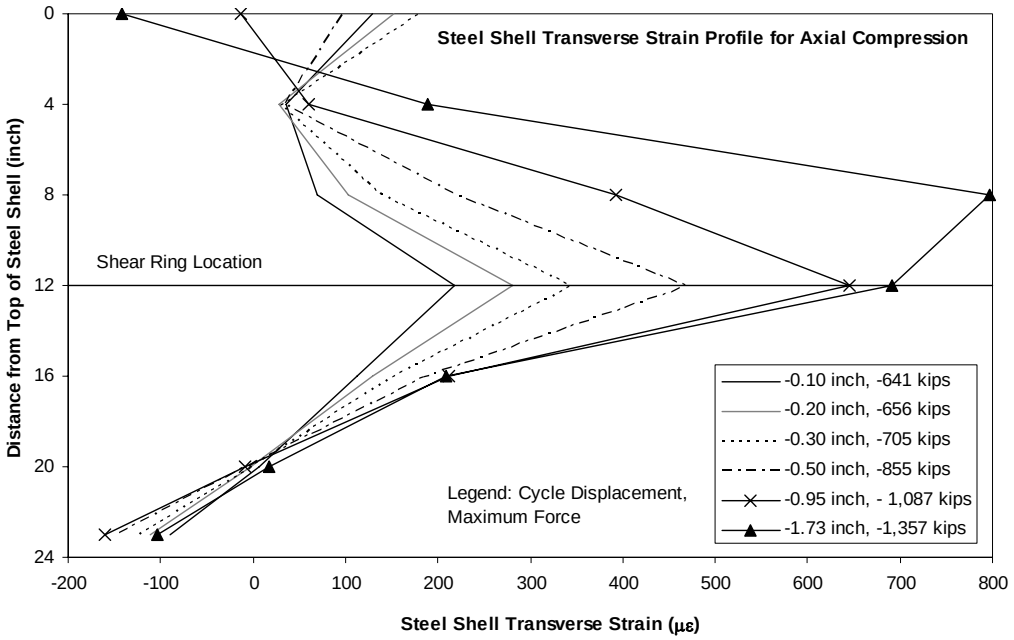


**Figure 9.15 Steel Shell Transverse Strain Profiles at Peak Cyclic Axial Compression Forces for Test Unit # 17**

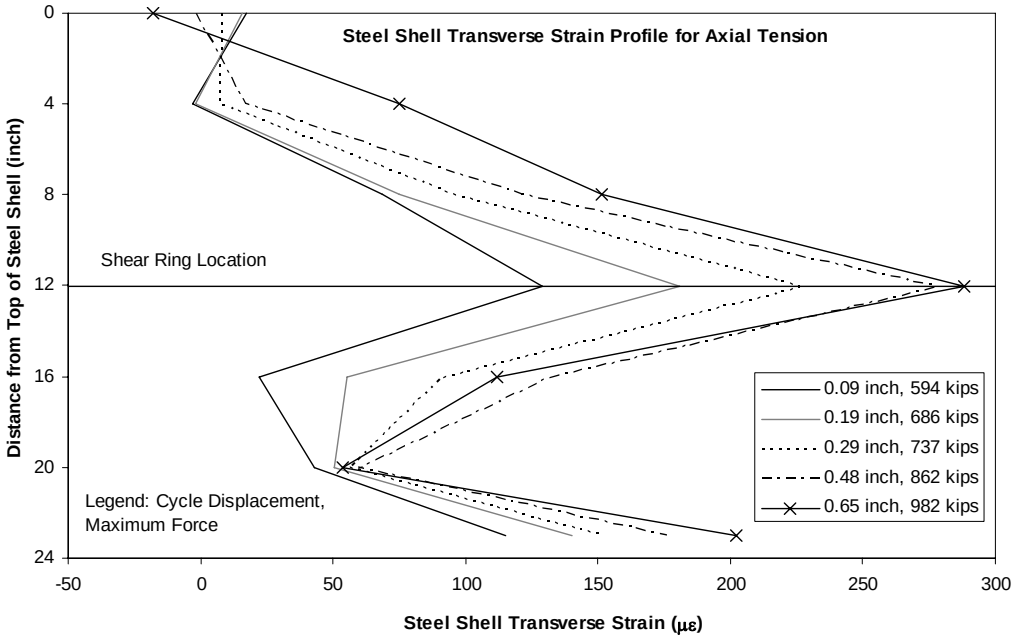


**Figure 9.16 Steel Shell Transverse Strain Profiles at Peak Cyclic Axial Tension Forces for Test Unit # 17**

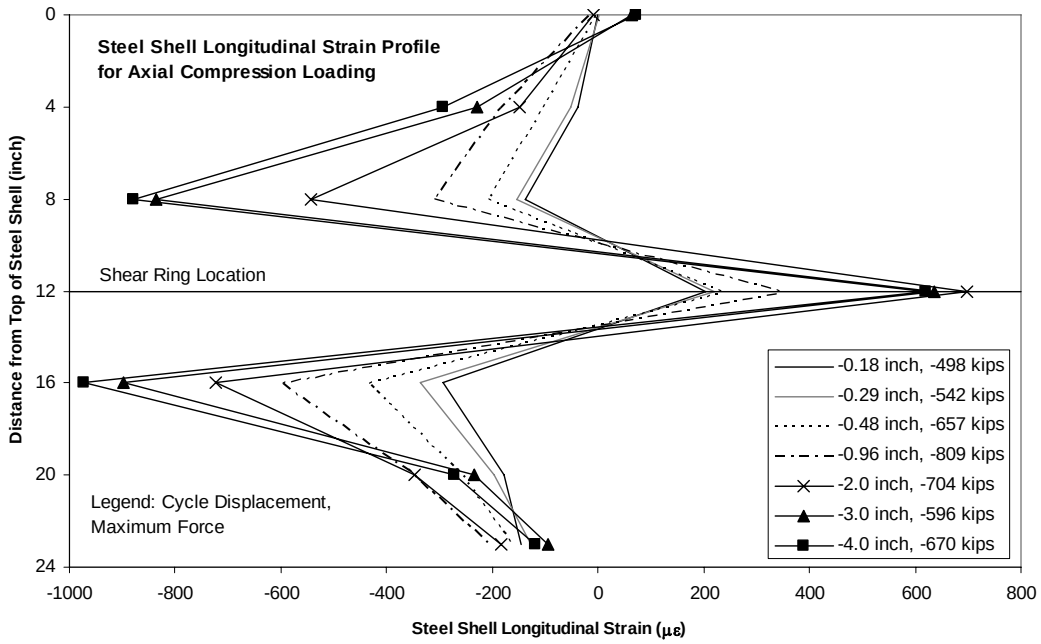


**Figure 9.17 Steel Shell Longitudinal Strain Profiles at Peak Cyclic Axial Compression Forces for Test Unit # 18**

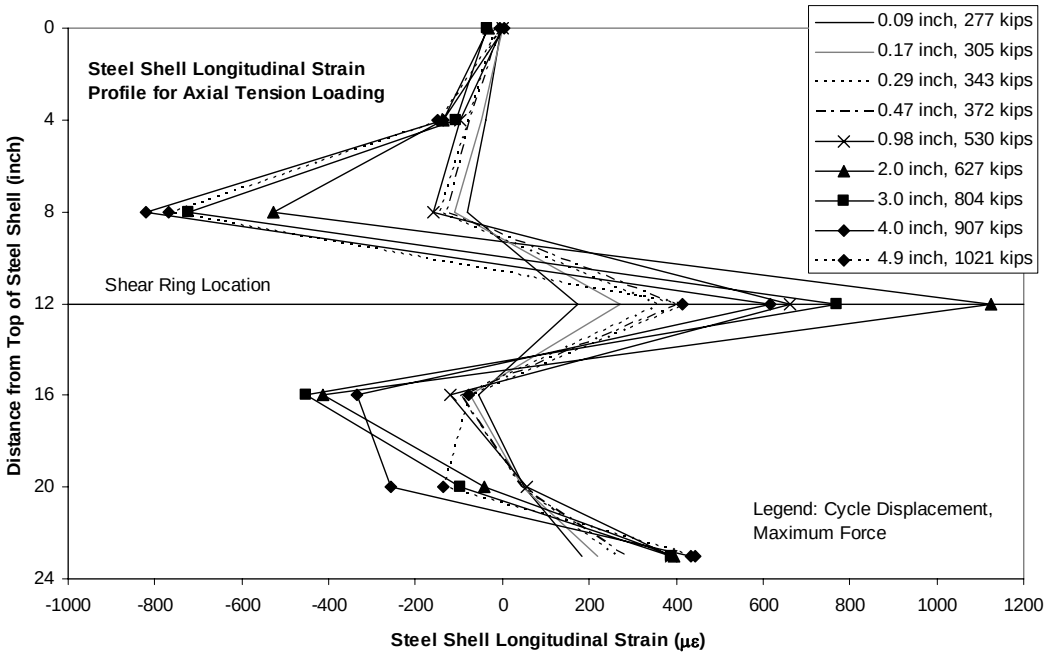


**Figure 9.18 Steel Shell Longitudinal Strain Profiles at Peak Cyclic Axial Tension Forces for Test Unit # 18**

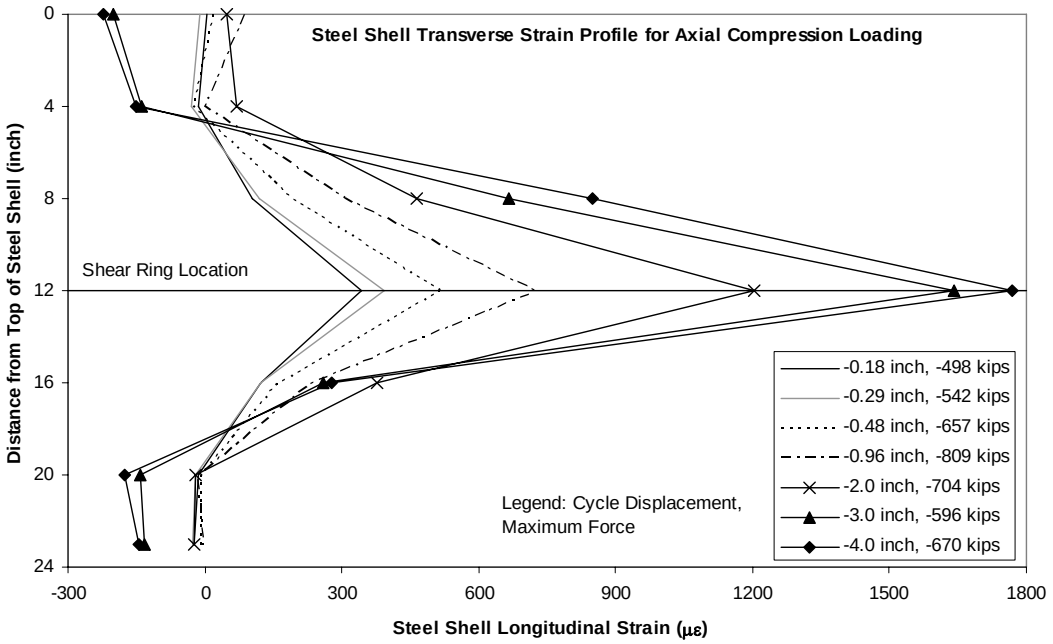


**Figure 9.19 Steel Shell Transverse Strain Profiles at Peak Cyclic Axial Compression Forces for Test Unit # 18**

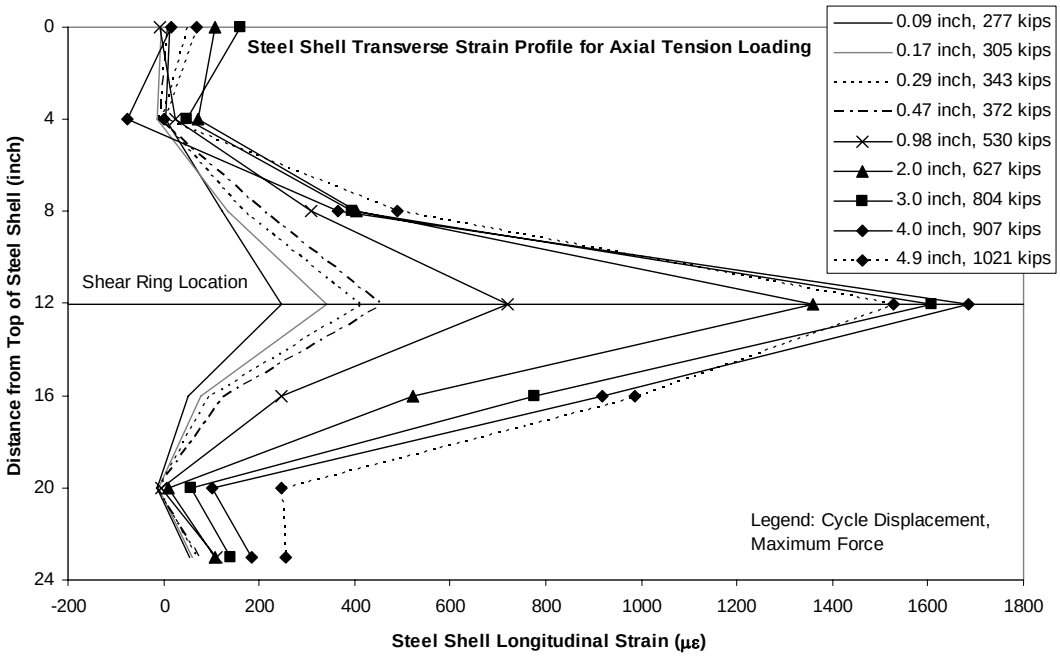


**Figure 9.20 Steel Shell Transverse Strain Profiles at Peak Cyclic Axial Tension Forces for Test Unit # 18**

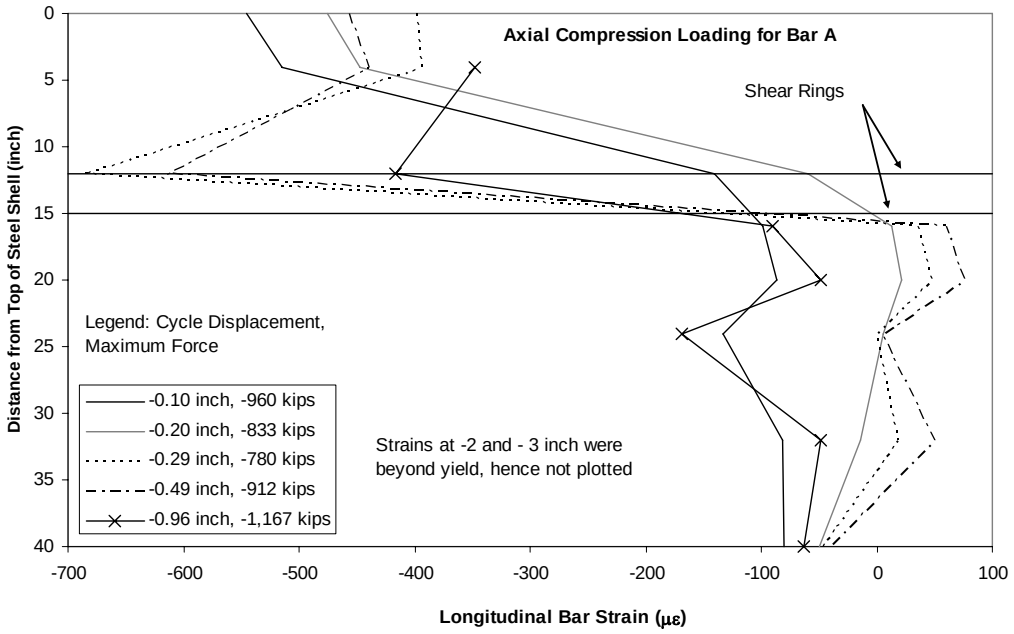


**Figure 9.21 Longitudinal Bar Strain Profiles at Peak Cyclic Axial Compression Forces for Test Unit # 19, Reinforcement Bar A**

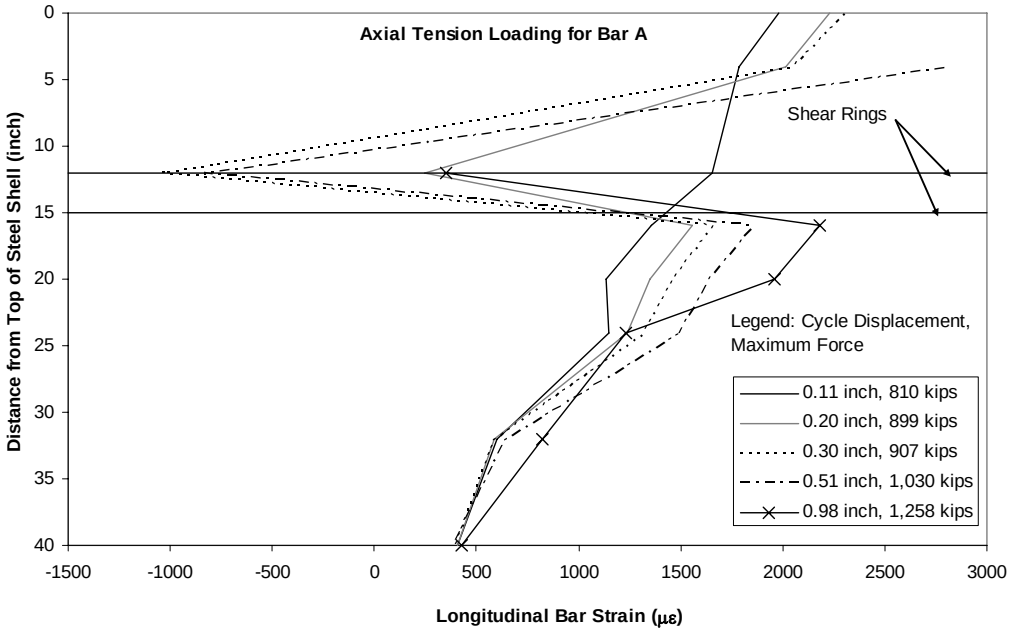


**Figure 9.22 Longitudinal Bar Strain Profiles at Peak Cyclic Axial Tension Forces for Test Unit # 19, Reinforcement Bar A**

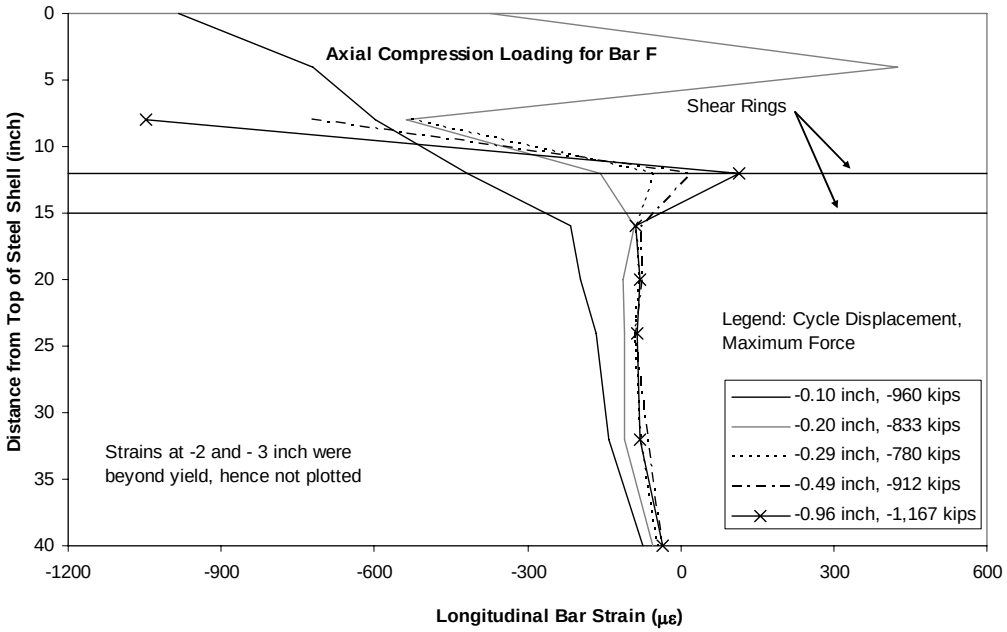


**Figure 9.23 Longitudinal Bar Strain Profiles at Peak Cyclic Axial Compression Forces for Test Unit # 19, Reinforcement Bar F**

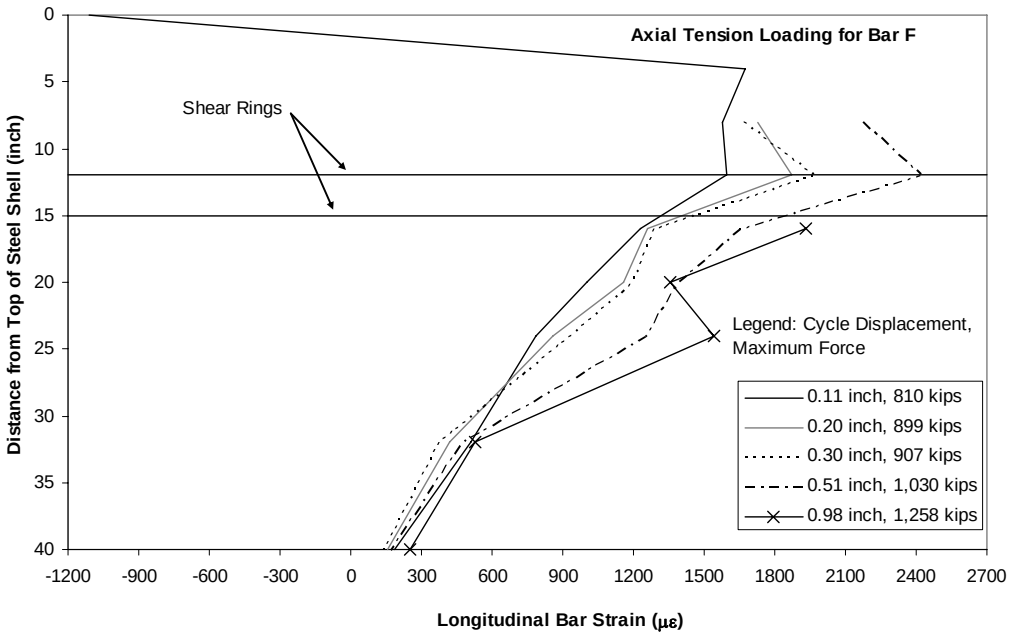


**Figure 9.24 Longitudinal Bar Strain Profiles at Peak Cyclic Axial Tension Forces for Test Unit # 19, Reinforcement Bar F**

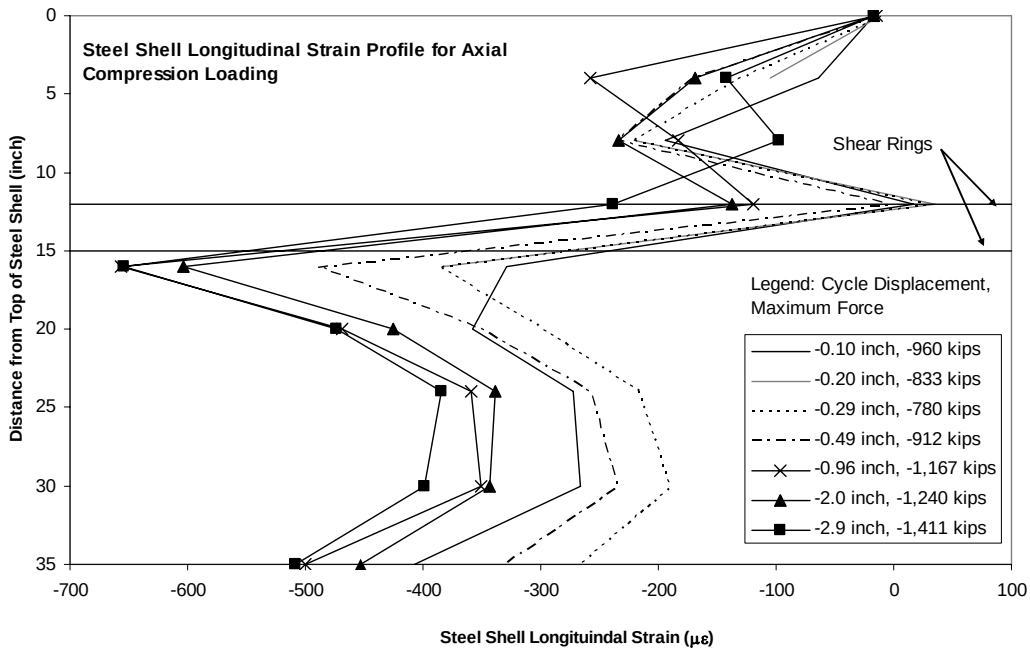


**Figure 9.25 Steel Shell Longitudinal Strain Profiles at Peak Cyclic Axial Compression Forces for Test Unit # 19**

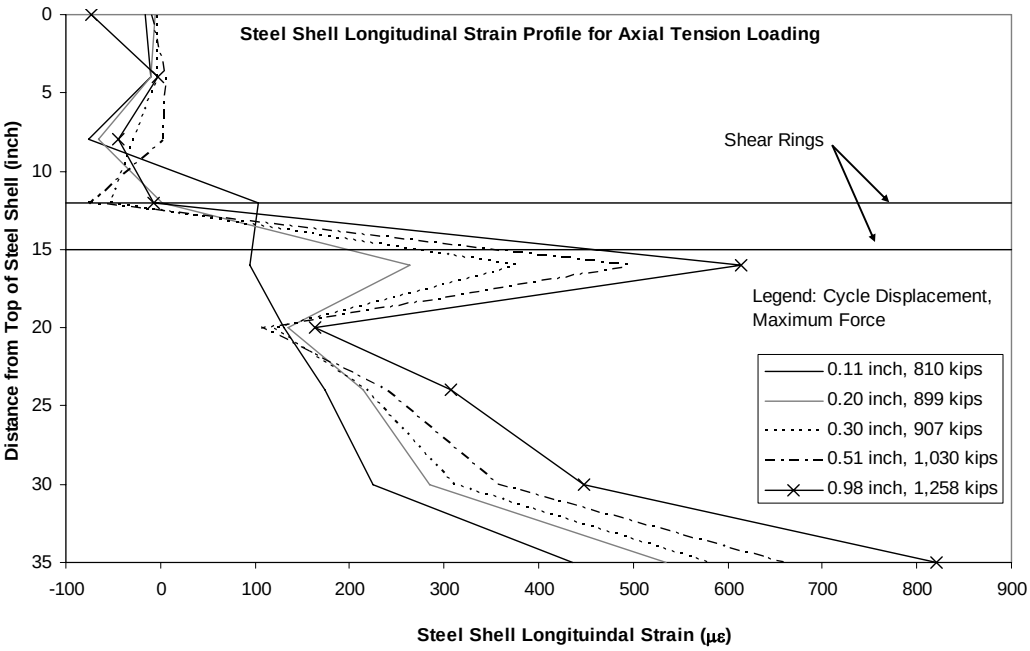


**Figure 9.26 Steel Shell Longitudinal Strain Profiles at Peak Cyclic Axial Tension Forces for Test Unit # 19**

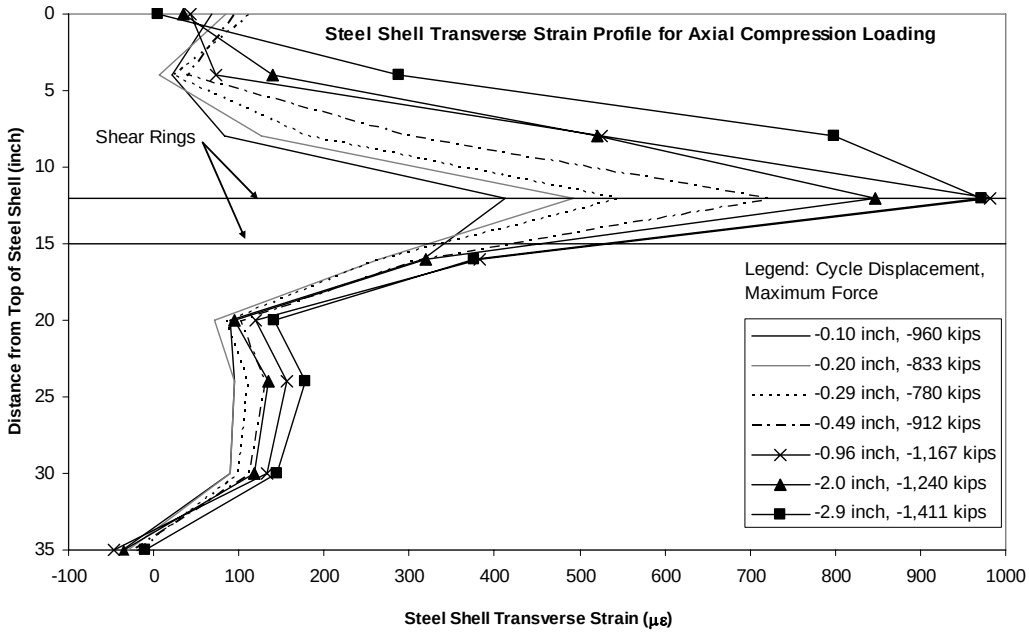


**Figure 9.27 Steel Shell Transverse Strain Profiles at Peak Cyclic Axial Compression Forces for Test Unit # 19**

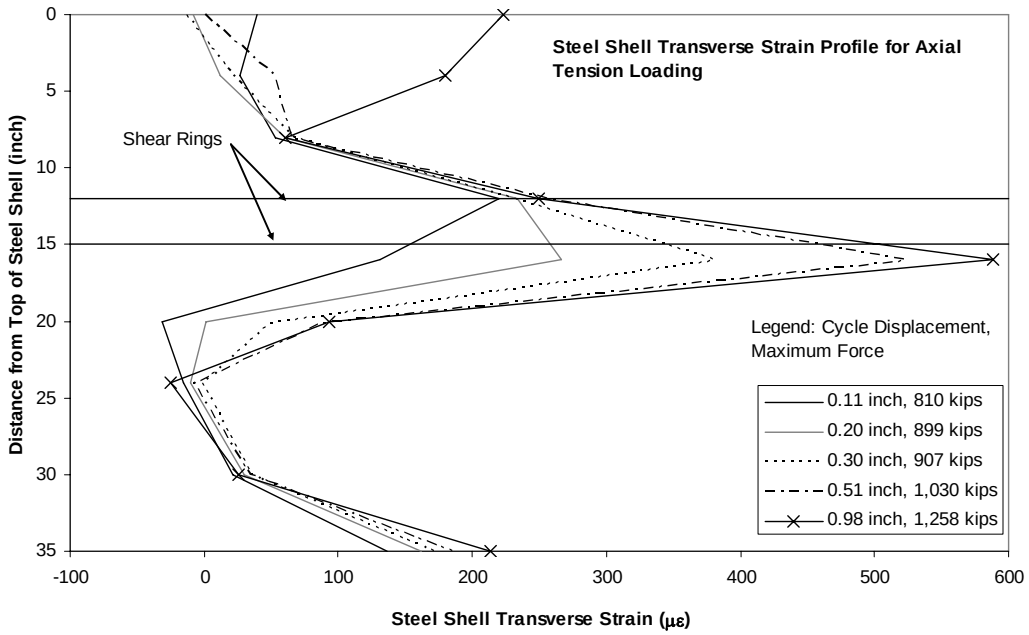


**Figure 9.28 Steel Shell Transverse Strain Profiles at Peak Cyclic Axial Tension Forces for Test Unit # 19**

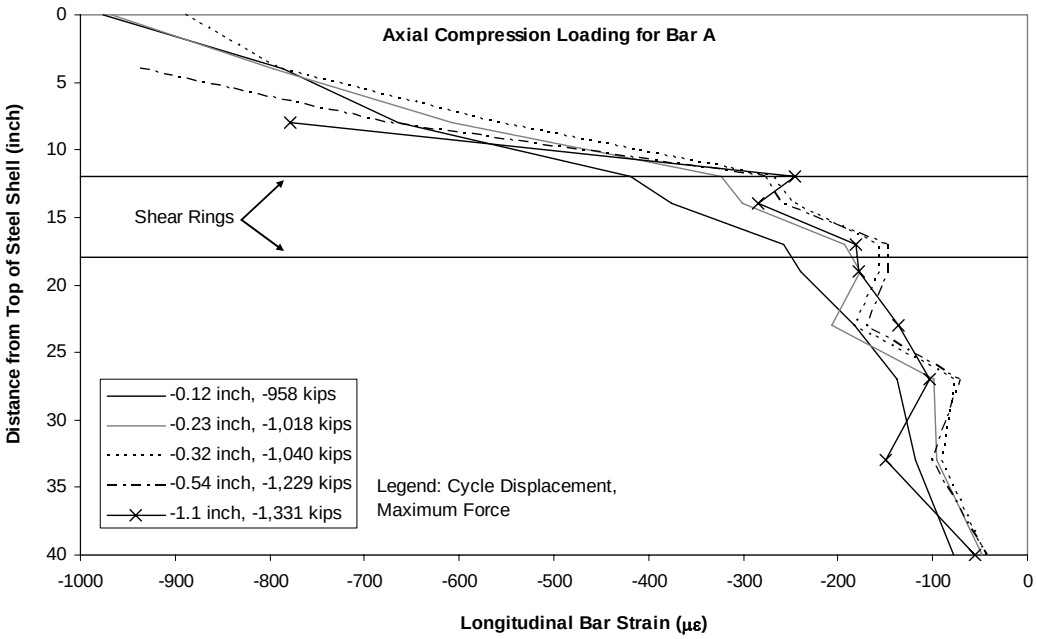


**Figure 9.29 Longitudinal Bar Strain Profiles at Peak Cyclic Axial Compression Forces for Test Unit # 20, Reinforcement Bar A**

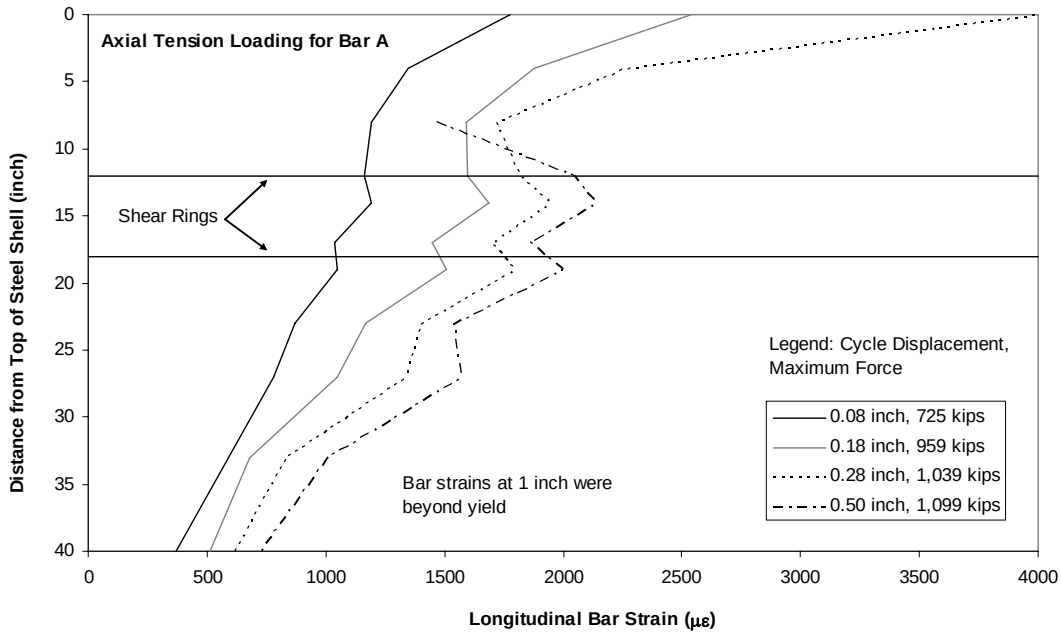


**Figure 9.30 Longitudinal Bar Strain Profiles at Peak Cyclic Axial Tension Forces for Test Unit # 20, Reinforcement Bar A**

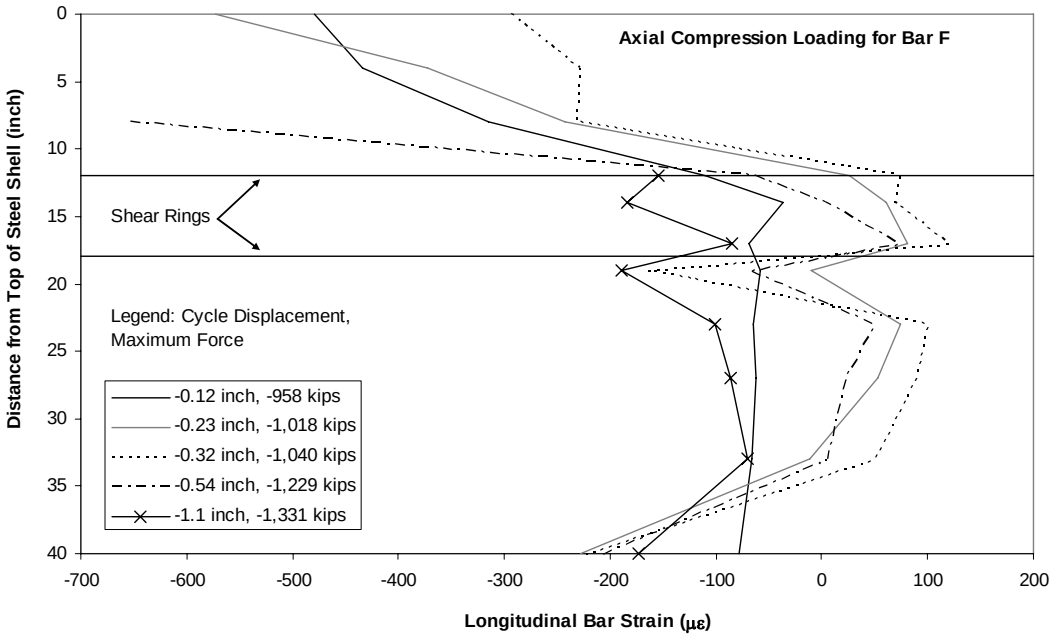


**Figure 9.31 Longitudinal Bar Strain Profiles at Peak Cyclic Axial Compression Forces for Test Unit # 20, Reinforcement Bar F**

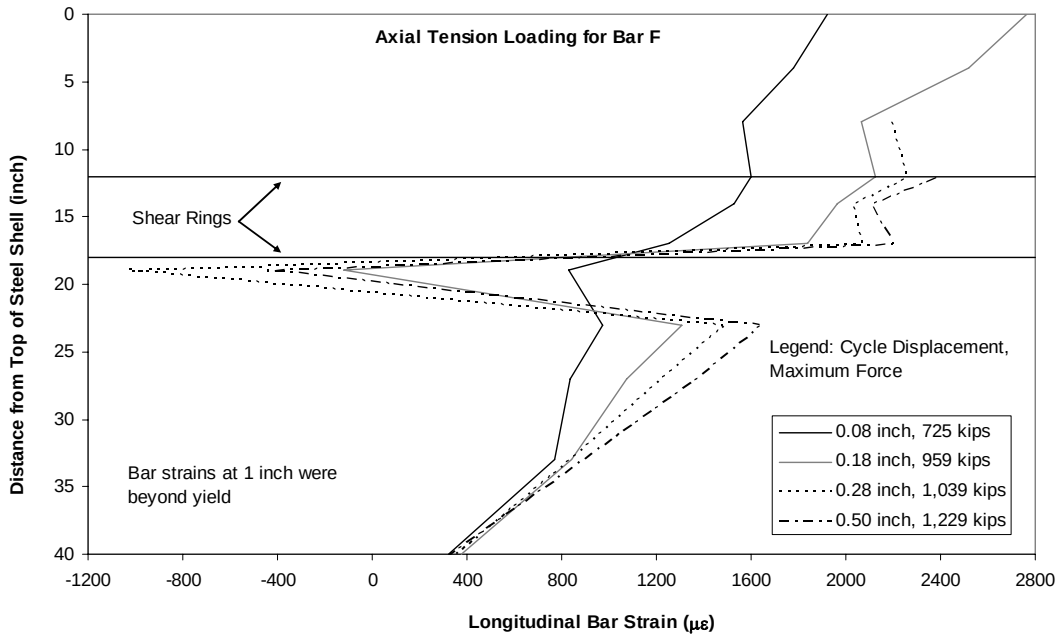


**Figure 9.32 Longitudinal Bar Strain Profiles at Peak Cyclic Axial Tension Forces for Test Unit # 20, Reinforcement Bar F**

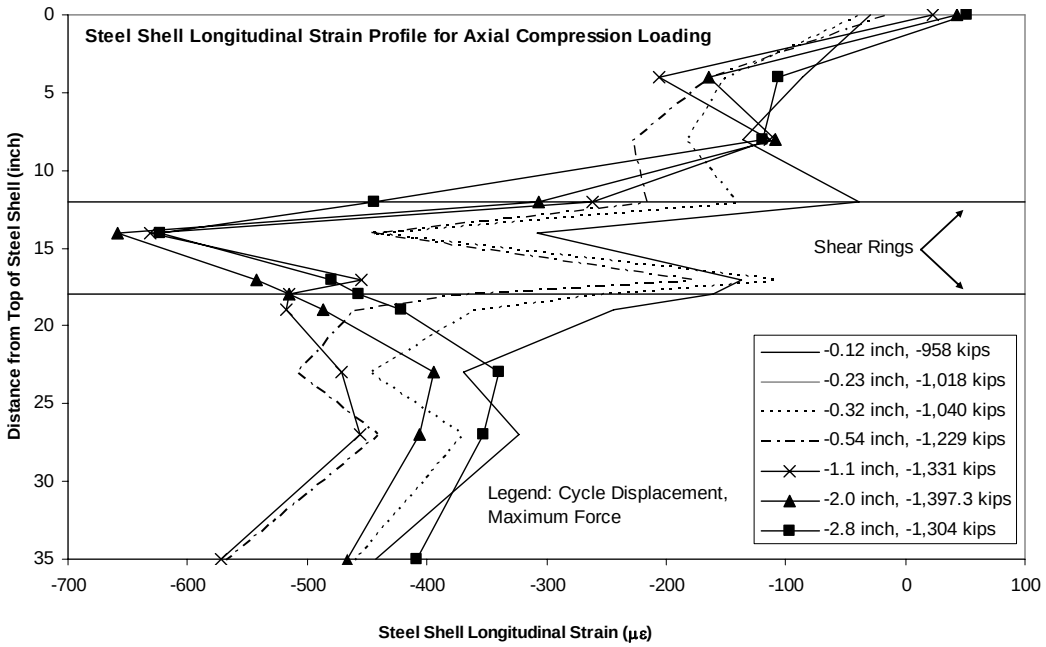


**Figure 9.33 Steel Shell Longitudinal Strain Profiles at Peak Cyclic Axial Compression Forces for Test Unit # 20**

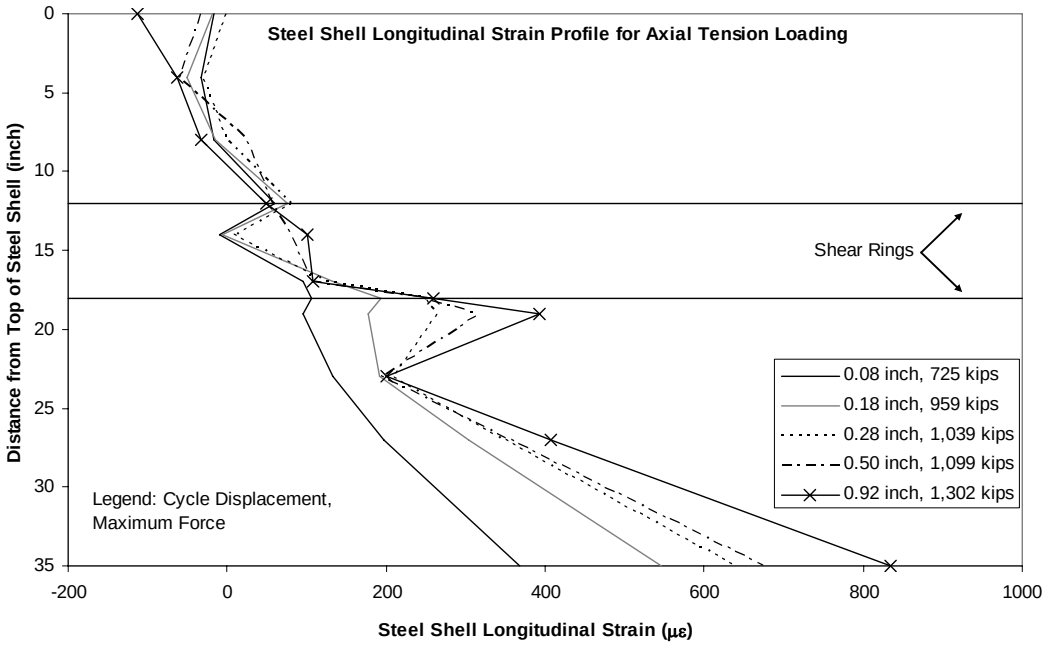


**Figure 9.34 Steel Shell Longitudinal Strain Profiles at Peak Cyclic Axial Tension Forces for Test Unit # 20**

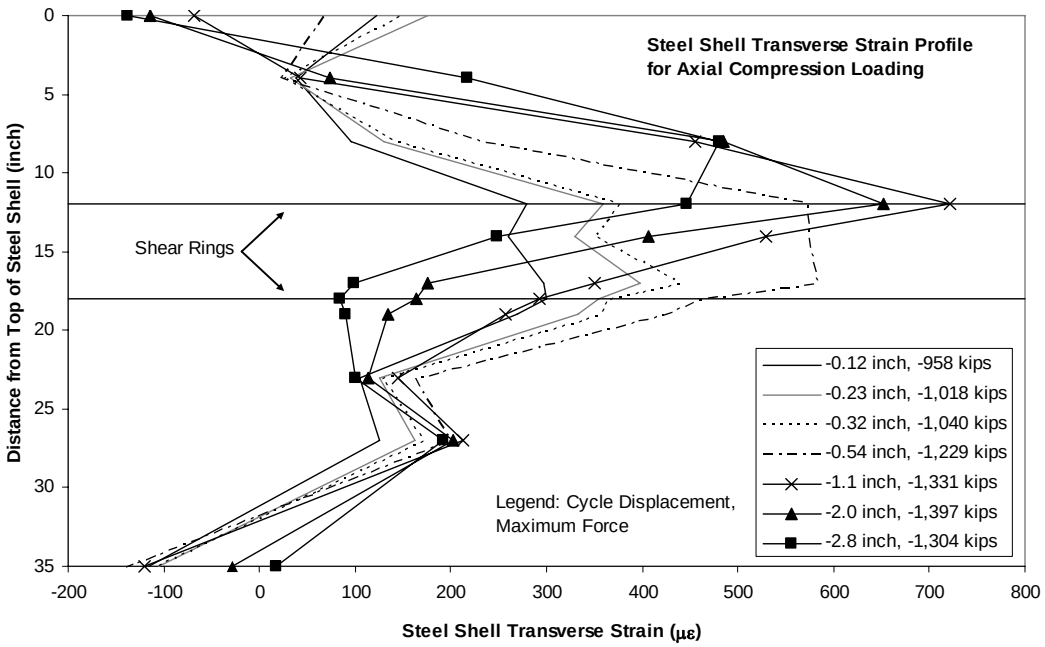


**Figure 9.35 Steel Shell Transverse Strain Profiles at Peak Cyclic Axial Compression Forces for Test Unit # 20**

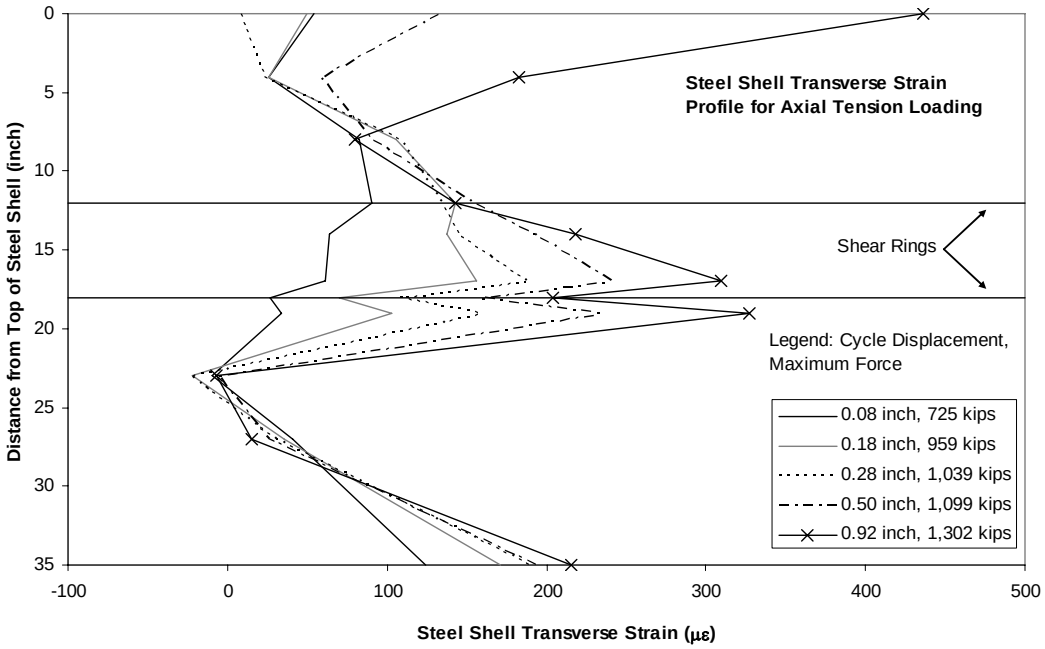


**Figure 9.36 Steel Shell Transverse Strain Profiles at Peak Cyclic Axial Tension Forces for Test Unit # 20**

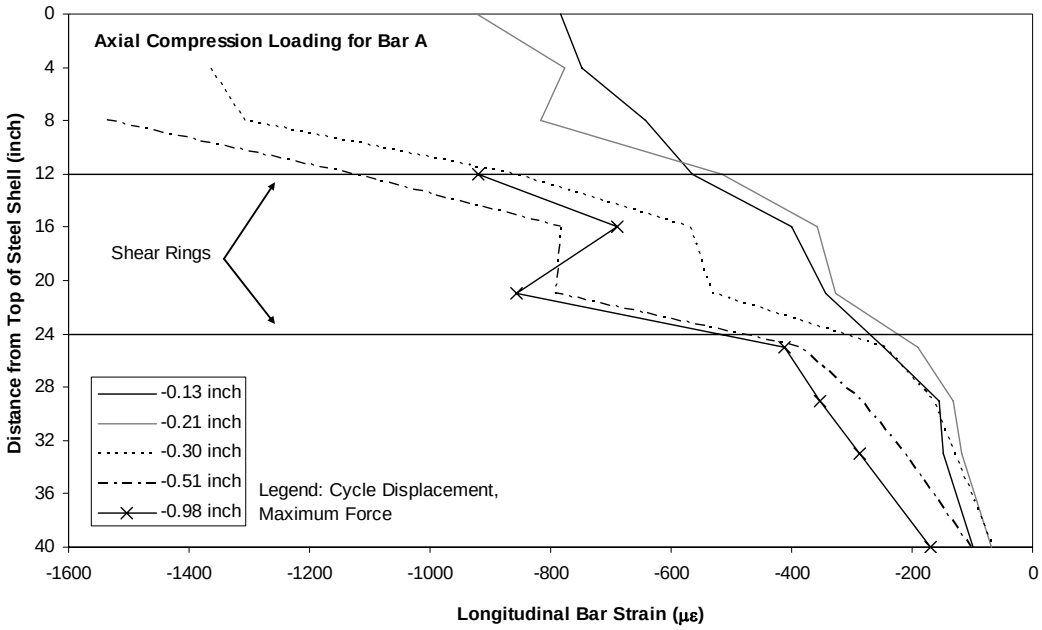


**Figure 9.37 Longitudinal Bar Strain Profiles at Peak Cyclic Axial Compression Forces for Test Unit # 21, Reinforcement Bar A**

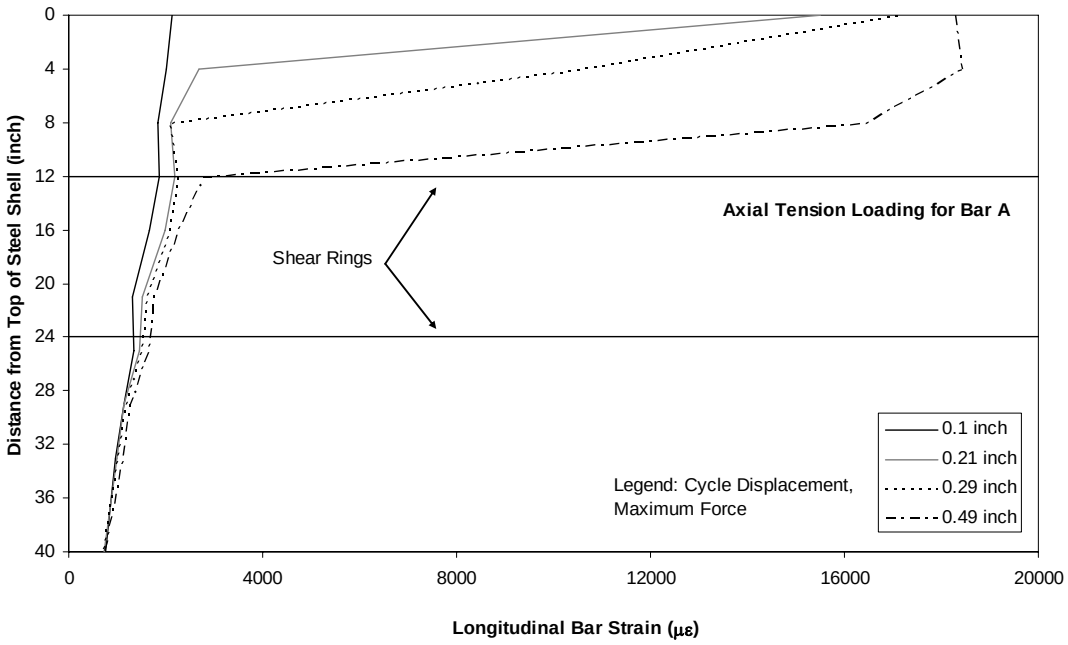


**Figure 9.38 Longitudinal Bar Strain Profiles at Peak Cyclic Axial Tension Forces for Test Unit # 21, Reinforcement Bar A**

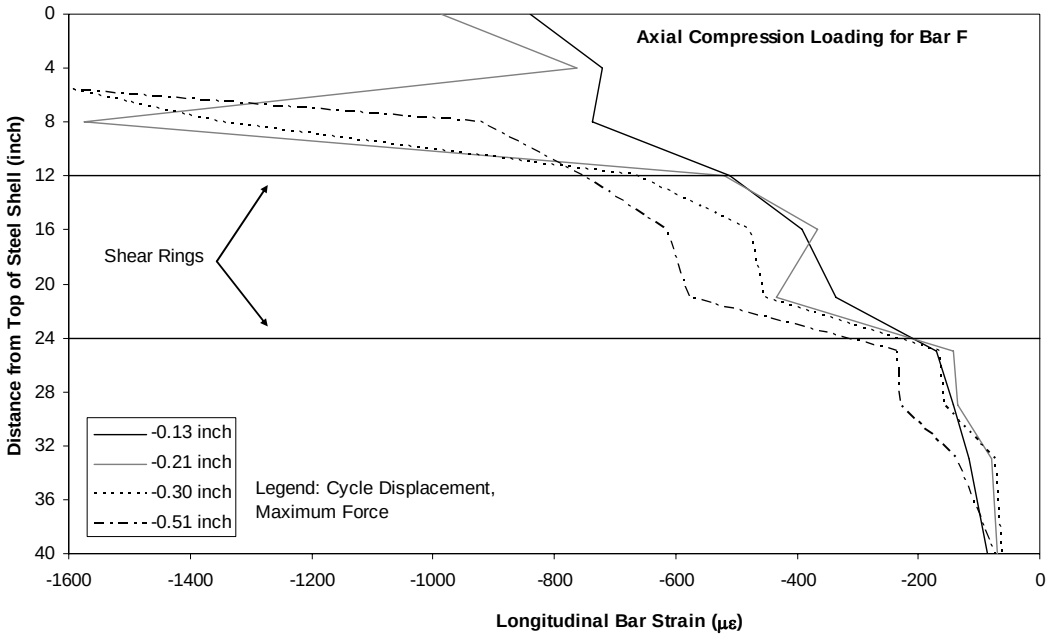


**Figure 9.39 Longitudinal Bar Strain Profiles at Peak Cyclic Axial Compression Forces for Test Unit # 21, Reinforcement Bar F**

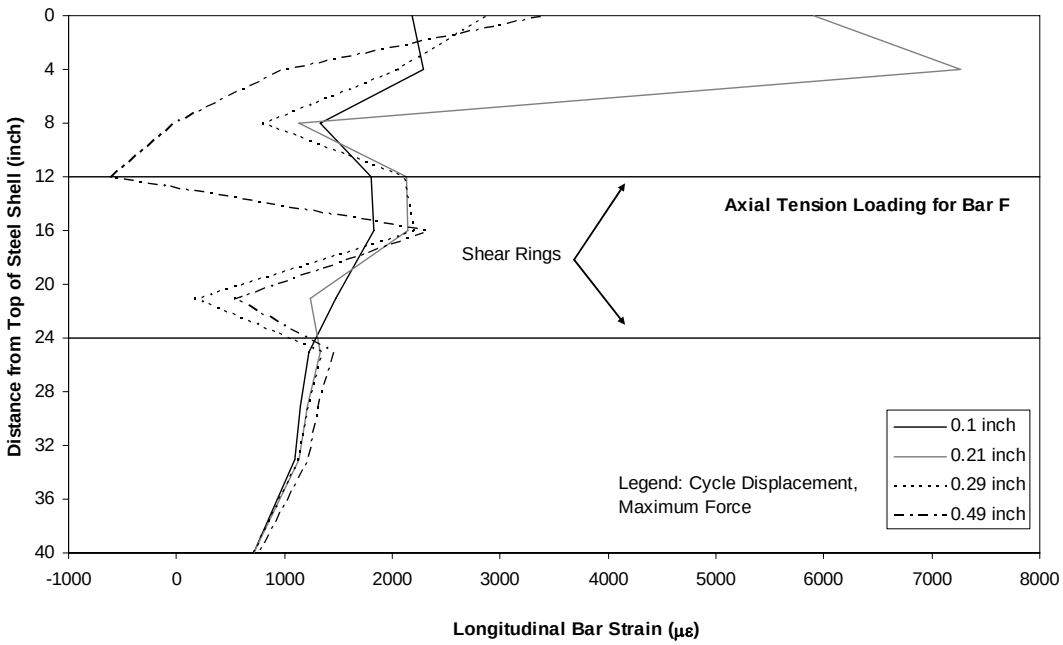


**Figure 9.40 Longitudinal Bar Strain Profiles at Peak Cyclic Axial Tension Forces for Test Unit # 21, Reinforcement Bar F**

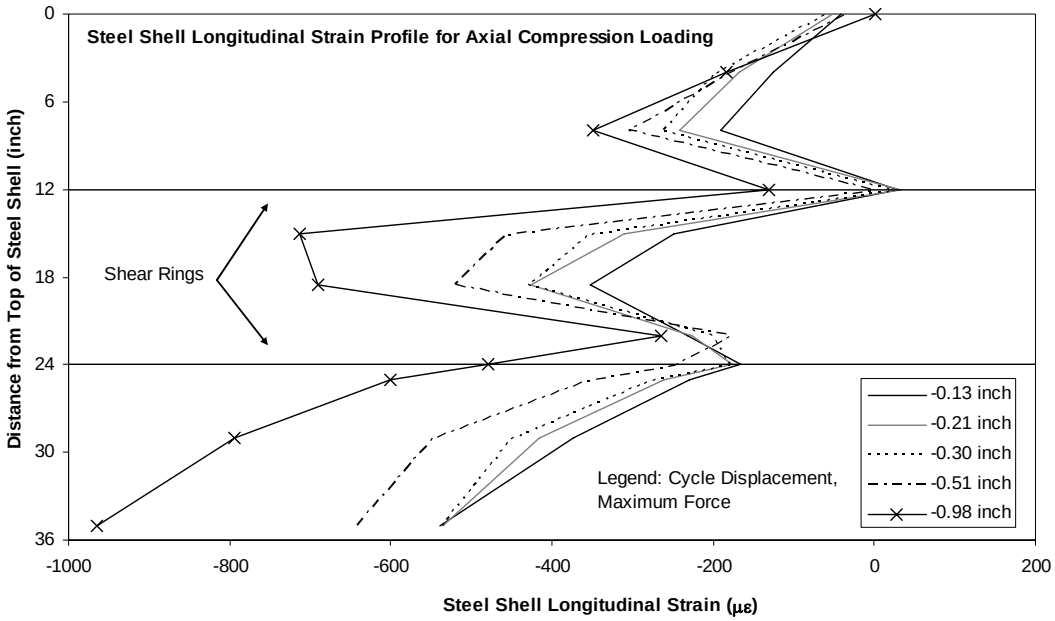


**Figure 9.41 Steel Shell Longitudinal Strain Profiles at Peak Cyclic Axial Compression Forces for Test Unit # 21**

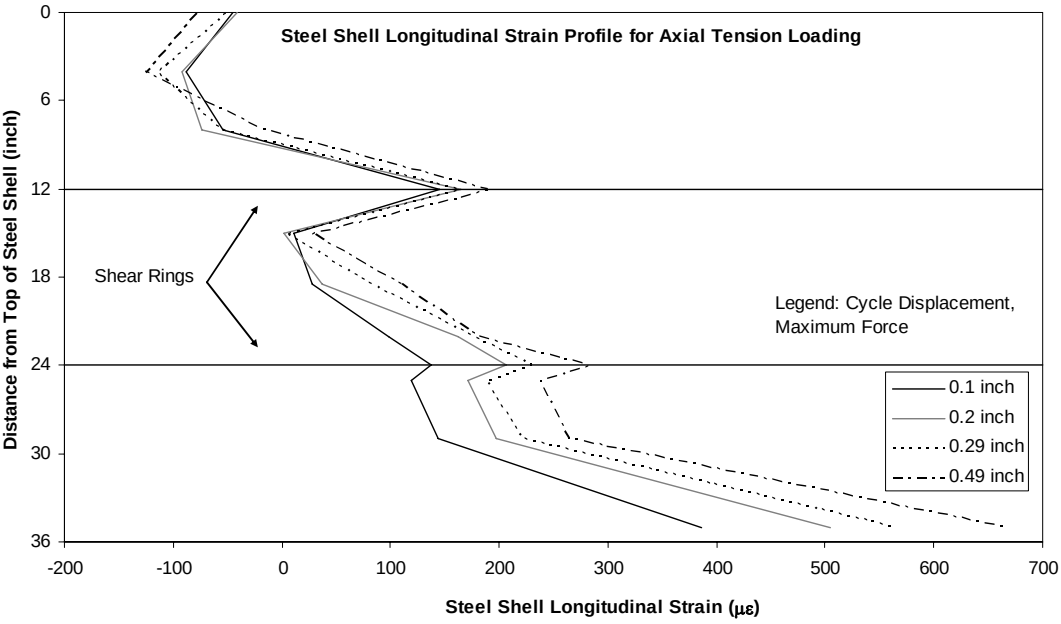


**Figure 9.42 Steel Shell Longitudinal Strain Profiles at Peak Cyclic Axial Tension Forces for Test Unit # 21**

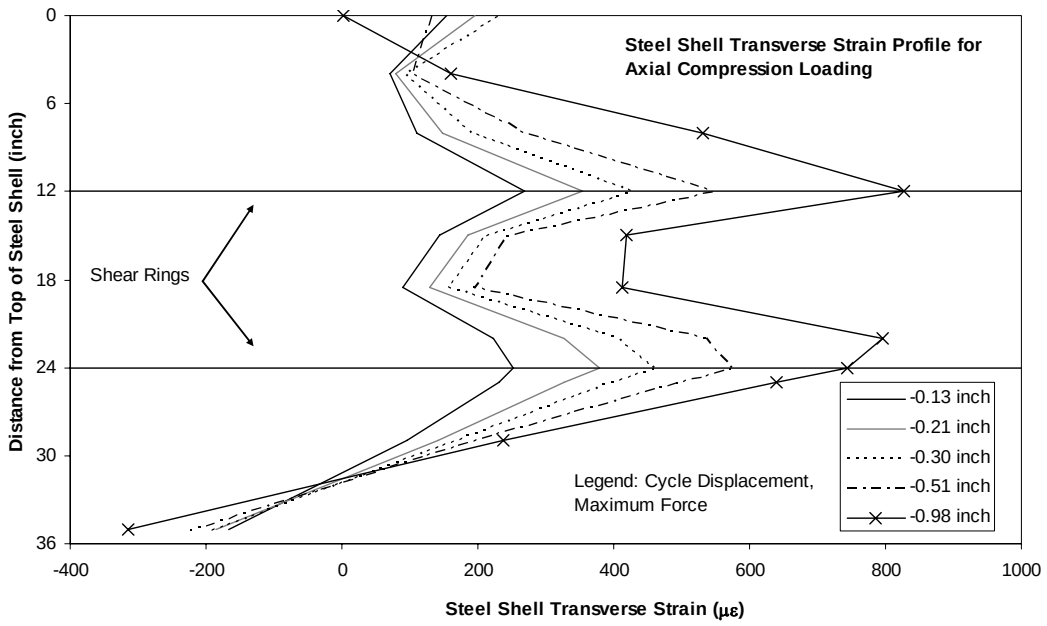


**Figure 9.43 Steel Shell Transverse Strain Profiles at Peak Cyclic Axial Compression Forces for Test Unit # 21**

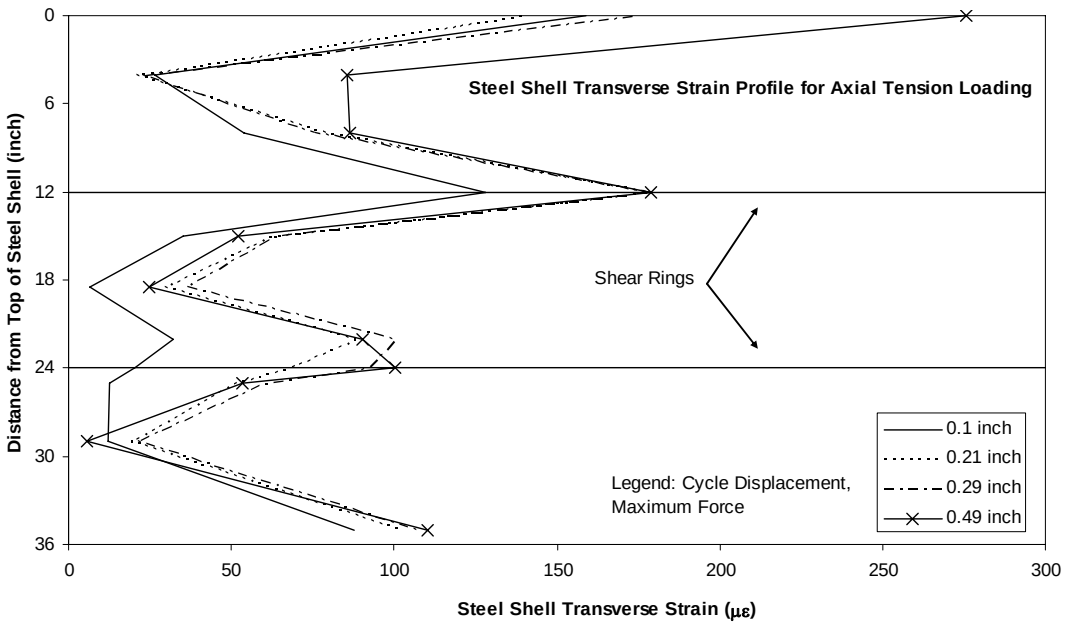


**Figure 9.44 Steel Shell Transverse Strain Profiles at Peak Cyclic Axial Tension Forces for Test Unit # 21**

# 10 APPENDIX - FINITE ELEMENT ANALYSIS

## 10.1 Introduction

This chapter presents the finite element models developed for this research. A description of the material properties, interaction, geometry, mesh, and elements used in the models are presented. Results from models of the shear ring mechanism and of the surface bond are compared to the experimental axial force-axial displacement results. Relevant plots of the von Mises stress distribution, and deformations are presented as well.

## 10.2 Program Used for Finite Element Analysis

The finite element analysis software program, ABAQUS 6.5.1, (ABAQUS, 2005) was used to develop a model of the axial force transfer through a shear ring mechanism. This program was used as the pre-processor, processor, and post processor for the model. Within the program two versions are available for the user: ABAQUS/Standard and ABAQUS/Explicit. *Standard* is typically used for static finite element analysis problems. *Explicit* is typically used for dynamic analysis and complex contact analysis problems, and was used in the analysis. *Explicit* finds a solution without iterating, it explicitly advances the kinematic state from a previous increment. This results in the need for a large number of increments, however, *Explicit* can be more efficient as *Standard* would require more iterations. *Explicit* typically uses less disk space and memory than *Standard* for the same simulation. The computational requirements of *Explicit* are proportional to the number of elements and inversely proportional to the smallest element size. The computational requirements of *Standard* are proportional to the square of the number of degrees of freedom. Other advantages to *Explicit* include an extensive library of elements, and a robust contact functionality which can solve complex formulations. *Explicit* is conditionally stable through its integration solution technique.

## 10.3 Three Dimensional Model

The computational requirements (in terms of time and memory) to analyze a three dimensional model was so substantial that a model could not produce enough data (results for comparison to the experiment) when ran on a desktop computer. This was overcome by gaining access to the San Diego Supercomputer Center (SDSC), located at UCSD. Three dimensional models were analyzed for comparison to the experimental results. Details pertaining to the models are presented in this section.

### 10.3.1 Test Units Modeled

The high computational cost of this analysis necessitated that only the most important issues are modeled with finite elements. These were judged to be the shear ring transfer mechanism and the friction bond. The axial force transfer through the shear ring was modeled for Test Units # 5 and # 17 which had D/t ratios of 128 and 24, respectively. This allowed for investigation of the two failure modes: yielding of the steel shell at the mechanism, and crushing of concrete at the mechanism. Test Unit # 4 with a weld bead, and Test Unit # 7 with a welded bar, were modeled to examine the effect of the mechanism radial width. The axial force transfer through only friction bond was investigated through modeling of Test Units # 1, # 2, and # 3.

### 10.3.2 Material Models

The elastic and inelastic properties of steel and concrete needed to be specified due to the highly nonlinear response observed in the experimental program. A damaged plasticity model was used for concrete with a tension stiffening and tension damage property to account for the tension present due to the reinforcing steel. A kinematic hardening property was specified for steel to model the cyclic degradation of steel. A description of these models is presented in this section.

#### 10.3.2.1 Concrete

A continuum damaged plasticity based model was selected to model the elastic and inelastic behavior of concrete subject to compression and tension. This model

accounts for the irreversible damage that occurs, such as concrete crushing and tensile cracking. This is accounted for through scalar (isotropic) damaged elasticity and multi-hardening plasticity.

This model can be used with a rebar layer option to model steel reinforcement bars. This option was not used due to the high computational requirements of the model. In addition the reinforcement was not included because the concrete core was subjected to only a monotonic axial compression, such that the reinforcement bar contribution could be assumed negligible. The tension stiffening property in the concrete model provided a level of representation of the tension present.

A mass density of 200.0 $kg/m^3$ ($2.246 \cdot 10^{-4} lb \cdot s^2/in^4$) was assumed. It should be noted that a mass density of $2.246 \cdot 10^{-7} kip \cdot s^2/in^4$ was assumed in the model because the unit of kips was used throughout the model, and had to be consistent. This mass density corresponds to a concrete with a unit weight of 2403 $kg/m^3$ (150 $lb/ft^3$).

Poissons ratio, $\upsilon$, was assumed as 0.2. This was assumed based on the research of Kupfer *et al.* (1969), which recommended a Poissons ratio, $\upsilon$, of 0.18 to 0.2 for concrete loaded in compression and tension. The elastic modulus, $E_c$, was assumed to be 21520 MPa (3122 ksi) based on Equation 10.1 with an $f_c^{'}$ of 20.7 MPa (3.0 ksi). It should be noted that the units for $f_c^{'}$, in Equation 10.1, are $lb/in^2$.

$$E_c = 57000 \cdot \sqrt{f_c^{'}} \tag{10.1}$$

In the damaged plasticity model, a dilation angle of 36.31°, which corresponds to the ratio of volume change to shear strain, was assumed. A wide range of values for the dilation angle has been used from approximately 10° to 40° (ABAQUS, 2005). A value of 36.31° was selected per successful usage of other UCSD researchers (Cheng, 2005).

The plasticity model under axial compression assumes a linear response until the initial yield stress, $\sigma_{ci}$, is obtained, as shown in Figure 10.1. After this initial yield

stress, the model is characterized by a stress hardening to the ultimate stress, $\sigma_{cu}$. After the ultimate stress, the response is characterized by strain softening. As shown in Figure 10.1, unloading from any point on the stress-strain curve after the ultimate stress will have a stiffness of $(d_c - 1) \cdot E_o$. In this unloading stiffness, $d_c$, is the compression damage variable and will be assumed to have a value of zero, such that any unloading has a stiffness, $E_o$, equal to the initial stiffness. The initial yield stress, $\sigma_{ci}$, was assumed as 10.3 MPa (1.5 ksi) at an inelastic strain of zero. The ultimate stress was assumed as 20.7 MPa (3.0 ksi) at an inelastic strain of 0.001.

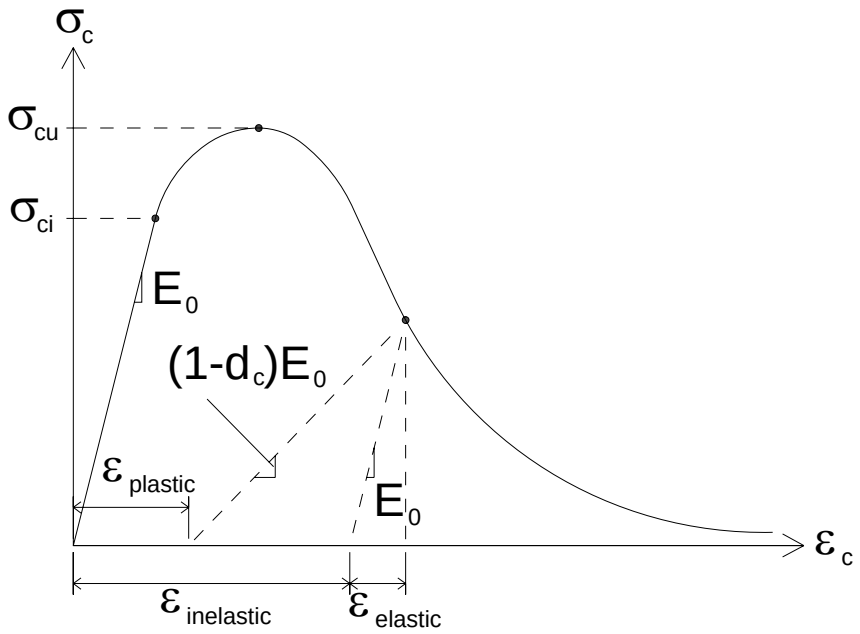


**Figure 10.1 Concrete Compression Stress-Strain Model Behavior**

The plasticity model, under axial tension, assumes a linear response until the failure stress, $\sigma_{ti}$, is obtained. After the failure stress is obtained micro-cracking occurs and is modeled by a softening in the stress strain response, as shown in Figure 10.2. The tensile behavior was modeled by specifying a stress-displacement curve, and a tensile damage curve. The tensile stress-displacement curve was specified, as shown in Figure 10.3, to capture the softening in the stress-displacement after obtaining the tension yield stress. The tension yield stress, $f_{ct}$, was calculated from the concrete compression stress, $f_c^{'}$, using Equation 10.2 with units of psi.

$$f_{ct} = 6.4 \cdot \sqrt{f_c^{'}} \tag{10.2}$$

The tension yield stress was multiplied by a dynamic amplification factor of 1.2 to account for rate effects. This resulted in a tension yield stress of 2.90 MPa (421 psi) for an assumed $f_c^{'}$ of 20.7 MPa (3000 psi). The tensile stress-displacement curve, shown in Figure 10.3, was used by Cheng (2005) in the modeling of a fiber reinforced polymer slab, and was judged suitable for use this model.

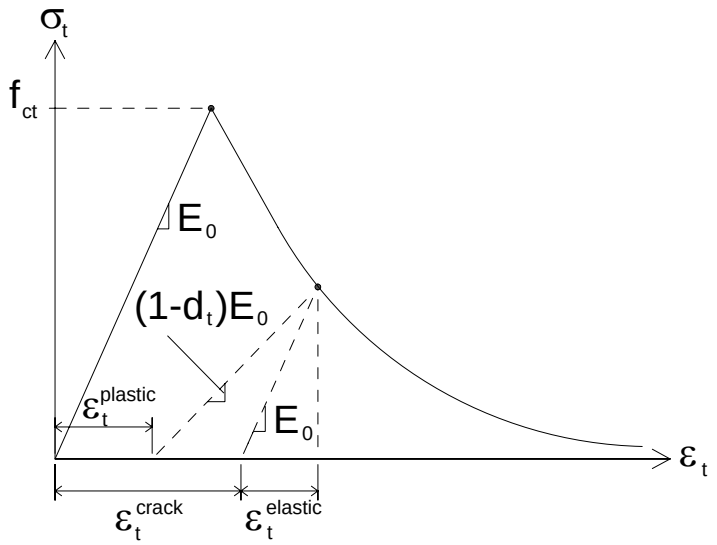


**Figure 10.2 Concrete Tension Stress-Strain Model Behavior**

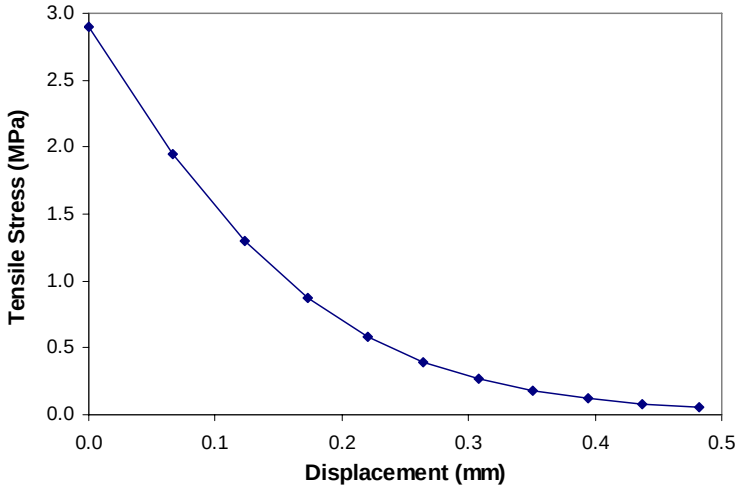


**Figure 10.3 Concrete Tensile Stress-Strain Model**

The tensile damage curve, as shown in Figure 10.4, was used to model the degradation in the unloading stiffness: $E_o \cdot (1 - d_t)$. The tension damage, $d_t$, ranges in

value from zero for no loss in stiffness, to one for a complete loss of stiffness. The tension damage curve, shown in Figure 10.4, was obtained from Cheng (2005).

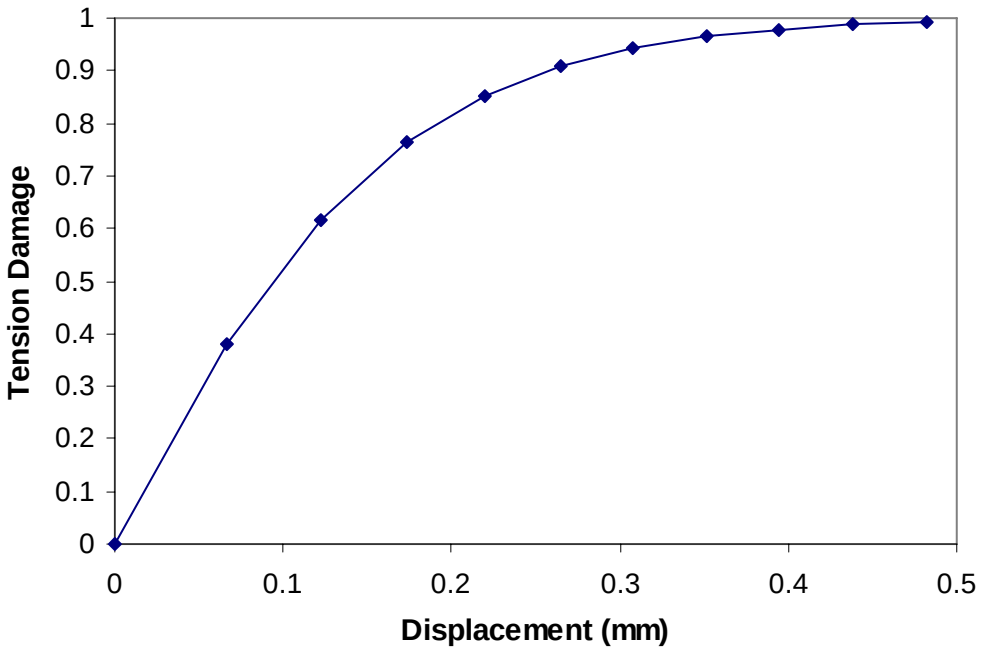


**Figure 10.4 Concrete Tensile Damage Model**

#### 10.3.2.2 Steel

A nonlinear kinematic hardening model was used to model the behavior of steel. This model is applicable for metals subjected to cyclic loading. In this model, the yield surface is modeled with a von Mises yield surface, as stated in the function, $F$, of Equation 10.3. The von Mises yield surface is pressure independent, such that yielding is independent of the pressure stress.

$$F = f(\sigma - \alpha_{vm}) - \sigma^0 = 0 \tag{10.3}$$

In Equation 10.3, $f(\sigma - \alpha_{vm})$ is the equivalent von Mises stress with respect to the backstress, $\alpha_{vm}$, and $\sigma^0$ is the yield stress. The equivalent von Mises stress can be stated as:

$$f(\sigma - \alpha_{vm}) = \sqrt{\frac{3}{2} \cdot (S - \alpha^{dev}) : (S - \alpha^{dev})} \tag{10.4}$$

In Equation 10.4, $S$ is the deviatoric stress tensor, and $\alpha^{dev}$ is the deviatoric part of the backstress tensor. The deviatoric stress tensor is defined as a function of the stress

tensor, $\sigma$, the equivalent pressure stress, $p$, and the identity tensor, $I_t$, as stated in Equation 10.5.

$$S = \sigma + p \cdot I_t \tag{10.5}$$

The hardening law, with temperature and field variable dependencies omitted, is stated as:

$$\dot{\alpha} = C \cdot \frac{1}{\sigma^0} \cdot (\sigma - \alpha) \cdot \dot{\bar{\varepsilon}}^{pl} - \gamma \cdot \alpha \cdot \dot{\bar{\varepsilon}}^{pl} \tag{10.6}$$

In Equation 10.6, $C$ is the initial kinematic hardening modulus and $\gamma$ is the rate at which the kinematic hardening modulus decreases as plastic deformation increases. The modulus, $C$, and rate, $\gamma$, are material properties determined from calibrated cyclic test data. Also in Equation 10.6, $\dot{\bar{\varepsilon}}^{pl}$ is the equivalent plastic strain rate, which is defined as the rate of plastic flow, $\dot{\varepsilon}^{pl}$, divided by the partial derivative of the von Mises yield surface function with respect to stress, as stated in Equation 10.7.

$$\dot{\bar{\varepsilon}}^{pl} = \left( \frac{\dot{\varepsilon}^{pl}}{\frac{\partial F}{\partial \sigma}} \right) \tag{10.7}$$

Finite element analysis of the cyclic behavior of steel eccentrically braced frames (Richards, 2004) determined that a yield stress of 438 MPa (63.5 ksi) and a kinematic hardening parameter, $C$, with a value of 406.18, provided adequate results. The calibration of the kinematic hardening parameter is presented in Richards (2004).

A mass density of 660.0 $kg/m^3$ ($7.46 \cdot 10^{-4} lb \cdot s^2/in^4$) was assumed. It should be noted that a mass density of $7.46 \cdot 10^{-7} kip \cdot s^2/in^4$ was used in the ABAQUS model because the unit of kips was used throughout the model, and had to be consistent. This mass density corresponds to steel with a unit weight of 7,979 $kg/m^3$ (498 $lb/ft^3$). Poissons ratio, $\upsilon$, was assumed to be 0.3. The elastic modulus, $E_s$, was assumed to be 206,820 MPa (30,000 ksi).

### 10.3.3 Steel Shell-Concrete Core Interaction Property

The interaction between the concrete core and the steel shell was specified through a contact pair. In the contact pair option the two surfaces in contact are assigned a surface interaction property as presented.

#### 10.3.3.1 Contact Formulation for Contact Pair

A kinematic constraint enforcement method was used to enforce contact constraints between a defined master surface and a slave surface. This enforcement method does not allow a node of the slave surface to penetrate an element of the master surface. However, the master surface can penetrate into the slave surface, if the mesh is coarse, and if hard contact is specified. The master surface was defined as all of the surfaces of the steel shell (including the edges and external surfaces) and the mechanism. This was done to prevent any potential wrapping of the concrete core elements around the steel shell and mechanism. The slave surface was defined as the concrete core, which pertains to the softer material, per ABAQUS recommendation. The slave surface includes the concrete surfaces in contact with the steel shell, mechanism, and also includes the top surface and bottom surface. The top and bottom surfaces were included to prevent any mesh distortion/deformation of these surfaces when the concrete core obtained the maximum displacement, or during the initial displacement. The sides of the concrete core, not in contact with the steel shell and mechanism, were not included in the slave surface definition as these sides had an applied boundary condition. A surface with a boundary condition was not recommended (ABAQUS, 2005) to also have a slave surface definition.

Hard contact was specified for the contact behavior normal to the surfaces. In hard contact, the surfaces will not separate as long as the contact pressure (in the normal direction) is greater than zero. Separation of the surfaces will occur when the pressure equals zero or is less than zero, as shown in Figure 10.5. This rapid change in the contact state, as shown in Figure 10.5, can result in a difficulty for ABAQUS/Standard to complete a simulation. However, ABAQUS/Explicit, can accommodate this form of

contact because iteration is not required. In the normal contact definition, an option is available to allow or disallow separation of the surfaces. This option was set to allow separation, as a gap between the steel shell and concrete core was expected to form underneath a mechanism subjected to axial compression.

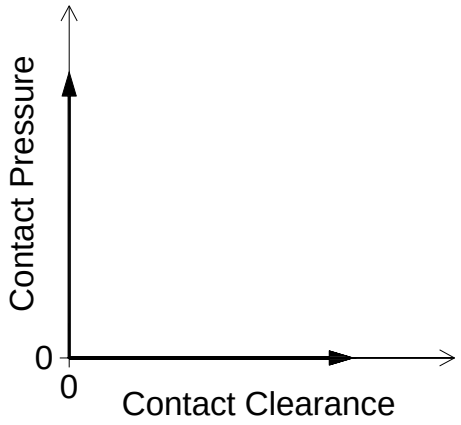


**Figure 10.5 ABAQUS Hard Contact**

Two options were available to specify the sliding contact between the surfaces: small sliding, and finite sliding. Small sliding provides an efficient analysis procedure, however it is only useful if the motion between the two contact surfaces is less than a typical element length. Finite sliding is useful when the motion between two contact surfaces is greater than a typical element length. In finite sliding, the slave surface cannot penetrate into the master surface, however, the master surface can penetrate into the slave surface. Finite sliding was used for the sliding contact between the core and steel shell surfaces.

#### 10.3.3.2 Surface Interaction Property

A friction model with an exponential decay was specified as the surface interaction property. In this model the friction, $\mu$, is a function of the static friction, $\mu_s$, kinetic friction, $\mu_k$, an exponential decay constant, $d_c$, and the slip rate, $\gamma_{eq}$, as expressed in Equation 10.8. After the initial static friction, $\mu_s$, is overcome, the friction

decays exponentially to the kinetic friction, $\mu_k$, as shown in Figure 10.6. The decay is proportional to a decay constant, $d_c$, and the slip rate, $\gamma_{eq}$, as shown in Equation 10.8.

$$\mu = \mu_k + (\mu_s - \mu_k) \cdot e^{-d_c \cdot \gamma_{eq}} \tag{10.8}$$

Values of 0.25 and 0.20 were used for the static and kinetic friction, respectively. The exponential decay constant and the slip rate were assumed as 0.003 and 0.001. These values were used in the models as the initial friction and were changed as necessary to provide an improved prediction of the experimental results.

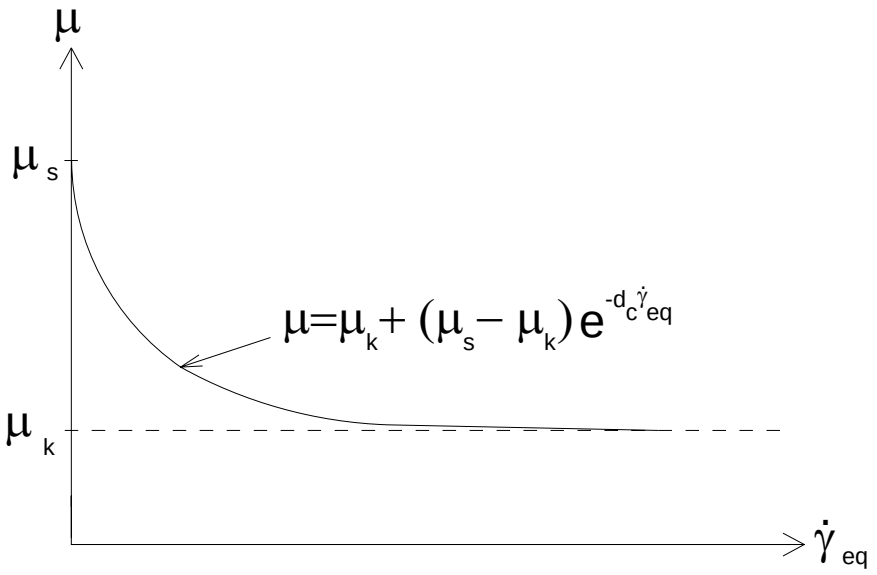


**Figure 10.6 Exponential Decay Friction Model**

### 10.3.4 Model Geometry

A balance between the number of elements, element size and the accuracy of the solution had to be obtained. The number of elements and the element size influence the accuracy of the solution as a fine mesh at regions of plasticity is needed. However, the number of elements and the element size is proportional to the computation time. The computation time for this contact analysis was very high, such that the models had to be run at the San Diego Supercomputer Center which itself was just adequate for this analysis. As a result of this high computational demand, a minimum number of elements had to be used, yet just the right amount had to be used to provide decent results.

The model geometry was simplified to facilitate an efficient run time. A three dimensional one-quarter section was modeled to take advantage of the radial symmetry and to save on computation time. Each model had a steel shell with a height of 711 mm (28.0 in.), and a concrete core with a height of 610 mm (24.0 in.), as shown in Figure 10.7. The steel shell extended 50.8 mm (2.0 in.) beyond the base of the steel shell to allow for contact between the concrete core and the steel shell to be maintained for up to 50.8 mm (2.0 in.) in axial compression. A height of 610 mm (24.0 in.) was used for the concrete core to minimize the number of elements in the model. This height was also selected to minimize any boundary effects of the concrete on the shear ring axial force transfer, because the shear ring mechanism was located at 305 mm (12.0 in.) from the top of the steel shell. This length provided a $45^{o}$ angle between the top corner of the concrete core, opposite of the steel shell, and the shear ring. The thickness of the steel shell and the radius pertained to the test unit being modeled, as listed in Table 10.1.

**Table 10.1 Element Usage in ABAQUS Finite Element Models**

| | | | Number of Elements | | |
|---|---|---|---|---|---|
| Test Unit # | D/t Ratio | Mechanism | Steel Shell | Concrete Core | Total |
| 1 | 128 | None | 470 | 568 | 1038 |
| 2 | 94 | None | 764 | 903 | 1667 |
| 3 | 46 | None | 581 | 911 | 1492 |
| 5 | 128 | Shear Ring | 1003 | 1564 | 2567 |
| 7 | 128 | Welded Bar | 1145 | 1669 | 2814 |
| 17 | 24 | Shear Ring | 1217 | 1549 | 2766 |

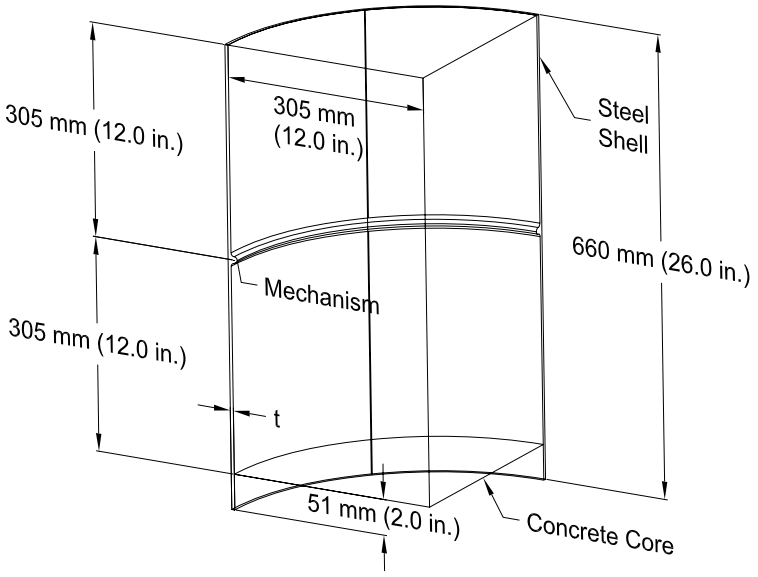


**Figure 10.7 Perspective View of a Typical ABAQUS Model**

The shear ring or weld bead or welded bar mechanisms and their corresponding welded connection to the steel shell did not fail in the experiment. Therefore the mechanism and its weld were incorporated as a part of steel shell. This was done to reduce the computational cost of the analysis. The shear ring, for the model of Test Unit # 5, had a radial width of 12.7 mm (0.5 in.), and a height of 12.7 mm (0.5 in.) The corners of the shear ring were rounded with a radius of 6.4 mm (0.25 in.), as was the intersection of the shear ring with the steel shell, as shown in Figure 10.8. This was done to prevent a singularity in the numerical solution at the corners of the shear ring. The shear ring for Test Unit # 17 had a height of 12.7 mm (0.5 in.), and a radial width of 6.35 mm (0.25 in.). The corners of the shear ring and the intersection with the steel shell were rounded with a radius of 6.4 mm (0.125 in.), as shown in Figure 10.8. The welded bar for Test Unit # 7 had a height of 9.53 mm (0.375 in.), and a radial width of 9.53 mm (0.375 in.). In the model the welded bar resembled the model with the shear ring mechanism to simplify the analysis, as shown in Figure 10.8. The assumed intersection of the top of the bar and bottom of the bar with the steel shell were rounded with a radius of 4.76 mm (0.1875 in.), as shown in Figure 10.8.

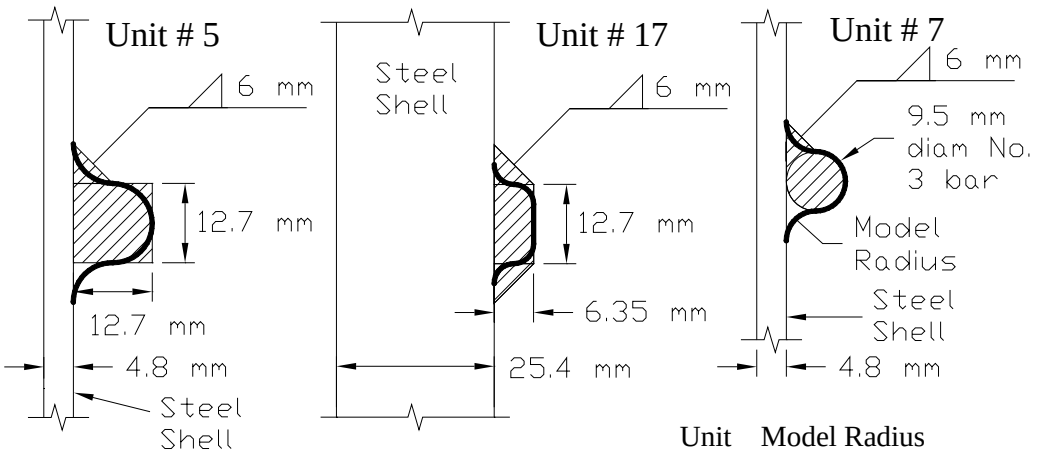


| Unit # | Model Radius mm (in.) |
|---|---|
| 5 | 6.4 (0.25) |
| 7 | 4.8 (0.19) |
| 17 | 3.2 (0.12) |

**Figure 10.8 Mechanism Geometry in the ABAQUS Models**

### 10.3.5 Model Partitioning and Mesh

The generation of a mesh for the models involved dividing the steel shell and the concrete core into partitions. Mesh seeds were then assigned to the partition edges to control the number of elements in a particular partition of the model. The partitions and seeds were placed such that more elements would be generated at the mechanism location where the stresses, deformation and displacement were the greatest in the experiment. A typical partitioning strategy for a test unit with a mechanism is shown in Figure 10.9. At regions of the model far from the mechanism, the stress concentrations were lower; therefore, the element size was increased for partition edges farther away from the mechanism location. The partition strategy allowed for this change in element size, as shown in Figure 10.9, with the larger partitions at the extremes of the concrete core, and smaller partitions at the shear ring. The mesh generated for models of Test Units # 1, # 2, # 3, # 5, # 7, and # 17 are shown in Figures 10.10, 10.11, 10.12, 10.13, 10.14, and 10.15, respectively.

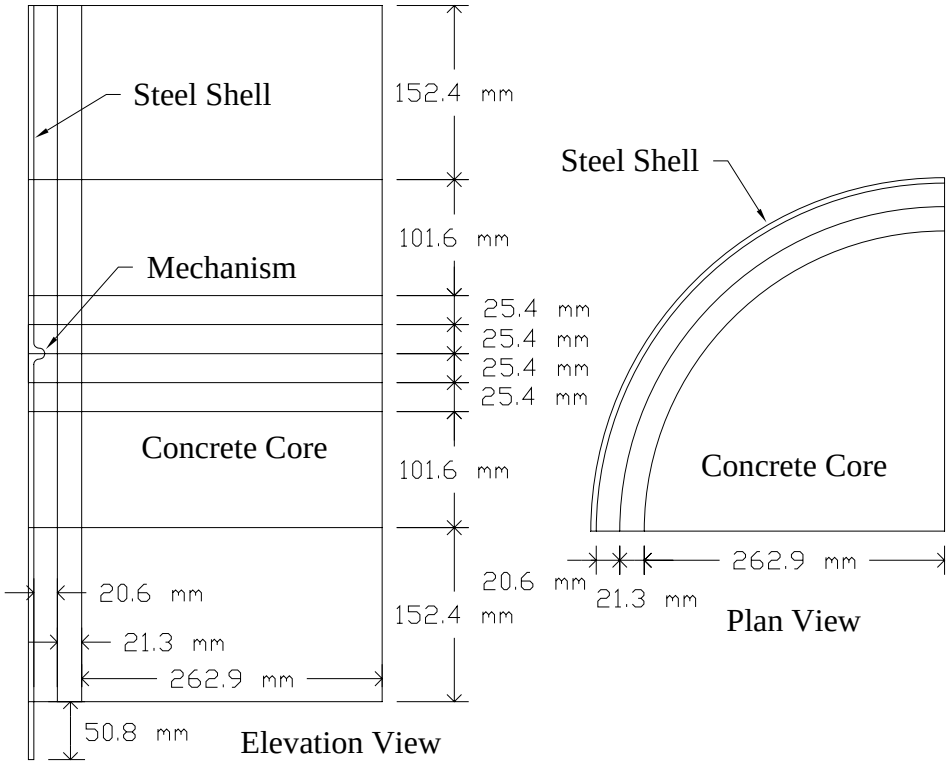


**Figure 10.9 Typical ABAQUS Partitioning Strategy**

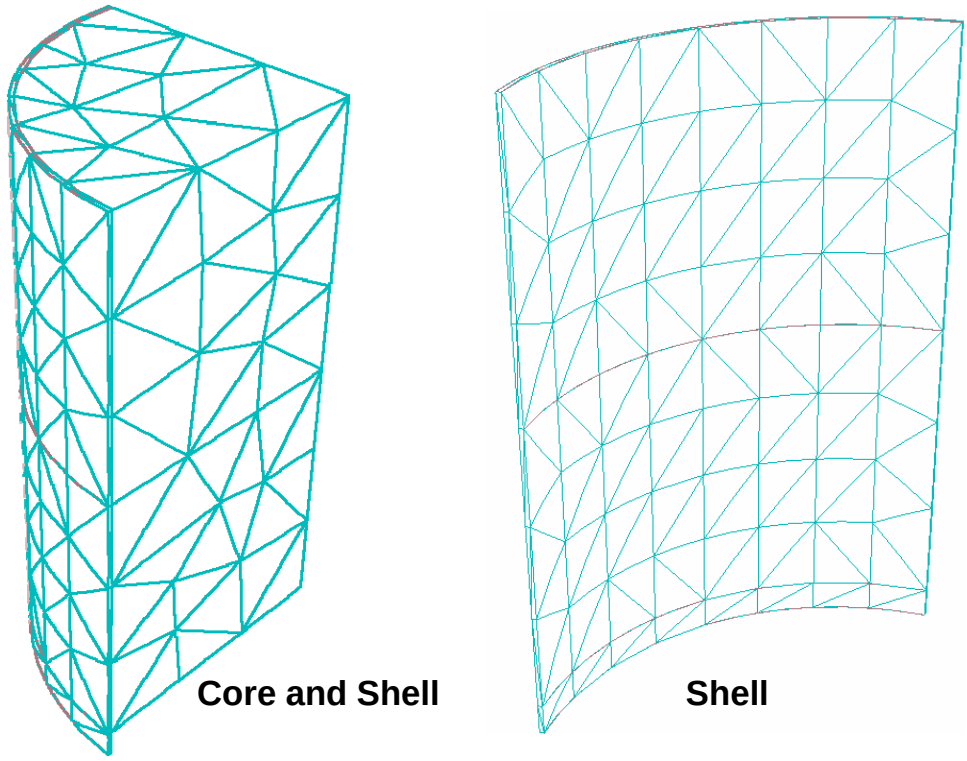


**Figure 10.10 Mesh for Model of Test Unit # 1 (D/t = 128)**

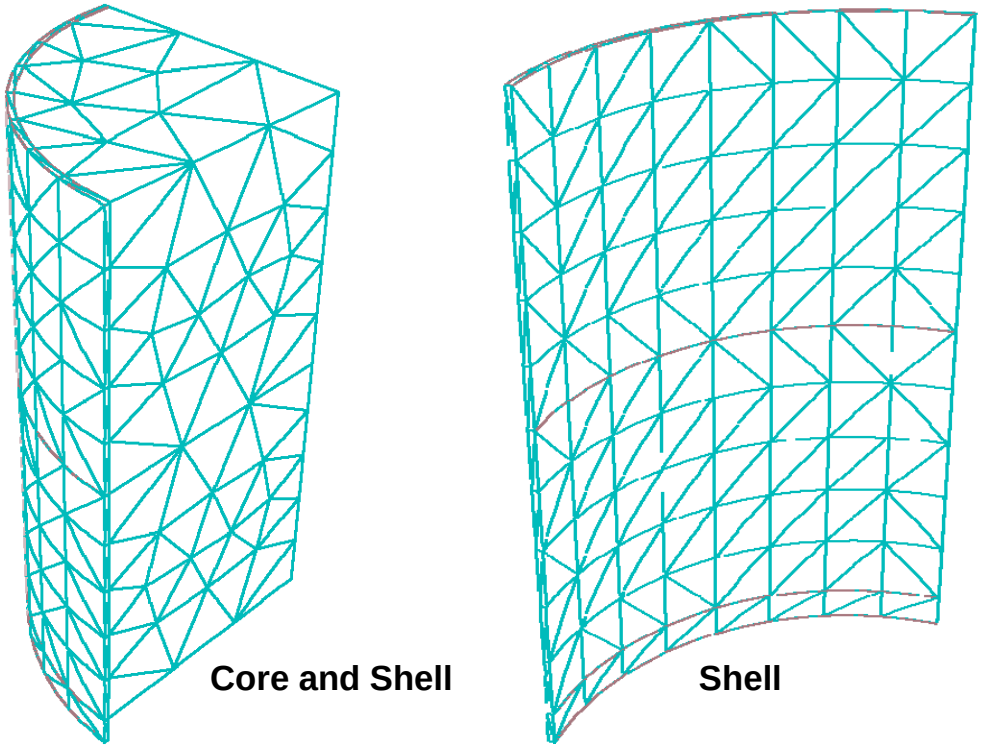


**Figure 10.11 Mesh for Model of Test Unit # 2 (D/t = 94)**

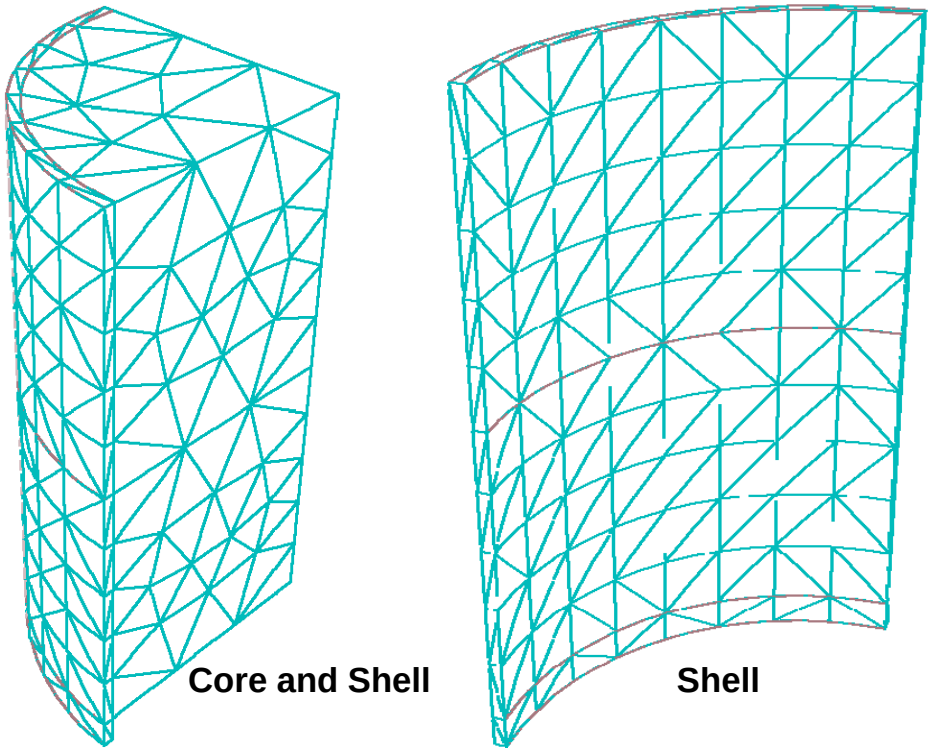


**Figure 10.12 Mesh for Model of Test Unit # 3 (D/t = 46)**

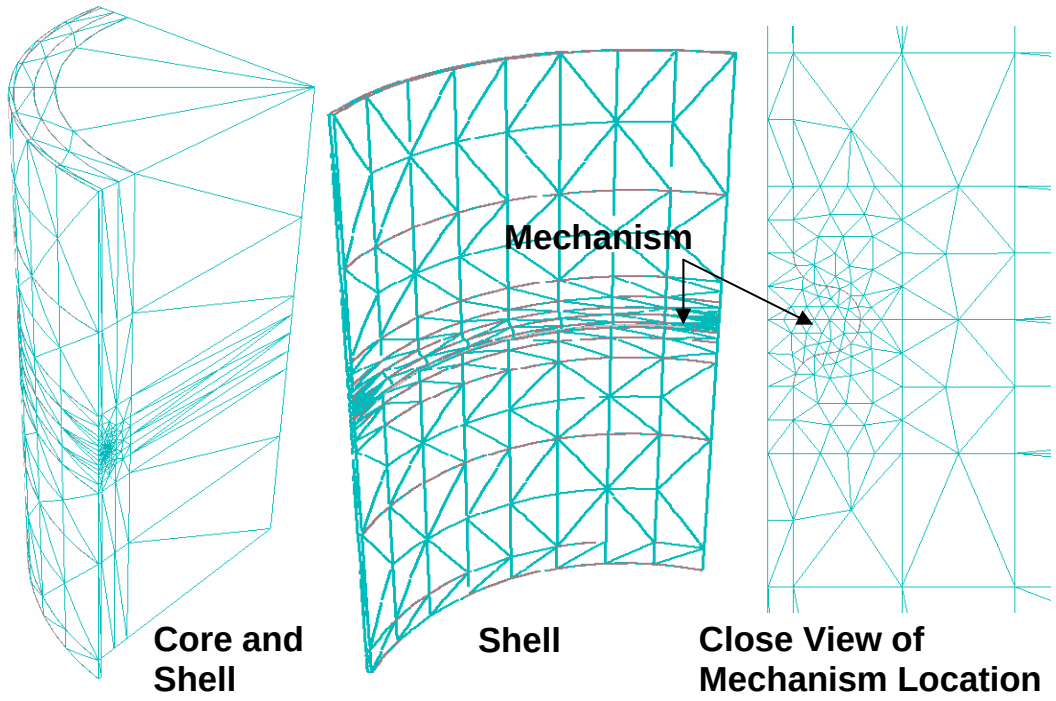


**Figure 10.13 Mesh for Model of Test Unit # 5 with a Shear Ring (D/t = 128)**

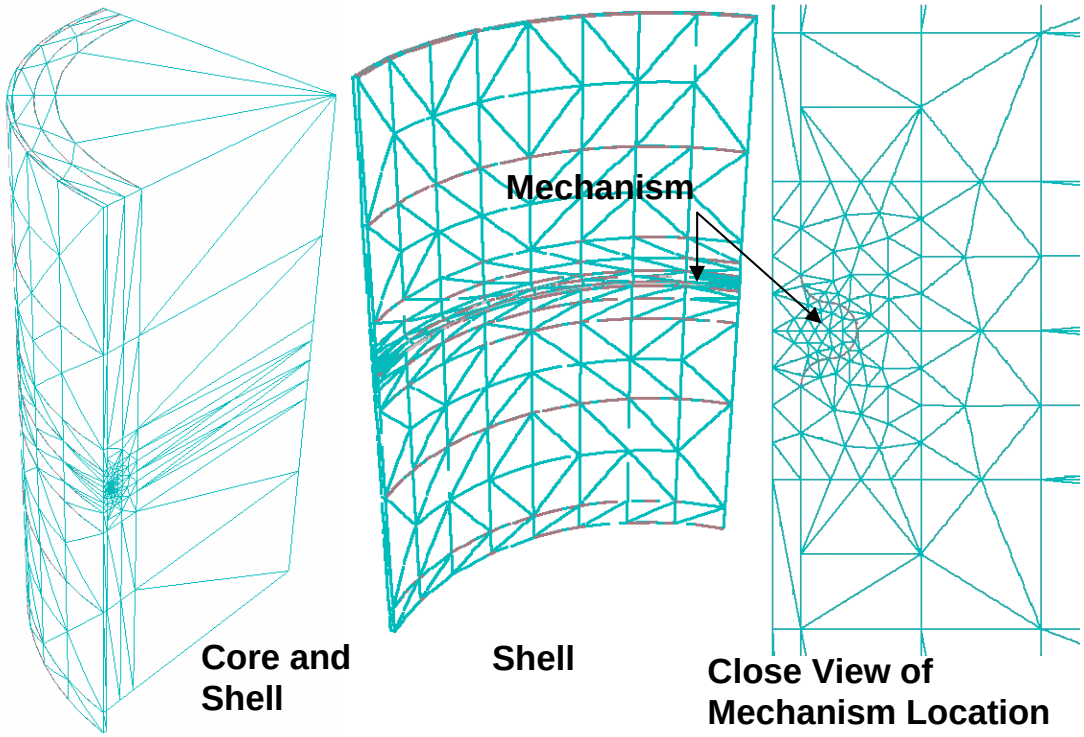


**Figure 10.14 Mesh for Model of Test Unit # 7 with a Welded Bar (D/t = 128)**

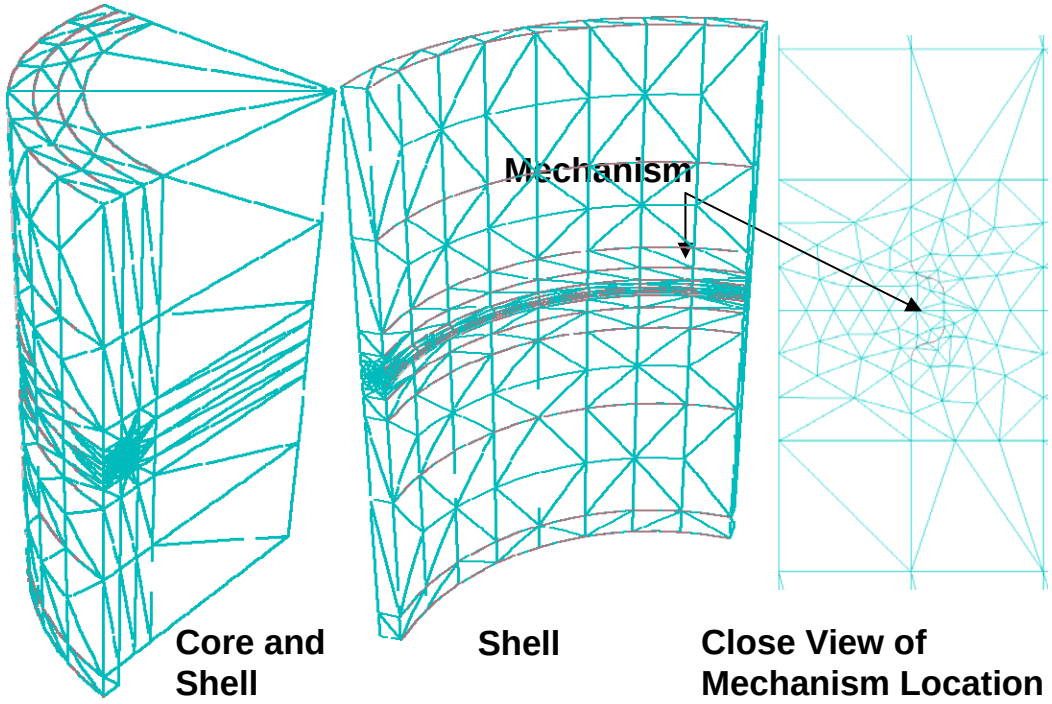


**Figure 10.15 Mesh for Model of Test Unit # 17 with a Shear Ring (D/t = 24)**

### 10.3.6 Elements

A modified second order tetrahedral element was used for the steel shell and the concrete core. This three dimensional continuum element, referred to as C3D10M in ABAQUS, was designed for complex contact analysis simulations. The modified designation, M, in the element name denotes that this element has non-zero contact forces at the element corners. The regular element, C3D10, has zero contact forces at the element corners: a poor representation for a contact analysis problem. The tetrahedral element, C3D10M, was selected over a more commonly used quadrilateral or hexahedral element, because of its capability at contact analysis.

The models typically had approximately 2,000 elements. As mentioned previously the number of elements influences the accuracy and the computational cost of the analysis. This target was set based on attempts to run models with fewer elements, and with more elements. Models with less than 2,000 elements had a severe distortion of the concrete core mesh, at the mechanism location, due to an insufficient number of elements to model the curvature of the region. Models beyond 2,000 elements had a

greater computational cost, such that an analysis could not generate any tangible results at the supercomputer center within the 18 hour run time limit. The number of elements used for the steel shell (including the mechanism) and the concrete core are listed in Table 10.1 for each test unit modeled.

### 10.3.7 Boundary Conditions

The three dimensional models took advantage of the radial symmetry by modeling a one-quarter section with the displacement restrained. Displacement was restrained in the out-of-plane directions on the concrete core and on the steel shell at radial planes corresponding to $\theta = 0^o$ and $90^o$, as shown in Figure 10.16. The vertical displacement of the concrete core and steel shell faces were not restrained, to allow for displacement. At the base of the steel shell, the displacement was restrained in all three directions to simulate the fixed base reaction. A fixed boundary condition was not applied to the top surface of the steel shell; this was done to simulate the top surface condition of the test unit. A fixed boundary condition was also not applied to the top and bottom surface of the concrete core because the applied displacement would result in these surfaces and the entire core to displace vertically.

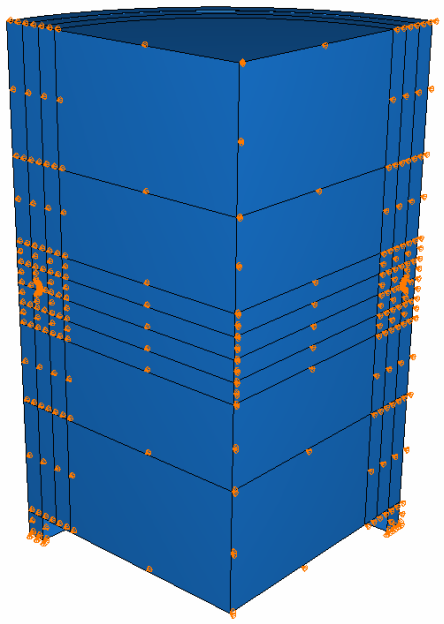

**Figure 10.16 Boundary Condition Applied to a Typical Concrete Core and Steel Shell to Simulate the Effects of Symmetry**

### 10.3.8 Applied Displacement

A vertical axial compression displacement of 50.8 mm (2.0 in.) was applied to the top of the concrete core. This displacement was applied over a time period of 1 second, with a linear ramp. A short time period was used because of the high computational requirements of the model. In the experiment, the axial displacement was applied at a rate of 1.27 mm/sec (0.05 in/sec) at the greater axial displacements. If this loading rate was used in the ABAQUS models then a time period of 40 seconds would be needed for the applied displacement. A time period of 40 seconds was impractical for analysis purposes as the computation would require additional increments of analysis for a long time period.

The axial compression displacement was specified in ABAQUS as a boundary condition applied to the top surface of the concrete core. Test units which had a mechanism had the axial compression displacement applied to the concrete core top surface, except the radial partition adjacent to the steel shell-concrete core interface, as shown in Figure 10.17. This was done because some of the nodes along the interface displaced in the opposite direction when the axial displacement was applied to the entire concrete core. The application of the axial displacement to the core, excluding the radial partition adjacent to the steel shell-concrete core interface reflected the test unit design. As presented in Chapter 4, the test units had a radial gap of approximately 12.7 mm (0.5 in.) between the top of the steel shell internal diameter and the concrete core section to which axial displacement was applied.

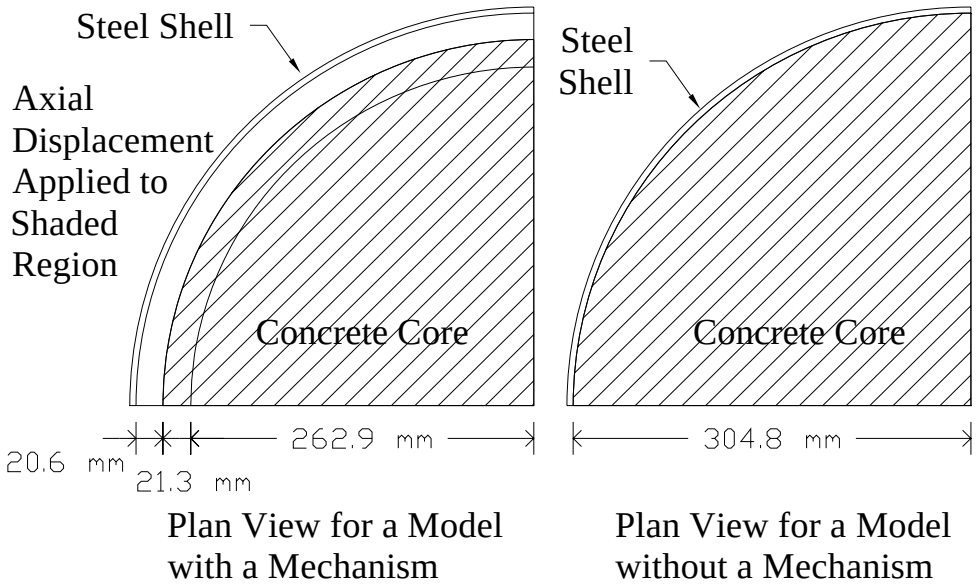


**Figure 10.17 Axial Displacement Applied to the Concrete Core**

## 10.4 Model Results

In this section, the results obtained from finite element modeling of test units with a mechanism, and test units without a mechanism are presented. Results include monotonic axial compression response curves and stress distributions within the steel shell, mechanism, and concrete core. The monotonic axial compression curves will be presented with the corresponding axial force-axial displacement hysteretic response loops for axial compression.

### 10.4.1 Shear Ring Model at a D/t Ratio of 128

The monotonic response for the finite element model of Test Unit # 5 with a shear ring at a D/t ratio of 128, was found to be influenced by the specified friction between the concrete core and the steel shell. A comparison between two of the monotonic curves, with different levels of friction, and the axial compression response of the test unit is shown in Figure 10.18. The model, u5v4, had a low level of friction, with a static coefficient of friction, $\mu_s$, kinetic coefficient of friction, $\mu_k$, and decay constant, $d_c$, of 0.01, 0.008, and 0.05, respectively. The model, u5v6, had a greater level of friction, with a static coefficient of friction, $\mu_s$, kinetic coefficient of friction, $\mu_k$, and decay

constant, $d_c$, of 0.175, 0.125, and 0.03, respectively. Both models had the same initial stiffness; however, the yield point and the response at greater axial displacements were different. The model with the greater friction slightly over-predicted the response, whereas the model with a low level of friction had a slight under-prediction of the response, as shown in Figure 10.18. The model with the greater level of friction was ran only to an axial displacement of -5.3 mm (-0.21 in.), due to limitations in the available computing power and time.

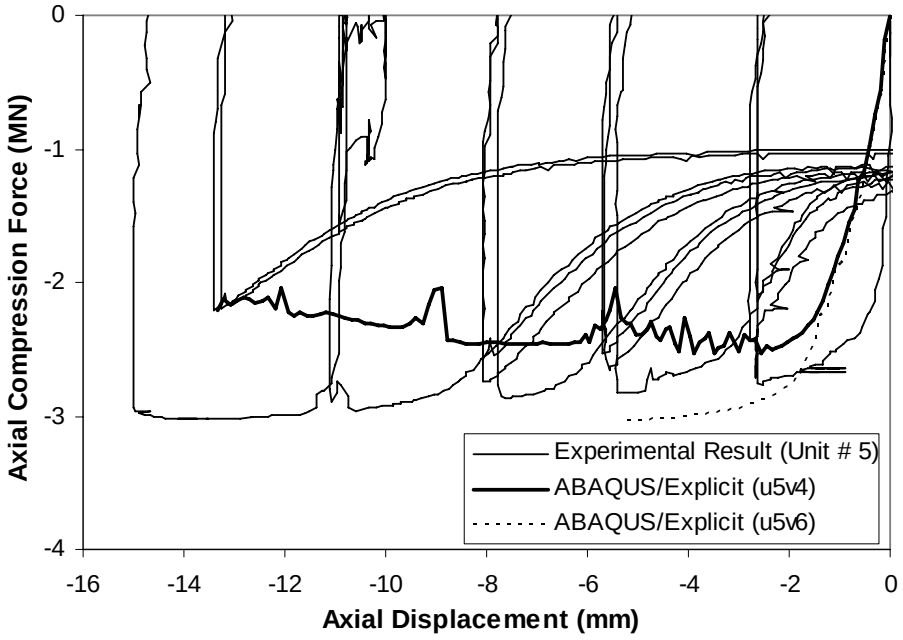


**Figure 10.18 Comparison of Experimental Results with a Monotonic Axial Compression Response Generated by ABAQUS for Test Unit # 5 (Shear Ring) at a D/t Ratio of 128**

Both of the aforementioned models had a failure mode similar to the actual test unit in that the steel shell deformed out-of-plane and concrete crushed at the shear ring location. Concrete crushing is shown in Figure 10.19 by the high stresses in the concrete core above the mechanism location where the stresses clearly exceeded $f_c^{'}$. In the three dimensional von Mises stress plot of the concrete core surface (in contact with the shell and shear ring), the maximum stress obtained was 2760 MPa (400 ksi). A high stress concentration occurred in a concrete core element, above the shear ring, and along the

model edge (for symmetry), as shown in Figure 10.20. This high stress concentration is a result of the coarse mesh used which was a necessity for an analysis to be conducted.

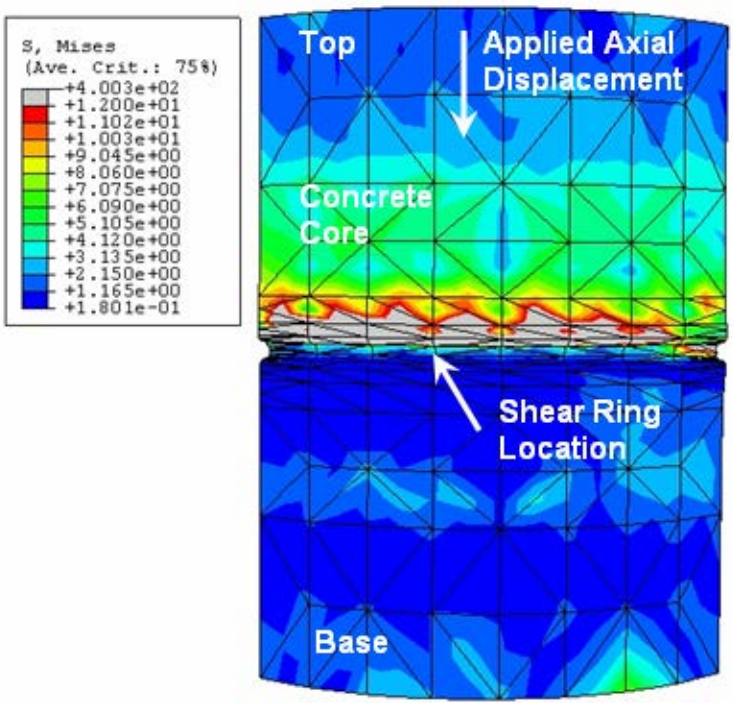


**Figure 10.19 Concrete Core of ABAQUS Model for Test Unit # 5**

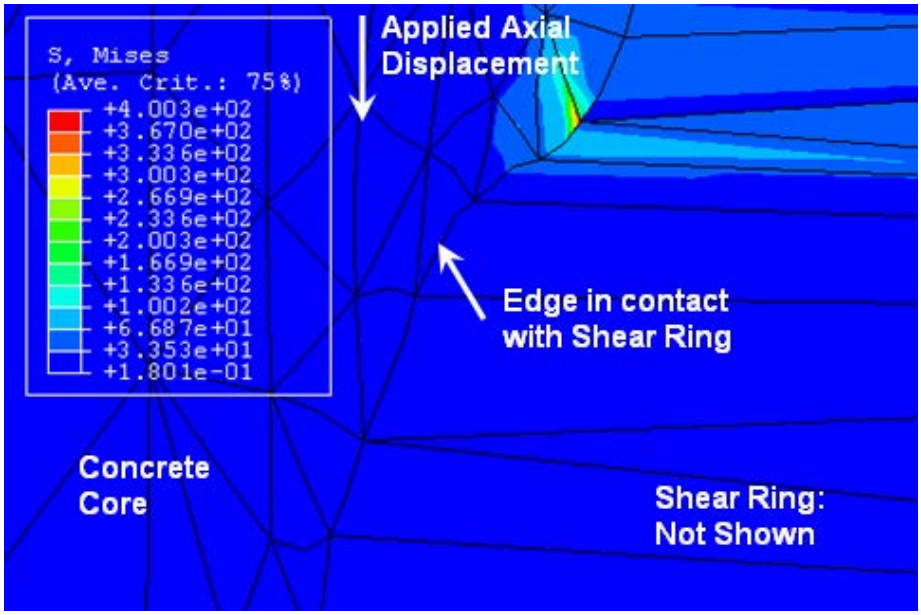


**Figure 10.20 High Stress Point on the Concrete Core above the Shear Ring Location of the ABAQUS Model for Test Unit # 5**

A void formed below the shear ring, as shown in Figure 10.21. This void formation and concrete crushing had a corresponding yielding and out-of-plane deformation of the steel shell, as shown in Figure 10.22. In the three dimensional von Mises stress plot of the steel shell exterior surface, the maximum stress obtained was 2760 MPa (400 ksi). This stress was obtained in several elements in the shear ring, as shown in Figure 10.23. This high stress concentration is the result of the necessity of a coarse mesh to allow for the analysis to be run. The von Mises stress plots of Figures 10.20, 10.21, 10.22, and 10.23 correspond to the last increment calculated at an axial displacement of -5.3 mm (-0.21 in.) for the model, E3Dunit5v6, which had the greater level of friction.

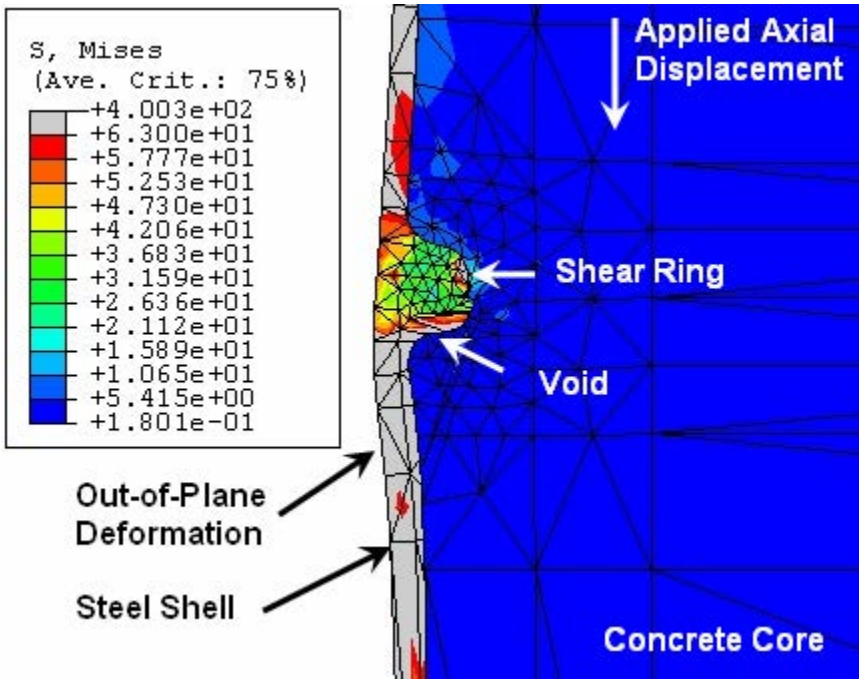


**Figure 10.21 Deformation of Shear Ring, in ABAQUS Model for Test Unit # 5**

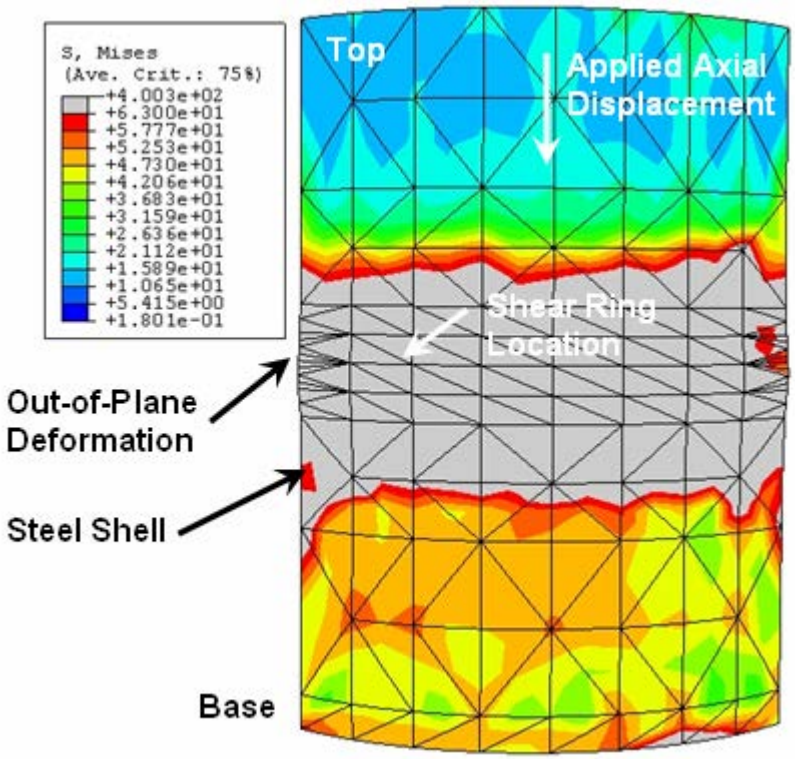


**Figure 10.22 Steel Shell of ABAQUS Model for Test Unit # 5**

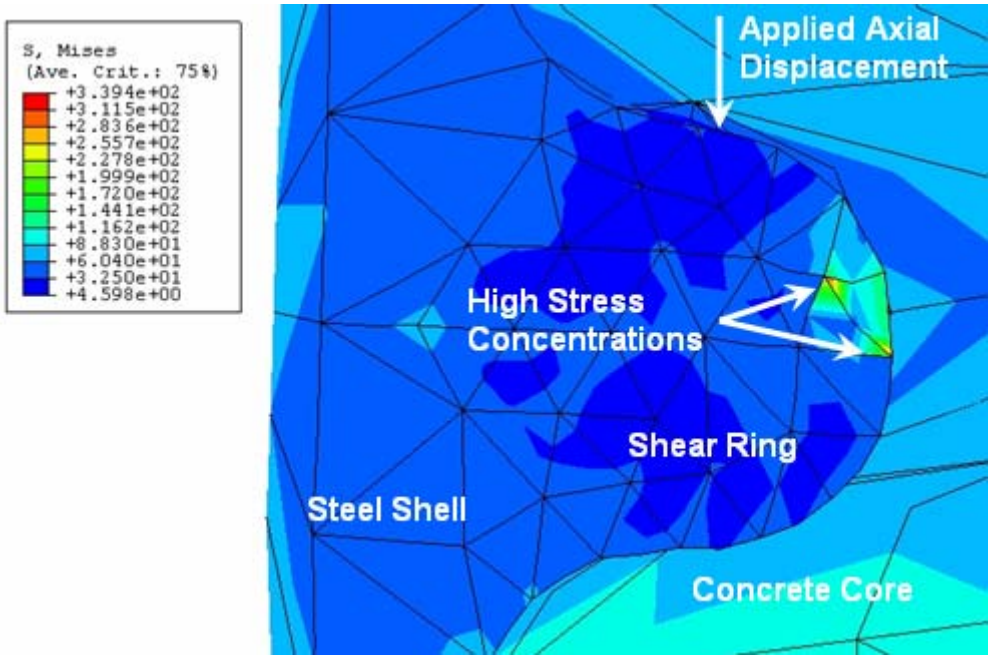


**Figure 10.23 High Stress Point on the Shear Ring of the ABAQUS Model for Test Unit # 5**

### 10.4.2 Welded Bar Model at a D/t Ratio of 128

The monotonic response for the finite element model of Test Unit # 7 with a welded bar at a D/t ratio of 128 is shown in Figure 10.24. This ABAQUS model had a level of friction with a static coefficient of friction, $\mu_s$, kinetic coefficient of friction, $\mu_k$, and decay constant, $d_c$, of 0.175, 0.125, and 0.03, respectively. This level of friction matched the greater level of friction used in the modeling of Test Unit # 5, as presented in the previous section. This model resulted in a monotonic curve with a close fit to the experimental hysteretic response, as shown in Figure 10.24. This model was executed to an axial displacement of -8.05 mm (-0.31 in.), due to limitations in the available computing power and time.

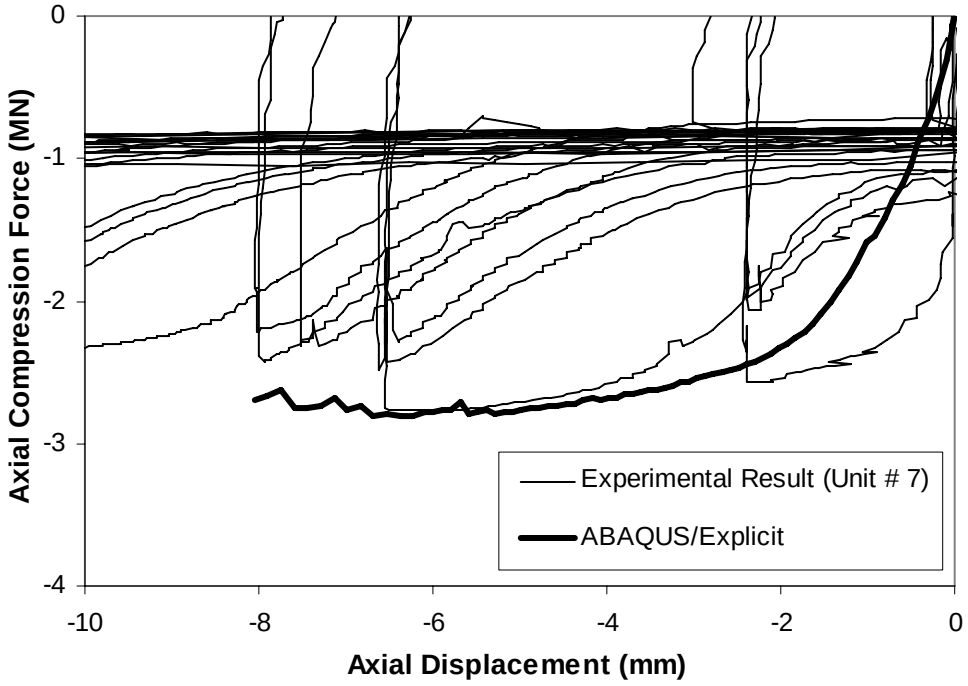


**Figure 10.24 Comparison of Experimental Results with a Monotonic Axial Compression Response Generated by ABAQUS for Test Unit # 7 (Welded Bar) at a D/t Ratio of 128**

This model had a failure mode similar to the actual test unit in that the steel shell deformed out-of-plane and concrete crushed at the shear ring location. Concrete crushing is shown by the high stresses in the concrete core above the mechanism where the stresses clearly exceeded $f_c^{'}$. As the concrete core displaced vertically relative to the

steel shell and the shear ring, the concrete above the shear ring crushed, as shown by the high stresses in the concrete core of Figure 10.25. In the three dimensional von Mises stress plot, of the concrete core surface (in contact with the shell and shear ring), the maximum stress obtained was 1720 MPa (250 ksi). A high stress concentration occurred in a concrete core element, above the shear ring, and along the model edge (for symmetry), as shown in Figure 10.26. This high stress concentration is a result of the coarse mesh used.

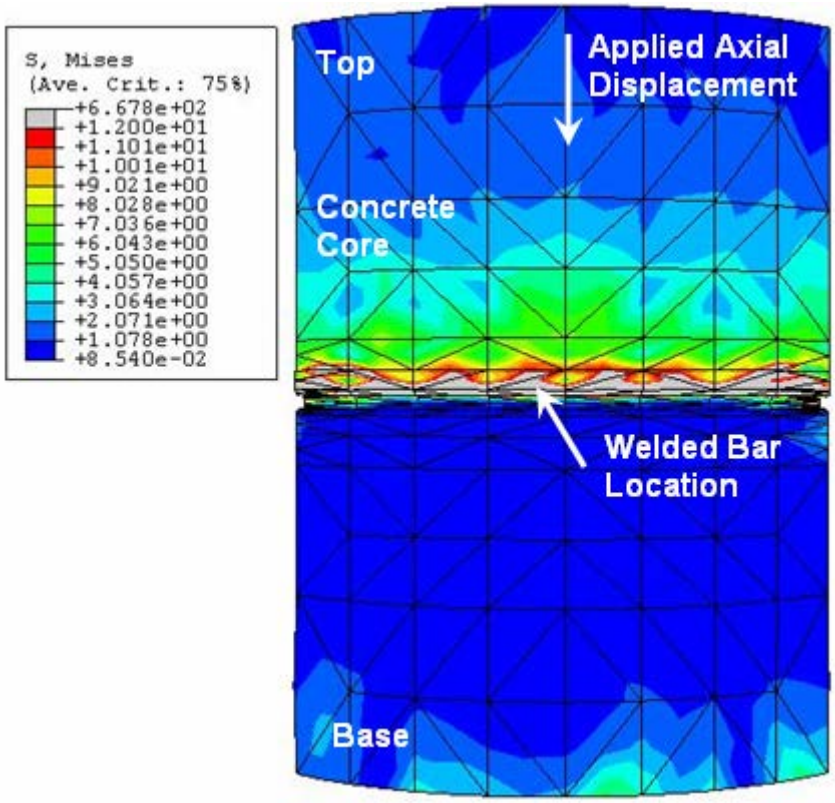


**Figure 10.25 Concrete Core of ABAQUS Model for Test Unit # 7**

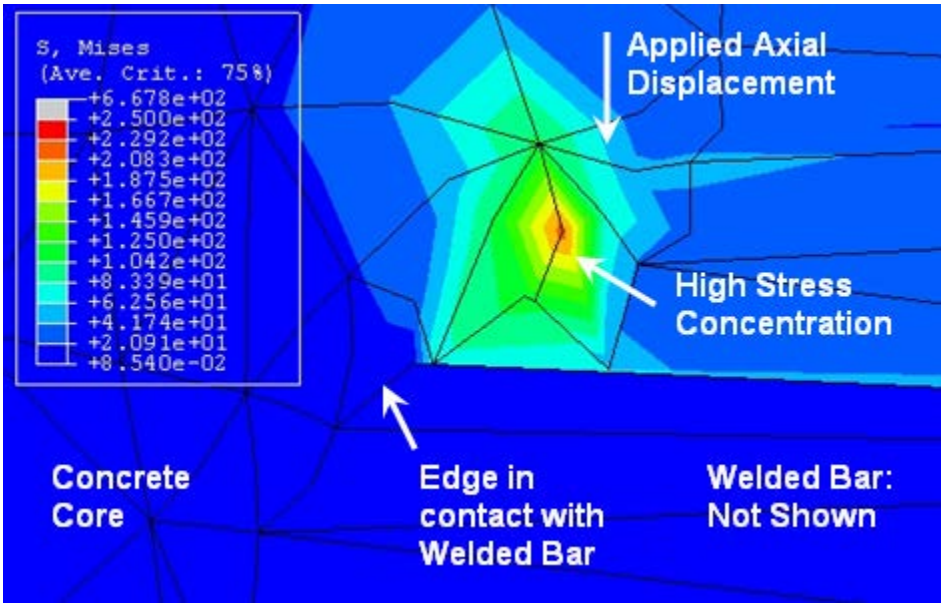


**Figure 10.26 High Stress Point on the Concrete Core above the Shear Ring Location of the ABAQUS Model for Test Unit # 7**

A void formed below the shear ring, as shown in Figure 10.27. This void formation and concrete crushing had a corresponding yielding and out-of-plane deformation of the steel shell, as shown in Figure 10.28. In the three dimensional von mises stress plot, of the steel shell exterior surface, the maximum stress obtained was 721 MPa (105 ksi). This stress was obtained in several regions of the steel shell, just below the welded bar, as shown in Figure 10.29. Figures 10.25, 10.26, 10.27, 10.28 and 10.29 correspond to the last increment calculated, at an axial displacement of -8.05 mm (-0.31 in.).

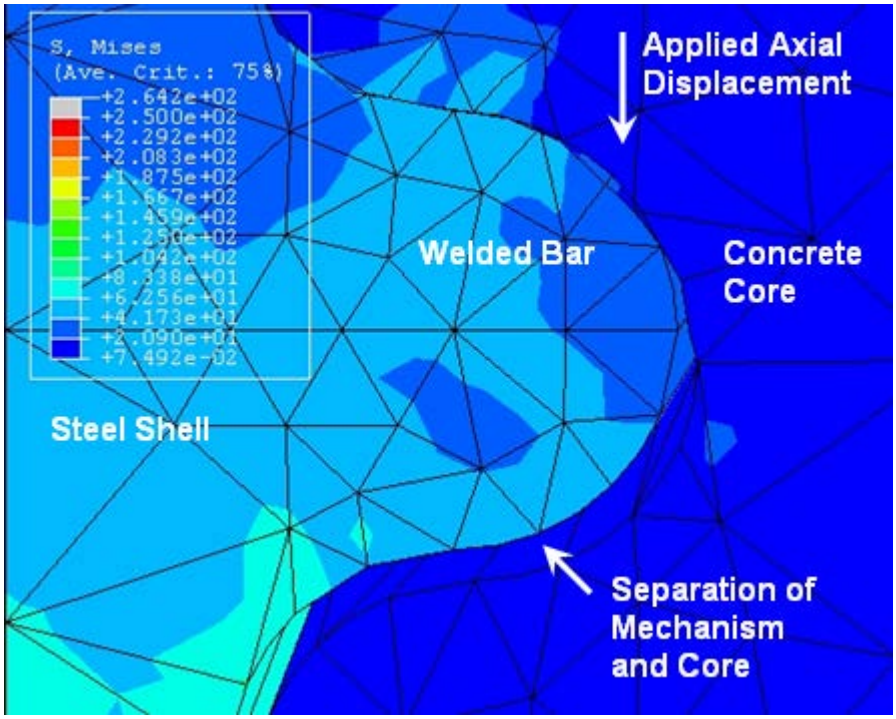


**Figure 10.27 Formation of a Void below the Shear Ring, in ABAQUS Model for Test Unit # 7**

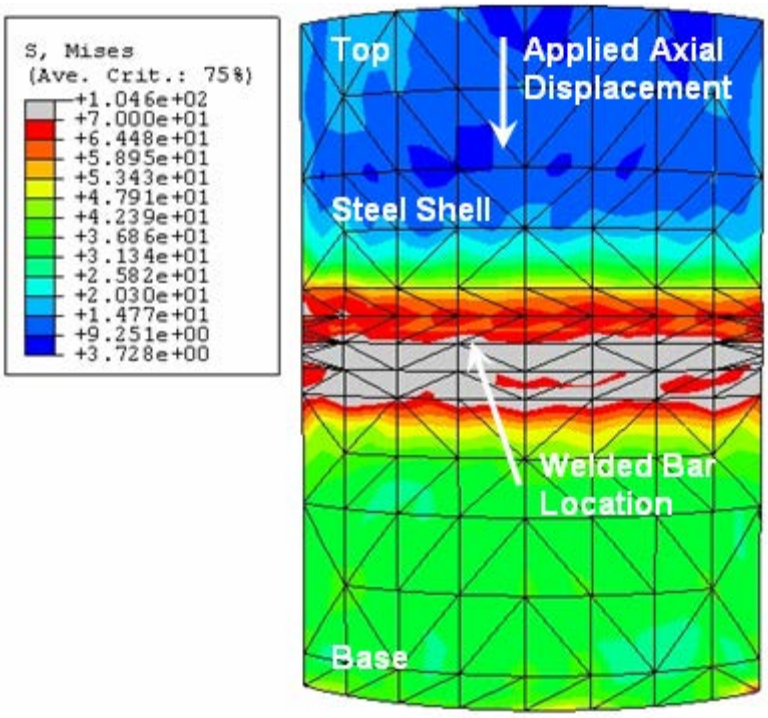


**Figure 10.28 Steel Shell of ABAQUS Model for Test Unit # 7**

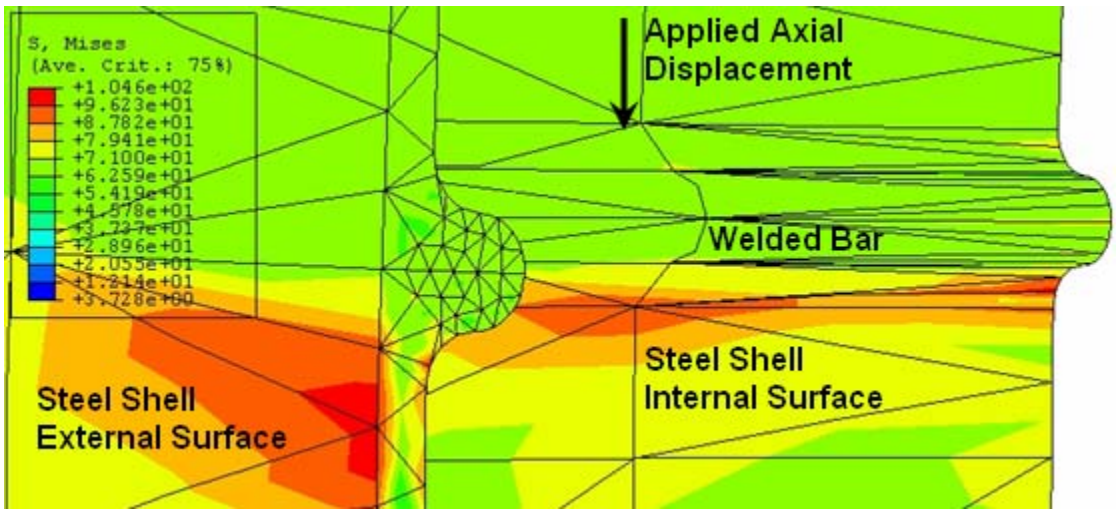


**Figure 10.29 High Stress Regions on the Steel Shell of the ABAQUS Model for Test Unit # 7**

### 10.4.3 Shear Ring Model at a D/t Ratio of 24

The monotonic response for the finite element model of Test Unit # 17 with a shear ring at a D/t ratio of 24 was found to be highly influenced by the specified friction between the concrete core and the steel shell. A comparison between three of the monotonic curves, with different levels of friction, and the axial compression response of the test unit is shown in Figure 10.30. The ABAQUS model, E3Dunit17v6a, had a low level of friction, with a static coefficient of friction, $\mu_s$, kinetic coefficient of friction, $\mu_k$, and decay constant, $d_c$, of 0.01, 0.008, and 0.05, respectively. The ABAQUS model, E3Dunit17v7, had a greater level of friction, with a static coefficient of friction, $\mu_s$, kinetic coefficient of friction, $\mu_k$, and decay constant, $d_c$, of 0.175, 0.125, and 0.03, respectively. The ABAQUS model, E3Dunit17v6a, had the greatest level of friction, with a static coefficient of friction, $\mu_s$, kinetic coefficient of friction, $\mu_k$, and decay constant, $d_c$, of 0.01, 0.008, and 0.05, respectively.

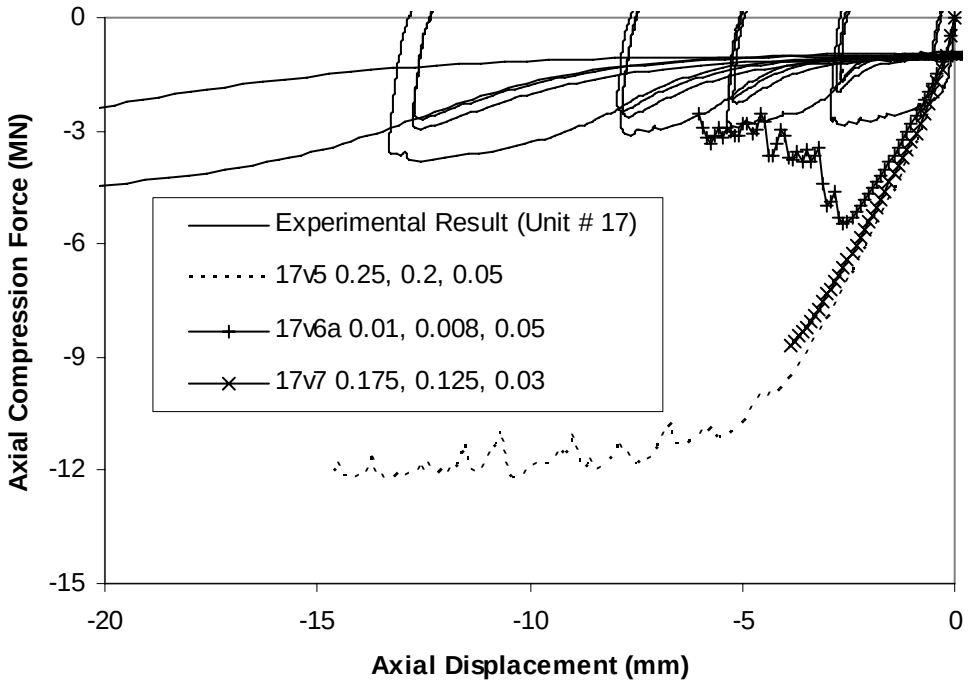


**Figure 10.30 Comparison of Experimental Results with a Monotonic Axial Compression Response Generated by ABAQUS for Test Unit # 17 (Shear Ring) at a D/t Ratio of 24**

All three models had approximately the same initial stiffness, as shown in Figure 10.30; however, the yield point and response at greater axial displacements varied. Both models with a high level of friction over-predicted the response. The model with a low level of friction, E3Dunit17v6a, initially over-predicted the response. However, after the yield point was obtained the axial force decreased sharply and approached the test unit hysteretic response. The model with the greater level of friction was ran only to an axial displacement of -14.6 mm (-0.58 in.), whereas the other two models were stopped at lesser axial displacements due to limitations in the available computing power and time.

All of the aforementioned models had a failure mode similar to the actual test unit in that concrete crushed at the shear ring location. The steel shell had no out-of-plane deformation and remained elastic. Concrete crushing is shown by the high stresses in the concrete core above the mechanism where the stresses clearly exceeded $f_c^{'}$. As the concrete core displaced vertically, relative to the steel shell and the shear ring, the concrete above the shear ring crushed as shown by the high stresses in the concrete core

of Figure 10.31. In the three dimensional von Mises stress plot of the concrete core surface (in contact with the shell and shear ring), the maximum stress obtained was 1230 MPa (179 ksi). A high stress concentration occurred in a concrete core element, above the shear ring, and along the model edge (for symmetry), as shown in Figure 10.32. This high stress concentration is a result of the coarse mesh used, which was a necessity for an analysis to be conducted. Figure 10.32 also shows the void space which formed below the shear ring.

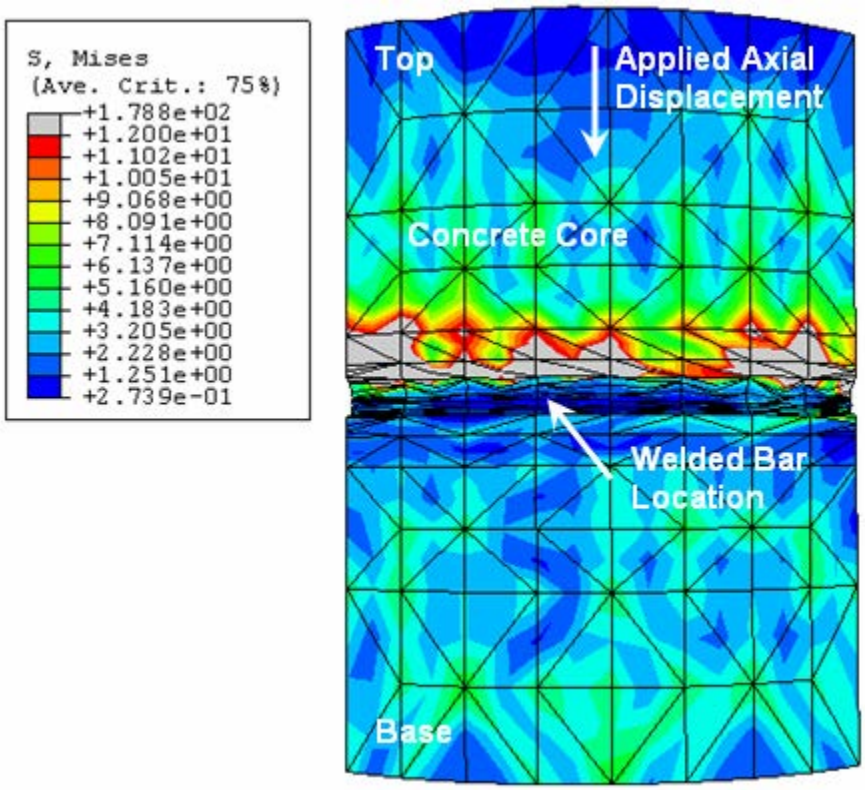


**Figure 10.31 Concrete Core of ABAQUS Model for Test Unit # 17**

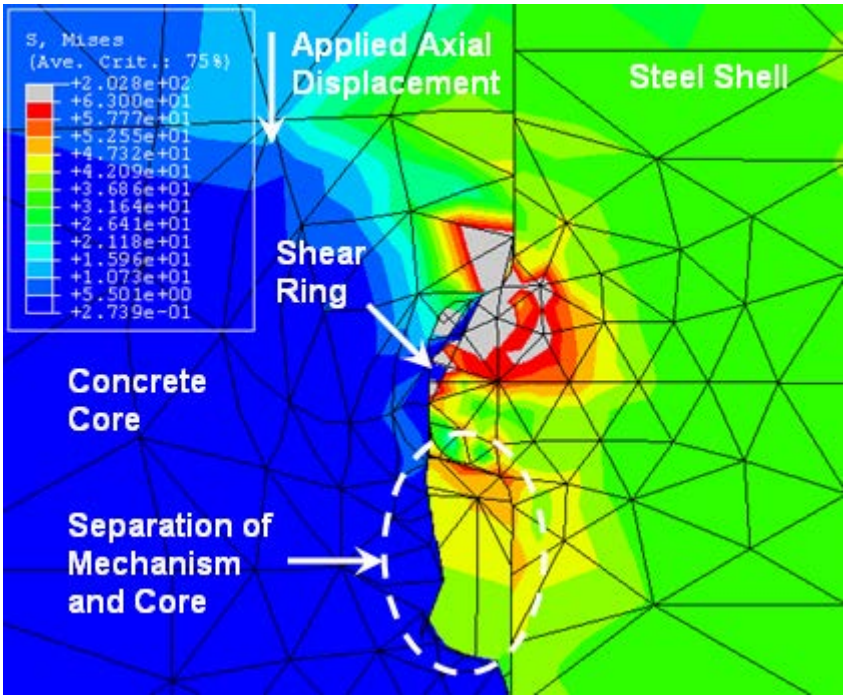


**Figure 10.32 Void Below Shear Ring, in ABAQUS Model for Test Unit # 17**

In the three dimensional von Mises stress plot, of the steel shell exterior surface, as shown in Figure 10.33, the maximum stress obtained was 2301 MPa (179 ksi). This stress was obtained in several shear ring elements, along the upper surface, as shown in Figure 10.34 and is the result of the necessity of a coarse mesh for analysis. Figures 10.31, 10.32, 10.33 and 10.34 correspond to the last increment calculated at an axial displacement of -14.6 mm (-0.58 in.) for the model E3Dunit17v6a which had the greater level of friction.

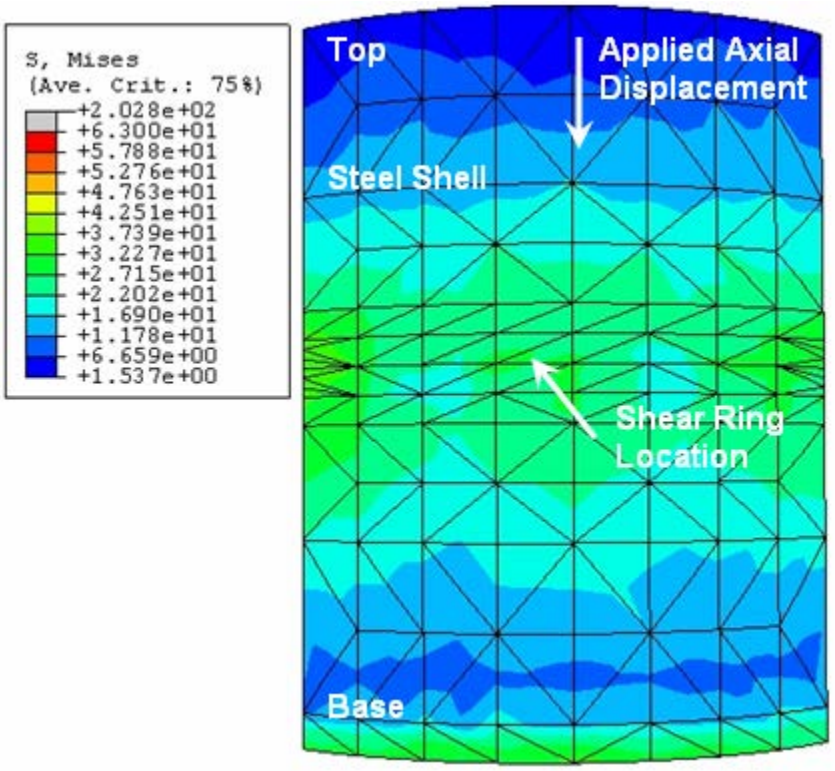


**Figure 10.33 Steel Shell of ABAQUS Model for Test Unit # 17**

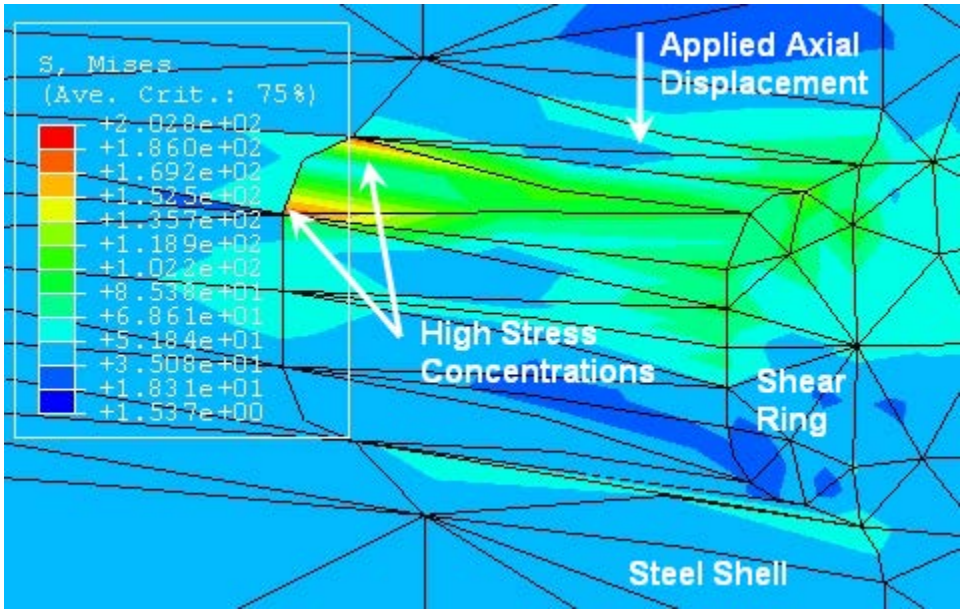


**Figure 10.34 High Stress Regions on the Shear Ring of the ABAQUS Model for Test Unit # 17**

### 10.4.4 Model of the Surface Bond at a D/t Ratio of 128

The monotonic response for the finite element model of Test Unit # 1 at a D/t ratio of 128 and without a mechanism was found to under-predict the initial stiffness. However, at axial compression displacements beyond 10 mm (0.39 in.), the model provided a better prediction of the friction. A comparison of the monotonic response from the ABAQUS model and the test unit axial compression hysteretic response is shown in Figure 10.35. The ABAQUS model response had a constant fluctuation (jagged profile) due to the nature of the problem, being a contact analysis problem. The model was executed until an axial compression displacement of 24 mm (0.94 in.) after which the model was terminated due to limitations on the computational time available. The interaction property used in this model had a static coefficient of friction, $\mu_s$, of 0.175, a kinetic coefficient of friction, $\mu_k$, of 0.125, and a decay constant, $d_c$, of 0.03. A level of friction lower than this would under-predict the response. This friction property was used as it provided decent results for the test units at D/t ratios of 94 and 46, without a mechanism, as presented in the following sections. In this model, the axial displacement was applied to the entire reinforced concrete core.

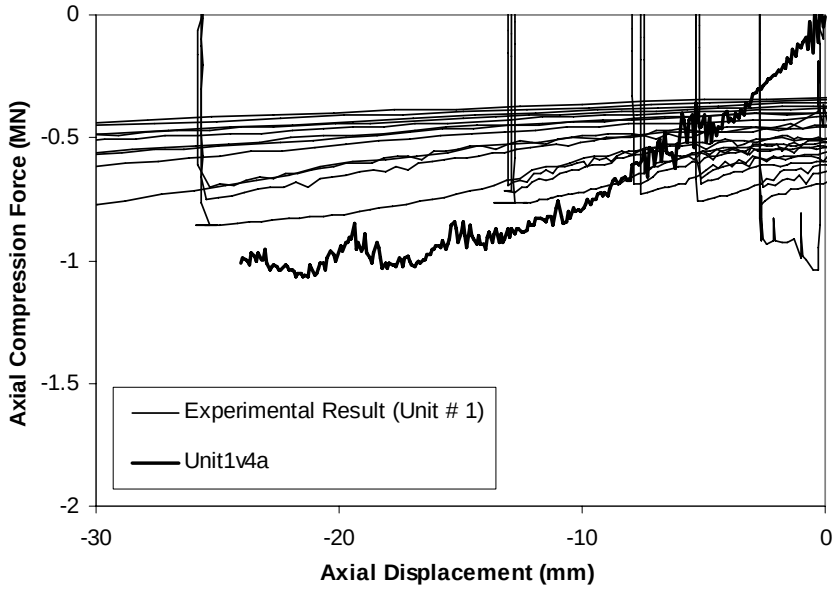


**Figure 10.35 Comparison of Experimental Results with a Monotonic Axial Compression Response Generated by ABAQUS for Test Unit # 1 at a D/t Ratio of 128**

The stress distribution in the steel shell was primarily below the yield stress, as shown in Figure 10.36. However, a maximum stress of 1080 MPa (157 ksi) was obtained in several elements due to the coarse mesh that was used. The stress distribution in the concrete core surface (in contact with the steel shell) is shown in Figure 10.37. The stresses in the core were primarily below the concrete compressive strength, $f_c^{'}$. However, a maximum stress of 1760 (255 ksi) was obtained in several elements. Stress concentrations of approximately twice the $f_c^{'}$, resulted along a portion of the base, which was similar to the experimental result in that concrete failure occurred in the base to the extent that longitudinal reinforcement bars were exposed. The final displaced state of the concrete core relative to the steel shell is shown in Figure 10.38.

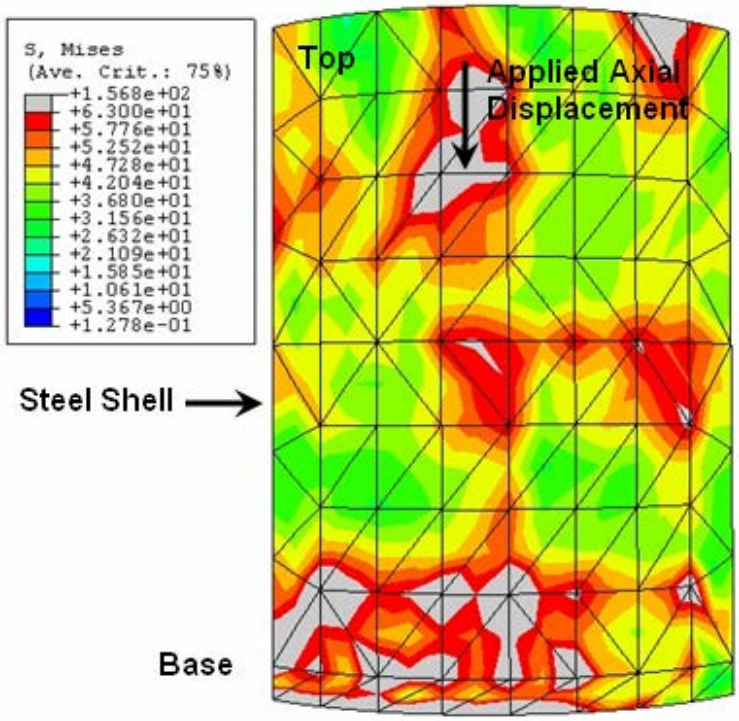


**Figure 10.36 Steel Shell of ABAQUS Model for Test Unit # 1**

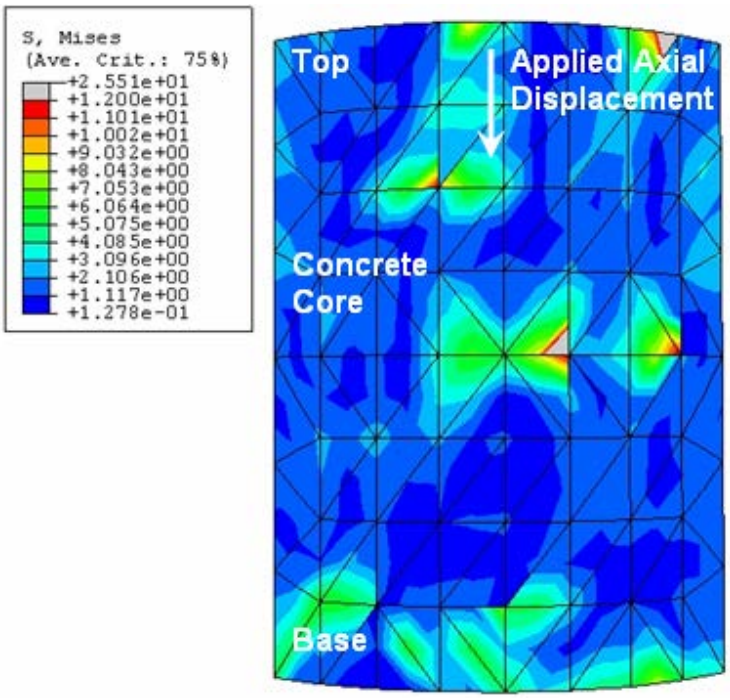


**Figure 10.37 Concrete Core of ABAQUS Model for Test Unit # 1**

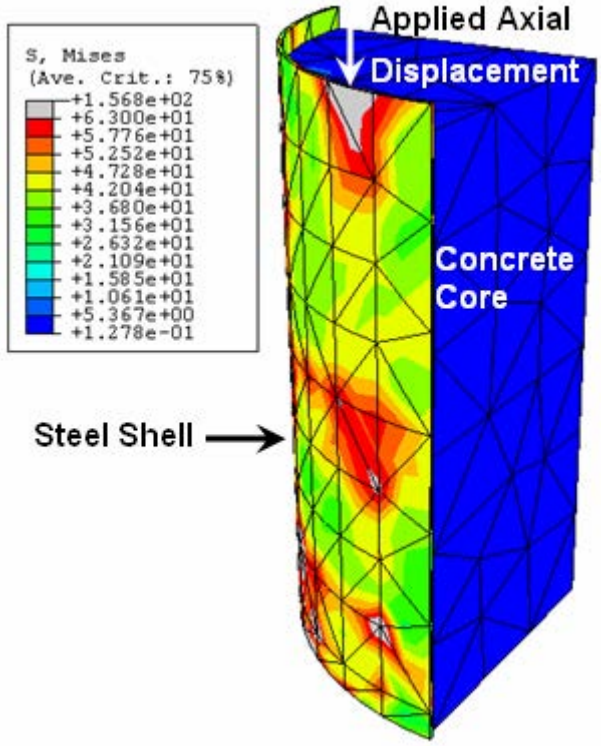


**Figure 10.38 Steel Shell and Concrete Core of ABAQUS Model for Test Unit # 1**

### 10.4.5 Model of the Surface Bond at a D/t Ratio of 94

The monotonic response for the finite element model of Test Unit # 2 at a D/t ratio of 94 and without a mechanism was found to under-predict the initial stiffness, and the axial force transferred. However, at axial compression displacements beyond 5 mm (0.20 in.) the model over-predicted the axial force transfer. A comparison of the monotonic response from the ABAQUS model and the test unit axial compression hysteretic response is shown in Figure 10.39. The ABAQUS model response had a constant fluctuation (jagged profile) due to the nature of the problem, being a contact analysis problem. The model was executed until an axial compression displacement of 24 mm (0.94 in.) after which the model was terminated due to limitations on the computational time available. The interaction property used in this model had a static coefficient of friction, $\mu_s$, of 0.175, a kinetic coefficient of friction, $\mu_k$, of 0.125, and a decay constant, $d_c$, of 0.03. This aforementioned friction property is the same as was used for the model of Test Unit # 1. In this model, the axial displacement was applied to the entire reinforced concrete core.

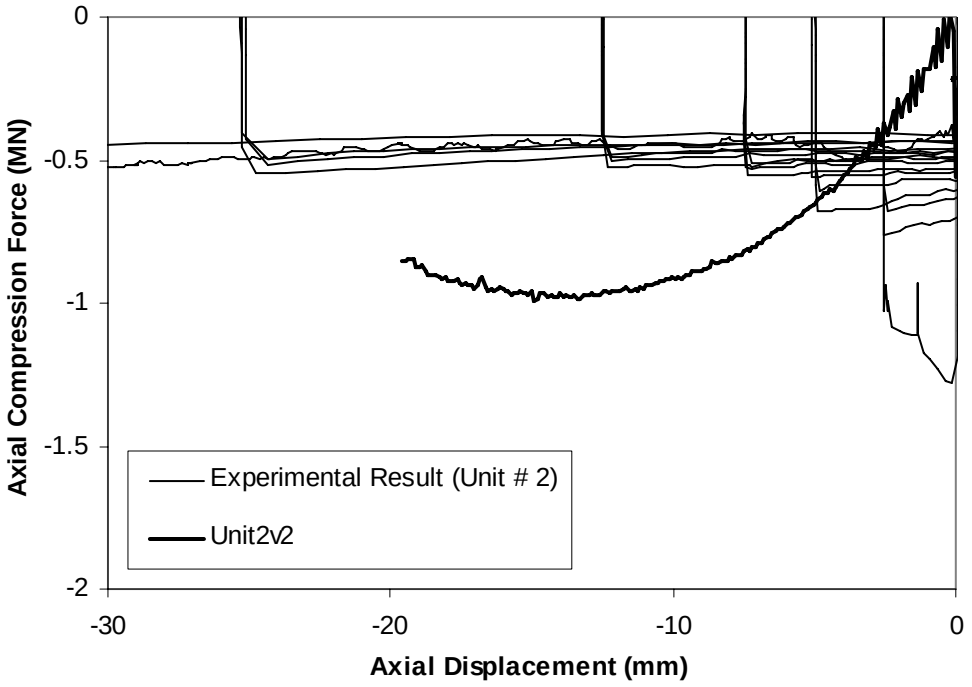


**Figure 10.39 Comparison of Experimental Results with a Monotonic Axial Compression Response Generated by ABAQUS for Test Unit # 2 at a D/t Ratio of 94**

The stress distribution in the steel shell was primarily below the yield stress, as shown in Figure 10.40. However, a maximum stress of 758 MPa (110 ksi) was obtained in several elements due to the coarse mesh that was used. The stress distribution in the concrete core surface (in contact with the steel shell) is shown in Figure 10.41. The stresses in the core were primarily below the concrete compressive strength, $f_c^{'}$. However, a maximum stress of 1370 MPa (198 ksi) was obtained in several elements. Stress concentrations equal to or slightly exceeding $f_c^{'}$ resulted along a portion of the base, which was similar to the experimental result in that concrete failure occurred in the base to the extent that longitudinal reinforcement bars were exposed. The final displaced state of the concrete core relative to the steel shell is shown in Figure 10.42.

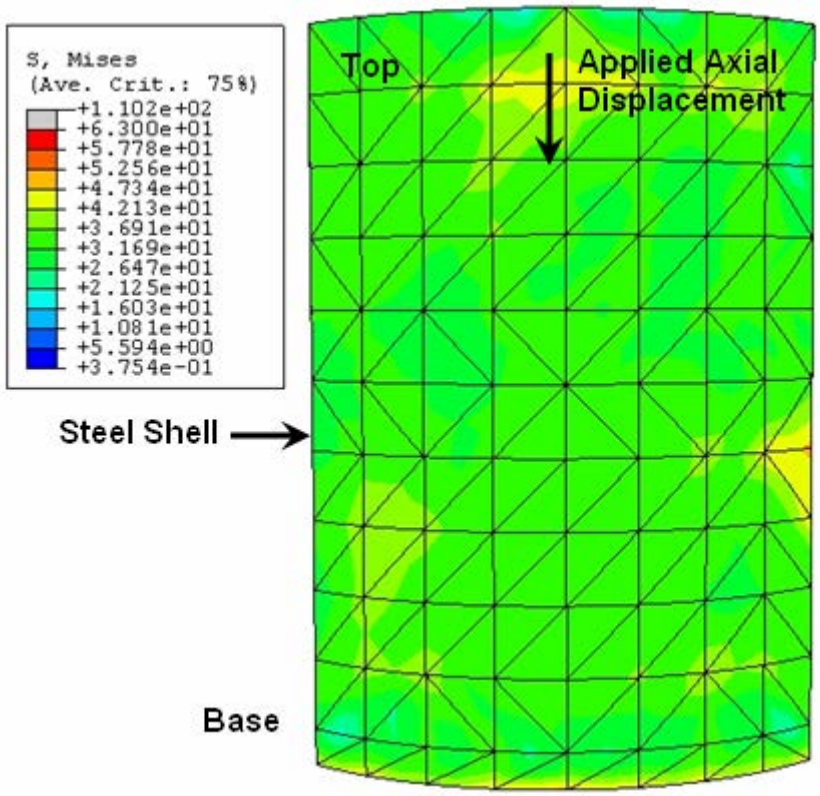


**Figure 10.40 Steel Shell of ABAQUS Model for Test Unit # 2**

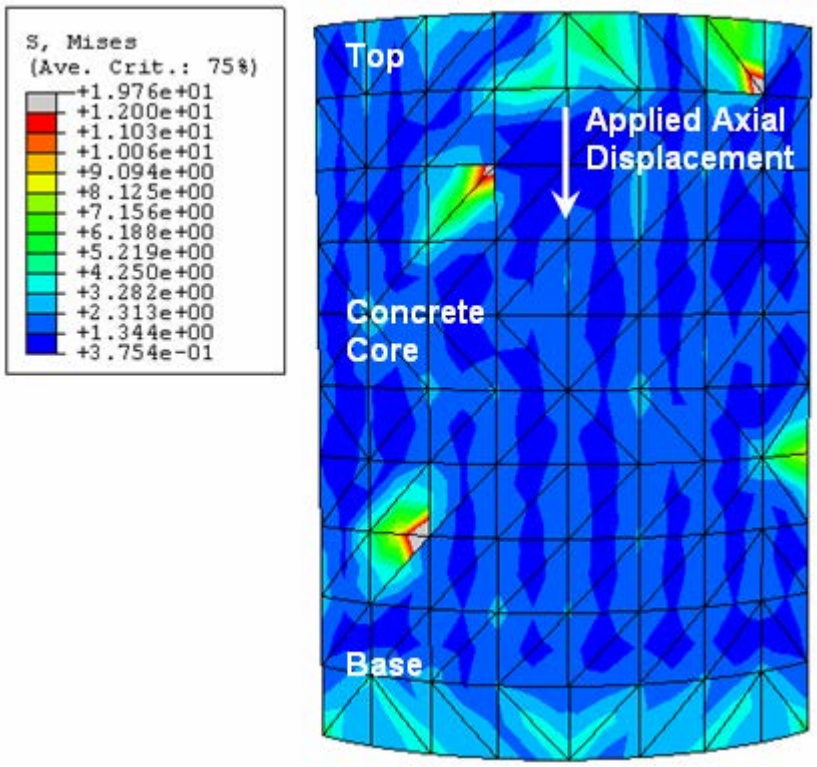


**Figure 10.41 Concrete Core of ABAQUS Model for Test Unit # 2**

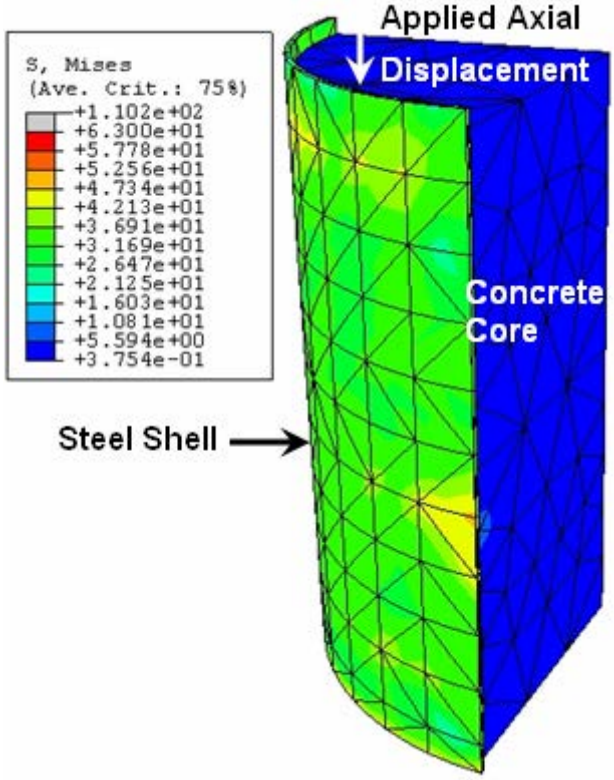


**Figure 10.42 Steel Shell and Concrete Core of ABAQUS Model for Test Unit # 2**

### 10.4.6 Model of the Surface Bond at a D/t Ratio of 46

The monotonic response for the finite element model of Test Unit # 3 at a D/t ratio of 46 and without a mechanism was found to have a poor prediction of the experimental result. A comparison of the monotonic response from the ABAQUS model and the test unit axial compression hysteretic response is shown in Figure 10.43. The model was executed until an axial compression displacement of 53 mm (2.1 in.) after which the model was terminated due to the concrete core displacing beyond the steel shell. The response of the model exceeded the test unit result at an axial displacement of 3.75 mm (0.15 in.), and continued to increase until a peak force transfer was obtained at a displacement of 15 mm (0.6 in.). This peak force transfer was similar to the peak obtained in the experiment. However, after this peak axial force was obtained the axial force decreased as displacement increased to 32 mm (1.25 in.), as shown in Figure 10.43. At this displacement, the base of the concrete core was at the base of the steel shell. Axial displacement applied to the core, beyond this displacement, resulted in the lower portion of the core losing contact with the steel shell. As the core displaced beyond the steel shell the axial force increased as if the test unit was being reloaded, as shown in Figure 10.43.

The interaction property used in this model had a static coefficient of friction, $\mu_s$, of 0.175, a kinetic coefficient of friction, $\mu_k$, of 0.125, and a decay constant, $d_c$, of 0.03. This aforementioned friction property is the same as was used for the models of Test Units # 1 and # 2. In this model the axial displacement was applied to the entire reinforced concrete core.

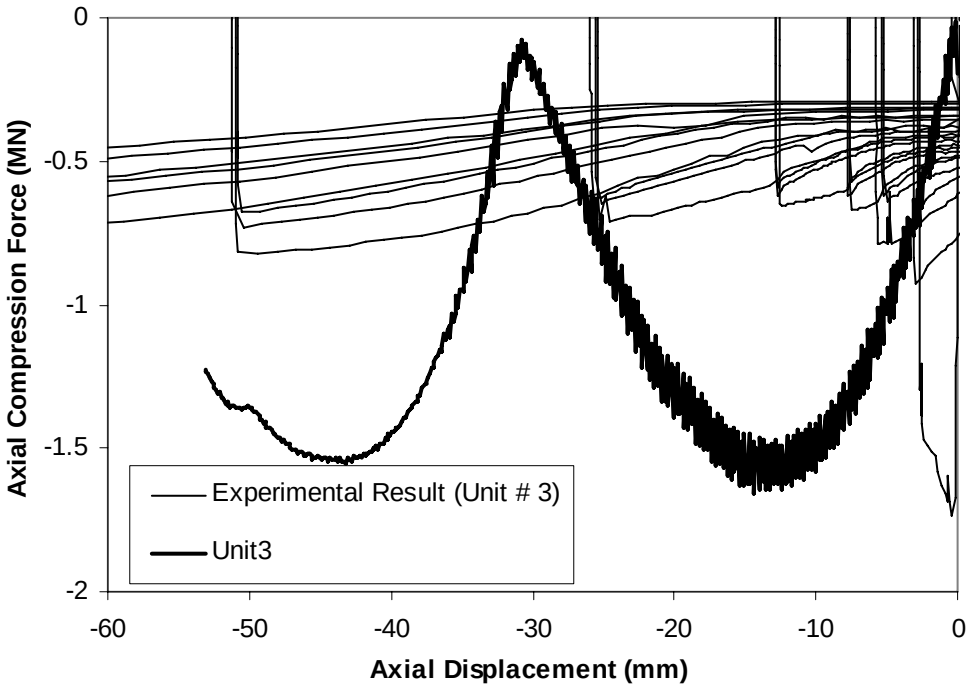


**Figure 10.43 Comparison of Experimental Results with a Monotonic Axial Compression Response Generated by ABAQUS for Test Unit # 3 at a D/t Ratio of 46**

The stress distribution in the steel shell was primarily below the yield stress, as shown in Figure 10.44. A maximum stress of 434 MPa (63 ksi), the yield stress, was obtained in several elements due to the coarse mesh that was used. The stress distribution in the concrete core surface (in contact with the steel shell) is shown in Figure 10.45. The stresses in the core were primarily below the concrete compressive strength, $f_c^{'}$. However, a maximum stress of 965 MPa (140 ksi) was obtained in several elements. Stress concentrations equal to or slightly exceeding $f_c^{'}$ resulted along a portion of the base which was similar to the experimental result in that concrete failure occurred in the base to the extent that longitudinal reinforcement bars were exposed. The final displaced state of the concrete core relative to the steel shell is shown in Figure 10.46.

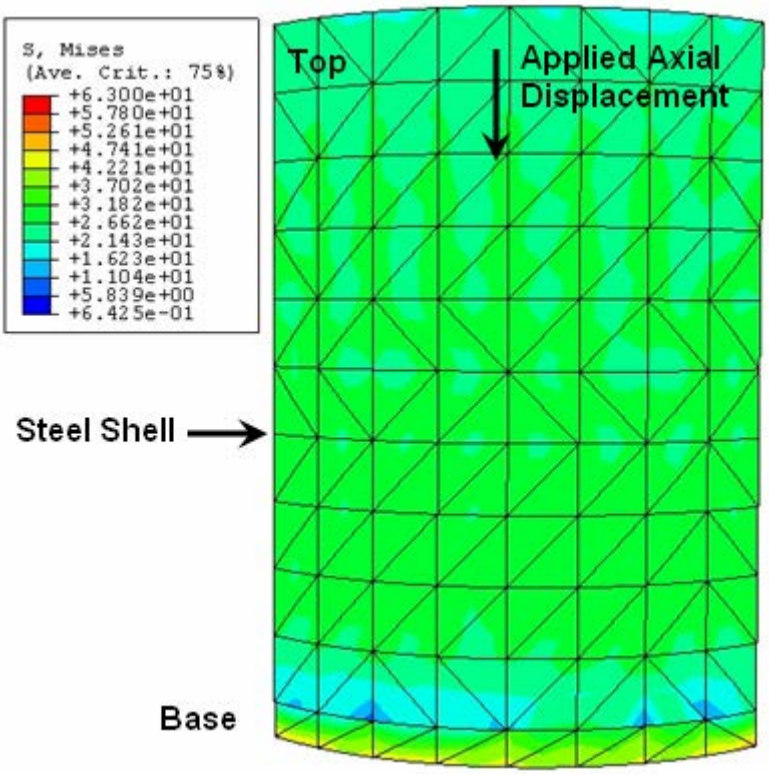


**Figure 10.44 Steel Shell of ABAQUS Model for Test Unit # 3**

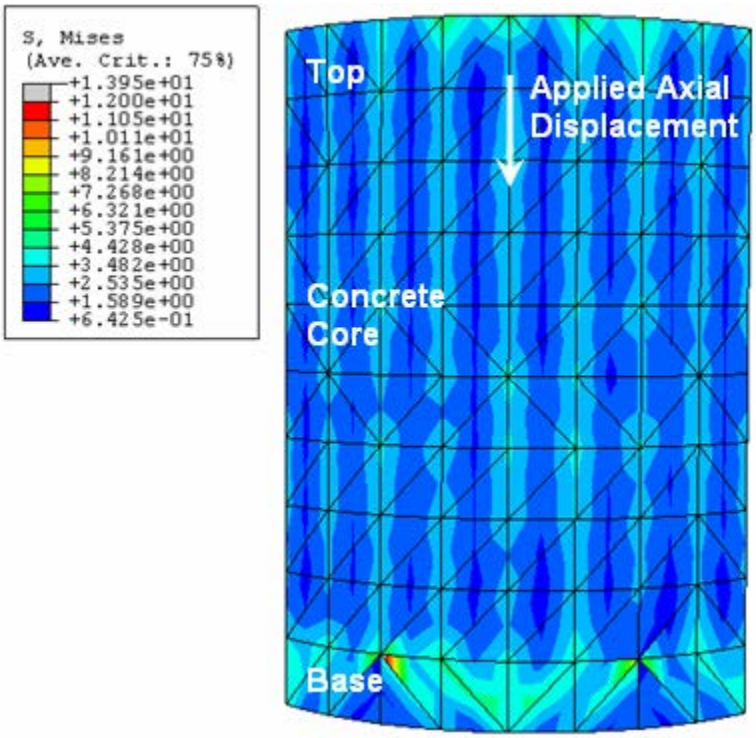


**Figure 10.45 Concrete Core of ABAQUS Model for Test Unit # 3**

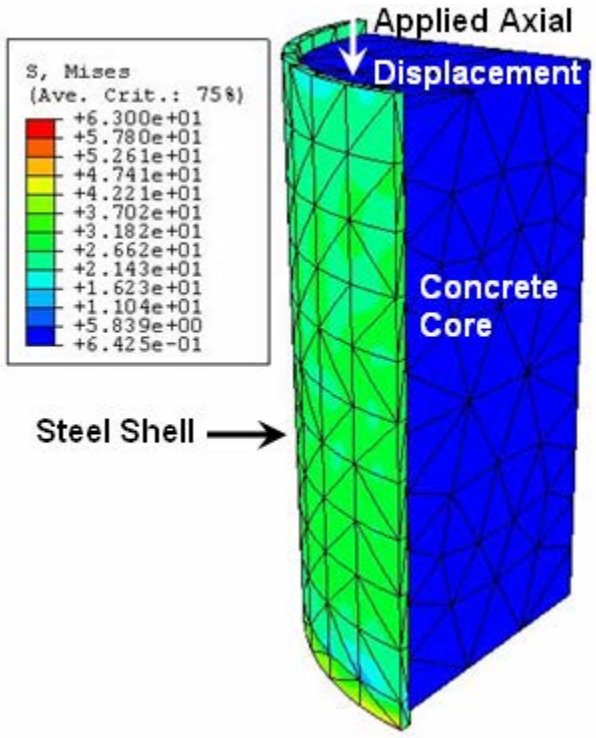


**Figure 10.46 Steel Shell and Concrete Core of ABAQUS Model for Test Unit # 3**

## 10.5 Summary of Finite Element Modeling

Finite element analysis was conducted to generate a model of the axial force transfer through a shear ring and through the surface bond. The models at a D/t ratio of 128 for the shear ring and the welded bar both resulted in axial force-axial compression curves that provided a decent envelope to the experimental results. In addition, both models matched the failure modes obtained in the test units, which consisted of concrete crushing above the mechanism, a separation (void) below the mechanism, and an out-of-plane deformation of the steel shell and the mechanism. The model of the shear ring at a D/t ratio of 24 over-predicted the axial force-axial displacement response. However, the model obtained failure through concrete crushing above the shear ring and a separation below the shear ring, which was obtained in the experiment.

Finite element modeling of the surface bond versus the variation of the D/t ratio provided mixed results. All models used the same friction property, as the friction between the concrete core and steel shell depends on the interface, not on the steel shell thickness. The model at a D/t ratio of 128 resulted in axial force-axial compression

displacement curves that provided a reasonable envelope to the experimental result. However, at lower D/t ratios of 94 and 46, the models over-predicted the response. If the friction coefficients were decreased for these two D/t ratios then a closer match would be obtained. This shows the friction in the model to either have dependence on the D/t ratio or on the mesh size used. In the experimental results the friction bond was not found to have a dependence on the D/t ratio, so the mesh size is the more likely reason for this discrepancy.

The stress distributions obtained for all models were highly non uniform, with high stress concentration regions. A stress distribution with clear and uniform radial stress contours in the steel shell, mechanism, and concrete core is expected. However, this was not obtained due the compromise that had to be made in the mesh size to allow for results to be generated.

# 11 REFERENCES


ABAQUS User's Manual (2005), Version 6.5.1, ABAQUS Inc.

American Concrete Institute Committee 223, "Standard Practice for the Use of Shrinkage-Compensating Concrete," Manual of Concrete Practice, Part 1, ACI 223-98, 2005.

American Petroleum Institute, "Recommended Practice for
Planning, Designing, and Constructing Fixed Offshore Platforms-Working Stress Design." API Recommended Practice 2A (RP 2A), 2002.

American Petroleum Institute, "Recommended Practice for
Planning, Designing, and Constructing Fixed Offshore Platforms-Load and Resistance Factor Design." API Recommended Practice 2A-LRFD (RP 2A-LRFD), 1993.

ASTM C 39, "Standard Test Method for Compressive Strength of Cylindrical Concrete Specimens," Annual Book of ASTM Standards, Vol. 4.02, ASTM International, 2004a.

ASTM A 370-03a, "Standard Test Methods and Definitions for Mechanical Testing of Steel Products," Annual Book of ASTM Standards, Vol. 1.03, ASTM International, 2004b.

Billington, C.J.; Lewis, G.H.G., "The Strength of Large Diameter Grouted Connections," Offshore Technology Conference, Paper OTC 3083, 1978, No. 1, pages 291-301, Houston, Texas.

Billington, C.J.; Tebbett, I.E., "The Basis for New Design Formulae for Grouted Jacket to Pile Connections," Offshore Technology Conference, Paper OTC 3788, 1980, No. 2, pages 449-458, Houston, Texas.

Cheng, Lijuan, "Development of a Steel-Free FRP-Concrete-Slab-on-Girder Modular Bridge System," Ph.D. Dissertation, University of California, San Diego, La Jolla, Calif., 2005.

Craig, Roy, Mechanics of Materials, John Wiley & Sons, 1996.

Day, Kevin, Concrete Mix Design, Quality Control and Specification, Second Edition, E & FN Spon, London, 1999.

Gebman, M.; Ashford, S.; Restrepo, J., Investigation of the Axial Load Transfer Mechanism in Cast-In-Steel-Shell Piles, *Test Research Report* No. TRR-04/02, Department of Structural Engineering, University of California-San Diego, La Jolla, Calif., May 2004, pp. 1-72.

Gebman, M.; Ashford, S.; Restrepo, J., Investigation of the Axial Load Transfer through Shear Rings in Cast-In-Steel-Shell Piles, *Test Research Report* No. TRR-05/02, Department of Structural Engineering, University of California-San Diego, La Jolla, Calif., March 2005, pp. 1-71.

Ichinose, L.H.; Watanabe, E.; Nakai, H., "An Experimental Study on Creep of Concrete Filled Steel Pipes," Journal of Constructional Steel Research, V. 57, 2001, pp. 453-466.

Karsan, D.I.; Krahl, N.W., "New API Equation for Grouted Pile to Sleeve Connections," Offshore Technology Conference, Paper OTC 4715, 1984, No. 2, pages 49-56, Houston, Texas.

Kupfer, H.; Hilsdorf, H.; Rusch, H., "Behavior of Concrete under Biaxial Stress," ACI Journal, Proceedings, Vol. 66, No. 8, August 1969, pp. 656-666.

Lewis, Gael; Livett, Ian; Mead, Kevin, "Cost Saving Design for Pile to Structure Connections as Applied to BP Magnus," Offshore Technology Conference, Paper OTC 3789, 1980, No. 2, pages 459-466, Houston, Texas.

Loset, Oystein, "Grouted Connections in Steel Platforms-Testing and Design," Offshore Structures: the use of Physical Models in their Design, Editors: Armer, G.S.T; Garas, F.K., Lancaster, England, 1981, Based on Proceedings from of an international seminar held at the UK Building Research Station by the Institution of Structural Engineers' Informal Study Group for 'Model Analysis as a Design Tool'"

Richards, Paul, "Cyclic Stability and Capacity Design of Steel Eccentrically Braced Frames," Ph.D. Dissertation, University of California, San Diego, La Jolla, Calif., 2004.

Richart, F.E.; Brandtzaeg, A.; Brown, R. L., "A Study of the Failure of Concrete Under Combined Compressive Stresses," Bulletin No. 185, Engineering Experiment Station, University of Illinois, Urbana, 1928.

Roeder, C. W.; Cameron, B.; Brown, C. B., "Composite Action in Concrete Filled Tubes," Journal of Structural Engineering, V. 125, No. 5, May 1999, pp. 477-484.

Sato, M.; Kato, C.; Miyoshi, H., "Mechanical Characteristics of Concrete-Filled Steel Pipes with Checkered Projections," Transactions of the Japan Concrete Institute, V. 3, 1981, pp. 431-438.

Tomii, M.; Yoshimura, K.; Morishita, Y., "A Method of Improving Bond Strength Between Steel Tube and Concrete Core Cast in Circular Steel Tubular Columns," Transactions of the Japan Concrete Institute, V. 2, 1980, pp. 319-326.

United Kingdom Department of Energy, "Offshore Installations, Guidance on Design Construction and Certification," Amendment No. 4, April 1982.

Virdi, K.W.; Woo, Y.S.; Schmidt, L.C.; Stevens, L.K., “Tests on Pushout Specimens with Cavaties at the Base of the Connector (Note 1),” AWRA Report P6-30-80, Vol. 10, Nov, 1981, pages 51-54.

Virdi, K. S.; Dowling, P.J., “Hollow Core Concrete Steel Tubular Columns,” Third International Colloquium Proceedings, Stability of Metal Structures, George Winter Memorial Session, 1983, pages 529-541

Yamasaki, Tokuya; Hara, Michihiko; Takahashi, Chiyomaru, “Static and Dynamic Tests on Cement-Grouted Pipe-To-Pipe Connections,” Offshore Technology Conference, Paper OTC 3790, 1980, No. 2, pages 467-476, Houston, Texas.